The Development of a Novel Silicon Microdosimeter for High LET Radiation Therapy

A thesis submitted in fulfilment of the requirements for the award of the degree

Doctor of Philosophy

from

University of Wollongong

by

Peter D. Bradley,

B.E. (Elec., 1st class honours, UNSW)

M.E. (Biomed. Eng., UNSW)

Grad. Dip. (Biomed. Eng., UNSW)

Department of Engineering Physics

2000

Certificate of Originality

I hereby declare that this submission is my own work and that, to the best of my knowledge and belief, it contains no material previously published or written by another person nor material which to a substantial extent has been accepted for the award of any other degree or diploma of a university or other institute of higher learning except where due acknowledgment is made in the text.

I also declare that the intellectual content of this thesis is the product of my own work, even though I may have received assistance from others on style, presentation and language expression.

(Signed).....

Acknowledgments

My thesis supervisor, Associate Professor Dr. Anatoly Rosenfeld was tireless in his support of this project. His motivation and flair for establishing international collaborations and finding a way to finance such ventures is impressive and added greatly to the content of this work. Many thanks are owed for his intellectual direction and encouragement. My appreciation is also extended to the following people for the use of their facilities and generous time and effort:

- John Burke and Peter Ihnat, *Department of Engineering Physics, University of Wollongong, Wollongong, Australia*: for superb skills in machining probe assemblies and PCB construction.
- Shigeo Satoh, *Fujitsu Laboratories Ltd., Atsugi, Japan*: for generous supply of prototype silicon microdosimeters.
- Assoc. Prof. Dr. Gernot Heiser: *Department of Computer Science and Engineering, University of New South Wales, Sydney, Australia*: for the use of computing resources and advice on semiconductor simulation tool DESSIS.
- Kin Kiong Lee, Assoc. Prof. Dr. David Jamieson, *Microanalytical Research Centre, Department of Physics, University of Melbourne, Melbourne, Australia*: for assistance and use of alpha and proton microbeam imaging.
- Prof. Dr. Richard Maughan, Dr. Chandrasekhar Kota, Jay Burmiester and Mark Yudelev, *Gershenson Radiation Oncology Center, Harper Hospital, Detroit, USA*: for assistance and use of the superconducting cyclotron, fast neutron therapy facility.
- Assoc. Prof. Dr. Tooru Kobayashi and Dr. Yoshinori Sakurai; *Kyoto University Research Reactor, Japan*: for assistance and use of the medical research reactor.
- Dr. Jeffrey Coderre Dr. Jacek Capala and staff at BMRR, *Medical Research Reactor, Brookhaven National Laboratory, Long Island, NY, USA*: for assistance and use of the medical research reactor.

- Assoc. Prof. Dr. Jacquelyn Yanch, *Department of Nuclear Engineering, Massachusetts Institute of Technology, Boston, USA*: for assistance and use of the BNCT tandem accelerator.

- Dr. Jay Flanz, Dr. Michael Goitein, Dr. Adrian. Van Meerbeeck, Dr. Jeff Schubert, Jim Bailey, J. Burns and R.M. Cataldo, *Harvard/ Northeastern Proton Therapy Centre, Massachusetts General Hospital, Boston, USA*: for assistance and use of the proton therapy facility.

- Dr. Y. Takada, Dr. A. Maruhashi, Dr. Y. Hayakawa, and Y. Kohno, *Proton Medical Research Center, University of Tsukuba, Tsukuba, Ibaraki, Japan*: for assistance and use of the proton therapy facility.

- Dr. Francois Lemeilleur, *CERN, Geneva, Switzerland*: for radiation hardness testing using the proton synchrotron.

- Prof. Dr. Barry Allen, *St George Hospital Cancer Care Center, Sydney, Australia*: for organization of experimental radiation oncology group meetings and discussions.

- Dr Dimitri Alexeiv, *Australian Nuclear Science and Technology Organisation, Sydney, Australia*: for assistance and use of tandem accelerator and current-voltage and capacitance-voltage measurement equipment.

- Iwan Cornelius, Greg Kaplan, Mark Reinhard and Michael Bailey, *Radiation Physics Group, Department of Engineering Physics, University of Wollongong, Wollongong, Australia*: for assistance with spectroscopy measurements.

- Dr. James Ziegler, *IBM*: for latest copy of SRIM software.

- Dr Mike Oldfield, *University of Surrey, Surrey, UK*.: for latest copy of PRISM software.

Finally, I would especially like to thank my wife Maria Bradley for her love and support and both our parents Campbell and Irene Bradley and Helen and Stan Kastrissios for their support and encouragement throughout my studies.

Abstract

This work is the first comprehensive investigation of the issues confronting silicon microdosimetry and its application to radiotherapy. Four main problems requiring investigation are identified and addressed including requirement specification with particular emphasis on device shape, tissue equivalence, noise minimization, and sensitive volume definition.

Analysis of device shape showed that a rectangular parallelepiped with a tissue equivalent converter on top of device (i.e. a silicon microdosimeter) provides a lineal energy spectrum that is closely equivalent to a sphere using the criteria of equal dose mean lineal energy. The tissue equivalent study demonstrated that under appropriate geometrical scaling (dimensions multiplied by 1/0.63) silicon detectors with well known geometry will record energy deposition spectra representative of tissue cells of equivalent shape. A novel prototype device using silicon-on-insulator (SOI) is presented. Silicon-on-insulator technology assists in defining the sensitive volume depth although the current device still suffers from lateral diffusion effects. I-V and C-V testing are performed and a noise optimization design model is presented. Methods for characterizing the collection efficiency and radiation hardness of silicon microdosimeters are presented and compared including alpha and proton microbeam spectroscopy, broadbeam alpha spectroscopy and 2D and 3D device simulation.

Results from testing the low noise prototype SOI device at several high LET clinical facilities including BNCT, proton therapy and fast neutron therapy facilities are presented. In the BNCT experiments, a simultaneous thermal neutron flux and microdosimetric measurement at a high spatial resolution is demonstrated. The use of SOI technology in experimental microdosimetry offers simplicity (no gas system or HV supply), high spatial resolution, low cost, high count rate capability and the possibility of integrating the system onto a single device with other detector types. The device also offers applicability in radiation protection and electronic single event upset (SEU) studies.

Table of Contents

1. INTRODUCTION 1

1.1 Background 1

1.2 Thesis Outline 3

2. LITERATURE REVIEW AND BACKGROUND 5

2.1 Historical Foundations 5

2.2 Basic Principles and Microdosimetric Quantities 7

2.3 Experimental Methods in Regional Microdosimetry 10

2.3.1 Proportional Counter Microdosimetry 11

2.3.1.1 Basic Principles of Proportional Counters 11

2.3.1.2 Performance of Proportional Counters: Uncertainties and Limitations 14

2.3.2 Semiconductor (Silicon) Microdosimetry 21

2.3.2.1 Basic Principles of Semiconductor Detectors 21

2.3.2.2 Performance of Silicon Microdosimeter 25

2.3.2.3 Review of Semiconductors in Microdosimetry 27

2.3.3 Other methods 33

2.3.3.1 Microstrip Gas Counters (MSGC) 33

2.3.3.2 Cloud Chambers 33

2.3.3.3 Optical Ionization Chamber 34

2.3.3.4 Autoradiography 34

2.3.3.5 Three Dimensional Optical Random Access Memories (3D ORAM) 34

2.3.4 Summary of Experimental Microdosimetry Methods 35

2.4 Applications of Experimental Microdosimetry 39

2.4.1 Radiobiology 39

2.4.2 Radiotherapy Applications 42

2.4.3 Radiation Protection Applications 45

2.4.4 Space applications and Radiation Effects on Microelectronics 46

2.5 Summary: Key Problems in Silicon Microdosimetry 47

3. SILICON MICRODOSIMETER REQUIREMENTS AND SHAPE ANALYSIS 49

3.1 Intended Applications 49

3.2 Sources of Fluctuations in Regional Microdosimetry 50

3.3 Detector Shape Considerations 53

3.3.1 Comparison of Chord Length Distributions 54

3.3.2 Comparison of Segment Length Distributions and finite range effects 60

3.3.2.1 Segment length distributions for RPP, cube and sphere under μ-randomness 60

3.3.2.2 Segment length distributions for infinite slab with converter overlayer 65

3.3.2.3 Segment length distributions for RPP with converter and overlayer 68

3.3.3 Equivalence of Shapes using Mean Energy per Event (ε_d) 69

3.3.3.1 Equivalence under μ-randomness 70

3.3.3.2 Equivalence under nonisotropic conditions and c-randomness 74

3.3.4 Equivalence of Shapes using Frequency Mean Energy per Event (ε_f) 77

3.3.5 Equivalent Lineal Energy Spectra and Straggling 79

3.3.6 Summary: Criteria for the Equivalence of Various Shapes in Microdosimetry 84

3.4 Combining Criteria for Shape Equivalence and Tissue Equivalence 85

3.5 Summary of Requirements 86

3.5.1 Geometrical Requirements and Considerations 86
3.5.2 Operational Requirements and Considerations 89

4. SILICON MICRODOSIMETER DESIGN AND NOISE ANALYSIS 91

4.1 Detector Description 92

4.2 Basic Electrical Characterization and Testing 95
4.2.1 Current-Voltage Measurements 95
4.2.2 Capacitance-Voltage Measurements 97

4.3 Probe Assembly #1 102

4.4 Probe Assembly #2 104

4.5 Design Equations, Noise Modeling and Optimization 106
4.5.1 Basic Design Equations and Noise Model 106
4.5.2 Optimization of Shaping Time 110
4.5.3 Optimization of Detector Voltage 111
4.5.4 Selection of Key Components and Parameters 114
4.5.5 Comparison with Device Performance 116
4.5.6 Ultimate Noise Performance 117

5. TISSUE EQUIVALENCE CORRECTION FOR SILICON MICRODOSIMETERS 120

5.1 Definition of Tissue and Detector Materials 121

5.2 Microdosimetry TE Correction Factor 123

5.3 Summary of Conditions for Tissue Equivalence 126

5.4 Boron Neutron Capture Therapy Tissue Equivalence 127
5.4.1 Comparison of Silicon and Tissue BNCT Range-Energy Relationships 127
5.4.2 Comparison of Silicon and Tissue BNCT Energy Deposition Spectra 133
5.4.2.1 Method: Monte Carlo Program 133
5.4.2.2 Results: Geometry Case 1 - Ion generation in RPP volumes with SV=GV 137
5.4.2.3 Results: Geometry Case 2-Ion generation above RPP volume 137

5.5 Fast Neutron Therapy and Proton Therapy Tissue Equivalence 138
5.5.1 Geometrical TE scaling factor for FNT and PT 138
5.5.2 Effect of converter atomic composition in FNT 143
5.5.3 Silicon versus tissue interactions in FNT and PT and range of secondary products. 146

5.6 Summary of Tissue Equivalence Study 153

6. CHARGE COLLECTION MODELING: SENSITIVE VOLUME AND RADIATION HARDNESS CHARACTERIZATION 154

6.1 Charge Collection Physics 155
6.1.1 Motion of Carriers 155
6.1.1.1 Carrier Drift 155
6.1.1.2 Carrier Diffusion 157
6.1.1.3 Recombination 157
6.1.1.4 Combined Model (Continuity and Poisson Equation) 162
6.1.2 Ion Interaction: Generation of Carriers 163
6.1.3 Ion Interaction: Motion of Carriers 165
6.1.4 Induced Currents by Carrier Motion (Ramos theorem) 172

6.2 Sensitive Volume Characterization 173
6.2.1 Spectroscopy Modeling Software 173
6.2.2 Numerical device simulation 177
6.2.2.1 Simulation Setup and Parameters 177
6.2.2.2 Collection Efficiency Simulations 181

6.2.2.3 Comparison of alpha and proton funneling in the 100×100 μm^2 bulk diode. 190
6.2.2.4 Simulation of angled BNCT alpha generated strike 194
6.2.3 Microbeam Spectroscopy 196
6.2.3.1 Collection efficiency derived from complete spectroscopy model 197
6.2.3.2 Collection efficiency derived from microbeam image 198
6.2.4 Broadbeam Spectroscopy 201
6.2.4.1 Results for 10×10 μm^2 , 2 μm SOI, undamaged and radiation damaged 202
6.2.4.2 Results for 10×10 μm^2 , 10 μm SOI, undamaged device 204

6.3 Radiation Hardness Characterization 205
6.3.1 Basic Radiation Damage Physics 205
6.3.2 Minority Carrier Lifetime Estimation 207
6.3.3 Damage Constant 213

6.4 Summary of Charge Collection Modeling 215
6.4.1 Collection Efficiency and Radiation Damage Summary 215
6.4.2 Implications for Mean Chord Length Estimation 217

7. APPLICATION TO BORON NEUTRON CAPTURE THERAPY 220

7.1 Background to BNCT 220

7.2 Thermal Neutron Sensitivity of Microdosimeter Construction 223

7.3 Experiments at Brookhaven National Laboratory (*Boron and U-235 Coating Investigation*) 227
7.3.1 Materials and Methods 227
7.3.1.1 Description of Brookhaven Medical Research Reactor(BMRR) 227
7.3.1.2 Description of probe assembly and device coating (B-10 and U-235) 228
7.3.1.3 Description of phantom 229
7.3.1.4 Microdosimetric measurements 229
7.3.1.5 Simulation of microdosimetric measurements and MCL estimation 229
7.3.2 Experimental Results and Discussion 232
7.3.2.1 Evaluation of boron coating methods 232
7.3.2.2 Evaluation of device orientation effects 235
7.3.2.3 Measurement using U-235 coated diode array 235
7.3.2.4 Comparison with Simulation 236
7.3.2.5 Comparison with Proportional Counter Microdosimetric Measurements 237

7.4 Experiments at Kyoto University Research Reactor (*Simultaneous microdosimetry and thermal neutron flux measurements*) 238
7.4.1 Materials and Methods 238
7.4.1.1 Description of Kyoto University Research Reactor (KUR) 238
7.4.1.2 Description of probe assembly and phantom 241
7.4.1.3 Microdosimetric measurements 242
7.4.1.4 Simulation of microdosimetric measurements and MCL estimation 242
7.4.2 Experimental Results and Discussion 246
7.4.2.1 Comparison BNL and KUR microdosimetric spectrum 246
7.4.2.2 Simulation (ion implanted boron and nitrogen in air) 247
7.4.2.3 Thermal neutron flux depth profile 252
7.4.2.4 Microdosimetric comparison of irradiation modes 254
7.4.2.5 Comparison sensitive volume depth variation (2 and 5 μm SOI) 256

7.5 Experiments at Massachusetts Institute of Technology (*Epithermal Neutron Beam Investigation*) 257
7.5.1 Materials and Methods 257
7.5.1.1 Description of facility 257
7.5.1.2 Microdosimetric setup and measurements 257
7.5.2 Experimental Results and Discussion 258

7.6 Summary of BNCT Applications 259

8. APPLICATION TO FAST NEUTRON THERAPY 262

8.1 Background to Fast Neutron Therapy 262

8.2 Materials and Methods 264
8.2.1 Description of fast neutron beam at Harper Hospital, Detroit. 264
8.2.2 Description of probe assembly and phantom 264
8.2.3 Microdosimetric measurements 267

8.3 Experimental Results and Discussion 268
8.3.1 Comparison of 2 μm and 10 μm SOI devices with the proportional gas counter. 268
8.3.2 Microdosimetric characterization of neutron beam using silicon microdosimeter 273
8.3.3 Tissue equivalence issues using a silicon microdosimeter in fast neutron beams 277

8.4 Summary of FNT Applications 278

9. APPLICATION TO PROTON THERAPY 281

9.1 Background to Proton Therapy 281

9.2 Experiment at PMRC-Tsukuba 283
9.2.1 Materials and Methods 284
9.2.1.1 Proton Therapy Facility at PMRC-Tsukuba 284
9.2.1.2 Experimental Setup at PMRC-Tsukuba 284
9.2.2 Results: Microdosimetric Spectra at PMRC-Tsukuba 285

9.3 Experiment at NPTC-Boston 288
9.3.1 Materials and Methods 288
9.3.1.1 Proton Therapy Facility at NPTC-Boston 288
9.3.1.2 Experimental Setup at NPTC-Boston 288
9.3.1.3 Simulation using SRIM and PRISM 290
9.3.2 Results 293
9.3.2.1 Microdosimetric Spectra at NPTC-Boston 293
9.3.2.2 Comparison with Simulation 294

9.4 Summary of Proton Therapy Applications 298

10. CONCLUSIONS AND FUTURE RECOMMENDATIONS 299

10.1 Key Findings 299

10.2 Future Recommendations and Proposed Design Outline 307

11. REFERENCES 310

APPENDICES 323

Appendix A: Prototype Fujitsu Silicon Microdosimeter, Packaging and Processing 323
A.1. Device Packaging 323
A.2. Device Processing 324

Appendix B: *Mathematica* Notebook - Analytical and Monte-Carlo Calculations of Chord and Segment Length Distributions in Various Shapes 332

Appendix C: Low Noise Microdosimeter Probe Design (Prototype #2) 333

List of Figures

Figure 2.1. Example Single Event Microdosimetric Distributions 8
Figure 2.2. Standard Representation of Microdosimetric Spectrums 10
Figure 2.3. Diagrams of the four types of wall effect in low pressure proportional counters 15
Figure 2.4. Setup required for experimental microdosimetry. With a proportional counter the gas system and high voltage supply are used. For a semiconductor microdosimeter detector the supply may often be low voltage and the gas system is not required. (LLD = lower level discriminator, ADC = Analog to Digital converter) 19
Figure 2.5. A schematic diagram of an abrupt p-n junction including the space charge density, electric field intensity, electrostatic potential and band diagram. The familiar band diagram (showing Fermi energy E_F, conduction E_C and valence bands E_V) may be thought of as the electron potential barrier. The left side shows plots for thermal equilibrium conditions with no bias voltage applied whilst the right hand side shows the same plots for a bias voltage of 10 V. The values selected to construct these graphs correspond to the silicon microdosimeter prototype (p doping Na=1.5 $\times$ 10^{15}/cm^3, n doping Nd=2 $\times$ 10^{20}/cm^3, effective density of states in valence band N_V =1.04 $\times$ 10^{19}/cm^3, effective density of states in conduction band N_C =2.8 $\times$ 10^{19}/cm^3, T = 300 K). 23
Figure 2.6. Resolution of proportional counter and silicon microdosimeter as a function of energy deposited for several preamplifier noise levels. Calculated using equations (2.20) and (2.29) with g=10^4 ,M=0.6, F=0.3,W=30 eV, R_{rest}=0 (TEPC), F=0.3, W=3.62 eV (Si microdosimeter) Also shown is the minimum energy measurable (E_m lower noise cutoff from equations (2.14) and (2.26)). The E_m for the proportional counter is not shown since it is very low (single ionization). 37
Figure 2.7. Quality factor $Q(L)$ as defined by ICRP publication 60 [53]. 45
Figure 3.1. Definition of rays interacting with a sensitive volume 49
Figure 3.2. Comparison of CLD under μ-randomness for a sphere, hemisphere and spheroid. $\bar{l}$ =2/3 in all cases. 57
Figure 3.3. Comparison of CLD under μ-randomness for a sphere various cylinders. $\bar{l}$ =2/3 in all cases. Numerical integration errors create small spikes in the cylinder CLDs. 57
Figure 3.4. Comparison of CLD under μ-randomness for a sphere, infinite slab and RPP. $\bar{l}$ =2/3 in all cases. 57
Figure 3.5. Comparison of CLD under μ-randomness for a cube, cylinder and oblate cylinder and oblate RPP. $\bar{l}$ =2/3 in all cases 58
Figure 3.6. Comparison of CLD under μ-randomness for a hemisphere and oblate spheroid. Volume is the same in both cases (0.88). $\bar{l}$ =0.66 for hemisphere and 0.72 for spheroid. 58
Figure 3.7. Hemisphere (r=0.75) and oblate spheroid (d=1.5,e=0.5) with CLDs shown in previous figure. These shapes provide identical CLDs for unidirectional radiation along the x-axis 58
Figure 3.8. Relative variance V_t of the chord length distribution as a function of elongation for oblate shapes 59
Figure 3.9. Effect of varying range (u) on segment length distribution for a sphere (r=1) 61
Figure 3.10. Effect of varying range (u) on segment length distribution for a RPP (a=b=1.33,h=0.66) 62
Figure 3.11. Relative variance of the segment length distribution as a function of particle fixed range for a sphere and cube 62
Figure 3.12. Fraction of crossers as a function of range for three different shapes with the same MCL 64
Figure 3.13. Fraction of stoppers+starters as a function of range for three different shapes with the same MCL 64
Figure 3.14. Fraction of stoppers+crossers as a function of range for three different shapes with the same MCL 64
Figure 3.15. Ratio of Range/MCL required for the given fraction of crossers or crossers and stoppers. This function applies for any convex shape. 65

Figure 3.16. Geometry of RPP detector with overlayer (thickness = a) and converter (thickness = h). Infinite slab case has the same cross section with the RPP having infinite length and width. 65
Figure 3.17. Segment length as a function of angle q for the infinite slab and overlayer/converter geometry. Examples given use R=5, h=1, and x=2 (Case 1) and x=4.25 (Case 2). In Region A, $s>h$ and two values of q correspond to each s value whilst for region B, $s£h$ and the inverse is unique. 67
Figure 3.18. Segment length distributions for an infinite slab under c-randomness. Various overlayer thickness (a) and particle range (R) configurations are compared. 68
Figure 3.19. Segment length distributions for a unit side length cube under c-randomness for two different overlayer thickness, a. The range R is 10. SLDs calculated assuming μ-randomness are shown for comparison....69
Figure 3.20. Height h and width d of the RPPs that have the same mean energy deposited as the unit diameter sphere (see also Table 3.6). For the specified elongations these RPPs are most closely equivalent to the unit diameter sphere 72
Figure 3.21. The geometric reduction factor $U(x)$ for the unit diameter sphere and for equivalent cylinder, cube and RPP. The largest difference occurs for the elongation that is not unity 73
Figure 3.22. Variation of mean energy deposited per event with particle range. The cube closely approximates a sphere for all ranges. The dimensions of each object were selected to obtain equivalent $\bar{e}_d$ assuming an infinite range. The LET L is assumed equal to 1. 74
Figure 3.23. Variation of mean energy deposited per event with particle range for isotropic and unidirectional beams. The unidirectional beam is normal to a cube face. The LET L is assumed equal to 1. (See also Figure 3.22)....75
Figure 3.24. Comparison of mean energy deposited per event with particle range for a unit diameter sphere and infinite slab. The infinite slab has a height of 0.176 (calculated to give equivalence at range = 100) and is exposed to a radiation field isotropically emitted from a converter 0.5 units above the slab. The LET L is assumed equal to 1. 76
Figure 3.25. Comparison of mean energy deposited per event with particle range for a unit diameter sphere and cube with various overlayers/converters. The sphere and cube lines are calculated under the condition of μ-randomness whilst the cube points for various overlayers are calculated using Monte-Carlo methods assuming c-randomness. 10000 segments were used in the Monte-Carlo calculation. The LET L is assumed equal to 1. 77
Figure 3.26. Comparison of chord length distribution under μ-randomness for a sphere, cube and cylinder with dimensions selected so that the $\bar{e}_d$ = 0.75 assuming an LET of 1. 82
Figure 3.27. Lineal energy spectra $f(y)$ under μ-randomness for equivalent sphere, cube and cylinder with straggling. LET assumed to be 100 keV/μm. Straggling standard deviation of 10keV/μm. 82
Figure 3.28. Lineal energy spectra $yd(y)$ under μ-randomness for equivalent sphere, cube and cylinder with straggling (10keV/um). LET assumed to be 100 keV/μm. See also Figure 3.27. 83
Figure 3.29. Lineal energy spectra $yd(y)$ under μ-randomness with a finite range = 5 μm. For range values approaching the shape dimensions the equivalence criteria is stricter. LET assumed to be 100 keV/μm. Straggling standard deviation of 10keV/μm. See also Figure 3.28....83
Figure 3.30. Comparison of lineal energy spectra $yd(y)$ for a cube (side length=0.837μm) and sphere (d=1μm) under μ-randomness and c-randomness with a particle range of 10 μm. Spectra calculated for two different overlayer thickness (a) are shown indicating that for the particle range selected the dose lineal energy is not significantly affected. LET assumed to be 100 keV/μm....83
Figure 4.1. Array sizes and overall layout of the prototype silicon microdosimeter....93
Figure 4.2: Basic SOI diode array structure 93
Figure 4.3. Scanning Electron Micrograph (SEM) photograph of a portion of the 10×10 μm diode array. (Note: Raised sections are aluminum tracks connecting contacts so that all diodes are electrically in parallel. The width of the photo is about 23μm.)....94
Figure 4.4. SEM of the prototype silicon microdosimeter. The 100×100 μm^2 arrays are at the top whilst the 10×10 μm^2 arrays are at bottom. The dark areas are due to charging effects

from previous high magnification images. The darker spot in array A4 (lower right array) corresponds to the location of Figure 4.3 image. 94
Figure 4.5. Example of the forward and reverse bias I-V characteristics for 2 μm SOI array A4. Only those components that passed the I-V tests are displayed with specific part numbers in the legend....96
Figure 4.6. Depletion width versus reverse bias voltage ($N_B = 1.5 \times 10^{15}$cm^{-3} and $V_{bi} = 0.74$)....98
Figure 4.7. Plot of $1/C_j^2$ versus reverse bias where C_j = detector capacitance per unit junction area. The 2 μm SOI is influenced by the insulating layer at the bias levels presented....99
Figure 4.8. Plot of $1/C_j^2$ versus reverse bias where C_j = detector capacitance per unit junction area. Arrays for a bulk device are compared....99
Figure 4.9. Plot of $1/C_{jc}^2$ versus reverse bias where C_{jc} = corrected detector capacitance per unit junction area. Arrays for a bulk device are compared. See also Figure 4.8. 99
Figure 4.10: Experimental setup for microdosimetry measurements using probe assembly #1 (original assembly)....103
Figure 4.11: Experimental setup for microdosimetry measurements using probe assembly #2 (low noise)....105
Figure 4.12. Probe assembly #2: PCB mounted electronics showing Fujitsu prototype microdosimeter, preamplifier and buffer amplifier. The board inserts into an aluminium box with the remaining air gaps filled by Lucite blocks. 106
Figure 4.13. Noise model of microdosimeter and charge sensitive pre-amplifier 108
Figure 4.14. ENC versus shaping time. Vb=10 V, All parameters as per Table 4.6. FET channel noise (series noise) dominates for large τ whilst bias current and resistor thermal noise dominates for small τ. The optimum occurs when these components are equal. 111
Figure 4.15. ENC versus detector bias supply voltage for each value of available shaping time. The absolute minimum ENC is also shown. In this case τ is free to vary to the optimal value (Optimal τ is large for small voltages and decreasing to smaller τ at larger voltages). 113
Figure 4.16. Optimal ENC versus voltage (top) and the corresponding shaping time (bottom) required to obtain the optimal ENC. Various values of detector resistance relative to the nominal 2×10^9 ohms are shown. At higher detector resistance values the detector current shot noise is reduced....113
Figure 4.17. Pulsar noise measurements performed on device #7, 10 μm SOI for two shaping time settings. The spectra were shifted to a peak at 0 eV. Acquisition time was 5 minutes. FWHM is 5.1 keV for τ=2 μs and 6.2 keV for τ=0.5 μs. 117
Figure 5.1. Comparison of BNCT ion product ranges in tissue and silicon. The silicon RPP dimensions have been scaled by 0.63 times the tissue dimensions. Note that the figure on the left (silicon) is an exact scale miniaturization of the figure on the right (tissue). These volumes will have equivalent microdosimetric spectra assuming equal concentrations of nitrogen and boron. 130
Figure 5.2. Range-Energy relationships for BNCT products (H, He, Li and C) in ICRU muscle and Silicon. The right-hand side shows the same plot as the left except for the silicon range scaled by 1/0.63. In addition, the plots display original SRIM generated data points used for the 5th order polynomial fit. 131
Figure 5.3. LET versus energy (left) and LET versus range(right) for BNCT Products (H, He, Li and C) in ICRU muscle and Silicon. The maximum range is plotted only up to the corresponding maximum energy. 132
Figure 5.4. Comparison of analytic and Monte Carlo generated segment length distribution (P(s)) for an RPP volume $3.5 \times 3 \times 2.5$ μm enclosed in a uniform isotropic field of 7 μm length rays. 134
Figure 5.5. Geometry Case 1 - SV and GV are identical in size and position....135
Figure 5.6. Geometry Case 1 (Example 1): Energy Deposition Spectra comparison of Silicon ($3.15 \times 3.15 \times 3.15$ μm) and Tissue ($5 \times 5 \times 5$μm). 135
Figure 5.7. Geometry Case 1 (Example 2): Energy Deposition Spectra comparison of Silicon ($5 \times 5 \times 5$ μm) and Tissue ($7.9 \times 7.9 \times 7.9$ μm). 135
Figure 5.8. Geometry Case 2 - GV is a large tissue volume above a much smaller silicon/tissue SV 136
Figure 5.9. Geometry Case 2 (Example 1): Energy Deposition Spectra comparison of Silicon ($3.15 \times 3.15 \times 3.15$ μm) and Tissue ($5 \times 5 \times 5$μm). 136
Figure 5.10. Geometry Case 2 (Example 2): Energy Deposition Spectra comparison of Silicon ($5 \times 5 \times 5$ μm) and Tissue ($7.9 \times 7.9 \times 7.9$ μm). 136

Figure 5.11. Initial spectrum of charged particles for a neutron fluence of 1 cm^{-2} of 14 MeV neutrons in ICRU tissue (from Caswell and Coyne [125] and ICRU report 36 p39 [11]). The symbols p, d and α refer to recoil protons, deuterons and alpha particles, respectively,.....139
Figure 5.12. Ratio of tissue range over silicon range as a function of ion energy for main ions in Neutron and Proton Therapy.....140
Figure 5.13. Range-Energy relationships for fast protons in ICRU muscle and Silicon. The right-hand side shows the same plot as the left except for the silicon range scaled by 1/0.63.....140
Figure 5.14. Range-Energy relationships for the main reaction products of fast neutron beams (H, He, C and O) in ICRU muscle and Silicon. The right-hand side shows the same plot as the left except for the silicon range scaled by 1/0.63.....141
Figure 5.15. LET versus energy (left) and LET versus range (right) for Fast Neutron Therapy Products (H, He, C and O) in ICRU muscle and Silicon. The maximum range is plotted only up to the corresponding maximum energy.....142
Figure 5.16. Comparison of analytic calculations of *yd(y)* of 20 MeV neutrons performed for ICRU tissue and for A150 plastic. (from Caswell and Coyne [190] and ICRU report 36 p42 [11]) 143
Figure 5.17. Relative contribution from interaction processes with different elements to kerma in muscle (skeletal) over the neutron energy interval 10 keV-30 MeV. (From p9 ICRU report 44 [32]).....144
Figure 5.18. Kerma Ratio of A150 and Acrylic to Muscle (Skeletal, ICRU 1989) as a function of neutron energy. The right hand side plot has both kerma ratios normalized to 1 at 0.01 MeV (see text for explanation). The left hand side is unnormalized.....145
Figure 5.19. Kerma Ratio of Silicon to Muscle (Skeletal, ICRU 1989) as a function of neutron energy 147
Figure 5.20. Dose distributions *d(y)k* for A150, Si, Al and SiO_2 at neutron energies of 5, 8, 15, 17, 34, 44 and 66 MeV (from Schrewe [37]). Note, to improve presentation, fixed offsets were added. In addition, take care to consider the different scale for the A150 plot.....148
Figure 5.21. Monte Carlo calculations of *yd(y)* of 5.85 MeV neutrons in TE A150 plastic and methane based TE gas (1 μm simulated diameter). Contributions of stoppers, starters, and crossers to the total. The contributions of insiders is insignificantly small. (from p42 ICR report 36 [11] and Fidorra and Booz [106].....151
Figure 5.22. Total (elastic+inelastic) cross section for neutrons interacting with silicon (left side) and hydrogen, carbon and oxygen (right side). Si data is from Evaluated Neutron Data File, ENDF/B-VI library (>10MeV) and JENDL-3(300K) library (<10MeV). H,C and O data is from ENDF/B-VI library [193]. 152
Figure 5.23. Inelastic (nuclear reaction) cross-section for neutrons interacting with silicon, carbon and oxygen. Data is from ENDF/B-VI library. [193]. Note that hydrogen, of course, does not undergo inelastic reactions.....152
Figure 5.24. Ratio of probability of interaction between silicon and muscle as a function of neutron energy. Left side is for all interactions (elastic+inelastic); right side is for inelastic reactions only.....153
Figure 6.1. Recombination mechanisms: (a) Shockley-Read-Hall, (b) Direct Radiative, (c) Direct Auger (d) Trap-Assisted Auger.....158
Figure 6.2. Plot of energy density profile as a function of radial distance from the center of an alpha and proton ion track based on Fageeha's implementation of Katz's model [211].....165
Figure 6.3. Cumulative fraction of dose deposited from the center of the track to the given radius. Fifty percent of the dose is within 2.5 nm of the center track.....165
Figure 6.4. Charge collection stages for an ion strike on a *n+/p* bulk diode. Most of the charge collection occurs during DR recovery (c) and the following stable DR (d).....166
Figure 6.5. Approximate minority carrier density (electron) during ambipolar diffusion around a 5 MeV alpha strike. The diffusivity constant was approximated to 1.5, 3 and 20 cm^2/s for the plots at 1, 10 and 100 ps respectively. 168
Figure 6.6. Summary of Edmonds approximate charge collection equations for a direct strike to the DR and a non-direct strike to the substrate. The equations for low (LLI) and high level injection (HLI) conditions are shown.....172
Figure 6.7. Flow diagram of spectroscopy modeling process.....175
Figure 6.8. Detailed cross-section of diode array *p*+-ohmic and *n*+-junction contacts with approximate dimensions. Overlayer and SOI thickness dimensions are identified for each region shown in the plan figure below.....176

Figure 6.9. Layout of 10 × 10 μm^2 (junction area) diode cell showing location of regions whose overlayer and SOI construction is identified in Figure 6.8. 176
Figure 6.10. Layout of 100 × 100 μm^2 (junction area) diode cell showing location of regions whose overlayer and SOI construction is identified in Figure 6.8. 177
Figure 6.11. Process simulator derived 2D geometry showing doping distribution. On the scale, positive is n type and negative is p type doping. Oxide region is colored gray. 178
Figure 6.12. The Katz-Fageeha model for 5 MeV alpha track density compared to the Gaussian model used by DESSIS (with r=2.25nm (best fit), r=100nm (typical simulation)) and also compared to a power law relationship (with n=2.6, r_o=0.35 nm, Q_o=5 ×10^{22} eh/cm^3) . The gaussian is a poor fit whilst the power law is a good approximation to the Katz model. 180
Figure 6.13. 2D simulation: Current Transient generated by a 5.3 MeV alpha particle traversing the 2D geometry given by Figure 6.11 at various distances x from the p+ contact edge of the simulation. Diffusion dominates from x=0 to 6-6.75 um. For x>6.75-15 funneling charge collection is present. 184
Figure 6.14. Current Transient at x=7.5 μm (conditions as for Figure 6.13) showing the points at which distribution plots have been made as shown in Figure 6.15, Figure 6.16 and Figure 6.17. Also shown is the collection efficiency CE as a function of time. 184
Figure 6.15. Hole density distribution for a 2D 5.3 MeV alpha particle transient simulation. Diode is the 10 × 10 μm junction size on 2 μm SOI substrate. The boundary denoted by S is the pre-ion strike (0 fs) depletion region boundary defined by the sharp transition in hole density. 185
Figure 6.16. Electron distribution for a 2D 5.3 MeV alpha particle transient simulation. Diode is the 10 × 10 μm junction size on 2 μm SOI substrate. The boundary denoted by S is the pre-ion strike depletion region boundary defined by the hole density distribution (see Figure 6.15). 186
Figure 6.17. Potential distribution for a 2D 5.3 MeV alpha particle transient simulation. Diode is the 10 × 10 μm junction size on 2 μm SOI substrate. The boundary denoted by S is the pre-ion strike depletion region boundary defined by the hole density distribution (see Figure 6.15). Note that the potential includes built in voltage and contact potentials, hence a range >10 V. 187
Figure 6.18. An example collection efficiency function with the parameters (L=55, (x_f, c_f) = (5,0.97) and (x_d, c_d) =(9,0.99)) derived from 5.3 MeV alpha broadbeam measurements of section 6.2.4.1. One quarter of the diode is shown with coordinates corresponding to the layout of Figure 6.9. 188
Figure 6.19. Voltage distribution for 2um SOI device, 100ps after 5.3MeV alpha strike at x=3.5,y=15um. (1/4 of device is shown, 15×15×2μm, center of diode is nearest to viewpoint). 189
Figure 6.20. Electron density for 2um SOI device, 100ps after 5.3MeV alpha strike at x=3.5,y=15um. (1/4 of device is shown, 15×15×2μm, center of diode is nearest to viewpoint). 189
Figure 6.21. Mesh construction used for the 3D simulation of a 5.3MeV alpha strike at x=3.5,y=15um. with voltage distribution also shown. 20000 vertices are required with refinement in high doping, depletion region and alpha strike region. 190
Figure 6.22. Comparison of current transient generated by 2 MeV proton and 5.3 MeV alpha particles. Device simulated was the 100 × 100 μm^2 bulk diode biased at 10 V with the ion incident on the junction center. The alpha current transient shows signs of funneling not evident in the proton response (such as the peak at 3 ps). 191
Figure 6.23. Transient 2D simulation of 2 MeV proton strike at center of 100 × 100 μm^2 (junction size) diode cell on bulk device. Strike is at (x=60, y=60) referring to Figure 6.10. The reverse bias is 10V. Each image is 60 μm wide and 58 μm deep although the actual simulation was performed on a 60 × 300 μm^2 section. Use of reflective boundary conditions are used so that only half the diode cell needs to be simulated. Two different time snapshots are displayed; 1 ps (left side) and 1 ns (right side) after the proton strike. Voltage distribution is displayed in the upper images whilst electron density is displayed in the lower images. 192
Figure 6.24. Transient 2D simulation of 5.3 MeV alpha strike at center of 100 × 100 μm^2 (junction size) diode cell on bulk device. Ion track is on the right edge. The reverse bias is 10V. Each image is 60 μm wide and 58 μm deep although the actual simulation was

performed on a 60 × 300 μm^2 section. Use of reflective boundary conditions are used so that only half the diode cell needs to be simulated. Two different time snapshots are displayed; 1 ps (left side) and 1 ns (right side) after the alpha strike. Voltage distribution is displayed in the upper images whilst electron density is displayed in the lower images. 193
Figure 6.25. 2D simulation of an angled 1750 keV alpha particle originating from the p+ contact. Device is the 10×10 × 2 μm^2 SOI diode. Electron and hole densities are shown for various. This models the recoiling alpha from a thermal neutron capture reaction with boron. See University of Wollongong web-site for dynamic GIF animation [231]. 195
Figure 6.26. Schematic of microprobe used at the Microanalytical Research Centre, University of Melbourne, Australia. 196
Figure 6.27. 2 MeV alpha spectra of energy deposited in the 10× 10 μm^2 2 μm SOI microdosimeter for the four main device regions. The spectra were calculated using the Monte Carlo transport program SRIM (10000 samples) based on the device cross-section of Figure 6.8. Scaling of the spectra counts was made according to the relative area of each region. 198
Figure 6.28. Comparison of 2 MeV alpha microbeam spectrum with spectroscopy model. The model is shown without Gaussian filtering and following 13 keV Gaussian filtering. The filtering is intended to imitate the statistics of charge collection. 198
Figure 6.29. Microbeam image (2MeV alpha) of 10×10μm 2μm SOI array. Black corresponds to lowest charge collection amplitude and white is highest amplitude. The top two rows show the image following median filtering of the bottom 12 cells. The bottom image was split into 12 cells and the median over all the cells was calculated for each cell pixel. 200
Figure 6.30. (a) Left side, processed microbeam image data for a quarter of the 2 μm SOI diode. (b) Right side, CE calculated from the data on the left using equation (6.53). 201
Figure 6.31. *Unirradiated* (left) and *Irradiated* (right) 2μm SOI device: 5.3MeV broadbeam alpha spectroscopy and a comparison with spectroscopy model. 204
Figure 6.32. *Unirradiated* (left) and *Irradiated* (right) 2μm SOI device: Collection efficiency function derived from 5.3MeV broadbeam alpha spectroscopy (Figure 6.32) and a comparison with 2D simulation results. 204
Figure 6.33. 10 μm SOI device, Collection efficiency derived from 5.3 MeV spectroscopy data. Left plot is the measured spectrum compared with the model. Right plot shows the CE function model in 2D form. 205
Figure 6.34. Parameters of Edmonds' charge collection model for large bulk devices. 208
Figure 6.35. Fit of diffusion model to proton microbeam peak charge collection data. All data is for 100×100 μm^2 diode size bulk devices except for the diamond which is for a 10 × 10 μm^2 diode size bulk device. 211
Figure 6.36. Fit of diffusion model to alpha broadbeam peak charge collection data. All data is for 100×100 μm^2 diode size bulk devices. Error in energy collected is estimated at ± 100 keV for alpha energy >2000 keV. The low energy data at 2000 keV has a larger error (± 200 keV) due to poorer resolution of incident alpha spectrum. 211
Figure 6.37. Capacitance versus voltage data for bulk devices before and after irradiation with 24 GeV/c protons at a fluence of 4.1 × 10^{13} p/cm^2. Irradiation was performed using the CERN-PS-T7 beam. A1 is an array with 100×100 μm^2 sized diodes and A4 has 10×10 μm^2 sized diodes. 212
Figure 6.38. Correction Diode Array Junction Capacitance versus voltage data for bulk devices before and after irradiation with 24 GeV/c protons at a fluence of 4.1 × 10^{13} p/cm^2. Irradiation was performed using the CERN-PS-T7 beam. A1 is an array with 100×100 μm^2 sized diodes and A4 has 10×10 μm^2 sized diodes. The slope of the data is related to the substrate doping density 212
Figure 6.39. CERN Proton Synchrotron transfer lines inside the tunnel. (Photo courtesy of CERN). 213
Figure 6.40. Estimated change in diffusion length with 1 MeV equivalent neutron fluence given a damage constant K_{1MeV} = 1.5×10^{-6} cm^2/n-sec 214
Figure 7.1. Schematic diagram of the epithermal beam and patient irradiation facility at the BMRR. [255] *A*, core of the reactor; B, moveable shutter; C, epithermal neutron filter. A patient is shown with his head in the neutron beam port. Filters and moderators adjust the energy spectrum to maximize neutrons in the epithermal energy range of ~1 eV to 10 keV and minimize those outside this range. 227

Figure 7.2. Cross-section of boron-coating simulation on top of 10×10 μm^2, 2 μm SOI diode array (40×120 diodes, each cell 30×30 μm^2). The GV is ($1215 \times 3615 \times 6.55$ μm^3) whilst the SV is (1200×3600 μm^2 with a depth of 2 μm in the *n*+, *p*+ regions and 1.82 μm elsewhere) . The maximum range of 1470 keV alpha particles in Lucite is 7.55 μm. The left side shows the boron coat configuration and the right side shows the boron lid configuration. 231
Figure 7.3. Segment length distribution produced by thermal neutron irradiation of a boron/Lucite coating and lid configurations above the 10×10 μm^2, 2 μm SOI diode array. Simulation geometry is depicted in Figure 7.2. 232
Figure 7.4: Microdosimetric spectra for non-boron coated device compared with boron coating. The spectra were obtained at a depth of 6.5 cm in the Lucite phantom with a reactor power of 300 kW. Note that the no coat spectrum is scaled up by a factor of 100. The peak at 200 keV/μm in the no coat spectrum arises from boron *p*+-dopant in the device. 234
Figure 7.5. Microdosimetric spectra for various coating options. The spectra were obtained at a depth of 6.5 cm in the Lucite phantom with a reactor power of 300 kW. 234
Figure 7.6. Bias dependence of U-235 Covered diode array at a depth of 6.5 cm in Lucite phantom, Reactor Power = 30 kW 235
Figure 7.7: Comparison of experimental results (1% B coated diode array (10x10μm) at 6.5 cm) with Monte-Carlo Simulation. The left side shows the energy probability distribution and the right side shows the same data presented in standard yd(y) form. 237
Figure 7.8: Comparison of proportional counter [262] with diode array at BMRR. The mean chord length for the diode array was 2.85 μm. 238
Figure 7.9. General layout of the 5 MW KUR clinical irradiation system [269] 240
Figure 7.10. Cross-section of epithermal neutron filter construction at KUR 240
Figure 7.11. Water head phantom used at KUR showing 3D actuator system (above right from phantom) and a rail mounted remote-patient carrier system. 241
Figure 7.12. Boron ion implantation during device fabrication showing boron deposition in LOCOS (SiO_2) and silicon *p*+ region. 244
Figure 7.13. Definition of Generation Volume for *p*+ doping BNCT simulation. The top inside layer of boron doped material (0.1 μm thick) is within the oxide (due to mask overlap during boron ion implantation) whilst the lower layer (0.2 μm thick) is within the silicon *p*+ region. 244
Figure 7.14. Segment length distribution produced by thermal neutron irradiation of the ion implanted region of a 10×10 μm^2, 2 μm SOI diode array. 245
Figure 7.15. Cross-section of nitrogen in air neutron capture simulation on top of 10×10 μm^2, 2 μm SOI diode array (40×120 diodes, each cell 30×30 μm^2). The GV is ($10000 \times 10000 \times 300$ μm^3) whilst the SV is (1200×3600 μm^2 with a depth of 2 μm in the *n*+, *p*+ regions and 1.82 μm elsewhere). The maximum range of 1010 keV protons in air is 10.42 mm. 246
Figure 7.16. Comparison of energy distribution from ion-implanted boron capture reaction at BNL and KUR. An identical microdosimeter was used, 10×10 μm^2, 2 μm SOI diode array. The air gap varied between the two experiments as shown in Figure 7.17. The data is normalized by integrating values > 450 keV. 247
Figure 7.17. Lucite lid configurations for measurements made using the ion implanted boron region of the microdosimeter. The hatched region is a Lucite lid present during the BNL measurements but not present during the KUR measurements. Therefore, t_{air} = 100 μm BNL and 300 μm KUR. The *p*+ boron is implanted in the top surface of the silicon wafer (~0.1-0.2 μm depth). No boron is present in any of the Lucite components in this diagram. 247
Figure 7.18. Comparison of boron ion implantation simulation with energy spectrum at 1 cm depth, mixed mode irradiation at KUR. The simulation was normalized to provide the same total number of counts greater than 450 keV as the experiment. 249
Figure 7.19. Illustration of possible variation in recombination with ion strike direction with respect to electric field. 249
Figure 7.20. Comparison of air gap (nitrogen) simulation with energy spectrum at 1 cm depth, mixed mode irradiation at KUR. The simulation was normalized to provide the same total number of counts within the energy range of 120 to 450 keV as the experiment. The fast proton simulation curve, representing events due to fast neutron generated

recoil protons, is calculated by subtracting the air simulation from the experimental data for E<250 keV. 250
Figure 7.21. Comparison of combined boron ion implantation, nitrogen in air and fast proton simulation data with energy spectrum at 1 cm depth, mixed mode irradiation at KUR. The simulation data from Figure 7.18 and Figure 7.20 has been combined to form this plot. 252
Figure 7.22. Comparison of gold foil and microdosimeter calculated thermal neutron flux profile. The depth profile for the mixed and epithermal irradiation modes are shown. 254
Figure 7.23. Energy spectrum for *mixed mode irradiation* at various depths in the water phantom. Spectra have been normalized so that the integral counts > 450 keV (thermal neutron events) are equal to unity. Differences in the fast proton contribution, E<200 keV, are highlighted. 255
Figure 7.24. Energy spectrum for *epithermal mode irradiation* at various depths in the water phantom. Spectra have been normalized so that the integral counts > 450 keV (thermal neutron events) are equal to unity. Differences in the fast proton contribution, E<200 keV, are highlighted. 255
Figure 7.25. Relative ratio of fast proton events to thermal neutron events at various depths in the water phantom. Ratio is normalized to unity at a depth = 1 cm for mixed mode. 255
Figure 7.26. Comparison of lineal energy spectrum for 2 μm SOI and 5 μm SOI devices (small diode array 10×10 μm junction size) under mixed mode irradiation at 1 cm depth. 256
Figure 7.27. Microdosimeter probe and water phantom with the D_2O moderator/graphite reflector at MIT 258
Figure 7.28. Lineal energy spectrum comparing the performance of Probe Assembly #1 and the improved low noise Probe Assembly #2. 259
Figure 8.1. Chord length distribution for proportional counter, 10 μm SOI silicon microdosimeter and 2 μm SOI silicon microdosimeter. SOI devices are approximated by an infinite slab geometry. 266
Figure 8.2. Microdosimeter probe, water phantom and collimator beam port used at Harper Hospital. The ionization chamber (Farwest Technology, 8150 TE plastic 1 cm^3) as indicated was used to monitor the total dose. Although not used in this study, the integrated charge data was collected for possible future analysis of microdosimetric spectra in terms of absolute dose. 267
Figure 8.3. Comparison of microdosimetric spectra for 2 μm and 10 μm SOI devices with the proportional gas counter. Measurements were performed at 10 cm depth on the central axis. The left side (a) shows the SOI diode array spectra with a MCL set to give the same dose mean lineal energy as the proportional counter. The right side (b) has the MCL for the SOI diode array set to provide the best peak fit to the proportional counter spectrum ($\bar{l}$ ~0.75 times the left side values) 268
Figure 8.4. Calculated energy deposition distributions for 9 MeV neutrons in ICRU tissue for a 1 μm and a 32 μm spherical cavity, showing the contribution of insiders, starters, stoppers and crossers. For the 1 μm cavity the crossers are so close to the total, that they are not drawn on the graph, while the insiders are negligible. (Reproduced from Caswell and Coyne [285]) 272
Figure 8.5. Lineal energy dose distribution measured using the 10 μm SOI silicon microdosimeter and proportional gas counter at two depths along the central axis of the beam. 274
Figure 8.6. Lineal energy dose distribution measured using the 10 μm SOI silicon microdosimeter and proportional gas counter at 7 cm off-axis from the center of the beam and 10 cm depth. 275
Figure 8.7. The weighting function y_{sat} used to correct the measured single event spectrum for saturation effects at lineal energies greater than 125 keV/μm. The weighted spectrum $y_{sat}yf(y)$ for the 2μm proportional counter (10 cm central axis) is shown compared to the standard spectrum $y^2f(y) = yd(y)$. The weighting function for the standard case is simply y. 276
Figure 9.1: Bragg peak of 200MeV proton beam (PMRC-Tsukuba) derived by MOSFET detector in Lucite phantom. Relative dose is the dose normalized to maximum dose at depth of 17.4 cm. 287
Figure 9.2: Microdosimetric spectra of 200MeV proton beam (PMRC-Tsukuba) at various depths in a Lucite phantom. Range of proton is approximately 18cm. 287
Figure 9.3: Comparison of microdosimetric spectrum obtained under Parasitic-Beam and Full-Beam modes at PMRC-Tsukuba with different vertical slit widths (depth in Lucite phantom =

17.9 cm). This example shows significant pile-up effects using the Parasitic Beam despite its much lower total intensity. To avoid pile-up in either mode the beam requires a vertical slit width of 2 mm in order to reduce the number of protons/spill. 287
Figure 9.4: Depth-Dose curve for the NPTC 191.6 MeV proton beam in water. Relative dose is defined as Dose(Markus)/Maximum Dose(Markus). The maximum dose is at 23.2 cm and the relative dose = 1 at this point. The depths at which microdosimetric measurements are made are shown. 290
Figure 9.5. Geometry used for PRISM simulation of 10 μm SOI microdosimeter..... 293
Figure 9.6: Microdosimetric spectra of 191.6 MeV proton beam at various depths in a water phantom. Range of proton is approximately 23.7 cm. 294
Figure 9.7. Proton energy spectrum following the transport using SRIM of 191.6 MeV protons (normal distribution with μ=191.6 MeV, σ=2.8 MeV) through 23.9 cm of water. Note also that 48.5% of protons are stopped completely in the water (i.e. E=0). 296
Figure 9.8. Probability distribution of proton angle of incidence with respect to the device normal. Calculated using SRIM transport of 191.6 MeV protons (normal distribution with μ=191.6 MeV, σ=2.8 MeV) through 23.9 cm of water 297
Figure 9.9. Experimental silicon microdosimeter spectrum at 23.9 cm in water phantom at NPTC compared to Monte-Carlo simulation results using PRISM and SRIM. 297
Figure 9.10. Experimental silicon microdosimeter spectrum at 2.2 cm in water phantom at NPTC compared to Monte-Carlo simulation results using PRISM and SRIM. 297
Figure 10.1. Cross-section of ideal proposed silicon microdosimeter. The TE material may be constructed with either A150, some other TE plastic or even the deposition of real tissue cells. Note that the protective qualities of the SiO_2 passivation overlayer are quite robust..... 308

List of Tables

Table 2.1. Design rules for radiation protection microdosimetry as given by Schroder [68] 32
Table 2.2. Comparison of proportional counter to silicon microdosimeter 36
Table 3.1. Typical ranges of recoil products in various radiation fields 50
Table 3.2. Summary of chord length distributions for various shapes 55
Table 3.3. Summary of mean chord length and relative variance for various shapes 59
Table 3.4. Summary of geometric reduction factor for various shapes 71
Table 3.5. Dimensions of a cylinder and cube with the same $\overline{e}_d$ as a unit diameter sphere. (assuming μ-randomness with infinite range tracks and constant LET) 72
Table 3.6. Dimensions of a RPP with the same $\overline{e}_d$ as a unit diameter sphere. (assuming μ-randomness with infinite range tracks and constant LET) 73
Table 3.7. Ratio of microdosimetric quantities in a cube of side length a and a sphere of diameter d 79
Table 3.8. Cell size data from the literature 87
Table 4.1. Summary of diode array dimensions used in this work 93
Table 4.2. Summary of reverse bias current for selected devices used in later experiments 96
Table 4.3. Parameters estimated for diode arrays from C-V data 101
Table 4.4. Correction capacitance values for each array 102
Table 4.5. Optimum detector bias supply voltage for each value of shaping time. 113
Table 4.6. Relative contribution of noise components in microdosimeter design 116
Table 4.7. Optimum noise performance of silicon microdosimeter with on-chip preamplifier. 119
Table 5.1. Elemental composition of important tissue types, substitutes and detector materials. 122
Table 5.2. Tissue equivalence scaling factor for A150, Lucite and Silicon 126
Table 5.3. Summary of Energy-Range data for ions produced by thermal neutron interactions with nitrogen and boron 127
Table 5.4. Summary of interaction data for selected BNCT conditions♣ 127
Table 5.5. Mean ratio of BNCT ion ranges in silicon and tissue 129
Table 5.6. Mean ratio of Fast Neutron/Proton Therapy ion ranges in silicon and tissue 139
Table 5.7. Calculated values of $\overline{y}_d$ in A150 and Muscle for various neutron energies En 143
Table 5.8. Neutron kerma coefficients (k in fGy m^2) for Si microdosimeter materials and ratio to A150 from Schrewe [37]. The ratio of Si to A150 kerma is shaded for clarity. 148
Table 5.9. Nuclear interaction cross sections for 14 MeV neutrons incident on silicon and muscle. 152
Table 6.1. Electron and Hole Mobility 156
Table 6.2. Lifetime parameters for damage constant estimation 212
Table 6.3. Summary comparison of charge collection modeling methods 215
Table 6.4. Collection efficiency parameters for 2 and 10 μm SOI devices 216
Table 7.1. Elements in silicon microdosimeter construction with isotopic abundance, thermal neutron reaction and cross-section. Reactions in bold produce ion products. Reaction data from Mughabghab [265]. Isotopic abundance from Krane (appendix C) [266]. 225
Table 7.2. Elements in overlayer materials (air and Lucite (unboronated)) with isotopic abundance, thermal neutron reaction and cross-section. Reactions in bold produce ion products. Reaction data from Mughabghab [265]. Isotopic abundance from Krane (appendix C) [266]. 226
Table 7.3. Relative probability of thermal neutron interaction with selected microdosimeter/overlayer elements. All elements selected produce ion recoil products through (n,p) or (n,α) reactions. 226
Table 7.4. Relative probability of thermal neutron detection with selected microdosimeter/overlayer elements. This is a revised and improved subset of Table 7.3. 251
Table 8.1. Estimated mean chord lengths for silicon microdosimeter compared with the expected range of values. 271
Table 8.2. Calculated values of $\overline{y}_d$ and y^* for proportional counter and 10 μm SOI device at various locations in the water phantom 276
Table 8.3. Nuclear interaction probabilities for 20 MeV neutrons incident on silicon and muscle. 278
Table 9.1. Probe assembly materials in front of the silicon microdosimeter and water equivalent thickness 290
Table 9.2. Beam items in nozzle of NPTC and proton energy attenuation 290
Table 10.1. Summary of requirements and design rules for silicon based radiation therapy microdosimetry 300

List of Publications by the Author

The following publications are by the author, several of which are used in this work:

(1) P. Bradley, "The effects of ionising radiation on implantable MOS electronic devices," in *Graduate School of Biomedical Engineering*, Sydney: University of New South Wales, 1996, 245 pages.

(2) P. D. Bradley, A. B. Rosenfeld, K. K. Lee, D. Jamieson, G. Heiser, and S. Satoh, "Charge collection and radiation hardness of a SOI microdosimeter for space and medical applications," *IEEE Trans. Nucl. Sci.*, vol. 45, no. 6, pp. 2700-2710, 1998.

(3) P. D. Bradley and A. B. Rosenfeld, "Tissue Equivalence Correction for Silicon Microdosimetry Detectors in Boron Neutron Capture Therapy," *Med. Phys.*, vol. 25, no. 11, pp. 2220-2225, 1998.

(4) P. D. Bradley and E. Normand, "Single event upset in implantable cardioverter defibrillators," *IEEE Trans. Nucl. Sci.*, vol. 45, no. 6, pp. 2929-2940, 1998.

(5) P. D. Bradley, A. B. Rosenfeld, B. J. Allen, T. Kobayashi, Y. Sakurai, C.Kota, R. L. Maughan, M.Yudelev, J. Coderre, and J. Capala, "Application of silicon diode arrays for microdosimetry in BNCT and FNT," *8th International Symposium on Neutron Capture Therapy for Cancer, La Jolla, USA, 14-18th Sep 1998*, 1998.

(6) P. D. Bradley, A. B. Rosenfeld, B. J. Allen, J. Corderre, and J. Capela, "Performance of silicon microdosimetry detectors in boron neutron capture therapy," *Radiat. Res.*, vol. 151, pp. 235-243, 1999.

(7) P. D. Bradley, A. B. Rosenfeld, M. Bailey, M. Reinhard, K. K. Kee, A. Saint, D. Jamieson, F. Lemeilleur, and S. Satoh, "Radiation hardness and charge collection in a SOI based diode array designed for medical microdosimetry," *Nuc. Inst. Meth. Phys. Res.*, In press 1998, submitted Feb 1998.

(8) A. B. Rosenfeld and P. B. Bradley, "Semiconductor microdosimetry in mixed radiation field and photon fields: present and future," *Radiation Protection Dosimetry*, vol. 85, no. 1-4, pp. 385-388, 1999.

(9) A. B. Rosenfeld, P. D. Bradley, I. Cornelius, G. I. Kaplan, B. J. Allen, J. B. Flanz, M. Goitein, A. V. Meerbeeck, J. Schubert, J. Bailey, Y. Takada, A. Maruhashi, and Y. Hayakawa, "A new silicon detector for microdosimetry applications in proton therapy," *IEEE Trans. Nucl. Sci.*, vol. 47, no. 4 (In Press), 2000.

In addition, the author has presented work at the following conferences:

(1) IEEE Nuclear Science and Medical Imaging Conference, Seattle USA, October 26-30, 1999. Poster: "A New Silicon Detector for Microdosimetry Applications in Proton Therapy"

(2) 5th National Workshop Experimental Radiation Oncology, Sydney Australia, Nov 27 1998. Poster: "Application of silicon diode arrays for microdosimetry in High LET Radiation Oncology"

(3) Engineering and the Physical Sciences in Medicine (EPSM98), Hobart, Australia, Nov 1998. Poster: "The Development of a Novel Silicon Microdosimeter for Radiation Oncology" (presented by A.B. Rosenfeld on authors behalf)

(4) 8th International Symposium on Neutron Capture Therapy for Cancer, La Jolla USA, Sep '98. Presentation: "Application of silicon diode arrays for microdosimetry in BNCT and FNT" (presented by A.B. Rosenfeld on authors behalf)

(5) IEEE Nuclear and Space Radiation Effects conference, Newport USA, July 20-24 1998. Presentation: "Single event upset in implantable cardioverter defibrillators" Presentation: "Charge collection and radiation hardness of a SOI microdosimeter for space and medical applications"

(6) Hiroshima@Melbourne Symp. semi-conductor tracking detectors, Melbourne Aust., Nov 1997 Presentation: "Radiation hardness and charge collection in a SOI based diode array designed for medical microdosimetry"

(7) 1st Symposium on Soft Errors, Radiation effects and Reliability in VLSI: Terrestrial Applications NASA/SEMATECH/SRC, NASA/Goddard Space Flight Center, Oct 27, 1997, Presentation: "Cosmic Ray Induced Single Event Upsets in Implantable Cardioverter Defibrillators", (presented by E. Normand (Boeing Defense and Space) on authors behalf)

1. Introduction

1.1 Background

Ionizing radiation deposits energy within matter via the processes of ionization and excitation. These interactions deposit energy in discrete highly concentrated packages distributed non-uniformly throughout an irradiated body. Although, the standard quantity for specification of irradiation is the absorbed dose, defined as the average energy deposited per unit mass, radiation effects are largely determined by the microscopic pattern of energy distribution relative to the sensitive structures of the irradiated body. For the case of biological effects, it is well known that radiation types with differing patterns of energy distribution will have different effects for the same absorbed dose. This effect is quantified by the term relative biological effectiveness (RBE). The field of microdosimetry evolved from a desire to understand the effects of different radiation sources through an analysis of the absorption of ionizing radiation at a scale comparable to the affected structures.

Microdosimetry is formally defined by Rossi and Zaider as [1] “the systematic study and quantification of the *spatial* and *temporal* distribution of absorbed energy in irradiated matter". Although, much of the historical development of microdosimetry has focused on its applications to radiobiology, the concepts have utility in a diverse range of applications such as radiation effects on electronics. The fields of radiation protection, radiobiology, radiotherapy and radiation effects on electronics require microdosimetry methods for measuring the pattern of energy deposition in small cell-sized volumes.

The scale of measurements in microdosimetry is typically at the micron level. At such small dimensions, the primary tool of experimental microdosimetry has been the low-pressure proportional counter. Although generally considered the best currently available detector, the proportional gas counter has several shortcomings. These include a relatively large physical size which limits spatial resolution and increases vulnerability to pileup effects (p198 [1]), the use of gas in the detection volume which leads to phase effects and wall effect errors [2], and an inability to simulate an array of cells.

In certain applications silicon based detectors offer significant advantages particularly with regard to spatial resolution. McNulty [3] proposed the use of arrays of silicon

reverse-biased p-n junctions for characterizing complex radiation environments inside spacecraft and aircraft primarily. The work was intended to have applications in determining single event upset (SEU) risks to microelectronics and as a biological microdosimeter for personnel monitoring. The detector is connected to a spectroscopic system in which charge collection induced by radiation interactions is recorded by a multi-channel analyzer. Such a detector removes several of the previously mentioned problems associated with proportional gas counters. Silicon diode array microdosimetry exploits the small size, rapid development, and current manufacturing capabilities of integrated circuit technology. Furthermore, the capabilities of such technology continue to grow at an astonishing pace enabling the development of new detector designs.

Fortunately, the requirements of a device designed to study SEU phenomena coincide with the requirements of a biological microdosimeter. This is a manifestation of the close correlation between SEU phenomenon, biological cell death, and microdosimetry [1, 4]. For example, an electronic memory state change (or bit flip) is analogous to cell death in radiobiology. Both applications demand an accurately defined sensitive volume (region of charge collection), an array of identical diodes to improve collection statistics and diode structure sizes of the order of a few microns. Therefore, in developing a silicon microdosimeter one may draw upon the wealth of study in single event upset phenomenon in electronic devices.

However, several problems have impeded the widespread application of silicon based microdosimetry in medical applications. These problems include the tissue equivalence of the device, insufficient low noise capability and a poorly defined sensitive volume. In this work, a novel high spatial resolution silicon based microdosimeter using silicon-on-insulator (SOI) technology is presented. The aim of this work was to develop methods that address the key problems impeding silicon microdosimetry using the SOI microdosimeter as a prototype test device. The feasibility of using the device in high linear energy transfer (LET) clinical environments was verified by experimentation at boron neutron capture therapy (BNCT), fast neutron therapy (FNT) and proton therapy facilities. Such an encompassing study of the problems affecting silicon microdosimetry and the application of such devices to medical radiation environments has not previously been attempted.

1.2 Thesis Outline

The organization of the thesis is shown in detail in the Table of Contents and described briefly as follows:

Chapter 1. Brief introduction and thesis outline

Chapter 2. The literature review summarizes past and current research in the areas relevant to the thesis topic. Emphasis is given to experimental methods in microdosimetry and particularly, previous research in developing and testing silicon based microdosimeters. The rationale behind utilizing silicon based microdosimetry in medical radiotherapy applications is discussed. Four main problems requiring investigation are identified (and addressed in chapters 3, 4, 5 and 6) including requirements especially device shape, noise minimization, tissue equivalence, and sensitive volume definition. Additional literature reviews occur throughout the thesis were it is necessary to introduce background material for improved understanding.

Chapter 3. The *requirements* of a silicon microdosimeter are discussed with a particular emphasis on *detector shape* considerations. Criteria for the equivalence of measurements made using a rectangular parallelepiped shaped silicon device, with a tissue equivalent converter, are determined.

Chapter 4. The *design* of the silicon-on-insulator (SOI) prototype device and associated electronics is described along with a *noise optimization* model used in the prototype design. I-V and C-V testing of the prototype is presented. Although not meeting all the desired requirements the device is an improvement on previously constructed silicon microdosimeters.

Chapter 5. The problem of *tissue equivalence* correction for silicon microdosimetry is addressed. A method for correcting microdosimetric measurements in silicon to tissue volumes is derived and confirmed using Monte-Carlo simulations.

Chapter 6. The device *sensitive volume* and *radiation hardness* is determined. Methods for characterizing the collection efficiency and radiation hardness of silicon microdosimeters are presented and compared including alpha

and proton microbeam spectroscopy, broadbeam alpha spectroscopy and 2D and 3D device simulation.

Chapter 7. Having fully characterized the device behavior and addressed the key problems the prototype was tested in several major high LET clinical facilities. In this chapter, initial testing of the device at three *boron neutron capture therapy* facilities is presented (BNL, MIT and KUR). The interaction of thermal neutrons with each of the device materials is analyzed. Simultaneous thermal neutron flux and microdosimetric measurement at a high spatial resolution is demonstrated.

Chapter 8. This chapter presents the first demonstration of a SOI based microdosimeter in a *neutron therapy* beam (Harper Hospital, Detroit) with results sufficiently promising to confirm the feasibility of the device in this application. A detailed comparison with a proportional counter is performed. Despite some deficiencies in the existing design, microdosimetric radiation quality variations may still be characterized qualitatively.

Chapter 9. Initial testing of the device in two *proton therapy* facilities (PMRC, and NPTC) is presented. Testing at the recently constructed NPTC facility in Boston demonstrated the capability of the device to record lineal energy spectra with high spatial resolution. High count rate measurements not previously performed were made at PMRC.

Chapter 10. Conclusion providing a summary of main results and suggested directions for further research.

In summary, the identified problems are addressed in chapters 3, 4, 5 and 6 whilst initial clinical facility testing follows in chapters 7, 8, and 9.

Finally some notes on presentation.

- The spelling in this thesis conforms to US English.
- References are presented in IEEE format. The use of "et.al" for references to papers with multiple authors is not used. The vast majority of papers have multiple authors and as such multiple authors may be assumed by default.

2. Literature Review and Background

2.1 Historical Foundations

The foundations of microdosimetry grew out of the study of radiation effects on living cells. Early attempts at understanding cellular radiation effects recognized that knowledge of the energy distribution at a scale comparable to the structures affected by irradiation was essential. Dessauer [5] and Crowther [6] in the 1920s developed the earliest forms of target theory which identified discrete energy transfers denoted as hits with individual ionization. The neglect of the spatial distribution of these events severely limited the predictive capability of this early work. The late 1940s saw the development of several important concepts, in particular the development of the concept of linear energy transfer (LET). Zirkle [7] in 1952 provided the first definition of LET although his work was closely linked to similar ideas introduced by Gray [8] and Lea [9]. ICRU report no 16 [10] defines LET as a measure of the loss of energy per unit distance along the path of a charged particle. This report also discusses some of the serious limitations of the LET concept in explaining relative biological effectiveness and the differences between radiation types.

Kellerer and Chmelevsky [10], have investigated the effect of these limitations and the ranges and energies over which they are important. There are several reasons for the limitations in the LET concept [11]. Firstly, delta ray energy distribution and its relationship to spatial dose distribution are not adequately considered. Particles with different velocities and charges can have the same LET but it is the particle velocity that largely determines the energy distribution of delta rays. In microscopic volumes, the delta ray distribution may be a significant factor in the spatial distribution of energy, particularly at higher ion energies and small site sizes. Secondly, the limited range of charged particles relative to the finite target structure influences the energy deposition by two possible mechanisms; a change in LET through the site or the possibility of the track beginning or ending within the volume. Such effects are more predominant at lower ion energies and in sites with larger dimensions. Finally, LET, being a non-stochastic average quantity, does not account for the random fluctuations in energy deposition which manifest as clustering of energy deposition and range straggling. The variance due to straggling may exceed the path length variations at high ion energies and small site sizes.

These limitations in LET lead to the formulation of a set of measurable stochastic quantities that provide the fundamental basis for the field of microdosimetry. The two principle quantities are specific energy and lineal energy. These quantities will be defined and discussed in section 2.2. It is the goal of experimental microdosimetry to measure these quantities in well-defined volumes.

Parallel to the theoretical development of radiation interaction with tissue were two main experimental developments [12]. The first main experimental development included studies of visible chromosome aberrations in cells which observed that ionizing radiation could induce exchanges of material between different radiation damaged chromosomes. This work was pioneered by Sax [13] and Lea and Catcheside [14] in the 1940s working on *Tradescantia* plant cells followed by Wolff [15] in the late 1950s and Neary [16] and coworkers in the 1960s. Analysis of the size of the affected chromosome structures under different types of ionizing radiation suggested an interaction distance between pairs of damaged chromosomes of between 0.1-1 μm. This compares with a typical cell diameter of 10 μm and a DNA molecule diameter of 0.002 μm.

Clearly, the measurement of radiation quantities in sites of comparable size to the cell or even the chromosome interaction distance are required. Of utility in such measurements was the development in the early 1950s of the low-pressure proportional counter, commonly called the Rossi counter after its pioneer [17]. This was the second main experimental development in microdosimetry and permits measurement of microdosimetric quantities at scales of the order of 1 μm. The operation and limitations of proportional counters will be described in section 2.3.1.

The site concept involves the definition of volumes of interest called sites in which the energy absorbed by ionizing radiation is considered without regard to the microscopic distribution of energy within the site. *Regional microdosimetry* is concerned with the measurement of energy deposition in sites and it is the principal objective of experimental microdosimetry [1]. Intuitively, it would seem likely that a link exists between microdosimetric experimental quantities and the observed effects of radiation on biological cells. The theory of dual radiation action, first proposed by Kellerer and Rossi in 1972 [18], seeks to establish the link between experimental radiation physics and cellular radiobiology. This theory and the applicability of experimental

microdosimetry to radiobiology, radiotherapy, radiation protection, and other applications is discussed briefly in section 2.3.3. Prior to the discussion on applications, the following sections will describe the important concepts of microdosimetry with particular emphasis on experimental microdosimetry. Current experimental methods will be reviewed to facilitate a comparison with silicon based microdosimetry. Past attempts at silicon microdosimetry are thoroughly examined. The main problems associated with silicon based microdosimetry are identified based on this review and the rationale behind utilizing silicon based microdosimetry in medical radiotherapy applications is presented.

2.2 Basic Principles and Microdosimetric Quantities

The formal definitions for the principal microdosimetric quantities are given by the International Commission on Radiation Units and Measurements [11]. Of primary importance is the concept of *lineal energy*, y, which is defined as the quotient of ε by $\bar{l}$, where ε is the energy imparted to matter in a volume by a single energy deposition event and $\bar{l}$ is the mean chord length in that volume:

$$y = \frac{\varepsilon}{\bar{l}} \tag{2.1}$$

Lineal energy is commonly presented in units of keV μm^{-1}. The mean chord length in a volume is the mean length of randomly orientated chords in that volume. Various types of randomness exist and the definition of $\bar{l}$ typically refers to *m*-randomness in which the body is exposed to a uniform isotropic field of infinite straight lines. Chord length distributions and randomness types are further discussed in section 3.3.1 and subsequent sections. According to a theorem by Cauchy, the mean chord length in a convex volume under *m*-randomness is given by

$$\bar{l} = \frac{4V}{S} \tag{2.2}$$

where V is the volume and S is the surface area of the body.

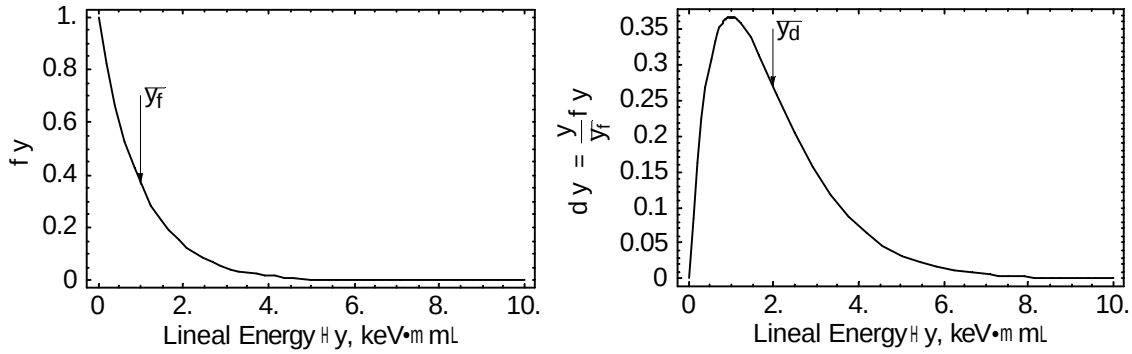
The measured lineal energy is subject to random fluctuations and hence is a stochastic quantity. The random fluctuations are due to all of the previously mentioned limitations in LET, that is, delta ray effects, variations in LET through the volume, and energy and range straggling as well as variations in the chord length through the sensitive volume.

The sources of variation that contribute to the distribution of lineal energy are discussed extensively in section 3.2.

The probability distribution of lineal energy (f(y)) is a fundamental function in microdosimetry. An example is shown in Figure 2.1 where a single set of measurements can be displayed as a frequency distribution (f(y) probability of event versus event size) or as a dose distribution (d(y), fraction of energy versus event size). The relationship between f(y) and d(y) is given by:

$$d(y) = \frac{y f(y)}{\bar{y}_F} \tag{2.3}$$

The dose distribution relationship simply reflects the fact that higher lineal energies deposit a higher dose.



(a) Frequency (event) distribution **(b) Dose distribution**

The lineal energy was assumed to be exponentially distributed, i.e. $f(y)=Exp(-y)$, with mean $\bar{y}_F = 1$ keV/μm. This is not too dissimilar to the measured distributions of single events in a spherical counter of 2 μm simulated tissue diameter irradiated with ^{60}Co γ rays [12]. The lineal energy distributions may be represented as frequency distributions as given by the left-hand diagram or as dose weighted distributions given by the right hand side.

Figure 2.1. Example Single Event Microdosimetric Distributions

The distributions displayed in Figure 2.1, have the following averages defined as

$$\bar{y}_F = \int_0^\infty y f(y)\,\mathrm{d}y \tag{2.4}$$

$$\begin{aligned} \bar{y}_D &= \int_0^\infty y d(y)\,\mathrm{d}y \\ &= \frac{1}{\bar{y}_F}\int_0^\infty y^2 f(y)\,\mathrm{d}y \end{aligned} \tag{2.5}$$

The first moment of f(y) is the frequency mean lineal energy, $\bar{y}_F$, whilst the second moment divided by the first is the dose mean lineal energy, $\bar{y}_D$.

Although not used in this work, another important microdosimetric quantity is specific energy, *z*, which is the quotient of *e* by the volume mass *m*. Similar microdosimetric distributions and averages also apply for this quantity.

Thus, from the single event lineal energy distribution and the site geometry one may calculate all microdosimetric distributions of interest. The representation of these fundamental microdosimetric spectra is traditionally displayed as a log-linear plot with the ordinate multiplied by y such that the area under the curve delimited by two values of y is proportional to the fraction of events (for f(y)) or the fraction of dose(for d(y)) delivered by events in this range of lineal energy values. This representation accommodates the wide lineal energy range often observed in microdosimetric spectra (from 0.1 keV/μm to several hundred keV/μm) but requires further scaling to preserve the dose to area correspondence. Specifically, the ordinate is displayed as *yf(y)* and *yd(y)* on a linear-log plot since

$$\int d(y)\mathrm{d}y = \int yd(y)\mathrm{d}(\ln y) = \ln(10)\int yd(y)\mathrm{d}(\log y) \tag{2.6}$$

and this integral is proportional to the dose deposited in the interval d*y*. Presented in this way, equal areas under different regions of the function *yd(y)* correspond to equal doses.

As an example, the spectra of Figure 2.1 are represented in standard semi-log form, in Figure 2.2. This form will be used where appropriate in the remainder of this work. A note of caution, when presenting spectra in semi-log form, care must be taken to perform correct normalization given a logarithmically binned histogram, as discussed in Appendix B of ICRU 36 [11]. Replication of Figure 2.1. and Figure 2.2, will assist in verifying the correct algorithms. By definition, the distribution *d(y)* is normalized to unity:

$$\int_0^\infty d(y)\mathrm{d}y = 1 \tag{2.7}$$

This normalization should remain unchanged when plotted versus a logarithmic scale of *y* using logarithmic binning. Using equation (2.6) and (2.7), the necessary relationship is:

$$\int_0^\infty yd(y)\mathrm{d}(\ln y) \approx \frac{\ln 10}{B}\sum_{i=0}^{\infty} y_i d(y_i) = 1 \tag{2.8}$$

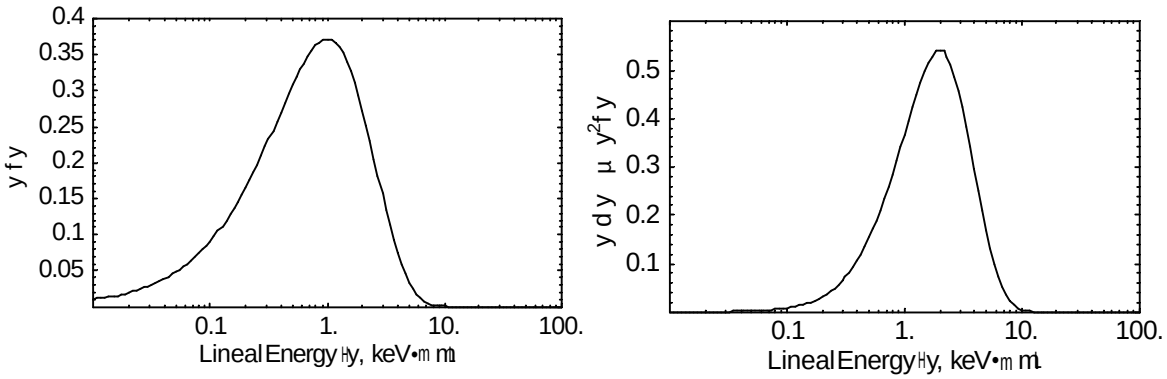
where the logarithmic scale of y is subdivided into B increments per decade such that the ith value of y is:

$$y_i = y_0 10^{i/B} \tag{2.9}$$

The approximation in equation (2.8) arises from the use of the relationship:

$$\mathrm{d}(\log y) \approx \Delta(\log y) = \frac{1}{B} \tag{2.10}$$

where the difference between d(log y) and Δ(log y) is negligible provided B is large enough. In all the plots used in this work B = 40 which was found to provide sufficient smoothing of the data, adequate display resolution and correct normalization.



(a) Frequency (event) distribution

(b) Dose weighted distribution

Semi-log representations of the spectrum of Figure 2.1. The ordinates have been multiplied by y such that area under the curve is proportional to the fraction of events (or dose) in the areas range.

Figure 2.2. Standard Representation of Microdosimetric Spectrums

2.3 Experimental Methods in Regional Microdosimetry

The following section summarizes current experimental methods in microdosimetry with particular emphasis on their performance capabilities and limitations. The methods discussed include proportional counters, autoradiography, and cloud chambers. The theoretical treatment of proportional counters is complex with limited experimental predictive capability. This review seeks only to elucidate in a largely qualitative manner, the principles of operation and limitations. Note that the use of semiconductor based dosimeters is discussed at length in section 2.3.2.

2.3.1 Proportional Counter Microdosimetry

2.3.1.1 Basic Principles of Proportional Counters

Historically, there have been several difficulties associated with measuring ionization in small micron sized solid devices. These include tissue equivalence problems, small device sizes, and construction difficulties. An alternative approach is to simulate a small tissue volume using a larger gas volume with the requirement that the energy loss of charged particles is identical in both tissue and gas volumes for equivalent trajectories. For a tissue sphere of diameter d_t, density r_t, and mass stopping power $(S/r)_t$ and a gas sphere with parameters d_g, r_g, and $(S/r)_g$, the required condition of equivalent energy loss is[11]:

$$\Delta E_t = (S/r)_t \, r_t d_t = (S/r)_g \, r_g d_g = \Delta E_g \tag{2.11}$$

where ΔE_t and ΔE_g are the mean energy losses from the charged particle in tissue and gas. Given a gas with an identical atomic composition to that of tissue and if the mass stopping powers are independent of density then the design criterion becomes:

$$r_t d_t = r_g d_g \tag{2.12}$$

Thus if the ratio of gas to tissue diameter is k_{gt}, then the density of the gas must be reduced from that of tissue by the same factor. The density of the gas may simply be adjusted by changing the gas pressure. As an example, a 2.5 cm diameter sphere filled with propane based tissue equivalent (TE) gas at 17 Torr is equivalent to a 1 μm diameter sphere of unit density material [19]. The absorbed dose is the same in both spheres but the number of charged particles per unit absorbed dose is multiplied by k_{gt}^2, the increase in the area cross section.

An important principle in the simulation of microscopic volumes is Fano's theorem [20]. In a medium of constant atomic composition, the fluence of secondary particles is constant if the fluence of primary particles is constant and that under this condition the fluence is independent of the density variations provided the interaction cross-section and stopping powers of the particles are independent of density. The conditions of this theorem must be fulfilled for a counter to correctly simulate tissue. In practice, the counter materials are made tissue equivalent with essentially identical atomic compositions. However, it should be noted that the requirement that mass stopping

powers are independent of density is not always met due to polarization effects in solids [21].

These principles are exploited in the low pressure proportional counter, the most common microdosimetric device. It consists of a spherical or cylindrical gas chamber with a central anode wire traversing the diameter and electrically isolated from the surrounding chamber wall. A voltage is applied between the anode and the conductive wall of the counter such that radiation induced ionization within the chamber results in the drift of ions along the electric field lines. The amount of charge collected is a measure of the number of ion pairs produced. If the average energy (W) required for producing an ion pair is known then the energy deposited within the counter volume may be calculated.

The size of the pulse produced at the anode depends on the applied voltage. At low voltages (a few volts), the ions move relatively slowly and recombination is a significant process. As the voltage increases, the so-called ion chamber region is reached in which almost all ions are collected. At still higher voltages, gas amplification (or avalanche production) occurs in which each ion or electron acquires enough energy to produce secondary and higher generation ions through collisions with gas molecules. In this region of operation, the charge collected is proportional to the energy deposited and the detector is termed a proportional counter.

The amplification or gas gain is a function, among other factors, of the reduced field E/p (where E is the field strength normally expressed in volts/cm and p is the gas pressure expressed in Torr); at sufficiently large values of E/p ionization by electrons can occur [1, 11, 22]. For the simple case of a cylindrical counter the reduced field at a radius r is given by (p163 [23]):

$$\frac{E}{p} = \frac{V}{p\,r\ln(r_2/r_1)}$$

where V is the applied voltage and r_1 and r_2 are the radii of the central wire and collection volume respectively . Thus, E/p decreases rapidly with r_2 and gas amplification typically only occurs in a very small proportion of the detector within a few wire diameters of the central anode. Consequently, the amount of charge collected is almost independent of the position of the incident ion and the resulting pulse is proportional to the number of primary ions. The shape of the outer wall results in a field

that is more intense at the ends of the collecting wire than in the center. In order to generate a uniform field in the multiplication region, the central anode wire is typically surrounded by an additional electrode shaped as a helix at a potential 80% of the shell voltage (p 89 [1, 11, 22]). A 12.5 mm radius counter at 28 Torr of TE gas simulating a 1 μm radius will typically have an anode radius of 0.0125 mm (1 mil wire) with a helix electrode radius of 1.5mm (p93 [1]).

As the gas pressure decreases (in an attempt to simulate smaller tissue volumes) the amplification region increases such that the counter output ceases to be independent of the spatial distribution of primary ion pairs in the sensitive volume. In order to maintain the amplification region within the confines of the helix electrode, the voltage must be reduced which has the effect of decreasing gain. Conflicting with the requirement of lower gain is that at lower pressures charged particles lose less energy in the counter. Thus, at low pressures the electronic gain must be significantly increased to provide an equal signal to the pulse height analysis system. Rossi (p94 [1]) states a factor of 10 increase in electronic gain from 1 μm simulated diameter down to 0.5 μm. Noise and stability considerations limit the possible electronic gain increases. The generally accepted limit on the simulated diameter due to expansion of the gas multiplication region is around 0.3 μm, although a well defined limit does not exist because it depends on the criterion used for the maximum tolerable spectrum deterioration as well as the applied electric field and gas pressure [11].

Aside from gas pressure decreases, the simulated volume may also be reduced by using smaller electrode diameters. Kliauga [22] has reported reasonable spectra measurements obtained from an ultra-miniature cylindrical counter 0.5 mm in length × 0.5 mm in diameter operating at 4.2 Torr and simulating a 5 nm diameter unit density volume. The successful operation of such a counter is not well predicted by current theories of electron multiplication in gases that may be more due to the inadequacies of theory as opposed to experimental limitations. More research is required to understand the behavior and possible spectrum quality issues associated with such a counter.

Note, that apart from these design restrictions a more fundamental limit [24, 25] on the minimum site size also exists due to the fact that the unit of measurement is ionizations and that excitations are not detectable. Single ionizations in tissue equivalent gas are equivalent to a mean energy deposition of 30 eV. At site diameters less than about 0.3

μm, errors in the conversion to energy may be quite large due to the small number of ionizations produced by individual low LET tracks with average energy below 30 eV.

2.3.1.2 Performance of Proportional Counters: Uncertainties and Limitations

The following discusses the important effects that create errors in the experimental measurements performed by proportional counters. Many of the significant sources of error have been listed in ICRU 36 [11] with a notable systematic study also given by Lindborg [26].

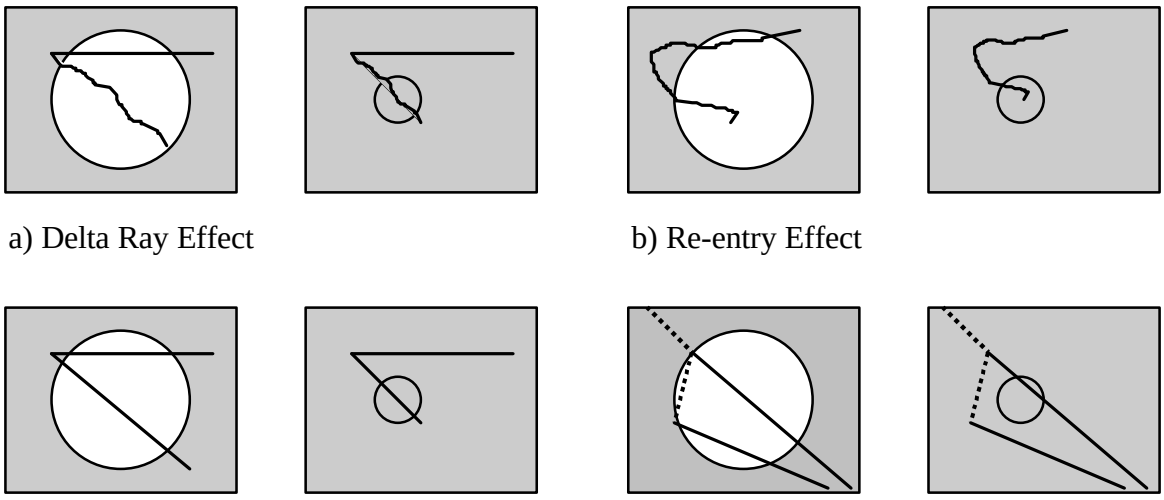
Wall Effects: Even if the wall and TE gas have the same atomic composition distortions in the microdosimetric spectra may occur due to density differences and the effect of the non-rectilinear particle traversals. The so-called wall effects are due to the scattering of particles and the production of secondary and tertiary particles. This leads to an increase in energy imparted by superposition of energy deposition events that would not simultaneously occur in a medium of uniform density. Rossi [27] was the first to suggest such effects with a detailed theoretical treatment subsequently given by Kellerer [2, 28]. Wall effects are classified into four types as depicted in Figure 2.3 and described as follows:

1. ***Delta-Ray Effect:*** A primary particle enters the cavity along with one of its delta rays. However, the distance between the particles is such that only one particle would enter the real tissue volume in the case of uniform density. This effect is most significant for high energy heavy charged particles (significant delta ray production) or for high energy electrons (delta ray and electron may have comparable energies). For heavy charge particles, the energy deposited by the delta ray is much less than the primary particle and hence $\bar{y}_D$ is much less affected than $\bar{y}_F$. Kellerer [2] estimated that for protons of energies above 5 MeV the frequency of double events is about 15% in 1 μm site sizes. For electron energies less than 1 MeV this frequency is less than 6% but the proportion increases at higher energies.

2. ***Re-entry Effect:*** An electron may re-enter the cavity after it has traversed it due to its tortuous path. The points of entry and re-entry may be far enough apart that the electron would not re-enter the high density microscopic volume. Only low energy electrons (<1 MeV) have sufficient curvature to create this effect. For such electrons, Kellerer [2] estimates about 20% of all energy deposition events will be double events due to the re-entry of the primary electrons.

3. ***V-Effect:*** The V-effect is similar to the delta ray effect except that the tracks are formed from two heavy charged particles from a non-elastic nuclear interaction. The two tracks make similar contributions and hence unlike the delta ray effect $\bar{y}_D$ as well as $\bar{y}_F$ are substantially overestimated. Oldenburg [29] has performed Monte-Carlo calculations which indicate that the V-effect is insignificant for neutrons up to 6 MeV but increases in importance above 10 MeV.

4. ***Scattering Effect:*** An uncharged primary particle produces two closely spaced charged particles which both enter the cavity. In the real microscopic region, the two particles may be sufficiently spaced that only one of the particles would enter the sensitive volume. This effect is not well investigated although it may be considered important for neutrons and photons that undergo multiple scattering.



a) Delta Ray Effect b) Re-entry Effect

c) V Effect d) Scattering Effect

Notes: The meandering tracks represent electron traversal, straight lines are heavier particles. and dashed lines represent uncharged(neutron or photon) primary particles. High-density material is represented by the shaded regions. Each type of wall effect has two diagrams: the left indicates behavior with a walled proportional gas counter and the right diagram illustrates the behavior in equivalent real tissue. In all cases the wall effect leads to an increase in energy imparted by superposition of energy deposition events (left diagrams) which would not occur simultaneously in a volume of uniform density (right diagrams).

Figure 2.3. Diagrams of the four types of wall effect in low pressure proportional counters

The wall-effect has motivated the development of “wall-less” counters of which two different approaches have been taken [11, 30, 31]. The first approach uses electric field lines, circumscribed by small field shaping electrodes, to define the collecting boundary. The main disadvantages of the field defined counter are poor boundary definition due to slight variations in the field and the extreme care required in set up adjustment. A second approach is to delineate the boundary using a fine material grid such that the amount of solid at the boundary is small. Although such a counter has a well defined

boundary and is relatively easy to use it has the disadvantage of not being truly wall-less. Finally, for all wall-less counters particular care should be taken to ensure that the container in which the counter is placed does not disturb radiation equilibrium [2].

Tissue Simulation: Traditionally, proportional counters have been designed to simulate energy deposition in small tissue volumes. Tissue equivalence requires that the mass collision stopping powers of charged particles in the counter and the interaction cross section of the counter materials are identical to tissue. This requirement is fulfilled by utilizing materials with elemental compositions approaching that of standard muscle tissue as specified by ICRU report 44 [32]. Such a requirement conflicts somewhat with practical constraints such as electrical conductivity, toughness, and manufacturability. Varieties of plastics have been developed which closely meet these requirements. The standard plastic formulation for use as a wall material was originally developed by Shonka and designated A-150 [33]. This conducting plastic is a mixture of calcium fluoride, polyethylene (for hydrogen), nylon (for nitrogen) and carbon (as a conductive replacement for oxygen).

The suitability of a tissue equivalent gas is determined by the quality of its elemental tissue composition, gas counting properties and homogeneity with the wall. Of several gas mixtures that meet these requirements two types are predominately used; A methane based mixture developed by Rossi and Failla [34] and a propane based mixture developed by Srdoc [19]. The propane mixture permits higher gas gains and is more homogeneous with A150 whilst the methane based mixture more closely models the ICRU standard.

The quality of the tissue substitute depends on the type and energy of the radiation under investigation. For photons of energy between 50 keV and 5 MeV, A-150 plastic combined with methane based tissue equivalent gas is considered tissue equivalent (p30 [11]). However, below 50 keV differences in total attenuation coefficient are discernible due to the photoelectric effect and above 5 MeV photonuclear reactions occur. For neutrons above 10 MeV the substitution of carbon for oxygen leads to poor tissue equivalence due to differences in non-elastic neutron interactions and inhomogeneity due to carbon-oxygen content differences between the gas and wall. The issue of tissue equivalent materials is revisited in more detail in chapter 5.

Calibration: Generally, the proportional counter is calibrated by irradiating the detector with a source of particles of known energy located near the inside surface of the counter [1, 35]. For high LET radiation, an α-source (e.g. ^{244}Cm, ^{210}Po) is used whilst for low energies, x-ray sources may be employed that emit accurately known K_α radiation that is totally absorbed in the gas by photoelectric absorption. The source spectrum should be fully characterized using a surface barrier detector since thick α sources may exhibit significant spectral spread. For a spherical counter, the maximum of the gaussian pulse-height distribution corresponds to the traversal of a particle across the diameter of the sphere. One may then use the known range-energy relationship for the calibration ion to determine the expected energy deposited. Calibration using an alpha particle source has several sources of uncertainty including source alignment errors, energy degradation of the alpha particle in the source and gain shifts frequently observed between calibration and actual measurements [36, 37].

In the case of neutron or proton irradiation, another convenient method, which does not involve calibration irradiation and removes many of the sources of uncertainty, is based on the phenomenon known as the proton and alpha edge [1, 35]. Microdosimetric spectra under neutron or proton irradiation generally exhibit a step in the spectrum corresponding to the maximum energy deposited by a proton near the end of its range, in the Bragg peak LET region. Specifically, the lineal energy position of the edge, y_{edge}, is given by:

$$\begin{aligned} y_{edge} &= dE_{\max} / \bar{l} \\ &= dE_{\max} / (2/3d) \quad \text{for spherical sensitive volume} \end{aligned} \tag{2.13}$$

where $dE_{\max}$ denotes the maximum energy loss of particles traversing the diameter d. The quantity $dE_{\max}$ is obtained by solving the implicit relation $R(E_i) - R(E_i - dE) = d$ and determining the maximum of dE by varying the initial energy E_i where $R(E)$ is the particle range-energy relationship. The maximum LET of protons in tissue is around 95 keV/μm (as seen in the Bragg curve) peaking at about 100 keV. Schrewe [37] calculates a proton edge $y_{p\text{-}edge}$ = 136 keV/μm and alpha edge $y_{a\text{-}edge}$ = 395 keV/μm for a typical 2 μm spherical TEPC. Pihet et.al. [36] have estimated an uncertainty of 2% each for the estimation of the proton edge position and the stopping power of protons at the edge. In practice, the proton and alpha edges are spread

somewhat due to energy and range straggling and the presence of heavier recoil products that produce events at a lineal energy above and around the edges.

Mean Energy Required per Ion Pair (W): *W* is the average energy required to generate an electron-ion pair and is frequently needed for calculations related to dose, noise, resolution and sensitivity. For most tissue equivalent gases, *W* is between 33 and 30 eV (p 88 [1] and [38, 39]). *W* is known to vary weakly with particle type and energy. For example, Goodman and Coyne [40] have shown that the W in a tissue equivalent methane gas mixture decreases from 32.8 to 31 eV as the energy of the neutrons increases from 0.l1 to 20 MeV. W is largely constant for high particle velocities but increases when the particle velocity becomes comparable to the orbital atomic electrons of the gas. Thus, W increases with particle mass (for a given energy) and decreases with particle energy (for a given mass). The uncertainty in W limits the accuracy of the proportional counter in measuring the energy absorbed to around 5% (p 88 [1]). However, one should note that the number of ions generated may well be a better metric for radiobiological efficacy.

Electronics and Sensitivity: The systems required for experimental microdosimetry measurements are shown in the spectroscopy setup of Figure 2.4. The most important component in terms of system noise is the preamplifier. The preamplifier noise is usually specified as the RMS (Root Mean Square) of the number of electrons referred to the preamplifier input. Modern preamplifiers typically have an RMS noise of 400 electrons although by integrating the preamplifier input FET into the counter design, preamplifier noise levels of 100 electrons RMS are achievable [41].

The minimum detection threshold (or Lower Level Discriminator (LLD) setting) of the multi-channel analyzer should generally be set to about 5 times the RMS noise to eliminate the recording of noise counts (p113 [1]). This "rule of thumb" is applicable to both proportional counters and semiconductor detectors. However, an LLD up to 10 times the RMS noise may be required if a low count rate is expected near the LLD energy.

Thus, for a proportional counter the minimum detectable energy E_m is given by:

$$E_m \approx 5\frac{e_{rms}W}{g} \tag{2.14}$$

where W is the average energy required to generate an electron-ion pair ~ 30 eV, g is the gas avalanche gain and e_{rms} is the system electronic noise referred to the preamplifier input. Typical values are W = 30 eV, $g = 10^4$, and e_{rms} = 400 giving an E_m = 6 eV which is less than the ionization energy for a single ion pair.

However, in order to measure single ions at the anode consideration must also be given to the distribution in charge collected from individual avalanches due to the distances covered between the ionizing collisions of electrons [42]. The spectrum for single electrons is well approximated by a Polya distribution. To ensure all counts are registered the average signal for a single ion-pair should be about 10 times as large as E_m [19]. That is, 10 $E_m = W$, which using equation (2.14) means that the gas gain must be 50 times the electronic noise e_{rms} or around 20000 using typical preamplifiers. Such a gas gain is not always achievable, depending on the counter design, and it is desirable to use methods mentioned previously to reduce preamplifier noise. For a given design, gas gain is varied by adjusting the high voltage (500-5000 V) supply. In summary, in order to measure the collection of single ions at the anode, the preamplifier noise should be as low as possible and the gas gain should be high.

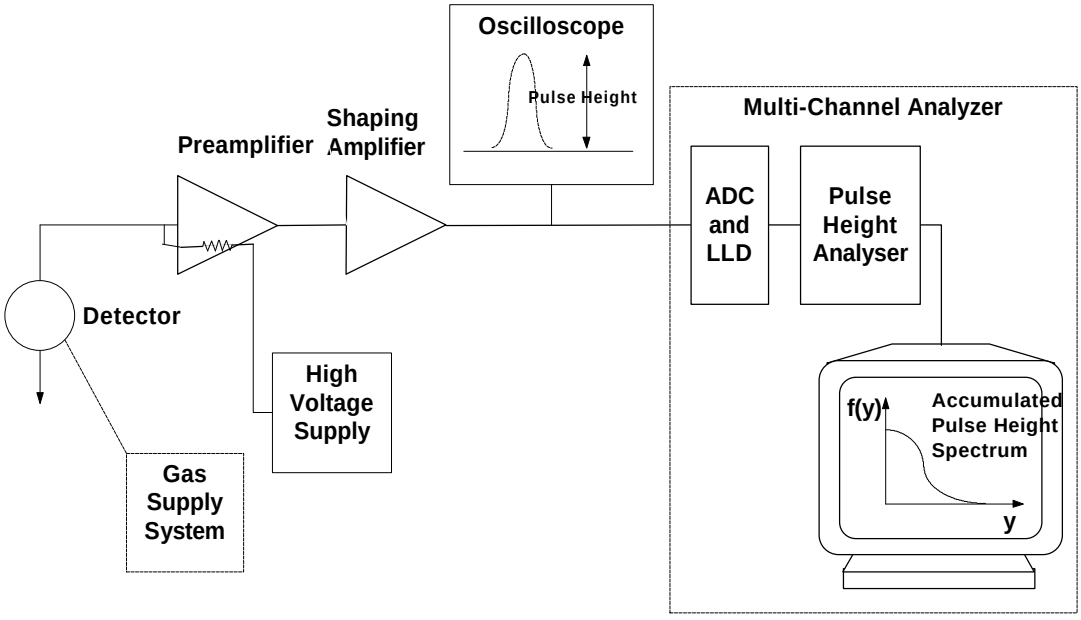


Figure 2.4. Setup required for experimental microdosimetry. With a proportional counter the gas system and high voltage supply are used. For a semiconductor microdosimeter detector the supply may often be low voltage and the gas system is not required. (LLD = lower level discriminator, ADC = Analog to Digital converter)

To optimize noise, a shaping amplifier is included in the spectroscopy experimental setup of Figure 2.4. A time constant of 0.1 μs is often employed for proportional counters which imposes a maximum count rate of 10^4-10^5 cps for most applications [1]. Noise optimization and shaping amplifier considerations are discussed in detail in chapter 4. The output of the shaping amplifier should be monitored with an oscilloscope to ensure correct pulse shaping (pole-zero adjustment) and no evidence of signal pile-up. The acquisition of the entire lineal energy spectra using the multi-channel analyzer may require two separate acquisitions with different amplifier gain settings due to the large dynamic range of the energy deposited. The two spectra may then simply be merged.

Energy Resolution: Given microdosimetric events of equal magnitude, the proportional counter will measure a range of energies deposited due to various statistical fluctuations. The resolution of a detector is defined as:

$$R_{FWHM}(\%) = 2.35\frac{s_E}{\overline{E}}100 \tag{2.15}$$

where $s_E / \overline{E}$ is the relative standard deviation of the distribution of energy collected. Two classes of fluctuations contribute to the distribution:

1. *Theoretical resolution, R_{thpc}*: Two inherent factors which are largely unavoidable in proportional counter operation contribute to the ultimate theoretical resolution. Firstly, the number of ions produced when energy T is absorbed varies about a mean T/W according to a relationship proposed by Fano [43]. The relative variance V_f is given by:

$$V_f = \frac{W}{T}F \tag{2.16}$$

where F is the Fano factor which is typically 0.3 for proportional counters (p 89 of [1]). Secondly, the previously mentioned statistics of gas multiplication results in another contribution with a relative variance V_m given by:

$$V_m = \frac{W}{T}m \tag{2.17}$$

where m is a multiplication factor which is typically 0.6 for proportional counters (p 96 of [1]). Adding the relative variances gives the theoretical resolution, R_{thpc}:

$$R_{thpc}(\%) = 2.35\sqrt{\frac{W}{T}\left[F+m\right]}100 \tag{2.18}$$

2. *Instrumentation Resolution, R_{instpc}*: Resolution is affected by imperfections in the counter design including preamplifier noise and variations in counter voltage, gas pressure and electric field uniformity. These contributions are typically less than 10% of the theoretical resolution. Note that the preamplifier noise, e_{rms}, must be corrected for the gas gain, g, to determine the contribution to resolution. Denoting non-preamplifier instrument resolution as R_{rest}, the instrumentation resolution may be expressed as:

$$R_{instpc}(\%) = 2.35\sqrt{\left(\frac{W}{T}\frac{e_{rms}}{g}\right)^2 + R_{rest}^2}100 \tag{2.19}$$

Combining equations (2.18) and (2.19) gives the estimated resolution R_{pc}:

$$\begin{aligned} R_{pc} &= \sqrt{R_{thpc}^2 + R_{instpc}^2} \\ &= 2.35\sqrt{\frac{W}{T}\left[F+m\right] + \left(\frac{W}{T}\frac{e_{rms}}{g}\right)^2 + R_{rest}^2}100 \end{aligned} \tag{2.20}$$

In summary, the dominant factor in the resolution is the gas multiplication variation. The instrumentation resolution is a minor contribution.

2.3.2 Semiconductor (Silicon) Microdosimetry

2.3.2.1 Basic Principles of Semiconductor Detectors

There are many references devoted to the physics of semiconductors. The following section is based on books by Sze [44], and Knoll [23] with the specific goal of providing a brief and basic framework for understanding the operation, capabilities and characteristics of silicon based radiation detectors. Note that the most common semiconductor material for room temperature radiation detection is silicon so the ensuing discussion will use silicon in all examples.

The usefulness of semiconductors as circuit elements and for radiation measurement stems from the special properties created at a junction where *n* and *p* type semiconductors are brought into good thermodynamic contact. To ensure excellent contact, the junction is created by ion-implantation or diffusion of appropriate dopants in a single crystal. These techniques and subsequent processing can create a variety of

doping profiles that affect the device characteristics. A useful approximation in many applications is the abrupt junction, which will be reviewed briefly.

Consider the *n*+-*p* junction shown in Figure 2.5 where the type change at the junction is taken to be a step function from a heavily doped *n* region to a lightly doped *p* region. The Fermi level (E_F) in the energy band diagram reflects the high concentration of electrons in the *n*+ region and the high concentration of holes in the *p* region. When the junction is first formed large carrier concentration gradients at the junction cause carrier diffusion. Holes from the *p*-side diffuse into the *n*-side leaving behind uncompensated negative acceptor ions (N_A^-) and similarly electrons from the *n*-side diffuse into the *p*-side leaving behind uncompensated positive donor ions (N_D^+). Note that the acceptors and donors are fixed in the semiconductor lattice while the holes and electrons are mobile. The result of this movement is the formation of a negative space charge on the *p*-side and a positive space charge on the *n*-side. The space charge region creates an electric field directed from the *n* to the *p*-side that results in a carrier drift current opposing the diffusion currents. Thus, at thermal equilibrium (i.e. no bias applied, steady state condition with no external excitation) the net current flow across the junction is zero.

The space charge region is also called the depletion region due to the very low mobile carrier density. This region acts, like a high resistivity parallel-plate ionization chamber making it feasible to use for radiation detection. The electric field separates electron-hole pairs formed by ionizing radiation and collects the carriers via drift. The rapid movement of carriers in the electric field generates a current pulse at the device electrodes. By applying, a reverse bias to the *n*+-*p* junction, the charge collection capabilities of the device may be improved. The presence of an external electric field in the same direction as the depletion region field (i.e. reverse bias) will cause additional majority carriers to vacate the junction region leaving more uncompensated impurities and thus expanding the depletion region. This effect is seen in Figure 2.5 where the space charge distribution, electric field distribution, potential distribution and band diagram are depicted for zero and 10 V reverse bias. The device selected has parameters similar to the prototype silicon microdosimeter used in this work and described in chapter 4.

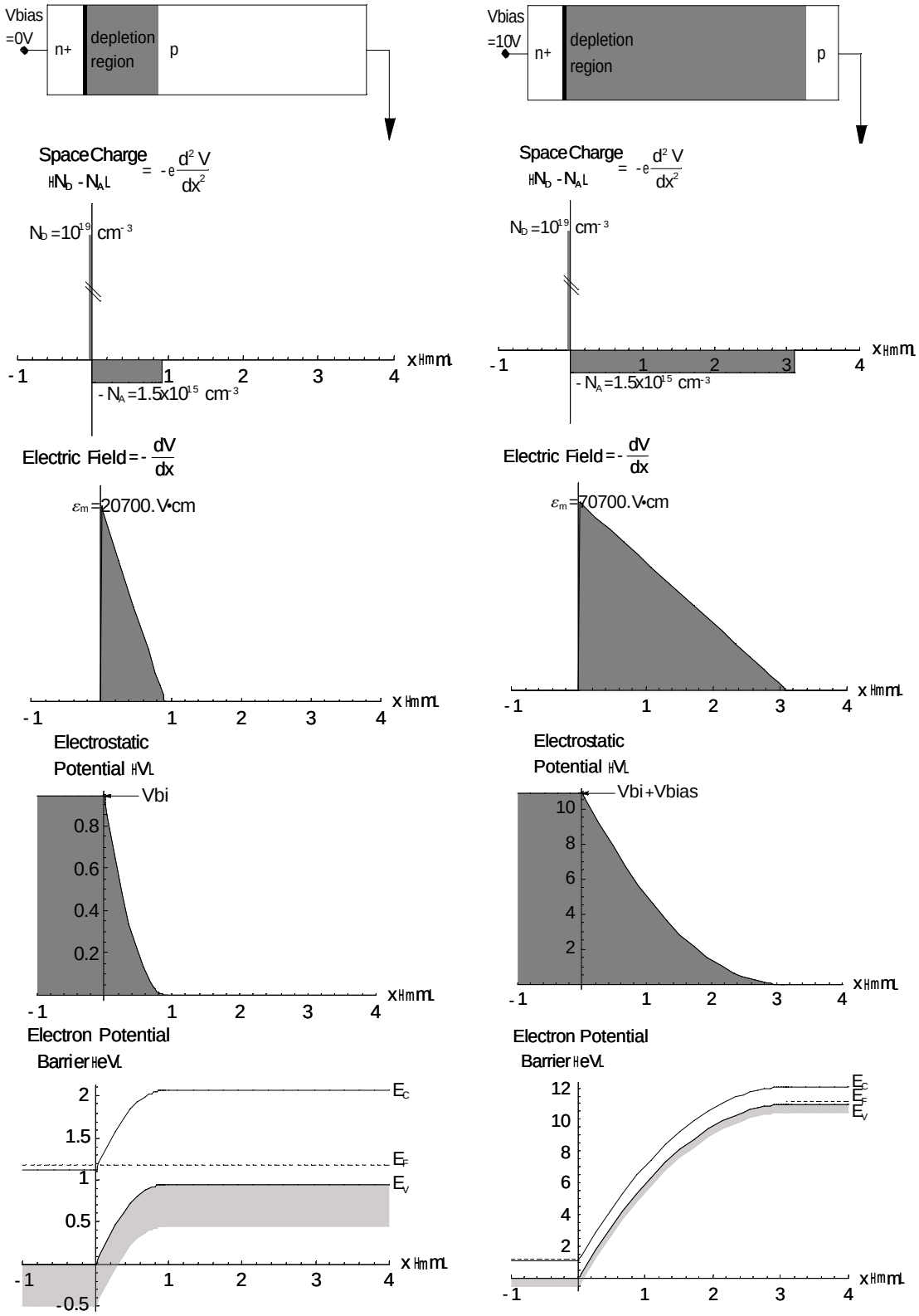


Figure 2.5. A schematic diagram of an abrupt p-n junction including the space charge density, electric field intensity, electrostatic potential and band diagram. The familiar band diagram (showing Fermi energy E_F, conduction E_C and valence bands E_V) may be thought of as the electron potential barrier. The left side shows plots for thermal equilibrium conditions with no bias voltage applied whilst the right hand side shows the same plots for a bias voltage of 10 V. The values selected to construct these graphs correspond to the silicon microdosimeter prototype (p doping Na=1.5 × 10^{15}/cm^3, n doping Nd=2 × 10^{20}/cm^3, effective density of states in valence band N_V =1.04 × 10^{19}/cm^3, effective density of states in conduction band N_C =2.8 × 10^{19}/cm^3, T = 300 K).

The equations used in the figures apply to a one-sided abrupt junction and are readily available in many texts such as Sze [44]. The key starting equation is Poisson's equation defined for the one-dimensional case as:

$$\frac{d^2V}{dx^2} = -\frac{r}{e_s} \tag{2.21}$$

where V is the electrostatic potential, e_s is the semiconductor dielectric permittivity and the r is the space charge density given by the sum of the charge carrier densities and the ionized impurity concentrations. That is,

$$r = q(p - n + N_D^+ - N_A^-) \tag{2.22}$$

In the depletion region, $r = q(N_D^+ - N_A^-)$ since there are no free carriers. Equation (2.21) may be solved for the electric field intensity and electrostatic potential given appropriate boundary conditions. Some useful results are now presented for the depletion region width, built in potential and maximum electric field intensity.

The depletion region width W [44] for a one sided abrupt junction is:

$$W = \sqrt{\frac{2e_s(V_{bi} - V)}{qN_B}} \tag{2.23}$$

where V is the reverse bias, V_{bi} is the built-in potential, q is the electron charge and N_B is the substrate doping concentration (= N_A in our example).

The built-in potential V_{bi} is given by [44]:

$$V_{bi} = \frac{kT}{q}\ln\left(\frac{N_A N_D}{n_i^2}\right) \tag{2.24}$$

where k is Boltzmann's constant (=1.38066 $\times$ 10^{-23} J/K), T = temperature (K), q = electron charge, N_A is the acceptor (p) doping concentration and N_D is the donor (n) doping concentration.

The maximum electric field strength e_{max} is given by [44]:

$$e_{\max} = \frac{qN_B W}{e_s} \tag{2.25}$$

Equations (2.21) through to (2.25) were applied in the construction of Figure 2.5 and will prove useful at various junctures in this work.

2.3.2.2 Performance of Silicon Microdosimeter

Many performance issues are discussed throughout this work. Given these detailed discussions, this section will summarize the performance to facilitate a comparison with the proportional counter provided in section 2.3.4.

Sensitive Volume Definition: In most attempts at silicon microdosimetry, particularly using existing commercial memory devices, the sensitive volume is poorly defined. This is an important problem in silicon microdosimetry that will be addressed in this work. Charge collection does not simply occur via drift in the depletion region. Diffusion from outside of the depletion region may be a significant contribution to charge collection. Further complicating matters is the funneling phenomenon associated with depletion region collapse following the injection of high carrier concentrations in the device. Clearly, the generation of ion tracks and evolution of the charge collection process are complex phenomenon and will be described in detail in section 6.1.

Radiation Hardness: High-energy radiation produces defect complexes in semiconductor materials which reduce minority carrier lifetime, change majority carrier density and reduce mobility. All of these effects reduce charge collection efficiency effectively altering the sensitive volume size. Radiation damage effects on silicon devices is discussed in detail in section 6.3.

Tissue Equivalence: The difficult issue of tissue equivalence in silicon microdosimeters is the subject of chapter 5. Silicon microdosimeters require a tissue equivalent converter on top of the device. Ideally, detected interactions should arise exclusively from events originating in the medium surrounding the detector (referred to for the remainder of this work as the *converter*). Therefore, the device should have a small overlayer thickness and the sensitive volume should be as small as possible to enhance crosser type particles and reduce direct nuclear interactions with silicon. In chapter 5 it will be shown that, assuming identical secondary charged particle spectra, the microdosimetric spectrum will be closely equivalent in a silicon volume and a tissue volume if the dimensions of the silicon volume are scaled by a factor of 0.63. The reader is referred to chapter 5 for more detailed analysis of tissue equivalence issues.

Mean Energy Required per Electron-Hole Pair (W): At room temperature the mean energy per electron-hole pair is 3.62 eV based on alpha particle measurements (p 348 [23]). This is about 10 times lower than for the proportional counter with positive implications for resolution as will be discussed below. The value of W varies with particle type and energy in a similar manner to TE gases. Differences as large as 2.2% have been observed between proton and alpha particles with smaller differences for other light ions and electrons [45]. The value of W is significantly higher for heavy ions and fission fragments than for alpha particle excitation leading to a lower than anticipated energy collected. This effect arises because as the velocity of heavy ions decreases the probability of losing energy via nuclear collisions rather than electronic collisions becomes significant. Wilkins (p 374 [23] from [46]) demonstrates, by irradiating a silicon surface barrier detector with (He, C, S, Ni, Ag, Au and U) ions, that pulse height versus ion energy does not deviate from linearity when using the He, C and S ions and pulse height deficits are seen for the remaining heavier ions. In this study we will mostly be concerned with ions of atomic weight less than S and W = 3.62 eV is a reasonable assumption.

Electronics, Calibration and Sensitivity: The system required for silicon microdosimetry measurements is similar to the proportional gas counter as shown in Figure 2.4. Important exceptions are the removal of the gas system and the need for only a low voltage supply (e.g. battery operated) in low resistivity silicon microdosimeters. System calibration using known energy sources is easy and similar to the proportional counter.

Again, the most important component in terms of system noise is the preamplifier. In fact, the influence of the preamplifier noise is more significant in the silicon microdosimeter because the device does not have any internal (or gas) gain. Thus, for a silicon microdosimeter the minimum detectable energy E_m is given by equation (2.14) with g=1:

$$E_m \approx 5 e_{rms} W \tag{2.26}$$

For the silicon prototype microdosimeter used in this work e_{rms} ~ 600 electrons giving E_m = 10.8 keV.

All other electronic considerations discussed previously for the proportional counter apply to the silicon microdosimeter since they share the same amplifier and MCA

components. Noise optimization and shaping amplifier considerations for the silicon microdosimeter will be discussed in detail in chapter 4.

Energy Resolution: The energy resolution of the silicon microdosimeter, like the proportional counter, may be divided into two classes of fluctuations:

1. *Theoretical resolution, R_{thpc}*: The ultimate theoretical resolution for the silicon device is better than the proportional counter for two reasons. Firstly, there is only one component given by the Fano relationship (equation (2.16)) and secondly the Fano factor is smaller for the silicon detector with a typical value of 0.1 employed (p340 [23]). Thus the theoretical resolution, R_{this}, is given by:

$$R_{thsi}(\%) = 2.35\sqrt{\frac{W}{T}F}100 \tag{2.27}$$

2. *Instrumentation Resolution, R_{instpc}*: The primary component defining instrumentation resolution is preamplifier noise. This is a more significant contribution to overall resolution than for the proportional counter since e_{rms}, is not divided by a gas gain factor in the expression for resolution. Thus, the instrumentation resolution may be expressed as:

$$R_{instsi}(\%) = 2.35\frac{W}{T}e_{rms}100 \tag{2.28}$$

Combining equations (2.27) and (2.28) gives the estimated resolution R_{si}:

$$\begin{aligned} R_{si} &= \sqrt{R_{thsi}^2 + R_{instsi}^2} \\ &= 2.35\sqrt{\frac{W}{T}F + \left(\frac{W}{T}e_{rms}\right)^2}\,100 \end{aligned} \tag{2.29}$$

At low energies (T) the preamplifier noise dominants whilst at high energies the Fano factor defines the resolution. The sensitivity and resolution of the silicon detector will be compared further in section 2.3.4.

2.3.2.3 Review of Semiconductors in Microdosimetry

Research on the development of semiconductor based microdosimetry may be classified into two general device types; *single* p-n junction diodes and p-n junction *arrays* based on commercial memory or charge coupled devices:

1) Single Diode Devices: The first (and most detailed to date) comparison of microdosimetric measurements between a spherical proportional counter and a single junction solid-state detector was made by Dicello [47] in 1980. Microdosimetric spectra for range-modulated negative pion beams (momentum=167 MeV/c) were made using a 1.3 cm spherical proportional counter with a simulated diameter of 2 μm and a 7 μm thick, 0.1 cm radius lithium drifted silicon detector.

Pions, as heavy charged particles, exhibit a Bragg-type depth dose distribution which is enhanced around the Bragg peak by the process of star formation arising from nuclear absorption of the pions and subsequent nuclear fragmentation. The secondary products from pion star formation consist of an isotropic emission of light and heavy ions from the fragmented nucleus along with neutrons and γ-rays. Experimental microdosimetry is a useful tool for analyzing the complex secondary particle distribution in pion beams.

For this type of beam, Dicello [47] found significant differences between the microdosimetric spectra obtained by the two detectors. Monte Carlo calculations demonstrated that the differences were largely attributable to the relatively large sensitive thickness of the silicon detector, that permitted a significant fraction of heavy ion stoppers, and the large diameter that permits large chord lengths. Events at large chord lengths although improbable deposit a high energy and may contribute substantially to the total dose. Moreover, low LET particles such as protons may erroneously produce events that contribute to the high lineal energy component of dose. Despite these difficulties, Dicello [47] acknowledged the potential for silicon microdosimetry due to its high spatial resolution, in-vivo capability and pile-up robustness.

The silicon device is advantageous in beams with high instantaneous count rates since the small area of the silicon detector and the higher noise cut-off reduce pile-up problems. The primary proton beam had a time structure of 120 pulses per second and a duty factor of 7.5%. Dicello [47] found the silicon detector was capable of measurements at full therapeutic beam intensity whilst the proportional counter measurements were complicated by a need to reduce beam intensity.

Later work by Dicello in 1986 [48, 49] focussed on the application of experimental microdosimetry to single event upset studies in silicon. Dicello designed a silicon walled proportional counter to study the energy deposition of pions and muons in

simulated 1 μm silicon site sizes. This work was directed towards the study of cosmic radiation induced single event upset since pions and muons are present in the atmospheric cosmic radiation spectrum

Other attempts at creating silicon microdosimeters using single diodes include the work of Orlic in 1989 [50] and later Kadachi in 1994 and onwards [51, 52]. Both efforts were directed towards radiation protection applications that may benefit from the silicon microdosimeters simplicity and portability. Orlic [50] used a silicon photodiode biased at zero voltage, to give an estimated sensitive thickness of 5 μm, and with a thick polyethylene converter mounted in front of the detector. A spectrum using a ^{252}Cf neutron-gamma source was obtained that distinguished the gamma and neutron microdosimetric spectrum. Kadachi [51] extended this work by comparing the response of a silicon PIN photodiode (sensitive depth ~ 8 μm at zero voltage, 13 mm^2 area) and a tissue equivalent proportional counter (TEPC) of 1 μm simulated diameter. The converter for the PIN diode was made by melting wax onto the diode surface. Measurements on both devices were performed during irradiation by an americium-beryllium neutron source. The dose mean lineal energy, $\bar{y}_D$, was found to be 52.1 keV/μm using the PIN diode and 67.5 keV/μm for the TEPC with the large difference attributable to the different sensitive volume size and the large path length of recoil protons in the PIN diode. These differences were also evident in the microdosimetric spectra for similar reasons.

Additional comparisons were later made by Kadachi [52] using a variety of silicon photodiodes (*p-n*, PIN and *pnn*) and sensitive depths (1,3,5 and 8 μm). The photodiodes were assembled with polyethylene and A-150 TE plastic converters. The effective quality factor, $\overline{Q}$, for irradiation using an Am-Be source was determined from the lineal energy spectra. For a TEPC, $\overline{Q}$ is given by:

$$\overline{Q} = \int Q_{60}(L) d(L) dL \tag{2.30}$$

where $Q_{60}(L)$ is the quality factor function given in ICRP report 60 [53] and d(L) is the normalized dose distribution. Kadachi assumes that the linear energy transfer *L* is equal to lineal energy *y*. For the silicon photodiodes, the computation of $\overline{Q}$ required two types of correction:

$$\overline{Q} = \int Q_{60}(L_s) C_Q(L_s) d(L_s) C_d(L_s) dL_s \tag{2.31}$$

where L is the LET of silicon and $C_Q(L_s)$ is a correction factor for the quality factor due to the difference in LET of water and silicon and $C_Q(L_s)$ is the ratio of the fractional relative dose of the converter and silicon. $C_Q(L_s)$ was taken by Kadachi to be approximately given by the ratio of the converter to silicon density. The effective quality factor was calculated as 7.9 for the Am-Be source using the TEPC and 8.1 using the 1 μm photodiode (*p*-*n*) which is quite a good comparison despite the significant spectral differences previously noted. For other applications such as $\bar{y}_D$ determination, the large area photodiode suffers from the problems identified by Dicello [47], namely, a chord length distribution which differs greatly from the proportional counter due to its large area. Furthermore, the sensitive volume of the device is not accurately defined due to the complexity of the charge collection process that includes diffusion and funnel assisted phenomenon (see section 6.1).

2) Arrayed Diode Devices: In 1983, Bradford [4] had clearly recognized the close correlation between radiation effects on microelectronics and radiobiological microdosimetry in a paper entitled "Microelectronic analogues to radiobiological microdosimetry". Single event upset phenomenon resulting from charge collection at a reverse biased node in the memory cell is analogous to biological cell death. Based on the detection ability of memory devices, due to the single event upset phenomenon, several researchers have pursued the idea of using dynamic random access memory (DRAM) circuits as neutron radiation dosimeters. Davis [54] experimented with the thermal neutron response of 16 Kbit DRAMs covered with ^{6}Li and ^{10}B converters. Similar experiments were also performed by other researchers using different DRAM devices [55-57]. In all these detection systems, a digital output is read from the DRAM and events are simply counted.

However, Abdel-Kader and McNulty [58] in 1987 proposed that the power supply lines of commercial memory devices may be connected to spectroscopic acquisition systems to record the energy deposited by events in reverse biased junctions within the device. Simplistically, a memory cell consists of two transistors in an on (conducting) state and two in a off state (non-conducting). A non-conducting transistor has a reverse-biased p-n junction which is connected via a conducting transistor to the power or ground line of the memory device. When configured with a spectroscopic system connected to the

power line, the device is essentially a radiation detector having a large array of p-n junction cells.

Irradiation with known energy sources is useful for characterizing the sensitive volume dimensions and charge collection regions [58-60]. This technique was further refined by the development of ion beam induced charge collection (IBICC) first performed on microcircuits by Breese [61] in 1992. Sexton [62] provides an excellent review of this subject. Briefly, a narrow (<1 μm) ion beam is magnetically scanned across the device and the charge collected is recorded along with the spatial position of the beam. The location, area and charge collection efficiency of the sensitive volume may then be determined more accurately then by using the broadbeam spectroscopy method (see section 6.2.3).

Roth and McNulty [63, 64] developed a silicon microdosimeter based on memory devices (993L422, 1 KByte) using the principle of power line spectroscopy. The system was intended for biological and electronic radiation monitoring in spacecraft and avionics. An important difference from previous systems is that it used an array of micro-volumes rather than one large detector. Unfortunately, the system was never flight-tested. Stassinopoulos [65] has recently developed a similar system that is undergoing flight-testing. The system uses a 32K × 8 SRAM with no applied bias and an estimated sensitive volume depth of 14 μm.

In 1994, Schroder [66-69] applied commercial memory devices to radiation protection applications such as personal neutron dosimetry. Schroder mainly selected radiation hardened memory devices (such as Harris HS6504RH, 4 Kbit) for two important reasons. Firstly, these devices provide designs that are more resistant to radiation damage such as oxide charge build-up (see section 6.3). Secondly, the sensitive volume depth is limited by a high p-doped region below the p-n junction that provides a potential barrier for minority carriers and limits the charge collection from deeper in the substrate. Schroder [68] tested a 4 Kbit radiation hard device with a 2 mm A150 TE converter separated from the device by a 2 mm air-gap and a 64 Kbit non-radiation hard device with a 100 μm thick polyamide layer directly coating the device. The sensitive depth and overlayer thickness were estimated using spectroscopy methods as (1.9 μm, 3.5 μm) for the 4 Kbit device [66] and (3.4 μm, 2 μm) for the 64 Kbit device [68]. Comparisons with a 1 μm simulated diameter TEPC in a 5.3 MeV mean energy neutron

field (cyclotron) were poor due to deficiencies in the memory device including an ill-defined sensitive volume, large overlayers that prevented heavy ion recoils from reaching the sensitive volume and little consideration to tissue equivalence corrections. The non-radiation hardened device exhibited spectral shifts during irradiation attributed to radiation damage effects.

Schroder [66] along with Pace [70] recognized the possibility of using charge coupled devices (CCD) for radiation protection microdosimetry. The disadvantages of this device are the need for readout control circuitry, the possibility of multiple hits in a single cell before cell readout, and the poor sensitive volume definition. For radiation protection applications, these problems are not as severe as for other applications such as radiotherapy.

Clearly, the recurring major problem in applying commercial memory devices and photodiodes to microdosimetry is the poorly defined sensitive volume compounded by the unwillingness of manufacturers to provide important device construction information. Buried wells are not completely effective at preventing charge collection from outside of the depletion region particularly for high LET particles due to the high charge density exceeding the doping density of such wells. As mentioned earlier, diffusion and funneling severely complicate the charge collection process. Schroder [67] attempted to reduce the effect of diffusion by adding a coupling capacitor following the detector that removed the slower time profile associated with diffusive charge collection. This idea is helpful but nevertheless very imprecise.

Schroder [68] concluded his work with a set of design rules for an optimized semiconductor chip to be used for personal neutron dosimetry. The rules are shown below in Table 2.1. These rules are not exhaustive and not thoroughly justified in the Schroder's paper [68]. This work intends to address the issue of formulating design rules and requirements for silicon microdosimetry.

Table 2.1. Design rules for radiation protection microdosimetry as given by Schroder [68]

Optimization of Design	Criterion
Small diode with $l_{\max} / \bar{l} \leq 3$ where l_{max} = maximum chord length and $\bar{l}$ = MCL	Fundamental microdosimetric requirement
Array of diodes with area of a few cm^2, radiation hardened SiO_2 passivation layer	Efficiency
Minimized SiO_2 thickness, simplified electronics	Threshold
TE converter on top of the chip	Tissue Equivalence

Finally, the concept of simultaneous macro and microdosimetry using a MOSFET was introduced by Rosenfeld in 1996 [71]. For macrodosimetry, the total dose was measured using threshold voltage changes arising from radiation-induced buildup of gate oxide charge. Simultaneously, the reverse-biased drain junction may be used for microdosimetry. Thus, silicon microdosimetry offers the possibility of integrating multiple detector types along with preamplifiers and processing circuitry onto a single small device.

2.3.3 Other methods

For completeness, a few less commonly used experimental microdosimetry methods are briefly described in the following. All the methods, except for microstrip gas counters, are directed at providing more detailed track information than is available using site based detectors such as the TEPC and silicon diode detectors. Recent useful reviews of detector developments are provided by Bartlett [72] and Barthe [73]. These reviews concentrate on neutron personal dosemeters which often use microdosimeter type detectors.

2.3.3.1 Microstrip Gas Counters (MSGC)

MSGCs are similar to multiwire proportional chambers except that the wires have been replaced by alternating anode and cathode strips formed on a supporting substrate. A drift electrode ~1-4 mm above the substrate (maintained at the same potential as the cathode) defines the gas volume. These devices are in the early stages of development for microdosimetry having been invented in 1988 by Oed [74]. The principle features of MSGCs of value to experimental microdosimetry are high count rate capability and high spatial resolution [75, 76]. Like the silicon microdosimeter, the tissue equivalence of the device materials (such as substrate) and the effect of the RPP device geometry on microdosimetric spectra need to be evaluated. Thus, some of the work presented in this thesis may have value in the development of MSGCs.

2.3.3.2 Cloud Chambers

Low-pressure cloud chambers have been employed in the study of track structures [77-79]. A three dimensional pattern of droplets created by individual ionizations may be resolved and stereoscopically photographed [79]. Cloud chamber dosimetry provides rich detail on the location of individual ionizations within the gas. However, it is a difficult process generally restricted to the research domain.

2.3.3.3 Optical Ionization Chamber

The three dimensional distribution of individual ionizations with a gas may also be determined using an optical ionization chamber proposed by Turner [80]. The electrons in the particle track are made to oscillate rapidly by the application of an external, short duration, high-voltage electric field. The excited electrons produce additional ionization and electronic excitation of the gas molecules in their immediate vicinity leading to copious light emission (fluorescence) from the gas allowing the location of the electrons to be determined. Two digital cameras perpendicular to one another record the light emission. Turner [80] predicts a resolution capability of ~10 nm, based on a position uncertainty of ~1mm at a gas pressure of 5 torr. This may prove a useful tool in the emerging field of nanodosimetry as well as for track structure analysis.

2.3.3.4 Autoradiography

Experimental microdosimetry has been criticized for using detector shapes which may not be representative of the real tissue. This problem is particularly manifest in boron neutron capture therapy where traditional microdosimetry fails to represent realistic tissue architecture and boron distribution. Zamenhof and Solares [81] addressed the issue in the development of high resolution quantitative autoradiography (HRQAR) combined with a novel 2D Monte Carlo simulation. HRQAR uses a 0.8 μm thick film of Lexan as the track detection medium placed in intimate contact with an equally thin tissue sample. Image processing techniques applied to the track detector film following exposure to thermal neutrons identify the boron atoms. Their hypothesis is that a full 3D characterization of the cellular architecture and the corresponding B-10 distribution can be mimicked by sectioning a single plane through many cells in the tumor matrix, deriving the boron distribution within this single plane by HRQAR, and performing a 2D Monte Carlo calculation within this plane over many cell sections to obtain the desired microdosimetric parameters. A spatial resolution of 1-2 μm and a sensitivity of 1 ppm boron may be achieved, although the process is very time consuming, taking 8 days for the HRQAR. In summary, autoradiography is a specialized time-consuming technique with excellent results for specific applications.

2.3.3.5 Three Dimensional Optical Random Access Memories (3D ORAM)

Three dimensional optical random access memories (3D ORAM) are bistable photochromic materials that can be converted from the stable non-fluorescent form to the quasi-stable fluorescent form (and vice versa) via two photon absorption using

intersecting laser beams. The use of this material for real-time dosimetry was first proposed by Moscovitch [82]. Theoretical calculations by Moscovitch and Emfietzoglou [83, 84] indicated that the energy deposited along a track due to passage of a charged particle through this material results in a local de-excitation of the less stable isomer. The track characteristics depend on the particle type and energy and thus dosimeters based on these materials could provide detailed information on particle type and energy distribution for neutrons and heavy charged particles [84, 85].

Readshaw [86] and Phillips [85] used a photochromic molecule spirobenzopyran (SB) embedded in polymethyl methacrylate (PMMA) to construct track detector films 60 μm thick. The material was read using a confocal laser scanning microscope. Successive two dimensional images formed by scanning across the focal planned (depth profiles) are layered to provide a three dimensional image. Image resolution of the track is approximately 1 μm in the scanning plane and several μm in the depth. Phillips [85] confirmed a fluorescent intensity that is proportional to dose over several orders of magnitude. In the range of energies investigated, the energy per nucleon can be determined from the width of the depth profile. Furthermore, the fluorescent intensity at a fixed dose varies with particle type and energy, a property that may prove useful for particle identification.

3D ORAM is in the early stages of development but promises to be a useful tool for microdosimetry studies of solid-state particle tracks.

2.3.4 Summary of Experimental Microdosimetry Methods

Particle track detection methods such as 3D ORAM, autoradiography, cloud chambers and optical ionization chambers are generally difficult and expensive experimental tools that are operationally time consuming. Site based devices such as the TEPC and the silicon microdosimeter are easier to use, generally applicable and quickly provide microdosimetric spectra and parameters. In this work, we are primarily focussed on developing a silicon based microdosimeter with performance characteristics that are competitive with the TEPC. The ultimate goal is to develop a device that exceeds the usefulness and performance of the TEPC for regional microdosimetry.

Table 2.2. Comparison of proportional counter to silicon microdosimeter

Category	Parameter	Proportional Counter	Silicon microdosimeter
Detector performance	Energy Resolution (Note ii)	Moderate	Moderate,
	Low energy sensitivity (Note iii)	Excellent, Single Ionizations, Minimum y = 0.05 keV/μm	Moderate, Minimum y = 0.4 keV/μm
	Sensitive volume definition	Good	Moderate
	Tissue Equivalence	Good	Moderate
	Radiation Hardness	Excellent	Moderate
	Spatial Resolution	Poor, 2.5 cm. 0.5 mm best case [22]	Excellent, 1 μm.
	Wall effect Immunity	Poor	Excellent
	Model cell array	No	Yes
	Shape design flexibility	Moderate	Moderate
Ease of Use	Calibration	Simple	Simple
	Cost	High	Low
	Portability	Moderate	Excellent
	System Complexity	Poor: Requires HV supply and gas supply.	Good: only requires low voltage supply.
	In-vivo use	No	Yes
	Integration	Poor	Excellent

Notes:

i) The shaded areas identify the best performance of the two devices for each parameter.

ii) See Figure 2.6 for energy and preamplifier noise dependence. The silicon microdosimeter has potentially better energy resolution (lower W=3.62 eVc.f. 30 eV, better Fano factor and no gas multiplication but needs low preamplifier noise)

iii) Assuming 2.5 cm spherical TEPC with simulated diameter d = 1μm capable of detecting single ionizations and 1 μm^3 cubic silicon microdosimeter with ultra low preamplifier noise ~15 erms. See section 4.5.6 for discussion of ultimate noise performance of silicon microdosimeter.

A comparison of the typical performance of the TEPC and the silicon microdosimeter is shown in Table 2.2 based on the previous sections discussion. Parameters for comparison are subdivided into "detector performance" criteria and "ease of use" criteria. The best performance for each criterion is shaded gray.

Energy resolution is dependent on preamplifier noise and energy deposited as indicated by equations (2.20) and (2.29). Figure 2.6 shows a resolution comparison of the TEPC and silicon microdosimeter as a function of energy deposited (T) for several preamplifier noise levels. For the TEPC, resolution is dominated by Fano and gas multiplication effects which vary according to $T^{-0.5}$ whilst for the silicon microdosimeter preamplifier noise is the dominant factor which varies according to T^{-1}. This accounts for the differing slopes in Figure 2.6.

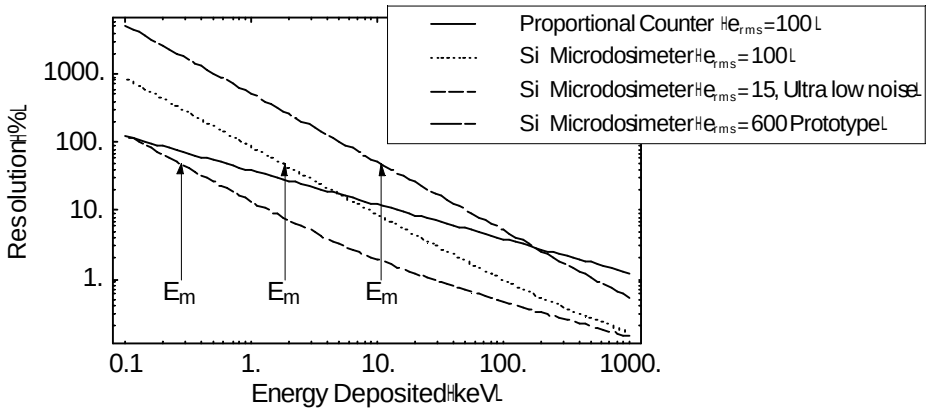


Figure 2.6. Resolution of proportional counter and silicon microdosimeter as a function of energy deposited for several preamplifier noise levels. Calculated using equations (2.20) and (2.29) with $g=10^4$,M=0.6, F=0.3,W=30 eV, R_{rest}=0 (TEPC), F=0.3, W=3.62 eV (Si microdosimeter) Also shown is the minimum energy measurable (E_m lower noise cutoff from equations (2.14) and (2.26)). The E_m for the proportional counter is not shown since it is very low (single ionization).

At higher energies the preamplifier noise is a less significant component of resolution and the theoretical contributions such as the Fano factor and gas multiplication are more significant. Therefore, the silicon microdosimeter has better resolution at higher energies since its theoretical resolution contributions (lower Fano, no gas multiplication) are smaller than the TEPC. The silicon detector's higher preamplifier noise component creates poor resolution at low energies. The minimum energy measurable, E_m, as provided by equations (2.14) and (2.26) is shown in Figure 2.6. The worst case resolution for the silicon detector at E_m is given by substituting equation (2.26) into (2.29). Noting that the Fano contribution is negligible at low energies, we obtain a resolution of 47% at E_m. For an equal preamplifier noise of e_{rms} equal to 100 eV, the silicon microdosimeter resolution is better for deposited energies greater than 4.9 keV. Thus, if a sufficiently low e_{rms} is obtained in the silicon microdosimeter design then the resolution will be better than the proportional counter over most of the measurable energy range. Furthermore, reducing e_{rms} is essential for obtaining an adequate low energy cutoff. Although the potential of the silicon microdosimeter in terms of resolution exceeds the proportional counter we classify both as moderate in Table 2.2 based on current performance as given by the prototype microdosimeter described in this work (e_{rms}=600).

The TEPC offers better performance in terms of low energy sensitivity since it is capable of single ionization detection. Sensitive volume definition is good (ignoring the wall effect) and tissue equivalence and radiation hardness are better than the silicon

microdosimeter. For both detectors, the ability to shape the sensitive volume is limited by construction methods. Silicon technology is capable of manufacturing most shapes except for the spherical shape. In all other categories, particularly those relating to ease of use, the silicon detector offers benefits. A higher spatial resolution is especially beneficial in many radiotherapy applications such as proton and heavy ion therapy.

Measurement in the solid phase offers the advantages of removing the wall effect, improving spatial resolution, reducing system size, and portability and offering the ability to model an array of cells. Kliauga [22] in an analysis of the limitations of experimental microdosimetry, recognized the restriction of measurements to the gas phase. He wrote, “Although there is a wide range of opinion as to how serious this constraint is in practice, there is no question that this is a valid issue for development in future research".

Theoretical calculations by Zaider [87, 88] have shown significant phase effects in the estimation of microdosimetric parameters. Calculations of the energy deposition from 30 keV electrons in water vapor and condensed water sites (d=1 μm) gave a 50% higher mean specific energy in condensed water relative to water vapor with commensurately large differences in the lineal energy spectra. Zaider's recent paper [88] stresses the need for development of a solid state microdosimeter suggesting a TE polymer solid state spectrometer as a possible device. To improve signal to noise internal gain could be achieved by operating at a high bias voltage in proportional counter mode rather than as an ionization chamber. Stoner [89] obtained gains of more than 1000 using 7.5 μm thick Kapton foil sheets although recombination is high so that only a maximum of 10% of carriers produced by an ion beam are collected. In this work, we contend that a silicon microdosimeter is a viable alternative (in which close to 100% of carriers produced by an ion beam may be collected), provided very low energy measurements are not required for the applications considered.

The rapidly improving integration capability of silicon technology offers the possibility of reduced system cost, increased reliability and improved performance. Such small systems are capable of in-vivo operation. Moreover, macrodosimetric detectors such as MOSFETs [71] and track structure analysis detectors [90] may be integrated onto the same device to provide high-resolution multi-function capability. However, as a first step towards acceptance a silicon microdosimeter must be developed.

2.4 Applications of Experimental Microdosimetry

The aim of this work is primarily focussed on technology development. Therefore, this section on applications will be a brief introduction. Note that high LET radiotherapy is the primary application pursued in this work. Aside from the discussion below, the various high LET therapy modalities are also discussed in more detail in later chapters.

2.4.1 Radiobiology

The link between experimental microdosimetry, based on regional or site measurements, and radiobiology was forged by Kellerer and Rossi in 1972 with the publication of the Theory of Dual Radiation Action (TDRA) [18]. The theory is based on a number of assumptions, including (from Goodhead [12]):

1. When a biological cell is exposed to ionizing radiation, the radiation produces *sublesions* within the cell and the number of sublesions is directly proportional to the energy imparted by the radiation.
2. A biological *lesion* is formed when two sublesions combine with one another, possibly over relatively long distances on a subcellular scale.
3. Each lesion has a fixed probability of leading to a given biological effect.

Most importantly, the original theory was developed in a site model form compatible with TEPC measurements in simple spherical or cylindrical shapes. This leads to the final simplifying assumption:

4. All pairs of sublesions within a sensitive site have an equal probability of combining and a zero probability outside the site.

Based on these assumptions the TDRA proposes that the mean number of lesions *e* after an absorbed dose *D* is:

$$e(D) = k(z\,D + D^2) \tag{2.32}$$

where k is a constant for a given biological system and z is the dose average of the specific energy (also written as z_D). The first term accounts for lesions formed by two sublesions that are produced in the same event (intra-track action) and the second term pertains to the case of sublesions combining from two separate events (inter-track action).

The relative biological effectiveness (RBE or R) of a high LET radiation *H*, relative to a low LET radiation *L*, is defined by:

$$R = \frac{D_L}{D_H} \tag{2.33}$$

where D_L and D_H are the absorbed doses of the two radiations causing equal effect. Utilizing equation (2.32) and equality of effect yields:

$$k(z_H D_H + D_H^2) = k(z_L D_L + D_L^2) \tag{2.34}$$

Substituting (2.34) into (2.33) gives:

$$R = \frac{1}{2D_H}\left[\sqrt{z_L^2 + 4D_H(z_H + D_H)} - z_L\right] \tag{2.35}$$

The site model formulation of TDRA correctly predicts the inverse square root variation of RBE with dose (i.e. $z_L << D_H << z_H$, $R \approx \sqrt{z_H / D_H}$). The domain in which the specific energy should be considered depends upon the average distance over which sublesions combine. Microdosimetric measurements of the neutron beams employed in biological experiments indicate that the sites typically have diameters of 0.2-2 μm [12, 18].

In the late seventies, it was recognized that the site model formulation of TDRA could not account for the effects of certain radiations such as soft X-rays [91, 92] or correlated pairs of charged particles [93, 94]. For instance, in the molecular ion beam experiment, it was found that if pairs of deuterons are separated by 90 nm the effect on the reproductive capability of V79 cells was significantly different then for a single particle with twice the LET. Yet the microdosimetric spectra for the two kinds of radiation are identical in volumes of the order of a few microns.

The TDRA was generalized by Kellerer and Rossi in 1978 with the introduction of the distance model formulation [95]. The generalized TDRA relaxed the site model assumption (4 above) and replaced it with:

4a. The probability *g(x)* of sublesions combining is a function of their distance apart *x*.

According to the distance model *z* in equation (2.32) becomes (p 242 Rossi [1]):

$$z = \int_0^\infty t(x)g(x)dx \tag{2.36}$$

where $t(x)$ is the proximity function (chapter V Rossi [1]) specifying the spatial properties of the deposition of radiation energy and $g(x)$ is the probability that two energy transfers separated by a distance x combine to form a lesion. The proximity function is a measure of the probability that the energy transfer points are separated by a distance x. On the other hand, the dose averaged specific energy is given by:

$$\bar{z}_D = \int_0^\infty t(x)\left[\frac{f_p(x)}{4\pi x^2 r}\right]dx \tag{2.37}$$

where $f_p(x)$ is the point pair distance distribution (ppdd) of the site where specific energy is measured. Comparing the above two equations indicates that a measurement of $\bar{z}_D$ yields the parameter z only if the microdosimeter and cell sensitive site have the same ppdd. That is;

$$g(x) = \frac{f_p(x)}{4\pi x^2 r} \tag{2.38}$$

Comparisons of experimentally determined $g(x)$ with the function given by the right-hand side of the above equation indicate that the spherical TEPC is a poor representation of the sensitive site geometry [94]. Finding a practically realizable detector structure that satisfies equation (2.38) may be difficult. However, Zaider and Rossi [96] have shown that that any function $g(x)$ may be represented as the algebraic superposition of ppdd's corresponding to spherical objects. Thus, the quantity z may be predicted from microdosimetric spectra measured in a series of spherical sites of different diameters. Implementations of these ideas suggest that 2-3 sites are sufficient. The site size required is very small of the order of tens of nanometres, which has consequently driven a demand for nanodosimetric detectors. Variance-covariance techniques (see section IV.5.2 Rossi [1]) may be used for measurements of $\bar{y}_D$ and $\bar{z}_D$ in such small volumes.

Further improvements to the TDRA include the compound dual radiation action theory (CRDA) developed in an attempt to correlate sublesions and lesions with biological entities such as chromosome breaks and chromosome exchange aberrations (p237, Rossi and Zaider [1]). Note that the validity of the TDRA and CDRA are open to much debate with research actively being pursued in alternative radiobiological models such as Goodhead's repair models [12] and work by Zaider and Katz on track structure theory

[97]. Thus, the application of regional experimental microdosimetry as a predictive tool in radiobiology is questionable and requires further research. Silicon based detectors with their flexible geometrical structures and greater design scope may offer new detectors capable of testing track structure theory as well as providing more traditional site based measurements.

2.4.2 Radiotherapy Applications

Microdosimetric methods are especially useful for high LET radiation therapy due to the requirement of quantitative specification of radiation quality. The high LET modalities in which microdosimetric methods have been applied include fast neutron therapy (FNT), boron neutron capture therapy (BNCT), proton therapy (at and beyond the Bragg peak), heavy ion therapy and negative pi-mesons (pions). The silicon microdosimeter developed in this work is tested in the more common modalities of FNT, BNCT and proton therapy.

To gauge the potential importance of these therapies, Wambersie [98] estimated the potential patient recruitment for high LET radiation therapy as about 1-1.5% of the total population. He assumed that cancer incidence is 25-30% of the population, 50% of patients require radiotherapy and about 10% of radiotherapy patients would derive some benefit from high LET radiation. There are about 30000 new cancer cases per year and per million inhabitants in the developed countries. Thus, in Australia (population ~20 million) about 30000 patients per year may potentially benefit from high LET radiotherapy. At present there are about 17 clinical centers worldwide using FNT [98], 14 using proton therapy [99], 7 using BNCT, 3 using heavy ions [100] and only 2 pion therapy facilities [98].

The benefit of high LET radiation therapy, over traditional radiation therapy, is based on two main considerations:

1. Except for protons, the LET is considerably higher than that of electrons. This is important because of the oxygen effect: At low LET, the sensitivity of aerated cells is 3 times greater than anoxic cells whilst at higher LET the difference is much less and the factor approaches 1 for an LET > 100 keV/μm [1]. Tumors are generally poorly oxygenated and thus at higher LETs a greater tumor dose may be delivered for the same normal tissue dose.

2. Except for FNT, the spatial specificity of dose delivery is improved with high LET therapy. The depth-dose profile due to the particle Bragg peak offers improved tumor to tissue absorbed doses. For BNCT, particular specificity may be gained due to the local deposition of high boron concentrations within a tumor.

For low LET radiations, absorbed dose is a good predictor of biological effect since the RBE does not vary significantly between X-rays, γ-rays or electrons in the energy range between about 1 to 50 MeV [98] and does not vary with position within the irradiated tissue. Thus, simple absorbed dose measurements suffice and microdosimetric studies are generally not needed for low LET radiations.

In contrast high LET radiations employing heavier particles (neutrons, protons, heavier ions, negative pi mesons) provide an RBE exceeding unity that may vary significantly with depth and beam parameters such as particle energy. For example the RBE of a fast neutron beam may approach 3 for the dose levels and biological endpoints relevant for therapy [98]. A problem specific to high LET radiations is the characterization of RBE spatial variation for a given beam compared to photons. Radiobiological studies such as intestinal crypt colony assay in mice [101] are typically used for RBE studies. However, radiobiological studies are prone to uncertainty due to their difficulty and the large number of parameters involved. Microdosimetric spectrum measurements are a valuable supplement to radiobiological studies in the characterization of RBE. Variations in microdosimetric spectra can identify regions or conditions in which more detailed radiobiological studies may be necessary. Considerable experimental time may be saved by such a protocol.

Mijnheer [102] calculated that the accuracy with which RBE must be calculated for neutron therapy is quite high (±3.5% 1 σ) and at least as stringent as for conventional therapy because of the steep rise and proximity of the curves relating tumor control and normal tissue complications to absorbed dose. The applied RBE directly influences the effective dose delivered to the patient and thus the accuracy requirement for dose also applies to RBE [98].

Calculation of RBE using equation (2.35) is not easily performed in experimental microdosimetry due to the difficulty in estimating the parameter z as discussed in the previous section. Instead empirical approaches have been developed based on calculating parameters from the microdosimetric spectrum $d(y)$ that correlate with RBE.

The parameter $\bar{y}_D$ is a measure of biological effectiveness (i.e. $\bar{y}_D \alpha$ R) under the conditions of low dose (quadratic term neglected in equation (2.32)), and minimal saturation effects. In an effort to improve the relationship between $\bar{y}_d$ and observed biological effects, Kellerer and Rossi [18] proposed a saturation correction to account for the excessive ionization density of high lineal energy particles over and above requirements for cell death. The saturation corrected dose mean lineal energy y^* is given by:

$$y^* = \frac{\int_0^\infty y_{sat} y f(y) dy}{\int_0^\infty y f(y) dy} \tag{2.39}$$

where the saturation correction function y_{sat} is:

$$y_{sat} = \frac{y_0^2}{y}(1 - e^{-(y/y_0)^2}) \tag{2.40}$$

with y_0 = 125 keV/μm. Several studies in FNT beams have demonstrated that RBE values calculated from the saturation corrected dose mean lineal energy y^* are fairly well correlated with RBE data derived from radiobiological data [103-105]. Microdosimetric spectra have been extensively used to investigate radiation quality of neutron therapy facilities [106-108]. Comparing the clinical performance of various facilities requires knowledge of the RBE of beams under consideration. Several researchers have compared the radiation quality of neutron therapy facilities using microdosimetric measurements [109-111]. These results have shown that microdosimetric measurements, despite there empirical nature, are capable of discerning even subtle changes in the radiation field and provide insight into the interpretation of such changes.

More references on the application of microdosimetry to FNT, proton therapy, heavy ion therapy and pion therapy may be found in ICRU report 36 (p69 [11]) and Rossi and Zaiders textbook [1] and these will not be repeated here. The specific role of microdosimetry in BNCT, FNT and proton therapy is discussed in more detail in chapters 7, 8 and 9, respectively.

2.4.3 Radiation Protection Applications

Radiation protection applications are primarily concerned with estimating the dose equivalent (*H*). For particles with a range of LET (*L*) the dose equivalent is defined as:

$$H = \int_0^\infty Q(L)D(L)dL \tag{2.41}$$

where $D(L)=Dd(L)$ is the dose distribution as a function of LET (unnormalized version of $d(L)$) and $Q(L)$ is a quality factor which weights the dose according to biological effect. Various forms of $Q(L)$ have been defined but the standard most recently adopted by the ICRU and ICRP is the definition of $Q(L)$ presented in ICRP publication 60 ([53] and p266 Rossi [1]) and shown in Figure 2.7:

$$Q(L) = \begin{cases} 1 & L < 10 \text{ keV}/\mu\text{m} \\ 0.32L - 2.2 & 10 \le L \le 100 \text{ keV}/\mu\text{m} \\ 300L^{-1/2} & L > 100 \text{ keV}/\mu\text{m} \end{cases} \tag{2.42}$$

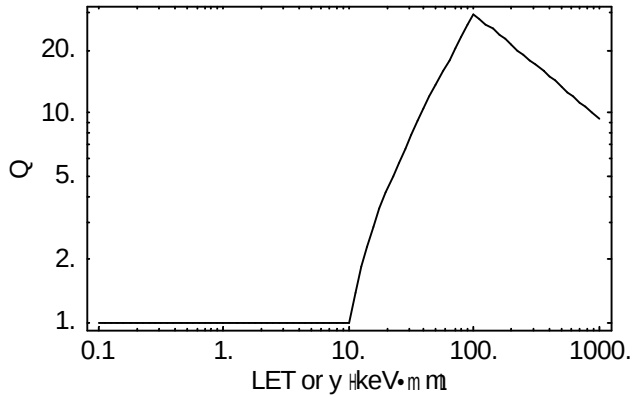


Figure 2.7. Quality factor *Q*(*L*) as defined by ICRP publication 60 [53].

Hartmann [112] considered 8 methods of deriving *H* from microdosimetric data obtained using a TEPC and concluded that all of them had sufficient accuracy for the commonly encountered neutron energy range of between 0.5 and 20 MeV. Note that the accuracy requirements are much less stringent in radiation protection compared to radiotherapy. An overall uncertainty of 30% is considered permissible [113] since many larger uncertainties exist in the application of radiation protection (e.g. position of best measurement, relationship to human body dose). The simplest method of determining *H* uses the expression $\int Q(y)D(y)dy$ based on the approximation $y \sim L$. Alternatively, Rossi [1] presents a method for determining $D(L)$ from $D(y)$. A more direct assessment of *H* may then be performed via equation (2.41) and (2.42).

In radiation environments that are essentially unknown or with high energy components, experimental microdosimetry is an important, if not indispensable, tool. However, at low energies in more common environments, factors such as simplicity, cost and portability often favor other approaches. Thus, the employment of microdosimeters in radiation protection has not been widespread despite the possibility of improved accuracy and versatility over current methods. The TEPC has also been known to suffer from aging effects mostly due to chemical gas interactions with material, gas cracking and outgasing of tissue equivalent materials. Despite these disadvantages, portable instruments using TEPCs have been developed, generally employing microprocessors to analyze and control device operation [114, 115].

A silicon based microdosimeter with its construction simplicity, capacity for system integration, and elimination of gas systems offers many benefits in radiation protection applications. However, several fundamental problems inherent in both silicon and TEPC microdosimeter systems must be recognized. At low neutron energies (<100 keV) the short range of recoils can cause substantial errors since the derivation of $D(L)$ from $D(y)$ assumes complete traversal of the sensitive volume. For a TEPC with a 1 μm diameter protons of energy less than 100 keV will not completely traverse the diameter. In addition, microdosimetric measurements in radiation protection are time consuming because of low count rates and may be incapable of measuring even slow changes in radiation quality. Rossi (p271 [1]) states that area monitoring measurements frequently use 10 cm diameter counters simulating 1 μm diameter sites. Typically, counting rates of 500/hr are observed in frequently occupied zones near reactors assuming an ambient dose equivalent rate of around 10 μSv/hr and an event frequency for fission neutrons of about 0.1 per Gy [1]. Kunz [115] estimated that as few as 16 channels (empirically determined width) are needed in the $d(y)$ spectrum (varying width). Even with this small number of channels, several hours may be required to obtain an adequate spectrum.

2.4.4 Space applications and Radiation Effects on Microelectronics

In a manner analogous to biological cell death, electronic memory cells may undergo state changes if sufficient energy is deposited in the sensitive region of the cell. The sensitive region is localized around the depletion region of reverse-biased p-n junctions. The first evidence of single event upsets (SEU) in memory cells was observed in 1975 by Binder [116] although the effect had been predicted in 1962 by Wallmark and

Marcus [117]. Since then the effect has been extensively studied as testified by the large number of IEEE Nuclear Science journal publications devoted to SEU.

Radiation effects on electronics are more common at high altitudes (avionics) and in space. Moreover, higher radiation levels in space naturally increase the biological risk in manned missions. To study the space environment, TEPCs have been flown on board the space shuttle [118] and Mir space station [119]. The recorded microdosimetric spectra have been used to test radiation transport models and calculations [118]. The development and testing of such models may provide a system for predicting radiation quality during the spacecraft design phase. Microdosimetric measurements have similarly been performed in aircraft in order to quantify radiation effects on personnel from secondary cosmic radiation [120, 121].

Microdosimetric principles and techniques have been applied to several SEU problems based on the previously discussed correlation (see section 2.3.2.3) between SEU and biological cell death (e.g. [122-124] and p291 Rossi [1]). This thesis directly exploits the close link between microdosimetry and SEU by employing a device originally designed to study radiation effects on microelectronics.

2.5 Summary: Key Problems in Silicon Microdosimetry

Based on the review presented in this chapter and summarized earlier in section 2.3.4 we may identify the essential problems impeding the development of silicon microdosimetry.

1. The *requirements* of silicon microdosimetry and particularly the influence of detector *shape* have not been dealt with thoroughly in the literature. This issue will be addressed in chapter 3.

2. The *low noise* requirements on the silicon microdosimeter are demanding and particular attention must be made in the design process to minimize electronic noise. A system noise model and optimization procedure is described in chapter 4.

3. The *tissue equivalence* of silicon microdosimeters has not been addressed in detail in the literature. Chapter 5 provides methods for converting silicon lineal energy spectra into TE spectra.

4. The *sensitive volume boundary* suffers from uncertainty in almost all previous attempts at silicon microdosimetry. Chapter 6 seeks to address the difficult issue of

characterizing the sensitive volume boundary and charge collection efficiency. The use of a parallel array of p-n junction diodes using silicon-on-oxide (SOI) technology, as described in chapter 4, is directed towards improving the definition of the boundary. *Radiation damage* may affect the performance of the silicon microdosimeter by reducing charge collection. This issue is intimately linked to the characterization of charge collection and thus will also be addressed in chapter 6.

If these problems are adequately addressed the many advantages of silicon microdosimetry may prove useful in future and current applications. These include:

- Good energy resolution
- High spatial resolution
- High count rate capability
- Solid-state measurement, wall effect immunity
- In-vivo design
- Manufacturable with good quality control
- Simple, low cost system
- Portable
- Enables integration of multiple detectors, preamplifiers and signal processing components.

3. Silicon Microdosimeter Requirements and Shape Analysis

This chapter analyses the requirements for the microdosimeter. Applications are presented followed by an analysis of the sources of fluctuations in microdosimetry. An extensive analysis of detector shape considerations is presented. Finally the microdosimeter requirements are summarised.

3.1 Intended Applications

Requirements are dictated by the intended applications. The use of a silicon based detector immediately places constraints on the range of applications for which such a device may be suitable. In particular, the interaction of radiation and the generation of secondary charged particles will differ in a given volume of silicon versus a tissue volume. In general, the silicon device will only be appropriate in radiation environments for which the dominant secondary charged particles produced in tissue have a range that is much longer than the mean chord length of the detector volume. That is, most events within the tissue volume must be crossers or stoppers as opposed to starters or insiders. The crossers or stoppers are generated by a tissue-equivalent converter on top of the detector. The definition of crossers, stoppers, starters and insiders is shown in Figure 3.1.

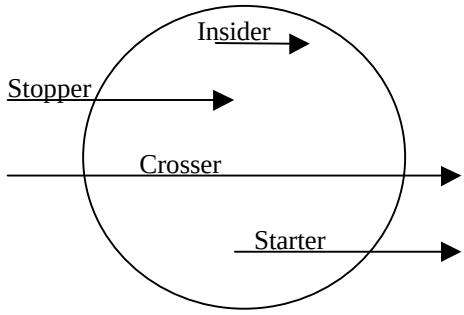


Figure 3.1. Definition of rays interacting with a sensitive volume

The extent to which the range of the secondary particles must exceed the dimensions of the detector volume is dependent on the application and the accuracy of the desired measurement. Typical ranges of recoil products in various radiation fields are shown in Table 3.1. In radiation protection, microdosimetric spectra may be used to determine the effective dose equivalent. Large uncertainties exist in the calculation method, which

relaxes the demands on high measurement accuracy. Measurement uncertainties of less than 30% are acceptable for radiation protection applications (p84, p251 [1]). Conversely, absorbed dose measurements in radiotherapy have a requirement for better than 5% accuracy due to the proximity of the curves relating tumor control and normal tissue complications to absorbed dose [98].

Table 3.1. Typical ranges of recoil products in various radiation fields

Environment	Typical Products	Range/μm(Note2)
Fast Neutron (14 MeV), (Note1)	7 MeV protons	615
	3.5 MeV alpha	21.2
	0.6 MeV oxygen	1.6
	1.6 MeV carbon	3.3
BNCT	1.47 MeV alpha	7.7
	0.84 MeV lithium	4.1
	0.59 MeV nitrogen	10.5
	0.04 MeV carbon	0.2

Note 1: Calculated by integrating initial spectrum of charge particles from Caswell and Coyne.[125]
Note 2: Range data from SRIM [126] for ICRU striated muscle.

The main applications discussed in this work are several high LET radiation oncology modalities including proton therapy, fast neutron therapy and boron neutron capture therapy. For each of these applications, we should consider the errors introduced by using the silicon/converter structure as opposed to the traditional spherical proportional chamber. The errors due to geometrical considerations need to be compared to other sources of variation in the measurement to gauge their significance. Therefore, an analysis of the sources of fluctuations in regional microdosimetry is required.

3.2 Sources of Fluctuations in Regional Microdosimetry

The shape of the pulse height distribution obtained by a microdosimeter is influenced by several random processes. Analysis by Kellerer [127] and Rossi [1] uses the concept of relative variance to quantify the relative significance of various processes. The relative variance (V) of a probability distribution, $f(x)$ is a measure of the width of the distribution and is defined as:

$$V = \frac{s^2}{m_1^2} = \frac{m_2}{m_1^2} - 1 \tag{3.1}$$

where s^2 is the variance and m_1 and m_2 are the first and second moments of $f(x)$.

The total relative variance (V_T) of the measured pulse height distribution is the sum of the relative variance of several statistical factors each characterized by a probability distribution. For single event spectrum, the following main distributions are evident (with relative variance symbol in brackets):

i) The distribution of *path lengths* traversed through the site. (V_t)

ii) The distribution of *particle LET* .(V_L)

iii) The distribution of the *number of collisions*.(V_c)

iv) The distribution of *energy imparted in individual collisions*.(V_e)

v) The distribution of the *fraction of energy retained in the site* (not escaping as delta radiation). (V_d)

vi) The distribution of the *number of electron/hole pairs* (or ions) formed by particles of the same energy (the Fano factor). (V_f)

vii) The distribution due to *measurement electronic noise and other measurement phenomena*. (V_m)

The most common geometry for microdosimetric measurements is a spherical volume using a proportional counter. This is the only geometry with an isotropic response. Furthermore, the relative variance due to the varying path lengths (V_t) is conjectured to be the minimum for any geometry (although this is unproven) [128]. Integrating the chord length distribution, given in Table 3.2, yields a value of 1/8 for V_t under the condition of large track lengths. As the particle range approaches the site diameter V_t drops and approaches zero for very short tracks. For other shapes with non-isotropic response, such as our proposed silicon detector with a rectangular parallelepiped (RPP) geometry, we need to consider the influence of shape on V_t. Rossi (p 80 [1]) notes that frequently $V_t << V_T$ so that non-spherical counters may be used without significantly affecting the measurement. A detailed discussion of detector geometry influences on spectrum shape, microdosimetric quantities and relative variance is provided in the next section.

Most microdosimetric applications involve multi-particle complex radiation fields with varying LET. The relative LET variance (V_L) varies considerably from about 0.3 for Co

γ radiation to greater than 0.8 for high energy (>2MeV) neutrons [1]. It is a significant contribution to the total variance in neutron measurements.

Factors (iii-v) are three aspects of range and energy straggling. They are best characterized by experimental measurements with monoenergetic sources since they are very geometry and radiation type dependent. Monte-Carlo simulations such as SRIM [126] are also useful for quantify straggling effects.

Factors (vi and vii) are features of the particular measurement system used. The number of electron-hole pairs formed in a semiconductor for a given energy deposited is subject to variation. Not all of the energy deposited in a semiconductor (or gas) is used to break covalent bonds. If the partitioning of energy between phonon production (lattice vibration) and bond breaking were completely uncorrelated the process would be described by Poisson statistics. However, some correlation exists and Fano [43] introduced an empirical correction (*F*) to the Poisson relation to give the experimentally observed variance.

$$V_f = \frac{F}{n} \tag{3.2}$$

where *F* = Fano factor and n is the average number of electron-hole pairs. *F* is usually around 0.1 for Silicon [23] and the minimum *n* is around 1000 (for silicon detectors at the electronic noise level). Therefore, V_f is negligible in comparison to other sources of variation in a microdosimeter.

The electronic noise for a semiconductor microdosimeter is dominated by the preamplifier electronics, which typically have noise rms levels (s_{pa}) of around 5 keV.

$$V_m = \frac{s_{pa}^2}{E_m^2} \tag{3.3}$$

Thus for even moderate mean energies (E_m), V_m is negligible in comparison to other sources. Electronic noise will be discussed in detail in section 4.5 since it is particularly important for determining the low energy threshold of the system.

The total relative variance of a microdosimetric spectrum is [1]:

$$\begin{aligned} V_T &= V_L + V_t + V_s + V_f + V_m \\ &\approx V_L + V_t + V_s \end{aligned} \tag{3.4}$$

where V_s is the total relative variance due to straggling and we assume that measurement variations (V_f and V_m) are negligible. Ideally in a microdosimeter, one would like to minimize the variation due to path length variations (Vt). This is particularly important for a non-isotropic radiation incident on a non-spherical detector. Therefore, a thorough analysis of the importance of detector shape and path length variations follows.

3.3 Detector Shape Considerations

Usually the intent of experimental microdosimetry is to model the energy deposited in volumes that are similar to critical tissue components such as cells or cell nuclei. Such components are frequently modeled as oblate spheroids or more simplistically as spheres. A spheroid is an ellipsoid with two axis of equal length and it is oblate if the third axis is smaller then the common axis length. The cells are usually randomly orientated unless they are in a flattened state characteristic of a tissue culture. Thus, even with a directional radiation source, the average response is that of a single cell in an isotropic field.

Traditionally, microdosimeters using proportional counters have employed a spherical or cylindrical counter. The spherical counter is preferred for two main reasons; the sphere is the only volume with an isotropic response and it has the lowest known relative variance. Cylindrical counters have evolved due to their simpler electrode design. Such counters do not have an isotropic response and simulation of an isotropic response, by the rotation of the counter under a constant fluence, is generally impractical. Kellerer provides an excellent paper [129] outlining the criteria for the equivalence of spherical and cylindrical proportional counters in microdosimetry. This work will be discussed in detail since it provides a basis for the comparison of other shapes with such counters.

The processing capability of integrated circuit technology is based on planar lithographic processes. Thus, structures with plane surfaces such as rectangular parallelepipeds (RPP) and, less readily, cylinders or hemispheres are manufacturable. In this section, chord and segment length distributions are analyzed for several shapes. Criteria for the equivalence of RPPs (in particular cubes) with spheres are discussed. Finally we compare lineal energy spectra produced by various shapes and include the effects of straggling on such spectra. The overall aim of the study is to obtain optimal

design criteria for the geometry of a silicon based microdosimeter. It is important to understand the conditions under which a planar geometry detector (particularly RPP) is sufficiently similar in performance to a spherical detector.

3.3.1 Comparison of Chord Length Distributions

In order to compare the microdosimetric spectrum produced by a spherical counter with other shapes such as RPP, infinite slab, hemisphere or cylinder we need to first calculate the chord-length distribution for each shape.

Chord-length distributions (CLD) result when convex bodies are intercepted by random straight lines. Several types of randomness result from the intersection of straight lines and convex bodies. The main types considered in the literature (originally defined by Coleman [130, 131] with revisions by Kellerer [132]) include *m-randomness* or *isotropic uniform randomness* in which the body is exposed to a uniform isotropic field of infinite straight lines; *n-randomness* or *weighted randomness* in which the ray passes in a uniformly random direction through an independently uniformly random point in the interior of the body (sometimes also called *I-randomness* or interior randomness); and *l-randomness* or *two point randomness* in which the ray passes through two points chosen independently and uniformly in the interior of the particle. Typically *m-randomness* conditions are used for comparing microdosimetric detectors since they most closely resemble microdosimetric experimental situations.

A review of the basic concepts of geometrical probability required in the calculation of chord length distributions may be found in Kendall and Moran [133]. There have been several attempts to derive analytical expressions for CLDs in various geometrical shapes. Simple analytical expressions of the CLD for the sphere and the infinite slab have been calculated [133, 134]. Kellerer [128] derived the expression for general cylinders and Mader [128, 135] presented numerical solutions for these expressions. Kellerer [132] also derived the formulae for prolate and oblate spheroids. The CLD for a hemisphere was derived by Langworthy [136]. Coleman [131] and Bradford [137] have derived solutions for RPPs based on rectangular CLDs calculated by Coleman [130, 138] and a formalism developed by Kellerer [128] to convert two-dimensional distributions into three-dimensional expressions. Note, that Bradford's work contains typographical errors with corrections presented by Ziegler [139]. Borak [140] recently presented a Monte-Carlo method for computing μ-randomness distributions. Appendix

B contains a Mathematica [141] based notebook which calculates all the CLDs and other calculations relevant to the shape analysis. Each of the distributions (*f(s)*) in the notebook was verified by calculating the mean chord length (MCL=$\bar{l}$) via integration techniques and comparing with Cauchy's equation as follows.

$$\bar{l} = \frac{4V}{S} = \int_0^\infty s f(s) ds \tag{3.5}$$

where V = volume and S = surface area

Table 3.2 summarizes some of the main CLDs. Equations provided in the notebook are correct (verified using the above method), however, almost all the papers cited contain typographical equation errors.

Table 3.2. Summary of chord length distributions for various shapes

Shape	Chord length distribution, *f(s)*
Sphere [132]	$\frac{2s}{d^2}$ $0 < s < d$, d = diameter
Spheroid [132]	$\frac{2s}{c_1 d^2}\left[c_2 + \frac{\sqrt{1-e^2}}{4(e^{-2}-1)}\left\{\sqrt{\left\lvert\frac{d^2}{s^2}-1\right\rvert}\left(\frac{d^3}{s^3}+\frac{3d}{2s}\right)+\frac{3}{2}ci\left(\frac{d}{s}\right)\right\}\right]$ $ci(x) = \begin{cases}\cos^{-1}(x) & \text{for } 0 \le x \le 1\\ \cosh^{-1}(x) & \text{for } x > 1\end{cases}$ $c_1 = \frac{1}{2} + \frac{e^2}{2\sqrt{1-e^2}}ci\left(\frac{1}{e}\right), \quad c_2 = \frac{1}{4e^2} + \frac{3}{4}c_1$ d = diameter, e = elongation
Hemisphere [136]	$\frac{2s}{3p^2}H(r-s) + \frac{1}{pr}c1 + \frac{2r}{3ps^2}\left(c1 + 2\frac{r}{s}\left(\cos^{-1}\left(\frac{s}{2r}\right) - \frac{p}{2}H(r-s)\right)\right)$ $c_1 = \sqrt{1-\frac{s^2}{4r^2}}$ r = radius, H = step function
Cylinder	Very lengthy (see Mader [135], Kellerer [132] and Appendix B)
Infinite Slab [132]	0 for $s \le h$ $\frac{2h^2}{s^3}$ for $s > h$ h= thickness
Cube [130]	$8/(3ap)$ $x = 0$ $k(8x^3 - 3x^4)$ $0 < x \le 1$ $k(6p + 6x^4 - 1 - 8(2x^2+1)\sqrt{x^2-1})$ $1 < x \le \sqrt{2}$ $k(6p - 3x^4 - 5 + 8(x^2+1)\sqrt{x^2-2} - 24Tan^{-1}(\sqrt{x^2-2}))$ $\sqrt{2} < x \le \sqrt{3}$ 0 $x > \sqrt{3}$ where $x = s/a$, a = side length and $k=1/(3apx^3)$
RPP	Very lengthy(see Bradford [137] corrections Ziegler [139] Kellerer [132], AppendixB)

Figure 3.2 to Figure 3.6 shows the CLD under μ-randomness for various shapes with an equal mean chord length (2/3) for all shapes. The mean chord length and relative variance for each of the shapes is given in Table 3.3. The relative variance is higher then the sphere relative variance for all shapes. Figure 3.2 illustrates that the prolate spheroid with a lower relative variance is a better approximation to the sphere then the oblate spheroid. Langworthy [136] identified some interesting similarities between the chord length distribution for an oblate spheroid, with $d=2r_{hemi}$ and elongation=0.5, and the hemisphere as shown in Figure 3.6 with the shapes illustrated in Figure 3.7. The distributions are remarkably close for $s>r_{hemi}$. For $s<r_{hemi}$ the functions are quite linear although the hemisphere exhibits a non-zero termination at $s=0$. Langworthy conjectures that all figures with dihedral corners such as cylinders, RPPs and hemispheres have a non-zero density at $s=0$. Furthermore, the oblate spheroid ($e=0.5$) and hemisphere have identical CLDs for unidirectional radiation parallel to the primary axis. This is evident on examination of Figure 3.7 by a simple geometrical argument. If we align at their midpoints chords in the hemisphere which are parallel to the x-axis then we obtain the spheroid shape. The importance of these results is that the hemisphere is a good approximation for modeling oblate spheroids ($e=0.5$) which in turn may be used to model a cell nucleus or cell. It is conceivable that a hemisphere could be constructed using integrated circuit (IC) processing methods. Alternatively, it may be possible to imitate the behavior of a hemisphere by using a number of different thickness RPP volumes connected electrically in parallel. This idea, however, will not be investigated in this work.

Figure 3.3 to Figure 3.5 indicate that the cube and cylinder with equal height and width have a CLD with a closer approximation to a sphere than shapes with none unity elongation. In both the cylinder and RPP as we increase elongation the CLD broadens as the maximum chord length increases and it appears that the coarse approximation to a sphere significantly worsens.

Th oblate cylinder or RPP is more amenable to IC processing and minimizes variance for directional radiation from a tissue equivalent converter located above the device. Figure 3.8 indicates the relative variance for various oblate shapes as a function of 1/elongation. For elongation>0.2 the spheroid offers the minimum variance. The RPP always has a higher relative variance than a cylinder of equivalent elongation, although

not significantly. Relative variance increases as the elongation differs from 1 due to a higher maximum chord length increasing the spread of possible chord lengths.

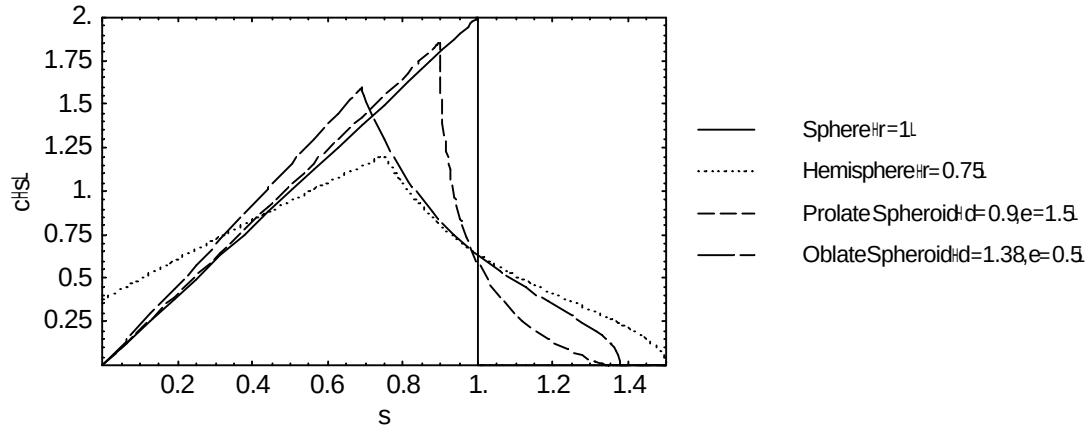


Figure 3.2. Comparison of CLD under μ-randomness for a sphere, hemisphere and spheroid. $\bar{l}$ **=2/3 in all cases.**

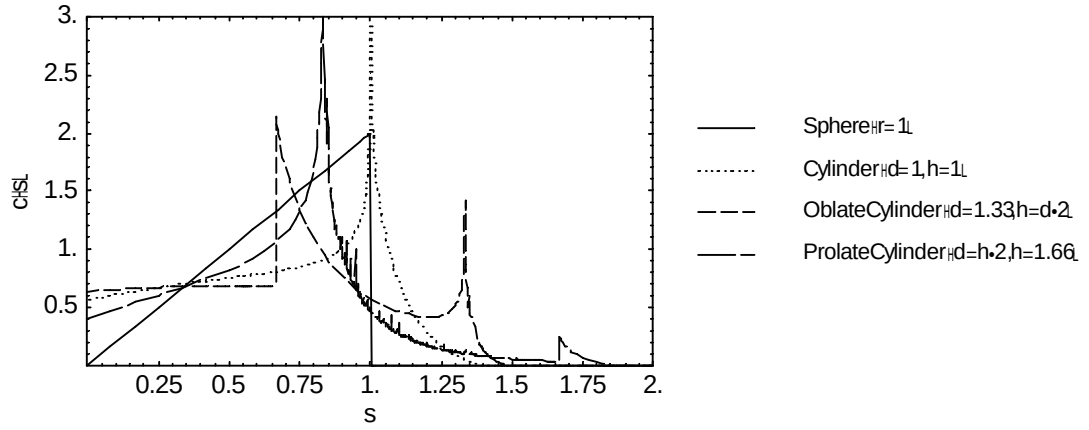


Figure 3.3. Comparison of CLD under μ-randomness for a sphere various cylinders. $\bar{l}$ **=2/3 in all cases. Numerical integration errors create small spikes in the cylinder CLDs.**

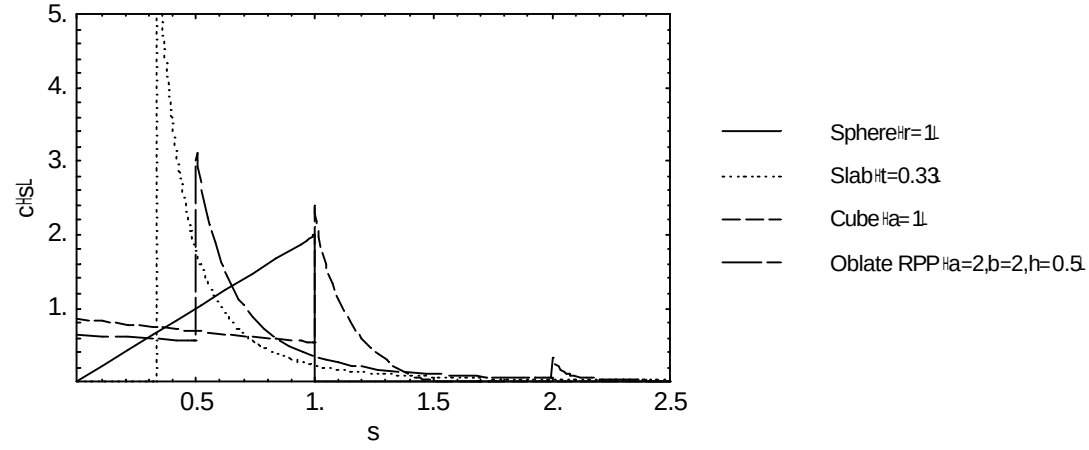


Figure 3.4. Comparison of CLD under μ-randomness for a sphere, infinite slab and RPP. $\bar{l}$ **=2/3 in all cases.**

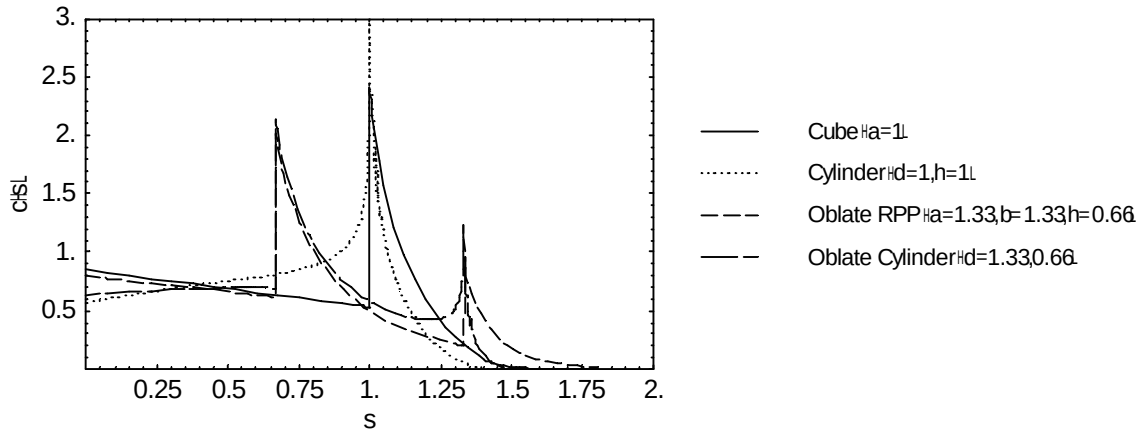


Figure 3.5. Comparison of CLD under μ-randomness for a cube, cylinder and oblate cylinder and oblate RPP. $\bar{l}$ **=2/3 in all cases.**

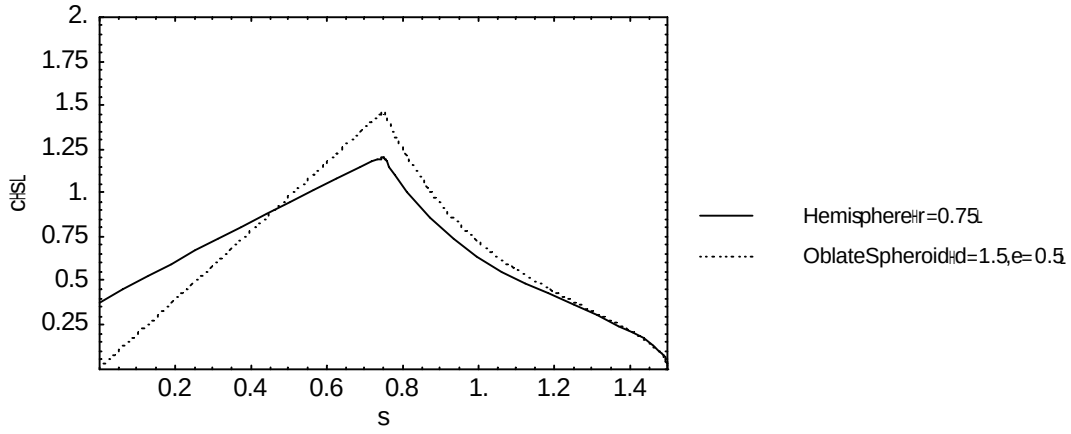


Figure 3.6. Comparison of CLD under μ-randomness for a hemisphere and oblate spheroid. Volume is the same in both cases (0.88). $\bar{l}$ **=0.66 for hemisphere and 0.72 for spheroid.**

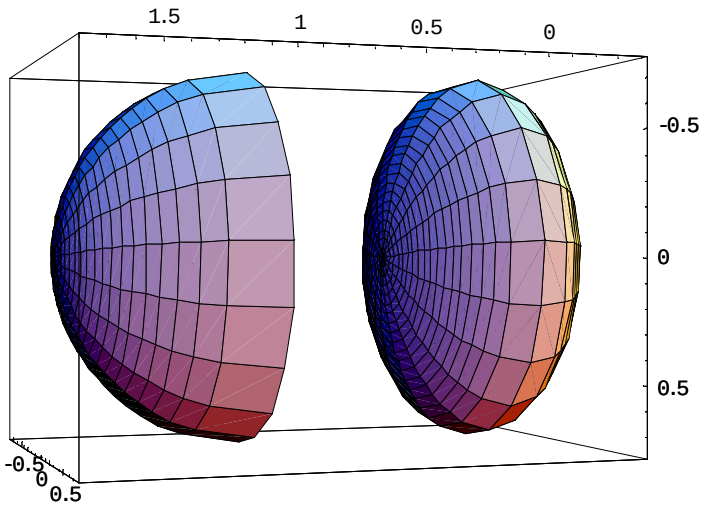


Figure 3.7. Hemisphere (*r*=0.75) and oblate spheroid (*d*=1.5,*e*=0.5) with CLDs shown in previous figure. These shapes provide identical CLDs for unidirectional radiation along the x-axis

Table 3.3. Summary of mean chord length and relative variance for various shapes

Shape	Mean Chord Length, $\bar{l}$	Relative Variance, V_t
Sphere	$\frac{2d}{3}$, d = diameter	0.125
Spheroid	$\frac{8de\sqrt{1-e^2}}{6\sqrt{1-e^2}+3e^2 Log\left(\frac{1+\sqrt{1-e^2}}{1-\sqrt{1-e^2}}\right)}$ e = elongation, d =main diameter	See Figure 3.8
Hemisphere	$\frac{8r}{9}$, r = radius	0.266
Cylinder	$\frac{2dh}{d+2h}$, d = diameter, h = height	See Figure 3.8
Infinite Slab	$2h$, h = height	Does not exist [135]
Cube	$\frac{2a}{3}$, a = side length	0.345
RPP	$\frac{2abh}{bh+ab+ah}$, h = height, a, b = side lengths	See Figure 3.8

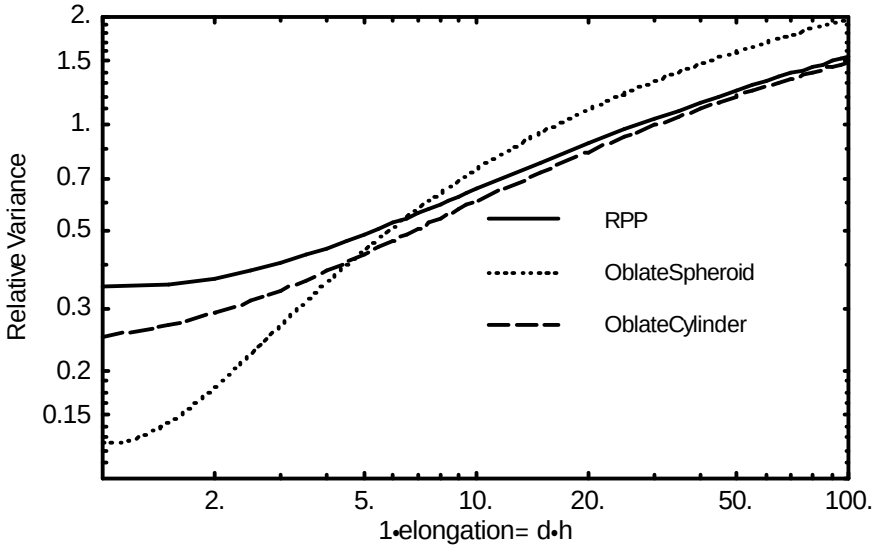


Figure 3.8. Relative variance V_t of the chord length distribution as a function of elongation for oblate shapes

3.3.2 Comparison of Segment Length Distributions and finite range effects

3.3.2.1 Segment length distributions for RPP, cube and sphere under μ-randomness

The previous section analyzed chord length distributions assuming μ-randomness with infinite range rays. Segment length distributions (SLD) are generated under similar conditions of randomness but with finite range rays. We can thus see the effect of finite range particles on the microdosimetric spectrum by considering SLDs. This is particularly important when our detector construction relies on a converter lying above a silicon volume.

Kellerer [128] provides an extremely useful expression for calculating SLDs given the CLD. The essential equations are repeated here due to their importance. Sum distributions are given in upper case and probability density distributions are in lower case. Assume that a convex body *K* has the sum distribution *F(s)* of chord length under μ-randomness and that it is exposed to an isotropic field of straight random tracks whose length u has the sum distribution *R(u)*. Note that the sum distributions are equal to the probability of exceeding a given value *s*. The resulting sum distribution of segment length in *K* is:

$$P(s) = k\left(F(s)\int_s^\infty R(x)dx + R(s)\int_s^\infty F(x)dx \right) \tag{3.6}$$

where $k = 1/(\bar{u} + \bar{l})$ and $\bar{u}$ = mean range, $\bar{l} = MCL$

In the special case where all tracks are of fixed length, u the formula reduces to

$$P(s) = \frac{1}{\bar{u} + \bar{l}}\left((u - s)F(s) + \int_s^\infty F(x)dx \right) \quad s < u \tag{3.7}$$

The mean segment length is given by Kellerer [128] as

$$\bar{s} = 1/(\bar{u}^{-1} + \bar{l}^{-1}) \tag{3.8}$$

Differentiating equation (3.6) we obtain the segment length probability density, *p(s)*,

$$p(s) = \frac{1}{\bar{u} + \bar{l}}\left(f(s)\int_s^\infty R(x)dx + r(s)\int_s^\infty F(x)dx + 2F(s)R(s) \right) \tag{3.9}$$

and in the special case of a fixed range *u*,

$$p(s) = \frac{1}{\bar{u} + \bar{l}} \left((u - s) f(s) + d(s - u) \int_u^\infty F(x) dx + 2F(s) \right) \quad s < u \tag{3.10}$$

Kellerer categorizes the three terms in equation (3.10) as distributions associated with crossers, insiders and starters+stoppers. If we split the sum segment distribution *P(s)* given by equation (3.7) into these categories, we obtain

$$\begin{aligned} P(s) = \quad & \frac{1}{\bar{u} + \bar{l}} \Bigg(F(s) \int_s^\infty R(x) dx - \int_s^\infty F(x) R(x) dx && \textit{crossers} \\ & + R(s) \int_s^\infty F(x) dx - \int_s^\infty F(x) R(x) dx && \textit{insiders} \\ & + 2 \int_s^\infty F(x) R(x) dx \Bigg) && \textit{starters} + \textit{stoppers} \end{aligned} \tag{3.11}$$

The SLD, *p(s)*, in the case of a fixed range *u*, has been calculated for the sphere, cube, and RPP as given in Appendix B. The sphere is a tractable integration whilst the RPP requires numerical integration methods. The effect of varying the fixed range on the distribution *p(s)* is shown for the sphere and RPP in Figure 3.9 and Figure 3.10, respectively. Clearly, the distribution shape changes significantly as *u* approaches the dimensions of *K*. The relative variance of the distributions is a maximum when the range *u* corresponds closely to the main dimension of the volume as shown in Figure 3.11. As will be seen in the following analysis, this is near the peak in the fraction of stoppers and starters.

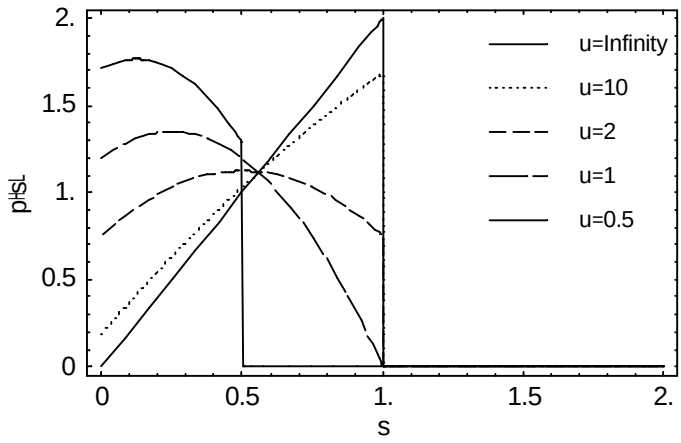


Figure 3.9. Effect of varying range (*u*) on segment length distribution for a sphere (*r*=1)

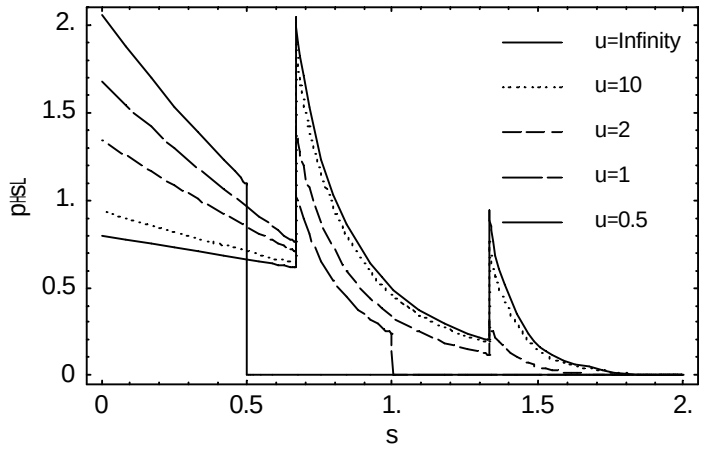


Figure 3.10. Effect of varying range (u) on segment length distribution for a RPP (*a*=*b*=1.33,*h*=0.66)

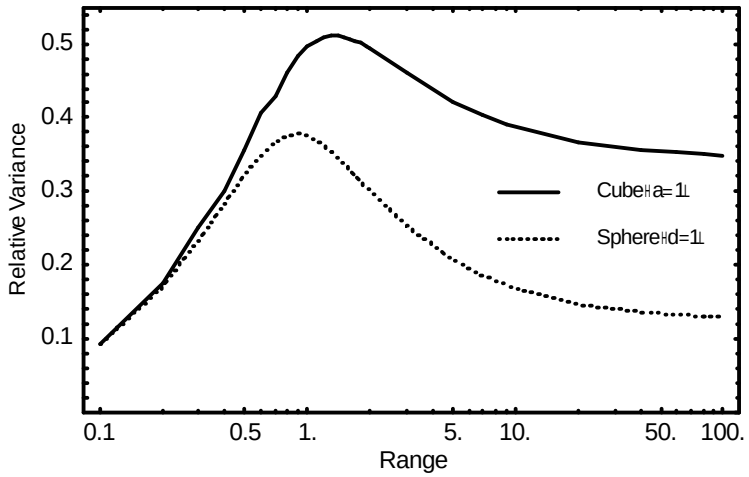


Figure 3.11. Relative variance of the segment length distribution as a function of particle fixed range for a sphere and cube

As noted previously, the use of a silicon structure requires that a high proportion of the chords are crossers or stoppers since we do not want to consider chords generated within the non-tissue equivalent silicon structure. It is useful to determine an expression for the fraction of chords that are generated from outside of *K* (i.e. stoppers and crossers). The equations for the fraction of crossers (b_{cross}) and stoppers (b_{stop}) are given by the first and third term of equation (3.11) at *s*=0.

$$b_{cross} = \frac{1}{\bar{u} + \bar{l}} \left(\bar{u} - \int_0^\infty F(x) R(x) dx \right) \tag{3.12}$$

$$b_{stop} = \frac{1}{\bar{u} + \bar{l}} \left(\int_0^\infty F(x) R(x) dx \right) \tag{3.13}$$

Note that we make use of the fact that $\bar{l} = \int_0^\infty F(s) ds$ and $\bar{u} = \int_0^\infty R(x) dx$.

If u is always greater than the maximum chord length ($u_{min} \geq s_{max}$), in which case there are no insiders and the sum range distribution $R(x)=1$ $x \leq s_{max}$, then we may simplify equations (3.12) and (3.13) to

$$b_{cross} = \frac{\bar{u} - \bar{l}}{\bar{u} + \bar{l}} \quad u_{\min} \geq s_{\max} \tag{3.14}$$

$$b_{stop} = \frac{\bar{l}}{\bar{u} + \bar{l}} \quad u_{\min} \geq s_{\max} \tag{3.15}$$

The summation of the fraction of stoppers and crossers to give the fraction of segments from outside K ($b_{start\_outside}$) requires no range assumptions to obtain a simple form. From equations (3.8), (3.12) and (3.13) we obtain:

$$\begin{aligned} b_{start\_outside} &= b_{cross} + b_{stop} \\ &= \frac{\bar{u}}{\bar{u} + \bar{l}} = \frac{\bar{s}}{\bar{l}} \end{aligned} \tag{3.16}$$

Solving equation (3.16) for $a = \frac{\bar{u}}{\bar{l}}$, the ratio of mean range to mean chord length, gives

$$a = \frac{b_{start\_outside}}{1 - b_{start\_outside}} \tag{3.17}$$

Note that these previously unreported equations are independent of shape for objects of the same MCL. Examples of equation (3.12) and (3.13) applied to a cube, RPP and sphere of equal MCL are shown in Figure 3.12 and Figure 3.13. As u decreases the proportion of crossers continuously drops whilst the proportion of insiders steadily rises. The proportion of stoppers and starters peaks at around the mean chord length. At range values greater than the maximum chord length, we observe identical crosser and stopper fractions for each shape reflecting the expected shape independence. The fraction which start outside (crossers + stoppers) is shown in Figure 3.14 with complete shape independence for all values of u.

Figure 3.15 shows the ratio of a=Range/MCL($\bar{l}$) required for a given fraction of start-outsiders. If we require a minimum of 80% of segments from outside of the detection volume K than the minimum allowable mean particle range is $4\bar{l}$. This provides a useful guideline for using a RPP volume with a converter structure for which we expect segments exclusively from outside of the RPP.

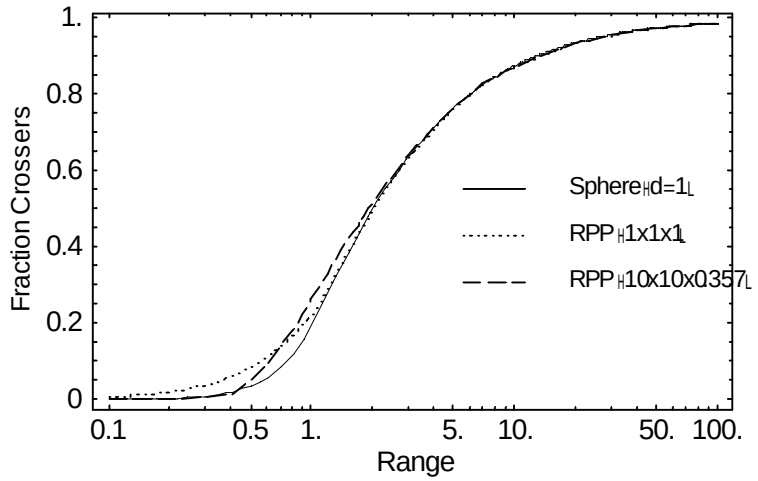


Figure 3.12. Fraction of crossers as a function of range for three different shapes with the same MCL

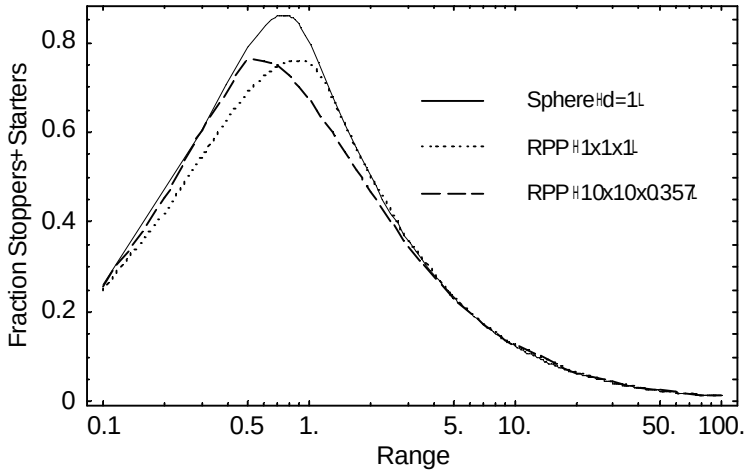


Figure 3.13. Fraction of stoppers+starters as a function of range for three different shapes with the same MCL

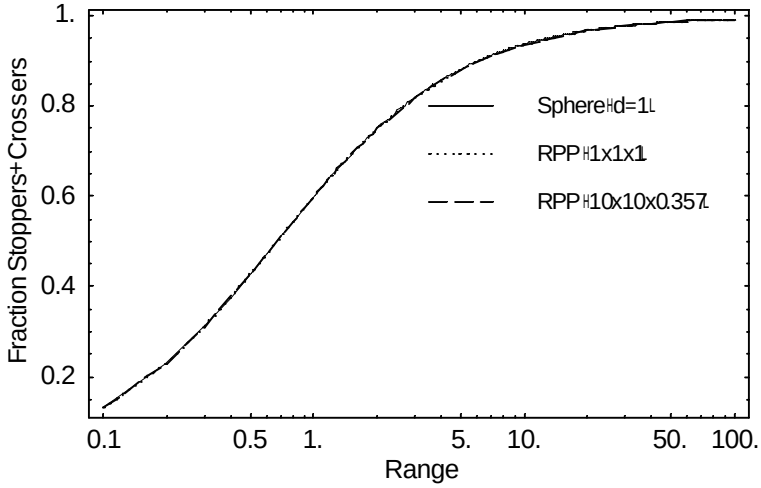


Figure 3.14. Fraction of stoppers+crossers as a function of range for three different shapes with the same MCL

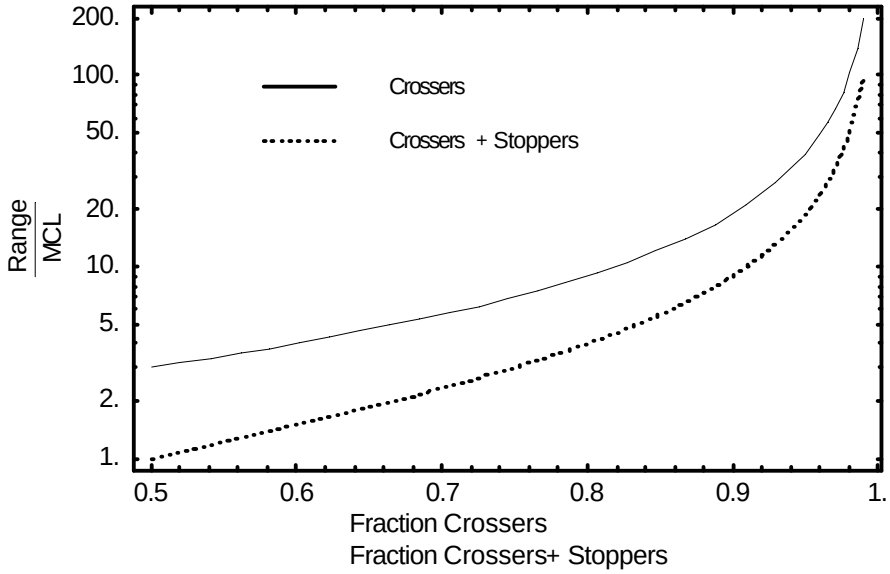


Figure 3.15. Ratio of Range/MCL required for the given fraction of crossers or crossers and stoppers. This function applies for any convex shape.

3.3.2.2 Segment length distributions for infinite slab with converter overlayer

The previously described segment length distributions considered the case of μ-randomness with finite range tracks. Practical implementations of silicon based detectors will initially incorporate a converter which is only above the detector. We define a new type of randomness which will be termed *c-randomness* (for converter) to describe the geometry shown in Figure 3.16 with finite range rays originating from a point uniformly distributed within the converter volume and emanating isotropically. The thickness of the converter and overlayer exceeds the particle range conforming to the typical dosimetry requirement of "dose equilibrium".

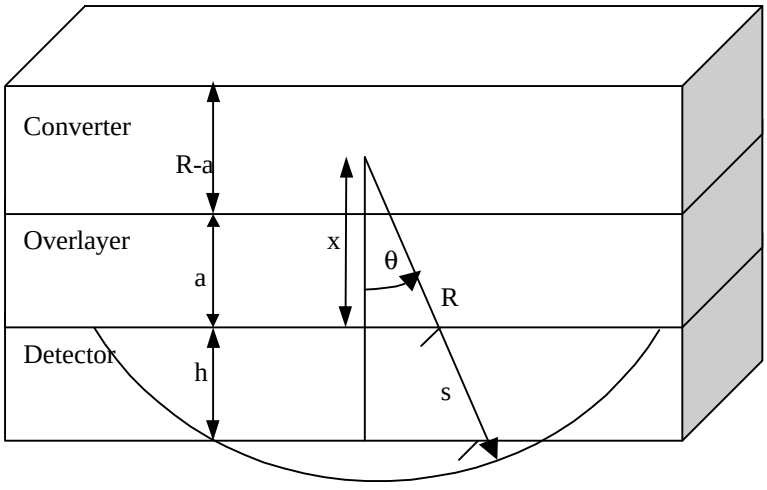


Figure 3.16. Geometry of RPP detector with overlayer (thickness = *a*) and converter (thickness = *h*). Infinite slab case has the same cross section with the RPP having infinite length and width.

It is relatively simple to derive an analytic solution for the case of an infinite slab and converter. The RPP case with c-randomness involves complex integrals so it is most simply handled using Monte-Carlo methods. The infinite slab calculation proceeds by considering a point x above the sensitive volume of thickness h with a ray of length (*R*) emanating isotropically from point x at an angle *q* with respect to the slab surface normal. The probability *p(q)dq* of emitting at an angle between *q* and *q+dq* is proportional to the partial area of the hemisphere $dA=2pr^2\ Sin(q)dq$ since the emission is isotropic. Normalising to the area of the hemisphere gives

$$p(q) = Sin(q) \tag{3.18}$$

Simple geometry gives the relationship between the segment length *s* and *q*.

For $x < R-h$, we have

$$s = \begin{cases} \dfrac{h}{Cos(q)}, & 0 \le q \le Cos^{-1}\left(\dfrac{x+h}{R}\right) \\ R - \dfrac{x}{Cos(q)}, & Cos^{-1}\left(\dfrac{x+h}{R}\right) \le q \le Cos^{-1}\left(\dfrac{x}{R}\right) \\ 0, & Cos^{-1}\left(\dfrac{x}{R}\right) \le q \le \dfrac{p}{2} \end{cases} \tag{3.19}$$

and for $x \geq R-h$ there are no crossers and we have

$$s = \begin{cases} R - \dfrac{x}{Cos(q)}, & 0 \le q \le Cos^{-1}\left(\dfrac{x}{R}\right) \\ 0, & Cos^{-1}\left(\dfrac{x}{R}\right) \le q \le \dfrac{p}{2} \end{cases} \tag{3.20}$$

These relationships are shown in Figure 3.17 for the two cases. We can now apply change of variable methods to determine the distribution of segment length.

$$p(s) = p(q)\left|\frac{dq}{ds}\right| \tag{3.21}$$

Care must be taken in applying the above equation since the inverse of *s(q)* is not unique for *s>h* as shown in Figure 3.17. We define two regions: A ($h<s\leq hR/(h+R)$) and B ($0\leq s\leq h$). For region A, we need to add the contribution due to *p(s)* for both solutions to *q(s)*. Applying equation (3.21) to (3.19) and (3.20) we obtain:

$$p(s,x) = \begin{cases} \dfrac{x}{R} & s = 0 \\ \dfrac{x}{(R-s)^2} & \text{Region B: } 0 < s \le h \\ \dfrac{h}{s^2} + \dfrac{x}{(R-s)^2} & \text{Region A: } h < s \le \dfrac{hR}{x+h} \end{cases} \tag{3.22}$$

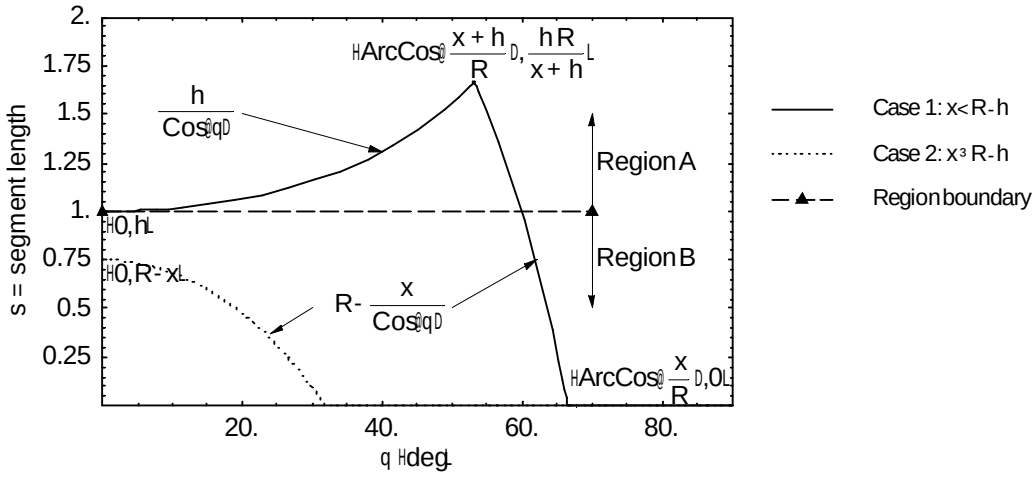


Figure 3.17. Segment length as a function of angle *q* for the infinite slab and overlayer/converter geometry. Examples given use *R*=5, *h*=1, and *x*=2 (Case 1) and *x*=4.25 (Case 2). In Region A, *s*>*h* and two values of *q* correspond to each s value whilst for region B, *s*£*h* and the inverse is unique.

Now we sum the probability over all x to remove the x variable and normalize appropriately. Care should be taken in selecting the integral bounds. The range of x is from the start of the converter at $x = a$ to the maximum value of x for each region given the finite range R.

$$p(s) = \begin{cases} k\int_a^{R-s} p(s,x)\,dx & \text{Region B: } 0 < s \le h \\ k\int_a^{\frac{hR}{s}-h} p(s,x)\,dx & \text{Region A: } h < s \le \dfrac{hR}{x+h} \end{cases} \tag{3.23}$$

Evaluating we obtain

$$p(s) = \begin{cases} k\left(\dfrac{1}{2} - \dfrac{a^2}{2(R-s)^2}\right) & \text{Region B: } 0 < s \le h \\ k\left(\dfrac{h^2 R}{s^3} - \dfrac{a^2}{2(R-s)^2} - \dfrac{h(2a+h)}{2s^2}\right) & \text{Region A: } h < s \le \dfrac{hR}{x+h} \end{cases} \tag{3.24}$$

$k = \dfrac{2R}{(a-R)^2}$ and $0 \le a < R$

An example of this function is shown in Figure 3.18. It is evident that the proportion of large segments for a given range is reduced by increasing the overlayer thickness. This function will be used later in section 3.3.3.

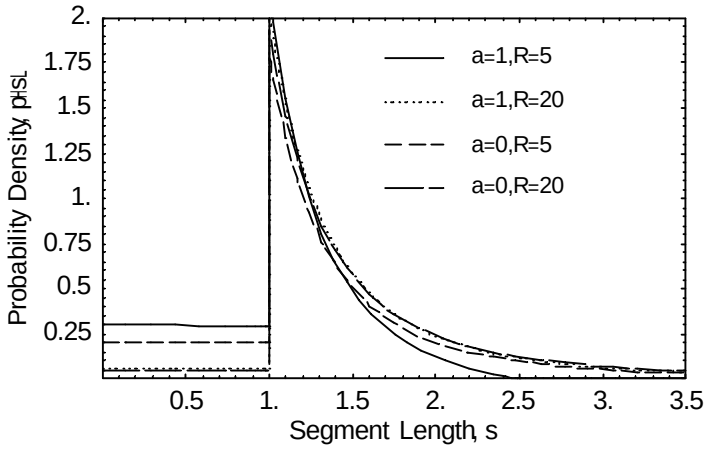


Figure 3.18. Segment length distributions for an infinite slab under c-randomness. Various overlayer thickness (*a*) and particle range (*R*) configurations are compared.

3.3.2.3 Segment length distributions for RPP with converter and overlayer

The structure of a RPP separated from a converter volume by an overlayer volume is the simplest geometry for a silicon based detector constructed using integrated circuit technology. The geometry is shown in Figure 3.16 with the tissue equivalent converter volume defining the region in which ionizing particles are generated. The randomness defined by such a construction was termed c-randomness in the previous section. An analytical solution to the segment length distribution for the RPP under c-randomness may be obtained following similar methods to the infinite slab case. However, the calculations are tedious so the Monte-Carlo method is employed. The process begins by randomly selecting points in the converter volume from which rays of a user-defined range are isotropically emitted. The segment lengths for rays intercepting the user defined sensitive volume are calculated and stored in order to form the segment length distribution. A more detailed description of the technique is provided in section 5.4.2. An example comparing the SLD for a unit cube under μ-randomness with the SLD under c-randomness using a ray with a range of 10 is shown in Figure 3.19. The calculations indicate that c-randomness is well approximated by μ-randomness particularly for larger ranges and minimum overlayer thickness. Increasing the overlayer thickness has the effect under c-randomness of reducing the probability of large segment lengths, which occur due to high angle intercepts (with respect to the

overlayer normal). A similar effect occurs for decreasing ranges under μ-randomness. Thus, an approximation to a c-random configuration with an overlayer of thickness *a* and particle range *R* is a cube under u-randomness with range *R-a*. An example of such an approximation is shown in Figure 3.19.

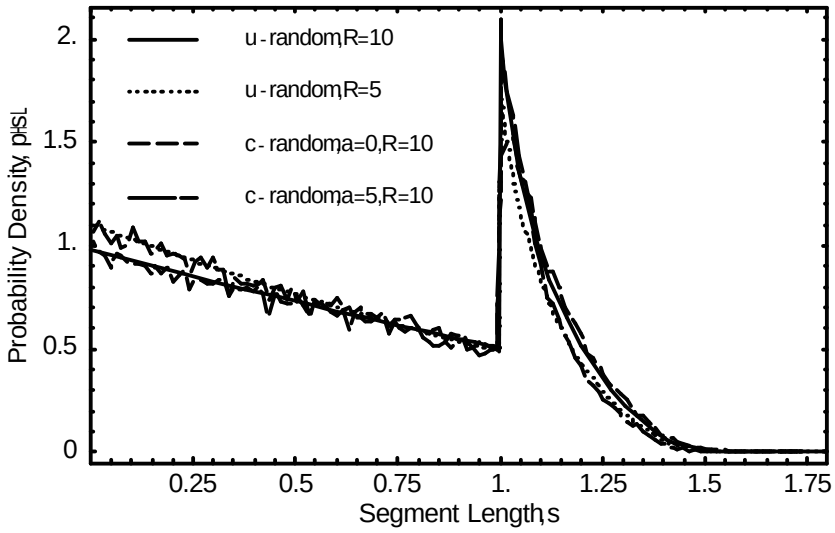


Figure 3.19. Segment length distributions for a unit side length cube under c-randomness for two different overlayer thickness, a. The range R is 10. SLDs calculated assuming μ-randomness are shown for comparison

3.3.3 Equivalence of Shapes using Mean Energy per Event (ε_d)

The previous sections detailed calculations of CLD and SLD are useful for comparing microdosimetric $f(y)$ spectra between shapes and predicting the expected number of crossers, stoppers, starters and insiders. In this section, we investigate parametric criteria for the equivalence of shapes.

Kellerer [129] proposed that a particularly suitable parameter for comparing the performance of microdosimetric shapes is the mean energy imparted per event ($\bar{e}_d$). This quantity is closely related to the dose average of lineal energy since

$$y_d = \frac{\bar{e}_d}{\bar{l}} \tag{3.25}$$

Both of these quantities are frequently used in microdosimetric applications since they often relate to the radiobiological effectiveness of the radiation. Moreover, they vary substantially with size and shape of the sensitive volume and radiation quality. From a

microdosimetric viewpoint, if the quantity $\bar{e}_d$ does not vary substantially between two detector shapes then the detectors may be considered largely equivalent.

There are two methods to calculate $\bar{e}_d$; one may integrate the previously calculated chord length distributions or use the proximity function method proposed by Kellerer [129, 142, 143]. Proximity functions applied to a volume are a measure of the probability distributions of the distances between points in a volume and when applied to a track relate to the distribution between energy transfers. The integral proximity function, *S(x),* of a region *S* is equal to the expected volume of the region that is contained in a sphere of radius *x* centered at a random point of *S*. The differential proximity function is the expected volume of *S* contained in a spherical shell of radius *x* and thickness *dx* centered at a random point of S. Kellerer [142] has shown that $\bar{e}_d$ may be calculated for a uniform isotropic radiation field given the proximity function *t(x)* of the radiation and the proximity function *s(x)* of a region.

$$\bar{e}_d = \int_0^{x_{\max}} \frac{s(x)t(x)}{4\pi x^2} dx = \int_0^{x_{\max}} U(x)t(x)dx \tag{3.26}$$

where *U(x)* is termed the geometric reduction factor. If a spherical shell of radius *x* is centered at a random point of *S*, then *U(x)* is equal to the average fraction of the shell that lies within *S*. The relation shown above applies rigorously for all radiations and arbitrary volumes and indicates that reference volumes with similar *U(x)* functions will be largely equivalent for all types of radiations. The advantage of using proximity functions over integrating the chord length distribution is that they are often simpler than the chord length distribution and contain fewer singularities.

3.3.3.1 Equivalence under μ-randomness

The geometric reduction factors for the sphere, cylinder and RPP under μ-randomness have been calculated by Kellerer [143] and are reproduced in Table 3.4 and calculated in Appendix B.

Kellerer assumes that radiation may be approximated by simple infinite straight-line tracks of constant energy transfer rate *L*. The proximity function is then equal to $t(x)=2L$. An improvement on Kellerer's work is provided by assuming finite range tracks which have a proximity function [142] given by:

Table 3.4. Summary of geometric reduction factor for various shapes

Shape	Geometric Reduction Factor, U(x)
Sphere	$U(x)=1-\frac{3x}{2d}+\frac{x^3}{2d^3}, \quad x\le d$, d = diameter
Cylinder	$U(x)=\frac{1}{2px}\int_{z_1}^{z_2}\left(1-\frac{z}{h}\right)\frac{s_c\left(\sqrt{x^2-z^2}\right)}{\sqrt{x^2-z^2}}dz$ $z1=\left(Max(0,x^2-d^2)\right)^{1/2}; \quad z2=Min(x,h); \quad 0<x\le\sqrt{h^2+d^2}$ For cylinder, $s_c(x)=4x\left(Cos^{-1}\left(\frac{x}{d}\right)-\frac{x}{d^2}\sqrt{d^2-x^2}\right), \quad x\le d$ h = height, d=diameter
RPP	As above but with For RPP, $s_c(x)=2x\begin{cases}\frac{x^2}{d^2}-\frac{4x}{d}+p & x\le d\\ p-2-4Cos^{-1}\left(\frac{d}{x}\right)+4\sqrt{\frac{x^2}{d^2}-1}-\frac{x^2}{d^2} & d\le x\le\sqrt{2}d\end{cases}$ and h = height, d = maximum diameter = $\sqrt{2}d$, d = side length

$$t(x)=2L\left(1-\frac{x}{R}\right), \quad x\le R \tag{3.27}$$

Using Kellerer's assumption that R is infinite, the mean energy imparted is proportional to the integral over $U(x)$ which is shown to be simply related to be mean chord length $\bar{l}_I$ for I-randomness (random chords through a random point in a convex body).

$$\begin{aligned}\bar{e}_d &= 2L\int_0^{x_{\max}}U(x)dx\\ &= L\bar{l}_I\end{aligned} \tag{3.28}$$

For the case of finite range tracks, $\bar{e}_d$ is obtained using equation (3.27) with the appropriate $U(x)$ applied to equation (3.26). A unit sphere may be considered a reference for the mean energy deposited. For a given range R, it is useful to determine the dimensions of a RPP or cylinder for which the calculated $\bar{e}_d$ is the same as for the reference unit sphere. Kellerer [129] considered first the infinite range case and compared a unit sphere with a cylinder and RPP both of unit elongation. The sphere has $\bar{e}_d$ =0.75 L whilst for a cube of unit side length, $\bar{e}_d$ =0.897 L. Therefore, the required dimensions for a cube to obtain the same $\bar{e}_d$ as for the sphere is 0.75/0.897=0.837. The results are summarized in Table 3.5.

Table 3.5. Dimensions of a cylinder and cube with the same $\bar{e}_d$ as a unit diameter sphere. (assuming μ-randomness with infinite range tracks and constant LET)

Shape	$\bar{e}_d$	Required Dimensions
Sphere (d=1)	0.75 L	d = 1
Cylinder (d=1,h=1)	0.838 L	d = h = 0.895
RPP (side length d=1,h=1)	0.897 L	d = h = 0.837

This process may be applied for various elongations' of a cylinder and RPP. Figure 3.20 gives those values of height and side length for a RPP which are associated with the same value of $\bar{e}_d$ as a unit diameter sphere. Table 3.6 lists corresponding numerical values. Figure 3.21 shows the value of $U(x)$ for the sphere, cube, cylinder (e=1) and RPP (e=0.1). The best approximation to the sphere $U(x)$ is obtained with an elongation of 1 for both the cylinder and RPP. The poor correspondence for the RPP with e=0.1 indicates that, although $\bar{e}_d$ is equivalent, the spectral shape and performance with varying range particles will be poor for elongation values significantly different from unity. Conversely, excellent correspondence of the cube with the sphere $U(x)$ is found over all x with the conclusion that a cube of side length d=0.837 is very nearly equivalent to a sphere of diameter d. Using a numerical analysis, Kellerer [129] showed that the difference between a cube and sphere $\bar{e}_d$ must always be less than 3.5% provided the function $t(x)$ is monotonically decreasing. The proximity function $t(x)$ is always a decreasing function of x except for small distances x below the microdosimeters resolution. Kellerer also claims that the difference between a cylinder and sphere must always be less than 1.7% under similar conditions for $t(x)$.

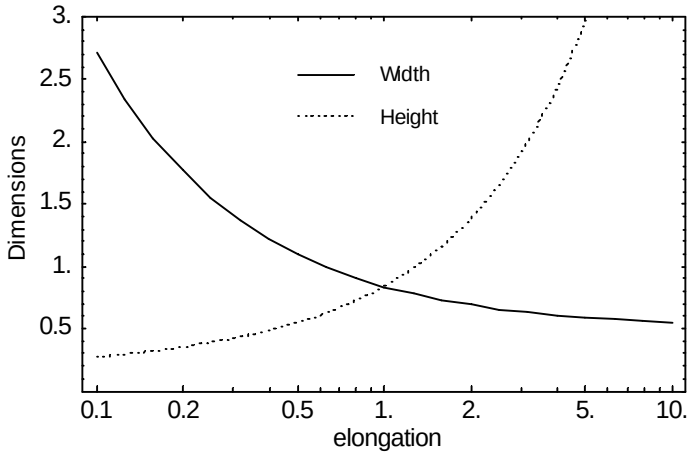


Figure 3.20. Height *h* and width *d* of the RPPs that have the same mean energy deposited as the unit diameter sphere (see also Table 3.6). For the specified elongations these RPPs are most closely equivalent to the unit diameter sphere

Table 3.6. Dimensions of a RPP with the same $\bar{e}_d$ as a unit diameter sphere. (assuming μ-randomness with infinite range tracks and constant LET)

Elongation (*e*)	**Height (*h*)**	**Diameter (*d*)**	$\frac{V}{V_{sphere}}$	$\frac{S}{S_{sphere}}$	$\frac{\bar{l}_m}{\bar{l}_{m,sphere}}$
1/32	0.194	6.192	14.17	25.94	0.546
1/16	0.234	3.747	6.279	10.06	0.624
1/10	0.272	2.721	3.849	5.658	0.680
1/8	0.294	2.354	3.117	4.413	0.706
1/4	0.389	1.556	1.800	2.313	0.778
1/2	0.549	1.098	1.262	1.534	0.823
1	0.837	0.836	1.118	1.336	0.836
2	1.380	0.690	1.255	1.516	0.828
4	2.434	0.609	1.722	2.122	0.811
8	4.504	0.563	2.727	3.431	0.795
10	5.531	0.553	3.232	4.090	0.790
16	8.599	0.537	4.743	6.067	0.782
32	16.73	0.523	8.740	11.32	0.772

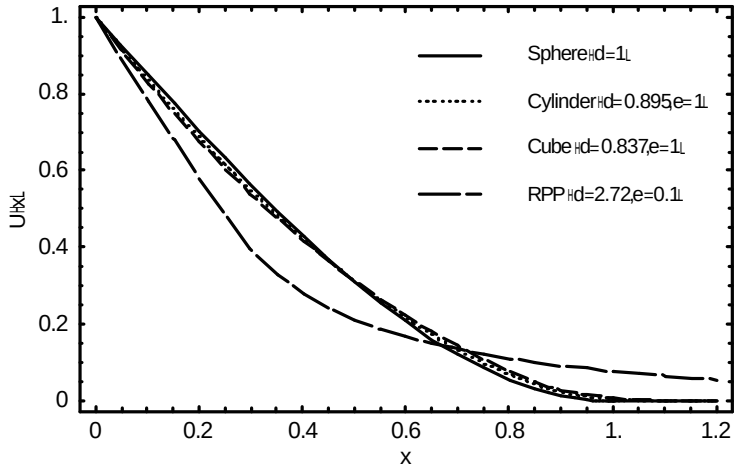


Figure 3.21. The geometric reduction factor *U*(*x*) for the unit diameter sphere and for equivalent cylinder, cube and RPP. The largest difference occurs for the elongation that is not unity

The previous discussion determined the optimal geometry for various shapes under the criteria that the mean energy deposited is identical to a unit diameter sphere assuming infinite range particles. If the particle range is finite, the mean energy deposited drops as the proportion of crossers drops. Figure 3.22 indicates that the rate of decrease is almost identical for the sphere and cube with deviations less than 2.1% for all ranges. For the RPP with small elongation (*e*=0.1) the equivalence with a sphere is quite poor (up to 15% difference) for ranges less than 10 as expected given the disparity in the *U*(*x*) functions.

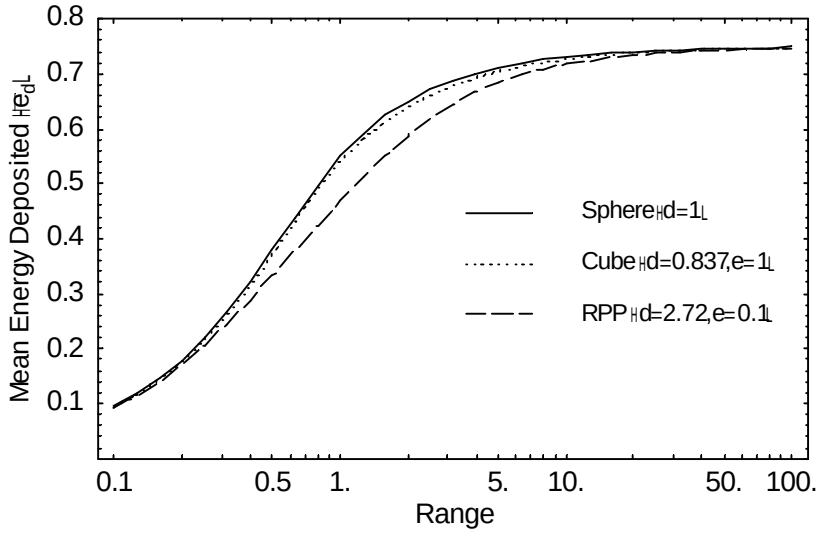


Figure 3.22. Variation of mean energy deposited per event with particle range. The cube closely approximates a sphere for all ranges. The dimensions of each object were selected to obtain equivalent $\bar{e}_d$ assuming an infinite range. The LET *L* is assumed equal to 1.

3.3.3.2 Equivalence under nonisotropic conditions and c-randomness

It is important to check the equivalence under non-isotropic conditions. Kellerer [143] performs this analysis for a cylinder by considering the extreme case of a unidirectional field perpendicular to the cylinder axis. This orientation is common in experimental applications with the particles then having a preferred direction in passing through the detector. A value of $\bar{e}_d$ =0.849 *L* was derived for the unit elongation cylinder under a unidirectional field, which is close to the isotropic case of $\bar{e}_d$ =0.838 *L*. The conclusion is that the cylinder remains closely equivalent to a sphere even under non-isotropic conditions.

Similarly, the cube or RPP is commonly orientated with the normal to a face plane parallel to the radiation beam. We consider the limiting case of particle tracks that are all normal to the selected face plane. In this case, the proximity function is that of a straight line of length equal to the thickness of the RPP (*d*) in the beam direction.

$$U(x) = 2\left(1 - \frac{x}{d}\right) \tag{3.29}$$

For an infinite range the mean energy deposited is simply $\bar{e}_d$ = *d L* since all chords intersecting the RPP have length *d*. Under these unidirectional conditions, the side length of a cube that is most nearly equivalent to a unit diameter sphere is *d* = 0.75 compared with a value of *d* = 0.837 for the isotropic case. Thus, a cubic detector

optimized for isotropic conditions will record in a unidirectional beam an $\bar{e}_d$ 11.6% higher than desired for equivalence to a sphere. However, if a cube with d = 0.75 is employed in unidirectional beams then the close equivalence with a sphere is preserved for all particle ranges as shown in Figure 3.23.

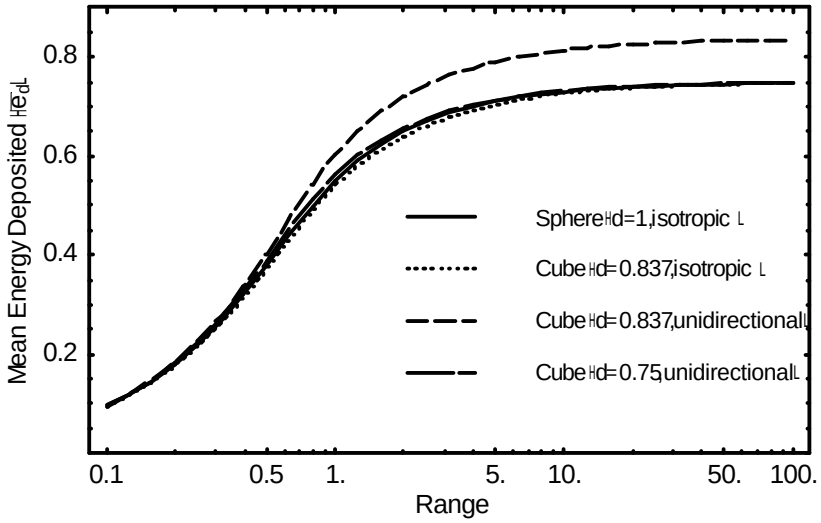


Figure 3.23. Variation of mean energy deposited per event with particle range for isotropic and unidirectional beams. The unidirectional beam is normal to a cube face. The LET *L* is assumed equal to 1. (See also Figure 3.22)

The use of a converter on top of a RPP under c-randomness is another form of non-isotropic radiation. For the infinite slab case discussed previously in section 3.3.2.2, the mean energy deposited $\bar{e}_d$ may be calculated by integrating equation (3.24) for the SLD $p(s)$ as follows:

$$\bar{e}_d = L\frac{\int_0^\infty s^2 p(s)ds}{\int_0^\infty s\,p(s)ds} = L\frac{\int_0^\infty s^2 p(s)ds}{\bar{l}} \tag{3.30}$$

For a given range, the slab thickness required to obtain the same $\bar{e}_d$ as a unit diameter sphere may be estimated. The thickness required varies considerably with range and overlayer thickness such that the equivalence between the infinite slab structure and a sphere is quite poor. An example of the large variation in $\bar{e}_d$ with range for an infinite slab structure is shown in Figure 3.24. The slab of height 0.176 and overlayer thickness 0.5 is selected to give a unit sphere equivalent $\bar{e}_d$ at a range of 100. The mean energy increases continuously with range due to the large segment lengths that arise as the

range increases. The large segments are at high angles with respect to the top face normal. RPPs of elongation closer to unity limit this rise and large variation of $\bar{e}_d$ with particle range since the maximum chord length is restricted.

Consider now the case of a cube under c-randomness. The SLD was calculated using Monte-Carlo methods in section 3.3.2.3. Again, the mean energy deposited may be estimated by numerically integrating the SLD as per equation (3.30) assuming for comparative purposes a fixed LET of 1. The number of segments in the calculated distribution was 10000, which leads to an error in $\bar{e}_d$ of around 0.7% (based on comparative studies with known spectra under μ-randomness). The cube under c-randomness with no overlayer closely approximates the sphere for ranges greater than the cube dimensions. When the range becomes close to the sum of the overlayer and detector thickness $\bar{e}_d$ drops faster than for a sphere since the proportion of crossers drops dramatically. The overlayer increases the range above which spherical equivalence is attained. In summary, the $\bar{e}_d$ equivalence of a RPP/overlayer/converter structure to a sphere is best attained by using a minimum sized cube (elongation=1) with no overlayer.

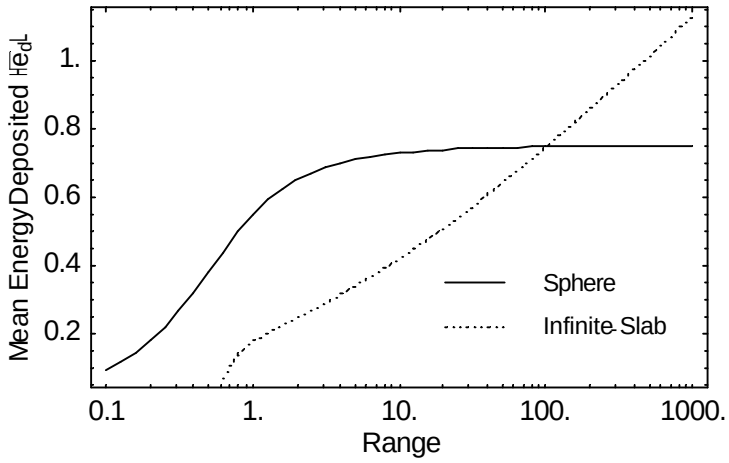


Figure 3.24. Comparison of mean energy deposited per event with particle range for a unit diameter sphere and infinite slab. The infinite slab has a height of 0.176 (calculated to give equivalence at range = 100) and is exposed to a radiation field isotropically emitted from a converter 0.5 units above the slab. The LET L is assumed equal to 1.

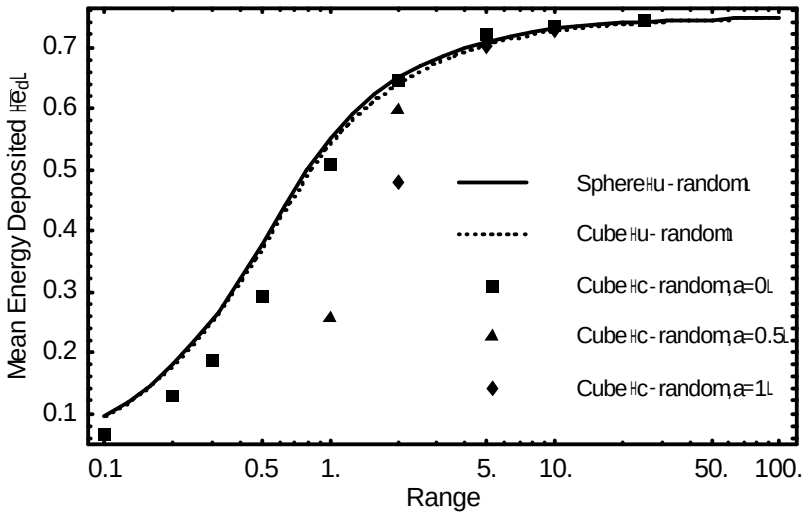


Figure 3.25. Comparison of mean energy deposited per event with particle range for a unit diameter sphere and cube with various overlayers/converters. The sphere and cube lines are calculated under the condition of μ-randomness whilst the cube points for various overlayers are calculated using Monte-Carlo methods assuming c-randomness. 10000 segments were used in the Monte-Carlo calculation. The LET L is assumed equal to 1.

3.3.4 Equivalence of Shapes using Frequency Mean Energy per Event (ε_f)

The previous sections have demonstrated a good equivalence between the sphere and cube with respect to the parameter $\bar{e}_d$. This equivalence is maintained even when using a converter/overlayer type geometry although the equivalence is reduced somewhat under the condition of unidirectional radiation. In most microdosimetric applications $\bar{e}_d$ and the closely related parameter $\bar{y}_d$ are of greatest interest. However, equivalence using the $\bar{e}_d$ parameter does not necessarily imply that other parameters and the microdosimetric spectra are in perfect agreement. Estimates of the remaining differences may be gauged by considering the frequency mean energy imparted per event $\bar{e}_F$ and the related event frequency Φ representing the average number of events per unit dose. Kellerer [143] performs the calculations for a sphere, cylinder and cube and the results are reproduced here supplemented by the non-isotropic case for the cube and consideration of the use of a converter with under c-randomness.

The relevant equations are

$$\bar{e}_F \Phi = m = \rho V \tag{3.31}$$

where m, V and ρ are the mass, volume and density of the volume. Kellerer considers two cases; short range and long range particles. For particles of short range $\bar{e}_F$ is equal

to the mean energy of the particles and is independent of the radiation directionality and detector shape. Therefore,

$$\frac{\bar{e}_F}{\bar{e}_{Fsphere}} = 1 \quad \text{and} \quad \frac{\Phi}{\Phi_{sphere}} = \frac{V}{V_{sphere}} = \frac{6a^3}{pd^3} \quad \text{for short range} \tag{3.32}$$

where a = side length of the cube and d = sphere diameter. For long range particles using the approximation of constant LET, L, $\bar{e}_F = L\bar{l}_m$ and applying equations (3.31) and (3.5) gives

$$\frac{\bar{e}_F}{\bar{e}_{Fsphere}} = \frac{\bar{l}_m}{\bar{l}_{msphere}} \quad \text{and} \quad \frac{\Phi}{\Phi_{sphere}} = \frac{S}{S_{sphere}} \quad \text{for long range} \tag{3.33}$$

which for isotropic conditions becomes

$$\frac{\bar{e}_F}{\bar{e}_{Fsphere}} = \frac{a}{d} \quad \text{and} \quad \frac{\Phi}{\Phi_{sphere}} = \frac{6a^2}{pd^2} \quad \text{for long range, isotropic} \tag{3.34}$$

and for unidirectional radiation

$$\frac{\bar{e}_F}{\bar{e}_{Fsphere}} = \frac{3a}{2d} \quad \text{and} \quad \frac{\Phi}{\Phi_{sphere}} = \frac{4a^2}{pd^2} \quad \text{for long range, unidirectional} \tag{3.35}$$

For long ranges, these equations are good approximations to the case of c-randomness with a converter and overlayer since the segment length distribution for c-randomness approximates μ-randomness. For short ranges, no rays intersect the sensitive volume under c-randomness.

The ratios of these microdosimetric quantities for a cube and sphere have been calculated in Table 3.7 with relevant ratios calculated for various RPP elongations in Table 3.6. These results indicate that the best overall equivalence to a sphere occurs for elongations close to 1. The event frequency and frequency average vary significantly with radiation direction for a cube due to the large difference in mean chord length with orientation. Given a cube optimized for a sphere equivalent $\bar{e}_d$, the ratio $\bar{e}_F / \bar{e}_{Fsphere}$ varies from 0.84 to 1.26 as we go from isotropic to unidirectional radiation. However, in practice $\bar{e}_F / \bar{e}_{Fsphere}$ will be somewhere between these values since the radiation pattern will be neither ideal isotropic nor unidirectional and a value closer to 1 may be expected. The condition of equal volumes for a sphere and cube provides a

reasonable overall equivalence for each of the parameters particularly if a case between isotropic and unidirectional is considered. However, it is important to note that equivalence based on event parameters is not as important as equivalence based on mean energy deposited, a point which will be further emphasized in the following section.

Table 3.7. Ratio of microdosimetric quantities in a cube of side length a and a sphere of diameter d

	Equal $\bar{e}_d$ $a = 0.837d$		**Equal Volume $a = 0.806d$**	
	Isotropic	**Unidirectional**	**isotropic**	**Unidirectional**
$\bar{e}_d / \bar{e}_{dsphere}$	1 - 1	1 - 1.12	1 -0.96	1 - 1.07
$\bar{e}_F / \bar{e}_{Fsphere}$	1 - 0.84	1 - 1.26	1 - 0.81	1 - 1.21
Φ / Φ_{sphere}	1.12 - 1.34	1.12 - 0.89	1 - 1.24	1 - 0.82

Note: The values to the left of the hyphen apply to short tracks whilst the values to the right apply to long tracks

3.3.5 Equivalent Lineal Energy Spectra and Straggling

Previously, the equivalence of various shapes to a sphere was studied using parameters such as $\bar{e}_d$. Attention must also be given to obtaining equivalence for the lineal energy spectrum and the important parameter of dose average lineal energy ($\bar{y}_d$). In this section, example lineal energy spectra will be presented, along with a study of the effect of straggling on the final spectrum. First, a method for constructing lineal energy spectra that are equivalent to a sphere must be derived.

The mean energy deposited in a volume *K* is proportional to the mean chord length assuming a constant LET and particles of range much larger than the dimensions of *K*. Therefore,

$$\frac{\bar{e}_{d,K}}{\bar{e}_{d,sphere}} = \frac{\bar{l}_K}{h\,\bar{l}_{sphere}}$$
$$\text{where } h = \frac{\bar{l}_{K\_eq}}{\bar{l}_{sphere\_eq}} = \begin{cases} 0.837 \text{ if shape = cube} \\ 0.895 \text{ if shape = cylinder(e = 1)} \end{cases} \qquad (3.36)$$

and $\bar{l}_{K\_eq}$ = mean chord length (μ-random) of *K* with dimensions such that mean energy deposited in *K*, $\bar{e}_{d,K\_eq}$ is equivalent to the reference sphere energy $\bar{e}_{d,sphere}$ and $\bar{l}_{sphere\_eq}$ = mean chord length for the reference sphere = 2d/3. So *h* is the ratio of the mean chord lengths for the volume *K* and for a sphere when the dimensions are selected to give

equal dose mean energy deposited per event. Using equation (3.25) and rearranging equation (3.36) provides an expression for the dose average lineal energy in a reference sphere, $\bar{y}_{d,sphere}$.

$$\begin{aligned}\bar{y}_{d,sphere} &= \frac{\bar{e}_{d,sphere}}{\bar{l}_{sphere}} \\ &= \frac{\bar{e}_{d,K}}{\bar{l}_K} h = \frac{\bar{e}_{d,K}}{\bar{l}_{Keff}}\end{aligned} \tag{3.37}$$

where the effective mean chord length $\bar{l}_{Keff}$ is given by:

$$\bar{l}_{Keff} = \frac{\bar{l}_K}{h} \tag{3.38}$$

Thus to obtain the same $\bar{y}_d$ as a reference sphere, the lineal energy for a given shape (composed of the same material as the reference sphere) must be calculated using an effective mean chord length $\bar{l}_{Keff}$ equal to $\bar{l}_K / h$. Ideally, one should select the dimensions of K such that $\bar{l}_K = \bar{l}_{K\_eq}$ since the scaling will then apply for finite range particles. The equation above is generally valid for ranges greater than the maximum of ($\bar{l}_K, \bar{l}_{K\_eq}$) such that a high proportion of crossers exists.

As an example, a cube of side length *a* may be used to approximate a 1 μm sphere provided the particle ranges are much greater than *a*. (e.g. *a* = 2μm, *h* = 0.837, $\bar{l}_K = 1.33$ μm and $\bar{l}_{Keff}$ = 1.59 μm). Nevertheless, the preferred option is to use a cube of side length 0.837 μm since the proportion of each type of segment (e.g. crosser) is better matched over a wide sweep of ranges as discussed in section 3.3.2.

Consider a cube, cylinder and unit diameter sphere with dimensions selected such that $\bar{e}_d$ is equivalent for each volume. A comparison of the chord length distributions is shown in Figure 3.26 with an improved qualitative agreement compared with distributions provided in Figure 3.3 to Figure 3.5 (where the MCL is constant).

Straggling varies considerably with ion energy and type. A typical case is provided here to illustrate the influence of straggling on the expected microdosimetric spectrum. Consider first some data obtained in chapter 5 for a 5.3 MeV alpha incident on a 2 μm thick detector. The energy deposited, calculated using SRIM [126], is gaussian

distributed with a mean of 262 keV and a standard deviation, induced by energy and range straggling, of about 1/10 the mean (28.8 keV). For simplicity, consider a 1 μm diameter sphere and equivalent cube and cylinder in a μ-random particle environment with the particle LET = 100 keV/μm. The lineal energy spectra are gaussian filtered with a standard deviation of 10 keV/μm to approximate straggling effects. The resulting lineal energy spectra in y vs. $f(y)$ format is shown in Figure 3.27. Straggling improves the match between the cube spectrum and the sphere, particularly at higher lineal energies. The cylinder is a slightly better approximation to the sphere than a cube; a result consistent with the previous section's analysis.

The poor approximation at lower lineal energies becomes negligible when the data is displayed in the most common format for microdosimetric data, the log(y) vs. $yd(y)$ format as shown in Figure 3.28. If one were to introduce other sources of variation (such as LET and range as described in section 3.2 or increased straggling), it is clear that the cube and cylinder would provide lineal energy spectra $yd(y)$ and $\bar{y}_d$ values which are indistinguishable from the reference sphere. Note, that if the appropriate calculation for lineal energy, as provided by equation (3.37), is not employed (such as setting h=1) then the spectra shift significantly and an extremely poor correspondence with a sphere is observed.

An example of the effect of finite range on equivalence and lineal energy spectra is shown in Figure 3.29 for a range of 5 μm. The lineal energy spectrum differs for spheres of diameter 1 μm and 2 μm due to the differing contribution of segment types (e.g. crossers). Similarly, a cube of side length 1.674 μm is a poor match to a 1 μm sphere, although its equivalence to a 2 μm sphere is maintained even for low ranges. This illustrates the importance of selecting dimensions for equivalence such that $\bar{l}_K = \bar{l}_{K\_eq}$ and therefore $\bar{e}_{d,sphere} = \bar{e}_{d,K}$, particularly when relatively small ranges are expected.

The final plot in Figure 3.30 shows the close spherical equivalence of a cube exposed to a c-random field. The range of the particles is 10 μm. This plot, along with previous discussions on the equivalence of $\bar{e}_d$, demonstrates the feasibility of utilizing a silicon detector with a converter structure to record a lineal energy spectra equivalent to sphere. Increasing the overlayer thickness to 5 μm did not significantly alter the $yd(y)$ spectrum

for the given range of 10 μm indicating that the equivalence of such a spectrum is robust to moderate overlayer thickness.

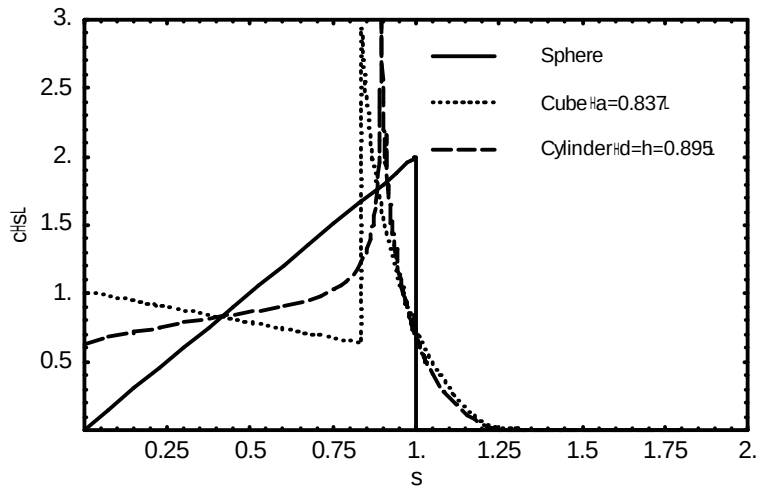


Figure 3.26. Comparison of chord length distribution under μ-randomness for a sphere, cube and cylinder with dimensions selected so that the $\overline{e}_d$ = 0.75 assuming an LET of 1.

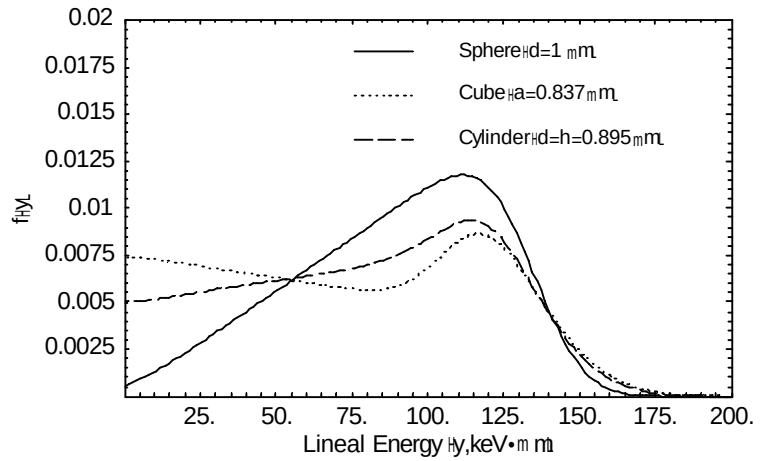


Figure 3.27. Lineal energy spectra *f*(*y*) under μ-randomness for equivalent sphere, cube and cylinder with straggling. LET assumed to be 100 keV/μm. Straggling standard deviation of 10keV/μm.

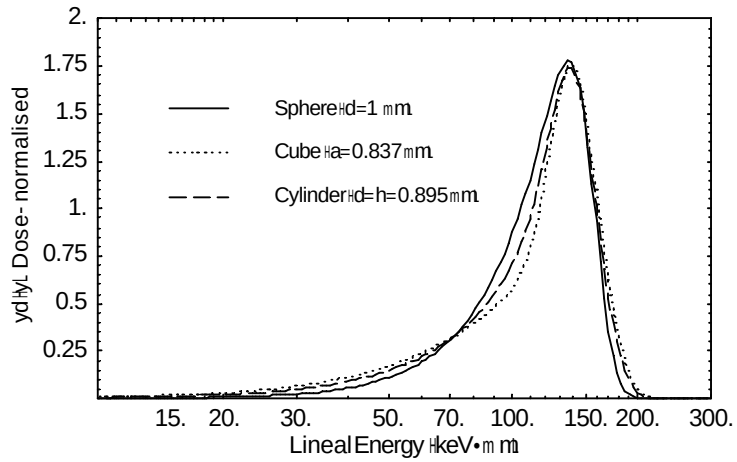


Figure 3.28. Lineal energy spectra *yd*(*y*) under µ-randomness for equivalent sphere, cube and cylinder with straggling (10keV/um). LET assumed to be 100 keV/µm. See also Figure 3.27.

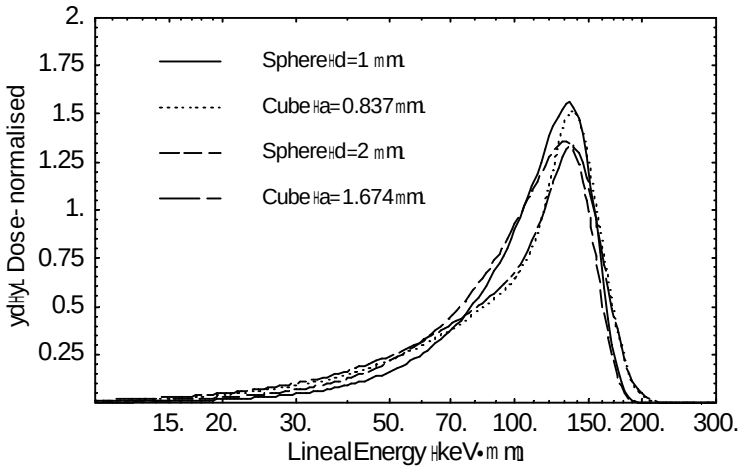


Figure 3.29. Lineal energy spectra *yd*(*y*) under µ-randomness with a finite range = 5 µm. For range values approaching the shape dimensions the equivalence criteria is stricter. LET assumed to be 100 keV/µm. Straggling standard deviation of 10keV/µm. See also Figure 3.28.

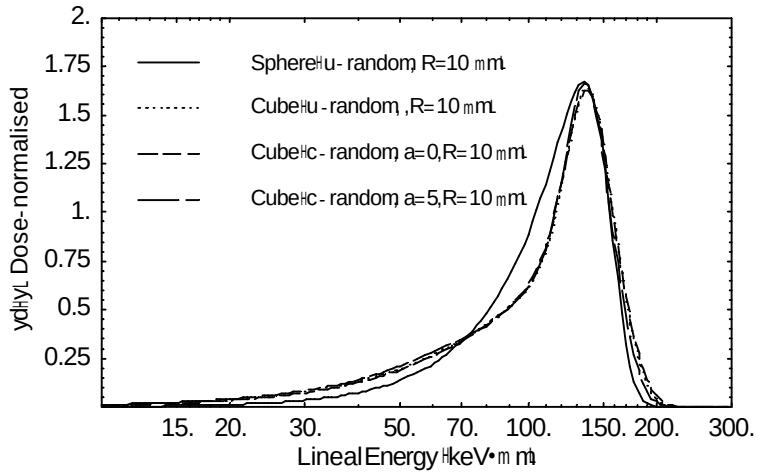


Figure 3.30. Comparison of lineal energy spectra *yd*(*y*) for a cube (side length=0.837µm) and sphere (d=1µm) under µ-randomness and c-randomness with a particle range of 10 µm. Spectra calculated for two different overlayer thickness (a) are shown indicating that for the particle range selected the dose lineal energy is not significantly affected. LET assumed to be 100 keV/µm.

3.3.6 Summary: Criteria for the Equivalence of Various Shapes in Microdosimetry

The following summarizes the shape analysis study.

- Should select detector volumes to minimize the relative variance due to chord length variations. A sphere has the minimum known relative variance. For a RPP and cylinder the minimum relative variance occurs for unit elongation. Large elongations increase the maximum chord length possible and thus the relative variance.

- The primary criterion for equivalence of microdosimetry volumes is equality of the dose mean energy imparted per event $\bar{e}_d$

- To obtain the same $\bar{y}_d$ as a reference sphere, the lineal energy for a given shape K must be calculated using a mean chord length equal to $\bar{l}_K / h$ where h is the ratio of the mean chord lengths for the volume K and for a sphere when the dimensions are selected to give equal $\bar{e}_d$. (h = 0.837 for a cube)

- A cube of side length 0.837d is closely equivalent to a sphere of diameter d for all radiation types and ranges. ($\bar{e}_d$ varies less than 2% over all ranges for constant LET, Kellerer [129] estimates maximum deviations of 4% under all isotropic conditions)

- A RPP detector optimized for isotropic conditions will record in a unidirectional beam an $\bar{e}_d$ 11.6% higher than desired for equivalence to a sphere.

- A RPP with an overlayer/converter structure (c-randomness) is closely equivalent to a sphere and RPP under μ-randomness. The equivalence holds within 10% for particle ranges $R > 2\ (a + \bar{l}\ )$ and within 2% for $R > 4\ (a + \bar{l}\ )$ where a = overlayer thickness.

- The overlayer thickness should be a minimum; ideally zero.

- The thickness of the detector should be minimized commensurate with the radiobiological requirements of the measurement.

- A hemisphere is an excellent approximation to an oblate spheroid with elongation = 0.5. This may prove useful in microdosimetric applications in which cells are modeled as oblate spheroids.

- Given a cube optimized for a sphere equivalent $\bar{e}_d$, the event frequency ratio $\bar{e}_F / \bar{e}_{Fsphere}$ varies from 0.84 to 1.26 as we go from isotropic to unidirectional radiation.

3.4 Combining Criteria for Shape Equivalence and Tissue Equivalence

The shape analysis thus far has assumed that both the reference sphere and an alternative shape *K* are composed of the same material. In chapter 5, a correction factor that enables the conversion of energy spectra measured in silicon shapes to tissue shapes is derived. Thus, to provide equivalent dose mean energy deposited and $\bar{y}_d$ as a reference sphere, two corrections to the tissue sphere diameter are required to determine the dimensions of the silicon detector.

1. *Shape Corrections*: To ensure the same dose mean energy deposited and $\bar{y}_d$ as a reference sphere, the lineal energy for a given shape *K* must be calculated using a mean chord length equal to $\bar{l}_K / h$ as determined in section 3.3.5.

2. *Tissue Equivalence(TE) Corrections*: A silicon volume, K_{si}, of a given shape, will record the same energy deposition spectrum as a tissue volume, K_t, of the same shape, if the linear dimensions of K_{si}, are scaled by a TE scaling factor z = 0.63 times the dimensions of K_t. This factor arises due to the differing range-energy relationships (and LET) for particles in silicon versus tissue and is discussed in detail in chapter 5. The TE lineal energy is calculated using the tissue mean chord length $\bar{l}_{Kt}$ equal to $\bar{l}_{Ksi} / h$.

Therefore, given a measurement of energy deposited e_{Ksi} in a silicon detector the TE lineal energy, y_{Kt}, is calculated using:

$$\begin{aligned} y_{Kt} &= \frac{e_{Ksi}}{\bar{l}_{Ksi}} hz \\ &= \frac{e_{Ksi}}{\bar{l}_{Keff}} \end{aligned} \tag{3.39}$$

where the effective MCL $\bar{l}_{Keff}$ is now given by:

$$\bar{l}_{Keff} = \frac{\bar{l}_{Ksi}}{hz} \tag{3.40}$$

This equation may be used for designing the silicon volume dimensions to meet the demands of $\bar{y}_d$ equivalence to a reference tissue sphere. The effective MCL is actually the reference tissue sphere MCL $\bar{l}_{Kt}$, if we desire equal dose mean energy deposited in both shapes (as is generally the case, see also section 3.3.5). Therefore, given a reference tissue sphere with a MCL = $\bar{l}_{Kt}$, the required MCL of a silicon volume $\bar{l}_{Ksi}$ is

$$\bar{l}_{Ksi} = \bar{l}_{Kt}\, hz$$
$$\text{where } hz = \begin{cases} 0.5 \text{ for a cube} \\ 0.54 \text{ for a cylinder (elongation = 1)} \end{cases} \tag{3.41}$$

Therefore, a silicon cube with side length 0.5 μm will have a similar lineal energy deposition spectrum and $\bar{y}_d$ as a 1 μm tissue sphere. Note, that the MCL used for calculating the TE lineal energy spectrum is not $\bar{l}_{Ksi}$, as would normally be the case, but is instead the tissue MCL, $\bar{l}_{Kt}$ (given by equation (3.40) with $\bar{l}_{Keff} = \bar{l}_{Kt}$). This is evident by inspection of the required lineal energy expression, equation (3.39).

3.5 Summary of Requirements

3.5.1 Geometrical Requirements and Considerations

The previous section discussed in detail the shape of the detector sensitive volume. Given the shape of the volume, dimensions of the detector should be selected based on two considerations. Firstly, the detector size should closely match the size of the biological entity that the detector is attempting to model in order to maximize the potential radiobiological information of the microdosimetric spectrum. Secondly, the size should be minimized in order to maintain as many crossers as possible. The microdosimetric spectrum will be more representative of particle LET, and possibly radiobiological effectiveness, if crossers dominate. Moreover, the use of a converter above a silicon detector is applicable under such circumstances.

Typical equivalent diameters for spherical and cylindrical proportional counters vary from around 1 μm to 10 μm. However, nanodosimetry miniature counters produced by

Kliauga [144-146] are capable of measurements down to a simulated site size of 10 nm. Some cell dimensions found in the literature are given in Table 3.8. Hartman [147] states that most types of tumor cells have cell diameters in the range 10-20 μm with temporal variations for each type depending on phase in the cell cycle. Smaller (8-10 μm for lymphoid tumors) and larger (~ 50 μm for epitheloid sarcomas) tumor cells have also been reported [148]. From the data presented in Table 3.8 the typical cell diameter is around 13 μm with a nucleus diameter of 9 μm. The calculations assume a spherical model for the cell although an ellipsoid is often more accurate. The cell diameter provides an upper limit on a microdosimeter's effective diameter. Interesting structures from the radiobiological viewpoint are present at the sub-cell nucleus levels (e.g. Chromosomes and DNA strands). Such structures are at the nanodosimetric scale and vary in size from 1.4 μm for a metaphase chromosome to 2 nm for the DNA double helix [1]. Therefore, the theoretical lower limit on the desired microdosimeter diameter is of the order of a few nanometers, well below sizes achievable with current experimental techniques. In practice, a range of sizes is desirable in order to study the effects of varying spatial distribution of energy.

Table 3.8. Cell size data from the literature

Cell Type	Cell Volume (μm^3)	Cell Diameter (μm)	Nucleus Volume (μm^3)	Nucleus Diameter (μm)	Comments
HeLa	1025	12	-	-	Ref [149]
V79 Chinese Hamster	1150	13	230	7.6	Ref [150]
9L Gliosarcoma	2140	16	690	11	Ref [151]
Lymphoid tumors	380	8-10	-	-	Ref [147, 148]
epitheloid sarcomas	65450	50	-	-	Ref [147, 148]
Melanoma (MeWo)	1550	14.4	640	10.7	Ref [152]

In the TDRA, briefly described in section 2.4.2, it was stated that the domain in which specific energy should be considered depends upon the average distance over which sublesions combine. Microdosimetric measurements of the neutron beams employed in biological experiments indicate that the sites typically have diameters of 0.2-2 μm [12, 18]. For this reason, along with practical design limitations and the desire to conform to Bragg-Gray cavity theory (see chapter 5), TEPC measurements are frequently performed in 1 and 2 μm site sizes. In summary, the ideal silicon microdosimeter should

have dimensions that approximate a tissue sphere of diameter ranging from around 13 μm to the minimum achievable given the device construction. Radiobiological studies indicate site sizes in the range less than 2 μm are of importance.

The silicon microdosimeter should be constructed with an array of sensitive volumes to improve collection statistics. The effective cross-sectional area required is dependent on the flux of the radiation environment. The lowest flux appears in radiation protection applications whilst the highest flux is observed in certain synchrotron based fast proton therapy facilities.

Proportional counters used in radiation protection have diameters of the order of 10-20 cm with gas pressure selected to simulate 1 μm diameter sites in tissue. Alternatively arrays of proportional counters may be employed [72]. For the same application and similar count rates of 500/hr at 10 μs/h, the required silicon detector area is also around 10 cm. Conversely, it will be shown in chapter 8, that the required area to avoid pile-up in fast proton therapy facilities is around 1 mm^2.

In summary the geometrical requirements are

- Given a reference tissue sphere with a MCL = $\bar{l}_{Kt}$, the required MCL of a silicon volume K is $\bar{l}_{Ksi} = \bar{l}_{Kt}\, hz$ where $hz = 0.5$ for a cube. Therefore, a silicon cube with side length 0.5 μm will have a similar TE lineal energy spectrum and $\bar{y}_d$ as a 1 μm tissue sphere. In addition, $\bar{l}_{Kt}$ (0.66 μm in this case) and not $\bar{l}_{Ksi}$ is used for calculating the TE lineal energy in the silicon volume.

- The ideal silicon microdosimeter should have dimensions that approximate a tissue sphere of diameter ranging from around 13 μm (the typical cell diameter) to the minimum achievable given the device construction.

- The detector should use an array of sensitive volumes to improve collection statistics. The total sensitive area of the volumes should be approximately 100 cm^2 for radiation protection applications and as small as 1 mm^2 for fast proton therapy measurements.

- A RPP with an overlayer/converter structure is appropriate. Such a structure is easily manufacturable. Furthermore, a RPP under c-randomness is closely equivalent to a sphere and RPP under μ-randomness. The equivalence holds within

10% for particle ranges $R > 2\ (a + \bar{l}\ )$ and within 2% for $R > 4\ (a + \bar{l}\ )$ where a = overlayer thickness.

- The elongation of the RPP should be as close to unity as practicable in order to minimize shape relative variance.
- A tissue equivalent converter should be used with a thickness greater than the maximum particle range expected to ensure charged particle equilibrium.
- The overlayer thickness separating the converter and detector should be minimized.

3.5.2 Operational Requirements and Considerations

In addition to the geometrical requirements, one must examine operational requirements such as electronic noise and charge collection behavior.

The application requires:

- An accurately defined sensitive volume. Minimization of charge collection complexity in particular diffusion and funneling effects. These effects are explained fully in chapter 6.
- Capable of measuring a lineal energy down to a minimum of ~1 keV/μm in tissue equivalent terms. For a silicon microdosimeter with a noise level e_{rms} (in rms electrons) and silicon MCL $\bar{l}_{Ksi}$, the minimum lineal energy in tissue $y_{Kt,\min}$ (in eV) is approximately given by inserting equation (2.26) into (3.39):

$$\begin{aligned} y_{Kt,\min} &\approx \frac{5 e_{rms} W}{\bar{l}_{Ksi}} hz \\ &\approx \frac{9 e_{rms}}{\bar{l}_{Ksi}} \end{aligned} \tag{3.42}$$

The radiobiological effectiveness begins to rise above unity as the lineal energy increase above ~1 keV/μm. From a microdosimetric standpoint, events below this lineal energy are not interesting since their RBE is close to unity [53]. Ideally one would like to measure the lineal energy >0.1 keV/μm to obtain the complete spectrum [88] in all radiation environments. However, in many practical examples of interest such as microdosimetric measurements in fast neutron therapy [153, 154] and proton therapy near the distal edge of the beam [155] the dose contribution below 1 keV/μm is small. Note that the energy of a proton with an LET of 1

keV/μm is 70 MeV. Therefore provided the radiation environment does not contain protons with energy greater than 70 MeV and is not dominated by gamma radiation then a minimum lineal energy of 1 keV/μm should suffice. Clearly, this specification is very application dependent and there are some cases in which a lower minimum lineal energy is desirable and a specification closer to 0.5 keV/μm may be more appropriate (e.g. see section 8.3.2). Low noise design and optimization is necessary to met such requirements and will be discussed in detail in chapter 4.

- The charge collection behavior should be resistant to radiation damage at typical application fluences. The radiation hardness of silicon detectors is discussed in chapter 6.

4. Silicon Microdosimeter Design and Noise Analysis

The requirements and recommendations arising from the previous section may be used to design a prototype silicon microdosimeter. An alternative to designing a custom device is to consider existing detectors and components. McNulty [3] has proposed the use of commercial memory cell arrays as microdosimeters. Random Access Memory (RAM) cells typically contain 4 to 6 transistors per cell. Reverse-biased junctions on various transistors, with their high electric field, are the most sensitive regions of a memory cell to radiation interactions. If sufficient charge is collected within the sensitive regions then the memory cell may change state from a 1 to a 0 or vice versa. This process is termed a single event upset (SEU) or bit-flip. SEU have been extensively studied; over the last 25 years due to their impact on memory reliability, particularly in space and avionics applications (see for example Ma and Dressendorfer [156], Ziegler [157] or issues of IEEE Nuclear Science). Cosmic ray induced terrestrial upsets have even been observed in life dependent implantable medical devices as was first reported by the author in 1996 [158, 159].

A memory cell is a remarkable analogue to a biological cell from a microdosimetric perspective. Cell death due to radiation interactions is directly analogous to single event upset in a RAM cell. The significant disadvantage of employing RAM cells in microdosimetry is the complexity of charge collection and the poorly defined sensitive volume boundaries. Charge collection efficiency varies dramatically over the cell area with multiple diode junctions, complex electric fields and varying effects of drift and diffusion present.

Memory cell designers have developed simulation tools to predict SEU performance in various environments [160-164]. In order to verify the simulation modeling, silicon devices with simple structures and easily defined charge collection regions are required. Fortuitously, the requirements of a SEU test device overlap with the requirements of a silicon microdosimeter. One such SEU test device was developed by Fujitsu Research Laboratories for verification of their SEU modeling software. The author was able to obtain 100 of these test devices, which provided an outstanding opportunity to test the concept of a silicon microdosimeter for medical applications. Significant time and expense were saved by avoiding the full development of a complete custom device.

The following sections will describe the device construction, basic electrical characterization and probe design. Care must be made in probe design and assembly in order to maximize noise performance. Characterization of the device charge collection, radiation hardness and compatibility (or otherwise) with geometrical requirements described in the previous chapter will be addressed in chapter 6.

4.1 Detector Description

The silicon microdosimeter prototype consists of a diode array test structure fabricated by Fujitsu Research Laboratories Ltd. The test structures were fabricated on bonded Silicon-On-Insulator (SOI) wafers with thickness 2, 5, and 10 μm. In addition, a bulk device (no SOI) was fabricated. The processing steps required to construct the device are provided in Appendix B, along with mask layouts and packaging details. The device was packaged in a 28 Pin DIL ceramic carrier.

An ideal silicon based microdosimeter collects charge in a reverse-biased p-n junction diode via drift driven separation of electron hole pairs in the depletion region. In reality, charge collection is complicated by additional charge collection via diffusion from outside of the depletion region. By using SOI structures, we preclude any charge collection from beneath the SOI layer due to the underlying insulating layer of SiO_2. Such a design creates a sensitive volume of well-defined depth and is a major advantage of using SOI technology for microdosimetry applications. As previously mentioned, the charge collection behavior and sensitive volume of the device will be fully characterized in chapter 6.

Four diode array structures as shown in Figure 4.1 are available on each device. For this work, the arrays A1 and especially A4 were used. These arrays are designated “large” (A1, 100×100 μm^2, 30×5=150 diodes) and “small” (A4, 10×10 μm^2, 120×40=4800 diodes) reflecting their respective junction sizes as shown in Table 4.1. The total N+ junction area and total diode area, including surrounding P+ junction, are also provided. Note that all diodes in a given array are connected in parallel.

The basic SOI structure is shown in Figure 4.2 with a more detailed cross-section of a 2 μm SOI diode provided in the charge collection chapter as Figure 6.8. Various cross-section regions with unique overlayer and SOI construction are identified in Figure 6.8 and depicted in plan view in Figure 6.9 for the small diode array A4 and Figure 6.10 for

the large diode array A1. The n+ and p+ silicon layers with depths 0.2 and 0.5 μm were constructed by arsenic and boron implantations at 30 keV and 5×10^{15} cm^{-2}. The impurity concentration of the P type silicon substrate was 1.5×10^{15} cm^{-3}. A SEM photo of the small cell array is shown in Figure 4.3 with a lower magnification view of the device following in Figure 4.4.

Table 4.1. Summary of diode array dimensions used in this work

Array/Name	Junction Size (μm)	Cell Size (μm)	Array Size	Total Junction Area (mm^2)	Total Diode Area (mm^2)
A1/Large	100×100	120×120	150 (30×5)	1.5	2.26
A4/Small	10×10	30×30	4800 (40×120)	0.48	4.40

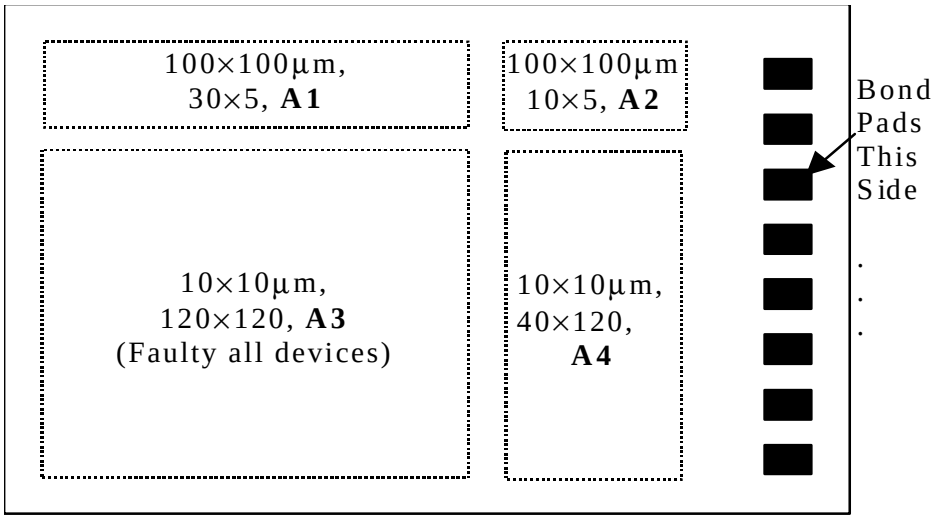


Figure 4.1. Array sizes and overall layout of the prototype silicon microdosimeter

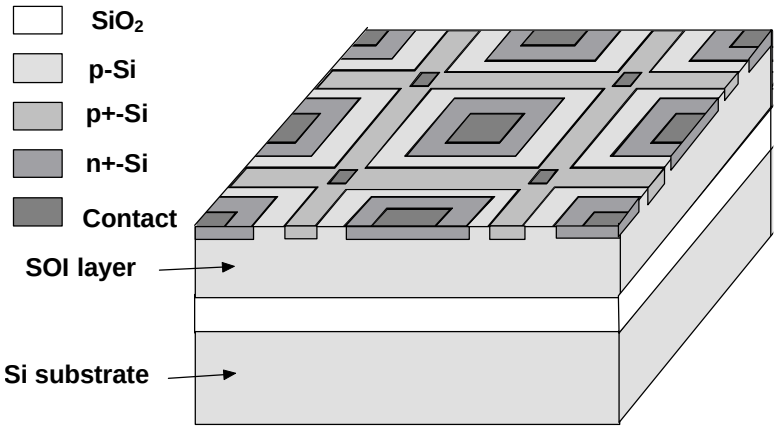


Figure 4.2: Basic SOI diode array structure

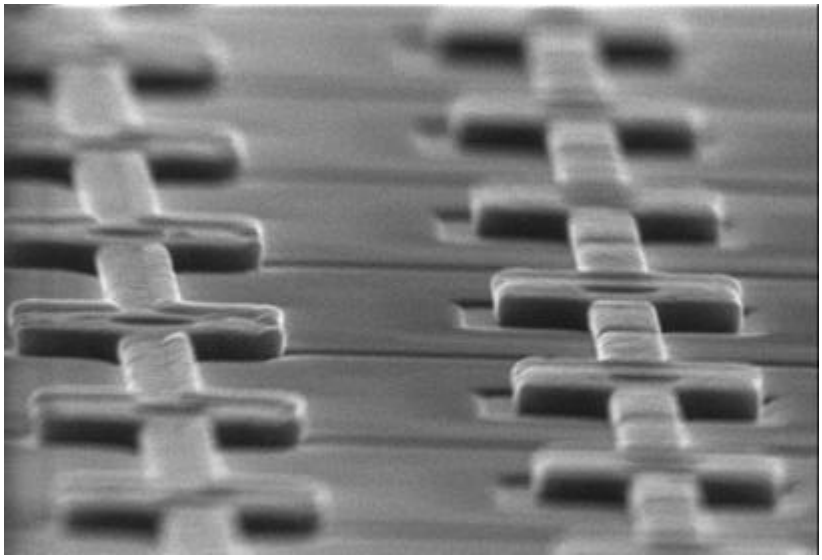


Figure 4.3. Scanning Electron Micrograph (SEM) photograph of a portion of the 10×10 μm diode array. (Note: Raised sections are aluminum tracks connecting contacts so that all diodes are electrically in parallel. The width of the photo is about 23μm.)

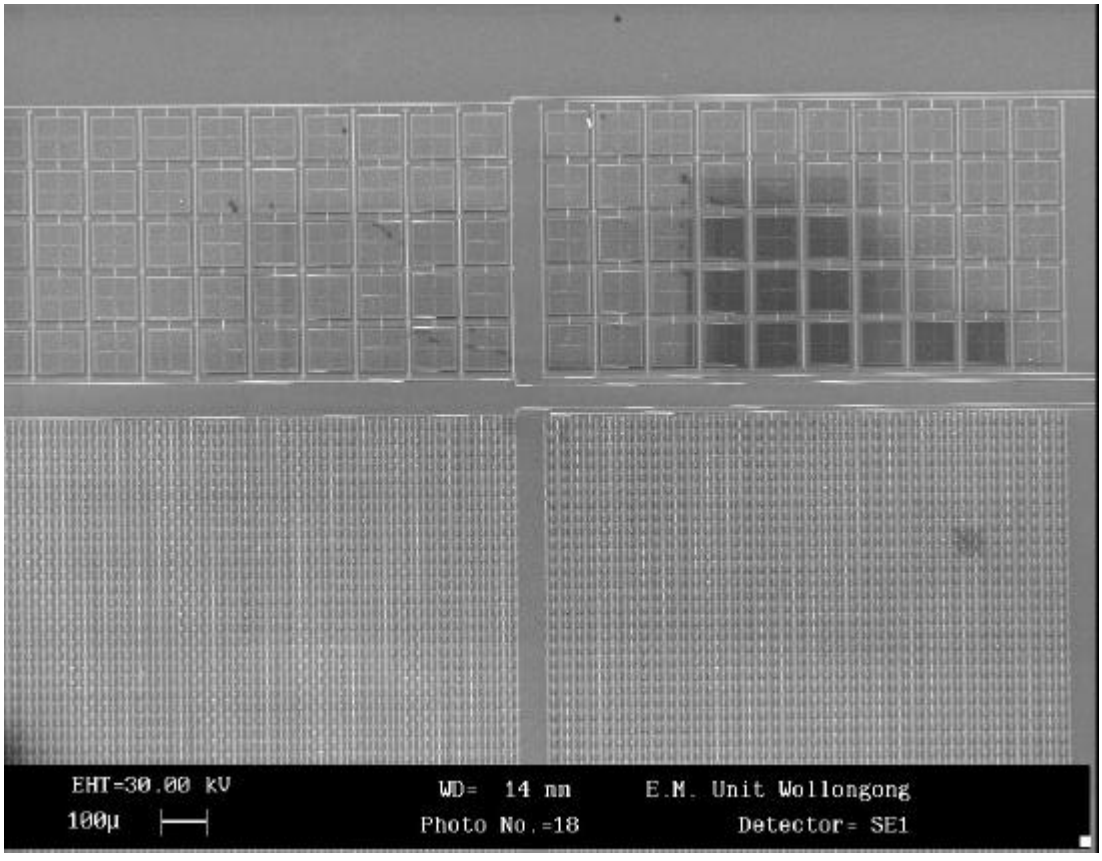


Figure 4.4. SEM of the prototype silicon microdosimeter. The 100×100 μm^2 arrays are at the top whilst the 10×10 μm^2 arrays are at bottom. The dark areas are due to charging effects from previous high magnification images. The darker spot in array A4 (lower right array) corresponds to the location of Figure 4.3 image.

4.2 Basic Electrical Characterization and Testing

4.2.1 Current-Voltage Measurements

Current-voltage (I-V) measurements were performed on all devices as a basic test of diode integrity. Measurements of reverse leakage current are also useful for noise calculations. A Keithley 237 High Voltage Measurement Unit dedicated to I-V measurements at the Australian Nuclear and Science Technology Organisation (ANSTO) was employed for the I-V measurements. The accuracy of the meter is within 0.3% in the 10nA range. The unit was computer controlled using Metrics Software (V2.1) with reverse bias measurements performed from -10 to 0 V in 0.1 volt steps and forward bias measurements from 0 to 0.45 volts in 0.05 volt steps. The current was limited at 100 μA and a 3 second settling time was allowed following each voltage step. I-V measurements are extremely temperature sensitive with the reverse leakage current exponentially dependent on temperature [44]. During these tests the temperature was not explicitly regulated (room temperature ~25 ± 3 °C) since the predominant aim was simply to identify working devices.

Nominal components were identified according to the following test criteria:

Test 1) I-V should be monotonic with positive derivative.
Test 2) I at specific V points should lie within desired ranges.
- a) -10 V: nominal range: -200 nA-0 nA
- b) 0 V: nominal range: -0.25 nA-0.25 nA
- c) 0.45 V: nominal range: 1-50 uA

An example of the I-V characteristic for the 2 μm SOI device is shown in Figure 4.5. A straight line may approximate the reverse bias I-V characteristic with a slope given by the reverse bias impedance. The main devices used for experiments in this work are summarised in Table 4.2. The equivalent resistance R_d is calculated by linear regression fitting to the reverse bias I-V and extracting the slope. The bias current I_b is then given by

$$I_b = V_d / R_d \tag{4.1}$$

where V_d is the voltage across the detector.

Table 4.2. Summary of reverse bias current for selected devices used in later experiments

Device	Bias Current (I_b nA) at V_d = -10V	Equivalent Resistance ($R_d \times 10^9 \Omega$)	Experiments
2 µm SOI, #6	2.2	4.6	BNCT (BNL)
2 µm SOI, #19	5.1	2.0	BNCT (MIT,BNL)
2 µm SOI, #23	5	2.0	BNCT (MIT, KUR), Neutron Therapy (Detroit)
5 µm SOI, #5	0.45	26	BNCT (KUR)
10 µm SOI, #7	4.6	2.2	BNCT (KUR) Proton Therapy (MGH, KEK), Neutron Therapy (Detroit) Radiation Protection (ANSTO)
Bulk, #20	0.3	34	BNCT (KUR)

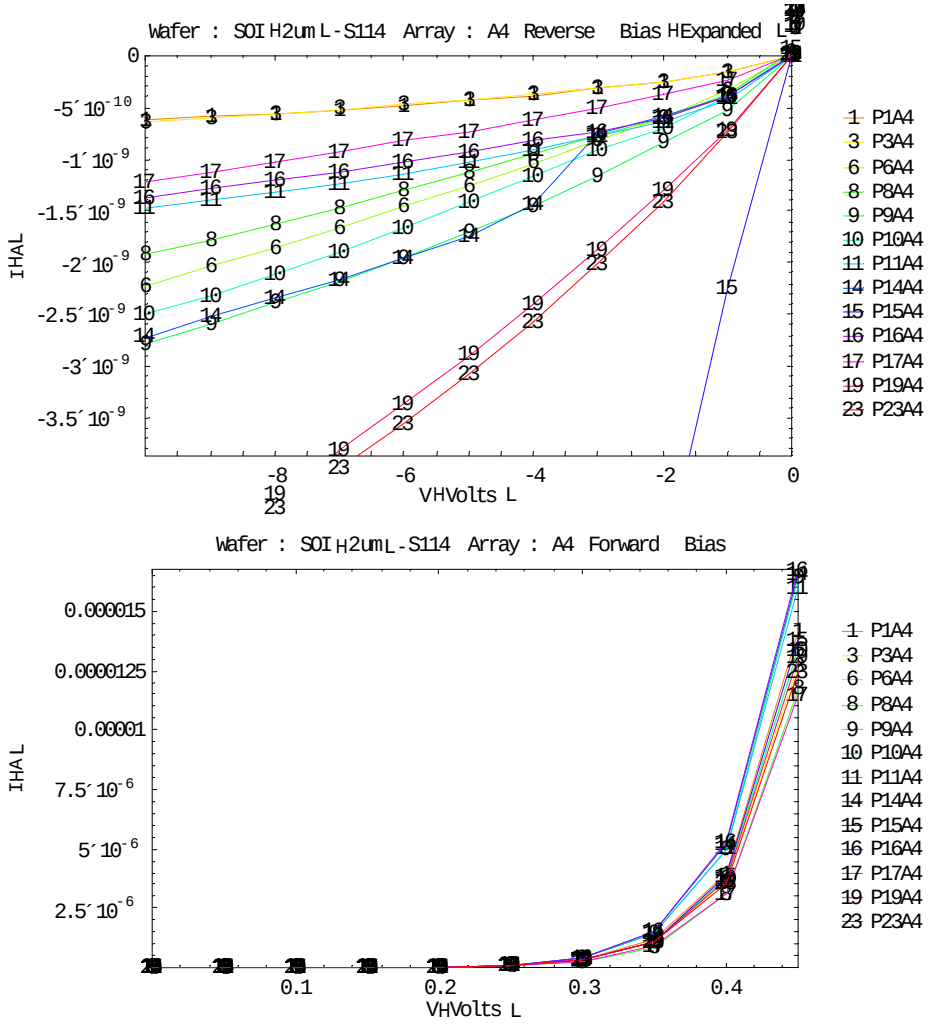


Figure 4.5. Example of the forward and reverse bias I-V characteristics for 2 µm SOI array A4. Only those components that passed the I-V tests are displayed with specific part numbers in the legend.

4.2.2 Capacitance-Voltage Measurements

Capacitance-Voltage measurements of the diode structures were performed on selected devices. Capacitance information is necessary for noise calculations and may provide information on substrate doping concentrations. A Boonton capacitance meter (Model 7200) controlled by a PC via an IEEE-488 interface was used for the measurements. The meter has a resolution of 0.01 pF and a measurement error of 0.5%. Wiring capacitance contributions are cancelled by zeroing the meter without the device connected.

The reverse bias capacitance of a diode is dominated by depletion capacitance. An increment of the reverse bias voltage *dV* uncovers an increment of space charge *dQ*, which causes an increase in the electric field by an amount $de = dQ / e_s$ (from Poisson's equation). Therefore, the depletion capacitance per unit area C_j is given by [44]:

$$C_j \equiv \frac{dQ}{dV} = \frac{dQ}{W_d \dfrac{dQ}{e_s}} = \frac{e_s}{W_d} \qquad \mathrm{F/cm^2} \tag{4.2}$$

where W_d is the depletion region width and e_s is the permittivity of silicon. This equation is valid for any arbitrary impurity distribution. Solving Poisson's equation for a one-sided abrupt junction (e.g. *n*+-*p* diode with constant doping *n*+ >> *p* doping) provides an equation for W_d:

$$W_d = \sqrt{\frac{2e_s(V_{bi} - V)}{qN_B}} \tag{4.3}$$

where V_{bi} is the built-in potential, *q* is the electron charge and N_B is the substrate doping concentration. The depletion width is plotted against reverse bias voltage in Figure 4.6. Equation (4.2) may be combined with equation (4.3) to give [44]:

$$\frac{1}{C_j^{\,2}} = \frac{2(V_{bi} - V)}{qe_s N_B} \tag{4.4}$$

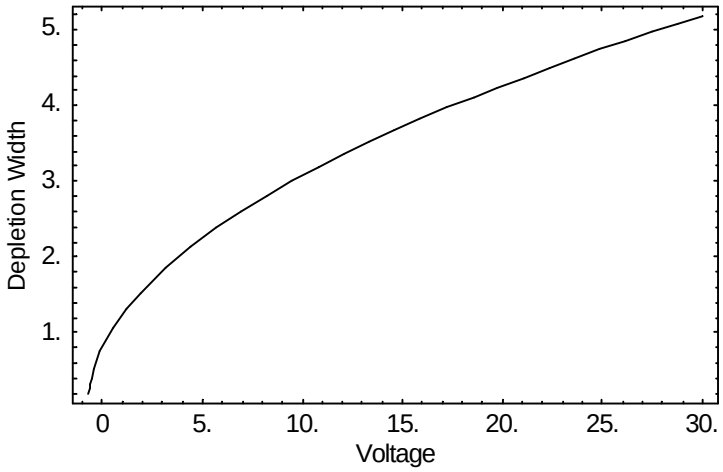


Figure 4.6. Depletion width versus reverse bias voltage ($N_B = 1.5 \times 10^{15}$cm^{-3} and $V_{bi} = 0.74$)

Thus, for a one-sided abrupt junction a plot of $1/C_j^2$ versus V produces a straight line. The slope gives the impurity concentration and the intercept at $1/C_j^2=0$ gives $V_{bi.}$ Plots of $1/C_j^2$ versus V for the small cell array were constructed. The 2 μm, 5 μm, 10 μm and bulk devices were compared as shown in Figure 4.7. The 2 μm SOI deviates significantly from the other devices due to the influence of the insulating layer at the bias levels presented. The C-V characteristic, for the diode topology used, is not well modeled by a parallel plate capacitor when the depletion region width approaches or consumes the silicon thickness. Figure 4.8 compares the arrays within a bulk device using a similar plot. If the model presented by equation (4.4) was correct than the curves should be identical for each array (since the capacitance is normalized to area).

None of the devices exhibits a straight line, indicating either changing impurity concentrations with depth or deviations from the simple one dimensional capacitance model. It will be shown that the latter applies in this case, particularly since capacitance per unit area is unequal between arrays. Such deviations from the simple model represented by equation (4.4) include the influence of capacitances other than the depletion capacitance and the effect of a finite cell width with respect to the cell depth. An analytical expression for the total capacitance to substrate, C_I, of an isolated pixel diode is provided by Cerdeira [165] based on the work of Kavadias [166].

$$\frac{C_I}{C_{1d}} = 0.965 + 2.27\frac{W_d}{L} \tag{4.5}$$

where C_{1d} is the planar one dimensional capacitance of the diode as per equation (2.28), L is the cell junction width and W_d is the one dimensional depth defined by equation

(4.3). Note that this expression is obtained by fitting the curve that results from the three dimensional numerical solution of the Laplace equation.

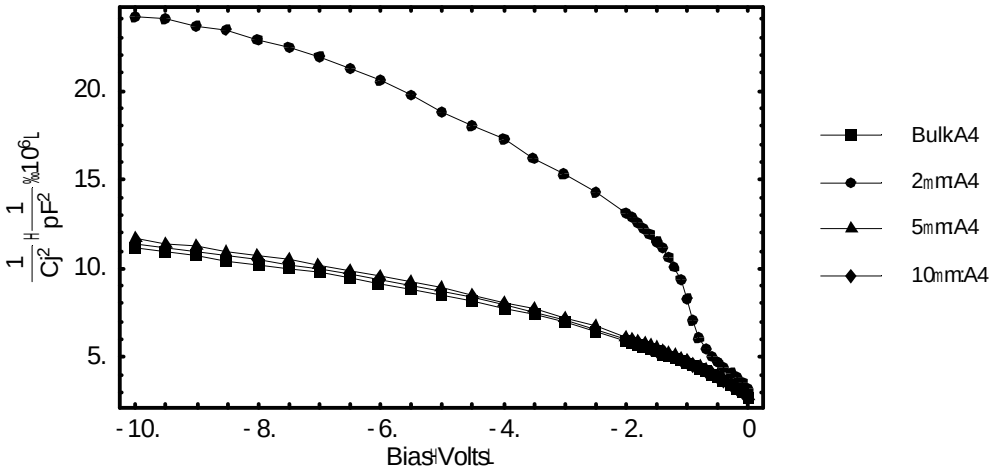


Figure 4.7. Plot of $1/C_j^2$ versus reverse bias where C_j = detector capacitance per unit junction area. The 2 μm SOI is influenced by the insulating layer at the bias levels presented

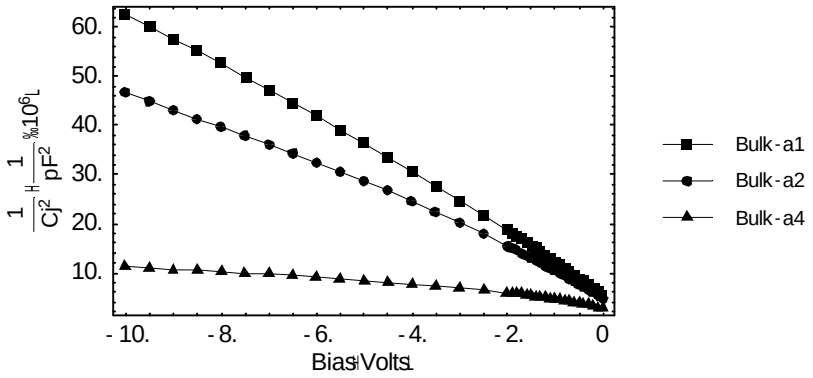


Figure 4.8. Plot of $1/C_j^2$ versus reverse bias where C_j = detector capacitance per unit junction area. Arrays for a bulk device are compared

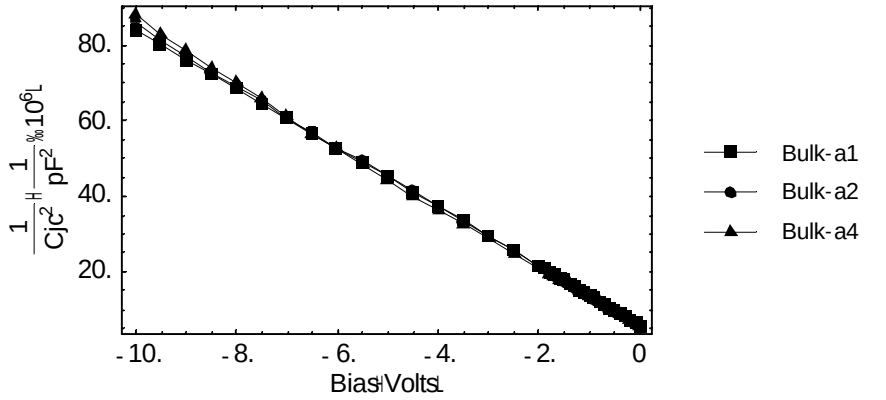


Figure 4.9. Plot of $1/C_{jc}^2$ versus reverse bias where C_{jc} = corrected detector capacitance per unit junction area. Arrays for a bulk device are compared. See also Figure 4.8.

The aluminium layer, which routes the reverse bias voltage to the junctions, contributes an additional capacitance C_{al} that should be included in our capacitance model. This capacitance is formed by the metal-oxide-substrate structure (i.e. a MOS diode) and consists of the oxide capacitance C_{ox} and the semiconductor depletion layer capacitance C_d in series [44]. Therefore

$$\begin{aligned} C_{al} &= \frac{C_{ox}C_d}{C_{ox}+C_d} \\ &= \frac{e_{ox}/d_{ox}}{1+\frac{e_{ox}W_m}{e_s d_{ox}}} = \begin{cases} 6\times10^{-5}\,pF/mm^2 \text{ if } d_{ox}=0.4mm \\ 3.6\times10^{-5}\,pF/mm^2 \text{ if } d_{ox}=0.78mm \end{cases} \end{aligned} \tag{4.6}$$

where e_{ox} is the permittivity of silicon dioxide, d_{ox} is the oxide thickness (see Figure 6.8) and W_m is the maximum width of the surface depletion layer (~0.5 μm from p186 ff. Sze [44]). In addition, there may exist some parasitic capacitance C_p. Using equations (4.2), (4.3) and (4.5) the final model for the measured diode array capacitance C_m with n_c cells is

$$\begin{aligned} C_m &= C_p + C_{al} + n_c\left(2.27e_sL + 0.965L^2\sqrt{\frac{qe_sN_B}{2(V_{bi}-V)}}\right) \\ &= C_c + n_c 0.965L^2\sqrt{\frac{qe_sN_B}{2(V_{bi}-V)}} \end{aligned} \tag{4.7}$$

where C_c is a capacitance term that groups together the first three terms for convenience.

$$C_c = C_p + C_{al} + n_c 2.27e_sL \tag{4.8}$$

If we define a corrected capacitance per unit junction area C_{jc} as

$$\begin{aligned} C_{jc} &= \frac{C_m - C_c}{n_c L^2} \\ &= k\sqrt{\frac{qe_sN_B}{2(V_{bi}-V)}} \text{ where } k = 0.965 \end{aligned} \tag{4.9}$$

then a plot of $1/C_{jc}^2$ versus V should produce a straight line provided the variables are correctly set. It is possible to simultaneously determine V_{bi}, N_B and the required correction capacitances C_c for each array using a non-linear fitting routine. The routine

uses the Levenberg-Marquardt method to minimize the χ^2 merit function given by the some of the squares of the residual. That is, χ^2 is calculated as

$$c^2 = \sum \frac{\left(C_{m\_fit}(V, N_B, V_{bi}, C_{c\_a1}) - C_{m\_data\_a1}\right)^2}{\left(C_{m\_data\_a1}\right)^2} + \sum \frac{\left(C_{m\_fit}(V, N_B, V_{bi}, C_{c\_a2}) - C_{m\_data\_a2}\right)^2}{\left(C_{m\_data\_a2}\right)^2} + \sum \frac{\left(C_{m\_fit}(V, N_B, V_{bi}, C_{c\_a4}) - C_{m\_data\_a4}\right)^2}{\left(C_{m\_data\_a4}\right)^2} \tag{4.10}$$

The process, programmed in Mathematica, calculated the parameters given in Table 4.3. Using these parameters $1/C_{jc}^2$ is plotted versus V for various arrays as shown in Figure 4.9. Good linearity over the entire voltage range is observed along with a close correspondence between different array and cell sizes. This is in stark contrast to the simpler model presented in Figure 4.8. The substrate doping concentration is within 7% of the value provided by Fujitsu: $N_B = 1.5 \times 10^{15}$ boron atoms/cm^3 [162].

Table 4.3. Parameters estimated for diode arrays from C-V data

Parameter	Data Fit	Other Calculations
N_B	1.6×10^{15}/cm^3	1.5×10^{15}/cm^3 (Note 1)
V_{bi}	0.74 V	0.9 V (Note 2)
C_{c_a1}	8.4 pF	9.0 pF (Note 3)
C_{c_a2}	6.4 pF	5.9 pF (Note 3)
C_{c_a4}	29.6 pF	20.5 pF (Note 3)

Note 1: From Fujitsu manufacturers.
Note 2: Very rough calculation based on ideal abrupt junction equation (4.11).
Note 3: Based on equations (4.6) and (4.8), see Table 4.4.

The other parameters may be roughly estimated. For an abrupt junction:

$$V_{bi} = \frac{kT}{q} \ln \frac{N_A N_B}{n_i^2} \tag{4.11}$$

where n_i = intrinsic carrier density. However, the junction is not perfectly abrupt and the appropriate value for the n+ region doping density is difficult to estimate. Using an average value of $N_A = 2 \times 10^{20}$ /cm^3 we obtain $V_{bi} = 0.9$ V. In this case, one would consider the value calculated using C-V methods as the best representation of built-in voltage.

The correction capacitance values may be estimated by using equation (4.6) and (4.8) with the total metal area not covering a junction included in the calculation. A parasitic capacitance of 0.5 pF was also included. The values and sub-components are shown in Table 4.4. The calculated values of C_c for diode arrays A1 and A2 are reasonably close (within 10%) to those extracted from the C-V curve fit model whilst A4 differs by 30%. Given the approximate nature of equation (4.6) the correspondence is quite reasonable and one can state that the detector capacitance is reasonably well modeled by metal-oxide track capacitance and the traditional pixel array depletion capacitance as quantified by equation (4.7). The method presented for calculating the model parameters (C_c, N_B, and V_{bi}) is simple and appears to provide a reasonably accurate estimate of substrate doping concentration that corresponds well with the manufacturers value. The model indicates the importance of minimizing metal-oxide track capacitance by having a thick oxide layer separating the metal from the substrate and minimum metal area. The capacitance model presented here will be used in future sections for noise calculations and optimization.

Table 4.4. Correction capacitance values for each array

Capacitance	Array 1 (pF)	Array 2 (pF)	Array 4 (pF)
C_p	0.5	0.5	0.5
C_{al}	4.9	4.2	8.5
$n_c 2.27 e_s L$	3.6	1.2	11.5
Total $=C_c$	9	5.9	20.5

4.3 Probe Assembly #1

Two different probe assemblies are used in this work corresponding to different stages in the project development. Prototype assembly #1 was the first assembly constructed and consists of the microdosimeter package inserted into a machined Lucite holder with a 1 m coaxial cable connecting the detector to a Canberra 2003T charge sensitive preamplifier (CSA) as shown in Figure 4.10. Noise was minimized by encapsulating the entire microdosimeter probe in an aluminum foil shielding which was then connected to the coaxial cable ground. This also ensured that the chip did not receive any light, which generates significant noise via surface photo-generation.

An 8-meter coaxial cable links the preamplifier to a Canberra 2024 Fast Spectroscopy amplifier. The output of this amplifier is a voltage pulse whose amplitude is proportional to the energy deposited in the sensitive volume of the microdosimeter.

Note that the microdosimeter collects charge generated by the traversal of an ion through the device's sensitive volume. The charge collected is proportional to the energy deposited, as it requires 3.6 eV to generate an electron hole pair in silicon. The pulse height from each event is digitized and stored using a PC based Multi-Channel Analyzer (MCA).

A two-point calibration of this system was performed using a polonium-210 alpha spectroscopy source with alpha peak energy of 5.301 MeV and an Americium-241 alpha-gamma source. The 60 keV gamma peak of the Am-241 source was used as a low energy reference point to ensure a good estimation of system offset. The diode array was replaced by a silicon ion implanted detector of similar capacitance, which collects charge corresponding to the total energy of the alpha particle.

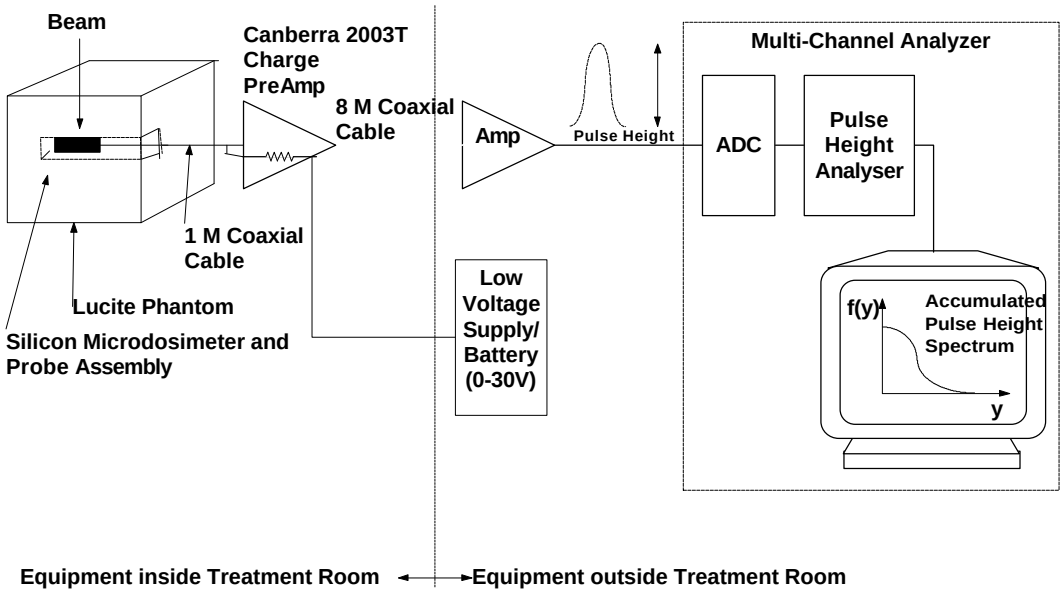


Figure 4.10: Experimental setup for microdosimetry measurements using probe assembly #1 (original assembly)

The supply voltage used varied from 0 to 20 V reverse bias with 10 V commonly used. The system electronic noise was measured at a bias voltage of 10 V using an Ortec 414 pulsar capacitively coupled to the pre-amplifier input. With an amplifier shaping time of t = 2 μs the FWHM noise was 8.5 keV (or 1000 electrons rms, see equation (4.23)). Minimum measurable energies are usually twice the FWHM. Thus, the minimum lineal energy even using the thick 10 μm SOI with a sensitive depth of 8.2 μm is quite high at approximately 2 keV/μm in silicon or 1 keV/μm in tissue, as per equation (3.42). There is no design margin with respect to the requirement of 1 keV/μm stipulated in the summary of chapter 3 and we would also prefer measurements in smaller sensitive

volumes. Thus, the noise performance was improved by a new more optimal design described in the next section.

4.4 Probe Assembly #2

The noise performance of the first prototype could be significantly improved by removing the 100pF capacitance added by the detector to CSA cable and improving shielding to gain immunity to external electromagnetic fields (particularly RF interference). The second prototype assembly, based on a printed circuit board design, uses an AMPTEK A250 radiation-hard CSA in close proximity to the detector. The A250 amplifier is designed specifically for low noise CSA applications in radiation environments up to 10^3 Gys. The amplifier allows for selection of all important components in order to optimize noise given the detector and signal characteristics. A system view of the low noise prototype is shown in Figure 4.11. The complete circuit diagram for the probe is shown in Appendix C and a photo of the probe is shown in Figure 4.12. Calibration of this low noise prototype is performed as per the older prototype discussed earlier.

The selection of most of the components and the design equations are fully described in the following section. Important considerations not discussed later are now presented.

- A JFET is used as the input transistor due to its high input impedance, high transconductance and low input capacitance.
- The A250 is not designed for driving long cables or large capacitance loads. Therefore a fast low noise buffer is used to drive the 8 M coax cable. An AD829 high speed operational amplifier was configured as a non-inverting buffer with adjustable gain from 3 to 45. The noise contribution to the signal is almost negligible as will be discussed in the following section. Each stage is AC-coupled to ensure DC stability.
- Fast rise time signals over long cables must be accurately impedance matched. However, if a signal has a rise time which is more than a few times the cable delay time then distortion of the leading edge of the pulse by reflections will be completely obscured by the inherent rise time of the signal, and there is no point in bothering to terminate the line with its characteristic impedance. Typical coaxial cables (50-100 ohm) have delay times of 5 ns/m. The rise time of the preamplifier

output is about 40 ns (from the A250 data-sheet). With 8 M cable lengths to the spectroscopy amplifier, correct termination of the cable with characteristic impedance was employed. Correct termination is even more important for the pulsar input since the rise time is of the order of a few nanoseconds.

- High quality ceramic disc bypass capacitors on both the A250 and AD829 power supplies assist in minimizing power supply coupled noise and instability. A battery powered +/- 6 volt DC regulated supply was constructed to power the probe electronics. A separate regulated supply adjustable from 0 to 15 V was used for the detector bias supply.

- The entire probe was encapsulated in an aluminium shield ($40\times25\times180 mm^3$, 0.4 mm thick sheet) to reduce external electromagnetic noise sources. The shield design includes as few non-conductive holes and gaps as possible. Air gaps between the electronics and shield are filled with Lucite blocks machined to fit the board contours.

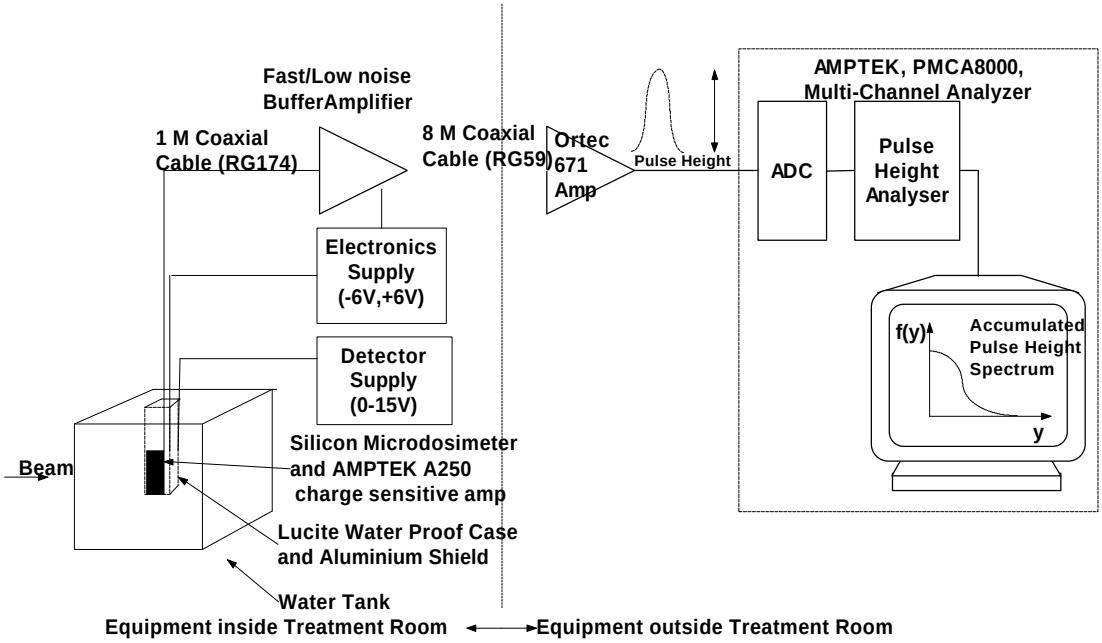


Figure 4.11: Experimental setup for microdosimetry measurements using probe assembly #2 (low noise)



Figure 4.12. Probe assembly #2: PCB mounted electronics showing Fujitsu prototype microdosimeter, preamplifier and buffer amplifier. The board inserts into an aluminium box with the remaining air gaps filled by Lucite blocks.

4.5 Design Equations, Noise Modeling and Optimization

4.5.1 Basic Design Equations and Noise Model

There are three main fundamental noise mechanisms in electronic circuits; thermal, shot and flicker noise [167, 168]. In this section, a model for the noise performance of the detector is presented based on these mechanisms. First, we briefly describe these noise phenomena.

Thermal Noise is due to the thermal excitation of charge carriers in a conductor. The Brownian type random motion of electrons produces noise that has a white spectral density and is proportional to absolute temperature. It should be mentioned here that thermal noise is also referred to as Johnson or Nyquist noise since it was first observed by J.B. Johnson and analyzed using the second law of thermodynamics by H. Nyquist in 1928 [169]. The thermal noise of a resistor R may be modeled as a current source in parallel with the resistor. The mean square value of the current noise source $\overline{i_{th}^2}$ is given by,

$$\overline{i_{th}^2} = \frac{4kTdf}{R} \tag{4.12}$$

where k = Boltzmann's constant and T = temperature (300 K).

Shot Noise was first studied by W. Schottky [170] in connection with current fluctuations in thermionic diodes but the effect also occurs for minority carriers in P-N junctions. This noise occurs because the dc bias current is not smooth and continuous

but instead is a result of pulses of current caused by the individual flow of carriers. Shot noise may be modeled as a current dependent white noise source $\overline{i_s^2}$ given by

$$\overline{i_s^2} = 2qI_b df \tag{4.13}$$

where q = electron charge and I_b is the dc bias current.

Flicker Noise is the least well understood of the three noise phenomena. It is found in all active devices where a dc current is flowing. Flicker noise usually arises due to traps in the semiconductor where carriers that would normally constitute dc current are held for some time period and then released. Flicker noise is also commonly referred to as 1/f noise since it is well modeled by a $1/f^{\alpha}$ spectral density, where α is between 0.8 and 1.3. For a JFET, flicker noise is modeled as a voltage noise source $\overline{v_f^2}$ in series with the gate, as follows.

$$\overline{v_f^2} = \frac{K_f}{C_g f} df \tag{4.14}$$

where C_g is the gate capacitance and K_f is a device dependent constant.

For the JFET channel, thermal noise associated with the channel resistance will vastly exceed any shot noise since the majority carrier current dominates. When the transistor is in the active region the channel resistance was found to be $R_{ch} = 1/(g\ g_m)$ where g_m is the transconductance and g is usually taken to be 2/3 [171]. The model for the JFET channel thermal noise $\overline{i_{ch}^2}$ is then given by

$$\begin{aligned} \overline{i_{ch}^2} &= 4kT / R_{ch} df \\ R_{ch} &= 1/(g\ g_m) \end{aligned} \tag{4.15}$$

The channel noise may be referred to the gate of the transistor by using the definition of transconductance (i.e. $\overline{v_g^2} = \overline{i_{ch}^2} / g_m^2$). Adding the flicker noise, we obtain the following noise model for the FET as a voltage noise source at the gate input.

$$\overline{v_{FET}^2} = \left(\frac{4kTg}{g_m} + \frac{K_f}{C_g f} \right) df \tag{4.16}$$

In order to optimize the noise performance of the detector a noise model of the system was developed based on the previously described mechanisms. The calculation follows noise analysis methods presented by Delaney and Finch [168] or Radeka [41]. The model, depicted in Figure 4.13, considers the primary noise sources as the bias resistor R_b thermal noise; feedback resistor R_f thermal noise; the detector current I_d shot noise; the thermal noise associated with the JFET channel resistance and the 1/f noise of the JFET.

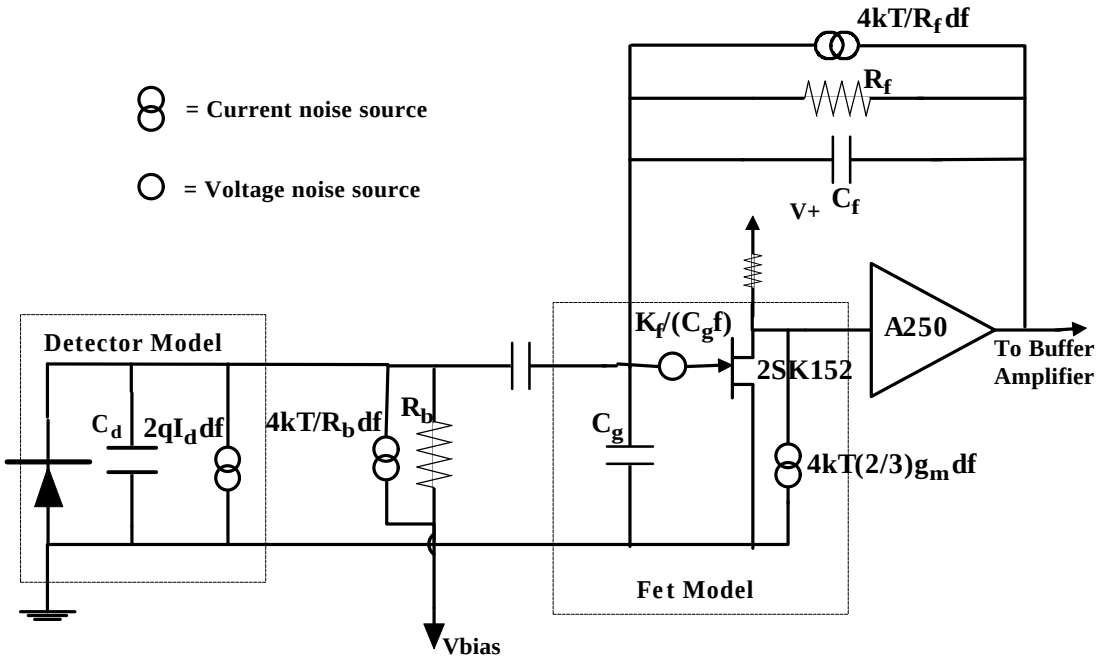


Figure 4.13. Noise model of microdosimeter and charge sensitive pre-amplifier

The first step in the noise calculation is to refer all the noise sources to the output of the amplifier. For the FET gate noise source, simple voltage division along with the assumption that the amplifier has a large open loop gain gives:

$$v_{out} = v_{FET}\left(\frac{Z_{in} + Z_f}{Z_{in}}\right) \tag{4.17}$$

where Z_{in} is the impedance looking back to the detector from the gate and Z_f is the feedback impedance. At the frequencies representative of a charge pulse (f>10 KHz), Z_{in} and Z_f are effectively the impedances of the detector capacitance C_d and the feedback capacitance C_f.

The other noise sources are all current sources, which charge up the feedback capacitance. They are referred to the output using the sensitivity equation for the CSA.

$$v_{out} = i_{in} Z_f$$
$$\therefore |v_{out}| \approx \frac{i_{in}}{wC_f} \tag{4.18}$$

Usually the sensitivity equation for the CSA is written in terms of Q_D, the charge released by the detector.

$$v_{out} = \frac{Q_D}{C_f} \tag{4.19}$$

Using the previous equations (4.12) to (4.19), the total differential rms noise at the output is given by

$$\overline{v^2_{total\_CSA}} = \left(\frac{4kT}{R_T} + 2qI_d\right)\left(\frac{1}{wC_f}\right)^2 + \left(\frac{4kTg}{g_m} + \frac{K_f}{C_g f}\right)\left(\frac{C_f + C_{in}}{C_f}\right)^2 \frac{dw}{2p} \tag{4.20}$$

where $1/R_T = 1/R_b + 1/R_f$ and $C_{in} = C_d + C_g + C_{stray}$, C_d = detector capacitance, C_g = JFET gate capacitance, C_{stray} = stray input capacitance and $w = 2pf$.

An important aspect of noise reduction is the spectroscopy amplifier that follows the CSA. This amplifier limits the bandwidth to significantly reduce noise. A general purpose wide-band amplifier has upper and lower fall off frequencies. It can be shown that the optimum signal to noise ratio for a spectroscopy system occurs when these frequencies are equal with a corresponding shaping time constant equal to t [167]. The amplifier frequency response is modelled by a simple RC-CR filter as follows.

$$A(w) = \frac{A_0 wt}{1 + w^2 t^2} \tag{4.21}$$

The optimum S/N is obtained using a cusp pulse shape. The simple RC-CR filter with a somewhat Gaussian shape exhibits a S/N that is 36% worse than the optimum. However, the spectroscopy amplifiers used in this study are capable of triangular shaping which provides performance within 7.5% of the optimum S/N. The total noise on the output of the spectroscopy amplifier is given by integrating equation (4.20) and (4.21) over all frequencies.

$$\overline{v_{total}^2} = \int_0^\infty A^2(w)\overline{v_{total\_CSA}^2}dw$$
$$= A_0^2\left[\frac{kTt}{2R_TC_f^2} + \frac{qI_dt}{4C_f^2} + \frac{kTg\left(C_f + C_{in}\right)^2}{3g_mtC_f^2} + \frac{K_f\left(C_f + C_{in}\right)^2}{2C_gC_f^2}\right] \quad (4.22)$$

The total noise is usually expressed using the concept of equivalent noise charge (ENC). This is defined as the genuine charge signal which will produce the same output as the RMS noise. ENC is usually presented in units of electrons RMS (e_{rms}) or as an FWHM (Full Width Half Maximum) expression in keV defined as:

$$FWHM(\text{keV Silicon}) = 2.35W/1000\, e_{rms} = 0.0085e_{rms} \quad (4.23)$$

where W is the mean energy expended per electron hole pair (3.62 eV). If a charge signal Q is deposited on the input of the preamplifier then the corresponding voltage step at the output of a wide-band amplifier is A_oQ/C_f. However, since the rise and fall times have been made equal the peak pulse height voltage will be less. Simple circuit analysis (See Delaney [168] p275 and p308) indicates that the gain is reduced by a factor Exp(1) down to $A_oQ/(C_f\,E)$. Equating the square of this signal value with $\overline{v_{total}^2}$ and solving for Q gives the *ENC*.

$$ENC = E\sqrt{\frac{kTt}{2R_T} + \frac{qI_dt}{4} + \frac{kT\left(C_f + C_{in}\right)^2}{3g_mt} + \frac{K_f\left(C_f + C_{in}\right)^2}{2C_g}} \quad (4.24)$$

Note that the calculation assumes that the feedback time constant (R_fC_f) and input time constant ($R_b\,C_{in}$) are much greater than t and that the buffer and spectroscopy amplifier contribute negligible noise.

4.5.2 Optimization of Shaping Time

From equation (4.24) it is evident that one may select an optimum t such that ENC is a minimum. Rewriting equation (4.24) we obtain

$$ENC^2 = Lt + \frac{MC_T^2}{t} + NC_T^2 \quad (4.25)$$

where we have simplified the equation by using constants L, M, and N and $C_T = C_f + C_{in}$.

$$L = E^2\left(\frac{kT}{2R_T} + \frac{qI_d}{4}\right),\ M = E^2\frac{kT}{3g_m},\ N = E^2\frac{K_f}{2C_g}$$

Differentiating to find the minimum yields:

$$t_{\min} = \sqrt{\frac{M}{L}} C_T \tag{4.26}$$

and then substituting back into equation (4.25) gives

$$ENC^2 = \sqrt{LM}\, C_T + \sqrt{LM}\, C_T + N C_T^2 \tag{4.27}$$

From equation (4.27) it is evident that we can minimize ENC by equalizing the contribution to noise of the bias and feedback resistor and detector shot noise (which increase with t) with the channel thermal noise (which decreases with increasing t). The former components are often called parallel noise sources since they are in parallel with the detector whilst the later are referred to as series noise sources. This optimization process is shown in Figure 4.14 with parameter values as selected in section 4.5.4.

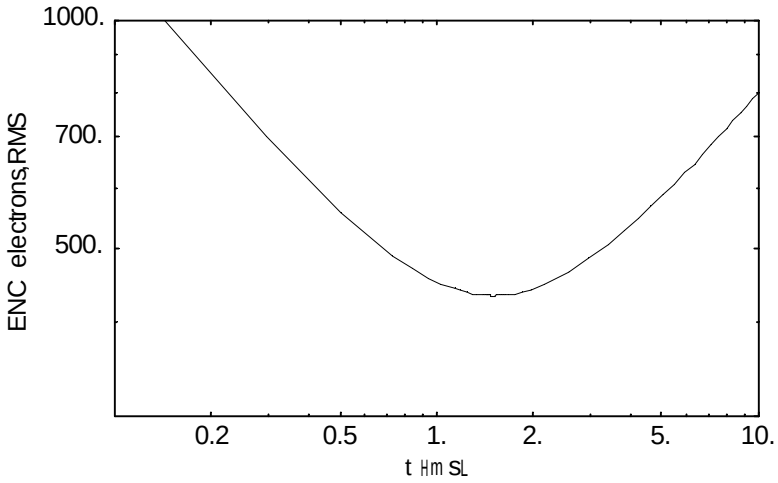


Figure 4.14. ENC versus shaping time. Vb=10 V, All parameters as per Table 4.6. FET channel noise (series noise) dominates for large τ whilst bias current and resistor thermal noise dominates for small τ. The optimum occurs when these components are equal.

4.5.3 Optimization of Detector Voltage

In general, the detector voltage should be set to fully deplete the SOI thickness. Under such conditions, the charge collection is drift driven and close to 100% efficient. The voltage required to fully deplete the SOI thickness is given by equation (4.3) and Figure 4.6. With a maximum reverse bias voltage before breakdown of around 30 V, it is evident that we may only fully deplete the 2 and 5 μm SOI devices. However, the requirement of full depletion is not a strict requirement for reasonable charge collection efficiency. Provided the minority carrier lifetime (and hence the diffusion length) of the silicon is relatively long, charge collection may still be efficient outside of the depletion

region. The charge collection behavior of the device will be fully discussed in chapter 6. Despite the general desire to fix detector voltage for full depletion, it is nevertheless instructive to determine the optimum ENC with respect to voltage assuming that charge collection is equally efficient for all depletion widths.

This second less obvious optimization may be performed by consideration of equation (4.24) with the substitution of the equations for capacitance (4.7) and bias current (4.1) as a function of detector bias voltage. The spectroscopy amplifiers used (Ortec Model 671, or Canberra Model 2020) have fixed shaping times of 0.5, 1, 2, 5 and 10 μsec. The ENC for the various allowable shaping times as a function of bias supply voltage is shown in Figure 4.15. For each shaping time the optimum voltage and corresponding ENC is given in Table 4.5. At low voltages the detector capacitance rises, which increases the channel noise, whilst the detector shot noise drops with the lower bias current. Therefore, the optimum t increases as the voltage drops since channel noise is reduced by increasing t (see Figure 4.15 and Figure 4.16). Occasionally the optimum t coincides with one of the available fixed shaping times as seen in Figure 4.15 for t = 1 μs and V = 20. The absolute minimum ENC as a function of voltage was calculated by using the optimum τ as given by equation (4.26). That is, the equation for capacitance (4.7) and bias current (4.1) were substituted into equation (4.27) and a steepest descent numerical algorithm was employed to find the minimum. Note that an analytical solution is possible if we assume that C_c and C_f are negligible in comparison with the $\sqrt{1/(V_{bi}-V)}$ capacitance (second term of equation (4.7)). This assumption is reasonable for low voltages. The quite complex solution is not presented here since it is too complicated to provide additional illumination and the more accurate numerical optimization is preferred. The minimum possible ENC of 344 electrons rms occurs at V = 0.15. If the detector current is reduced, by selecting a device with a lower resistance, then the shot noise is reduced. To obtain equal series and parallel noise sources, the capacitance must rise to increase the channel noise. Hence, the absolute optimum ENC is found at higher voltages and higher shaping times as the detector resistance rises. This effect is shown in Figure 4.16. This is a valuable result since it emphasizes the great benefit in reducing leakage current. Moving the optimum ENC to higher voltages corresponds with our desire to fully deplete the SOI thickness as discussed earlier. Note that to fully deplete the 2 μm and thicker SOI devices a voltage greater than 5V is required.

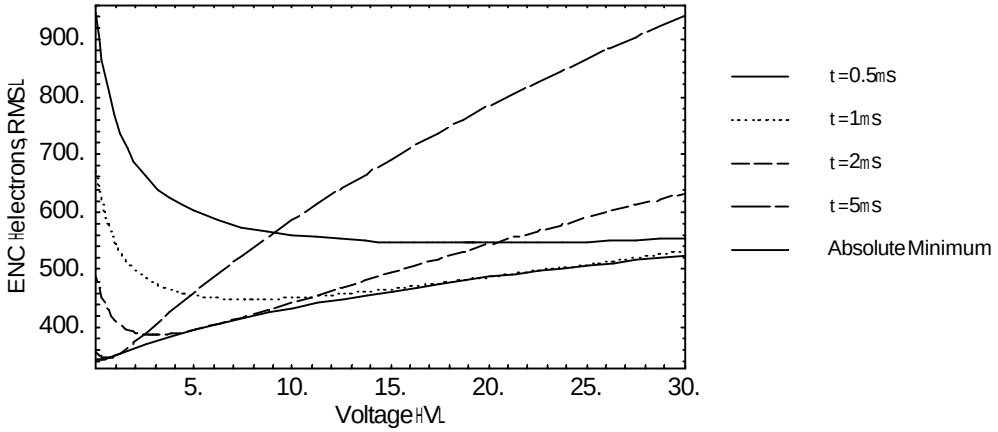


Figure 4.15. ENC versus detector bias supply voltage for each value of available shaping time. The absolute minimum ENC is also shown. In this case τ is free to vary to the optimal value (Optimal τ is large for small voltages and decreasing to smaller τ at larger voltages).

Table 4.5. Optimum detector bias supply voltage for each value of shaping time.

Shaping Time (μs)	Optimal Voltage(V)	ENC (rms, electrons)
0.5	19.1	546
1	7.73	449
2	2.95	387
5	0.52	347

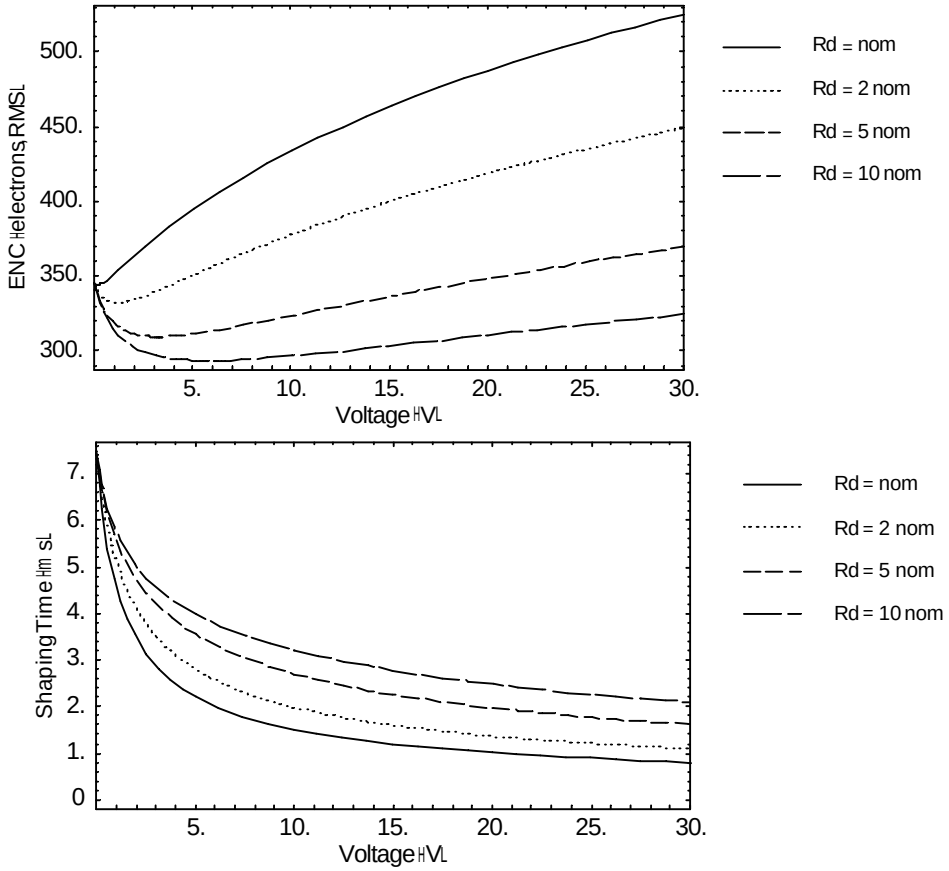


Figure 4.16. Optimal ENC versus voltage (top) and the corresponding shaping time (bottom) required to obtain the optimal ENC. Various values of detector resistance relative to the nominal 2 × 10^9 ohms are shown. At higher detector resistance values the detector current shot noise is reduced.

4.5.4 Selection of Key Components and Parameters

Before adjusting t to obtain the desired equalization of noise contributions one should first select circuit components to minimize ENC as given by Equation (4.24). Several conflicting design requirements arise as will be discussed in the following summary of component selection.

FET: A good quality FET with high g_m, small gate capacitance and a low flicker noise coefficient should be selected. A large FET transconductance conflicts with the need for low gate capacitance. Consequently, the FET is usually designed with a very large width and minimum length. The 2SK152 FET was selected for its excellent g_m/C_g ratio and relatively low flicker noise. The bias current of the FET was set to 6mA using resistor R9 (see Appendix C) which provides a g_m = 20mS and C_g = 7pF. The current was selected as high as possible (to maximize g_m) whilst still providing a safe operating margin with respect to absolute ratings. In addition, the amplifier is battery operated so power consumption was also considered. For the purposes of noise calculations, the FET noise model was fitted to noise data from the 2SK152 data sheet. In order to obtain a good match, the parameters g = 4/3, g_m = 20mS C_g = 7pF are required.

C_f: The feedback capacitance primarily determines the preamplifier sensitivity or gain via equation (4.19). The A250 amplifier conveniently has an in-built 1 pF capacitor which provides an adequate gain of 44 mV/MeV. Note that too high a gain affects the maximum count rate attainable by the preamplifier before output saturation as given by equation (4.28). It will be shown later (in the R_f discussion) that the gain is appropriate.

R_f: The resistor noise should be minimized by selecting large values of R_f. However, the maximum value of R_f is limited by the need to discharge the feedback capacitor between pulses. The maximum counting rate tolerated by ac-coupled preamplifiers r_{max} is controlled by the signal fluctuations and the maximum voltage V_m allowed at the charge loop output [172].

$$r_{\max} = \frac{1.2 V_m^2 e^2 C_f}{E_s^2 R_f} \times 10^{25} \tag{4.28}$$

where E_s is the energy deposited in MeV, e = energy to form e-h pair = 3.62 eV and r_{max} is in counts/second . Using the proposed values of R_f = 300 Mohms and C_f = 1

pF and with E_s = 3 MeV (300 keV/μm particle in 10 μm thick detector) and V_m = 5V (given 6V supply to preamplifier) we obtain a value of $r_{max} = 1.44 \times 10^6$ /s. So the system is limited not by the preamplifier but by the spectroscopy amplifier with its minimum allowable time constant of 0.5 μs. Note that if the discharge time is set too low in comparison with the charge collection time (<10ns in our case), the signal may not be completely integrated (the so-called ballistic deficit effect). This phenomenon, sometimes called the ballistic deficit effect, is not an issue in this case since the fall time ($R_f C_f$ = 0.3 ms) is much greater than the charge collection time (<10 ns).

τ: The shaping time constant selection is influenced by two factors; the maximum count rate expected and the minimization of noise as discussed fully in sections 4.5.2 and 4.5.3. In our case, we often have high count rate requirements in radiation therapy applications. The shaping time was set to 0.5, 1 or 2 μs with 0.5 the dominant setting. Selecting the lower shaping time compromises somewhat our minimum ENC as shown in Figure 4.15. Note, that a smaller detector area would be useful to reduce the count rate, thus allowing a higher t, whilst simultaneously reducing noise by decreasing detector capacitance.

R_b: The resistor noise should be minimized by selecting large values of R_b. However, the maximum value of R_b is limited by the required voltage V_d across the detector. That is, $V_d = V_b - I_b R_b$, where V_b is the input bias supply voltage. From section 4.2.1 the bias current is given by equation (4.1) so the ratio of detector voltage to input bias voltage is given by

$$\frac{V_d}{V_b} = \frac{1}{1 + \frac{R_b}{R_d}} \tag{4.29}$$

R_b was set to 100 MΩ, the highest readily available resistor. The lowest value of R_d from Table 4.2 is $R_d > 2 \times 10^9 \Omega$ giving $V_d / V_b > 0.95$ which is sufficiently close to unity.

I_b: The detector bias current should be minimized to reduce shot noise. Selecting components with low bias currents, as determined from I-V testing, is recommended. Low bias currents may also be achieved by reducing the detector

bias voltage V_d but, as discussed in the previous section, this may not be compatible with the desired depletion width.

V_b: In this work a bias voltage V_b of between 9-20 V is most frequently used. Such a voltage range enables full depletion of the 2 μm SOI. Other SOI types are not fully depleted but voltages higher than 20V were avoided to provide adequate breakdown voltage margin. Furthermore, a bias voltage of 9-10V was easily available using a battery supply. Figure 4.15 provides a useful guideline for selecting the voltage based on minimum ENC considerations for different shaping times.

The component values and the relative noise contributions are summarized in Table 4.6. The contribution to noise of the buffer amplifier is also included based on modeling of amplifier and input resistor thermal noise sources. Note that the AD829 has a low input bias noise current of 1.5 pA/Hz$^{1/2}$ and low voltage noise of 1.7 nV/ Hz$^{1/2}$. The noise contribution calculated adds less than 0.1 keV to the final FWHM.

Table 4.6. Relative contribution of noise components in microdosimeter design

Noise Source	Relevant Values	Noise (t = 0.5 μs) Electrons (RMS)	Noise (t = 2 μs) Electrons (RMS)
R_b	100 MΩ	55	109
R_f	300 MΩ	32	63
I_d, R_d	5 nA, 2×10^9 ohms	166	331
JFET (2SK152)	K_f = 5 10^{-28}J, C_g = 7pF, g_m = 20mS, g =4/3	531 (channel) 6 (1/f)	265 (channel) 6 (1/f)
Other parameters	V_b=10 V. C_d = 45pF, C_{stray} = 5pF C_f = 1 pF	-	-
Buffer amplifier	AD 829, R3,R4 (See Appendix C)	111	55
Total		571 erms=4.8 keV	446 erms=3.8 keV
Experiment		6.2 keV	5.1 keV

4.5.5 Comparison with Device Performance

Pulsar noise test measurements were performed on device #7, 10 μm SOI for two shaping time settings. The acquisition time was 5 minutes using an Ortec 414 pulsar connected to the detector input of the CSA via a 2.2 pF capacitor. The system was calibrated using alpha and americium sources as previously described. The pulsar spectra are shown in Figure 4.17 with the peaks shifted to zero keV. The FWHM is 5.1 keV for τ=2 μs and 6.2 keV for τ=0.5 μs compared with theoretical estimations of 3.75 keV and 4.74 keV respectively. The higher observed noise may be attributable to

additional leakage current on the PCB board, variation in transistor specifications and imperfect shielding of the detector from external noise sources. The latter factor is likely since pulsar measurements performed at different experimental facilities (all other conditions equal) varied by around 1 keV. Nevertheless the difference in noise between τ=0.5 μs and τ=2 μs of 1 keV corresponds well with theoretical calculations (1.1 keV).

Given that lower level discriminator settings on multi-channel analyzers are typically twice the FWHM we may expect to be able to measure down to around 1.3 keV/μm (Si) or 0.65 keV/μm (Tissue, see equation (3.42)) with a 10 μm thick SOI device. For this prototype, an improved noise performance may be gained by paralleling 2 FETs to improve the transconductance. In this case, the optimum noise of around 300 electrons rms or 2.5 keV would be attained with a shaping time of 5 μs and a supply voltage of only 0.1 V. This condition, however, was not tested due to limited FET availability.

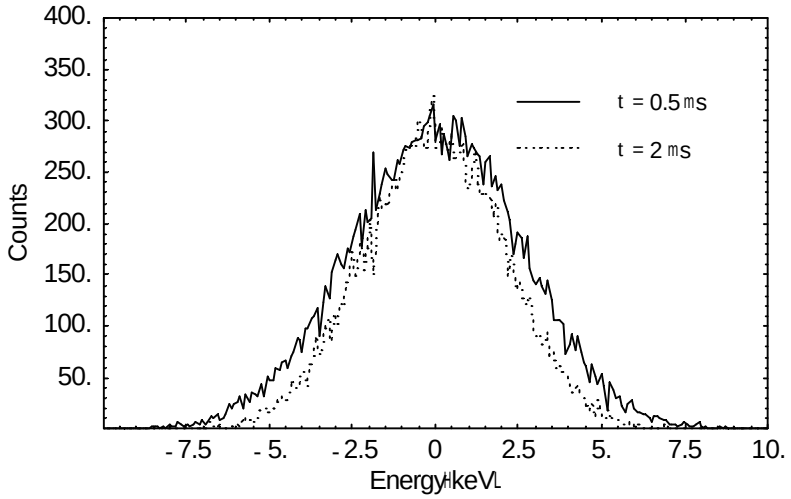


Figure 4.17. Pulsar noise measurements performed on device #7, 10 μm SOI for two shaping time settings. The spectra were shifted to a peak at 0 eV. Acquisition time was 5 minutes. FWHM is 5.1 keV for τ=2 μs and 6.2 keV for τ=0.5 μs.

4.5.6 Ultimate Noise Performance

We conclude this section by determining the ultimate noise performance attainable by a silicon microdosimeter. To improve noise performance, the detector, input FET, preamplifier (and possibly the shaping amplifier) should be located on the same integrated circuit. Most silicon detectors use high resistivity silicon, which is not readily compatible with the lower resistivity requirements of standard CMOS electronic design. Fortunately, our detector design with a small depletion width is compatible with low resistivity silicon thus simplifying the task of integrating the preamplifier and detector.

First, consider the variation of device performance with the main geometrical factors of area A and thickness W_d. Primarily the detector area should be reduced to minimize detector capacitance and leakage current. Substituting equation (4.2) into the FET term of equation (4.24) and assuming FET channel noise dominates yields:

$$\begin{aligned} ENC &\propto C_{in} \\ &\propto A / W_d \end{aligned} \tag{4.30}$$

Now as W_d varies the energy deposited will change proportionally if we assume particles are primarily crossers with constant LET. Therefore, the signal to noise ratio *(S/N)* will vary according to W_d/ENC, which gives.

$$S / N \propto W_d^{\,2} / A \tag{4.31}$$

Reducing the detector thickness, has a two fold effect in dropping the signal level whilst raising capacitance and noise. However, as discussed in the previous chapter, the device thickness is determined largely by microdosimetric considerations. Some variation and latitude may exist in cell sizes in which case equation (4.31) provides guidance on the S/N implications of geometrical factors.

For the remainder of this discussion, we assume a device volume of 1 μm^3 in silicon with a doping concentration of $N_B = 1.5 \times 10^{15}$ /cm^3. A voltage of only 0.4 V is required to deplete such a small volume as given in Figure 4.6. Consider two arrays; one 20 times smaller in area than the prototype (array A4) with 24000 $\times$ 1 μm^3 diodes in parallel and another 200 times smaller with 2400 $\times$ 1 μm^3 diodes in parallel. The detector capacitances (4 and 0.4 pF) and detector leakage current (10 and 1 pA) are simply scaled from the previous prototype using these area scaling factors. The transconductance g_m and gate capacitance C_g of the input FET in the active region are given by [173] :

$$g_m = \sqrt{2mC_{ox}(W / L)I_D} \tag{4.32}$$

$$C_g \approx \frac{2}{3} WLC_{ox} \tag{4.33}$$

where I_D = drain current, W = transistor width, L = transistor length, m = mobility and C_{ox} = oxide capacitance

Typically, a PMOS FET is used in preference to a NMOS due to its lower flicker noise although a higher drain current is required to compensate for the lower mobility. Selecting values of W/L = 1000/0.8 μm, I_d = 5mA and using typical values of mobility (m = 0.02 m^2/Vs) and oxide capacitance (C_{ox} = 1.9 × 10^{-3} pf/μm^2) we may obtain a transconductance of 20 mS with a gate capacitance of 1 pF. On chip feedback and bias resistor values of 3 GΩ are attainable using custom designs as shown by O'Connor[174]. The selected component values and the relative noise contributions are summarized in Table 4.7. For the 24000×1 μm^3 array a noise of 47 electrons rms or 400 eV FWHM is predicted whilst for the 2400×1 μm^3 detector a noise of 19 electrons rms or 160 eV FWHM is predicted. Thus, it is not unreasonable to expect a minimum lineal energy of around 0.26 keV/μm(tissue) for the smaller array. This is well within the requirements discussed in the previous chapter. A smaller detector volume may be considered with volumes of around 0.3 μm^3 still capable of measuring lineal energies down to 1 keV/μm(tissue).

This section has been an approximate estimation of attainable noise performance. As an ultimate benchmark, one may emulate the work of O'Connor [174]. A 100 eV resolution preamplifier was designed and tested for X-ray spectroscopy. The detector (C_d = 0.3 pF) and circuit were cooled to -75 degC (reducing thermal noise and leakage current) to achieve an ENC of 13 electrons rms. Thus, for a 1 μm^3 detector the minimum lineal energy measurable would be around 0.18 keV/μm(tissue). This represents the absolute limit for this size detector. To achieve reasonable count rates for small detector arrays several detector/preamplifier channels would be required to increase the total area.

Table 4.7. Optimum noise performance of silicon microdosimeter with on-chip preamplifier.

	24000 × 1 μm^3 arrays (C_d = 4 pF)		**2400 × 1 μm^3 detector (C_d = 0.4 pF)**	
Noise Source	**Relevant Values**	**Noise Electrons (RMS)**	**Relevant Values**	**Noise Electrons (RMS)**
R_b	3000 MΩ	10	3000 MΩ	14
R_f	3000 MΩ	10	3000 MΩ	14
I_d	10 pA	7	1 pA	3
FET	K = 2 × 10^{-25}J, C_g = 1pF, g_m = 20mS, g=2/3	38 (channel) 32 (1/f)	K = 2 × 10^{-25}J, C_g = 1pF, g_m = 20mS, g=2/3	7 (channel) 8 (1/f)
Other parameters	t = 1 μs, V_b =0.4V C_d = 4 pF, *Cstray* =0pF C_f = 1 pF	-	t = 0.5 μs,V_b=0.4V. C_d = 0.4 pF, *Cstray* = 0pF C_f = 0.1 pF	-
Total		47 erms=0.40 keV		19 erms=0.16 keV

5. Tissue equivalence correction for silicon microdosimeters

ICRU report 44 [32] states "Tissue substitutes are often mixtures formulated so that their radiation interaction properties rather than their atomic composition, match those of the body tissue to the degree necessary for the specific application". Similarly, radiation detectors due to operational and construction requirements (such as electrical conductivity, stability, mechanical strength, and shape construction) are rarely made of components with identical composition to tissue. Instead, the pertinent radiation characteristics and mass densities of the body tissue and detector are evaluated and correction factors frequently employed.

The *macrodosimetric* tissue equivalency of silicon or silicon dioxide for integral low LET photon irradiation is well established [175]. However, methods for converting silicon based *microdosimetric* measurements to tissue volumes have previously not been investigated.

For macrodosimetric measurements, dose may be scaled according to the Bragg-Gray theorem [176-178]. Assuming that the detector is small in comparison with the range of secondary particles then the relationship between detector dose $D_{detector}$ and tissue dose D_{tissue} is given by:

$$D_{tissue} = \frac{\left(\bar{S} / r\right)_{tissue}}{\left(\bar{S} / r\right)_{detector}} D_{detector} \tag{5.1}$$

where $\bar{S} / r$ is mass collision stopping power averaged over the energy spectrum of charged particles. For photons, provided the detector does not perturb the photon spectrum, equation (5.1) becomes

$$\begin{aligned} D_{tissue} &= \frac{\left(\bar{m}_{en} / r\right)_{tissue}}{\left(\bar{m}_{en} / r\right)_{detector}} D_{detector} \\ &= k\, D_{detector} \quad \text{for Silicon Detector} \end{aligned} \tag{5.2}$$

where $\bar{m}_{en} / r$ is the mass energy absorption coefficient averaged over the photon spectrum. The scaling factor k is simply 1.09 for silicon with photons in the energy range 0.3 to 3 MeV [179].

For microdosimetric measurements, a spectrum is produced as opposed to a single dose measurement. A simple method for interpreting silicon microdosimetric spectra as equivalent tissue measurements is described in this chapter.

The results are presented using boron neutron capture therapy (BNCT) as a test case. We first compare silicon and tissue range-energy relationships for H, He, Li and C ion deposition. The Monte-Carlo method is used to compare energy deposition spectra for some simple geometrical cases relevant to boron neutron capture therapy. The tissue equivalency of silicon detector/converter systems under fast neutron and proton irradiation is also considered.

5.1 Definition of Tissue and Detector Materials

Before comparing silicon to tissue, the composition of tissue must first be defined. Biological tissue composition varies significantly between tissue types and individuals. The subject of tissue references is comprehensively discussed in ICRU report #44 [32] and a report by the ICRP [180]. These reports identified the most important tissues needing simulation as muscle, adipose tissue and the skeleton. Together these make up over 70% of the body mass. Lung tissue is also important due to its large density difference. Muscle includes the connective tissue, blood vessels, blood, lymph, etc., generally associated with skeletal (striated) muscle. Adipose tissue is composed of a protein matrix supporting cells (adipocytes) highly specialized for the storage of lipids. The most common tissue reference in microdosimetric literature [11], and the one we shall use here, is commonly identified as muscle (striated, ICRU, 1964) [181]. ICRU report 44 [32] identifies a composition called muscle (skeletal, ICRU, 1989) as the recommended muscle composition. However, the difference with muscle (striated) is small (an additional 2% carbon content and 2% less oxygen content) and we maintain conformity with the literature in using muscle (striated). The composition of muscle (striated ICRU, 1964), heretofore called muscle, is defined in Table 5.1. In addition, the term "tissue equivalent" refers to muscle (striated ICRU, 1964) equivalence. The primary elements in tissue are hydrogen, carbon, oxygen and nitrogen. For a given tissue substitute the quality of the tissue approximation depends on the composition and density matching along with the type and energy of the radiation being used. Also described in Table 5.1 are the composition and some relevant properties of several materials (A150, Lucite, and silicon) which will be compared to muscle.

The standard wall material used in the majority of proportional gas counters is a plastic designated A150, which is considered "muscle equivalent". A150 is a mixture of polyethylene, nylon, carbon and calcium fluoride, which is easily molded, welded and machined. The material was originally developed by Shonka and collaborators [33] and subsequently modified by Smathers [182]. The elemental composition of A150 is very close to muscle in regard to hydrogen and nitrogen content. However, the oxygen content is much lower and this has been substituted by an increased carbon content to obtain suitable electrical conductivity. Note that no usable solid exists with the required oxygen content of tissue. The effect of this discrepancy in elemental composition on neutron microdosimetric measurements is discussed further in section 5.5.

Lucite (or Perspex) is a readily available material often used as a tissue substitute in phantoms. The tissue converter placed above the silicon microdosimeter in this work was constructed of Lucite. This material was selected due to availability, low cost and construction ease. The hydrogen content is slightly lower than for muscle and there is no nitrogen. Like A150, the carbon and nitrogen contents do not correctly reflect muscle. Again, the effect of this discrepancy in elemental composition will be discussed further in section 5.5.

Table 5.1. Elemental composition of important tissue types, substitutes and detector materials.

			Muscle(Striated ICRU, 1964)		**A150**		**Lucite**		**Silicon**
Atom	**Z**	**A**	**Atomic %**	**Mass %**	**Atomic %**	**Mass %**	**Atomic %**	**Mass %**	**Mass & Atomic %**
H	1	1.01	63.31	10.2	58.26	10.1	53.33	8.05	-
C	6	12.01	6.41	12.3	37.61	77.7	33.33	59.98	-
N	7	14.01	1.56	3.5	1.45	3.5	-	-	-
O	8	16.00	28.51	72.91	1.89	5.2	13.33	31.96	-
F	9	19.00	-	-	0.52	1.7	-	-	-
Na	11	22.99	0.02	0.08	-	-	-	-	-
Si	14	28.09	-	-	-	-	-	-	100.00
P	15	30.97	0.04	0.2	-	-	-	-	-
S	16	32.06	0.10	0.5	-	-	-	-	-
K	19	39.10	0.05	0.3	-	-	-	-	-
Ca	20	40.08	0.001	0.007	0.26	1.8	-	-	-
Mean Atomic Mass				14.10		11.80		12.40	28.09
Density (g/cm^3)				1.04		1.127		1.2	2.32
Atomic Density $\times 10^{23}$ atoms/cm^3				1.00		1.17		1.08	0.50
Electron Density $\times 10^{23}$ atoms/cm^3				3.44		3.73		3.90	6.99

Note 1: The Mean Atomic Mass was calculated as the mass weighted average (i.e. sum(mass fraction$_i \times A_i$))
2: Lucite (or Perspex) is Polymethyl Methacrylate, $C_5H_80_2$ [126].
3: Definition of Muscle (Striated ICRU,1964) and A150 from Appendix C [11]

5.2 Microdosimetry TE Correction Factor

Frequently when analyzing microdosimeter performance researchers have often concentrated on LET. However, the energy deposited in a microdosimeter depends upon the *integral* of the particle LET over the chord length traversed. This implies that one should consider the particle range-energy relationship rather than the LET-range relationship as a starting point in analyzing microdosimetry tissue equivalence. The equation for range of a particle with initial energy E_{max} is

$$R = \int_0^{E_{max}} \left(-\frac{dE}{dx} \right)^{-1} dE \tag{5.3}$$

where *dE/dx* is the particle LET or linear stopping power. Particles primarily lose energy via coulomb interactions with the material's electrons. An approximate relationship for *dE/dx* is given by the Bethe formula based on relativistic quantum mechanics [23]:

$$-\frac{dE}{dx} = \frac{4pe^4z^2}{m_0v^2} NZ\left[\ln\frac{2m_0v^2}{I} - \ln(1-\frac{v^2}{c^2}) - \frac{v^2}{c^2} \right] \tag{5.4}$$

where *v* and *ze* are the velocity and charge of the particle, *N* and *Z* are the number density and atomic number of the absorber atoms, m_0 is the electron rest mass, and *e* is the electronic charge. The parameter *I* represents the average excitation and ionization potential of the absorber and is normally treated as an experimental parameter for each element. The following approximate empirical formula may be used to estimate the *I* value in eV for an element with atomic number *Z* [183].

$$I = \begin{cases} 19.0 \text{ eV}, Z = 1 \text{ (hydrogen)} \\ 11.2 + 11.7Z \text{ eV}, \ 2 \le Z \le 13 \\ 52.8 + 8.71Z \text{ eV}, \ Z > 13 \end{cases} \tag{5.5}$$

When the material is a compound or mixture, the stopping power may be calculated by simply adding the contributions from the individual constituents (Bragg additivity rule). If there are *T* elements with the *i*-th element described by an atomic density N_i atoms/cm^3, atomic number Z_i and mean excitation energy I_i then we use:

$$n \ln I = \sum_{i=1}^{T} N_i Z_i \ln I_i \tag{5.6}$$

where n is the total number of electrons/cm^3 in the material (= NZ). For non-relativistic particles, only the first term in the brackets of equation (5.4) is significant. In comparing different materials as absorbers dE/dx depends primarily on NZ (the electron density), which is outside the logarithmic term.

Unfortunately, the integral formed by applying equation (5.4) into (5.3) does not have a simple analytic solution. Nevertheless, a semi-empirical scaling formula for range (sometimes called the Bragg-Kleeman rule) enables the comparison of ranges in different materials [23].

$$\frac{R_2}{R_1} \cong \frac{r_1\sqrt{A_2}}{r_2\sqrt{A_1}} \tag{5.7}$$

where r and A represent density and atomic weight and the subscripts refer to different materials. The accuracy of this estimate diminishes with large differences in atomic number. Note that the equation is independent of the ion type, charge or energy. Higher accuracy in range comparisons may be gained by using Ziegler's SRIM (Stopping and Ranges of Ions in Matter) program [126, 184]. Note that the range considered in this discussion is the mean range since as discussed in chapter 3, range and energy straggling produce a distribution of ranges for a given incident particle energy.

The general shape of the range-energy and LET-range relationships is quite similar between different materials for all ion types. Therefore, the range-energy curve in one material $E_1(R)$ will approximate the range-energy curve of another $E_2(r)$ provided the ranges are scaled appropriately according to equation (5.7) or using other range calculations. That is,

$$E_1(R) \cong E_2(zR)$$
$$\text{where } R = \text{range and } z = \frac{R_2}{R_1} \cong \frac{r_1\sqrt{A_2}}{r_2\sqrt{A_1}} \tag{5.8}$$

The energy deposited E_{dep1} by a charged particle traversing a reference volume with material denoted by subscript 1 is given by

$$\begin{aligned} E_{dep1} &= \int_{a1}^{b1} \frac{dE_1}{dx} dx \\ &= E_1(b_1) - E_1(a_1) \end{aligned} \tag{5.9}$$

where $s_1 = b_1 - a_1$ is the chord length. Similarly, for another volume of differing material denoted by subscript 2 the energy deposited E_{dep2} is given by

$$\begin{aligned} E_{dep2} &= \int_{a2}^{b2} \frac{dE_2}{dx} dx \\ &= E_2(b_2) - E_2(a_2) \end{aligned} \tag{5.10}$$

where $s_2 = b_2 - a_2$ is the chord length. Using equation (5.8) substituted into (5.10) gives

$$E_{dep2} \cong E_1(b_2 / z) - E_1(a_2 / z) \tag{5.11}$$

Comparing equations (5.9) and (5.11) indicates that the energy deposited in the two volumes will be equal ($E_{dep1} = E_{dep2}$) provided that $b_1 = b_2/z$ and $a_1 = a_2/z$ which equates to $s_2 = z s_1$. That is, the energy deposited is equal in the two volumes if the chord lengths are scaled by the factor z. For multiple chords, the scaling requires equivalent shapes (and chord length distribution shape) with a scaling of the linear dimensions. *More generally, assuming identical charged particle spectra, the microdosimetric energy spectrum will be equivalent in two volumes of differing composition if the shape of the volumes is the same and the dimensions are scaled by the factor z.*

For a tissue rectangular parallelepiped (RPP) with dimensions $x \times y \times z$ the required scaling is z $x \times z$ $y \times z$ z of silicon. Note that this holds for any RPP (it is not necessary that $x=y=z$) and for other shapes such as a cylinder (the radius and length are scaled) or a sphere (radius scaling only). The scaling factor simply applies to each linear dimension. To obtain equal TE lineal energy ($E/\bar{l}$) in both a tissue volume and a correctly scaled silicon volume we must use the same mean chord length $\bar{l}$, corresponding to the *tissue* volume, since the energy deposited is the same.

The required scaling factor z may be estimated by equation (5.7). Values calculated for various materials with respect to muscle are shown in Table 5.2. The scaling factor calculated for 1 MeV protons, using the projected range algorithm (PRAL) option of SRIM [126, 184], is within 7% of the factor calculated using the approximate equation (5.7). The tissue equivalence factor for Lucite is quite close (within 5%) of the factor for A150.

Note that the possible equivalence of silicon and tissue via a geometrical scaling factor assumes that the charged particle spectra are equivalent. To obtain equivalent charged

particle spectra the atomic composition of the volumes should closely match in order to obtain the same interactions (capture, elastic, inelastic and nuclear reactions) and subsequent reaction products. In the case of a silicon detector, we require the use of a tissue substitute converter lying above the detector. Furthermore, the range of recoil particles should be such that crossers and stoppers dominate the microdosimetric spectrum as discussed extensively in chapter 3.

Table 5.2. Tissue equivalence scaling factor for A150, Lucite and Silicon

	A150	Lucite	Silicon
z from equation (5.7)	0.84	0.81	0.63
z from PRAL (1MeV protons)	0.88	0.84	0.68

Note: The range of 1 MeV proton in muscle is 23.03 um calculated using PRAL, the projected range algorithm option of SRIM [126, 184]

5.3 Summary of Conditions for Tissue Equivalence

In summary, to obtain tissue equivalence the silicon detector/ TE converter must satisfy four main conditions

1. The geometrical TE scaling factor for the silicon detector (z = 0.63) should apply to all ion products
2. T.E converter must closely approximate tissue atomic composition with respect to atoms generating the dominant secondary charged particles.
3. The proportion of interactions with silicon must be negligible in comparison with converter interactions. That is, events should originate from converter recoil products or primary ions rather than from within silicon.
4. The range of recoil particles should be such that crossers and stoppers dominate the microdosimetric spectrum as discussed extensively in chapter 3

The effect of tissue substitute composition will be further discussed in section 5.5 were we consider Fast Neutron Therapy (FNT) and Proton Therapy (PT) conditions. The concept of scaling ranges to establish tissue equivalence will be further clarified by consideration of the Boron Neutron Capture Therapy (BNCT) reactions in the following section.

5.4 Boron Neutron Capture Therapy Tissue Equivalence

The principle and application of microdosimetry to BNCT is described in chapter 7. In this section, the interaction of neutron capture products with silicon and tissue will be considered in detail to test TE relationships uncovered in the previous section.

5.4.1 Comparison of Silicon and Tissue BNCT Range-Energy Relationships[1]

The BNCT reactions provide an excellent platform for testing the geometrical TE factor discussed in the previous section. Four ion types over a range of energies are involved. The primary thermal neutron reactions with tissue are as follows:

$$^{14}_{7}N + ^{1}_{0}n \longrightarrow {}^{14}_{6}C + ^{1}_{1}p \qquad Q = 630keV$$

$$^{10}_{5}B + ^{1}_{0}n \xrightarrow{6.3\%} {}^{7}_{3}Li + ^{4}_{2}He \quad Q = 2790keV$$

$$\xrightarrow{93.7\%.} {}^{7}_{3}Li + ^{4}_{2}He + g \quad Q = 2310keV$$

Table 5.3. Summary of Energy-Range data for ions produced by thermal neutron interactions with nitrogen and boron

Reaction	Ion	Energy (keV)	Range(μm)	
			Tissue	Silicon
^{14}N(n,p)^{14}C	p	590	10.5	7.2
	^{14}C	40	0.20	0.12
^{10}B(n,α)^{7}Li	α (6.3%)	1780	9.3	6.3
	^{7}Li (6.3%)	1010	4.6	2.8
	α (93.7%)	1470	7.7	5.1
	^{7}Li (93.7%)	840	4.1	2.5

Table 5.4. Summary of interaction data for selected BNCT conditions♣

Reaction	σ (barns/atom)	Interactions/ μm^3	Ions	P(ion pair emitted)
^{14}N(n,p)^{14}C	1.81	0.0272	p, ^{14}C	0.37
^{10}B(n,α)^{7}Li	3837	0.0462	α, ^{7}Li (6.3%)	0.04
			α, ^{7}Li (93.7%)	0.59

♣ Both reactions are for a neutron fluence of 10^{13} n/cm^2 [186]
Nitrogen concentration 3.5g/100g, Boron concentration 20μg/g.
For other concentrations and fluence the interactions per unit volume changes proportionally.
P(ion pair emitted) is the proportion of interactions which produce the respective ion pair.

The ion products and their energies are summarized in Table 5.3. Ion range and energy data for each of these ions was calculated using the computer code SRIM [126]. The data was calculated for both silicon and tissue using the projected range algorithm

[1] The work presented in this section and the following one was originally published by the author in 1998 [185] P. D. Bradley and A. B. Rosenfeld, "Tissue Equivalence Correction for Silicon Microdosimetry Detectors in Boron Neutron Capture Therapy," *Med. Phys.*, vol. 25, pp. 2220-2225, 1998..

(PRAL) option of SRIM [126, 184]. This option provides range-energy tables that are within a few percent of the more accurate but time consuming TRIM-Monte-Carlo calculations available in SRIM. The accuracy of PRAL was considered adequate for our purposes given that we are primarily interested in a comparative study between silicon and tissue. TRIM-Monte-Carlo calculations using the ion/energy combinations given in Table 5.3 yielded average longitudinal range estimates within 2% of the PRAL estimated ranges.

Tissue was modeled as per ICRU striated muscle, which is defined with an elemental composition and density given in Table 5.1. Using these models, the range-energy data is plotted in Figure 5.2 for the ions relevant to BNCT. The corresponding LET versus energy and LET versus range relationships are provided in Figure 5.3 as a useful reference. A 5th order polynomial was fitted to the range-energy data for each of the ion/target combinations with the results given below.

H, He, Li and C ions in Silicon:

$$E(r, H, Silicon) = -0.07492r^5 + 1.713r^4 - 13.27r^3 + 34.89r^2 + 80.99r$$
$$E(r, He, Silicon) = -0.2455r^5 + 15.81r^4 - 51.49r^3 + 198.7r^2 + 9.229r$$
$$E(r, Li, Silicon) = 4.398r^5 - 44.75r^4 + 141.6r^3 - 63.99r^2 + 141.1r$$
$$E(r, C, Silicon) = -2.442 \times 10^6 r^5 + 862600r^4 - 109200r^3 + 5922r^2 + 211.8r$$

H, He, Li and C ions in Muscle:

$$E(r, H, Mucsle) = -0.01148r^5 + 0.398r^4 - 4.787r^3 + 21.2r^2 + 40.05r$$
$$E(r, He, Muscle) = 0.00564r^5 + 0.1188r^4 - 5.84r^3 + 58.06r^2 + 17.36r$$
$$E(r, Li, Muscle) = 0.03762r^5 - 1.534r^4 + 11.73r^3 + 6.404r^2 + 72.66r$$
$$E(r, C, Muscle) = -1.660 \times 10^5 r^5 + 97530r^4 - 20210r^3 + 1727r^2 + 146.5r$$

The above equations are only valid up to the ion ranges specified in Table 5.3. Comparison of the range-energy relationships for tissue and silicon indicates that the data may be related by a simple scaling factor, z. Scaling the silicon plots by substituting 0.63 r (z = 0.63) into the above equations yields a close approximation to the tissue range-energy relationship as shown in the right hand plots of Figure 5.2. These results are completely consistent with the previous discussion and value of z given in Table 5.2. As predicted by equation (5.7), the ratio z of the ion range in silicon to the range in tissue is only weakly dependent on the ion species and energy. Note that

the geometrical scaling is not obvious by inspection of the LET curves provided in Figure 5.3.

An average value of *z* was calculated for each ion using the following equation:

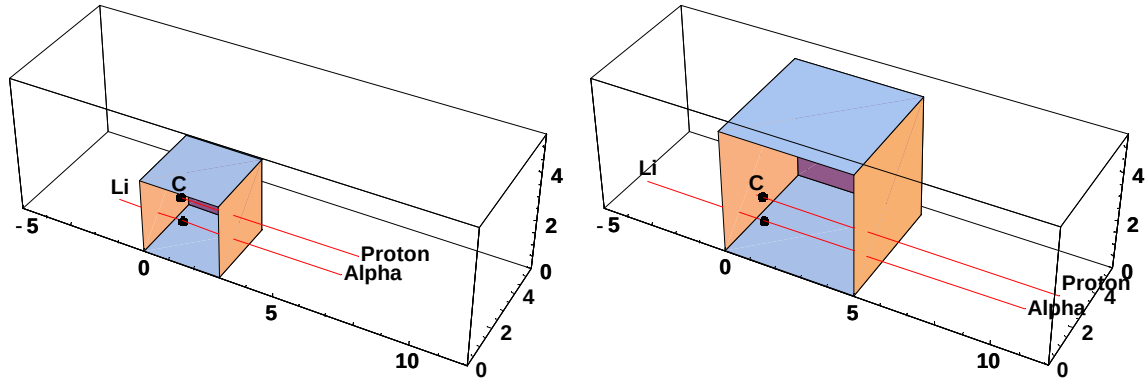
$$z(ion) = \frac{1}{E_{\max}} \int_0^{E_{\max}} \frac{R(E, ion, silicon)}{R(E, ion, tissue)} dE \tag{5.12}$$

where *R(E, ion, target)* is the range as a function of energy (*E*) for the required *ion* and *target*. Values of *z* for each ion are shown in Table 5.5. The optimum scaling factor, *z*, is dependent on the contribution of each ion to the energy deposition spectra which in turn is dependent on the segment length distribution of the sensitive volume, ion energy and relative frequency of ion generation. An approximate scaling factor was calculated by weighting each ion according to the energy of the ion and the relative frequency of generation. The required cross-section and boron and nitrogen concentrations are given in Table 5.4 taken from typical values used by Charlton [186]. The final weighted average scaling factor is *z* = 0.63. The maximum deviation from this scaling factor is 8% and occurs for the highest energy proton. This factor is in excellent correspondence with the approximate range ratio equation (5.7). Note, that a more accurate weighting of ions would consider the difference in contribution to dose mean lineal energy $\bar{y}_D$ of the various ions. Ions depositing a higher energy (usually higher LET ions) contribute more to $\bar{y}_D$ and thus should be assigned a higher weighting factor.

Table 5.5. Mean ratio of BNCT ion ranges in silicon and tissue

Ion	*z*	Weight
H	0.65	0.13
He	0.64	0.55
Li	0.60	0.31
C	0.60	0.01
Weighted Av.	0.63	

Note: Weight is an approximate measure of the contribution of the ion to BNCT energy deposition spectra



Silicon (RPP: 3.15×3.15×3.15μm^3) **Tissue (RPP: 5×5×5μm^3)**

Figure 5.1. Comparison of BNCT ion product ranges in tissue and silicon. The silicon RPP dimensions have been scaled by 0.63 times the tissue dimensions. Note that the figure on the left (silicon) is an exact scale miniaturization of the figure on the right (tissue). These volumes will have equivalent microdosimetric spectra assuming equal concentrations of nitrogen and boron.

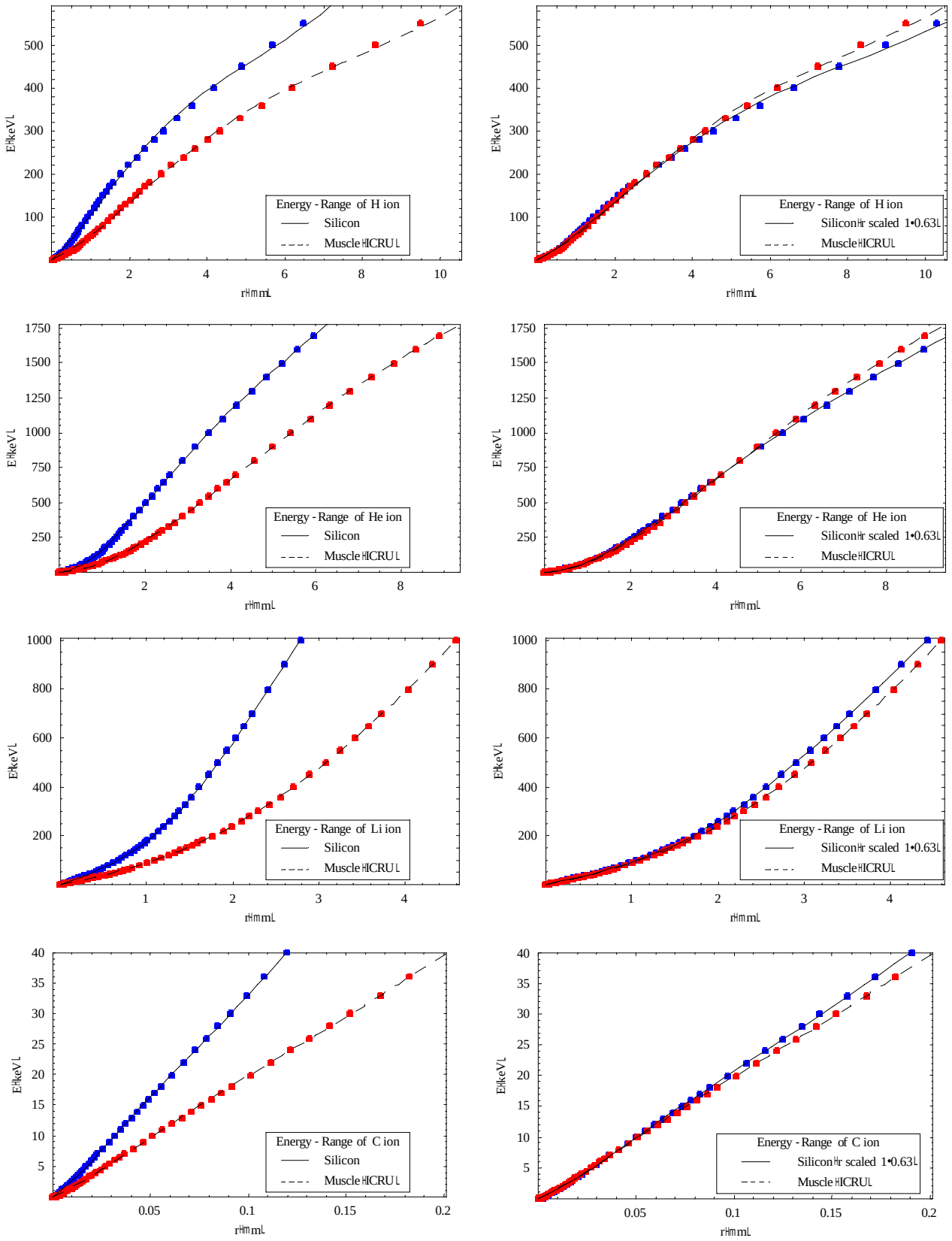


Figure 5.2. Range-Energy relationships for BNCT products (H, He, Li and C) in ICRU muscle and Silicon. The right-hand side shows the same plot as the left except for the silicon range scaled by 1/0.63. In addition, the plots display original SRIM generated data points used for the 5th order polynomial fit.

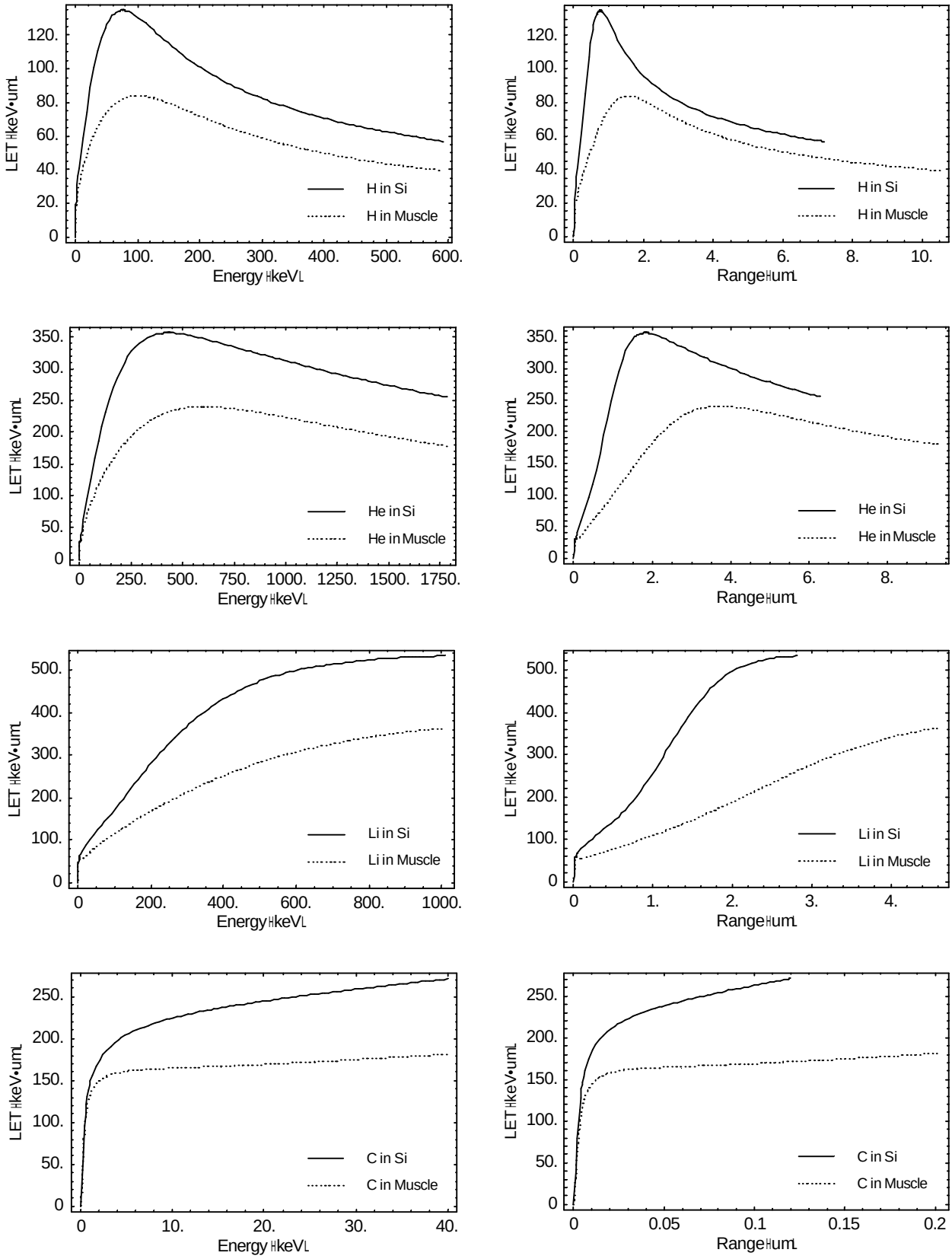


Figure 5.3. LET versus energy (left) and LET versus range(right) for BNCT Products (H, He, Li and C) in ICRU muscle and Silicon. The maximum range is plotted only up to the corresponding maximum energy.

5.4.2 Comparison of Silicon and Tissue BNCT Energy Deposition Spectra

5.4.2.1 Method: Monte Carlo Program

A Monte Carlo program was developed in order to confirm that the energy deposition in appropriately scaled silicon volumes may approximate the deposition in tissue. The use of Monte Carlo methods to calculate microdosimetric spectra in cell sized volumes exposed to BNCT and other high LET ions is well established [186]. It is generally assumed that the path of the ions follow straight lines with negligible straggling and that the width of the track is negligible in comparison to the volume size. These assumptions are valid for micrometer sized volumes and low energy ions as confirmed by comparative calculations performed by Charlton [187] on detailed track structure versus simple chord length/LET calculations.

The program description begins by defining two types of volumes:

1. *Generation volume (GV)* in which ions are generated assuming a nitrogen concentration of 3.5 g/100g and a boron concentration of 20 μg/g. These are typical values as used by Charlton [186]. The probability of formation of the various ion pairs and the number of interactions per μm^3 are given in Table 5.4.

2. *Sensitive volume (SV)* in which we compute the energy deposited by the traversal of ions generated in the GV.

The shape of both volumes is defined as an RPP with dimensions $x \times y \times z$ all in μm. Such a shape is selected on the basis that the SV of silicon reverse biased p-n junctions has traditionally been modeled as an RPP (See chapter 3 for a complete discussion on detector shape). The position of the GV with respect to the SV has no restriction with partial or even complete overlapping allowed.

The Monte Carlo process may be summarized by the following steps:

1. Randomly select an ion pair with initial energy and range given by Table 5.3 according to the probability specified in Table 5.4.

2. Randomly select the position of the interaction within the GV and the angle of ion emission with equal probability for all points within the GV and all angles. Note that ion pairs are emitted at 180 degrees.

3. Calculate the points of intersection of the emitted ions with the SV. This may be approached by solving the simultaneous equations of a line intersecting an RPP in a similar manner as Charlton [188] for an ellipsoid. Alternatively, one may incrementally follow the ion path at sufficiently small increments (0.01μm), testing at each increment to check for traversal of the SV boundary. The latter approach was adopted despite the longer computation time since it is more adaptable to future versions that may operate on complex geometry.

The main Monte-Carlo routines were coded in C for computational speed. These routines were encapsulated within a Mathematica [141] based input/output framework to provide flexibility in program input and output analysis.

Software validation of such programs is a non-trivial task since it is often difficult to construct cases of sufficient simplicity that analytic solutions may be derived for result comparison. The software was modified slightly to calculate segment length distributions. Such distributions have been analytically derived by Bradford [122, 137] (based on the work of Kellerer [128]) for an RPP volume under the condition of μ-randomness and fixed length tracks as discussed in chapter 3. Exact segment length distributions were calculated using the Mathematica notebook shown in Appendix B (and described in chapter 3) and compared against the Monte Carlo results. Figure 5.4 displays the close correspondence between the analytic and Monte Carlo derived distributions thus validating a substantial portion of the software. The remainder of the software was tested by thorough review and testing of individual functions.

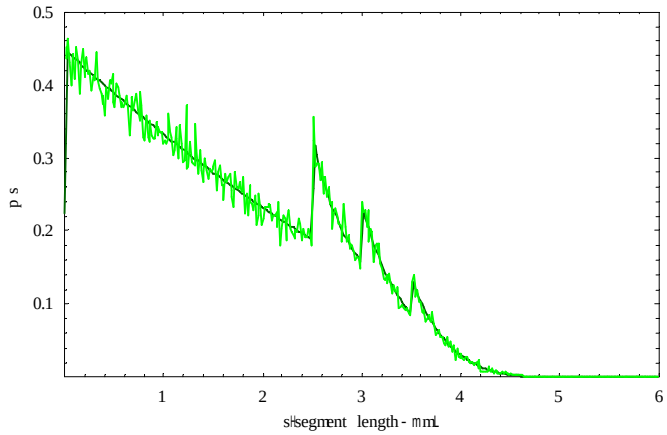


Figure 5.4. Comparison of analytic and Monte Carlo generated segment length distribution (P(s)) for an RPP volume 3.5 × 3 × 2.5 μm enclosed in a uniform isotropic field of 7 μm length rays.

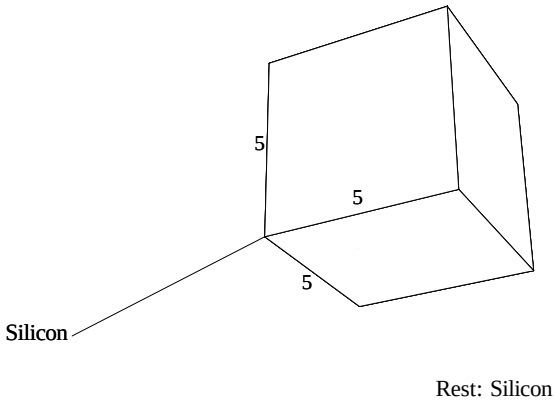


Figure 5.5. Geometry Case 1 - SV and GV are identical in size and position

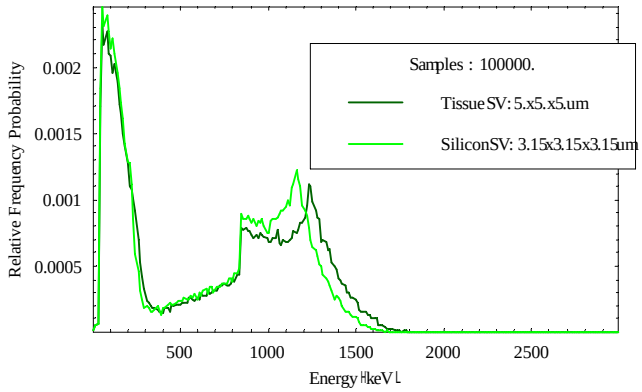


Figure 5.6. Geometry Case 1 (Example 1):
Energy Deposition Spectra comparison of Silicon (3.15 × 3.15 × 3.15 μm) and Tissue (5 × 5 × 5μm).

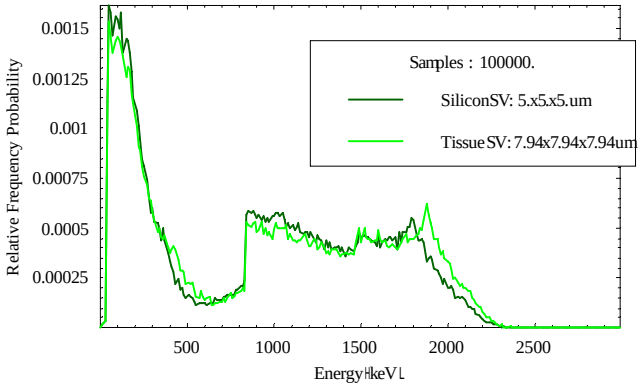


Figure 5.7. Geometry Case 1 (Example 2):
Energy Deposition Spectra comparison of Silicon (5 × 5 × 5 μm) and Tissue (7.9 × 7.9 × 7.9 μm).

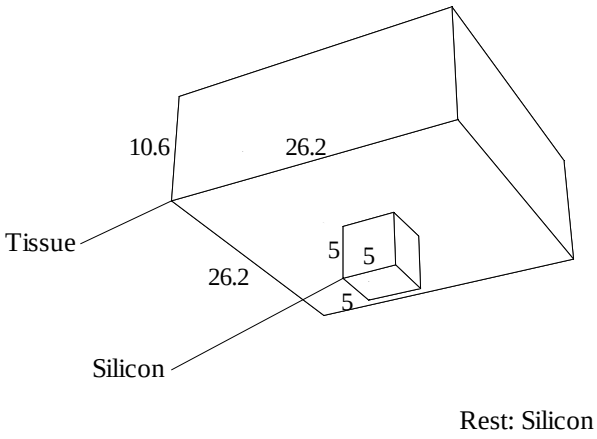


Figure 5.8. Geometry Case 2 - GV is a large tissue volume above a much smaller silicon/tissue SV

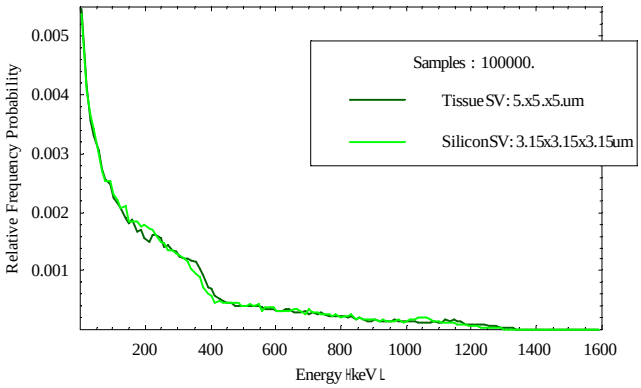


Figure 5.9. Geometry Case 2 (Example 1):
Energy Deposition Spectra comparison of Silicon ($3.15 \times 3.15 \times 3.15$ μm) and Tissue ($5 \times 5 \times 5$μm).

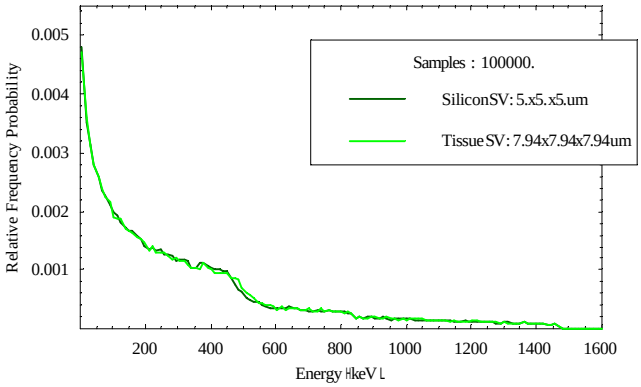


Figure 5.10. Geometry Case 2 (Example 2):
Energy Deposition Spectra comparison of Silicon ($5 \times 5 \times 5$ μm) and Tissue ($7.9 \times 7.9 \times 7.9$ μm).

5.4.2.2 Results: Geometry Case 1 - Ion generation in RPP volumes with SV=GV.

Geometry Case 1 consists of identical SV and GV of the same material (silicon or tissue). Figure 5.5 illustrates the case for a 5×5×5 μm^3 volume of silicon. We assume that both silicon and tissue contain the same concentration of boron and nitrogen. This case corresponds to the BNCT scenario in which a B-10 compound is uniformly distributed throughout the cell. However, a corresponding silicon detector cell is limited to measuring only the boron capture component. Boron may be easily introduced by using *p* doped Si arrays as proposed by Rosenfeld [71]. The introduction of nitrogen into the body of a silicon diode is a much more difficult proposition. Nitrogen concentrations required for an acceptable probability of nitrogen capture are too high for maintaining device operation. Note, that nitrogen may be introduced into surrounding insulating layers (e.g. Si_3N_4 is commonly used for passivation). Nevertheless, for the purpose of testing the silicon/tissue scaling factor, we compare a hypothetical device assuming tissue concentrations of nitrogen and boron.

Figure 5.6 and Figure 5.7 illustrate the energy deposition spectra (normalized) for silicon and tissue with the dimensions of silicon scaled by 0.63 in each case. Clearly, the energy deposition spectra are vastly different for similar volumes of tissue and silicon. However, a comparison of silicon volumes scaled by z =0.63 with tissue volumes indicates quite good correspondence between spectra. Note that the step in probability at 840 keV corresponds to the lithium ion as given in Table 5.3. This ion has a range small enough to be a complete insider. A similar step occurs at 40 keV corresponding to the carbon recoil.

5.4.2.3 Results: Geometry Case 2-Ion generation above RPP volume

Geometry Case 2 consists of a large GV placed directly on top of a much smaller SV. The GV material is tissue whilst the remaining volume including the SV consists of either tissue or silicon. This case is not hypothetical since it is easy to construct an overlayer with the appropriate concentrations of boron and nitrogen without compromising silicon device operation. Figure 5.8 illustrates the case for a silicon SV of dimensions 5×5×5 μm^3. The GV dimensions are selected such that the boundaries are further from the SV than the longest range ion (590 keV proton -10.5 μm). Thus, we effectively model a volume of infinite extent away from the SV. Such a situation models a layer of tissue equivalent plastic (or real cells) impregnated with appropriate boron concentrations and placed above a silicon cell (within an integrated circuit). We

then compare the energy deposition in an appropriately scaled silicon cell to that which may occur if a tissue cell was substituted as the SV. Again the normalized results shown in Figure 5.9 and Figure 5.10 confirm that, with appropriate geometrical scaling, silicon detectors with well known geometry will record energy deposition spectra representative of tissue cells of equivalent shape. Again, note the significant differences in spectra between the two figures (tissue 5×5×5 μm^3 in Figure 5.9 and silicon 5×5×5 μm^3 in Figure 5.10) indicating the importance of using an appropriate scaling factor.

5.5 Fast Neutron Therapy and Proton Therapy Tissue Equivalence

Experimental microdosimetry is commonly applied to the characterization of fast (>1 MeV) neutron and proton beams. The conditions necessary for TE of a silicon/TE converter microdosimeter were summarized in section 5.3. Each of these conditions will now be addressed for the case of fast neutron therapy (FNT) and proton therapy (PT). The emphasis will be on FNT since for PT the absorbed dose for proton energies less than 250 MeV is dominated by electronic interactions with the protons. The recoil products in PT are similar in energy and type (but not relative contribution) to FNT so the discussion on TE of FNT is largely applicable to PT. Further discussion of neutron therapy and proton therapy are provided in chapter 8 and chapter 9, respectively.

5.5.1 Geometrical TE scaling factor for FNT and PT

The main ion products from fast neutron reactions include protons, alphas, and heavy ion recoils (carbon, oxygen recoil and to a lesser extent nitrogen). As an example, the initial spectrum of charged particles for 14 MeV neutrons in ICRU tissue was calculated by Caswell and Coyne [125] and shown in Figure 5.11. From this data for 14 MeV neutrons; protons have energies up to 14 MeV, alphas may have energies up to about 13 MeV, carbon up to 6 MeV and oxygen up to 3 MeV. The range-energy relationships for these ions are shown in Figure 5.14 and the LET relationships are given in Figure 5.15. In addition, the range-energy relationship for fast protons is displayed up to 200 MeV in Figure 5.13. The mean ratios of ranges in tissue and silicon, calculated as per equation (5.12), are displayed in Table 5.6. In general, the previously calculated scaling factor of 0.63 is reasonable, although the mean ratio drops to 0.58 for high energy protons. For microdosimetric spectrum dominated by high energy protons, one may consider reducing the geometric scaling factor. Note, that in

many cases the higher LET ions, although relatively infrequent, contribute significantly to the dose mean lineal energy. Additional weighting should then be applied to such ions when estimating the optimal scaling factor.

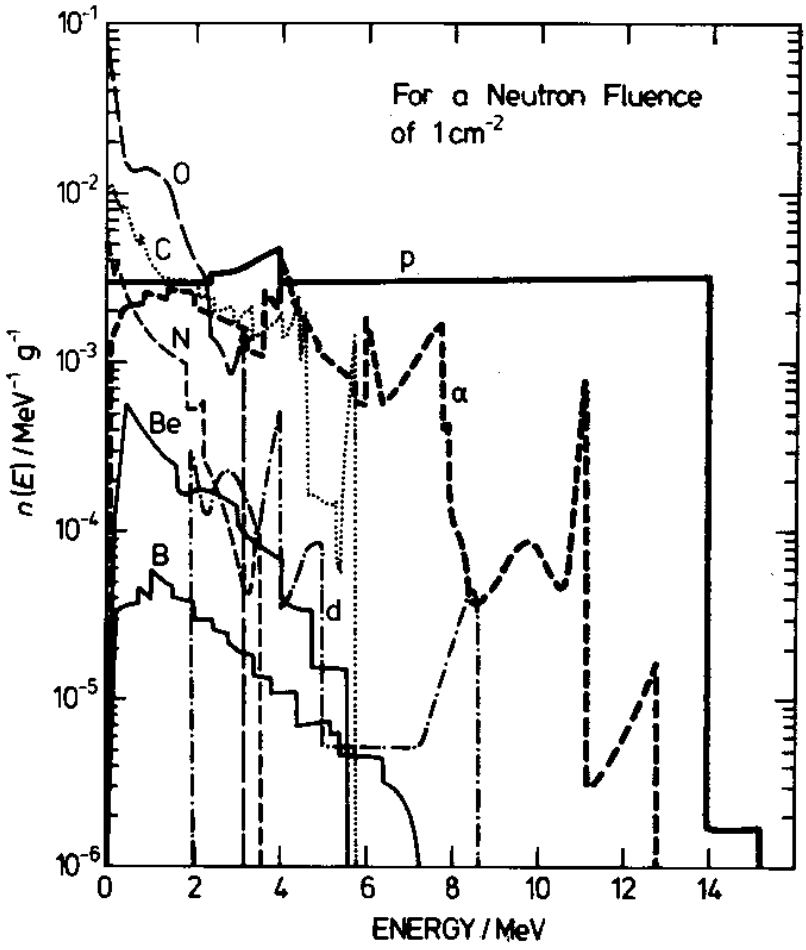


Figure 5.11. Initial spectrum of charged particles for a neutron fluence of 1 cm^{-2} of 14 MeV neutrons in ICRU tissue (from Caswell and Coyne [125] and ICRU report 36 p39 [11]). The symbols p, d and α refer to recoil protons, deuterons and alpha particles, respectively,

Table 5.6. Mean ratio of Fast Neutron/Proton Therapy ion ranges in silicon and tissue

Ion	*z*
H (0-14 MeV)	0.62
H (0-200 MeV)	0.56
He	0.66
C	0.63
O	0.61

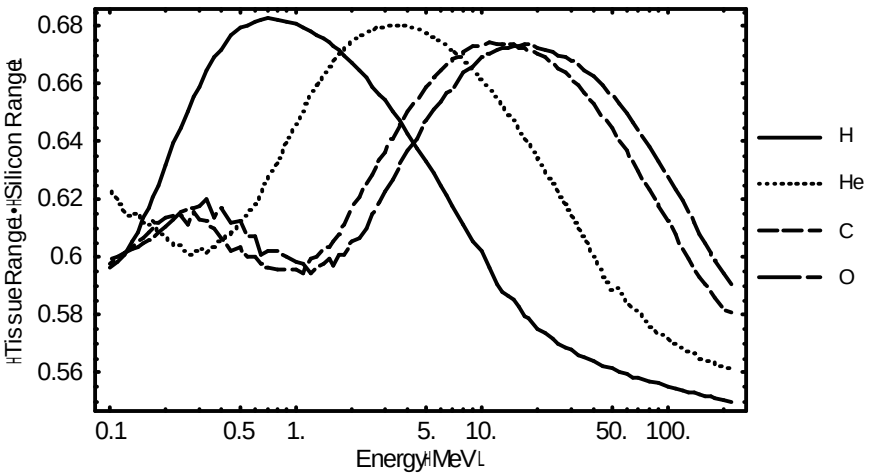


Figure 5.12. Ratio of tissue range over silicon range as a function of ion energy for main ions in Neutron and Proton Therapy.

The ratio of tissue range over silicon range as a function of ion energy is shown for various ions up to 200 MeV in Figure 5.12. This provides a useful reference for calculating the required *z* factor given information on the energy spectrum of secondary recoil products. Curves for different ions follow a common shape shifted to the right according to the ion's atomic number. The Bragg peak in the LET curve for each ion shifts to higher energies as the atomic number rises, although the main peak in Figure 5.12 is at an energy somewhat higher than the Bragg peak for each ion. An empirical equation should be extractable from Figure 5.12, with ion atomic number as a parameter, although this was not attempted.

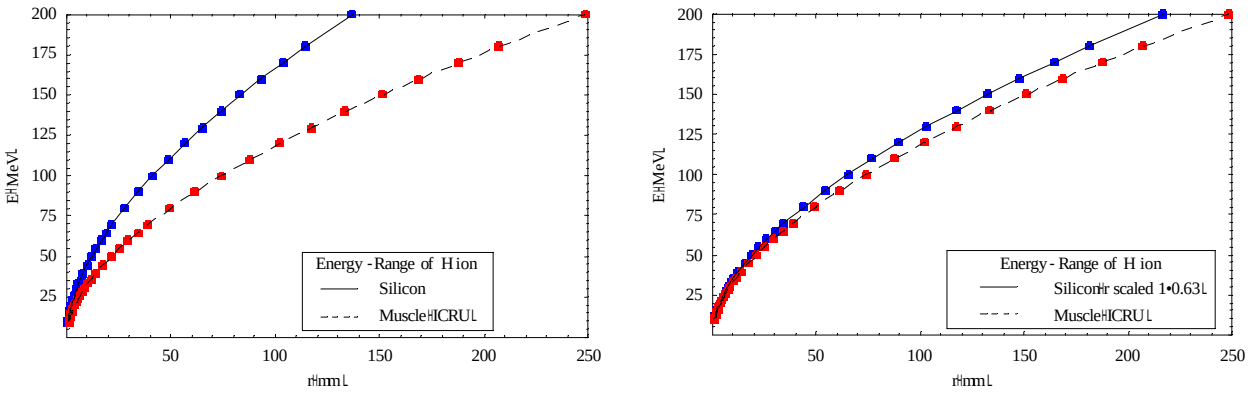


Figure 5.13. Range-Energy relationships for fast protons in ICRU muscle and Silicon. The right-hand side shows the same plot as the left except for the silicon range scaled by 1/0.63.

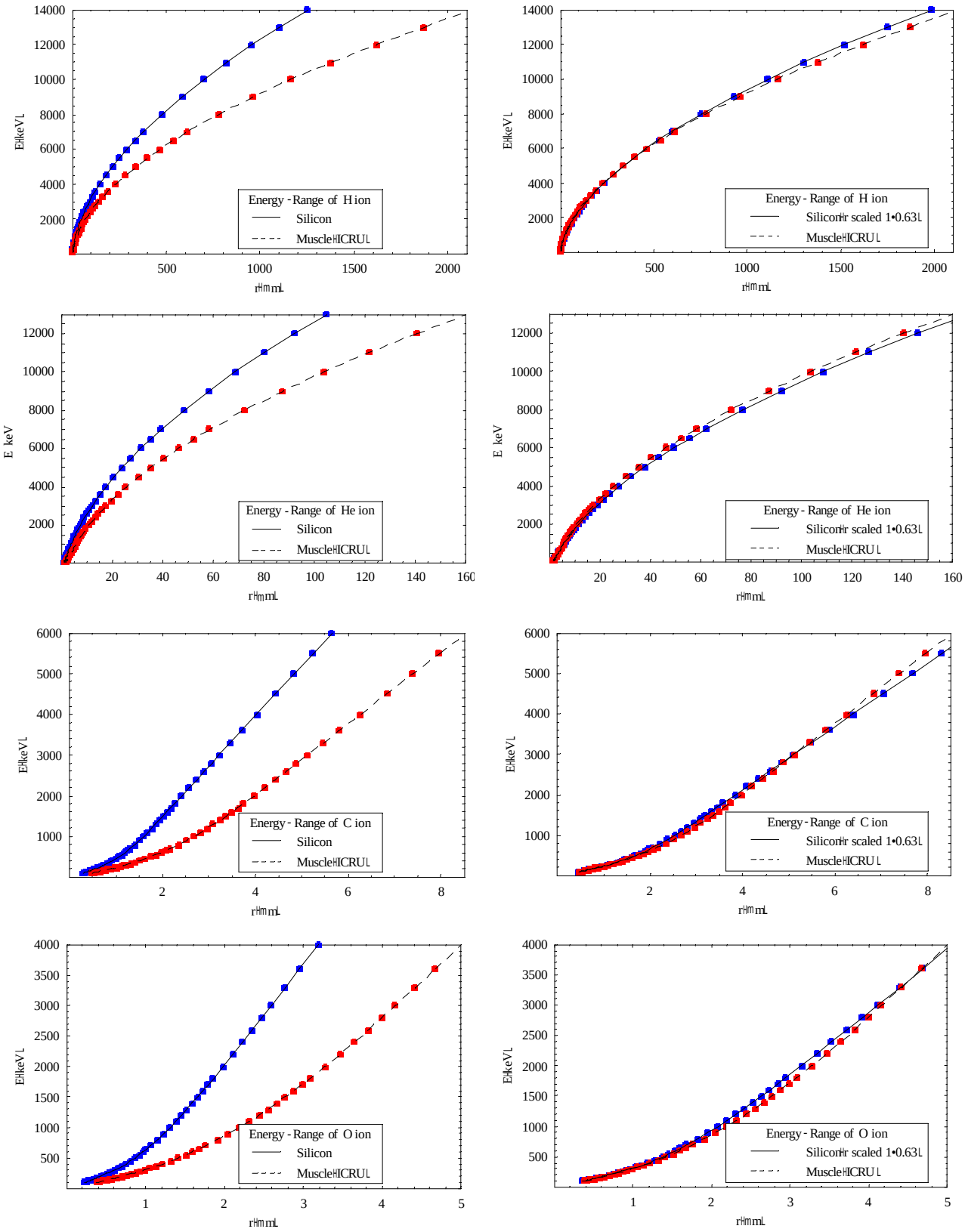


Figure 5.14. Range-Energy relationships for the main reaction products of fast neutron beams (H, He, C and O) in ICRU muscle and Silicon. The right-hand side shows the same plot as the left except for the silicon range scaled by 1/0.63.

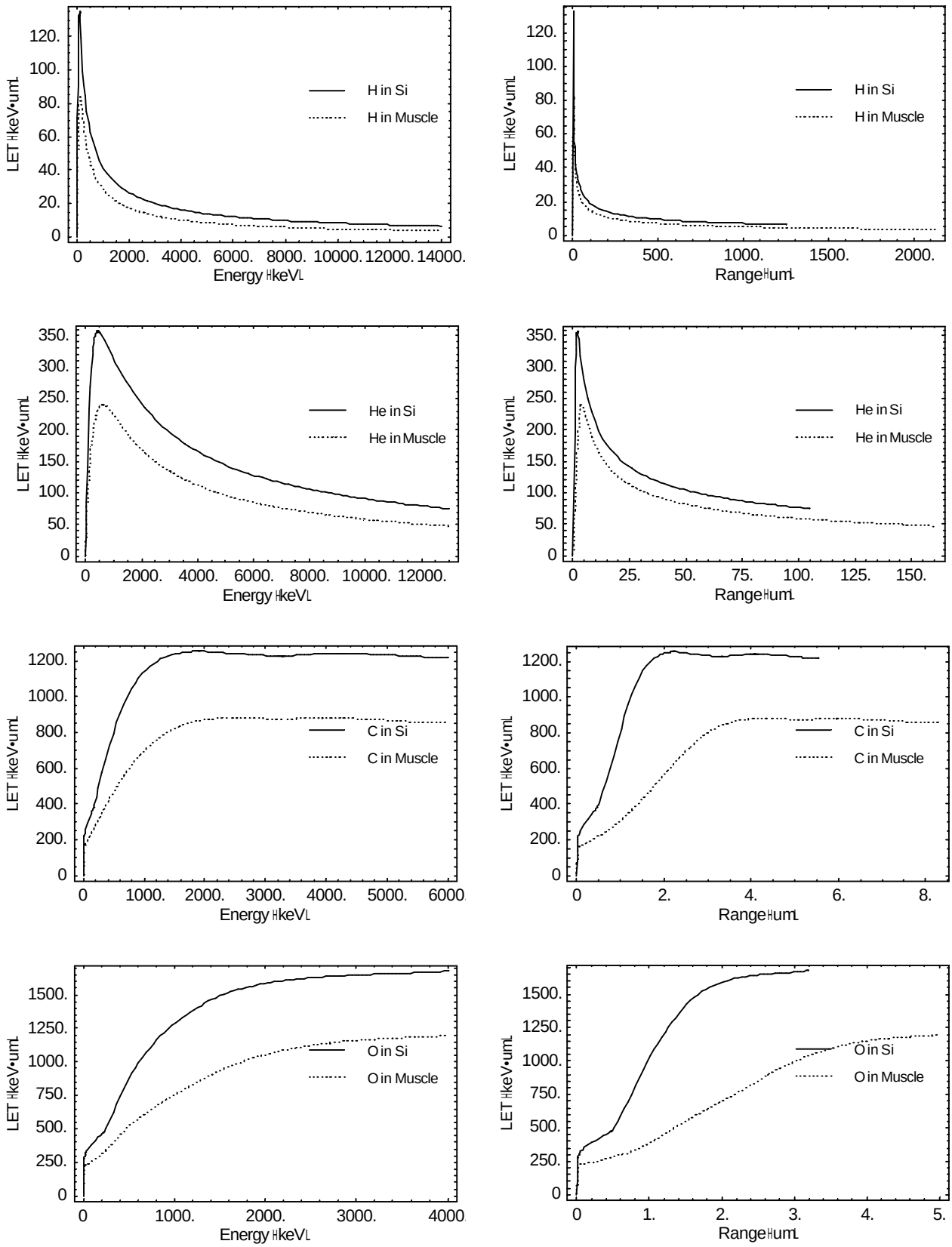


Figure 5.15. LET versus energy (left) and LET versus range (right) for Fast Neutron Therapy Products (H, He, C and O) in ICRU muscle and Silicon. The maximum range is plotted only up to the corresponding maximum energy.

5.5.2 Effect of converter atomic composition in FNT

Given that the TE geometrical scaling factor $z = 0.63$ is a reasonable approximation for a wide range of ion types and energy, one must now consider the production of secondary particles in a fast neutron environment. At neutron energies below 10 MeV the bulk of absorbed energy is due to hydrogen recoils except for some narrow resonances in heavy elements. The proportion of hydrogen in muscle is well approximated by A150 and 20% lower than desired in Lucite. Both A150 and Lucite substitute carbon for oxygen in their atomic composition when compared with the desired muscle composition as shown in Table 5.1. At higher neutron energies elastic and inelastic collisions with carbon and oxygen become important and appreciable (>20%) TE induced errors in $\bar{y}_d$ may occur. Table 5.7 gives values of $\bar{y}_d$ for various substances calculated theoretically by Green [189]. Furthermore, calculations by Caswell and Coyne [190] have shown considerable differences in the lineal energy spectra for 20 MeV neutrons between a simulated A150 proportional counter and ICRU muscle as shown in Figure 5.16.

Table 5.7. Calculated values of $\bar{y}_d$ in A150 and Muscle for various neutron energies En

Material	En=5 MeV	En=10 MeV	En=15 MeV	En=19.5 MeV
A150	53.8	73.4	101.1	124.7
Muscle	49.3	60.3	68.9	64.7

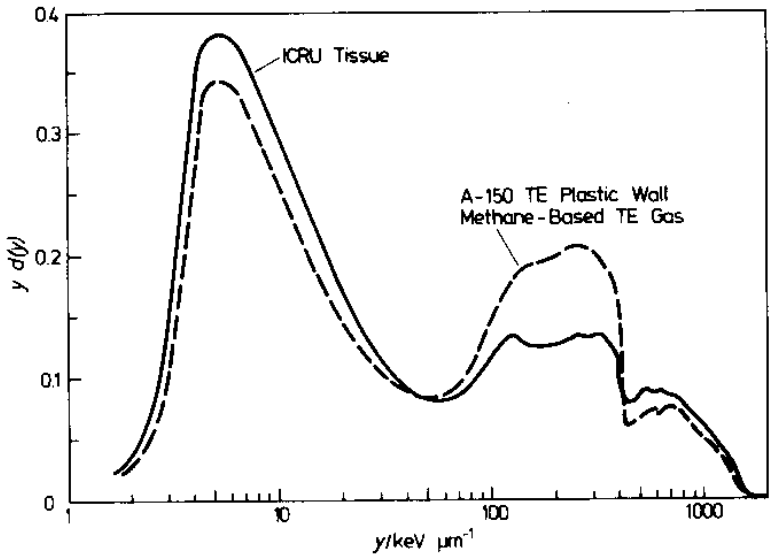


Figure 5.16. Comparison of analytic calculations of *yd(y)* of 20 MeV neutrons performed for ICRU tissue and for A150 plastic. (from Caswell and Coyne [190] and ICRU report 36 p42 [11])

Aside from simulation comparisons, a first order comparison of tissue equivalent performance may be gauged by comparing kerma ratios. Kerma is defined as the initial kinetic energy of all charged particles liberated by the radiation per unit mass and has the unit of Grays. Kerma data for various materials are tabulated in ICRU report 44 [32] based on the work of Caswell and Coyne [191]. Data is readily available for Acrylic, A150 and Muscle (Skeletal-ICRU 44). Acrylic ($C_6H_4O_2$, ρ = 1.17 gm/cm^3, H = 7%, C = 56%, O = 37%) is quite close in composition and density to Lucite ($C_5H_8O_2$, ρ = 1.2 gm/cm^3, H = 8%, C = 60%, O = 32%) and will be used in this comparative study. Note that the Acrylic mass composition provided in Appendix A of ICRU report 44 is fortunately in error since it corresponds to Lucite's mass composition. As mentioned in section 5.1, Muscle (Skeletal-ICRU 1989) is quite close in composition to Muscle (Striated-ICRU 1964) and sufficient for this comparative study.

The kerma ratio of A150 and Lucite to muscle (Skeletal, ICRU 1989) is shown in Figure 5.18. The Lucite kerma is generally 20% lower than A150 due to the 20% lower hydrogen content. The dips at 0.4 and 1 MeV occur due to oxygen elastic reactions, which are present in muscle and not in the plastics due to their lower oxygen content. These reactions have several resonances in the cross-section above 0.4 MeV as shown in Figure 5.22. The relative contribution of each element to tissue kerma is shown in Figure 5.17. Above 10 MeV the ratio rise is due to the effect of increasing carbon kerma contribution from the plastics.

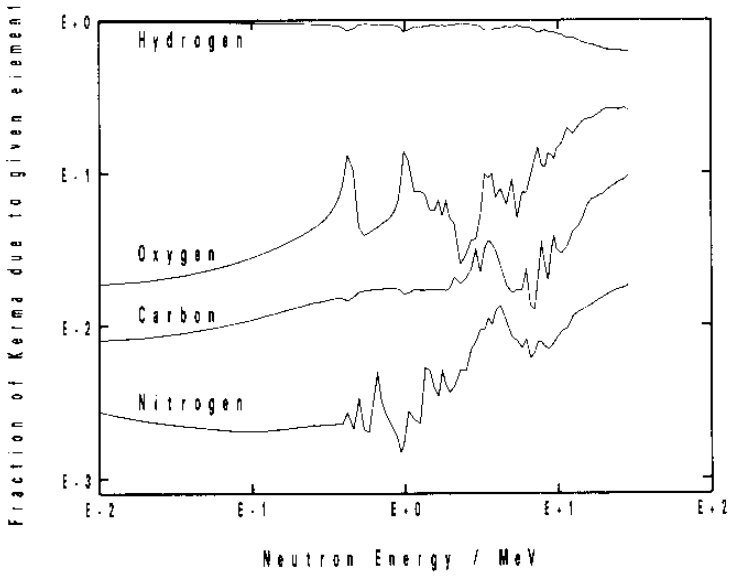


Figure 5.17. Relative contribution from interaction processes with different elements to kerma in muscle (skeletal) over the neutron energy interval 10 keV-30 MeV. (From p9 ICRU report 44 [32])

The final microdosimetric spectrum is normalized to unity since it is a probability distribution. Therefore in comparing kerma it is reasonable to normalize to unity at a low energy (were hydrogen interactions dominate) as shown in the right hand side of Figure 5.18. The normalization is slightly more complicated in that we only normalize the percentage of the kerma due to hydrogen interactions as provided by Figure 5.17. Deviations in the normalized kerma ratio from unity will crudely translate to differences in the normalized microdosimetric spectrum, particularly at higher lineal energies were the carbon and oxygen recoil contribute. Viewed in this manner, for neutron energies below 30 MeV, Lucite is a better approximation to tissue than A150 since its carbon and oxygen composition is better than A150. This is reflected in a normalized kerma ratio for Lucite which is closer to 1 than the A150 ratio.

A final important comment evolves from this discussion. The silicon/converter microdosimeter offers a potential tissue equivalent advantage over the A150 based proportional counter. Specifically, the silicon microdosimeter converter may be constructed using actual tissue cells or materials with precise muscle equivalent composition without regard for electrical conductivity, mechanical and construction requirements. This approach was not investigated in this work but is highly recommended for future consideration. A multi-layer converter structure may prove useful and amenable to construction. A thin layer of tissue cells may be sandwiched between TE plastic and the detector below. The longer range protons may primarily originate from the plastic whilst oxygen and carbon recoils originate from the cells. Each layer has the correct atomic composition for recoil products that are likely to intercept the detector.

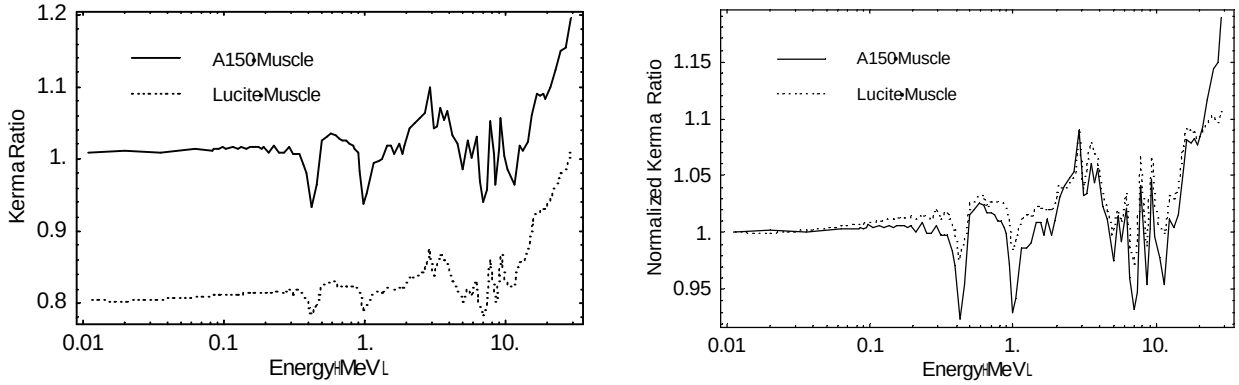


Figure 5.18. Kerma Ratio of A150 and Acrylic to Muscle (Skeletal, ICRU 1989) as a function of neutron energy. The right hand side plot has both kerma ratios normalized to 1 at 0.01 MeV (see text for explanation). The left hand side is unnormalized.

5.5.3 Silicon versus tissue interactions in FNT and PT and range of secondary products.

To maintain tissue equivalence the silicon microdosimeter must generate a relatively low proportion of insiders and starters compared with the tissue converter crossers and stoppers. Therefore, a brief summary of neutron-silicon and proton-silicon interactions is appropriate, followed by an analysis of relative kerma with tissue.

The important nuclear interactions of neutrons with silicon are summarized as

- $Si^{28}(n,n)Si^{28}$ elastic scattering
- $Si^{28}(n,n`)Si^{28}$ inelastic scattering
- $Si^{28}(n,p)Al^{28}$ nuclear reaction
- $Si^{28}(n,\alpha)Mg^{25}$ nuclear reaction Q=-2.654 MeV

For neutron energies above a few MeV, nuclear reactions begin to contribute to the silicon kerma. Nevertheless, elastic scattering dominates the total cross-section (~2 barns) for energies in the tens of MeV range. The silicon recoil energy is often small. with the maximum recoil energy from an elastic scatter reaction occurring for a backward scatter event. In this special case, the recoil energy is 0.133 E, where E is the nucleon incident energy [192]. Small recoil energies are much more probable and these result in much lower silicon recoil energies.

Similar nuclear reactions also occur for protons incident on silicon. The characteristics of high-energy proton-nucleus and neutron-nucleus reactions are very similar above 100 MeV. Below 100 MeV, the proton cross-section for silicon interactions is slightly lower than for neutrons. From about 20 MeV or below, the proton reaction cross section decreases rapidly because of the proton-nucleus Coulomb barrier. This barrier, however, does not apply to neutrons.

In general, microdosimetric measurements in proton therapy are only important at the end of the proton range. In this region, the relevant interactions correspond to no more than the tens of MeV energy range of fast neutron therapy. Therefore, we restrict the remainder of this comparative study to fast neutron therapy with typical neutron energies of less than 30 MeV.

We may consider the kerma ratio with tissue to ascertain the relative probability of silicon interactions as shown in Figure 5.19. The kerma ratio of silicon to tissue is less than 0.05 for neutron energies less than 5 MeV. Above this value, the cross-section for silicon neutron interactions rises more rapidly than for tissue resulting in the kerma ratio increasing to 0.2 at 15 MeV. The total cross-section (elastic + reaction(inelastic)) is high for silicon in the tens of MeV range, typically about 2 barns, with the inelastic reaction cross-section being 40% of the total cross-section as shown in Figure 5.22 and Figure 5.23.

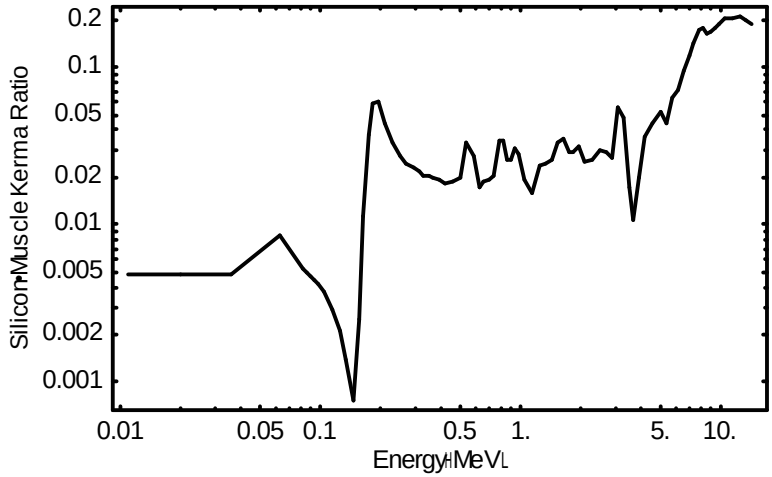


Figure 5.19. Kerma Ratio of Silicon to Muscle (Skeletal, ICRU 1989) as a function of neutron energy .

Some useful data is provided by Schrewe [37] in a very recent and excellent paper on the experimental estimation of kerma coefficients and dose distributions in various materials (C, N, O, Mg, Al, Si, Fe, Zr, A-150 plastic, Al_2O_3, AlN, SiO_2 and ZrO_2) for neutron energies up to 66 MeV. Proportional counters of various wall construction were used to measure dose in mono-energetic neutron fields which under charged particle equilibrium (CPE) conditions is almost equal to kerma. More precisely, the kerma coefficients (k_F or k= kerma/fluence) were derived by the following sequence: measure the absorbed dose in the cavity gas of the microdosimeter, derive the absorbed dose in the wall using Bragg-Gray cavity theory, determine the kerma in the wall under CPE conditions, and then correct for the neutron fluence attenuation in the wall. The kerma coefficients for materials in the silicon microdosimeter and their ratio to A150 plastic are shown in Table 5.8.

Table 5.8. Neutron kerma coefficients (k in fGy m^2) for Si microdosimeter materials and ratio to A150 from Schrewe [37]. The ratio of Si to A150 kerma is shaded for clarity.

Material	5 MeV	8 MeV	15 MeV	17 MeV	34 MeV	44 MeV	66 MeV
A150 (k)	4.546	5.364	6.732	7.505	8.67	8.07	7.95
(k/k_{A150})	1	1	1	1	1	1	1
Si (k)	0.175	0.812	1.436	1.571	2.75	3.05	3.84
(k/k_{A150})	0.038	0.151	0.213	0.209	0.32	0.38	0.48
SiO_2 (k)	0.406	0.757	1.914	2.048	3.62	3.99	4.77
(k/k_{A150})	0.089	0.141	0.284	0.273	0.42	0.49	0.60
Al (k)	0.196	0.438	1.140	1.436	2.40	2.82	3.82
(k/k_{A150})	0.043	0.082	0.169	0.191	0.28	0.35	0.48

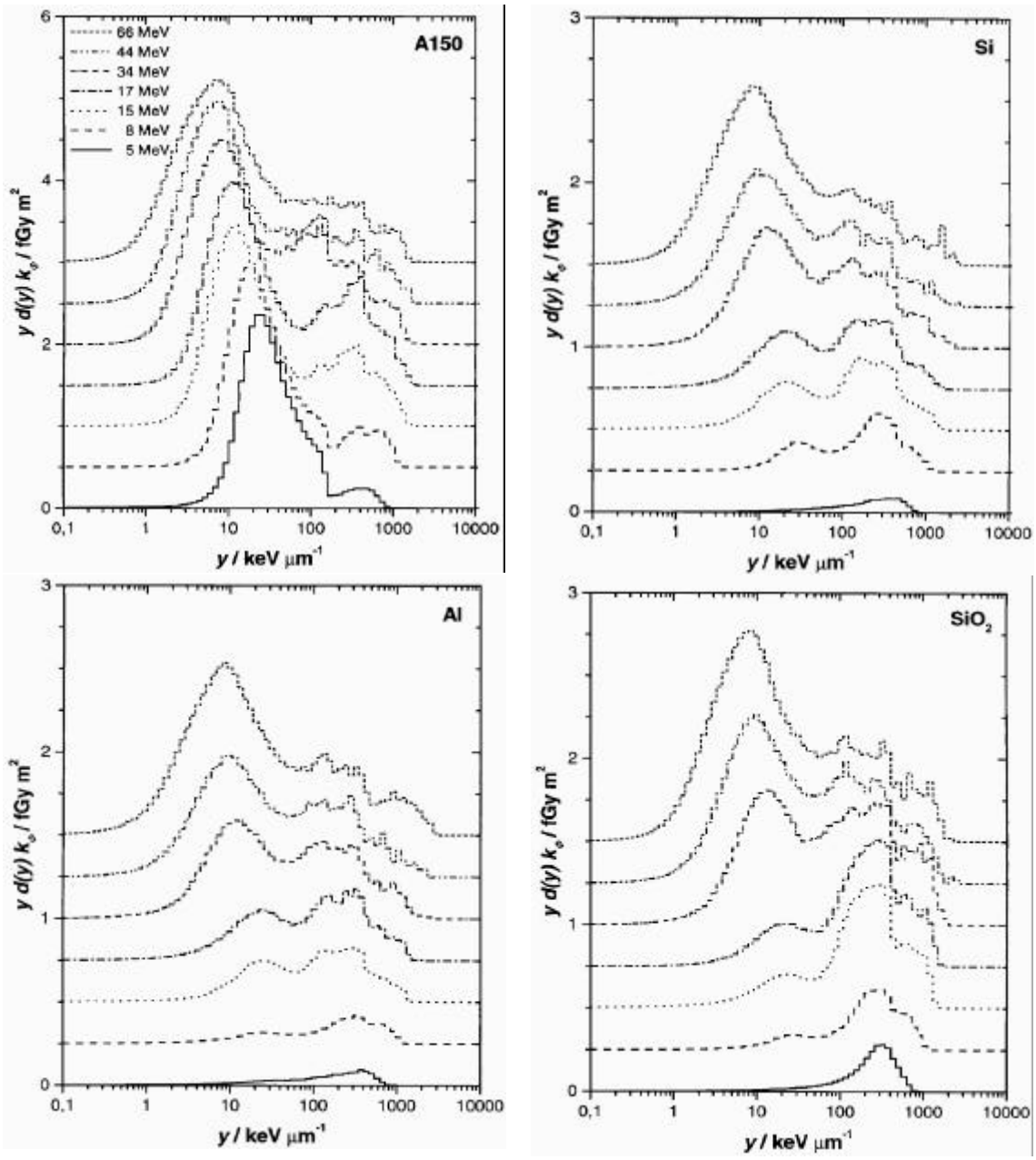


Figure 5.20. Dose distributions $d(y)k$ for A150, Si, Al and SiO_2 at neutron energies of 5, 8, 15, 17, 34, 44 and 66 MeV (from Schrewe [37]). Note, to improve presentation, fixed offsets were added. In addition, take care to consider the different scale for the A150 plot.

The values of tissue to silicon kerma derived from Schrewe's data [37] and given in Table 5.8 are in good agreement with Figure 5.19 although they extend the ICRU data to several higher energies. The kerma ratios with A150 for the main materials present in the detector overlayer (Al, SiO_2) are similar to Si. The Al ratio is generally lower by a few percent and the SiO_2 kerma ratio with A150 is 20-25% higher than Si at neutron energies above 15 MeV due to inelastic reactions with oxygen.

Schrewe [37] also provides dose distributions $d(y)k_F$ weighted by the kerma coefficient for measurements made using microdosimeters constructed with various materials and filled with a tissue equivalent propane gas mixture to provide an equivalent site diameter of 2 μm. These distributions, as shown in Figure 5.20, enable an approximate estimation of the expected contribution from different elements in the device construction to the silicon/converter microdosimeter dose distribution. Consider a hypothetical device with equal volumes of A150 and Si contributing to the detected secondary charged particle. This may be a reasonable first order approximation to the current device with an A150 converter located above the detector. At low neutron energies (<8 MeV) the contribution from silicon to the dose distribution is relatively small as reflected in the kerma ratio and visual comparison of the dose distributions. As the neutron energy increases above 8 MeV the contribution to the dose distribution increases particularly for lineal energies greater than 100 keV/μm. Given that as much as 30% of the dose may be due to silicon interactions at these lineal energies then one may expect discernible spectral distortion at neutron energies between 8 and 34 MeV. Clearly, the minimisation of silicon versus converter volume is required, a point that will be discussed later in this section. Interestingly, at high neutron energies >34 MeV, the distortion will be less significant since the shape of the dose distribution for both a silicon and A150 device are quite similar, particularly at 66 MeV. This behaviour arises from the decrease in significance of hydrogen reactions and the increased importance of inelastic reactions with sufficiently similar secondary product deposition spectra in silicon and A150.

An alternative analysis based on cross-section data will now be presented. Given appropriate cross-section data the probability of an interaction with silicon and tissue may also be compared. For sufficiently thin volumes the probability P_c of an incident particle encountering a nuclear collision is estimated by:

$$P_c \cong r\ s\ t \tag{5.13}$$

where r is the atomic density (in atoms/cm^3), s is the cross section (in cm^2) and t is the thickness (in cm). Total interaction cross-section data for silicon and the important elements of tissue are shown in Figure 5.22 with the inelastic (reaction) cross-sections compared in Figure 5.23. The hydrogen total cross-section is relatively high for energies less than about 8 MeV. Above 10 MeV, the cross-section magnitudes are in order of atomic number with silicon having the highest cross section.

As an example, the relevant data for 14 MeV neutrons is provided in Table 5.9 along with the probability of interaction for a particle traversing 1 cm of material. The probability of an interaction is similar in both silicon and tissue. However, 40% of the interactions in silicon are elastic collisions with poor energy transfer to the recoiling nucleus. The tissue, with its high hydrogen content, obtains high energy transfer due to the efficient energy exchange in elastic reactions with hydrogen. The difference in the energy of the secondary particles accounts for the higher kerma in tissue than in silicon.

The probability of interaction in 1 cm was calculated for energy ranges from 0.1 to 150 MeV in tissue and silicon. The ratio of these interaction probabilities for both total interactions and inelastic events is displayed in Figure 5.24. The total interaction ratio ranges from 0.2 to just over 1 in the energy range of most interest to fast neutron therapy. At neutron energies greater than 20 MeV the ratio steadily rises. For inelastic reactions, the high silicon cross-section produces a probability of inelastic reaction which is 2-3 times higher in silicon than tissue.

Nuclear reactions (inelastic) and elastic reactions with oxygen and carbon are of particular interest in microdosimetry since they produce recoil products with high LET. The recoil products typically have ranges of the order of a few microns as shown in Figure 5.14 and Figure 5.15. The alpha and proton by-products of inelastic reactions have longer ranges typically in the tens of micron range. In comparing silicon to tissue, the volume in which secondary particles are generated is important in assessing the probability that an excessive number of events will be generated from within the silicon compared to the tissue converter. To reduce the probability of silicon events, the silicon volume should be as small as practicable subject to the shape requirements discussed in chapter 3 and the practical signal to noise issues discussed in chapter 4. Accurate estimation of the maximum allowable silicon detector dimensions requires considerable

work in completely simulating (Monte Carlo) the interaction of the required neutron and proton environments with various tissue converter, overlayer and silicon detector constructions. Such time consuming calculations were not pursued in this work although they are highly recommended for follow-on studies. As an interim solution to gauge the extent of this problem we consider existing calculations for A150 proportional counters.

Fidorra and Booz [106] performed Monte Carlo simulations of a 5.85 MeV neutron beam incident on an A150 proportional counter with a simulated site size of 1 μm diameter. As shown in Figure 5.21 the proportion of starters and insiders within the tissue volume is quite small. The same volume of silicon would have even fewer starters and insiders since the ratio of interaction probabilities is 0.9. Thus, a silicon microdosimeter and TE converter with silicon dimensions of around 1 μm should provide a microdosimetric spectrum which is reasonably free of silicon interactions. The microdosimetric spectrum produced by thicker silicon detectors in fast neutron environments will have silicon interaction products contributing to spectral components at high lineal energies.

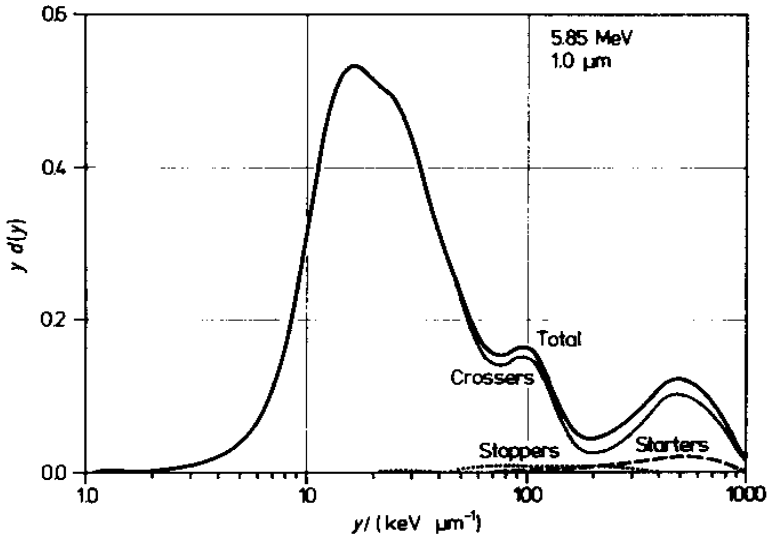


Figure 5.21. Monte Carlo calculations of *yd(y)* of 5.85 MeV neutrons in TE A150 plastic and methane based TE gas (1 μm simulated diameter). Contributions of stoppers, starters, and crossers to the total. The contributions of insiders is insignificantly small. (from p42 ICR report 36 [11] and Fidorra and Booz [106].

Complicating matters is the fact that the silicon microdosimeter is not completely surrounded by the TE converter, which is placed above the detector. For elastic collisions, this is not a significant problem since the neutron beam is generally normally incident to the detector. In this configuration, the majority of recoils will originate from

above the detector. Products from inelastic events are more isotropic and may originate from the silicon substrate. This may be a concern in silicon microdosimeters exposed to neutron energies around 10 MeV, where the inelastic cross-section is relatively high.

The implications of these results are significant for silicon microdosimetry design and experimentation. The silicon microdosimeter should be as small as practicable with the maximum amount of tissue equivalent material surrounding the detector.

Table 5.9. Nuclear interaction cross sections for 14 MeV neutrons incident on silicon and muscle.

Material	Nuclear Reactions		All Nuclear Interactions	
	$\sigma_{inelastic}$ **at 14 MeV (barns)**	**P(interaction) in 1 cm**	σ_{total} **at 14 MeV (barns)**	**P(interaction) in 1 cm**
Silicon	1.09	0.05	1.75	0.09
Muscle	Note 1	0.02	Note 1	0.1
Ratio(Si/Muscle)		2.5		0.9

Note 1: Muscle calculation uses elemental cross-sections from Figure 5.22 and Figure 5.23 and atomic density from Table 5.1.

Note 2: $\sigma_{total}=\sigma_{elastic}+\sigma_{inelastic}$

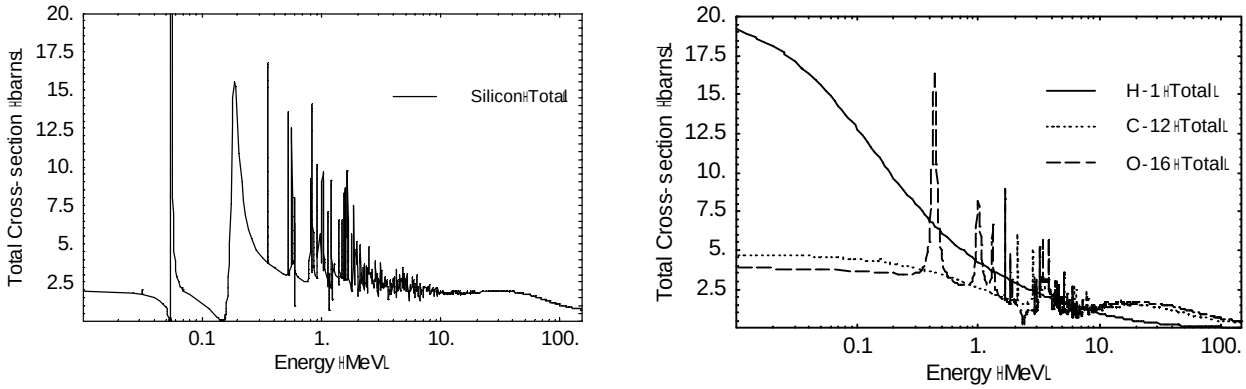


Figure 5.22. Total (elastic+inelastic) cross section for neutrons interacting with silicon (left side) and hydrogen, carbon and oxygen (right side). Si data is from Evaluated Neutron Data File, ENDF/B-VI library (>10MeV) and JENDL-3(300K) library (<10MeV). H,C and O data is from ENDF/B-VI library [193].

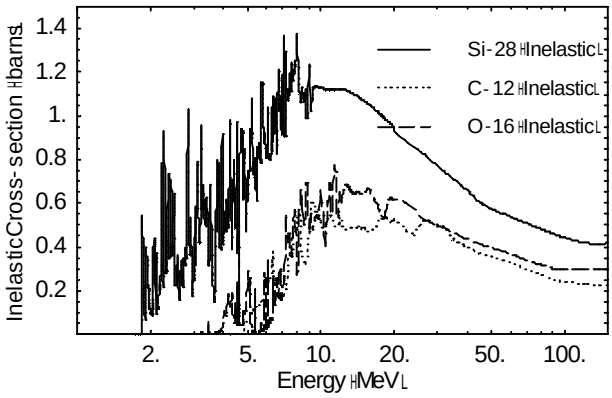


Figure 5.23. Inelastic (nuclear reaction) cross-section for neutrons interacting with silicon, carbon and oxygen. Data is from ENDF/B-VI library. [193]. Note that hydrogen, of course, does not undergo inelastic reactions.

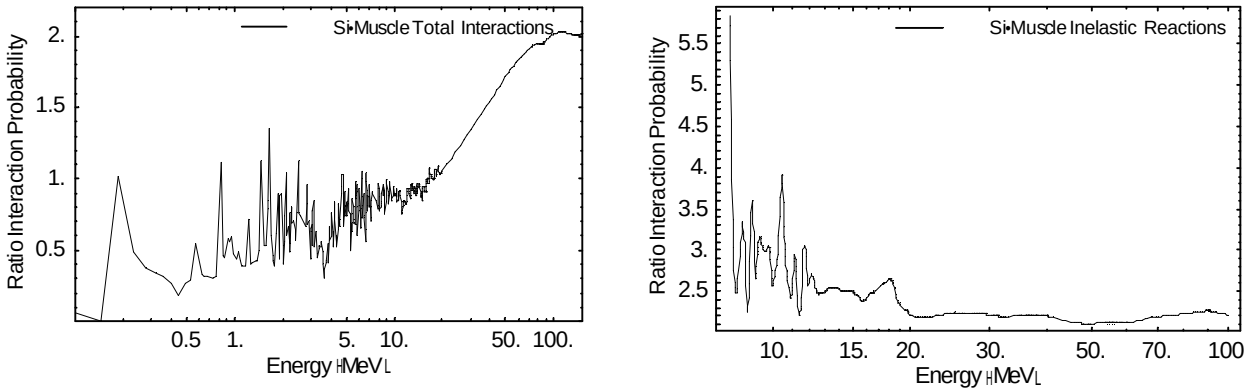


Figure 5.24. Ratio of probability of interaction between silicon and muscle as a function of neutron energy. Left side is for all interactions (elastic+inelastic); right side is for inelastic reactions only.

5.6 Summary of Tissue Equivalence Study

The requirements for TE were summarized in 5.3. To obtain tissue equivalence, the silicon detector/ TE converter should have a geometrical TE scaling factor of 0.63, a converter composition closely approximating tissue, and a minimum silicon detector size subject to shape and noise considerations (as discussed in chapters 3 and 4, respectively) in order to reduce the probability of nuclear interactions with silicon.

A Monte-Carlo program was developed to simulate the energy deposition of ions in a BNCT radiation field. The Monte Carlo results confirm that with appropriate geometrical scaling (z = 0.63) silicon detectors with well-known geometry will record energy deposition spectra representative of tissue cells of equivalent shape. That is, silicon is tissue equivalent for BNCT ion products under appropriate linear geometrical scaling. The scaling factor is also applicable to FNT but may need to be reduced for PT to around 0.56.

A brief study comparing tissue and silicon neutron interactions in FNT was described. For neutron energies less than 5 MeV, microdosimetric measurements in silicon volumes with dimensions of the order of 1 μm will not be significantly affected by events generated within the silicon. At higher neutron energies, the spectrum at high lineal energies may be affected by silicon elastic and inelastic reactions. A more detailed study is required to fully ascertain design requirements and the conditions under which satisfactory operation may be achieved. As a general guideline, the silicon microdosimeter should be as small as practicable with a maximum amount of tissue equivalent material surrounding the detector. The issue of tissue equivalence will be further discussed in the analysis of experimental results in subsequent chapters.

6. Charge Collection Modeling: Sensitive Volume and Radiation Hardness Characterization

A key problem impeding the widespread application of silicon based microdosimetry is the poor definition of the sensitive volume. The effects of diffusion and funneling may be minimized by the use of SOI structures. In this chapter, we present a study of the charge collection behavior of the prototype microdosimeter.

The aim of this work is to accurately define the sensitive volume and charge collection characteristics of this device. Three methods were used in this study; alpha and proton microbeam spectroscopy, broadbeam alpha spectroscopy and 2D and 3D device simulation. Broadbeam alpha spectroscopy refers to the use of a standard alpha spectroscopy source with a beam area larger than the microdosimeter area. Conversely, microbeam spectroscopy uses a submicron diameter beam scanned across the device under test. It has the important advantage of directly providing information on charge collection as a function of position on the device.

Experiments were performed on 2 and 10 μm SOI devices and the bulk structure. The results quantify the spatial response of the detector for various conditions including varying bias and radiation damage levels. The dangers in interpretation of broad-beam spectroscopy data are highlighted. In particular, lateral diffusion effects may complicate charge collection especially for small diode areas. The extent of lateral funneling effects is also determined. A software model is presented which accurately fits both broadbeam and microbeam data and determines the components which influence the resolution of spectroscopy methods.

A radiation hardness study is performed to determine the devices suitability for medical and space applications. Radiation induced displacement damage results in a reduction in minority carrier lifetime. The calculation of minority carrier lifetime was performed using microbeam spectroscopy methods. The radiation hardness study used 2 μm SOI and bulk devices only. Several devices of both types were radiation damaged at CERN using 24 GeV/c protons with fluences of 4.1×10^{13}pcm^{-2}. The different parts are designated “unirradiated” and “irradiated” throughout this chapter. Initial phases of this

work were originally presented by the author at the Nuclear Space and Radiation Effects Conference 1998 [194].

The basics of charge collection are described in section 6.1, section 6.2 describes the various sensitive volume characterization methods whilst section 6.3 applies such methods to the analysis of radiation hardness.

6.1 Charge Collection Physics

This section describes the basic physics of ion interactions with a reverse biased diode [44]. The simple case of a p-type bulk diode (n+-p) is generally used along with appropriate observations on behavior in SOI devices. The necessary background for subsequent detailed analysis of the microdosimeter charge collection volume is provided.

6.1.1 Motion of Carriers

The interaction of an ion with silicon produces electron-hole pairs. Such charge carriers are influenced by three main effects: drift due to an electric field, diffusion due to a concentration gradient and recombination of carriers through mid-gap recombination centers.

6.1.1.1 Carrier Drift

Under zero bias conditions at room temperature, charge carriers (holes in the valence band and electrons in the conduction band) are essentially free particles, which move rapidly due to thermal energy. The random thermal motion may be visualized as a succession of scattering collisions with lattice atoms, impurity atoms and other scattering centers. The random motion leads to zero net displacement over a sufficiently long time period. The thermal velocity of electrons is about 10^7 cm/s at 300 K with a mean free time between collisions of about 1 ps.

Application of an electric field, results in the net movement of carriers in a direction governed by the electric field and the carrier polarity. This process is called carrier drift. Mobility m is the proportionality factor that describes how strongly carrier motion is affected by the electric field strength $\vec{E}$. Thus, the drift velocities for holes $\vec{u}_p$ and electrons $\vec{u}_n$ are given by:

$$\vec{u}_p = m_p \vec{E} \tag{6.1}$$

$$\vec{u}_n = -m_n \vec{E} \tag{6.2}$$

The carrier mobility is determined by various scattering mechanisms including lattice scattering and impurity scattering. Lattice scattering results from thermal vibrations disturbing the lattice periodic potential thus allowing energy to be transferred between carriers and the lattice. Impurity scattering results when a charge carrier is deflected by Coulomb interaction with an ionized dopant impurity. Scattering processes and hence mobility are carrier type, temperature, doping and electric field dependent. At 300 K, intrinsic silicon has an electron mobility of 1350 cm^2/Vs and a hole mobility of 480 cm^2/Vs. The mobility of the *p*-substrate of the prototype microdosimeter is reduced somewhat although still dominated by lattice scattering whilst the *n*+ and *p*+ junction regions have much lower mobility due to high impurity scattering as shown in Table 6.1. Note that the electron mobility is approximately 3 times the hole mobility due to the lower effective rest mass of the electron.

Table 6.1. Electron and Hole Mobility

Doping Concentration	Electron Mobility (cm^2/Vs)	Hole Mobility (cm^2/Vs)
Intrinsic	1350	480
Na = 1.5×10^{15} (*p* substrate)	1337	458
Na = 2×10^{20} (*p*+,*n*+ contacts)	49	46

The linear relationship between drift velocity and electric field assumes that the time between collisions is independent of the applied field. At high electric field strengths (> 5×10^4 V/cm) the drift velocity becomes comparable to the thermal velocity of carriers and the linear relationship no longer holds. Thus, at sufficiently high electric fields the drift velocity approaches a saturation value v_{sat}. Experimental results are well approximated by the Caughey-Thomas [44, 195] empirical expression:

$$m(E) = \frac{m_{low}}{\left[1 + \left(\frac{m_{low} E}{v_{sat}}\right)^b\right]^{1/b}} \tag{6.3}$$

where E is the electric field in the direction of current, m_{low} is the low field mobility given in Table 6.1, v_{sat} is the saturation velocity (1.07×10^7 cm^2/s for electrons and 8.37 $\times 10^6$ cm^2/s for holes) and b is a constant (0.87 for electrons and 0.52 for holes) (from DESSIS manual [196]).

From equations (6.1) and (6.2) the drift current densities for holes and electrons are given by

$$\vec{J}_{p,drift} = qm_p p\vec{E} \tag{6.4}$$

$$\vec{J}_{n,drift} = qm_n n\vec{E} \tag{6.5}$$

where p is the hole density and n is the electron density.

6.1.1.2 Carrier Diffusion

Diffusion current results from the random thermal motion of carriers in a concentration gradient. The governing equations for hole and electron diffusion current densities are [44]:

$$\vec{J}_{p,diff} = -qD_p \nabla p \tag{6.6}$$

$$\vec{J}_{p,diff} = qD_n \nabla n \tag{6.7}$$

For an electron density that increases with a distance x, the gradient is positive and electrons will diffuse in the negative direction. Current flow is positive and flows in the direction opposite to the electrons. The holes also diffuse in a direction opposite to their concentration gradient. However, the current flow is negative in this case since positive charge is moving in the negative direction.

6.1.1.3 Recombination

At thermal equilibrium, the mass action law $np = n_i^2$ is valid. Recombination is the process of electron-hole pair cancellation that works towards restoring equilibrium under conditions where an excess of carriers exists, i.e. $np > n_i^2$. The recombination lifetime t_r is the average time it takes for an electron-hole pair to recombine when excess carriers exist.

The equilibrium electron and holes densities are denoted by n_0 and p_0 and by the mass action law [44]:

$$n_o p_o = n_i^2 \tag{6.8}$$

If we inject excess carriers *Dn* and *Dp* then the electron and hole densities are given by:

$$n = n_0 + \Delta n\,; \quad p = p_0 + \Delta p \tag{6.9}$$

The injection of carriers is categorized into two conditions; low level and high level injection. Low level injection occurs when the excess carrier density is much less than the majority carrier density. Conversely, high level injection occurs when the excess carrier density is much greater than the majority carrier density. For a p-type semiconductor with a doping N_a we have

Low level injection: $Dp=Dn << p=N_a$

High level injection: $Dp= Dn >> p=N_a$

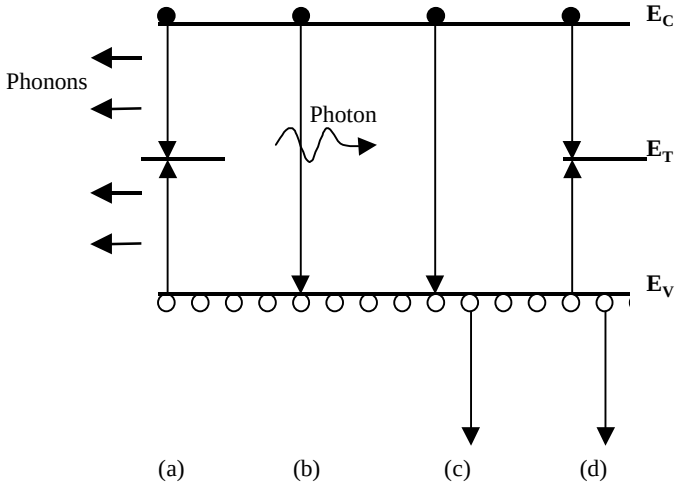


Figure 6.1. Recombination mechanisms:
(a) Shockley-Read-Hall, (b) Direct Radiative, (c) Direct Auger (d) Trap-Assisted Auger

There are four main mechanisms for recombination in semiconductors as summarized in Figure 6.1 and discussed below:

(a) *Shockley-Read-Hall*:

The basic theory of electron-hole pair recombination was initially developed in 1952 by Hall [197] and Shockley and Read [198]. During SRH recombination, electron hole pairs recombine through deep level impurities characterized by the impurity density N_T, energy level E_T in the bandgap and capture cross sections sn and sp and for electrons and holes, respectively. The energy liberated by the recombination event is dissipated by phonons or lattice vibrations. Shockley calculated the SRH lifetime t_{SRH} as:

$$t_{SRH} = \frac{t_p(n_0 + \Delta n + n_1) + t_n(p_0 + \Delta p + p_1)}{p_0 + n_0 + \Delta n} \tag{6.10}$$

where p_0 and n_0 are the equilibrium hole and electron densities, *Dn* and *Dp* are the excess carrier densities taken to be equal in the absence of trapping and n_1, p_1, t_n, t_p are defined as:

$$n_1 = n_i e^{(E_T - E_i)/kT}; \quad p_1 = n_i e^{(E_i - E_T)/kT} \tag{6.11}$$

$$t_p = \frac{1}{s_p v_{th} N_T}; \quad t_n = \frac{1}{s_n v_{th} N_T} \tag{6.12}$$

The corresponding recombination rate R_{SRH} per unit volume is given as [44]

$$R_{SRH} = \frac{pn - n_i^2}{t_p(n + n_1) + t_n(p + p_1)} \tag{6.13}$$

Note that we have used the relationships $p = p_0 + \Delta p$ and $n = n_0 + \Delta n$ along with the fact that the recombination rate is equal to the ratio of excess carriers to lifetime. If the centers are near the midgap such that p>>p_1 and if n>>p then the recombination rate is

$$R \cong \frac{\Delta n}{t_n} \tag{6.14}$$

Thus, the recombination is only dependent on the minority carrier lifetime and excess carrier concentration. The rate-limiting step in the recombination process is the capture of the minority carrier since there are an abundance of majority carriers available for recombination at a center.

(b) *Direct Radiative*:

In direct radiative recombination, the electron-hole pairs recombine directly from band to band with the energy carried away by photons. Radiative recombination is highly unlikely in indirect band-gap semiconductors such as silicon but it is important in direct bandgap semiconductors such as GaAs [44]. For completeness the radiative lifetime t_{rad} is given by :

$$t_{rad} = \frac{1}{B_{rad}(p_0 + n_0 + \Delta n)} \tag{6.15}$$

where $B_{rad} = 2 \times 10^{-15}$ cm^3/s for silicon.

(c) Direct Auger:

During Auger recombination, the recombination energy is absorbed by a third carrier. For a p-type semiconductor, the lifetime is given by [199]:

$$t_{Auger} = \frac{1}{C_p(p_0^2 + 2p_0\Delta n + \Delta n^2)} = \frac{1}{C_p p^2} \quad \text{assuming } \Delta n = \Delta p \tag{6.16}$$

where C_p is the Auger recombination coefficient. The general recombination rate for any doping and injection levels is given by:

$$R_{Auger} = (pn - n_i^2)(C_n n + C_p p) \tag{6.17}$$

where $C_n = 6.7 \times 10^{-32}$ cm^6/s and $C_p = 7.2 \times 10^{-32}$ cm^6/s [199].

Auger recombination is important in high injection conditions or regions of high doping (carrier concentrations > 10^{19} cm^{-3}). The following approximation applies at high injection levels and assuming *Dp=Dn*.

$$R \cong C_p \Delta p^3 \tag{6.18}$$

Note that since three carriers are now involved the recombination rate is proportional to the cube of the excess carrier density

(d) *Trap-Assisted Auger*:

The trap assisted Auger lifetime t_{trap} is given by [199]:

$$t_{trap} = \frac{1}{B_{trap}(p_0 + n_0 + \Delta n)} \tag{6.19}$$

where $B_{trap} \sim 1 \times 10^{-15}$ to 9×10^{-15} cm^3/s for silicon. Note the similarity with equation (6.15). This process is relatively unimportant except when many traps are present in which case B_{trap} may be much higher.

These mechanisms combine to determine the average recombination lifetime according to the relationship [200]:

$$\frac{1}{t_r} = \frac{1}{t_{SRH}} + \frac{1}{t_{rad}} + \frac{1}{t_{auger}} + \frac{1}{t_{trap}} \tag{6.20}$$

Of course, the recombination rates simply add to give the total recombination rate R.

$$R = R_{SRH} + R_{rad} + R_{auger} + R_{trap} \tag{6.21}$$

At high carrier densities (either injection or doping), the dominant recombination process is Auger recombination whilst at low densities SRH multi-phonon recombination is dominant.

All of the above mechanisms may operate in the silicon bulk. In addition, SRH recombination may occur at surfaces due to interface states that span the bandgap. These states are introduced by the discontinuity in the lattice structure, at the interface between surfaces. The primary interface in the silicon microdosimeter is the Si/SiO_2 interface, which bounds the top and bottom of the silicon SOI layer. Analogous to the SRH bulk lifetime of equation (6.13), the SRH surface recombination velocity is given by:

$$s_r = \frac{p_{0s} + n_{0s} + \Delta n_s}{(1/s_p)(n_{0s} + \Delta n_s + n_{1s}) + (1/s_n)(p_{0s} + \Delta p_s + p_{1s})} \tag{6.22}$$

where

$$s_n = s_{ns} v_{th} N_{it}; \quad s_p = s_{ps} v_{th} N_{it} \tag{6.23}$$

At low injection levels, s_r may vary from about 5000 cm/s to as low as 20 cm/s [199]. The subscript "s" refers to the appropriate quantity at the surface. Carrier densities are in units of cm^{-3} and interface trap density N_{it} is in units of cm^{-2}. The number of carriers recombining at the surface per unit area and unit time is the surface recombination rate R_s, given by an expression analogous to equation (6.13):

$$R_s = \frac{p_s n_s - n_i^2}{(1/s_p)(n_s + n_1) + (1/s_n)(p_s + p_1)} \tag{6.24}$$

Surface recombination is more complex than bulk recombination because it depends not only on the density of traps but also on the state of the surface. For example, positively charged surface states in p-type silicon may induce a depleted surface that presents an attractive potential for minority carriers. The enhancement of surface recombination via this mechanism will depend on the injection level since the surface potential may be reduced as injection levels rise.

The main features of recombination have been discussed. For a more detailed discussion of lifetime refer to Schroder [199, 200] and Bullis [201].

6.1.1.4 Combined Model (Continuity and Poisson Equation)

The overall effect of drift, diffusion and recombination on the semiconductor is encapsulated in the continuity equations. The spatial and temporal distribution of carrier density and electrostatic potential may be obtained by solving the continuity equations and Poisson's equation for the device. Classical electrodynamics relates the electric field $\vec{E}$ to the charge density r by Poisson's equation:

$$\nabla . e\vec{E} = r \tag{6.25}$$

where e is the dielectric permittivity of silicon = 1.05 pF/cm and the net charge density r is given by

$$r = q(p - n + N_d^+ - N_a^-) \tag{6.26}$$

where n and p denote the concentrations of electrons and holes, respectively, and N_d^+ and N_a^- are the concentrations of ionized acceptors and donors.

Conservation of charge conditions and the spatial and time continuity of carrier concentrations is expressed by the continuity equations for each carrier type [44]:

$$\nabla . \vec{J}_n = q\left(R - G + \frac{\partial n}{\partial t} \right) \tag{6.27}$$

$$\nabla . \vec{J}_p = -q\left(R - G + \frac{\partial p}{\partial t} \right) \tag{6.28}$$

where R is the total recombination rate given by the sum of bulk and surface recombination components (equations (6.21) and (6.24)) and G is the carrier generation rate.

These equations must be solved together with the constitutive relationships for current density (the actual drift-diffusion equations obtained by combining equations (6.4) to (6.7)) are:

$$\vec{J}_n = q\mu_n n\vec{E} + qD_n \nabla n \tag{6.29}$$

$$\vec{J}_p = qm_p p\vec{E} - qD_p \nabla p \tag{6.30}$$

One should also note the important relationship between mobility and diffusivity provided by the Einstein relationship:

$$D_n = \frac{kT}{q} m_n \tag{6.31}$$

where kT/q is 0.026 V. This relationship also applies between D_p and m_p. In addition to the conduction currents, there is the displacement current given by:

$$\vec{J}_d = e\frac{\partial \vec{E}}{\partial t} \tag{6.32}$$

These currents add up to give the total current at a point in the semiconductor:

$$\vec{J}_T = \vec{J}_d + \vec{J}_n + \vec{J}_p \tag{6.33}$$

6.1.2 Ion Interaction: Generation of Carriers

An energetic ion passing through a material predominantly deposits energy via coulomb collisions with the material's atomic electrons. The energy loss per unit path length or Linear Energy Transfer (LET) may be approximated by the Bethe equation provided in section 5.2. The numerous collisions slow down the ion until it eventually stops and has only the thermal energy of the surrounding material. Importantly, the energy deposition is not entirely along the trajectory of the incident ion but has a finite radial extension around the incident track trajectory. Liberated electrons, called delta rays (δ-rays), have sufficient energy to follow trajectories away from the incident track. Delta rays travel in a zigzag pattern and similarly lose energy from coulomb collisions until they are thermalized. The δ-rays account for roughly half of the collisional energy [202]. The rest are accounted for in soft collisions, between the ion and atomic electrons, which produce essentially thermal electrons that mainly contribute to the electron-hole pairs in the plasma core.

For a semiconductor material, the deposited energy is converted directly into a dense population of electron-hole pairs. The familiar conversion rate in silicon is 3.62 eV/e-h pair. Thus, if the initial energy distribution is known then the initial electron-hole pair distribution may be calculated. In microdosimetry, it is important to understand the extent of the electron-hole pair plasma that remains following the thermalization of

delta electrons. Many calculations assume that the track width is negligibly small in comparison with microdosimeter dimensions. Furthermore, semiconductor device simulations require as input the initial electron-hole pair distribution.

Several researchers [203-211] have investigated the track structure of ions traversing silicon and other materials. Monte Carlo calculations [204] have provided quite accurate information on track structure but are time consuming and largely incompatible with other semiconductor simulation codes. Much of the effort has focussed on obtaining an accurate semi-empirical analytical expression for the energy density deposited in a cylindrical shell about the ion track trajectory.

The current approach, which most accurately corresponds with Monte Carlo results and experiment, is based on a method initially proposed by Kobetich and Katz [203] and frequently called Katz theory. They utilized two empirical relations for electron range in aluminium and electron transmission through thin foils, to determine the energy deposition of δ-rays traveling in straight lines perpendicular to the incident track. Also required is a relationship for the delta ray energy distribution (i.e. spectrum; the number of delta rays per cm per energy). Note that electron range, expressed in gm/cm^2, is approximately the same for materials of similar atomic number. Hence the use of aluminium data to approximate other materials.

Many improvements have been made to the initial model, including work by Waligorski [205] who introduced a correction factor to the dose that provides better agreement with experiment and Monte-Carlo and Katz [209] who extended the work to mediums other than water. For silicon, the most recent and accurate Katz model is attributable to Fageeha [211]. The equations given by Fageeha were implemented in a relatively simple Mathematica program (Note that Fageeha wrote a program called REDCHP).

The electron hole pair density formed in silicon from a 5 MeV alpha particle and 2 MeV proton is shown in Figure 6.2. For these ions, high injection conditions occur in a cylindrical region less than about 0.1 μm radius. Auger recombination will be dominant in the region of radius less than about 5-10 nm. An alternative form of presentation is to plot the radial profile of the cumulative fraction of total dose as shown in Figure 6.3. (calculated as the cylindrical integral of Figure 6.2 divided by the total dose). From this figure, we see that the two ions have similar radial dose profiles except for almost an order of magnitude lower total dose for the 2 MeV proton. The lower total dose is

simply due to the lower LET. In both cases, fifty percent of the dose is within 2.5 nm of the center track and almost the entire dose is within 150 nm.

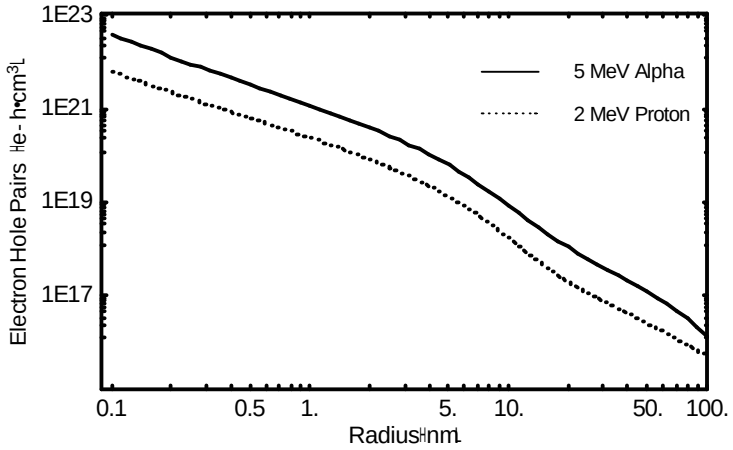


Figure 6.2. Plot of energy density profile as a function of radial distance from the center of an alpha and proton ion track based on Fageeha's implementation of Katz's model [211].

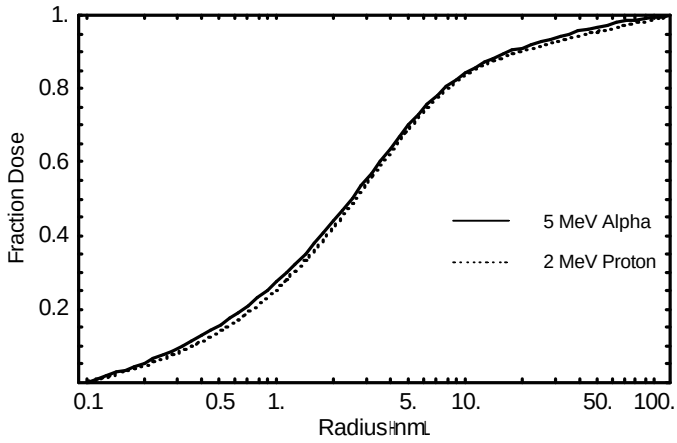


Figure 6.3. Cumulative fraction of dose deposited from the center of the track to the given radius. Fifty percent of the dose is within 2.5 nm of the center track.

6.1.3 Ion Interaction: Motion of Carriers

Having determined the initial carrier density following an ion strike, the evolution of the plasma column and the collection of carriers will now be described. We will consider an ion strike normally incident from above the device and intercepting the depletion region (DR, a strong space charge region) of a n+/p diode as shown in Figure 6.4. Three separate processes transpire, denoted by DR collapse, DR recovery and then stable DR operation. Charge collection may occur during each of these processes but to varying degrees depending on the time of the process. DR collapse and DR recovery are characterized by high injection conditions with a dynamic depletion region boundary

(DRB) whilst stable DR operation occurs in low level injection conditions and maintains a stationary DRB.

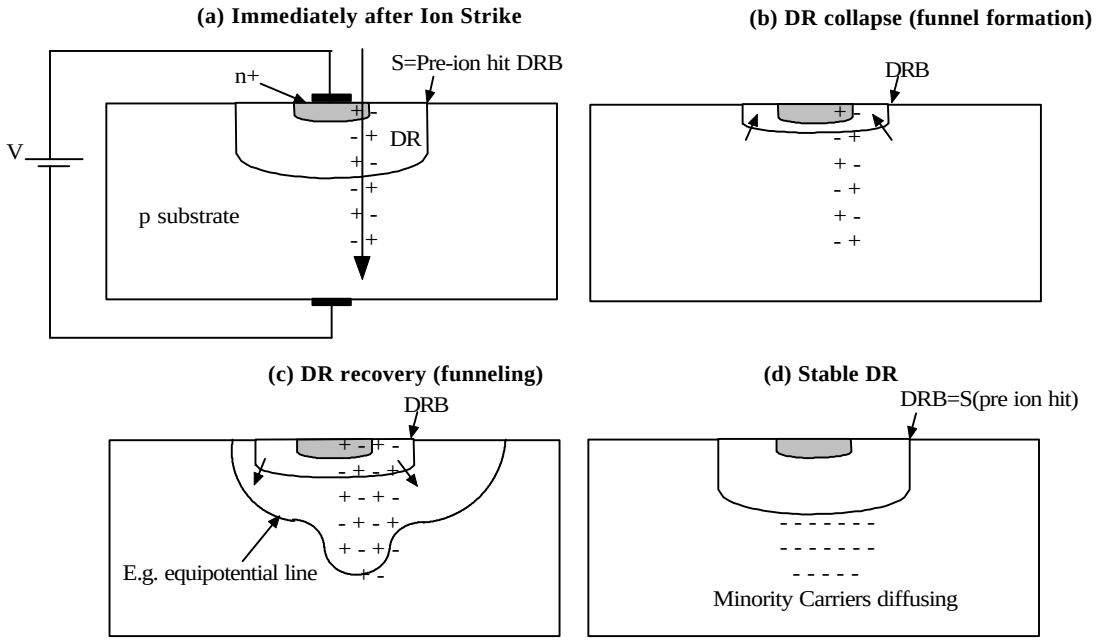


Figure 6.4. Charge collection stages for an ion strike on a *n+/p* bulk diode. Most of the charge collection occurs during DR recovery (c) and the following stable DR (d).

The ***DR collapse*** is caused by a rearrangement of charge carriers located above the initial DRB. The strong electric field in the depletion region very quickly produces a redistribution of carriers liberated by the ion track until many of the previously unshielded impurity ions become shielded by carriers. Thus, the DR shrinks and the quasi-neutral region of the track extends upwards. A quasi-neutral region is defined by the property that the charge imbalance is small compared to the majority carrier density. Below the DRB, under high injection conditions, the track is quasi-neutral because the electron and hole densities are equal and much larger than the substrate doping defining the majority carrier density.

An implication of a collapsed or partially collapsed DR, first discovered by Hsieh [212], is that it supports much less voltage then prior to the hit. Voltage formally across the depletion region now occurs across the quasi-neutral region and substrate. The substrate voltage drops enhances minority carrier (electron) flow from the substrate to the DR, a phenomenon called funneling. A simulation of a 5.3 MeV alpha particle incident on a p+/n bulk diode is shown in Figure 6.24 (and described in more detail in section 6.2.2.3). Even as short as 1 ps following the ion strike one can see the funnel shaped

voltage distribution. The end of the first stage is characterized by the DR at a minimum, the beginning of funneling, but with very little charge collected due to the very short time frame.

It has been assumed thus far that the DR collapse is caused by an ion strike intercepting the depletion region. However, if the track misses the junction there can still be a DR collapse producing a voltage across the quasi-neutral region. In this case, the collapse is more gradual since carriers must first diffuse to the DR to generate the collapse. Furthermore, the distinction between collapse and recovery is not as clear as for the direct strike since the DRB is quite well defined at all times and both collapse and recovery are gradual.

Throughout the collapse and subsequent recovery, the cylindrical electron-hole pair plasma expands radially outward by ambipolar diffusion. The diffusion is ambipolar as the plasma attempts to remain charge neutral [213]. Since the electron diffusion constant is higher than the hole diffusion constant the charge will attempt to separate. However, any charge imbalance is quickly rectified by strong electrostatic restoring fields. The common ambipolar diffusion constant is given by McKelvey [214, 215] as:

$$\begin{aligned} D &= \frac{(n+p)D_n D_p}{nD_n + pD_p} \\ &\approx \frac{2D_n D_p}{D_n + D_p} \qquad \text{High injection: if } n = p >> N_a \\ &\approx D_n \qquad \text{Low injection} \end{aligned} \tag{6.34}$$

Note that mobility is reduced at higher carrier concentrations. This further decreases diffusivity at early times in the plasma track evolution via Einstein's relationship between mobility and diffusivity (equation (6.31)). The diffusivity constant will typically vary from 1.5 cm^2 /s under high injection conditions to 35 cm^2 /s under low injection conditions. Ambipolar diffusion requires high level injection. Once the carrier density approaches the substrate doping level then electron and hole diffusion may occur at separate rates since the restoring electrostatic fields are no longer supported.

Assuming ambipolar diffusion is the dominant process, high level injection conditions with a constant diffusivity and including only SRH recombination then equation (6.14), (6.27) and (6.29) reduce to:

$$D\nabla^2 n - \frac{n}{t} = \frac{\partial n}{\partial t} \tag{6.35}$$

which has the solution for a Dirac delta function initial condition, *n(r,t=0)= N* e-h/unit length [215, 216]:

$$n = \frac{N}{4pDt}\exp\left(\frac{-r^2}{4Dt} - \frac{t}{t}\right) \tag{6.36}$$

As an example, the above equation was calculated for a 5 MeV alpha particle (LET=150 keV/μm, $N = 4.2 \times 10^8$ e-h/cm) at 1, 10 and 100 ps with t = 1 μs. The diffusivity constant was approximated to 1.5, 3 and 20 cm^2/s for the plots at 1, 10 and 100 ps respectively. We note that this equation is very much an approximation since the diffusivity constant will vary spatially and temporally with carrier density. However, it still provides some rough insight into the time scale of various processes. For the time periods considered, SRH recombination is not significant although Auger recombination may contribute for time periods less than about 5 ps when carrier densities exceed 10^{19} cm^{-3}. Ambipolar diffusion may occur for the first 500 ps after which the carrier density returns to low level injection conditions.

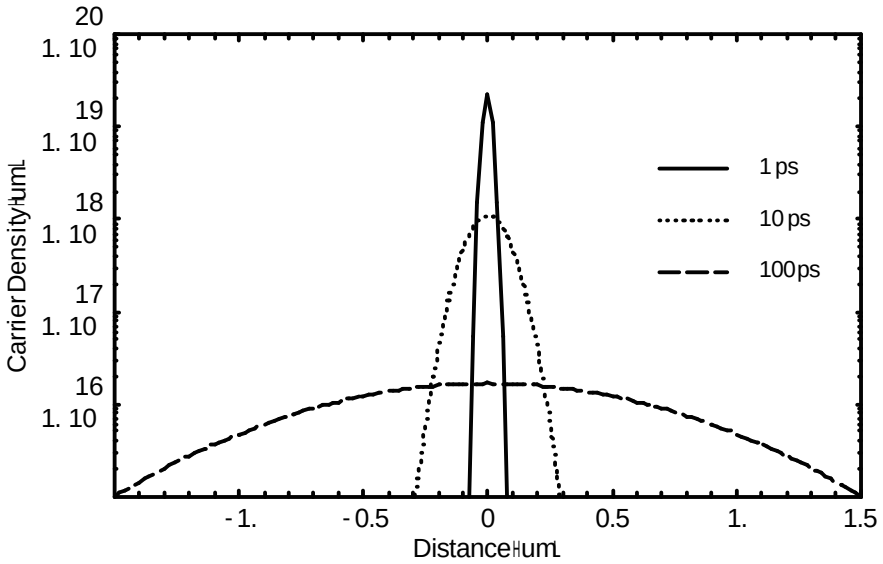


Figure 6.5. Approximate minority carrier density (electron) during ambipolar diffusion around a 5 MeV alpha strike. The diffusivity constant was approximated to 1.5, 3 and 20 cm^2/s for the plots at 1, 10 and 100 ps respectively.

An important concept highlighted by Edmonds [217] is that a strong current may flow longitudinally through a quasi-neutral region radially expanding via diffusion. The current does not require a charge separation because carriers leaving a volume element

can be replaced by others moving in. Thus, the ambipolar diffusion equation may describe the carrier density but says very little about carrier flow. A full description incorporating current flow requires complete solution of the continuity and Poisson equations over the entire device, a problem usually solved using device simulators as described in section 6.2.2.

A qualitative discussion of carrier flow is provided by considering the second stage of ***DR recovery*** in some detail. The collapsed DR begins to expand because the electric field continues to push holes down so that they move below the negative acceptor ions that they were previously screening. There are essentially no replacement holes coming from the n+ region since high recombination in the heavily doped n+ region eliminates virtually all holes. Thus, the downward flow of holes produces an expanding space charge region. However, the region is not depleted of electrons because the large electron supply in the quasi-neutral region and particularly the lightly doped *p* region are capable of replacing electrons that are moving up and out of the DR to the upper electrode. Much of the DR is characterized by a high electron density with virtually no holes.

Recovery time is much longer than collapse time, but this time may range from tens of picoseconds to nanoseconds depending on substrate doping and ion track characteristics. The recovery concludes when all the holes have been pushed out of the pre-ion hit DRB. This time corresponds with the drop in plasma column carrier density to values close to the substrate doping density at which stage there is no opposing hole diffusion current. Therefore, a strong diffusion current slows down the process because the upward hole diffusion at points below the DRB opposes the downward flow. For example, a thick substrate with an ion track long enough to produce a strong and long-lasting diffusion will result in a long recovery time.

Charge collection during recovery consists of the longitudinal funnel assisted drift collection of electrons at the *n*+ junction. The funnel is essentially a weak field ambipolar region with moderate longitudinal drift. The pre-ion hit electric potential is gradually restored as the carrier density approaches the substrate density. The potential restoration proceeds from the outer surface of the plasma column into the center. From the above discussion, we can see that current flow is the cause and the voltage across the quasi-neutral region (i.e. the funnel) is an effect.

The extent of funnel assisted charge collection is heavily dependent on whether the substrate is *p* or *n* type doping. For long tracks, the *n*-type substrate retains a significant portion of its voltage whilst the p-type readily exhibits funnel behavior [217]. The difference in mobility of electrons and holes is the fundamental reason. Edmonds [218, 219] has investigated this effect theoretically extending the earlier work of Hu [220] and McLean and Oldham [221] whilst Dodd has also investigated funneling using device simulation [222, 223].

Following the DR recovery, charge collection will still occur under a condition of ***stable DR operation***. The predominant current at this time is minority carrier diffusion from the substrate. Note that for a low LET ion strike, such as a proton, the DR collapse and recovery is very fast and almost all of the charge collection occurs under the condition of a stationary DR.

Edmonds [224] presented a simple model for calculating the total charge collected under the condition of funneling. The model assumes high injection conditions with the electron density *n* very nearly equal to the hole density *h*. In addition, the ratio of electron and hole diffusion constants is equal to ratio of electron and hole mobilities as given by equation (6.31). Combining these observations with equations (6.4) to (6.7) gives the following relationships:

$$\vec{J}_{n,drift} = (m_n / m_p)\vec{J}_{p,drift} \tag{6.37}$$

$$\vec{J}_{n,diff} = -(m_n / m_p)\vec{J}_{p,diff} \tag{6.38}$$

Combining equations (6.29), (6.30), (6.37), (6.38) and (6.33) gives the total current density:

$$\vec{J}_T = (1 + m_n / m_p)\vec{J}_p + 2\vec{J}_{n,diff} \tag{6.39}$$

This is conveniently integrated over the stationary surface S representing the pre-ion hit DRB to obtain the current. As mentioned earlier, because of the lack of replacement holes from the *n*+ region, the time integrated hole current passing through S corresponds to the initial number of holes created. Using this fact and integrating equation (6.39) with respect to time gives Edmond's final model for charge collected $Q_T(t)$ at a time *t*.

$$Q_T(t) = (1 + m_n / m_p)Q_D + 2Q_{diff}(t), \quad t > t_r \qquad \text{High level injection} \qquad (6.40)$$

where $Q_{diff}(t)$ is the total collected diffusion charge at time t. The equation is valid for times greater than the DR recovery time t_r. The physical explanation for why Q_T exceeds Q_D is that both kinds of carriers contribute to the collected charge. The contribution from holes moving from the DR to the substrate is Q_D and the remainder of (4.20) is the contribution of electrons moving from the substrate to the DR. The factor of two for the diffusion component arises fundamentally from the high injection level assumption, which gives rise to an electron drift current (equal to $(m_n / m_p)Q_D + Q_{diff}(t)$) and due to the plasma column high conductivity), as well as a diffusion current. Both the electron drift and diffusion currents are in the same direction and hence add together.

The opposite assumption of low level injection conditions predicts a total current given by the sum of the hole drift current Q_D and an electron diffusion current Q_{diff}.

$$Q_T(t) = Q_D(t) + Q_{diff}(t), \qquad \text{Low level injection} \qquad (6.41)$$

Low injection conditions occur during the post DR recovery stage. In addition, a low injection strike may occur for a low LET particle, such as a proton, where equation (6.41) is always applicable.

When an ion strike misses the DR the hole drift current Q_D is zero for both low and high injection conditions. For an indirect strike, under high injection, holes diffuse into the DR to create the collapse but the same number flow back out during recovery to give a net hole flow of zero. The electron drift and diffusion currents are equal and in the same direction hence the total charge collected is simply twice the minority carrier diffusion current.

A summary of Edmonds approximate charge collection equations for a direct strike to the DR and a non-direct strike to the substrate are given in Figure 6.6. In practice, if the charge collection process begins with high injection conditions then the total charge collected is not determined strictly by equation (6.40) since low level injection conditions eventually occur in which case equation (6.41) applies. If most of the collected charge occurs when the DR is still recovering, implying high injection conditions, then equation (6.40) is a good approximation. A useful area of research would be to obtain a simple expression that merges the two regions of operation.

Charge collection simulations and device behavior specific to the microdosimeter devices will be discussed further in the device simulation section 6.2.2.

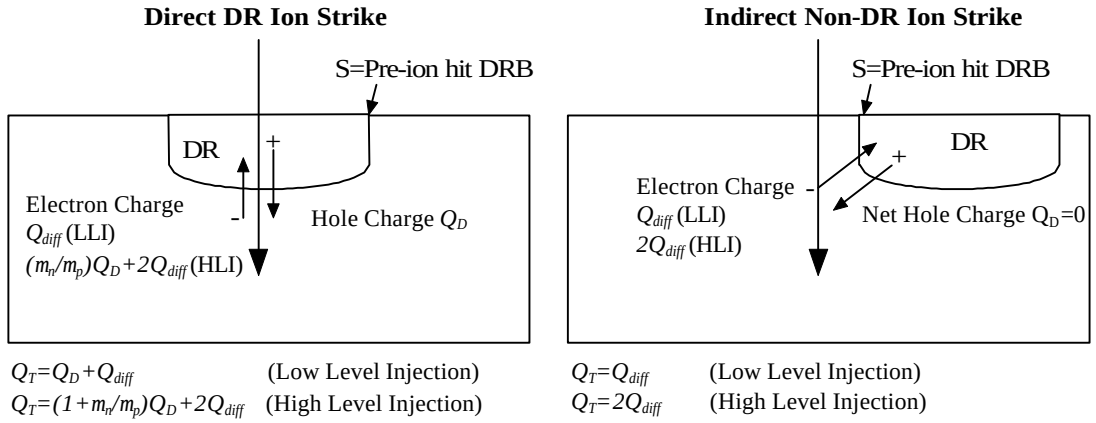


Figure 6.6. Summary of Edmonds approximate charge collection equations for a direct strike to the DR and a non-direct strike to the substrate. The equations for low (LLI) and high level injection (HLI) conditions are shown.

6.1.4 Induced Currents by Carrier Motion (Ramos theorem)

An important theorem relating to charge carrier motion in an electric field is due to Ramo [225]. Currents may be induced in electrodes prior to the arrival of any electrons and holes due to the instantaneous change in electrostatic flux lines which end on the electrode. The instantaneous current induced by a single carriers motion I is given by

$$I = qvE_v \tag{6.42}$$

where q is the carrier charge, v is the carrier velocity and E_v is the electric field component in the direction of v which would exist at the carriers position under the following circumstances: electron removed, given electrode raised to unit potential, all other conductors grounded. For the case of parallel infinite electrodes, frequently assumed in semiconductor detectors this equation becomes

$$I = qmE / d \tag{6.43}$$

where d is the electrode spacing, E is the electric field strength at the carriers position and m is the carrier mobility. Equation (6.43) may be integrated over time and over each carrier contribution to obtain the final total collected charge. For n electron hole pairs generated a distance x from the anode, the total collected charge will be nqx/d from the electron and $nq(d-x)/d$ from the holes giving at total charge collected of nq as expected assuming drift collection and no recombination.

This theorem proves useful for analyzing current profiles where charge collection occurs purely by drift. Hence it is particularly relevant for fully depleted semiconductor detectors [226] and ionization chambers (p 153 Knoll, [23]). Knoll derives a similar result based on energy conservation across a capacitor. A good example of the application of drift-diffusion equations to calculate electron density and Ramo's theorem to calculate the induced charge on an electrode is given by Toney [227].

The theorem is provided here for completeness. The complex microdosimeter charge collection includes drift and diffusion components and is more easily analyzed using semiconductor simulation methods.

6.2 Sensitive Volume Characterization

Sensitive volume characterization involves determining the proportion of generated charge which is collected (i.e. the charge collection efficiency (CE)) as a function of deposited position within the sensitive volume. To characterize the sensitive volume, three methods are employed including semiconductor device simulation, microbeam spectroscopy and broadbeam spectroscopy. These methods provide information for a spectroscopy model which is implemented in software and determines the charge collection efficiency.

6.2.1 Spectroscopy Modeling Software

To characterize the performance of a microdosimeter it is important to accurately model the statistical processes of energy deposition and measurement that lead to the spread in spectrum obtained by spectroscopy measurements. A software model was developed which incorporates source energy distribution, source angular distribution, ion energy and range straggling, overlayer variation, sensitive depth variation, system electronic noise, and the variation of collection efficiency with ion strike position. Successful comparison between the model and spectroscopy measurements implies that the collection efficiency function is well defined. Conversely, the model may also be used to extract the collection efficiency spatial function from spectroscopy data, which is particularly useful when only broadbeam data is available.

A flow diagram of the modeling process is shown in Figure 1. The software uses the SRIM [126] Monte-Carlo program to transport ions through the device. The entire process is encapsulated in a flexible Mathematica [141] framework coded to automatically run the SRIM program, generate input conditions and process output

results. The source is described by its energy spectrum and angular distribution. The angular distribution is derived from source/device geometrical considerations. The Monte-Carlo ion transport program SRIM [126] can use as input a file specifying individual ion energy and direction. This file is constructed by randomly sampling the energy and angular distributions of a user selectable number of ions (typically> 10000 ions).

Inspection of the device fabrication masks for the small diode array as provided in Appendix A identifies 5 regions of differing overlayer construction and SOI thickness. Figure 6.8 shows the cross-section associated with the various regions and the location of each region on the device. Figure 6.9, for the 10×10 μm^2, diode and Figure 6.10, for the 100×100 μm^2, diode are representations of the discrete function *Region(x,y)* which assumes values from 1 to 5 corresponding to each region. Note that the SOI thickness is only 2 μm in the n+ and p+ regions and around 1.8 μm in other areas due to consumption of silicon in the local oxidation (LOCOS) process. SRIM is run for each region to produce the SOI energy deposition spectra, *Edep(E, region)*.

The spectrum for the energy collected by the device assuming a normally incident particle at a point (x,y) is given by scaling down the deposition spectrum by the collection efficiency and

$$Ecol(E,x,y) = \frac{1}{C(x,y)} Edep\left(\frac{E}{C(x,y)}, Region(x,y) \right) \tag{6.44}$$

where *C(x,y)* is the spatially dependent collection efficiency defined as the proportion of energy collected to energy deposited for a normally incident ion traversing through the point (*x,y*). That is, the energy deposition spectrum is scaled down by the CE function with appropriate normalization (*Ecol* is a probability distribution function). Previously we mentioned that the SRIM input may consider the angular distribution of the incident ions. For simplicity, we apply equation (6.44) even for these ions. This approximation assumes a slowly varying CE and relatively small angular deviations. The CE is also assumed to be independent of depth (*z*). This is a reasonable assumption provided the diffusion length is much larger than the device depth dimensions. The CE may be estimated from microbeam experiments or device simulation.

The final energy spectrum excluding electronic noise is given by integrating equation (6.44) over the device area:

$$Etotal(E) = \int_0^{y\max} \int_0^{x\max} Ecol(E,x,y)dxdy \tag{6.45}$$

In practice equation (6.45) is calculated numerically with a spatial resolution of 0.3 μm and *ymax* and *xmax* =15 μm. The final energy spectrum including electronic noise is given by convolving *Etotal* with a Gaussian noise spectrum having a standard deviation s_n.

$$Etotaln(E) = \int_{E-3s_n}^{E+3s_n} Etotal(u)\frac{Exp\left((E-u)^2/2s_n^2\right)}{\sqrt{2p}\,s_n}du \tag{6.46}$$

Microbeam spectroscopy will produce an image which is defined by taking the median energy of equation (6.44) for each pixel. Both microbeam and broadbeam spectroscopy may produce a spectrum given by equation (6.46).

Note that the model presented thus far does not consider the statistics of the charge collection process which would increase the spread of the final spectrum. Ideally *C(x,y)* should be defined as a distribution to incorporate charge collection variability. It also does not consider diode to diode variation and non-discrete transitions between the defined regions (e.g. LOCOS "birds-beak"). Later sections will further discuss the application and limitations of the model.

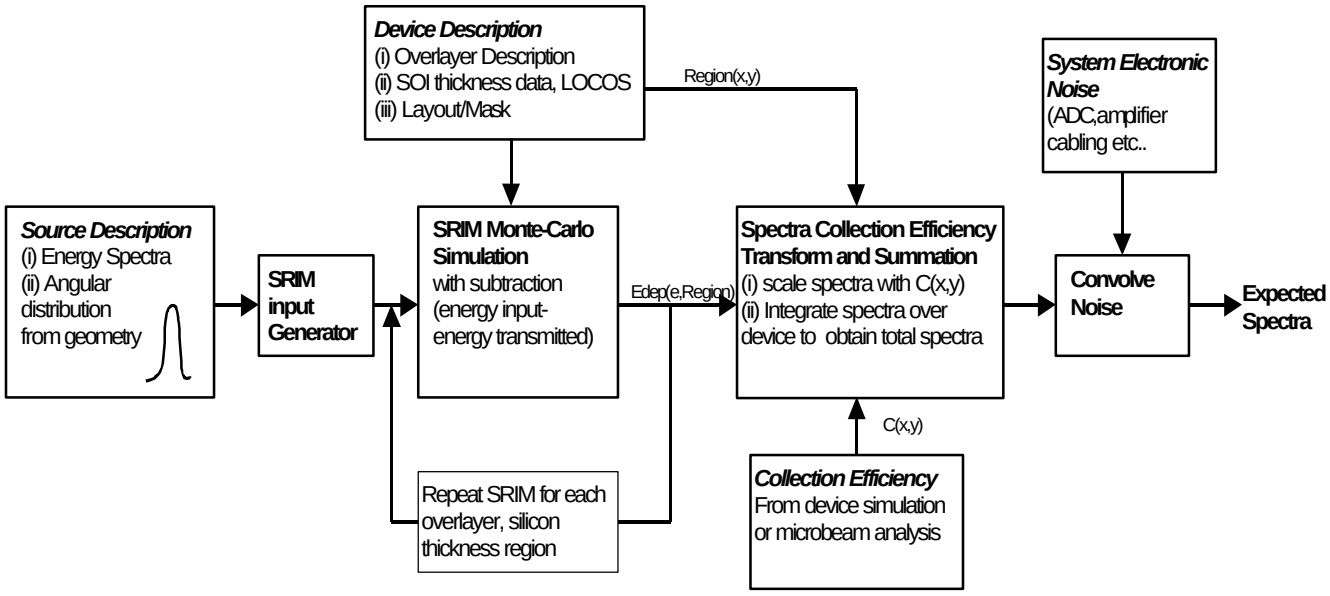


Figure 6.7. Flow diagram of spectroscopy modeling process

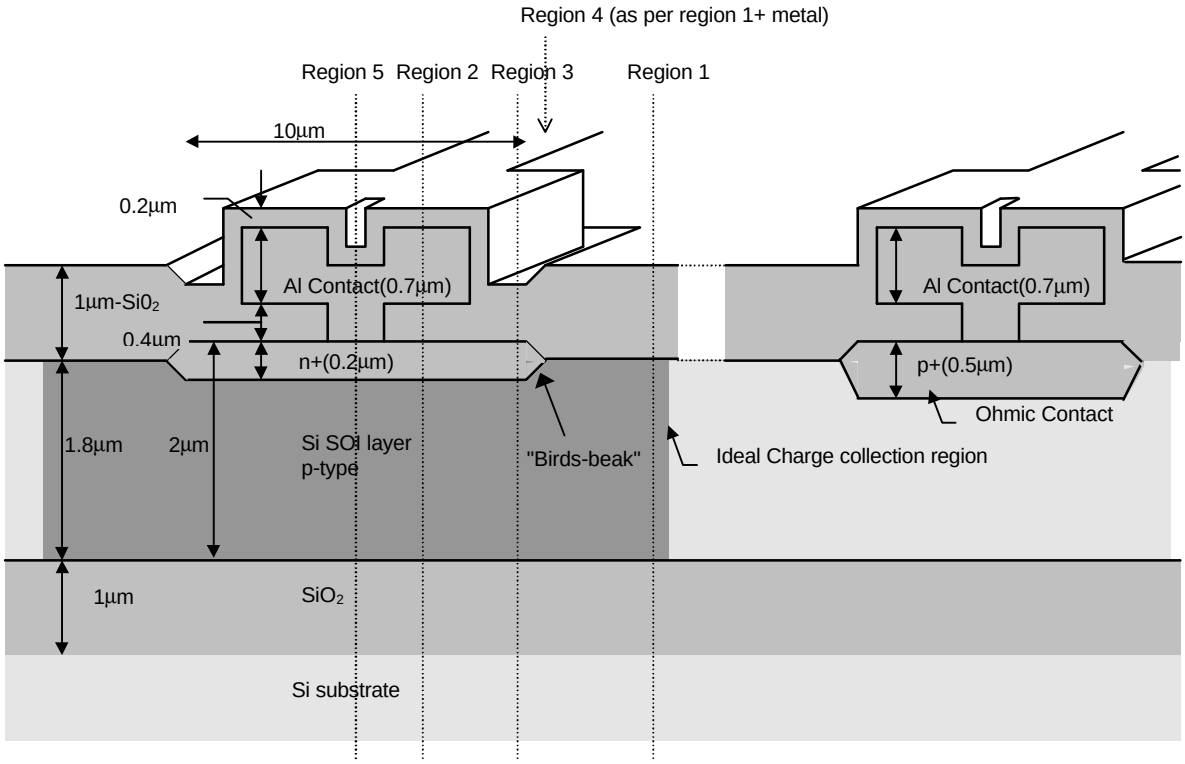


Figure 6.8. Detailed cross-section of diode array *p*+-ohmic and *n*+-junction contacts with approximate dimensions. Overlayer and SOI thickness dimensions are identified for each region shown in the plan figure below.

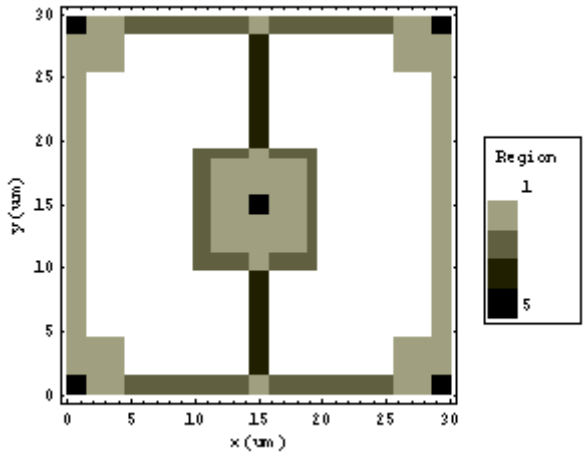


Figure 6.9. Layout of 10 × 10 µm^2 (junction area) diode cell showing location of regions whose overlayer and SOI construction is identified in Figure 6.8.

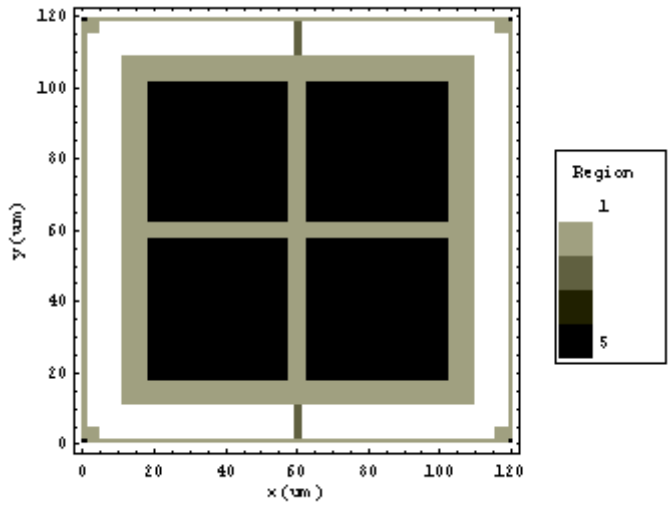


Figure 6.10. Layout of 100 × 100 μm^2 (junction area) diode cell showing location of regions whose overlayer and SOI construction is identified in Figure 6.8.

6.2.2 Numerical device simulation

Two and three dimensional numerical device simulations have been performed on the 2μm SOI, 10×10μm array using the DESSIS code [196]. The objective of the simulations was to determine the characteristics of the CE function, in particular the variation with bias and minority carrier lifetime and the effect of funneling.

6.2.2.1 Simulation Setup and Parameters

2D simulations have been predominantly used due to the lengthy computation time required for 3D simulations. For both simulation types the device simulated was constructed using a process simulator (LIGAMENT, PROSIT (3D) and TE2DIOS (2D) [196]) with manufacturer mask information and process specifications directly used as provided in Appendix A. The 2D simulation considered a cross-section, referring to Figure 6.9, along the line (0,15) to (15,15) whilst the 3D simulation considered the area with minimum coordinates (0,0) and maximum (15,15). In both cases, we exploit device symmetry to minimize the eventual simulation grid size. The cross-section of the 2×10×10 μm SOI device, constructed by the process simulator, is shown in Figure 6.11. Note the accurate formation of the LOCOS region including the characteristic "birds-beak" at each end. The top portion of the upper oxide layer was trimmed following the process simulation to reduce the simulation size.

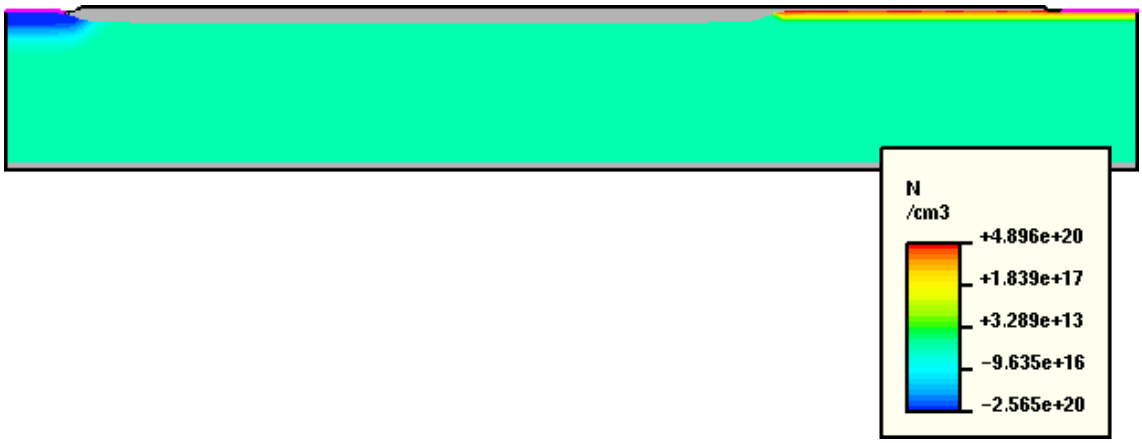


Figure 6.11. Process simulator derived 2D geometry showing doping distribution. On the scale, positive is n type and negative is p type doping. Oxide region is colored gray.

The DESSIS code incorporates drift-diffusion, hydrodynamic and thermodynamic models. In our case we neglect self-heating effects and use the drift-diffusion model. This model solves the transient semiconductor equations comprising the Poisson equation and the current continuity equations as described in section 6.1.1.4. Current density is expressed by the conventional drift-diffusion constitutive relations again provided in section 6.1.1.4. The numerical method employed to solve the boundary value problem involves a spatial discretization of the partial differential equations using the box method [228]. The discretized non-linear equations are solved using a fully coupled Newton method developed by Bank and Rose [196, 228].

The physics included in the simulation setup included doping dependent Shockley-Read-Hall (SRH) recombination, Auger recombination, and trap-assisted Auger recombination. Surface recombination at oxide interfaces above and below the SOI layer were included in the model. Surface recombination velocity was set to a typical value of 5000 cm^2/s, from Schroder [199]. The field dependence model for recombination was not employed since the maximum electric field was less then 3×10^5 V/cm. The intrinsic density model used was the Bennett-Wilson model with bandgap narrowing [229]. Deviations from Boltzmann statistics due to degeneracies at high doping concentrations are treated by replacing the intrinsic concentration by an effective intrinsic concentration determined by the Bennett-Wilson bandgap narrowing model. A doping and field dependent (Caughey Thomas, equation (6.3)) mobility model was used. Carrier-carrier scattering models were not included in the simulations to save simulation time. The ramifications of this exclusion are discussed in later sections.

The ions modeled were a 5.3 MeV alpha particle corresponding to a Polonium-210 alpha spectroscopy source and a 2 MeV proton typical of microbeam sources. A varying LET along the length of the path was used based on an accurate fit to SRIM [126] calculations over the 2 μm SOI region. The radial distribution of charge generation used a Gaussian model with a standard deviation radius of r_o = 100 nm. As seen from Figure 6.2 and Figure 6.3, the same radial profile exists for the 2 MeV proton as for the 5 MeV alpha and thus the standard deviation radius remains unchanged between these ions types. The ion strike was modeled as Gaussian in time with a characteristic decay time of 20 fs. The decay time of 20 fs is reasonable given that the maximum delta electron energy is 2.6 keV with a typical range of 135 μm for a 5 MeV alpha strike. If we assume the delta electron travels twice this distance due to scattering and that a linear range-energy relationship applies then the electron travel time is close to 20 fs.

These ion track parameters are consistent with previous simulations in the literature [222]. Note that literature estimates of track radius may sometimes quote the effective radius (radius at which carrier density corresponds to doping density) rather than a model parameter. It is important to consider the radial distribution in some detail, since the initial charge density may affect recombination rates. The gaussian radial distribution model is the only one available in DESSIS.

$$Q(r) = Q_0 e^{-\frac{r^2}{2r_0^2}} \tag{6.47}$$

Unfortunately, the gaussian profile is a poor fit to the Katz model described in section 6.1.2. The best gaussian fit to the Katz model occurs for r_o = 2.25 nm compared with the typical simulation value of 100 nm. The various track structure models are compared in Figure 6.12. A significantly better fit is a power-law relationship such as:

$$Q(r) = Q_0\left[1+\frac{r}{r_0}\right]^{-n} \quad \text{r} < 135\text{nm(max delta)} \tag{6.48}$$

where n = 2.6, r_o = 0.35 nm, $Q_o = 5 \times 10^{22}$ eh/cm^3 for a 5 MeV alpha particle. Dussault [230] has studied the effect of track structure variations on simulation results and found a less than 8% difference in collected charge and current transient between the gaussian model and the power law model. A 100 MeV Fe ion was used with 100 nm standard

deviation radius track incident on a *p+/n* bulk diode. This ion has a similar profile to the alpha and proton under consideration but with a much higher LET. In terms of funneling behavior, the *p+/n* diode with a high LET ion will behave like a *n+/p* diode with a lower LET, so we may expect Dussault's results to be broadly applicable to our case.

Note that the large gaussian radius of r_o = 100 nm used in the simulations severely underestimates the center track density and simulations may then underestimate Auger recombination. However, the time scale for ambipolar diffusion to attain the densities given by the 100 nm gaussian model (5.9×10^{17} cm^{-3}) is only about 20 ps as given by equation (6.36) and Figure 6.5 so the recombination error is not expected to be significant. Moreover, the process of ambipolar diffusion will tend to reshape the track towards a gaussian profile within this time frame.

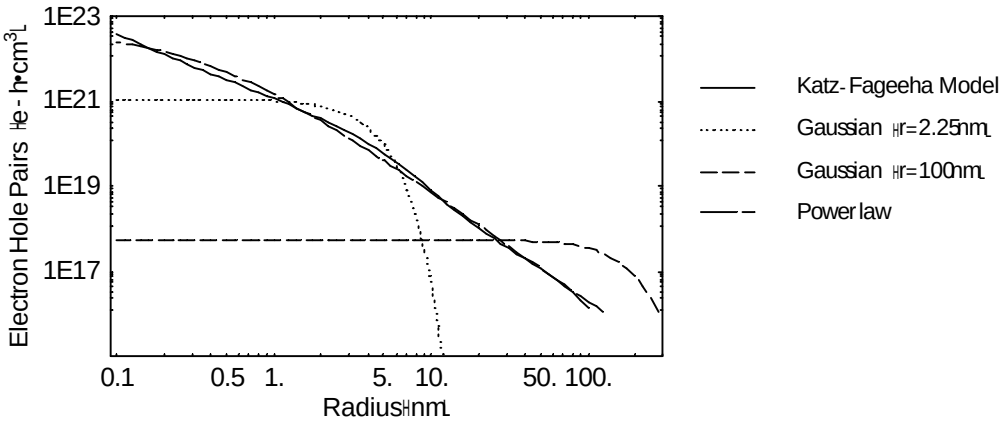


Figure 6.12. The Katz-Fageeha model for 5 MeV alpha track density compared to the Gaussian model used by DESSIS (with r=2.25nm (best fit), r=100nm (typical simulation)) and also compared to a power law relationship (with n=2.6, r_o=0.35 nm, Q_o=5 $\times 10^{22}$ eh/cm^3) . The gaussian is a poor fit whilst the power law is a good approximation to the Katz model.

Of critical importance in numerical device simulation is the use of correct spatial and transient discretization. The grid resolution was refined in the depletion, doping, and alpha particle track regions. Typically, 2000 and 20000 nodes (or vertices) were used for 2D and 3D simulations, respectively. An example 3D grid is shown in Figure 6.21. Time discretization is equally important and the time step was controlled so that at early periods in the simulation the maximum allowable step was very small, 5 fs at 100 fs, which progressively increased exponentially to 1ns at 10ns. To confirm that sufficient resolution was achieved all simulations have been run without recombination to ensure charge conservation is observed. In all cases, the total charge collected is within 2% of

charge deposited for 2D and 5% for 3D simulations. If the charge conservation conditions are not met then insufficient discretization is almost always the reason.

Note however, that one should avoid excessive discretization if possible because the simulation time varies according to $O(n^a)$ where n is the number of nodes and a is between 1.5 and 2 [223]. The 2D simulations with 2000 nodes typically take less than 30 minutes whilst the 3D simulations with 20000 nodes take over 24 hrs running on a DEC alpha processor with 1 GByte memory. Currently, a reasonable limit for such a system is 50000 nodes.

6.2.2.2 Collection Efficiency Simulations

2D simulations were performed every 0.75 μm along the line (0,15) to (15,15) (referring to Figure 6.9), from the $p+$ to the $n+$ region. A 5.3 MeV alpha particle strike was modeled for each of the 21 simulations. Two different minority carrier lifetimes, corresponding to a normal device and a radiation damaged device, were simulated along with two sets of voltages (0 and 10 V). The lifetimes were calculated from proton microbeam measurements, described later in section 6.3.2. The substrate doping density for the undamaged device is 1.5×10^{15} cm^{-3} whilst the radiation damaged device has a lower doping density of 1×10^{15} cm^{-3}. In addition, the maximum mobility was adjusted to account for radiation damage effects as discussed in section 6.3.2.

The CE was calculated for each point with the results shown in Figure 6.32. Charge collection efficiency approaches 100% in the depletion region since drift collection is strong for an unirradiated device. As we move away from the depletion region a transition region occurs in which a combination of funneling and diffusion takes place. In this region, the charge carriers diffuse into the depletion region with a sufficient carrier density to cause depletion region collapse. The lateral funnel effect, confirmed by simulation voltage distribution plots, has been reported previously by Edmonds [218, 219]. Eventually we reach a point at which only diffusion occurs and the efficiency decays exponentially with a constant that is related to the effective recombination time, which depends on both surface and bulk recombination. The diffusion length is long relative to the device dimensions so the exponential decay is approximately linear as shown in Figure 6.32. However, simulations were performed with shorter lifetimes that confirmed the exponential drop in CE. The onset of funneling corresponds to the transition point between the exponential decay and the constant high CE as we move

toward the junction. For example, x = 6 μm in Figure 6.32 for the 10V unirradiated device.

The point at which funneling disappears is easily identified by observing the simulation current transients as plotted in Figure 6.13 for the undamaged device. As the strike moves closer to the depletion region (increasing x) from the p+ contact, the collection time decreases since the diffusion distance is less. A larger current provides for a larger collected charge despite the shorter collection time. For x ≥ 6 μm, the trailing edge of the current transient exhibits a "kink" corresponding to the reformation of a collapsed depletion region. Funneling begins much more rapidly for strikes (x ≥ 8 μm) to the depletion region since no preceding diffusion process is required. All of these strikes have high currents at times early in the transient (<1-10 ps) due to fast drift collection.

Interestingly, the fastest collection time occurs for an ion strike, x = 9 μm, through the depletion region at a point were the pre-strike electric field is orientated radially to the ion strike. Both drift and diffusion currents flow radially towards the junction; a direction that minimizes recombination, decreases collection time and enhances the reformation of the collapsed DR. In contrast, the drift flow is longitudinal and the diffusion flow radial for an ion strike at the center of the junction x = 15 μm. Thus, designing the detector with the electric field orientated perpendicular to the most typical ion direction will maximize CE.

A more detailed examination of the lateral funneling behavior was performed by considering an ion strike at x = 7.5 μm. Hole and electron density distributions along with potential distributions were generated for various simulation times as shown in Figure 6.15, Figure 6.16 and Figure 6.17, respectively. The times selected were t = 0, 1 ps, 100 ps, 500 ps, 1 ns and 2 ns as identified for reference on the corresponding current transient plot shown in Figure 6.14. The DR collapse associated with funneling is most clearly recognized by consideration of the hole density distribution. The pre-strike DRB denoted by S is distinctly demarcated by the sharp transition in hole density from the substrate doping concentration to the extremely low values of the DR. For the first picosecond, little charge collection occurs as ambipolar diffusion spreads the high injection plasma track. However, after a period of tens of picoseconds, sufficient carriers have diffused into the pre-strike DR to shield previously uncompensated acceptor impurities and generate DR collapse as described in 6.1.3. (Note that the

surface S is only about 0.8 μm from the ion strike and one may use equation (6.36) to determine the approximate diffusion time). The quasineutral region electric field, characteristic of funneling, is clearly evident in the voltage distribution plots for times greater than 100 ps (but less than 2 ns). The maximum collapse of the DRB (1.2 μm) occurs at 500 ps as given by the hole density distributions. Shortly after 1 ns the reformation of the DRB begins when the opposing hole diffusion current from the quasi-neutral region has dropped, electric fields are restored and low level injection conditions begin to apply. Almost all of the charge collection occurs during the funneling process. The CE plot (= $Q(t)/Q_{deposited}$) of Figure 6.14 indicates that only 10% of charge is collected after 1 ns so post funneling diffusion is minimal.

Finally, one should mention an interesting effect not previously seen in the literature that appears in the voltage distribution plots. The potential drops to -4.8 V in the potential distribution at 1 ps. During ambipolar diffusion quasineutrality is not perfect which means that the electron density may still deviate from the hole density by small amounts [217]. At high carrier concentrations, this is sufficient to generate electrostatic fields and the unusual potential effect seen in this simulation. The effect disappears as the plasma density drops.

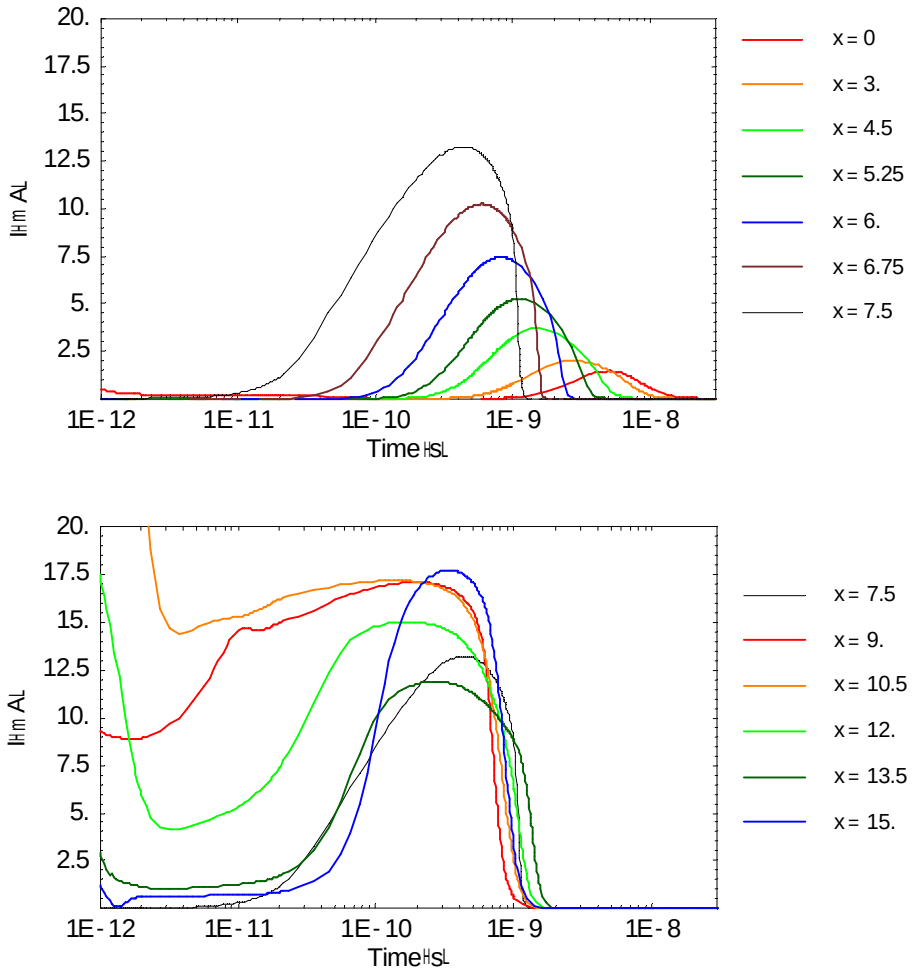


Figure 6.13. 2D simulation: Current Transient generated by a 5.3 MeV alpha particle traversing the 2D geometry given by Figure 6.11 at various distances x from the p+ contact edge of the simulation. Diffusion dominates from x=0 to 6-6.75 um. For x>6.75-15 funneling charge collection is present.

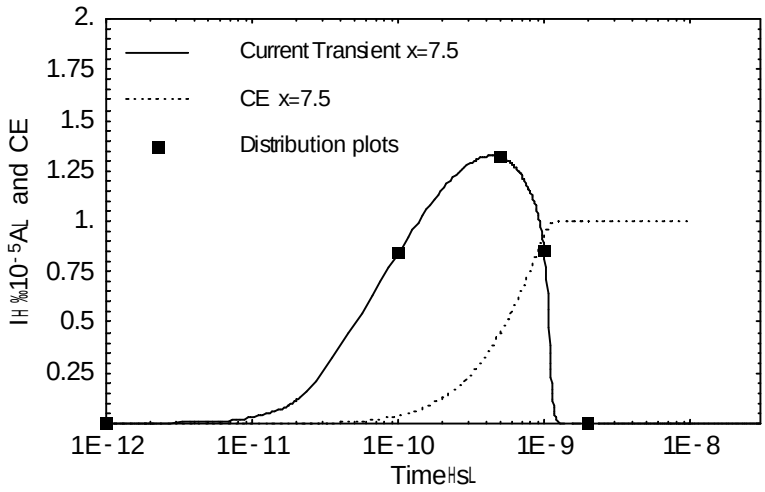


Figure 6.14. Current Transient at x=7.5 µm (conditions as for Figure 6.13) showing the points at which distribution plots have been made as shown in Figure 6.15, Figure 6.16 and Figure 6.17. Also shown is the collection efficiency CE as a function of time.

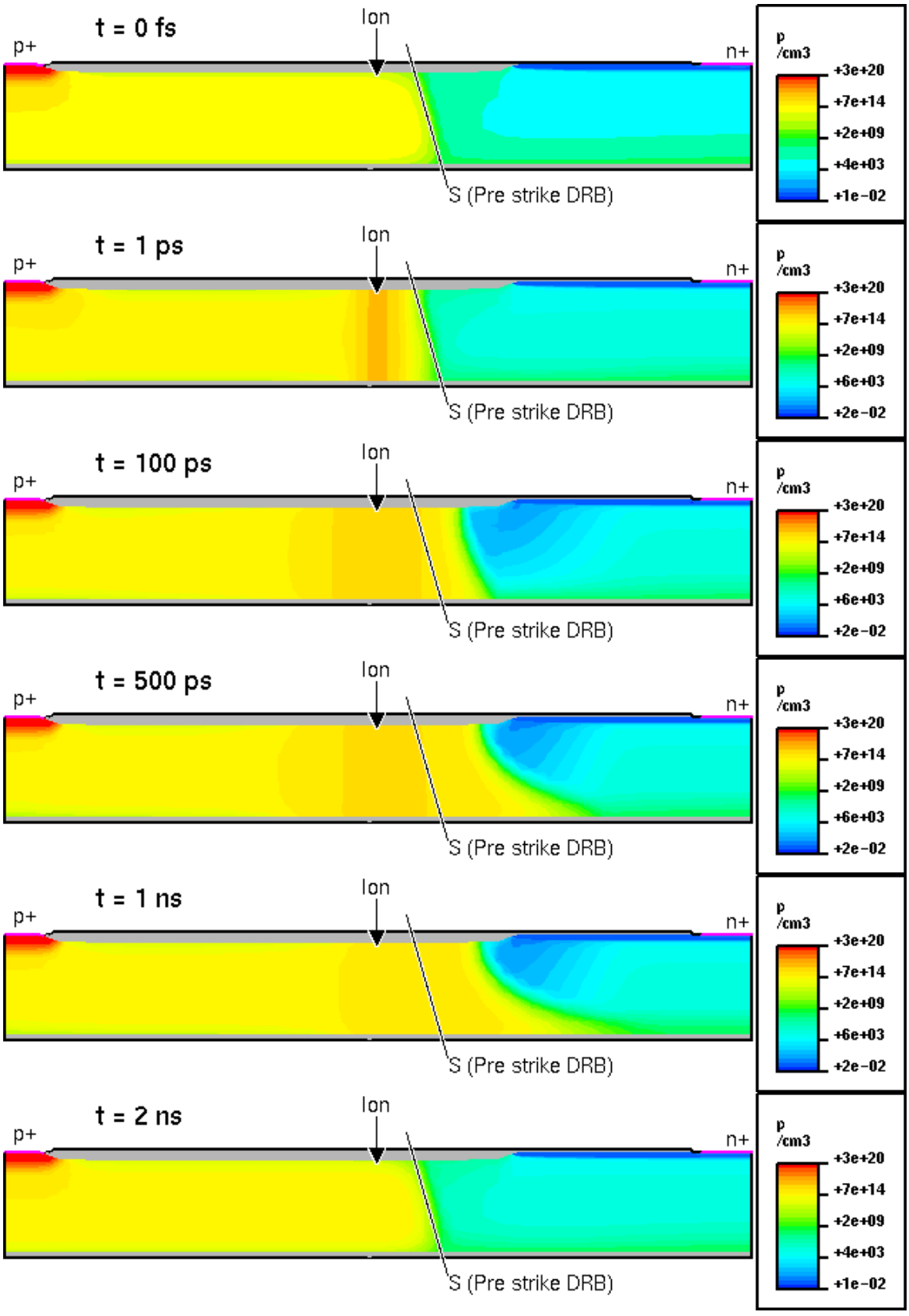


Figure 6.15. Hole density distribution for a 2D 5.3 MeV alpha particle transient simulation. Diode is the 10 × 10 µm junction size on 2 µm SOI substrate. The boundary denoted by S is the pre-ion strike (0 fs) depletion region boundary defined by the sharp transition in hole density.

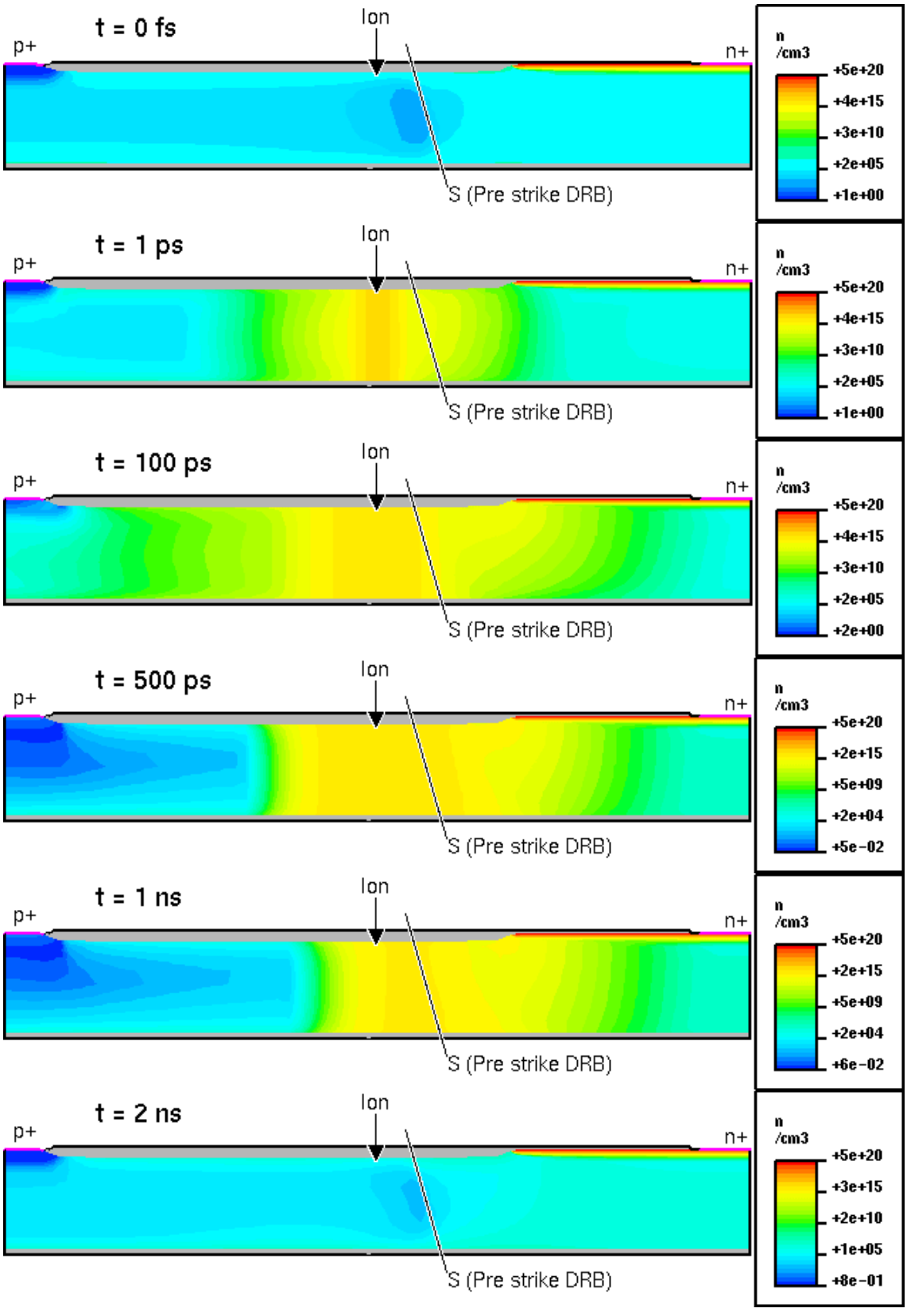


Figure 6.16. Electron distribution for a 2D 5.3 MeV alpha particle transient simulation. Diode is the 10 × 10 µm junction size on 2 µm SOI substrate. The boundary denoted by S is the pre-ion strike depletion region boundary defined by the hole density distribution (see Figure 6.15).

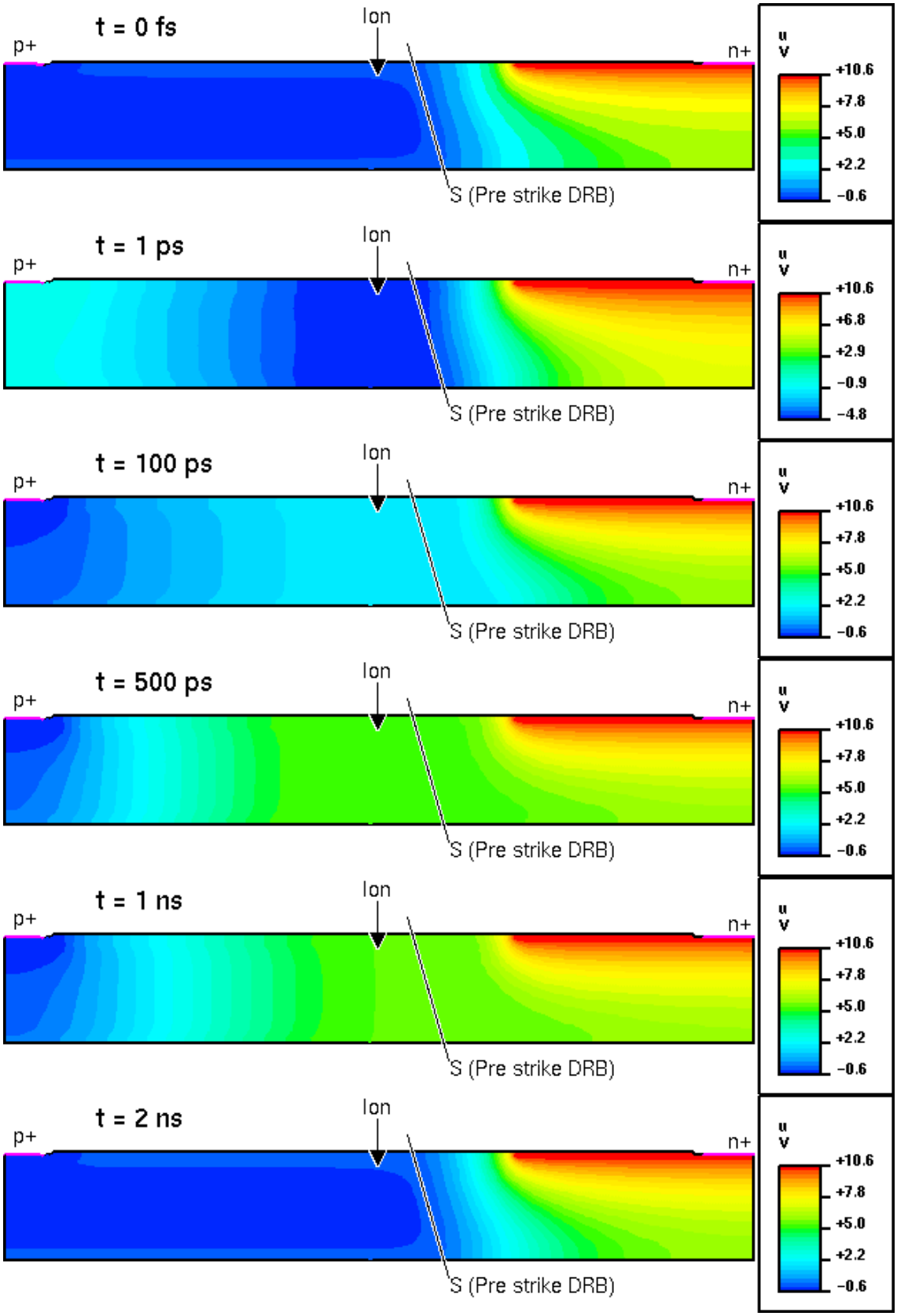


Figure 6.17. Potential distribution for a 2D 5.3 MeV alpha particle transient simulation. Diode is the 10 × 10 μm junction size on 2 μm SOI substrate. The boundary denoted by S is the pre-ion strike depletion region boundary defined by the hole density distribution (see Figure 6.15). Note that the potential includes built in voltage and contact potentials, hence a range >10 V.

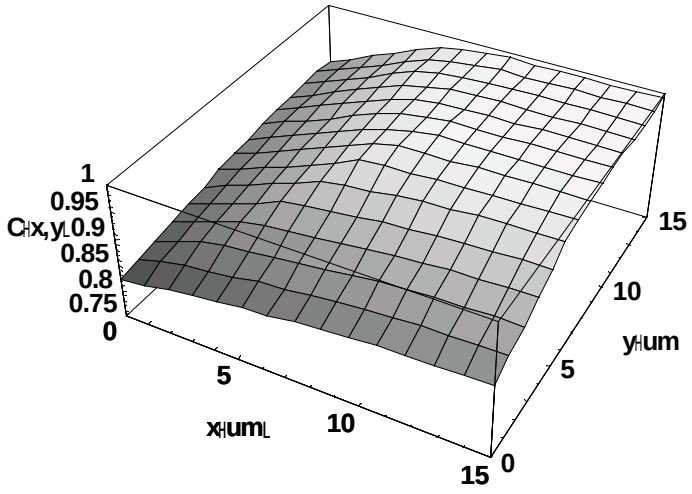


Figure 6.18. An example collection efficiency function with the parameters (L=55, (x_f, c_f) = (5,0.97) and (x_d, c_d) =(9,0.99)) derived from 5.3 MeV alpha broadbeam measurements of section 6.2.4.1. One quarter of the diode is shown with coordinates corresponding to the layout of Figure 6.9.

Following these results, the CE is modeled by a 3-parameter function. As shown in the equation below, three regions are defined: a constant region corresponding to the depletion region, an exponential region characterized by a parameter L, and a transition region between these two regions, which is defined by a quadratic. The parameters defining the boundaries of the transition region are (x_f, c_f) and (x_d, c_d). The derivative of the transition function is zero at the depletion region boundary x_d.

$$C_{2D}(x) = \begin{cases} c_f e^{(x-x_f)/L} & 0 \le x < x_f \\ a_2 x^2 + a_1 x + a_0 & x_f \le x < x_d \\ c_d & x_d \le x < 15 \end{cases} \qquad (6.49)$$

$$\text{where } a_2 = \frac{c_f - c_d}{(x_d - x_f)^2},\ a_1 = -2x_d a_2,\ a_0 = \frac{c_f x_d^2 + c_d x_f^2 - 2x_d x_f c_d}{(x_d - x_f)^2}$$

$$C_{3D}(x,y) = C_{2D}(10) = c_d \quad \begin{matrix} 10 \le x \le 15 \\ 10 \le y \le 15 \\ c_d > 10 \end{matrix} \qquad (6.50)$$

$$C_{2D}(10 - d1) \quad \textit{else where}$$

where *d1* = the distance from (*x*,*y*) to (*x1*,*y1*) with (*x1*,*y1*) defined as the intercept of a line drawn from (*x*,*y*) to the center of the *n*+ region (15,15). The 2D function is used to approximate the 3D function by effectively rotating the 2D function around the center of the diode (15,15) whilst observing a constant value of c_d within the *n*+ region. Note that the parameter L is not the diffusion length (L_d) although it may be closely related. An example 3D CE function is shown in Figure 6.18.

It is important to point out that the 3D CE may decay faster then an exponential and that the function presented above is a first order approximation. In order to determine the extent of this geometrical error a 3D simulation was performed at the point (3.5,15) for the unirradiated device at 10V bias. At this point, the ratio of 3D to 2D CE was only 0.93 indicating that the above equation may be a reasonable first order approximation. The voltage distribution and electron density at 100 ps following this strike are shown in Figure 6.19 and Figure 6.20. Note that the SOI is fully depleted at this bias level and funneling is not evident. Additional 3D simulations would be useful in order to calculate an improved CE function, although these are extremely time consuming. The comparison of simulation results with experimental results is discussed further in sections 6.2.3 and 6.2.4.

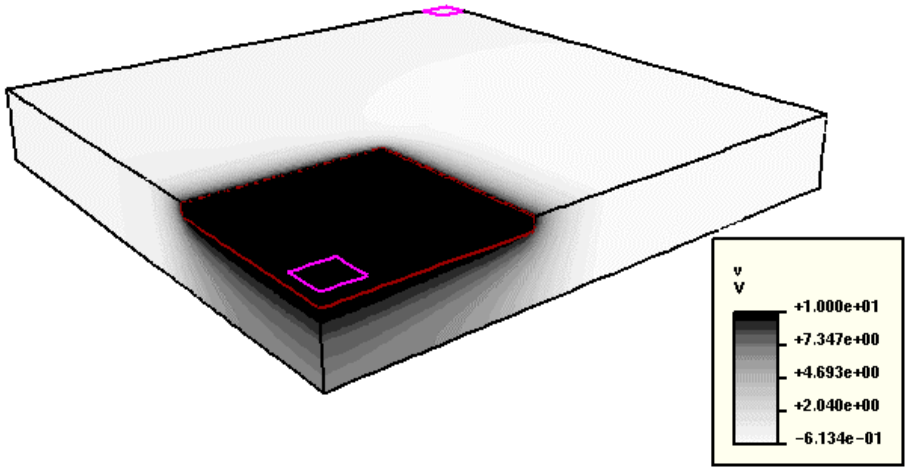


Figure 6.19. Voltage distribution for 2um SOI device, 100ps after 5.3MeV alpha strike at x=3.5,y=15um. (1/4 of device is shown, 15×15×2µm, center of diode is nearest to viewpoint).

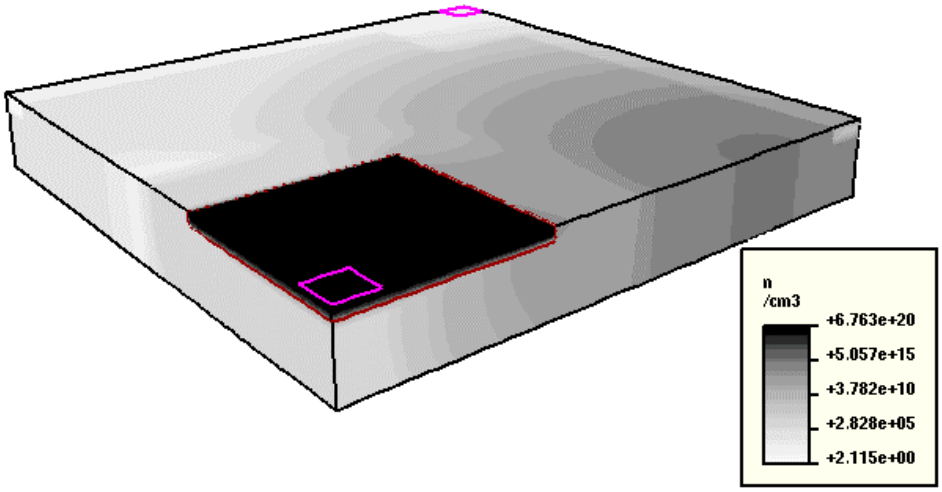


Figure 6.20. Electron density for 2um SOI device, 100ps after 5.3MeV alpha strike at x=3.5,y=15um. (1/4 of device is shown, 15×15×2µm, center of diode is nearest to viewpoint).

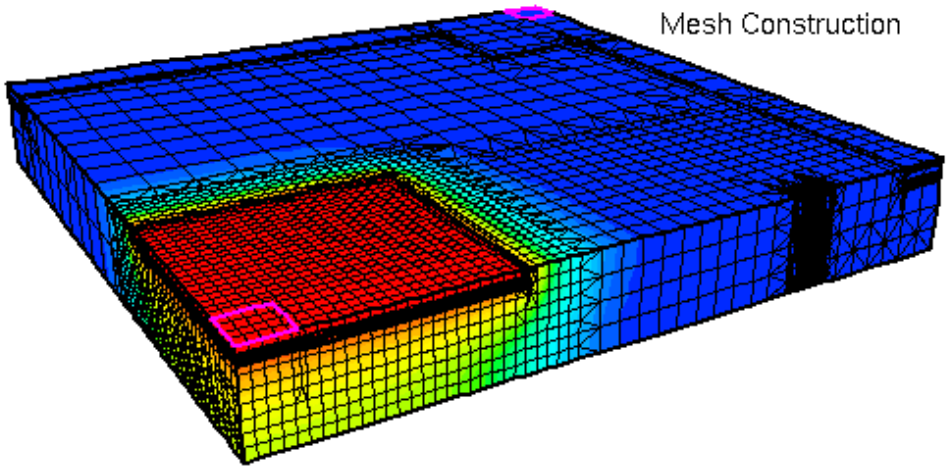


Figure 6.21. Mesh construction used for the 3D simulation of a 5.3MeV alpha strike at x=3.5,y=15um. with voltage distribution also shown. 20000 vertices are required with refinement in high doping, depletion region and alpha strike region.

6.2.2.3 Comparison of alpha and proton funneling in the 100 × 100 μm^2 bulk diode.

Later calculations of minority carrier lifetime given in section 6.3.2 use a model that assumes negligible funneling and charge collection dominated by diffusion. The model uses data from experiments performed on the 100 × 100 μm^2 bulk diode using a 1-3 MeV proton microbeam. Protons have a lower LET and are expected to produce smaller degrees of funneling then the higher LET alpha. The aim of this section is to check the assumption that funneling is negligible for a proton strike to the junction center of the 100 × 100 μm^2 bulk diode. A comparison with a 5.3 MeV alpha strike is also provided.

The 2D simulation considered a cross-section of the 100 × 100 μm^2, referring to Figure 6.10, along the line (0,60) to (60,60). The thickness of the bulk device was taken to be 300 μm. The ion strike was along the right edge of the simulation region. The current transients associated with the ion strikes are compared in Figure 6.22. The voltage potential and electron density distributions at 1 ps and 1 ns are shown in Figure 6.23 and Figure 6.24 for the proton and alpha, respectively. The electron distributions are useful for indicating the track size and injection levels. The injection levels at the center of the alpha track are an order of magnitude higher than the proton and the total charged deposited is 2.65 times higher. The proton voltage distribution shows a small funnel formation at 1 ps which is quickly restored and not evident at 1 ns. This contrasts markedly with the alpha voltage distributions that show classical funnel shaped equipotentials at 1 ps and significant depletion voltage collapse across the entire substrate by 1 ns.

The current transient response of Figure 6.22 shows an early peak at around 3 ps. This behavior has been previously noted by Dussault [230]. During the first few picoseconds the funnel collapse process is occurring; holes are beginning to screen negative acceptor ions in the depletion region and electrons are moving upwards predominantly via drift. The depletion region electric field still exists to some extent to assist charge collection. The depletion region collapse, formation of funnel-like equipotentials and movement of the potential distribution into the substrate occur in the first few picoseconds (see Figure 6.24 at t = 1 ps). Once the depletion region is completely collapsed then the collection current drops since drift is temporarily suspended. This accounts for the drop in current after 3 ps for the alpha transient of Figure 6.22.

The charge collection time for the proton is shorter than for the alpha even though the proton track is longer and minority carrier diffusion is the dominant charge collection process for the proton. Again, the earlier description of charge collection processes (6.1.3) provides an explanation for this behavior. The DR recovery is slow for the alpha strike due to the strong hole diffusion current from the long track opposing the downward flow of holes (shielding acceptor ions) necessary for depletion region recovery.

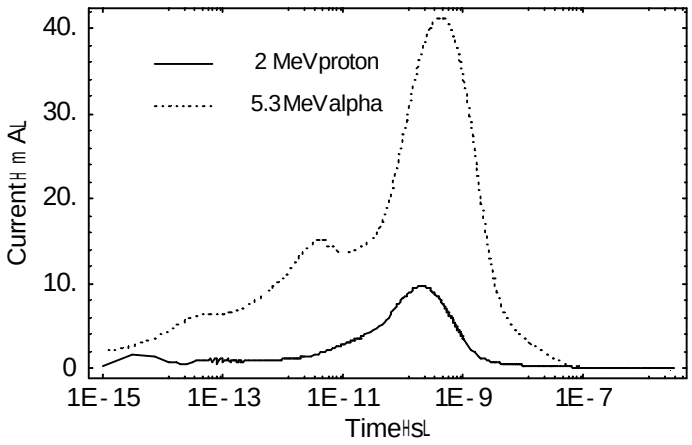
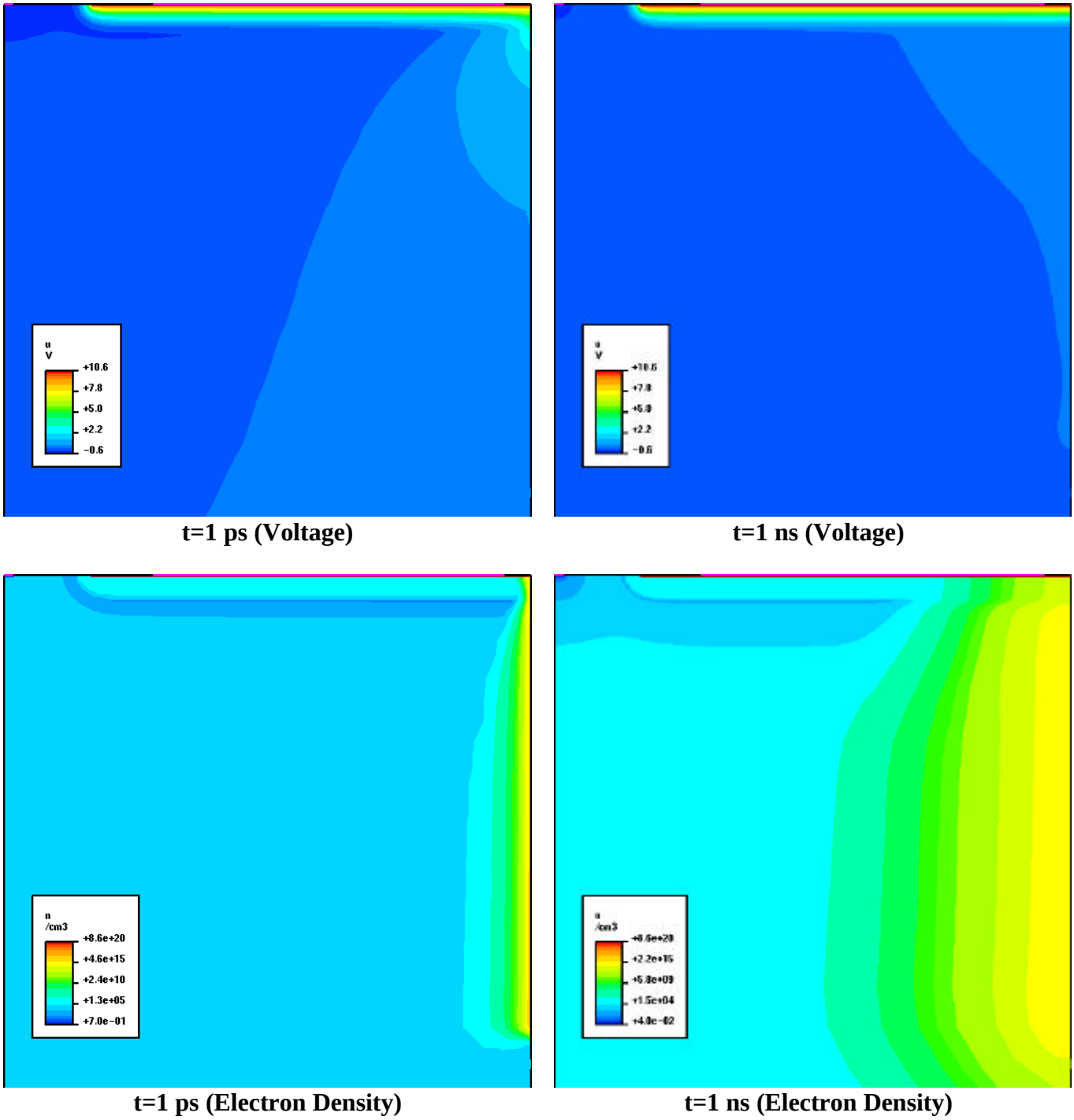


Figure 6.22. Comparison of current transient generated by 2 MeV proton and 5.3 MeV alpha particles. Device simulated was the 100 × 100 μm^2 bulk diode biased at 10 V with the ion incident on the junction center. The alpha current transient shows signs of funneling not evident in the proton response (such as the peak at 3 ps).

Proton Strike

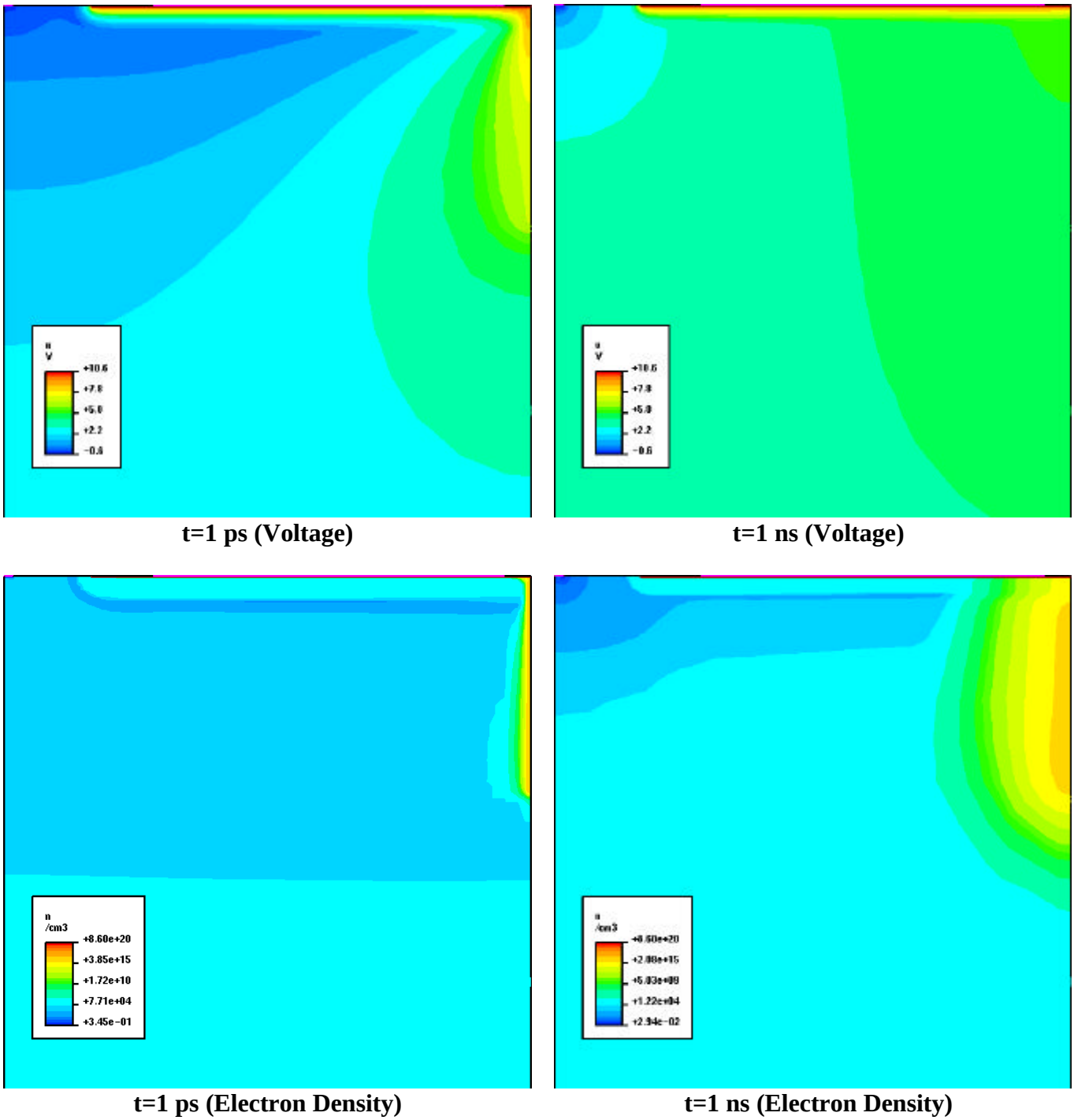


t=1 ps (Voltage) **t=1 ns (Voltage)**

t=1 ps (Electron Density) **t=1 ns (Electron Density)**

Figure 6.23. Transient 2D simulation of 2 MeV proton strike at center of 100 × 100 μm^2 (junction size) diode cell on bulk device. Strike is at (x=60, y=60) referring to Figure 6.10. The reverse bias is 10V. Each image is 60 μm wide and 58 μm deep although the actual simulation was performed on a 60 × 300 μm^2 section. Use of reflective boundary conditions are used so that only half the diode cell needs to be simulated. Two different time snapshots are displayed; 1 ps (left side) and 1 ns (right side) after the proton strike. Voltage distribution is displayed in the upper images whilst electron density is displayed in the lower images.

Alpha Strike



t=1 ps (Voltage) **t=1 ns (Voltage)**

t=1 ps (Electron Density) **t=1 ns (Electron Density)**

Figure 6.24. Transient 2D simulation of 5.3 MeV alpha strike at center of 100 × 100 μm^2 (junction size) diode cell on bulk device. Ion track is on the right edge. The reverse bias is 10V. Each image is 60 μm wide and 58 μm deep although the actual simulation was performed on a 60 × 300 μm^2 section. Use of reflective boundary conditions are used so that only half the diode cell needs to be simulated. Two different time snapshots are displayed; 1 ps (left side) and 1 ns (right side) after the alpha strike. Voltage distribution is displayed in the upper images whilst electron density is displayed in the lower images.

6.2.2.4 Simulation of angled BNCT alpha generated strike

The aim of this simulation is twofold; firstly to check that the CE function is independent of depth and secondly to model a typical BNCT generated alpha particle. Chapter 7 discusses in detail BNCT. A typical reaction product is a 1.75 MeV alpha particle emanating from the p+ region of the device with its high boron content. An angle of 80 degrees is assumed for this simulation although the emission is isotropic.

The CE has thus far been treated by considering normally incident ions and the CE function is assumed to be independent of depth. This assumption may be verified by simulating an angled strike. The total charge collected for the angled strike Q_{asim} is compared with the expected value Q_{est} (in fC) based on integrating the normally derived CE function over the ion range. That is calculate:

$$Q_{est} = \frac{1}{K}\left(\int_0^R \frac{dE}{dx_1} C_{2D}(x_1 Cos(q)) dx_1 \right) \tag{6.51}$$

where $C_{2D}(x)$ is the 2D simulation CE function using normally incident ions (quadratic interpolation of data from Figure 6.31 was used), x_1 is the distance along the ion track dE/dx is the ion LET as used by DESSIS, q is the ion angle and K is the conversion from keV to pC = 22.5 keV/fC.

The simulation was setup as per previous simulations discussed in section 6.2.2.1 except for the energy and angle of the alpha. The starting point for the track was 0.3 μm to minimize contact with the p+ electrode. Note that one should avoid placing ion tracks too close to electrodes in device simulations because the boundary conditions at the electrode are not good physical models for very high injection conditions (assumes local thermal equilibrium which implies quasi-Fermi potentials equal to the Fermi potential).

The estimated value from the ion strike was Q_{est} = 69.2 fC or 89% CE compared to the angle simulation value of Q_{asim} = 67.8 fC or 87%. This excellent correspondence of within 2% indicates that CE with no depth dependence is a reasonable approximation for the 2 μm SOI device. For thicker devices, with dimensions approaching the diffusion length, the approximation is not expected to be valid as CE will decrease with depth.

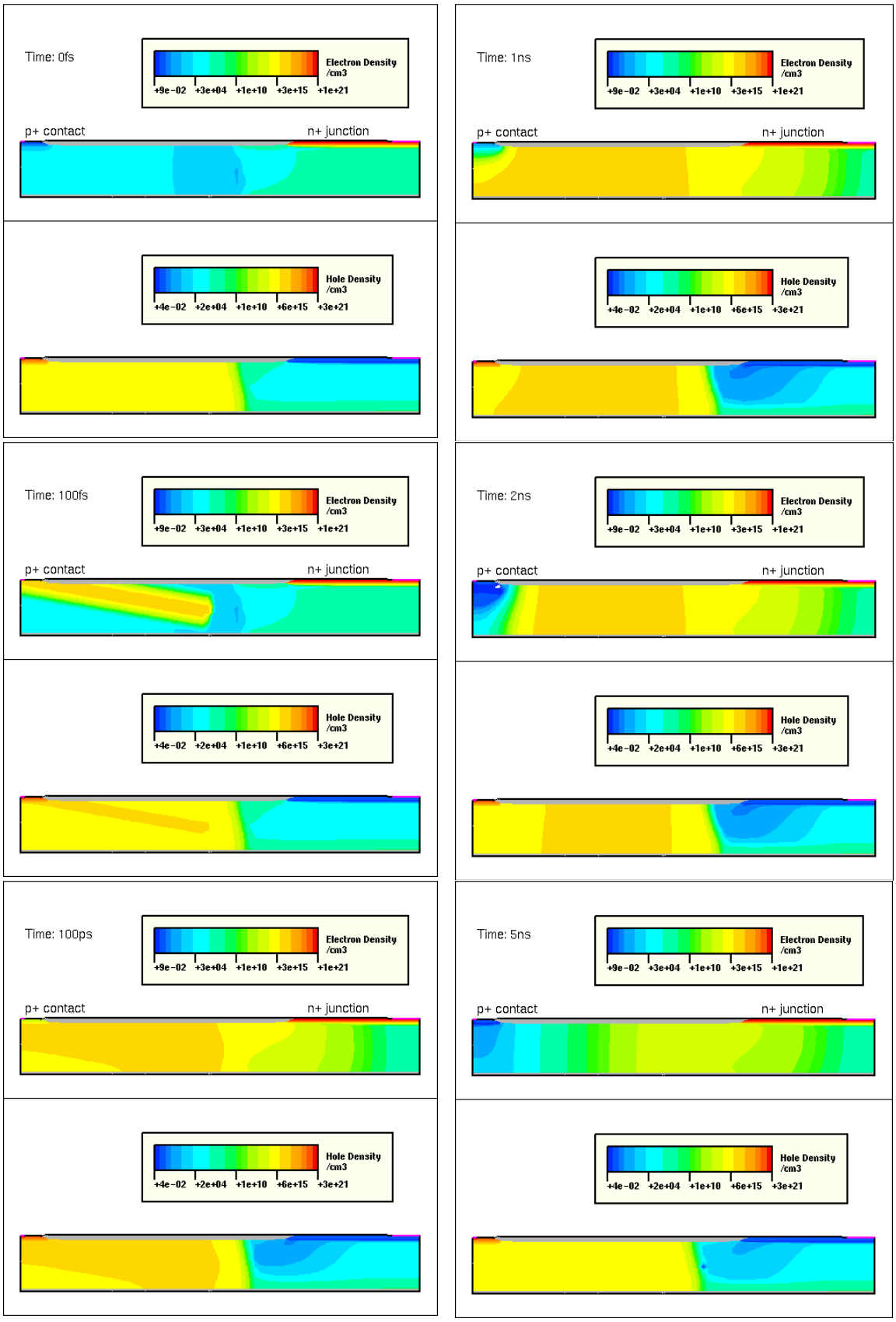


Figure 6.25. 2D simulation of an angled 1750 keV alpha particle originating from the p+ contact. Device is the 10×10 × 2 μm^2 SOI diode. Electron and hole densities are shown for various. This models the recoiling alpha from a thermal neutron capture reaction with boron. See University of Wollongong web-site for dynamic GIF animation [231].

Carrier density distributions resulting from the angle simulation at various times are shown in Figure 6.25. Ambipolar diffusion proceeds until sufficient carries have diffused into the junction to create DR collapse. The collapse is not as complete as for the previously described normally incident strike at x = 7.5 μm since the carrier diffusion is not as rapid and large.

6.2.3 Microbeam Spectroscopy

Microbeam spectroscopy (or Ion Beam Induced Charge (IBIC)) experiments were carried out using the NEC 5U Pelletron accelerator at the Microanalytical Research Centre, University of Melbourne, Australia [232, 233]. IBIC was performed on the unirradiated diodes with H, H_2 and He ion beams. A schematic of the facility is shown in Figure 6.26. The beam was initially focussed to a micron spot size on the target and was further reduced to submicron by reducing the diameter of both the object and collimator diaphragms. The adjustment and beam alignment process was carried out on a reflective region neighboring the diode array to avoid radiation damage to the device. The focussed beam was rastered across the array and the IBIC signals were individually amplified, digitized, and stored along with beam coordinate data.

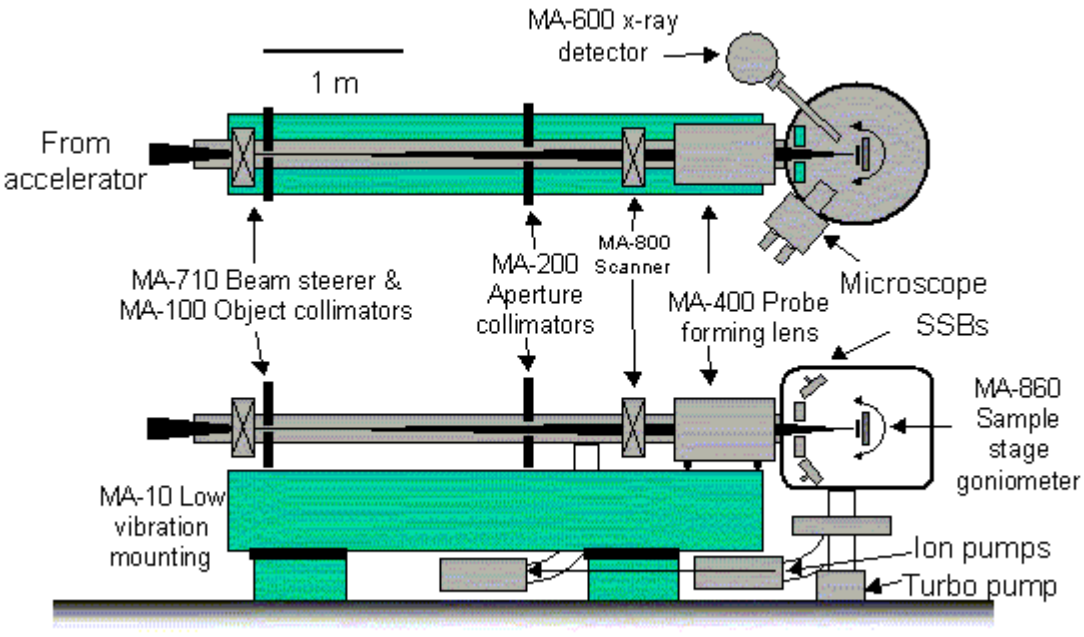


Figure 6.26. Schematic of microprobe used at the Microanalytical Research Centre, University of Melbourne, Australia.

6.2.3.1 Collection efficiency derived from complete spectroscopy model

In order to test the spectroscopy modeling software and determine the device CE function, we compare a 2 MeV alpha microbeam spectrum with the spectroscopy model for a 10×10 μm^2 junction size, 2 μm SOI device. The parameters for the CE function were calculated by iterative adjustment of the model to the measured data using 2D simulation results as a starting point. Figure 6.28 compares the experimental spectrum with the model spectrum. The best fit was obtained for a constant 100% CE.

The spectra for each region, calculated using SRIM [126] and scaled according to the relative areas, are shown in Figure 6.27. Note that the spectral broadening caused by energy straggling is 30 keV. The model predicts a spectrum with two peaks with the lowest energy peak originating by diffusion from region 1 and the highest from drift collection in region 2 which has a thicker SOI and overlayer. These peaks are smoothed out in the experimental spectrum due to effects that are not initially included in the model. In particular, the statistical process of charge collection creates a variation in CE for a given point. Inadequacies also exist in the modeling of the device between regions. For example, the "birds-beak" associated with the edge of the LOCOS region (see Figure 6.8 and Figure 7.12), which accounts for about 10% of device area, is not modeled. Finally, actual overlayer and device thickness may differ. In particular the SOI thickness across the wafer may vary from 1.8 to 2.5 μm. Note that the microbeam measurement has the advantage of minimizing any cell-to-cell variation in charge collection that may exist under broadbeam conditions.

To account for these effects the input charge deposition spectrum was gaussian filtered with the filter standard deviation progressively increased to obtain the best match between the model and experimental data. The charge collection statistics and device modeling inadequacies required a Gaussian standard deviation of 13 keV with the resultant spectrum shown in Figure 6.28. The final spectrum was also filtered (Gaussian, σ=5keV from pulsar measurements) to simulate electronic noise. Clearly, such a result highlights the inadequacy of finite-element type device simulators which do not model charge collection statistical variations versus Monte-Carlo device modeling methods [234]. However, Monte-Carlo methods are very computationally intensive and not as widely available. The remainder of this work uses the Gaussian filter as calculated above.

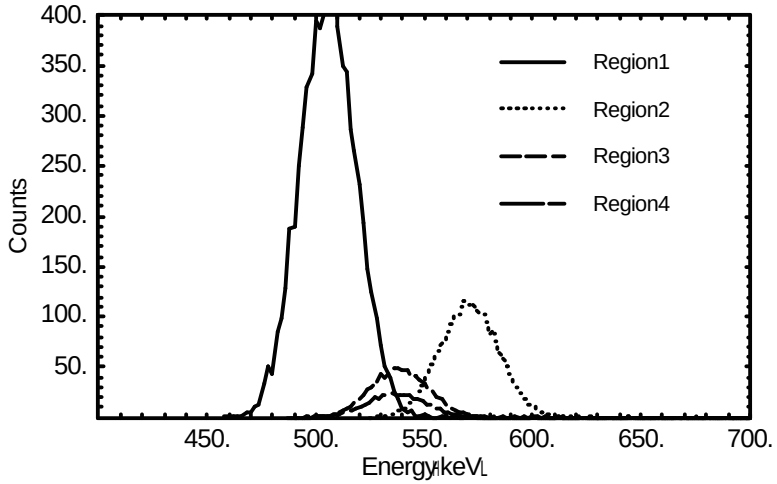


Figure 6.27. 2 MeV alpha spectra of energy deposited in the 10× 10 μm^2 2 μm SOI microdosimeter for the four main device regions. The spectra were calculated using the Monte Carlo transport program SRIM (10000 samples) based on the device cross-section of Figure 6.8. Scaling of the spectra counts was made according to the relative area of each region.

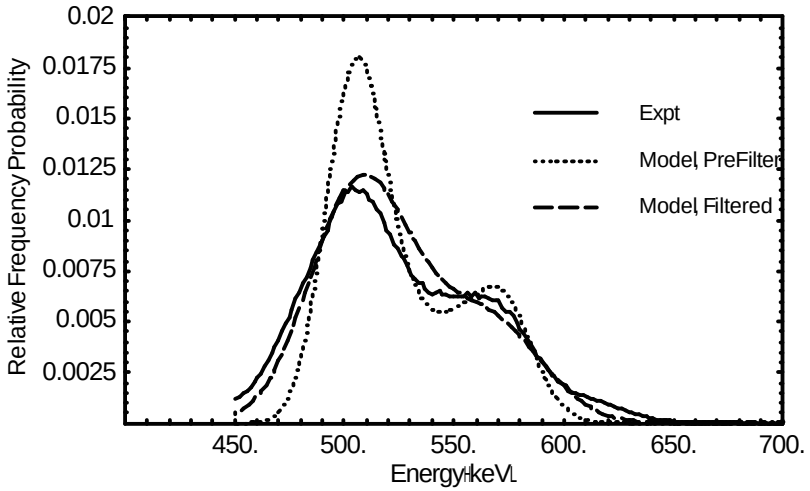


Figure 6.28. Comparison of 2 MeV alpha microbeam spectrum with spectroscopy model. The model is shown without Gaussian filtering and following 13 keV Gaussian filtering. The filtering is intended to imitate the statistics of charge collection

6.2.3.2 Collection efficiency derived from microbeam image

A microbeam image for the 2 MeV alpha is shown in Figure 6.29. The image shows the spatial charge collection information directly available from scanned microbeam methods. The CE function $CE_{mbeam}(x,y)$ may be derived directly from such data since we may calculate the energy deposited at a given position $E_{dep}(x,y)$ using knowledge of the device construction and SRIM calculations such as provided by Figure 6.27. Thus,

$$CE_{mbeam}(x,y) = E_{mbeam}(x,y) / E_{dep}(x,y) \tag{6.52}$$

where $E_{mbeam}(x,y)$ is the microbeam image data. The raw data shown by the bottom 12 cells of Figure 6.29 is obtained by taking the median average of all events traversing a given pixel location. The image data for the single diode cell may be improved further by splitting the image into 12 cells and taking the median over all the cells for each pixel. For a given cell we may use cell symmetry to produce the best possible data for a 1/4 diode by calculating the median of the four quarters with appropriate image reflections. The result calculated using Matlab software [235] has been displayed in the top 8 cells of Figure 6.29 with each cell identical. The left-hand side of Figure 6.30 shows the data E_{mbeam} for a quarter diode and the right hand side is the calculated CE_{mbeam}.

Using this method CE_{mbeam} is expected to have discontinuities at the boundaries between regions since $E_{dep}(x,y)$ is defined to have a single value in each region given by the mean of the distributions in Figure 6.27. The acquisition time was not long enough to obtain a sharper image so data at the boundaries between regions is blurred and the microbeam's effective spatial resolution is weakened. Furthermore, the calculated CE will be greater than 1 in some regions due to the image noise. Obtaining adequate image statistics was a major difficulty during experiments since great care had to be taken to avoid radiation damage of the device given the relatively large minimum beam currents at the time. Ideally, we would have preferred a system with single ion control of the beam synchronized to beam position on the device.

Nevertheless, the data is valuable qualitatively for investigating the CE within a given region. In particular the dominant region 1 shows a gradual drop in CE as we move away from the central n+ junction. This result is consistent with later broadbeam spectroscopy analysis and device simulation with the gradual drop indicating a large diffusion length in comparison with device dimensions. Given the relatively small drop it is not unreasonable that the previous section analysis derived a constant CE of 100%.

In general, the CE method proposed in this section is preferred over others due to the direct spatial information derived and well defined ion energy. However, to fully utilize the benefits of microbeam IBIC, reasonable data statistics are needed. A further improvement in this approach would be to use data from a minimum of two other alpha energies and simultaneously extract the CE, overlayer thickness and SOI thickness without any a-priori information regarding device structure. Assisting this approach is

that lower alpha energies are particularly sensitive to overlayer structures due to the sharply changing LET as a function of range (a reason the higher 2 MeV energy was used here). In addition, the range-energy and LET functions for the different overlayer materials are similar so one could assume an overlayer constructed purely of the one material (SiO_2). Equation (6.52) may be written as:

$$CE_{mbeam}(x,y) = E_{mbeam_i}(x,y,a_i) / E_{dep}(x,y,a_i,t_{ol},t_d) \tag{6.53}$$

where a_i is the i-th alpha energy. A minimum of 3 equations (or alpha energies) is required to solve for the 3 unknowns, CE, t_{ol} the overlayer thickness and t_d the SOI thickness at each point (x,y). E_{dep} may be calculated using range-energy or LET relationships as described later in equation (6.56) (with diffusion term removed).

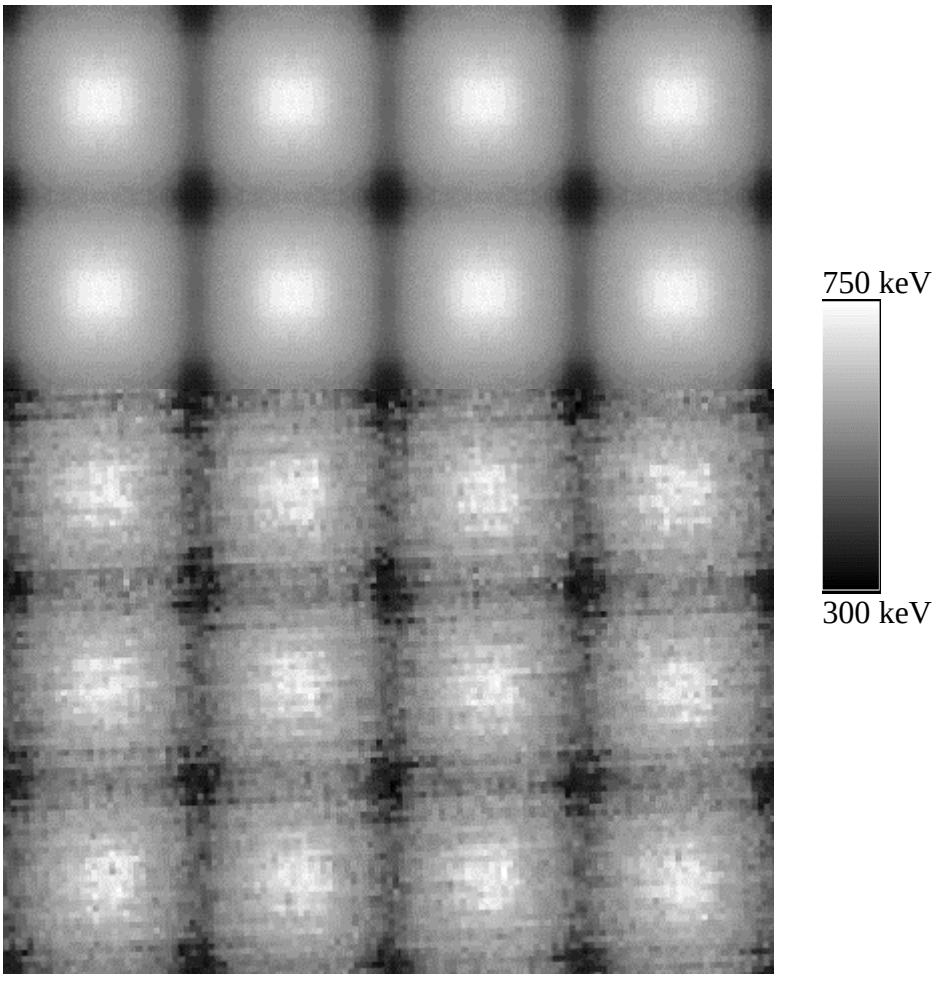


Figure 6.29. Microbeam image (2MeV alpha) of 10×10μm 2μm SOI array. Black corresponds to lowest charge collection amplitude and white is highest amplitude. The top two rows show the image following median filtering of the bottom 12 cells. The bottom image was split into 12 cells and the median over all the cells was calculated for each cell pixel.

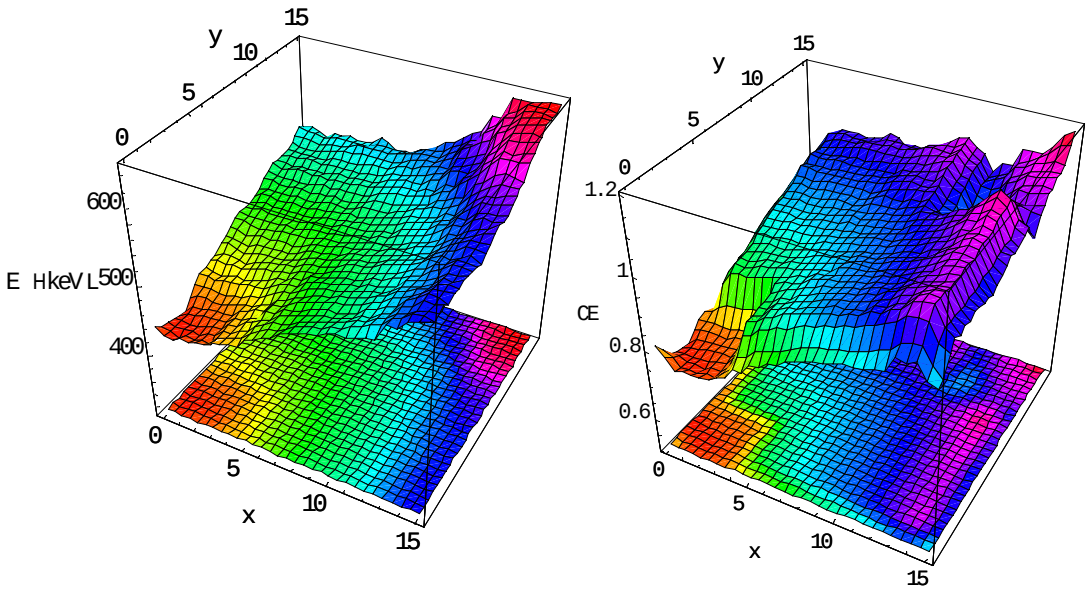


Figure 6.30. (a) Left side, processed microbeam image data for a quarter of the 2 μm SOI diode. (b) Right side, CE calculated from the data on the left using equation (6.53).

6.2.4 Broadbeam Spectroscopy

The aim of this section is to further test the spectroscopy modeling software and again determine the device CE function that provides the best comparison between experimental results and the model. A comparison with 2D device simulation results is also discussed.

Alpha spectroscopy was performed using a 7401 Canberra alpha spectroscopy amplifier which contains a vacuum chamber, preamplifier and shaping amplifier in a single module. A Po-210 (5.3 MeV) alpha source was placed in close contact with the device under test in the vacuum chamber. Energy spectra were recorded using a PC-based multi-channel analyzer (Amptek Pocket MCA8000) connected to the 7401 amplifier output. A note of caution: one should use a new good quality spectroscopy source with constant energy emission. Older sources often exhibit a low energy tail, which extends over time, possibly due to oxidation effects on the source surface. The results in this section supersedes previously published work [194] which was moderately affected by this phenomenon.

The source was placed 5 mm from the diode array. Since the diode array dimensions are 3.63×1.21 mm, the alpha particle may strike at an angle of up to 20° assuming a point alpha source. This geometrical consideration is accounted for in the spectroscopy modeling as described earlier in section 6.2.1. The calculated energy deposition spectra

have typical FWHM widths of 31 keV composed of 2 keV due to the angle effect, 0.5 keV due to spread in the source energy and 28.5 keV due to ion energy straggling effects.

6.2.4.1 Results for 10×10 μm^2 , 2 μm SOI, undamaged and radiation damaged

Both the damaged and undamaged devices were tested at two voltages 0 and 10V bias. Figure 6.31 compares the experimental spectra with the model spectra whilst Figure 6.32 show the CE functions used in the model spectra. The parameters for the CE function were calculated by iterative adjustment of the model to the measured data. Figure 6.32 also shows the CE calculated using 2D device simulation. The surface velocity (2000 cm/s) was adjusted to provide the best match between the CE calculated using the model and the CE calculated using 2D device simulation.

For the 10V unirradiated device the CE parameters (see equation (6.49), and (6.50), L = 55 μm, transition points (5,0.97),(9,0.998)) provide a CE with a gradual drop consistent with the relatively large diffusion length (61 μm measured in section 6.3.2) indicated by the microbeam analysis results. Small differences between the 2 MeV alpha and 5.3 MeV alpha spectra such as a slight increase in funneling for the lower energy alpha, due to it higher LET, are not discernable using these analysis methods. Generally, the comparison between calculated spectra and experimental results shown in Figure 6.31 is excellent and the extracted CE functions may be considered to be reasonable models.

The 2D simulations, on the other hand, do not correspond well with the experimentally derived model and do not predict some of the CE features of the radiation damaged device as seen in Figure 6.32. The intention of the simulations is to provide a qualitative understanding of the basic CE function features such as the drop in overall CE with lifetime decreases and the fall in CE away from the junction region. Poor absolute correspondence occurs due to the many inadequacies of the 2D simulation.

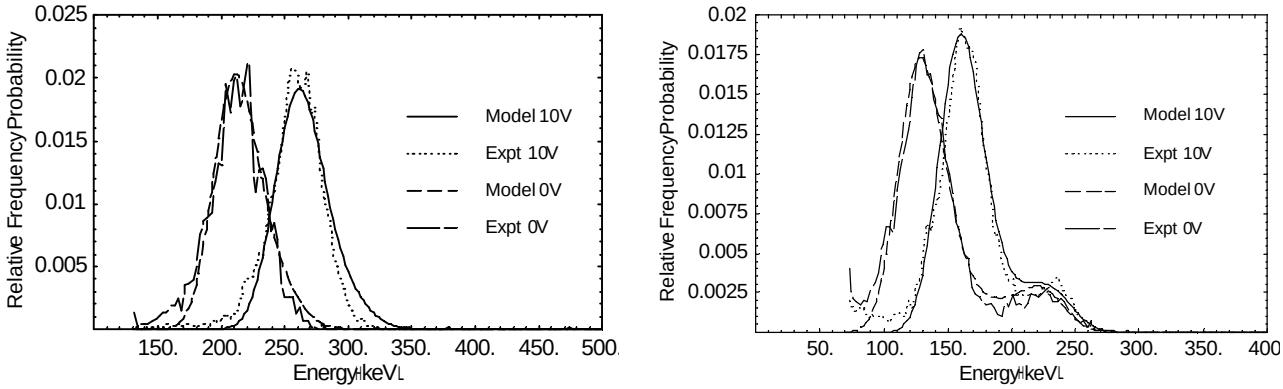
In general, due to geometrical effects the 2D simulation results will overestimate the charge collection by lateral diffusion even if recombination parameters (lifetime and surface recombination velocity) are correctly defined. Essentially, the 2D model overestimates the area of the collecting junction as seen by charge diffusing from the substrate.

The difference in 2D simulation results from the experimentally derived CE is more than one would expect from device geometrical effects, particularly at 0 V bias. The difference even extends to the depletion region where charge collection is drift dominated and rapid. With 0V bias, drift collection is relatively weak and recombination is dramatically increased as seen by the substantial drop in CE. If we increase recombination in the simulation we may obtain a drop in CE, even in the depletion region: however, the decrease in collection from lateral diffusion becomes much too large (i.e. the parameter L in equation (6.49) is too large). So the observed difference in Figure 11 cannot be largely attributed to uncertainty in lifetime parameters. This result implies that the 2D simulation poorly models recombination within the plasma column for the irradiated device.

For 2D simulations, due to ion track geometrical effects, either the correct total charge or the correct charge density can be simulated but not both [223, 236]. DESSIS ensures total charge conservation and so the initial ion track charge density is underestimated. This will affect correct simulation of high injection effects such as Auger recombination and carrier-carrier scattering (CCS). The underestimation is further compounded by the use of a Gaussian ion-track profile which has a much reduced peak ion track density in comparison to more accurate ion track models [208, 211, 230]. A 2D simulation of a 5.3MeV alpha particle was performed which accounted for CCS via the unified mobility model and included self-heating effects by using a thermodynamic model. The simulation indicated negligible self-heating and only a 2% drop in total charge collected versus a model without CCS. Future work should investigate 3D simulations of the irradiated device with an improved ion track model, in order to accurately investigate the effect of CCS, auger recombination, and trap-assisted Auger recombination. This requires both extensive simulation time and a revised track model provided by the software manufacturers.

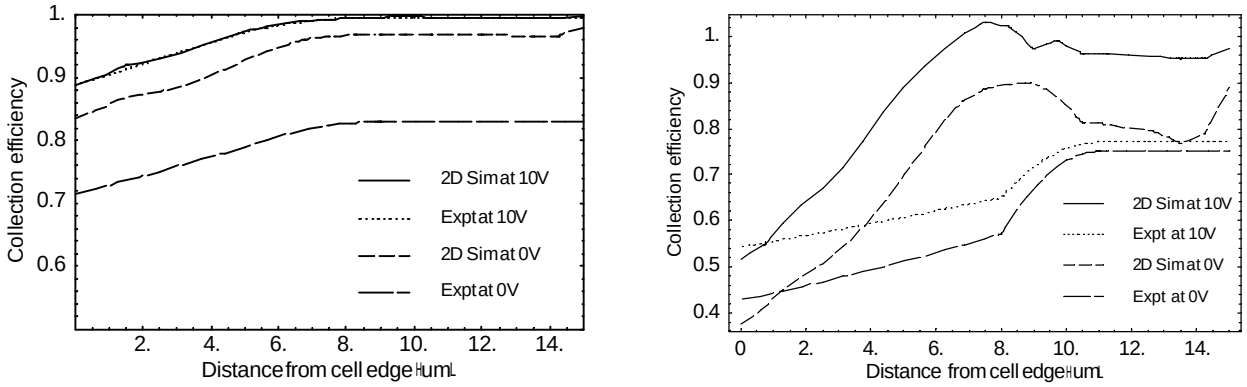
The correct simulation of the radiation damaged device is particularly challenging. The simulation included the damage effects of a decrease in lifetime, decrease in mobility and change in effective substrate doping density. The large decrease in CE seen outside of the junction region may be due to the build-up of interface traps at the Si/SiO_2 interface in conjunction with the above substrate effects. The traps are formed initially by the migration of holes arising from ionization in the oxide regions. They can substantially alter the effective surface recombination velocity depending on their

charge state [199]. The simulator used (DESSIS) has a facility for introducing interface traps into a simulation. However, attempts at such simulations met with unsolved convergence problems. In summary, accurate device simulation of SOI structures requires good estimation of recombination parameters, 3D device geometry and reasonable ion track models.



Unirradiated 2 μm SOI Irradiated 2 μm SOI

Figure 6.31. *Unirradiated* (left) and *Irradiated* (right) 2μm SOI device: 5.3MeV broadbeam alpha spectroscopy and a comparison with spectroscopy model.



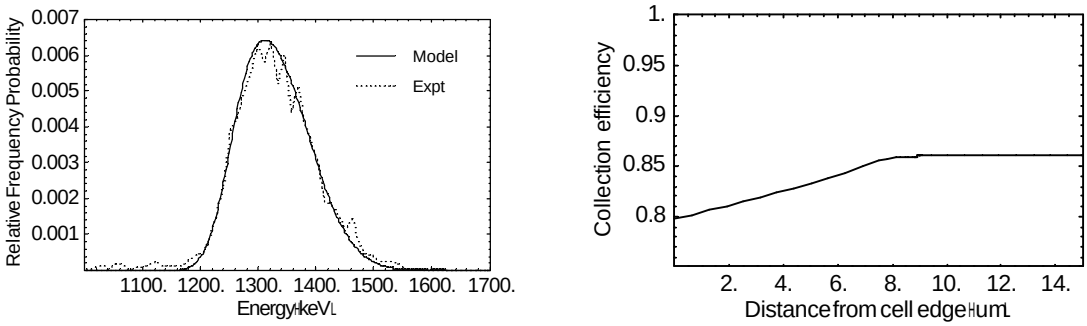
Unirradiated 2 μm SOI Irradiated 2 μm SOI

Figure 6.32. *Unirradiated* (left) and *Irradiated* (right) 2μm SOI device: Collection efficiency function derived from 5.3MeV broadbeam alpha spectroscopy (Figure 6.32) and a comparison with 2D simulation results.

6.2.4.2 Results for 10×10 μm^2 , 10 μm SOI, undamaged device

The spectroscopy model was applied to the 10 μm SOI device since this device is used in some of the experiments discussed in later chapters. The raw and modeled alpha spectroscopy data collected at 10 V bias, and the derived collection efficiency are shown in Figure 6.33. The model is an excellent fit to the data providing confidence in the models validity. The extracted parameters are L = 115 μm and transition points ((6,0.84),(9,0.86)). Unlike the 2 μm SOI device, the 10 μm SOI is not fully depleted

under the junction since the depletion depth is about 3 μm. Therefore, CE is 86% for ions traversing the junction due to diffusive charge collection and higher recombination below the depletion region. Additional recombination due to slow lateral diffusion creates the drop in CE as we move away from the junction. In many cases, the CE may be approximated to a constant 0.82, since the spatial variation in CE is quite small. For particles of effectively constant LET, the sensitive volume is reasonably modeled as a 8.2 μm thick slab.



(a) 5.3 MeV alpha spectrum (b) Spectroscopy model derived CE

Figure 6.33. 10 μm SOI device, Collection efficiency derived from 5.3 MeV spectroscopy data. Left plot is the measured spectrum compared with the model. Right plot shows the CE function model in 2D form.

6.3 Radiation Hardness Characterization

High-energy radiation produces defect complexes in semiconductor materials which reduce minority carrier lifetime, change majority carrier density and reduce mobility. In this study, we determine the damage constant describing the change in minority carrier lifetime. Calculating the damage constant will enable us to determine the number of patient treatment cycles (for fast hadron therapy) that the device will withstand before the charge collection behavior significantly alters. A brief summary of radiation damage mechanisms is provided prior to the main calculations.

6.3.1 Basic Radiation Damage Physics

The sensitivity of silicon electrical properties to radiation damage was first discovered in 1948 by Johnson and Lark-Horowitz [237]. Subsequently, many investigators have extensively studied the effect of radiation damage. Excellent summaries of the nature of the damage process and associated electrical property changes have been written [238-240]. This section will draw upon the key elements presented in these summaries to give a brief overview of the current understanding of radiation damage on silicon.

Radiation damage refers to the effect of radiation which produces atomic displacements in a crystal lattice. The first phase of the process is the collision of a high energy particle with an atom in the lattice. The displacement cross-section for neutrons impacting silicon atoms is ~3 barns so an incident neutron will probably undergo only one interaction before exiting the device [240]. Thus, most of the damage is actually done by the primary recoil (knock-on) atom (PKA). The PKA rapidly loses energy in the immediate vicinity of the collision due to both ionizing and non-ionizing energy losses. The displacement threshold for silicon is ~ 20 keV so the PKA can continue to produce displacements until its energy is below this threshold. Thus defects form in cascading subclusters with typically 1-3 terminal subclusters per track. Simulations and experiments have provided insight into the damage track structure [241, 242]. Most tracks are less than 1000 $\mathring{A}$ with terminal subcluster dimensions of 50 $\mathring{A}$. The first phase of the damage process ends when the PKA is at rest.

The damage produced consists of Frenkel defects (interstitial silicon and vacancy pairs) along the track and subclusters. Most of the Frenkel pairs are separated by only a few atomic spacings and have a high probability of recombination. Approximately 95% of defects are repaired immediately. The second phase of the damage process involves the diffusion of the remaining vacancies and interstitials, both of which are mobile even at liquid nitrogen temperatures. The interstitials do not appear to form electrically active defect sites which can contribute to damage effects. However, the vacancies are effective recombination and trapping sites capable of diffusing to form stable defect complexes with n-type dopants (E centers), oxygen impurities (A-center) and other vacancies (divacancies). These vacancy defect complexes are effective recombination and trapping sites and are responsible for the observed decrease in minority carrier, and reduction in majority carrier density and carrier mobility. Trapping of majority carriers reduces mobility because the trapped carriers convert the trapping center into fixed charge scattering centers. The scattering centers reduce the mobility of the remaining carriers. Both of these effects reduce material conductivity.

The changes in the electronic properties of the silicon are interpreted by the anomalous defect levels in the band-gap which are often deep levels with behavior unlike the more common shallow dopant levels which are mostly ionized. The divacancy is predominant in p-type material with a trapping and recombination center ~0.35 eV above the valance

band and another at mid-band level. Note that all of these defects may be annealed by elevated temperatures.

These radiation damage effects translate into significant differences in device performance. The lower lifetime results in increased leakage current and hence poorer resolution and reduced charge CE whilst the lower effective majority carrier density result in a decreased capacitance for a given reverse bias voltage.

6.3.2 Minority Carrier Lifetime Estimation

The reduction of minority carrier lifetime (τ) is given by the following equation:

$$\frac{1}{t} = \frac{1}{t_i} + kq_n \tag{6.54}$$

where k is the damage constant and θ_n is the neutron/proton fluence. This proportionality is valid up to neutron levels where the damage regions begin to overlap. An approximate estimate of the fluence where non-linear effects may appear can be made by calculating the reciprocal of the volume of the largest damage regions and applying the equation $q_{n,\max} \sim 1/(sN_aV)$ where s is the displacement cross section (3×10^{-24} cm^2), N_a = silicon atomic density = 0.5×10^{23} atoms/cm^3 and V is the largest damage volume. Given that most tracks are less than 100 $\mu m \times 50$ Å $\times 50$ Å [242] then nonlinear effects will not occur until neutron fluence values exceed 2.5×10^{15} n/cm^2 [240]. This is well above irradiation fluence levels considered in this study.

In order to calculate the damage constant we measure the minority carrier lifetime via charge collection spectroscopy methods as proposed by Edmonds [243]. Edmonds' model considers a planar device as shown in Figure 6.34. The upper surface of the silicon substrate is assumed to consist entirely of a depletion region acting as a perfect charge collection sink. Charge generated by ionizing particles traversing the depletion region is 100% collected by drift processes. Below the depletion region the charge collected by diffusion is given simply by the solution of the one dimensional continuity equations with appropriate boundary conditions. Thus, the charge collected Q_c by the depletion region from charge generated Q_o a distance x_1 below the depletion region is given by

$$Q_c = Q_o Exp(-x_1 / L_d) \tag{6.55}$$

where L_d is the diffusion length. Given a calibrated system, energy and charge are equivalent. Therefore, the energy collected from both the depletion region of thickness t_{dr} and substrate regions is given by

$$E_{collected} = \int_0^{t_{dr}} \frac{dE}{dx} dx + \int_{t_{dr}}^{R(E_1)} \frac{dE}{dx} e^{-\frac{x-t_{dr}}{L_d}} dx \tag{6.56}$$

where x is measured from the top of the depletion region t_{dr} is the depletion thickness given by equation 4.3, and $E_1 = E_i - \int_0^{t_{ol}} \frac{dE}{dx} dx$.

Note that the depletion region incident energy (E_1) is calculated by correcting for the overlayer thickness t_{ol}. The range of a particle with energy E_1 is given by the function $R(E_1)$.

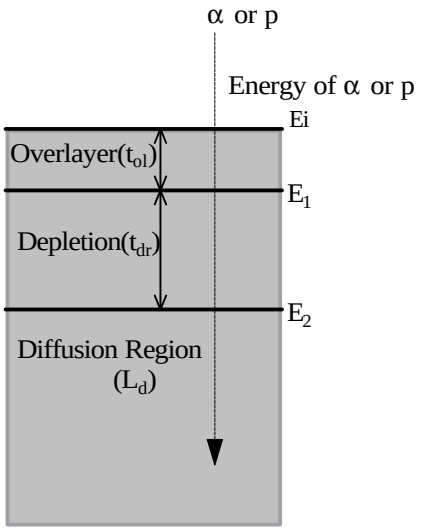


Figure 6.34. Parameters of Edmonds' charge collection model for large bulk devices.

The diffusion length L_d is calculated for various input ion energies E_i using a numerical non-linear curve fitting routine (Levenberg-Marquardt method) [141]. This routine minimizes the least square difference between the measured and calculated energy collected given by equation (6.56). Minority carrier lifetime then follows from:

$$t = L_d^{\,2} / D_n \tag{6.57}$$

where D_n is the diffusivity of electrons in silicon (37.6 cm^2/s in pure silicon). Diffusivity is related to mobility m_n via the Einstein relation.

$$D_n = \left[\frac{kT}{q}\right] m_n \tag{6.58}$$

where k = Boltzmanns constant, T = temperature, and q = electron charge. At T = 300K, kT/q = 0.026 V.

As mentioned previously, radiation damage may reduce mobility. Experiments by Leroy [244] indicate that the mobility of electrons in silicon is reduced linearly from 1345 cm^2/V-s to 1060 cm^2/V-s when exposed to 24 GeV/c protons. The linearity is observed up to 5×10^{-13} p/cm^2 after which saturation occurs. Thus we may express the mobility (in cm^2/V-s) as a function of 24 GeV/c proton fluence f_p (in p/cm^2)

$$m_n = 1345 - 6.95 \times 10^{-12} f_p \tag{6.59}$$

Equation (6.55) assumes that the depletion region boundary is a perfect charge sink consisting of a plane of infinite extent. This assumption is best satisfied by the 100×100 μm bulk device operating at 10V bias since the junction/depletion region covers a relatively high proportion of chip area (75%) as shown in Figure 6.10. Deviations from complete charge collection at the upper surface result in an underestimation of diffusion length.

The above method was applied to both the irradiated and unirradiated bulk devices. The bulk devices were irradiated at CERN with 24 GeV/c protons at a fluence of 4.1×10^{13} p/cm^2 using the CERN Proton Synchrotron (PS) T7 beam [245]. An image of the PS beam line exit is shown in Figure 6.39. Fluence measurements were performed with aluminium foils having the same area as the microdosimeter. The error in fluence measurements was estimated to be ± 7% [246].

Measurements of charge collection were performed on the large diode array (100×100 μm^2) bulk devices biased at 10V, using 1, 2 and 3 MeV proton microbeam data. The energy collected was taken as the energy of a particle traversing the middle of the diode. The maximum error in the measured collected energy was estimated to be ± 40 keV. Figure 6.35 shows the excellent fit to the data achieved by the model and Table 6.2 gives the extracted diffusion length and minority carrier lifetime. The diffusion length was reduced from 61.4 μm to 7.9 μm following irradiation due to the effects of displacement damage reducing the minority carrier lifetime from 1 μs to only 23 ns.

Also shown in Figure 6.35 are measurements for protons incident on the small diode array ($10 \times 10\ \mu m^2$) bulk device under identical conditions. The junction/depletion area occupies a smaller fraction of the upper surface area in the small diode array (20%) compared with the large diode array (75%) as shown in Figure 6.9 and Figure 6.10. This reduced junction area results in a 20-30% loss of charge due to surface recombination at the upper Si/SiO_2 interface. Clearly, Edmonds' one dimensional model given by equation (6.56) is inappropriate for the smaller diode array. However, the minority carrier lifetime may still be estimated given an improved model, which accounts for the surface recombination and reduced junction area. Such a model may be derived analytically using a 3 dimensional solution of the electron continuity equations or solved numerically using a simulation package such as DESSIS. Moreover, such a model may be used to derive both the bulk lifetime and the recombination surface velocity by fitting to measurements performed on both the small and large diode arrays.

Proton microbeam measurements have significant advantages over alpha broadbeam experiments since the lower LET protons are much less susceptible to funneling (as shown in section 6.2.2.3) and the imaging method allows us to select the ion position which best satisfies the model assumptions. As a comparison, alpha broadbeam measurements were also used to extract the diffusion lengths. In this case, the depletion width was included as a fit parameter since funneling has historically been modeled by an artificial increase in the depletion width [212]. The energy collected is estimated by extracting the peak in the alpha spectrum corresponding to ion traversal through the depletion region. A Po-210 (5.3 MeV) source was placed in a vacuum with incident alpha energy varied by using thin plastic films. The results shown in Table 6.2 indicate a large difference between proton microbeam and alpha broadbeam methods (a factor of 4.3 lower) due to alpha funneling effects. Note that the drift component for the alpha experiment is higher than one might expect from estimates of the depletion width. The additional charge collection is due to funneling.

For the proton microbeam modeling, the depletion width and majority carrier density were determined from C-V measurements as per previous measurement discussed in section 4.2.2. Note that trapping levels introduced by displacement damage may reduce the majority carrier density. The decrease in capacitance due to the change in effective substrate doping is shown in Figure 6.37. The junction capacitance per unit area was calculated and corrected for stray and track capacitance (as per section 4.2.2) with the

results displayed in Figure 6.38. These measurements indicate a drop in substrate doping density from 1.6 to $1\times10^{15}cm^{-3}$, which is directly reflected in the slope differences of Figure 6.38. Such a reduction will increase the depletion width following irradiation from 3.1 to 3.8 μm (at 10V) as a shown in Table 6.2

In summary, the effects of radiation damage on reducing lifetime and majority carrier density have been measured using spectroscopy techniques and C-V measurements. The importance of using measurements conforming with the assumptions of Edmonds' model is highlighted. In particular, proton microbeam measurements on large area diodes should be used for accurate results.

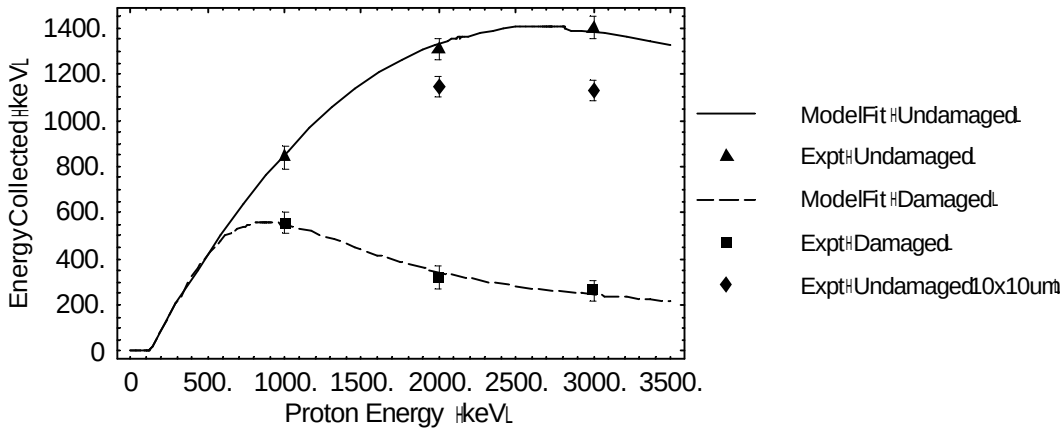


Figure 6.35. Fit of diffusion model to proton microbeam peak charge collection data. All data is for 100×100 μm² diode size bulk devices except for the diamond which is for a 10 × 10 μm² diode size bulk device.

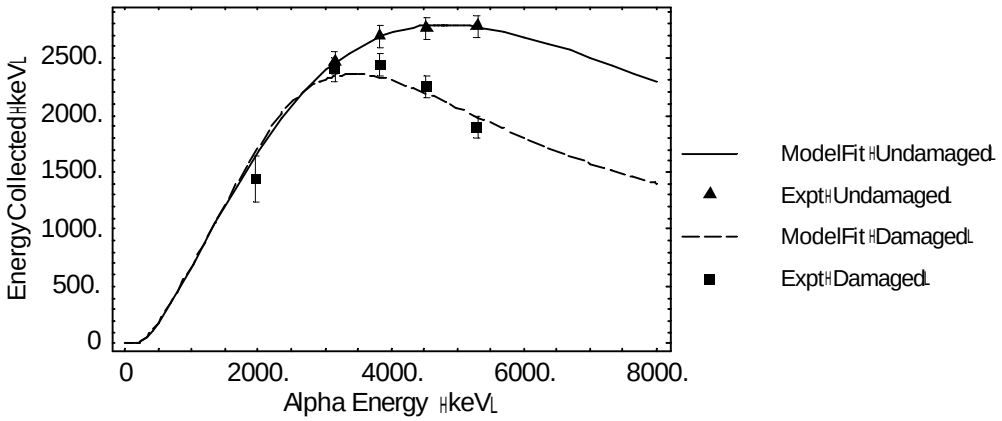


Figure 6.36. Fit of diffusion model to alpha broadbeam peak charge collection data. All data is for 100×100 μm² diode size bulk devices. Error in energy collected is estimated at ± 100 keV for alpha energy >2000 keV. The low energy data at 2000 keV has a larger error (± 200 keV) due to poorer resolution of incident alpha spectrum.

Table 6.2. Lifetime parameters for damage constant estimation

	Proton μbeam			α broadbeam (Note 1)		
	Drift (μm)	**L_d (μm)**	**τ (nsec)**	**Drift (μm)**	**L_d (μm)**	**τ (nsec)**
Unirradiated	3.1	61.4	1080	3.9	14.3	59
Irradiated	3.8	7.9	23	5.4	6.6	16
Damage Constant	1.5×10^{-6} cm^2/n/s			1.7×10^{-6} cm^2/n/s		

Note 1: Results indicate that α broadbeam measurements are severely affected by funneling enhanced charge collection. Drift or depletion width is determined by C-V measurement data for the proton μbeam and by Edmonds model fitting for the α-broadbeam.
Note 2: The minority carrier lifetime has been calculated using equations (6.57) to (6.59) which correct for a decrease in mobility due to radiation damage.

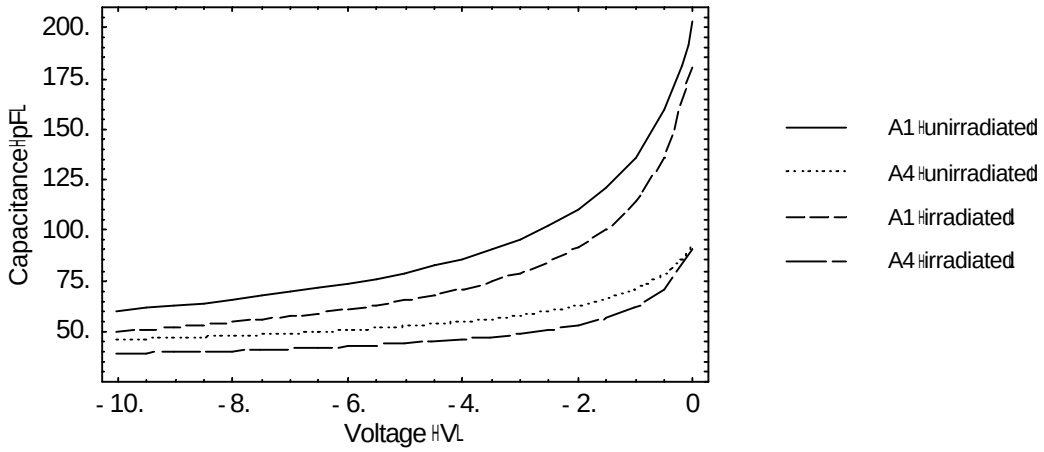


Figure 6.37. Capacitance versus voltage data for bulk devices before and after irradiation with 24 GeV/c protons at a fluence of 4.1×10^{13} p/cm^2. Irradiation was performed using the CERN-PS-T7 beam. A1 is an array with 100×100 μm^2 sized diodes and A4 has 10×10 μm^2 sized diodes.

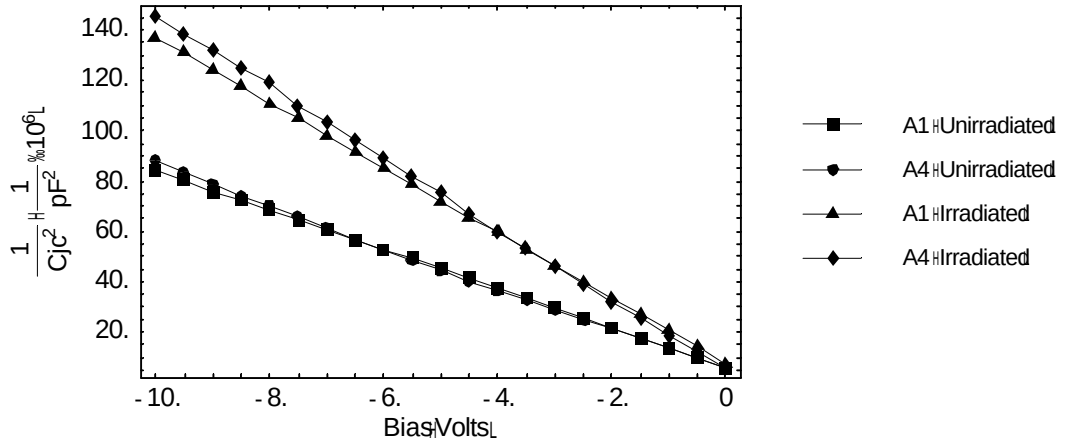


Figure 6.38. Correction Diode Array Junction Capacitance versus voltage data for bulk devices before and after irradiation with 24 GeV/c protons at a fluence of 4.1×10^{13} p/cm^2. Irradiation was performed using the CERN-PS-T7 beam. A1 is an array with 100×100 μm^2 sized diodes and A4 has 10×10 μm^2 sized diodes. The slope of the data is related to the substrate doping density

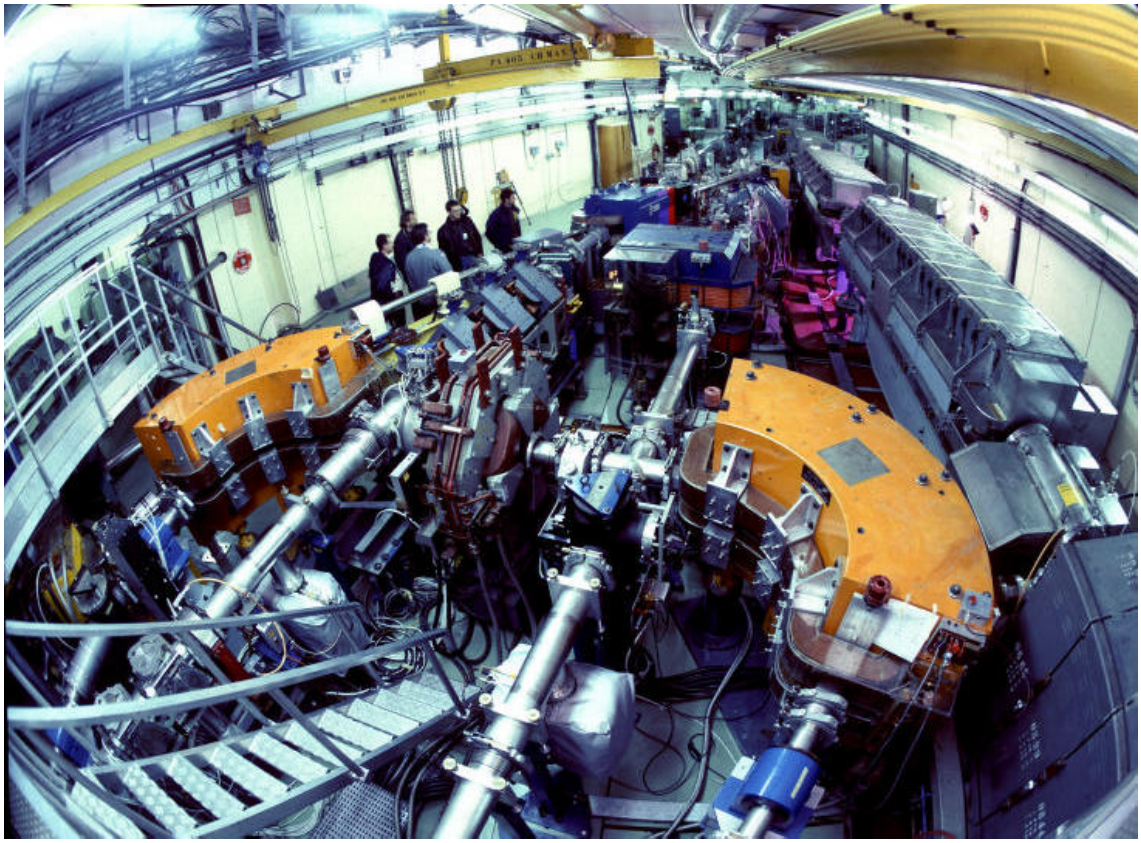


Figure 6.39. CERN Proton Synchrotron transfer lines inside the tunnel. (Photo courtesy of CERN)

6.3.3 Damage Constant

It has been demonstrated in several papers [247-249] that the displacement damage effects from a variety of particles may be correlated based on the nonionizing energy loss (NIEL). NIEL is the calculated energy loss per unit mass due to atomic displacements and does not include any energy loss to ionizing effects (i.e. creation of electron-hole pairs). The calculation of NIEL S_{di} for a monoatomic material consists of evaluating the expression [250]:

$$S_{di} = \frac{N}{A} \sum s_j(E) T_j(E) \tag{6.60}$$

where N is Avogadro's number, A is the atomic mass of the target atom, E is the energy of the incident particle, $s_j(E)$ is the displacement cross-section, and $T_j(E)$ is the average energy of the recoil atom for the j-th type of interaction .

The NIEL factor is frequently applied to normalize bulk radiation damage effects induced by various particles to that induced by 1 MeV neutrons [239, 240, 247-249]. The theoretical relative hardness of the 24 GeV/c protons, which is the ratio of the NIEL factors of the 24 GeV/c protons to that of 1 MeV neutrons is approximately 0.5-0.7

from [247, 248]. Note that the displacement cross-sections are 65.15 MeVmb for 24 GeV/c protons and 95 MeVmb for 1 MeV neutrons [251] which provide a similar ratio.

Using the proton microbeam data for the 100×100×bulk large diode array (Table 6.2) applied to equation (6.54) we obtain the 24 GeV/c damage constant as $K_{24GeV/c} = 1\times10^{-6}$ cm^2/n-sec. Applying the NIEL factor of 0.7 gives a final 1 MeV neutron equivalent damage constant of $K_{1MeV} = 1.5\times10^{-6}$ cm^2/n-sec. This result is in reasonable agreement with damage constants estimated by Messenger and Ash [239] assuming high injection ratios. The variation of diffusion length with equivalent 1 MeV neutron fluence is shown in Figure 6.40. Note that diffusion length is closely linked to CE. Given that 1 cGy is approximately equivalent to 4.1×10^{8} n/cm^2 (1MeV neutrons) [252] and assuming 100 cGy per patient treatment, then we may expect a 10% change in diffusion length after 3.4 treatments. This is a reasonable result given the low cost of each device and the possibility of using shorter exposure times during phantom measurements. Future devices may be designed to minimize radiation damage effects by operating the entire sensitive volume in a fully depleted mode and by using a smaller sensitive volume with faster collection times.

Bulk devices were also irradiated at the Australian Nuclear Science and Technology Organization (ANSTO) using 1MeV neutrons at fluences of 10^{10}-10^{12} n/cm^2. The spectrum shift at the highest fluence was approximately 5% compared to an expected change in diffusion length of 40%. We can conclude that the damage constant calculated above is quite conservative.

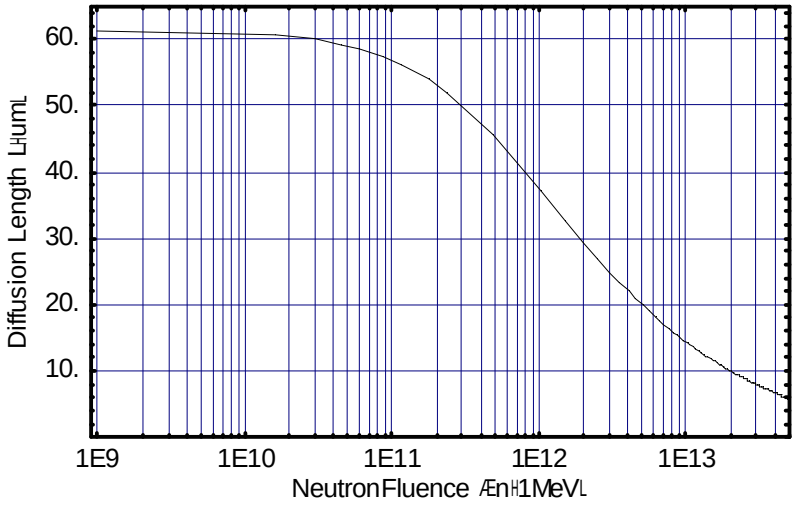


Figure 6.40. Estimated change in diffusion length with 1 MeV equivalent neutron fluence given a damage constant $K_{1MeV} = 1.5\times10^{-6}$ cm^2/n-sec

6.4 Summary of Charge Collection Modeling

6.4.1 Collection Efficiency and Radiation Damage Summary

The three basic methods employed in this analysis for charge collection modeling are summarized in Table 6.3. Potentially microbeam spectroscopy offers the most accurate estimation of device CE due to the unambiguous spatial information provided. The microbeam has several important advantages including the use of a proton beam to minimize funneling, a mono-energetic source, and localization of charge collection. However, in our experiments the sub-micron resolution of the microbeam system could not be achieved due to radiation damage effects limiting exposure time and thus statistical accuracy. The microbeam measurements should use the highest energy alpha available in order to minimize the influence of the overlayer. A proposed further improvement in microbeam analysis would be to use data from a minimum of two other alpha energies and simultaneously extract the CE, overlayer thickness and SOI thickness without any a-priori information regarding device structure.

Table 6.3. Summary comparison of charge collection modeling methods

Characterization Method	Advantages	Disadvantages
Microbeam Spectroscopy	- proton beam available which minimizes funneling effects - mono-energetic source - localization of charge collection and capable of directly extracting spatial CE	- Difficult and expensive experiment not readily available - Care must be taken to avoid radiation damage => require low current single ion control for best results
Broadbeam Spectroscopy	- Inexpensive and readily available	- limited source energies - proton not available - no spatial charge collection data => Easy to incorrectly associate peaks in the spectrum with various charge collection regions
Device Simulation	- Fast evaluation of new designs - Increases understanding of charge collection process - Provides basic CE profile	- Requires 3D simulation with accurate track profile models and recombination parameters for accuracy => Very time consuming - Does not model statistical variations in CE - 2D modeling has limited accuracy

The broadbeam results are used for CE definition in this work due to the greater availability of such measurements and the previously mentioned difficulties with microbeam experiments. Care must be taken in the interpretation of broad-beam data to

avoid associating peaks in the spectrum directly with drift collection regions. The effect of significant lateral diffusion is to shift the spectrum to lower energies due to reduced CE. The spectroscopy modeling presented assists in correctly interpreting data by including, as far as practicable, all the sources of variation that contribute to the measured spectral character.

The CE parameters for the 2 and 10 μm SOI devices are summarized in Table 6.4. The results indicate that the CE does not vary greatly with (x,y) position. Small decreases in CE away from the junction are observed, consistent with a diffusion length larger than diode cell dimensions. The area averaged broadbeam derived CE at 10 V was 0.944 for the 2 μm SOI and 0.825 for the 10 μm SOI device. Note that the CE was extracted from 5.3 MeV alpha measurements. The CE using other radiation types and energy may differ due to funneling and recombination variations. These difference are not expected to introduce significant changes in CE since the efficiency is quite high and relatively uniform. However, further study of CE variations with ion type and energy is encouraged. Such future studies may use 3D device simulation with more accurate track modeling than presented in this work.

Table 6.4. Collection efficiency parameters for 2 and 10 μm SOI devices

Device	CE (see equation (6.49), and (6.50))
10V undamaged 10×10 μm^2 junction size, 2 μm SOI	Broadbeam measurement (5.3 MeV alpha): L = 55 μm, (x_f, c_f) = (5,0.97) and (x_d, c_d) =(9,0.998) see Figure 6.31, Figure 6.32, section 6.2.4.1. Microbeam measurement (2 MeV alpha): (a) 100% CE using spectroscopy model, section 6.2.3.1. (b) Slight decrease in CE away from junction, consistent with broadbeam measurement see Figure 6.30, section 6.2.3.2.
10V undamaged 10×10 μm^2 junction size, 10 μm SOI	Broadbeam measurement (5.3 MeV alpha): L = 115 μm, (x_f, c_f) = (6,0.84) and (x_d, c_d) =(9,0.86) see Figure 6.33, section 6.2.4.2.

Device simulation was extensively used in this chapter to assist in understanding the charge collection process. Collection efficiency simulations described in section 6.2.2.2 and 6.2.4.1 were in poor absolute agreement with broadbeam spectroscopy modeling as shown in Figure 6.32. The differences were attributable to inadequacies in 2D simulations. Accurate device simulation of SOI structures requires good estimation of recombination parameters, 3D device geometry and reasonable ion track models. Nevertheless, despite the possible inaccuracies of 2D simulations they do provide

qualitatively useful information such as the reduction in CE away from the junction and identification of funnel dominated charge collection.

In particular, simulations on bulk devices indicated that protons would be largely immune from funneling effects in contrast to alpha particles. Radiation damage studies determined the minority carrier lifetime before and after radiation damage. Edmonds' spectroscopy method for determining lifetime was employed. Accurate results demanded, firstly, the use of proton microbeam methods to reduce funneling effects and, secondly, large area bulk diodes to conform with the Edmonds model. The reduction in lifetime with radiation damage is described by the calculated 1 MeV neutron equivalent damage constant of $K_{1MeV} = 1.5\times10^{-6}$ cm^2/n-sec. In addition, C-V measurements quantified the drop in majority carrier density from 1.6 to 1×10^{15}cm^{-3} following irradiation with 24 GeV/c protons at a fluence of 4.1×10^{13} p/cm^2.

In summary, the ability of SOI technology to create a well-defined sensitive *depth* has been confirmed by the charge collection studies. In using a p-n diode array it was initially hoped that the *lateral* charge collection would be dominated by drift in the junction region with much reduced charge collection outside that region. However, the charge collection studies demonstrated that lateral diffusion and funneling are dominant processes due to a diffusion length (61 μm) much larger than cell dimensions. Reducing diffusion by lifetime reduction methods such as radiation damage was found to also affect charge collection in drift dominated regions.

The main implication is that future SOI microdosimeter designs should introduce methods such as oxide isolation boundaries to minimize lateral diffusion. Such technology has recently (1998) been developed for radiation hard applications. The TEMIC Matra MHS D-MILL 10 MRad process available from Europractice ASIC service [253] is a good example process in which CMOS and bipolar and JFET technology are available with complete isolation between device structures. Smaller cell volumes would reduce the dependence of charge collection on minority carrier lifetime and thus enhance radiation hardness.

6.4.2 Implications for Mean Chord Length Estimation

Lateral diffusion has created a sensitive volume for the SOI devices that closely approximates an infinite slab (or a very elongated RPP) rather than the desired RPP, discussed in chapter 3, with small or preferably no elongation. For the 2 μm and 10μm

SOI devices, the average sensitive depths (corrected for CE and SOI thickness variations) are 1.78 μm and 8.15 μm, respectively. The device width is 1214 μm and length is 3626 μm.

Despite this non-ideal shape and chord length distribution, later chapters test the current device in clinical beams. The potential of the device and useful future design information may still be gauged by experimenting with the current prototype microdosimeter. Microdosimetric spectra in these studies require an estimate of the mean chord length, $\bar{l}$, for the sensitive volume.

Assuming μ-randomness, the $\bar{l}$ for an infinite slab of thickness *h* is 2*h* (from Table 3.3). However, the assumption of μ-randomness or infinitely long isotropic random tracks, is questionable for volumes with exceedingly high maximum chord lengths and high CLD variance. For many practical radiation types the charged particles are not longer than the maximum device dimension (~3.8 mm) and the irradiation from the TE converter is not always isotropic. Therefore, it is appropriate to explore alternative estimations of $\bar{l}$ that are appropriate for the radiation field under investigation. In addition, geometrical considerations made in chapter 3 regarding equivalence to a sphere and in chapter 5 regarding TE corrections should be incorporated where possible.

Four basic methods are employed in the remainder of this work.

1. **Monte-Carlo simulation:** An accurate value of $\bar{l}$ may be obtained via Monte-Carlo simulation methods which transport charged particles through the experimental setup and determine the path length traversed through the device. In the case of BNCT, Monte-Carlo software was developed and applied to $\bar{l}$ determination as discussed in chapter 7. Corrections to the calculated $\bar{l}$ to obtain y_d equivalence to a spherical shape and TE correction are discussed in detail in section 7.3.1.5 and 7.4.1.4.

2. **Dose Mean Lineal Energy y_d Equivalence:** In chapter 3, the dimensions of a cube required for equivalence to a spherical proportional counter were calculated based on providing equal y_d for both shapes. Where TEPC measurements exist, the mean chord length for the silicon microdosimeter measurements may be iteratively adjusted to provide the same value of y_d as the proportional counter. This method is applied to fast neutron therapy measurements discussed in chapter 8.

3. **Proton Peak or Edge Methods:** Another method for estimating $\bar{l}$ simply involves adjusting $\bar{l}$ to provide the best alpha and proton peak fit between the TEPC and silicon microdosimeter *yd(y)* spectra. Again this method is applied to fast neutron therapy measurements discussed in chapter 8. Related to this technique is an excellent method of calibrating microdosimetric measurements involving the use of the "proton edge" described earlier in section 2.3.1.2. The proton edge represents the maximum lineal energy that protons can have in the detector volume. This occurs at the end of the proton range in the Bragg peak. For sensitive volumes that have a well defined maximum chord length, the proton edge provides an excellent and convenient calibration technique that is independent of beam energy spectrum. Note, that adjusting $\bar{l}$ and calibrating the spectra via a gain adjustment have the identical effect of scaling the lineal energy axis in the *yd(y)* spectra. For elongated RPPs the maximum chord length is improbable and the proton edge method is difficult to implement. However, if the incident radiation is largely normal to the device then the proton edge may be more clearly defined corresponding to the sensitive depth of the detector.

4. **Normally Incident:** For some radiation types, such as proton beams discussed in chapter 9, the secondary particles are approximately normal to the device. In this case, a reasonable first order approximation approximates $\bar{l}$ as the sensitive depth of the device. (i.e. 1.78 μm for the 2 μm SOI and 8.15 μm for the 10 μm SOI). For the proton therapy application discussed in chapter 9 device operation is emphasized and results are presented using the silicon mean chord length without TE correction.

Clearly, high elongation RPPs introduce uncertainty in mean chord length estimation. This is an additional compelling reason for using cubic shaped devices.

7. Application to Boron Neutron Capture Therapy

7.1 Background to BNCT

Boron neutron capture therapy (BNCT) involves the thermal neutron irradiation of a tumor site that has been selectively sensitized to thermal neutrons via the concentration of boron-10 (B-10) within or near cancer cells [254]. The B-10 is administered by injection of tumor specific boron compounds. Several excellent reviews are available including Barth on general topics [255], Coderre on radiation biology [256], and Zamenhof on microdosimetry in BNCT [257].

BNCT was proposed in 1936 by Locher [258] and the first clinical trials took place at Brookhaven National Laboratory (BNL) in 1951-52 and Massachusetts Institute of Technology (MIT) in 1959-61 [259, 260]. Initial clinical trials were unsuccessful due to normal tissue necrosis attributed to high concentrations of boron in normal brain capillaries and the poor penetration depth of thermal neutron beams. BNCT was resumed in Japan in 1968 using more selective boron compounds. Results were encouraging although they indicated that the survival times of these patients were no better than for those receiving conventional radiotherapy [256, 261]. Recently, several improvements have been made in boron delivery agents and epithermal neutron beam design. Clinical trials were resumed at BNL in 1994 for glioblastoma multiforme (a particularly insidious form of cerebral cancer), at MIT in 1996 for cutaneous and intracerebral melanoma and at the high flux reactor in Petten, Netherlands in 1998 for glioblastoma.

The concept of BNCT is attractive in principle: the thermal neutrons are selective and the range of the fission products limits damage to the cell containing boron. The kinetic energy of thermal neutrons (0.025 eV) is below the threshold for ionization and only inelastic events such as neutron capture produce significant energy deposition. In tissue, hydrogen and nitrogen have significant cross-sections for thermal neutron capture (0.33 and 1.75 barns respectively). They produce 2.2 MeV γ rays and 0.6 MeV protons, respectively. However, provided B-10 concentrations are sufficiently high a large proportion of dose will be due to the capture of thermal neutrons by B-10 with a cross section of 3800 barns. The subsequent nuclear fission process is:

$$\begin{aligned} {}^{10}_{5}B + {}^{1}_{0}n &\xrightarrow{6.3\%} {}^{7}_{3}Li + {}^{4}_{2}He \qquad Q = 2790\,keV \\ &\xrightarrow{93.7\%.} {}^{7}_{3}Li + {}^{4}_{2}He + g \qquad Q = 2310\,keV \end{aligned} \tag{7.1}$$

The alpha and lithium reaction products are high LET particles that deposit their energy in ranges of 4.1 and 7.7 μm respectively, comparable to typical mammalian cell dimensions. Information on the energy and ranges of the main BNCT products is provided in section 5.4.

The energy deposition is highly localized in nature and depends strongly on the subcellular spatial deposition of the B-10 nuclei and the subcellular morphology. In addition to the dose due to B-10 neutron capture, many other dose components are present:

1. Protons as recoil products from the interaction of fast and epithermal neutrons with H-1 nuclei and
2. Protons as a product of N-14 neutron capture.
3. Gamma rays arise from H-1 neutron capture and from the neutron source and surrounding materials.

Studying complex radiation environments with such localized energy deposition is accomplished using the tools of experimental and theoretical microdosimetry. In particular, experimental microdosimetry provides techniques for separating varying LET components and measuring dose due to B-10 neutron capture, total dose, beam quality and dose enhancement factors. The separation of LET components using microdosimetric methods is important due to the varying biological effectiveness of these components.

Historically, the primary experimental tool for microdosimetric measurements is the proportional gas counter [11]. Wuu [262] first applied a Rossi type proportional counter to BNCT dosimetry. This has been followed by other studies by Maughan [263] and Kota [154, 264].

Wuu's experiments used paired TE and TE + boron chambers in the epithermal beam at BNL with some results shown later in section 7.3.2.5. The 2.5 cm diameter TE Rossi proportional counter was built with 50 ppm boron incorporated into the 3 mm thick walls. The same concentration of boron was also incorporated into the gas. The various

dose components of the beam, as described above, may be quantified. Gamma rays and fast protons occur at low LET (2-3 keV), Bragg peak protons at moderate LET (80 keV), heavy recoils and BNCT products at high LET (300 keV). The dual chamber method assists in discriminating the boron dose from other components. Zamenhof writes that such microdosimetric measurements "may contribute to a better understanding of the radiobiology of the B-10 reaction as well as that of the associated background dose components" [257].

However, proportional counter microdosimetry does not accurately reflect the cellular distribution of boron, which is dependent on the delivery agent and subcellular structure. Zamenhof and Solares [81] addressed the issue in the development of high resolution quantitative autoradiography (HRQAR) combined with a novel 2D Monte Carlo simulation. HRQAR uses a 0.8 μm thick film of Lexan as the track detection medium placed in intimate contact with an equally thin tissue sample. Image processing techniques applied to the track detector film identify boron. Their hypothesis is that a full 3D characterization of the cellular architecture and the corresponding B-10 distribution can be mimicked by sectioning a single plane through many cells in the tumor matrix, deriving the boron distribution within this single plane by HRQAR, and performing a 2D Monte Carlo calculation within this plane over many cell sections to obtain the desired microdosimetric parameters. A spatial resolution of 1-2 μm and a sensitivity of 1 ppm boron may be achieved, although the process is very time consuming, taking 8 days for the HRQAR.

Silicon microdosimetry can not achieve the information quality of the autoradiography method although it will offer benefits over the proportional gas counter without the complexity of autoradiography. These benefits include high spatial resolution and the ability to vary the spatial localization of boron to reflect real tissue distributions.

This chapter provides the first reported measurements using boron coated silicon diode arrays as microdosimetric detectors in BNCT. The purpose is to present some preliminary results for this new detector technology. Experiments were performed at BNL, Kyoto University Research Reactor (KUR) and MIT, in chronological order. At BNL, the effects of various boron-coating options on microdosimetric spectra are investigated along with device orientation effects. A U-235 coating is also tested to simulate device behavior in a heavy ion therapy beam. At KUR, the internal $p+$ doping

boron was extensively used to simultaneously record microdosimetric spectra and thermal neutron flux measurements. Finally, the experiments at MIT tested the microdosimeter under an epithermal accelerator source.

The subject of tissue equivalence of silicon based microdosimetric measurements in BNCT was discussed in section 5.4. This work demonstrated that under appropriate geometrical scaling (0.63) silicon detectors with well-known geometry will record energy deposition spectra representative of tissue cells of equivalent shape.

7.2 Thermal Neutron Sensitivity of Microdosimeter Construction

A necessary step in establishing the thermal neutron response of the microdosimeter is to examine the device elemental composition and thermal neutron capture cross-section as shown in Table 7.1. A similar table was constructed for the main materials on top of the detector; air and Lucite as shown in Table 7.2. Materials below the detector may be neglected since the silicon substrate is 300 μm thick and ion products from thermal neutron reactions will not have sufficient range to enter the SOI sensitive volume. Within each table, the reactions that produce ion products through (n,p) or (n,α) reactions are highlighted in bold typeface. For each of these reactions, the relative probability of a thermal neutron interaction within the microdosimeter construction was calculated. The probability of an interaction with N atoms is given by the macroscopic cross-section S (in cm^2) for the interaction of thermal neutrons defined as

$$\Sigma = s\ N \tag{7.2}$$

where s is the thermal neutron cross-section for the element (sometimes called the microscopic cross-section), and N is the number of atoms present. Thus, the count rate R (in counts/s) generated in the detector is given by

$$R = k_r \Sigma \Phi_n \tag{7.3}$$

where F_n is the thermal neutron flux (in neutrons/cm^2/s) and k_r is a correction factor which accounts for the proportion of generated recoil products that reach the sensitive volume and are detected above the microdosimeter noise threshold. Note that given accurate values for k and S (or N), the thermal neutron flux may be accurately derived from count rate measurements using equation (7.3).

The boron-10 within the detector *p*+ region will be used frequently in this work as a thermal neutron detector material. The relative probability of an interaction with a material is calculated as the ratio of the thermal neutron count rate for that material to the count rate for the *p*+ region B-10. For all reactions except the $^{14}N(n,p)^{14}C$ reaction we assume that all reactions produce a detectable event (i.e. $k_r = 1$). That is, the relative probability is simply the ratio of macroscopic cross sections. This assumption is a course approximation useful for this preliminary analysis. Later simulations will provide more accurate values of k_r where appropriate. In half of the $^{14}N(n,p)^{14}C$ reactions, a 40 keV carbon ion recoil will be ejected in the direction of the sensitive volume. This recoil will generally either not reach the sensitive volume or will have an energy below the noise threshold. Thus $k_r \cong 0.5$ for the $^{14}N(n,p)^{14}C$ reaction. Table 7.3 summarizes macroscopic cross-sections for ion product producing components and the corresponding relative probabilities. The following points arise from the comparison shown in Table 7.3:

- The important count rate generating materials are (in order of importance), 1% B-10 in a Lucite coat or cover (optional, if present), B-10 in the *p*+ region, N-14 in air (if present, may not have an air gap above the device), N-14 from the TiN barrier layer.
- The relative number of events due to O-17 (in air, Lucite or oxide) or Ar-36 (in air) reactions are negligible.
- Similarly, the number of thermal neutron reaction events due to B-10 in the substrate is negligible by four orders of magnitude in comparison with B-10 in the *p*+ region.
- The relative number of thermal neutron reaction events due to N-14 in the TiN is quite small, about 6%.
- A 200 μm air gap (with N-14) on top of the detector may produce an appreciable (30%) thermal neutron count rate in comparison with the *p*+ region.
- A 1% B-10 impregnated Lucite cover on top of the detector will produce a thermal neutron count rate up to 1300 times larger than the *p*+ region. This will be an overestimate since $k_r<1$ for the boron cover.

These findings are useful for understanding the spectra produced by the experiments discussed in the following sections.

Table 7.1. Elements in silicon microdosimeter construction with isotopic abundance, thermal neutron reaction and cross-section. Reactions in bold produce ion products. Reaction data from Mughabghab [265]. Isotopic abundance from Krane (appendix C) [266].

Element	Isotope	Isotopic Abundance (%)	Reaction	Cross-section (barns)	Comments
Boron	${}^{10}_{5}B$	19.61	**^{10}B(n,α)^{7}Li**	3837	*p*+ doping and substrate doping
	${}^{11}_{5}B$	80.39	^{10}B(n,γ)^{12}B	5.5×10^{-3}	
Nitrogen	${}^{14}_{7}N$	99.635	**^{14}N(n,p)^{14}C**	1.83	TiN Barrier layer
	${}^{15}_{7}N$	0.365	^{14}N(n,γ)^{15}N	2.4×10^{-5}	
Oxygen	${}^{16}_{8}O$	99.759	^{16}O(n,γ)^{17}N	1.9×10^{-4}	Oxide (SiO_2) layer
	${}^{17}_{8}O$	0.037	**^{17}O(n,α)^{14}C**	0.235	
	${}^{18}_{8}O$	0.204	^{18}O(n,γ)^{19}N	1.6×10^{-4}	
Aluminium	${}^{27}_{13}Al$	100	^{27}Al(n,γ)^{28}Al	0.231	Metal tracks
Silicon	${}^{28}_{14}Si$	92.23	^{28}Si(n,γ)^{29}Si	0.177	Substrate
	${}^{29}_{14}Si$	4.67	^{29}Si(n,γ)^{30}Si	0.101	
	${}^{30}_{14}Si$	3.1	^{30}Si(n,γ)^{31}Si	0.107	
Titanium	${}^{46}_{22}Ti$	8.2	^{46}Ti(n,γ)^{47}Ti	0.59	TiN Barrier layer
	${}^{47}_{22}Ti$	7.4	^{47}Ti(n,γ)^{48}Ti	1.7	
	${}^{48}_{22}Ti$	73.7	^{48}Ti(n,γ)^{49}Ti	7.84	
	${}^{49}_{22}Ti$	5.4	^{49}Ti(n,γ)^{50}Ti	2.2	
	${}^{50}_{22}Ti$	5.2	^{50}Ti(n,γ)^{51}Ti	0.179	
Arsenic	${}^{75}_{33}As$	100	^{75}As(n,γ)^{76}As	4.5	*n*+ doping
Gold	${}^{197}_{79}Au$	100	^{197}Au(n,γ)^{198}Au	98.65	Attaching/wires

Table 7.2. Elements in overlayer materials (air and Lucite (unboronated)) with isotopic abundance, thermal neutron reaction and cross-section. Reactions in bold produce ion products. Reaction data from Mughabghab [265]. Isotopic abundance from Krane (appendix C) [266].

Element	Isotope	Isotopic Abundance(%)	Reaction	Cross-section (barns)	Comments
Hydrogen	${}^{1}_{1}H$	99.985	^{1}H(n,γ)^{2}H	0.33260	53.33 atom% in Lucite
	${}^{2}_{1}H$	0.015	^{2}H(n,γ)^{3}H	5.19×10^{-4}	
Carbon	${}^{12}_{6}C$	98.89	^{12}C(n,γ)^{13}C	3.53×10^{-3}	33.33 atom% in Lucite
	${}^{13}_{6}C$	1.11	^{13}C(n,γ)^{14}C	1.37×10^{-3}	
Nitrogen	${}^{14}_{7}N$	99.635	**^{14}N(n,p)^{14}C**	1.83	75.50 atom% in Air
	${}^{15}_{7}N$	0.365	^{14}N(n,γ)^{15}N	2.4×10^{-5}	
Oxygen	${}^{16}_{8}O$	99.759	^{16}O(n,γ)^{17}N	1.9×10^{-4}	23.20 atom% in Air
	${}^{17}_{8}O$	0.037	**^{17}O(n,α)^{14}C**	0.235	13.33 atom% in Lucite
	${}^{18}_{8}O$	0.204	^{18}O(n,γ)^{19}N	1.6×10^{-4}	
Argon	${}^{36}_{18}Ar$	0.337	**^{36}Ar(n,α)^{33}S**	5.5×10^{-3}	1.30 atom% in Air
			^{36}Ar(n,γ)^{37}Ar	5.2	
	${}^{38}_{18}Ar$	0.063	^{38}Ar(n,γ)^{39}Ar	0.8	
	${}^{40}_{18}Ar$	99.60	^{40}Ar(n,γ)^{41}Ar	0.66	

Table 7.3. Relative probability of thermal neutron interaction with selected microdosimeter/overlayer elements. All elements selected produce ion recoil products through (n,p) or (n,α) reactions.

Element/Component	Number Atoms	Micro X-section (10^{-24} cm^2)	Macro X-Section (cm^2)	Relative Prob.	Comments
^{10}B in *p*+ region	2.22×10^{13}	3837	8.52×10^{-8}	1	Area of *p*+ region is 0.022 cm^2 and boron ion implant fluence 1.5×10^{15} atoms/cm.
^{10}B in substrate	2.62×10^{9}	3837	1.01×10^{-11}	10^{-4}	Substrate thickness = 2 μm, area = small diode array (40×120 cells @ 30×30μm^2)
^{10}B in 1% B Lucite	2.89×10^{16}	3837	1.11×10^{-4}	1300	Lucite thickness = 6.1 μm (range of 1470 keV α recoil) area = small array 0.044 cm^2
^{14}N in TiN	5.57×10^{15}	1.83	1.01×10^{-8}	0.06	TiN thickness = 0.1 μm, area = 0.011 cm^2, Density TiN=5.33 gm/cm^3.[267]
^{14}N in Air	3.31×10^{16}	1.83	6.07×10^{-8}	0.30	Air thickness = 200 μm, area = small array 0.044 cm^2
^{17}O in SiO_2	1.47×10^{14}	0.235	3.46×10^{-11}	4×10^{-4}	SiO_2 thickness = 2 μm (1 μm above and 1 μm below SOI), area = small array 0.044 cm^2
^{17}O in Air	3.77×10^{12}	0.235	8.86×10^{-13}	10^{-5}	Air thickness = 200 μm, area = small array 0.044 cm^2
^{17}O in Lucite	1.41×10^{14}	0.235	3.31×10^{-11}	4×10^{-4}	Lucite 6.1 μm thick.
^{36}Ar in Air	1.92×10^{12}	5.5×10^{-3}	1.06×10^{-14}	10^{-7}	Air thickness = 200 μm, area = small array 0.044 cm^2

Note 1: See chapter 4 for a device description and Appendix B for additional layout information.

2: Macro X-Section = Micro X-Section × Number atoms,
Relative probability = Macro X-Section/ Macro X-Section for ^{10}B in *p*+ region

7.3 Experiments at Brookhaven National Laboratory (*Boron and U-235 Coating Investigation*)

7.3.1 Materials and Methods

7.3.1.1 Description of Brookhaven Medical Research Reactor(BMRR)

The 3 MW BMRR is an adjunct to the Medical Research Center at Brookhaven National Laboratory (BNL). BMRR has three irradiation facilities: an epithermal neutron irradiation facility (ENIF), a thermal neutron irradiation facility, and a broadbeam facility. For this study, we used the ENIF since this beam is used for current clinical trials. A complete description of the facility and collimator design is provided by Liu [268] with a diagram shown in Figure 7.1. In our case, a Lucite cubic phantom was positioned at the irradiation treatment port immediately adjacent to the collimator. The center of the cube was aligned to the center of the collimator. The reactor power used for the experiments was 300 kW for boron coating measurements and 30 kW for the U-235 studies selected at the maximum power allowable without significant pile-up effects observed. The thermal neutron flux at 6.5 cm depth in the Lucite phantom was calculated [268] as 6.29×10^{7} n/cm^2/s.

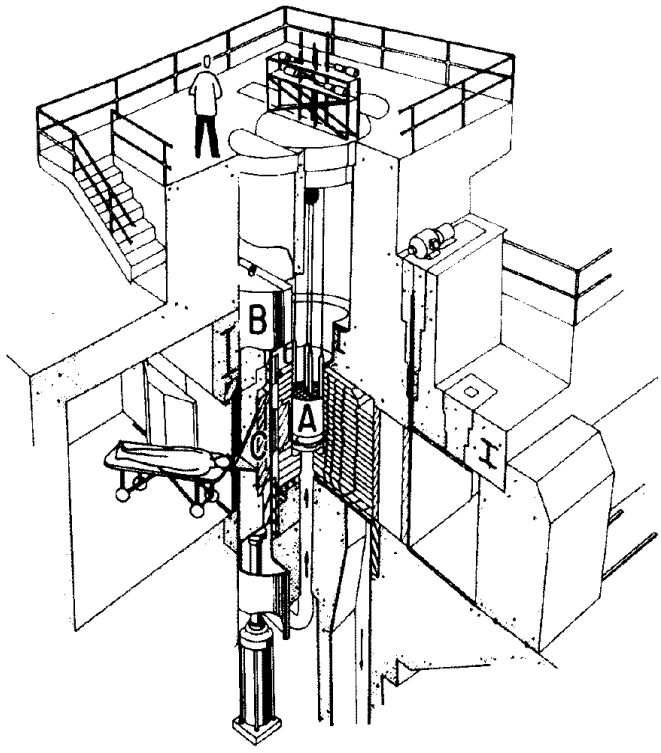


Figure 7.1. Schematic diagram of the epithermal beam and patient irradiation facility at the BMRR. [255] *A*, core of the reactor; B, moveable shutter; C, epithermal neutron filter. A patient is shown with his head in the neutron beam port. Filters and moderators adjust the energy spectrum to maximize neutrons in the epithermal energy range of ~1 eV to 10 keV and minimize those outside this range.

7.3.1.2 Description of probe assembly and device coating (B-10 and U-235)

The microdosimeter probe assembly used was "Probe Assembly #1" fully described previously in section 4.3. The microdosimeter used was a 2 μm SOI device with the small diode size (10×10 μm^2 junction) array selected. This device was selected because the sensitive volume was the smallest available. The charge collection characteristics of the device were fully described in section 6.2.4.1. The device was reverse biased at 10V.

Two devices were prepared. One without boron coating and the other with a Lucite coating containing 1% B-10. The boron coating models the biological situation where boron accumulates on the cell surface (e.g. boron attached to monoclonal antibodies) and we are interested in the microdosimetric spectra within the cell nuclei from a two dimensional array of cells. The device overlayer of between 1-1.35 μm (composed of SiO_2 and Al) crudely represents the cytoplasm spacing between the cell nucleus and surface. The coating was developed by dissolving Lucite shavings in dichloroethane. Decaborane was then added to obtain the required concentration of B-10 to an accuracy of ±5%. Drops of the solution were then placed onto the circuit and allowed to dry (~20 minutes). Note that extreme care should be taken in this process. Dichloroethane is volatile, its fumes are poisonous, and a mixture of decaborane and dichloroethane is known to be shock sensitive.

The minimum coating thickness required is given by the range (7.4 μm) of a 1.78MeV alpha produced by boron neutron capture. Conversely, too large a thickness may attenuate the thermal neutron fluence. Alpha spectroscopy was performed as an indicator of coating thickness. Since a 5.3MeV alpha has a range in Lucite of 31.9 μm, we would expect no charge collected by the device with a coating greater than this thickness. This was observed after 5 coatings.

However, once coated the device cannot be used for non-boron measurements or alpha spectroscopy experiments. A possible solution is to use a detachable boron coated Lucite lid in close proximity to the detector's surface. A thin Lucite lid with a 1% boron coating was constructed for comparison with the direct coating approach. The air gap between the lid and the detector surface was estimated to be between 100-200 μm.

A third Lucite lid was fabricated with a thin film of aluminum backed Uranium-235 glued to the underside of the lid. U-235 has a high thermal neutron fission cross-section

(580 barns). The U-235 nucleus splits in some 40 or so modes following the absorption of a thermal neutron. An average energy of 195 MeV is released in the fission process with a large portion of the energy (162 MeV) carried away by the charged fission fragments. Thus, a U-235 coated lid may be used to test the microdosimeter's performance under simulated heavy ion treatment conditions.

7.3.1.3 Description of phantom

The phantom consists of a sequence of Lucite blocks each 2.5×15×15 cm^3. Using a Lucite nut and bolt, 6 blocks are connected together to form a 15 cm sided cube. A similar Lucite cube has been used at BNL for previous dosimetry and Monte-Carlo studies. One block is designed with a recess for insertion of the microdosimeter probe. Thus, by rearranging the blocks we may move the probe to different positions within the cube. The primary position for measurements in this paper was 6.5 cm depth along the central axis. A 1-meter BNC compatible coaxial cable runs through the probe to connect the microdosimeter to a preamplifier.

7.3.1.4 Microdosimetric measurements

Using the facilities and techniques described in the previous sections microdosimetric spectra were obtained for each coating and lid condition (i.e. boron coating, boron lid and U-235 lid). Experiments were also performed to determine the effect of device orientation on microdosimetric spectra.

The multi-channel analyzer provides a spectrum of the number of events recorded at different energies. The energy deposited by each event is divided by the mean chord length to give the lineal energy (y). To convert to a tissue equivalent microdosimetric spectrum the mean chord length of the silicon device is simply scaled by a factor of 1/0.63 as described in section 5.4. Furthermore, the mean chord length should be such that the dose mean lineal energy is equivalent to that produced by a spherical proportional counter. The estimation of the mean-chord length was determined using simulation methods, based on these considerations, as described in the following section.

7.3.1.5 Simulation of microdosimetric measurements and MCL estimation

Simulation of the microdosimetric measurements may be performed using the Monte Carlo program developed in section 5.4.2. Such simulations provide increased understanding of experimental spectra and may also be used to estimate mean chord

lengths (MCL) required for lineal energy spectra presentations. The program was modified to take into account the collection efficiency within the sensitive volume. The Monte Carlo program transports an ion along its range in small increments of Dr = 0.01 μm. Within the sensitive volume, the energy deposited in Dr is multiplied by the collection efficiency at the current ion position to give the energy collected. The total charge collected E_{col} is simply the sum over all ion positions within the sensitive volume:

$$E_{col} = \sum_{i=1}^{i=n} (E(r_{i+1}) - E(r_i))C(x_i, y_i)$$
$$\text{where} \quad r_{i+1} = r_i - \Delta r, \quad \Delta r = 0.01um \tag{7.4}$$
$$x_1 = x_s, x_{i+1} = x_i + d_x \Delta r, \quad y_1 = y_s, y_{i+1} = y_i + d_y \Delta r,$$

and r_1 is the range of the ion upon entering the SV, $E(r)$ is the energy-range relationship, (x_i,y_i,z_i) is the ion position, (x_s,y_s,z_s) is the first point on entering the SV, (x_n,y_n,z_n) is the last point on exiting the SV or the point at the end of the ion range (whichever comes first), (d_x,d_y,d_z) are the direction cosines of the ion, and $C(x,y)$ is the collection efficiency. The collection efficiency function for the 10 × 10 μm^2, 2 μm SOI device was estimated in section 6.2.4.1. Note that the collection efficiency is defined in two dimensions and assumed constant in the z direction. The program can also calculate the chord length l as follows:

$$l = \sum_{i=1}^{i=n} \Delta r C(x_i, y_i) \tag{7.5}$$

The mean chord length was calculated for both the boron lid and boronated Lucite coating on top of the 10 × 10 μm^2, 2 μm SOI device. The dimensions of each of the simulations are shown in Figure 7.2. The entire device of 40 × 120 diodes was simulated with the collection efficiency for each diode as determined in section 6.2.4.1. Note, that the diode sensitive depth is 2 μm in the $n+$, $p+$ regions and 1.82 μm elsewhere with the variation due to the LOCOS region consuming silicon. The generation volume, consisting of the boron coating layer, need only extend above the sensitive volume to the maximum range of the generated alpha particles (7.55 μm) in Lucite. The overlayer was simplified to consist of the predominant material (SiO_2) with an average thickness calculated as 1.05 μm. Also note that the simulation assumes negligible nitrogen content in any of the components compared with the high boron

concentration in the Lucite. The simulations will be further discussed in the following results section.

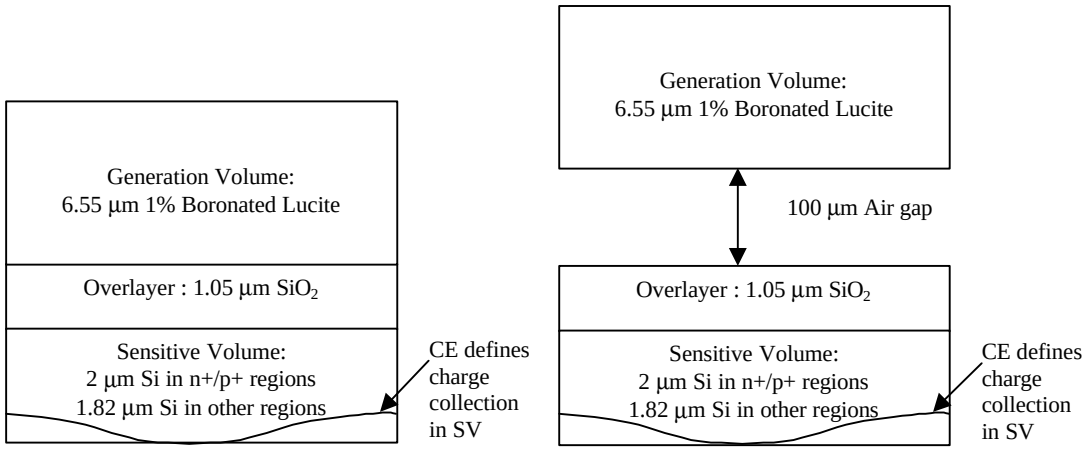


Figure 7.2. Cross-section of boron-coating simulation on top of 10×10 μm^2, 2 μm SOI diode array (40×120 diodes, each cell 30×30 μm^2). The GV is ($1215 \times 3615 \times 6.55$ μm^3) whilst the SV is (1200×3600 μm^2 with a depth of 2 μm in the *n*+, *p*+ regions and 1.82 μm elsewhere) . The maximum range of 1470 keV alpha particles in Lucite is 7.55 μm. The left side shows the boron coat configuration and the right side shows the boron lid configuration.

The calculated chord length distributions are shown in Figure 7.3. The mean chord length $\bar{l}_{Ksi}$ is 1.16 μm for the coat and 1.12 μm for the lid, a value quite low compared to the 2 μm thick sensitive volume. This low value arises from the large number of stoppers due to the short range of the lithium and alpha particles relative to the overlayer and sensitive volume thickness. Two corrections to the MCL are required. Firstly, the MCL should be adjusted so that the dose mean lineal energy is equivalent to that produced by a spherical proportional counter and secondly the tissue equivalent correction is required.

As discussed in detail in chapter 3, the spherical shaped counter is the main reference used in microdosimetric measurements. Therefore, the MCL is corrected to provide a dose mean lineal energy $\bar{y}_d$ that is equivalent to a sphere. Recall from section 3.4, the corrected effective MCL $\bar{l}_{Keff}$ is :

$$\bar{l}_{Keff} = \frac{\bar{l}_{Ksi}}{hz} \tag{7.6}$$

where z = 0.63 is the TE correction factor discussed in section 5.4, and h is a shape correction factor given by equation (3.37) as:

$$h = \frac{\bar{y}_{d,sphere}}{\bar{y}_{d,K}} \tag{7.7}$$

The dose mean lineal energy for a sphere is $\bar{y}_{d,sphere}$ = 9/8 L, where L is the particle LET (assumed constant, see section 3.3.3.1). From the data of Figure 7.3, the dose mean lineal energy for the boron-coated geometry is $\bar{y}_{d,K}$ = 1.42 L giving h = 0.79 and for the boron-lid geometry is $\bar{y}_{d,K}$ = 1.43 L giving h = 0.79. Thus, the corrected MCL for the boron coating and lid measurements are $\bar{l}_{Keff}$ (coating) = 2.32 μm and $\bar{l}_{Keff}$ (lid) = 2.26 μm.

The MCL used for displaying measurements made using the U-235 coating use the same MCL as the boron coated device. An accurate MCL is not required for this measurement since the purpose of the experiment was a comparative study of the variation in charge collection spectra with voltage under heavy ion irradiation.

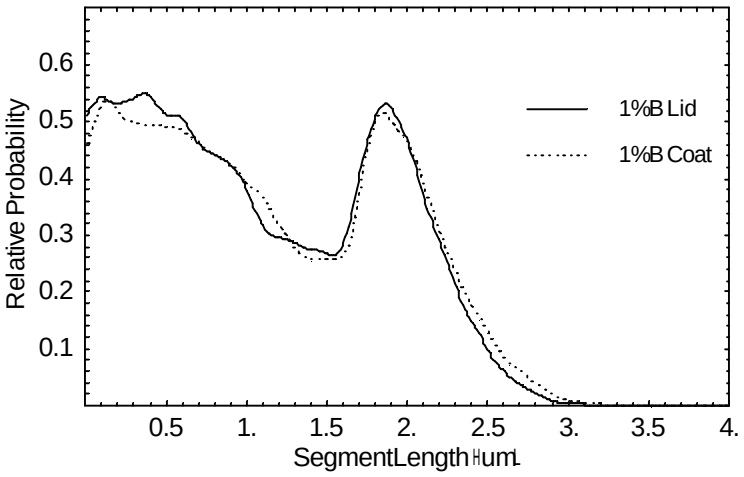


Figure 7.3. Segment length distribution produced by thermal neutron irradiation of a boron/Lucite coating and lid configurations above the 10×10 μm^2, 2 μm SOI diode array. Simulation geometry is depicted in Figure 7.2.

7.3.2 Experimental Results and Discussion

7.3.2.1 Evaluation of boron coating methods

A microdosimetric spectrum was obtained for a device with no boron coating in order to determine the influence of boron used in the construction of the device. Boron is used as the p-type dopant in the $p+$ regions of the chip. The spectrum shown in Figure 7.4, and

scaled by a factor of 100 to compare with a boron coated device, indicates the relatively small contribution from boron fission events within the device's *p*+ doped region compared to the boron coating. The excellent fast neutron filtering of the epithermal beam is also demonstrated by the small recoil proton component at lower lineal energies.

This spectrum also indicates the validity of ion implanting boron directly into the chip in order to simulate boron deposition in various regions of a cell, an idea recently proposed by Rosenfeld [71]. Such local B-10 concentration variation is not possible with a proportional gas counter. The *p*+ region is manufactured by ion implantation of 5×10^{15} boron ions/cm^2 at an energy of 30 keV and over an area 17% of the total diode area. This gives a B-10 concentration of approximately 1×10^{20} atoms/cm^3 or 2000 ppm for 20% isotopic abundance and assuming uniform B-10 distribution within a 0.1 μm depth region. Concentrations of 50 ppm, which are equivalent to clinically achievable conditions, could easily be obtained by reducing the implant to 1.2×10^{14} boron ions/cm^2. The distribution of boron through the cell may also be varied by changing the *p*+ layout or increasing the substrate boron doping concentration. The latter strategy would require substrate doping of the order of 1.2×10^{19} B-atoms/cm^3 to obtain a uniform B-10 concentration of 50 ppm. However, device operation would be severely compromised at such a high concentration due to carrier lifetime and collection efficiency reduction. Note that in the current design thermal neutron interactions with the boron *p*+ region will greatly exceed reactions with any of the overlayer constituents (Aluminium, Silicon, Oxygen, Titanium and Nitrogen) or the boron within the bulk silicon (see section 7.4). This is due to the relatively high thermal neutron capture cross-section of boron and a sufficiently large number of ions implanted. The use of the boron *p*+ region for thermal neutron studies is investigated in more detail in section 7.4.

A comparison was made of the microdosimetric spectra obtained using direct boron coating versus a detachable boron coated lid. As shown in Figure 7.5, the spectrum for the lid has a comparatively smaller high LET component and a reduced integral count rate. The 100-200 μm air gap when using the lid accounts for the small reduction in high LET components. The alpha and lithium ions will typically be past their Bragg peak upon entering the sensitive volume since they must pass through the device overlayer structures. Therefore, any additional overlayer will decrease the total energy

deposited. A 100 μm air gap is equivalent to 0.07 μm of SiO_2, in terms of energy loss of the BNCT ions, which effectively amounts to a 7% thicker overlayer. Thus, the additional energy loss and reduction in mean chord length is relatively small.

Despite the relatively small difference, direct coating of the chip is the preferred method of boron deposition given the attenuation of energy in the air gap and the possible large variation in the air gap distance using the lid method. Based on these observations, the coated device was used for the remainder of the BNL work. The acquisition time for the spectra obtained in Figure 7.4 and Figure 7.5 was only 3 minutes at 300 kW reactor power. The ability of the silicon microdosimeter to function at full reactor power is an additional advantage over the proportional gas counter.

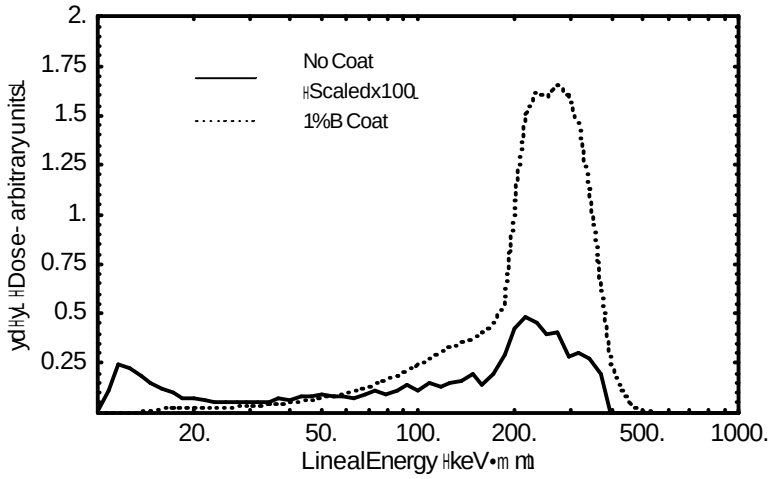


Figure 7.4: Microdosimetric spectra for non-boron coated device compared with boron coating. The spectra were obtained at a depth of 6.5 cm in the Lucite phantom with a reactor power of 300 kW. Note that the no coat spectrum is scaled up by a factor of 100. The peak at 200 keV/μm in the no coat spectrum arises from boron *p*+-dopant in the device.

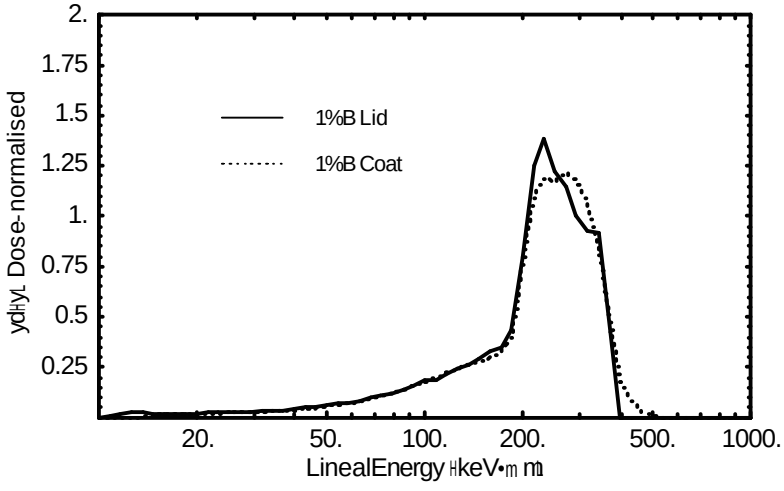


Figure 7.5. Microdosimetric spectra for various coating options. The spectra were obtained at a depth of 6.5 cm in the Lucite phantom with a reactor power of 300 kW.

7.3.2.2 Evaluation of device orientation effects

In order to determine the sensitivity of the device to beam orientation, the Lucite phantom was rotated with the detector positioned in the center of the phantom. The horizontal detector position gave a reduction in integral counts of 6.8% when compared to the vertical (possibly due to a small variation in device depth) with minimal changes in spectral character. Thus, the device is relatively insensitive to orientation. This result is to be expected given the isotropic nature of thermal neutrons.

7.3.2.3 Measurement using U-235 coated diode array

Measurements were performed on the diode array with a small piece of U-235 coated aluminum foil placed on the underside of a Lucite lid. The lid fits onto the recess in the device package, which contains the diode array. The air gap distance between the foil and device is estimated at between 100-200 μm. The fragments produced by the U-235 fission are heavy ions which produce dense plasma tracks in the silicon. Thus, the device must be sufficiently reverse biased to minimize recombination of electron-hole pairs in the plasma track. The purpose of this experiment was to determine the required reverse bias for heavy ions. This provides valuable information for possible future experiments at heavy ion therapy facilities. Figure 7.6 indicates that for voltages greater than 5 volts the difference between spectra is minimal. Therefore, under heavy-ion conditions, the minimum recommended bias voltage is approximately 5 volts, although higher voltages give slightly improved performance. Note that at zero bias recombination significantly reduces the charge collected by the microdosimeter.

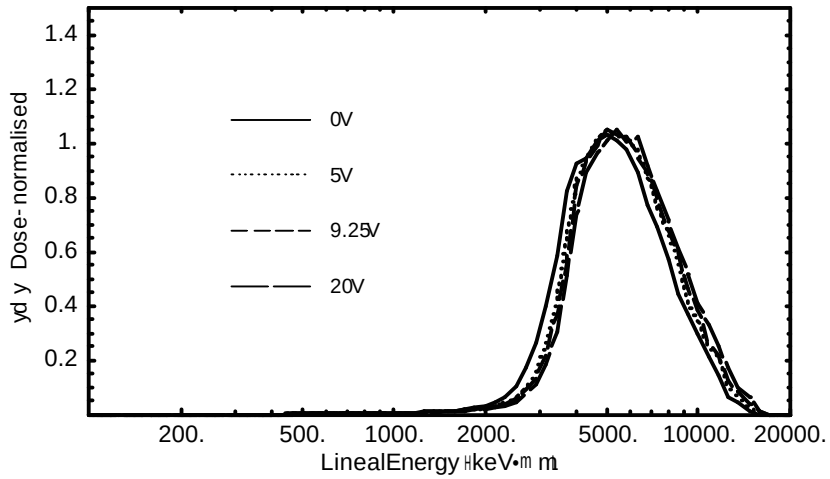


Figure 7.6. Bias dependence of U-235 Covered diode array at a depth of 6.5 cm in Lucite phantom, Reactor Power = 30 kW

7.3.2.4 Comparison with Simulation

The simulations indicate some discrepancies with experimental results as shown in Figure 7.7. The peak at 500 keV in the energy distribution for the coated device is located at 600 keV in the simulation and the simulation has a higher number of low energy events less than 200 keV. Reducing the device overlayer thickness and SOI thickness provides an improved match, although such simulations are not shown here. The simulation shown indicated that 78% of events arise from α-particle interactions with the remainder being lithium ion events. The lithium events contribute to the spectra only for energies less than 300 keV since a significant proportion of the lithium ion energy is absorbed in the overlayer. This is shown in Figure 7.7, where all energies greater than 300 keV are due to α events.

Note that the lineal energy dose distribution offers a better correspondence than the energy distribution since it involves a higher degree of smoothing and emphasizes high energy events which show a reasonable match.

Deviations between the Monte-Carlo simulation and measurements may be attributable to one or more of the following:

- Variations in overlayer structures are neglected. The overlayer is assumed uniform in thickness and composition. Inclusion of overlayer variations will broaden the spectra, which should improve the correspondence between theory and experiment
- The charge collection model is inadequate. The ions generated by BNCT reactions are close to their Bragg peaks as seen by the figures of section 5.4.1. The collection efficiency was calculated using normally incident 2 MeV alpha particles (LET~250 keV/μm) and 5 MeV alpha particles (LET~150 keV/μm). Larger peak LETs approaching 350 keV/μm are observed for the isotropic BNCT alpha. It is conceivable that recombination losses may be larger in the higher LET particles. Future work should examine the variation, if any, in CE with high LET particles.

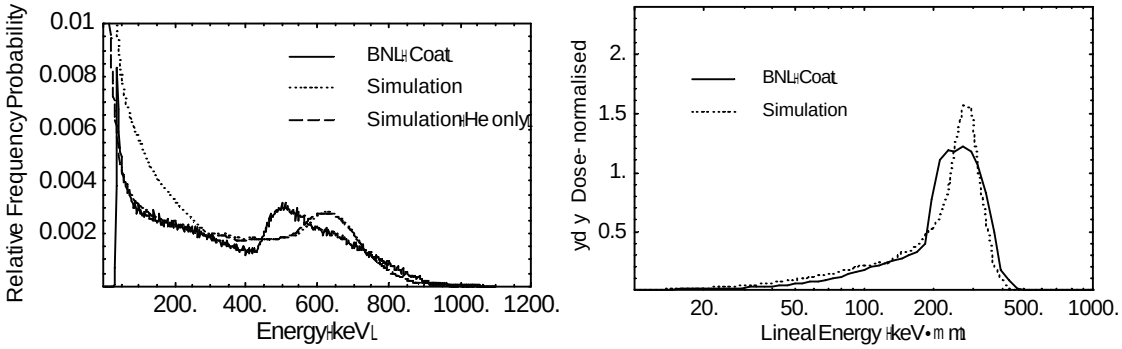


Figure 7.7: Comparison of experimental results (1% B coated diode array (10x10μm) at 6.5 cm) with Monte-Carlo Simulation. The left side shows the energy probability distribution and the right side shows the same data presented in standard yd(y) form.

7.3.2.5 Comparison with Proportional Counter Microdosimetric Measurements

Only a few studies have been performed using proportional gas counters to measure BNCT microdosimetric spectra [154, 262-264]. The study performed by Wuu [262] is most appropriate for comparison with the diode array since both measurements were performed at BMRR. Wuu performed measurements using a 2.5 cm spherical TE proportional gas counter with 50 ppm TE walls and gas. Site diameters of 2 and 6 μm, corresponding to mean chord lengths of 1.3 and 4 μm, were simulated by varying gas pressure.

Figure 7.8 provides a comparison of these measurements with the diode array. The spectra show similar peaks although a direct comparison with the diode array is difficult since the pattern of boron deposition differs significantly between detectors. Boron deposition is throughout the entire detector for the proportional counter whilst only on the surface of the diode array. Differences in the spectra may be expected primarily due to different chord-length distributions between a spherical counter geometry and the diode array's RPP type geometry. Wuu's device contains boron within the counter so "starters" and "insiders" are included whilst the boron coated diode array measures only "crossers" and "stoppers" (See section 3.1 for terminology definition). Furthermore, the diode array overlayer of 1.05 μm (on average) separates the boron from the detector. This will reduce somewhat the energy of alpha and lithium ions as well as altering the chord length distribution. Such effects account for the lower lineal energy recorded by the diode array.

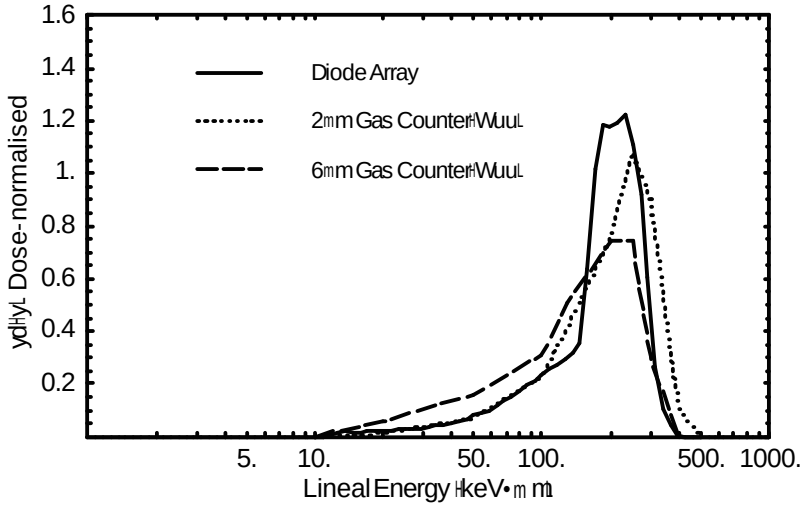


Figure 7.8: Comparison of proportional counter [262] with diode array at BMRR. The mean chord length for the diode array was 2.85 µm.

7.4 Experiments at Kyoto University Research Reactor (*Simultaneous microdosimetry and thermal neutron flux measurements*)

Based on experience gained in the previously discussed experiments, work was performed at the Kyoto University Research Reactor (KUR) principally using the boron *p+* region of the microdosimeter as the thermal neutron sensitive component. Using the *p+* region of the device removes the attenuating effect of the overlayer and presents a boron spatial distribution more nearly representative of possible biological boron distributions. However, the lower boron content makes the device more sensitive to neutron reactions with nitrogen in the TiN and air gaps as indicated in section 7.2. The performance of the *p+* region as a thermal neutron detector and the effect of the air gap will be studied in this section.

7.4.1 Materials and Methods

7.4.1.1 Description of Kyoto University Research Reactor (KUR)

The heavy water thermal neutron facility at KUR utilizes a 5 MW full power reactor. The reactor runs continuously at full power and the beam spectrum and thermal neutron flux are varied using heavy water, Boral and cadmium filters. A complete description of the facility and collimator design is provided by Kobayashi [269, 270] with diagrams shown in Figure 7.9 and Figure 7.10. In order, from the reactor core, the filters consist of an epithermal neutron moderator (80% aluminium plates/20% heavy water, 66 cm total thickness), a neutron energy spectrum shifter (consisting of 3 D_2O tanks, 10, 20 and 30 cm thick), a 30 cm D_2O water shutter, two thermal neutron filters (consisting of

1 mm Boral and 6.4 mm cadmium plates), and an adjustable bismuth layer typically 18.4 cm thick. Various irradiation modes are possible depending on the state of the filter such as open, closed, tank empty or tank full. The irradiation mode is specified by a coding scheme as shown below.

Cadmium Filter	Boral Filter		30 cm D_2O	20 cm D_2O	10 cm D_2O		Bismuth (F=18.4 cm)		Collimator Filter (E1=epithermal)	
C	B	—	1	1	1	1	—	F	—	E1	All filters in place, D_2O tanks full
O	O	—	0	0	0	0	—	E	—	E1	All filters in open, D_2O tanks empty

The presence of the boral or cadmium filter is designated by a "C" or "B", respectively, and the absence by an "O". A full D_2O tank is assigned a "1" and an empty tank a "0". The bismuth filter and collimator filter for all our experiments are in the F-E1 positions corresponding to 18.4 cm of bismuth and the E1 epithermal collimator.

There are three standard irradiation modes at KUR for BNCT:

1. The standard *thermal* neutron irradiation mode, OO-0011-F: tumor seated within a few cm of the surface such as melanoma.

2. The standard *mixed* thermal neutron irradiation mode, OO-0000-F: tumor seated comparatively deeper, from a few cm to almost 5 cm.

3. The standard *epithermal* neutron irradiation mode, CO-0000-F: BNCT for deep-seated tumor without craniotomy.

The mixed mode is the main current treatment mode undergoing clinical trials. The thermal mode has been used in the past and the epithermal mode is planned for future clinical trials. In this study, the mixed and epithermal modes will be used. The thermal neutron flux depth distribution for each mode is provided in section 7.4.2.3.

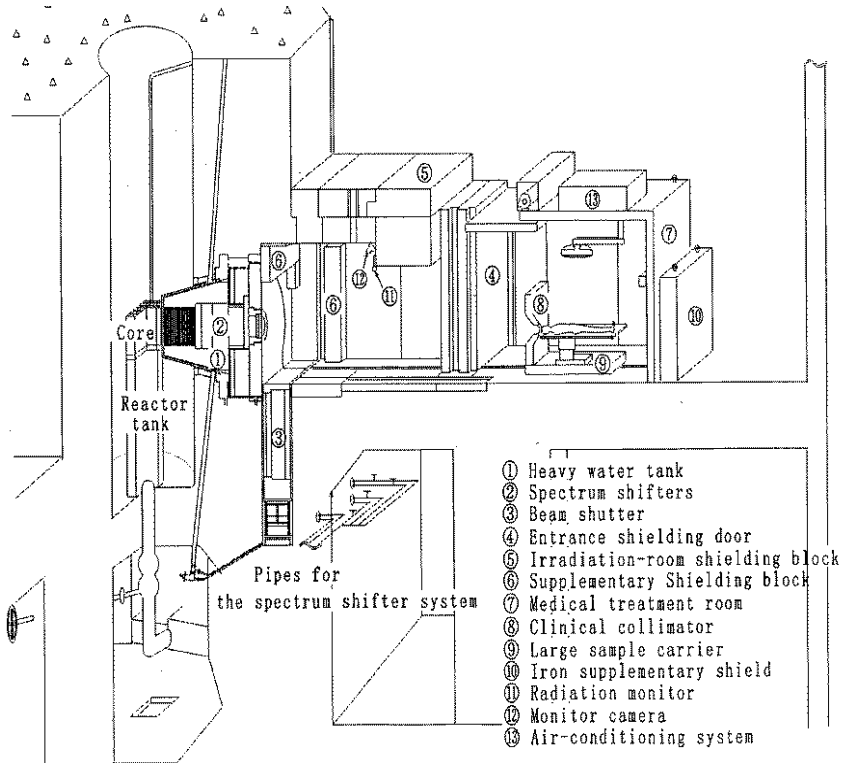


Figure 7.9. General layout of the 5 MW KUR clinical irradiation system [269]

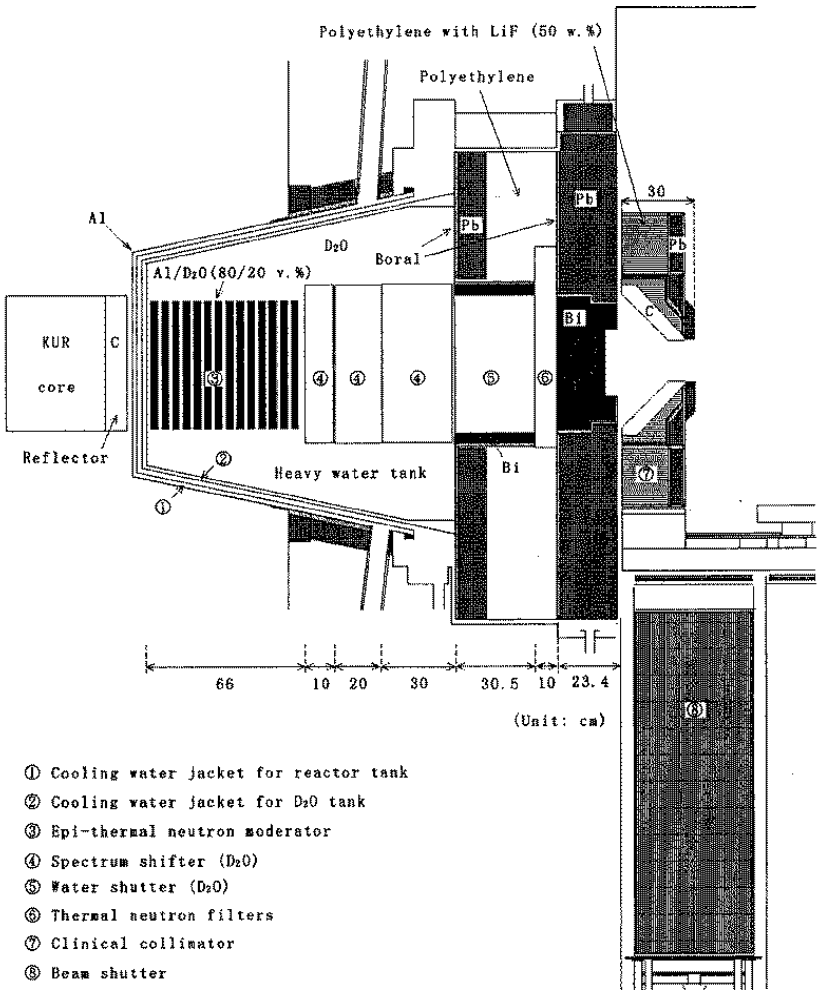


Figure 7.10. Cross-section of epithermal neutron filter construction at KUR

7.4.1.2 Description of probe assembly and phantom

The microdosimeter probe assembly used was "Probe Assembly #1" fully described previously in section 4.3. The microdosimeters used were the 2 and 5 μm SOI devices with the small diode size (10×10 μm^2 junction) array selected. For most experiments, the 2 μm device was used and configured in its "raw" state without boronated Lucite coatings or lids. This device was selected because the sensitive volume was the smallest available and offered the best LET or particle type discrimination capability given the short range of the BNCT ion products. The boron doping in the *p*+ region is used as the main thermal neutron detection element. In addition, the probe has a 300 μm air gap above the chip compared to 100 μm for the previous experiments at BNL. A comparison of the raw device configurations at BNL and KUR is shown in Figure 7.17. The lid insert used at BNL was not used at KUR (at the time it was, mistakenly, not considered important). The charge collection characteristics of the device were fully described in section 6.2.4.1. The device was reverse biased at 10V.

A cylindrical water head phantom was used as shown in Figure 7.11. The longitudinal axis of the water phantom was aligned with the central axis of the beam and the phantom was placed up against the collimator. The detector was then positioned to intercept the central axis of the beam. A 3D remote controlled actuator system was used to accurately position the microdosimeter (+/-2 mm) along the central axis and minimize personnel radiation exposure during measurements.

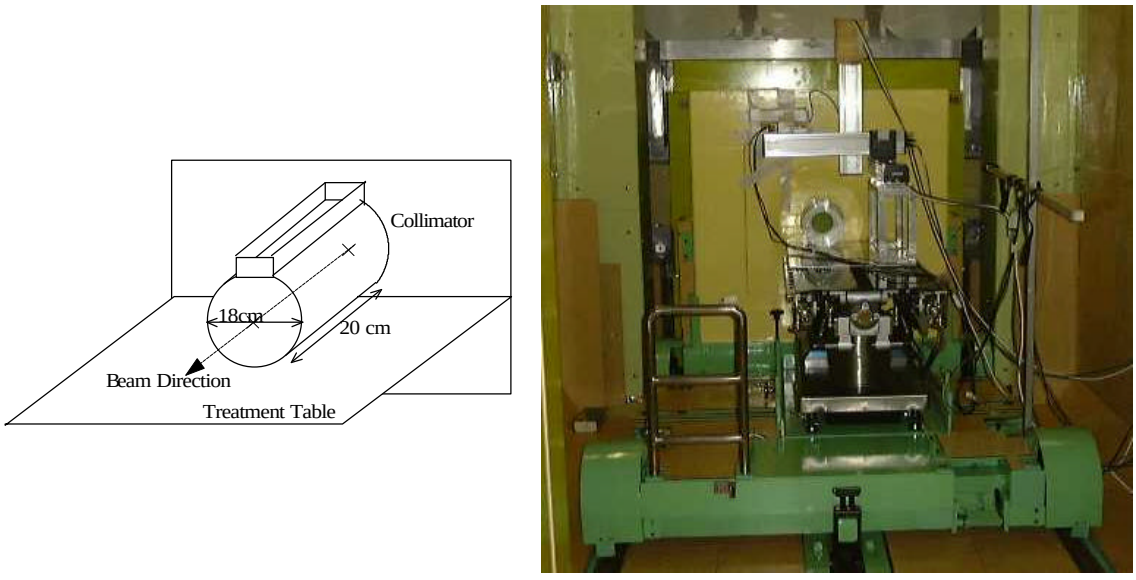


Figure 7.11. Water head phantom used at KUR showing 3D actuator system (above right from phantom) and a rail mounted remote-patient carrier system.

7.4.1.3 Microdosimetric measurements

Microdosimetric measurements were made at distances of 10, 20, 30, 40, 50, 60, 80 and 100 cm from the front face of the phantom. This direction, along the beam axis, will be referred to as the depth direction. The measurements were made for the mixed and epithermal modes with the intention of determining the thermal neutron flux depth distribution. The thermal neutron flux was determined using equation (7.3) with a correction factor k_r determined from simulations as discussed in the results section 7.4.2.3.

In addition, microdosimetric spectra may be compared to determine the relative contribution of various radiation components such as recoil protons from elastic fast neutron scattering. Thus, the principal aim was to examine the capability of the microdosimeter *p+* region for simultaneously extracting the thermal neutron flux and a microdosimetric spectrum. Most spectra will be presented in energy probability distribution form (i.e. calibrated MCA spectrum). For these measurements, greater spectral character is provided using the energy distribution rather then the standard *y-d(y)* format.

The ability of the microdosimeter to delineate events of differing LET depends upon a thin sensitive volume. A comparison between the response of the 2 and 5 μm SOI arrays was made at a depth of 20 cm using the mixed irradiation mode.

7.4.1.4 Simulation of microdosimetric measurements and MCL estimation

Monte Carlo simulations of the microdosimetric measurements provide an increased understanding of experimental spectra and may also be used to estimate mean chord lengths (MCL) required for lineal energy spectra presentations. Inspection of Table 7.3 indicates that there are two important regions to consider for the raw SOI device based on the relative probability of interactions.

1. The *p+* boron doped region: $^{10}B(n,\alpha)^{7}Li$ capture reaction, emitting alpha and lithium recoil products.
2. The nitrogen in the air layer above the device: $^{14}N(n,p)^{14}C$ capture reaction, emitting proton and carbon recoil products.

Simulations as per the Monte Carlo method discussed in sections 5.4.2.1 and 7.3.1.5 and 7.3.2.4 were performed for each of these regions as described below.

***The p+ boron doped region simulation*:**

The GV for the *p*+ doping is shown in Figure 7.13. The *p*+ ion implantation process uses a mask that overlaps the LOCOS region (see appendix B for device and process details). Therefore, the top of the LOCOS region will receive the same ion implantation as the substrate *p*+ region as shown in the cross-section of Figure 7.12. The ion implantation of 30 keV boron produces a typical range in silicon of 0.11 μm and 0.12 μm in SiO_2. The initial boron profile following ion implantation is spread via diffusion during the annealing phase of device construction. However, the diffusivity of boron in SiO_2 is very much lower than silicon (3×10^{-19} cm^2/s compared to 10^{-15} cm^2/s at 900 degC [44]) and there is almost no diffusive spread of the boron in oxide. For simplicity, the gaussian doping profiles typical of ion implantation and subsequent diffusion are approximated in the simulation by the uniform profiles of the RPP shaped GV. The thickness' of the oxide and *p*+ region GVs were selected as 0.1 μm and 0.2 μm, respectively (reflecting the differing diffusivity) and the LOCOS thickness is 0.377 μm based on measurements performed by Fujistu. In addition, the implant "birdsbeak" region associated with the LOCOS oxide growth is not precisely modeled since we represent the implant as a single discrete step from the silicon region to the oxide as shown in Figure 7.13. The final simulation was decomposed using cell symmetry to four GV regions:

```
GV =  {{Silicon, Cuboid({0,4,-0.2},{1,15,0}])},
      {Silicon, Cuboid({0,0,-0.2},{4,4,0})},
      {Oxide, Cuboid({1,4,0.0885},{4,15,0.1885})},
      {Oxide, Cuboid({4,4,0.0885},{7,7,0.1885})}
```

where the RPPs or Cuboids are specified by the bottom left {x,y,z} and top right vertices. The response of the device to the total GV is calculated by adding together the responses of these GVs weighted (weight factors 2,1,2,1) according to their relative contribution. The SV was defined as the 4 diode cells closest to the GV regions that may receive ion products:

SV = {Silicon, Cuboid({-30,-30,-2},{30,30,-2 + x_d})}

where the diode sensitive depth x_d is 2 μm in the *n*+, *p*+ regions and 1.82 μm elsewhere due to the LOCOS region consuming silicon. The collection efficiency within each

diode cell was modeled as given in section 6.2.4.1 and accounted for in the simulation as per equation (7.4). For the simulation, SiO_2 occupies space not defined by the above regions.

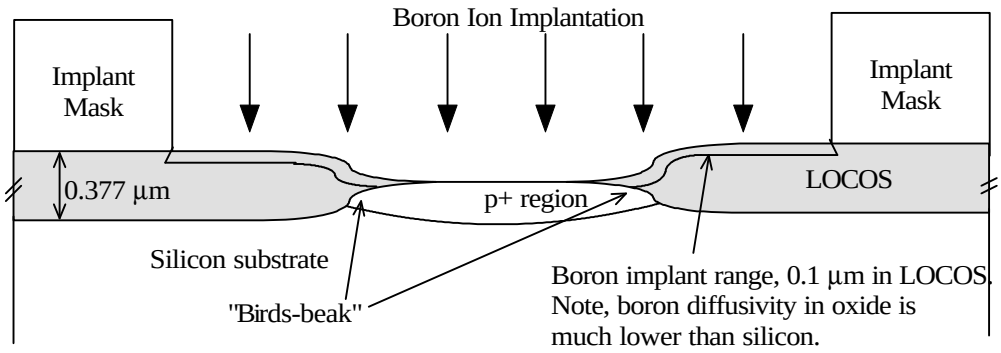
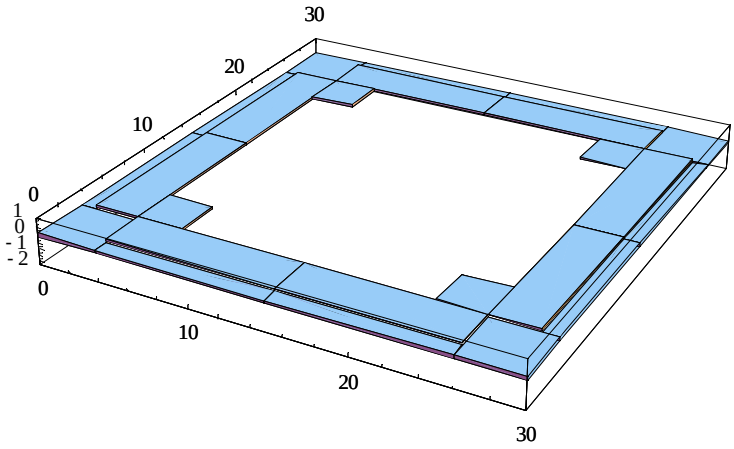
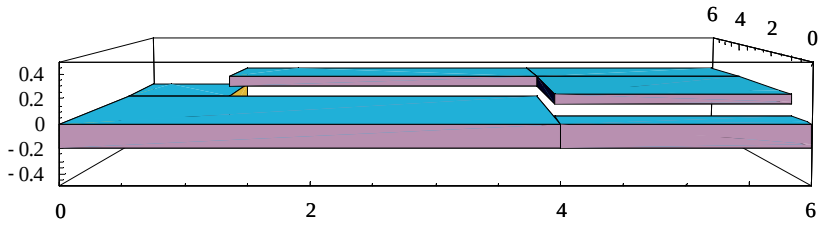


Figure 7.12. Boron ion implantation during device fabrication showing boron deposition in LOCOS (SiO_2) and silicon *p*+ region.



(a) Complete Single diode cell



(b) Expanded side view of a corner portion of a single diode cell

Figure 7.13. Definition of Generation Volume for *p*+ doping BNCT simulation. The top inside layer of boron doped material (0.1 µm thick) is within the oxide (due to mask overlap during boron ion implantation) whilst the lower layer (0.2 µm thick) is within the silicon *p*+ region.

The mean chord length was calculated for the boron implant BNCT simulation following the same process as for the BNL simulations described in section 7.3.1.5. The chord length distribution is shown in Figure 7.14. The mean chord length $\bar{l}_{Ksi}$ is 2.45 μm, a value higher than for the BNL coating and lid simulations due to the absence of overlayer effects. The correction factor ***h*** for obtaining an equivalent dose mean lineal energy to a sphere is 0.96. Therefore, the corrected MCL $\bar{l}_{Keff}$ (ion implant) = 4.05 μm. This MCL will be used in all measurements using the "raw" device as a thermal neutron detector since the boron generated events are of primary interest.

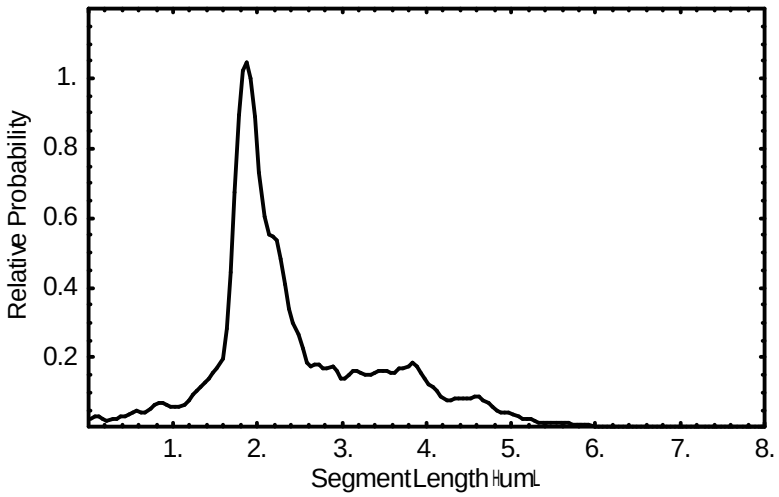


Figure 7.14. Segment length distribution produced by thermal neutron irradiation of the ion implanted region of a 10 × 10 μm², 2 μm SOI diode array.

***The air gap (nitrogen) simulation*:**

This simulation is very similar to the BNL coating and lid simulations discussed in section 7.3.1.5. The geometry is described in Figure 7.15. The range of a 590 keV proton in air produced by a capture reaction with nitrogen is 10.42 mm. This exceeds the 10mm side length of the package recess housing the microdosimeter wafer as displayed in Figure 7.17. Therefore, the GV dimensions (in μms) were adjusted to model the entire air gap within the package recess as follows:

GV = {Air, Cuboid({-6000,-2500,1.05},{4000,7500,301.05})}

The SV was defined as the entire 40 × 120 array of diode cells with the origin at the bottom left corner of the array:

SV = {Silicon, Cuboid({0,0,-2},{1200,3600, -2 + x_d })},

where the diode sensitive depth x_d is 2 μm in the *n*+, *p*+ regions and 1.82 μm elsewhere due to the LOCOS region consuming silicon. The collection efficiency within each diode cell was modeled as given in section 6.2.4.1 and accounted for in the simulation as per equation (7.4). For the simulation, SiO_2 occupies space not defined by the above regions. The simulations will be further discussed in the following results section.

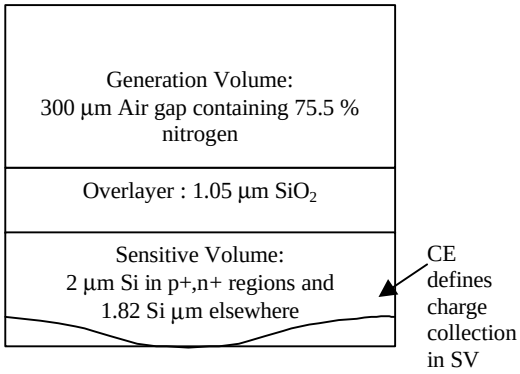


Figure 7.15. Cross-section of nitrogen in air neutron capture simulation on top of 10×10 μm^2, 2 μm SOI diode array (40×120 diodes, each cell 30×30 μm^2). The GV is ($10000 \times 10000 \times 300$ μm^3) whilst the SV is (1200×3600 μm^2 with a depth of 2 μm in the *n*+, *p*+ regions and 1.82 μm elsewhere). The maximum range of 1010 keV protons in air is 10.42 mm.

7.4.2 Experimental Results and Discussion

7.4.2.1 Comparison BNL and KUR microdosimetric spectrum

A comparison of the energy spectrum obtained at BNL and KUR under similar conditions is shown in Figure 7.16. (BNL: 6.5 cm in Lucite phantom, KUR: 6 cm in water phantom using mixed irradiation mode). The data are normalized by integrating values greater than 450 keV. Above this energy, the spectra are nearly identical. From 80 keV to 450 keV the KUR data exhibits significantly more counts peaking at around 110 keV. This peak is also present in the BNL data although it is much less prominent. Such an energy deposition corresponds to a normally incident 590 keV proton in silicon with an LET of around 60 keV/μm. Therefore, the difference in spectra may be due to additional nitrogen present in the KUR experiment. A slightly different lid configuration was used in the two experiments as shown in Figure 7.17. The air-gap above the device was 100 μm at BNL and 300 μm at KUR. The effect of the air-gap was not fully appreciated at the time of the KUR experiments. The following section describes a simulation that confirms the air influence.

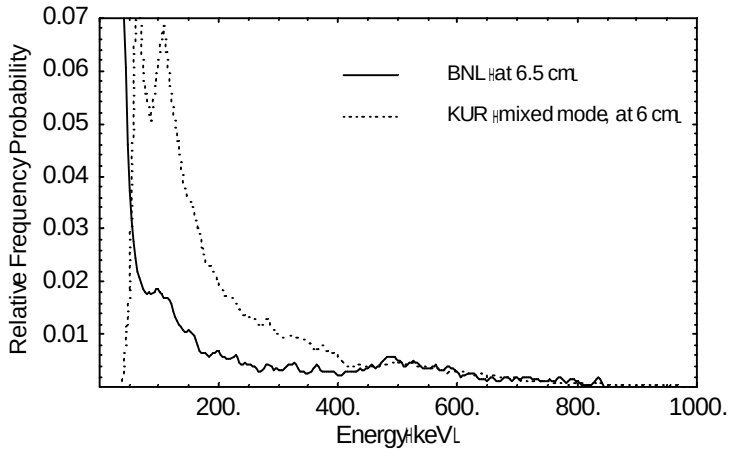


Figure 7.16. Comparison of energy distribution from ion-implanted boron capture reaction at BNL and KUR. An identical microdosimeter was used, 10×10 μm^2, 2 μm SOI diode array. The air gap varied between the two experiments as shown in Figure 7.17. The data is normalized by integrating values > 450 keV.

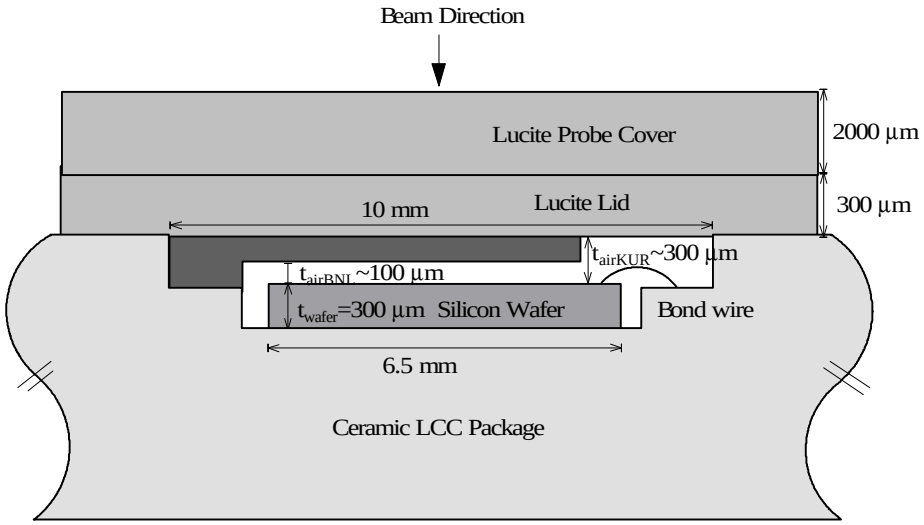


Figure 7.17. Lucite lid configurations for measurements made using the ion implanted boron region of the microdosimeter. The hatched region is a Lucite lid present during the BNL measurements but not present during the KUR measurements. Therefore, t_{air} = 100 μm BNL and 300 μm KUR. The *p*+ boron is implanted in the top surface of the silicon wafer (~0.1-0.2 μm depth). No boron is present in any of the Lucite components in this diagram.

7.4.2.2 Simulation (ion implanted boron and nitrogen in air)

The detector responses to neutron capture reactions with ion implanted boron and nitrogen in the air gap were simulated using the previously described Monte Carlo method.

***The p+ boron doped region simulation*:**

A comparison of the ion implanted boron simulation with a spectrum from KUR (obtained at 1 cm depth using mixed mode irradiation) is shown in Figure 7.18. The

simulation was normalized to have the same number of counts as the data for energies greater than 450 keV. In this region only counts are expected from the ion implant boron reactions. This spectrum was selected for its high thermal neutron flux and hence excellent acquisition statistics. The simulation correctly predicts the peak at 600 keV but offers a poor match at higher energies. The simulation shows three peaks at 590, 690 and 1120 keV. The lower two peaks are due to lithium ions originating in the silicon *p*+ doping for the higher energy (690 keV) and in the silicon dioxide for the lower energy (590 keV). Predominantly (93.7% of the time, equation (7.1)), an 840 keV lithium is generated with a range in silicon of 2.4 μm. Most of the ions originating from the silicon dioxide will intercept the device in the LOCOS region where the thickness is 1.81 μm compared to 2 μm in the *p*+ doped region. Furthermore, any additional overlayer reduces the energy deposited since the lithium ion is past the Bragg peak. The two peaks present in the simulation appear as a single peak at 600 keV. The difference may be attributable to the simulation's simplistic modeling including the step approximation to the "birds-beak" region and the uniform distribution of boron.

The higher energy peak of the simulation is due to alpha particles originating from boron within the *p*+ region and the silicon dioxide. The alphas have a typical range of 5.1 μm with an initial energy of 1470 keV. The larger range makes the alpha less sensitive to overlayer thickness than the lithium ion. The reason for the discrepancy at high energies, between this simulation peak and experimental results, is not clear. These high energy events (>1000 keV) are due to high angle (60°-90°, typically 70°) alpha tracks arising from the *p*+ silicon substrate region. In heavily doped regions the carrier lifetime is reduced. The collection efficiency function may not correctly model the recombination losses in these regions particularly at high angles. Any electric field present in the substrate due to funneling may possibly increase recombination since drift collection is in a direction which may increase the likelihood of electron-hole pair recombination as shown schematically in Figure 7.19. These effects were not seen in the 2 D simulation presented in section 6.2.2.4. Further 3 D simulations of the 1470 keV alpha at high angles are required. Angled microbeam or broadbeam experiments may also be useful in further characterization of the device collection efficiency.

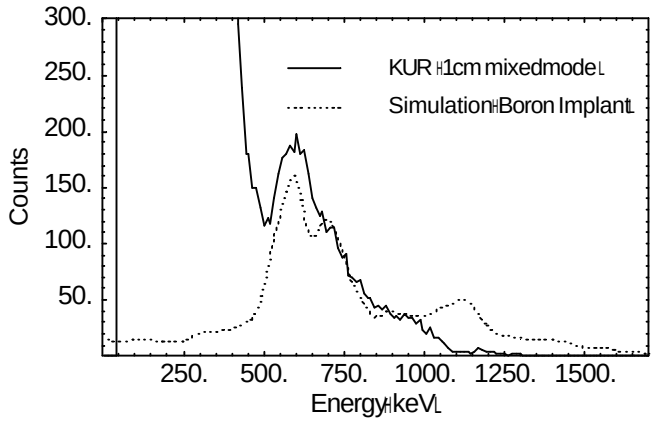


Figure 7.18. Comparison of boron ion implantation simulation with energy spectrum at 1 cm depth, mixed mode irradiation at KUR. The simulation was normalized to provide the same total number of counts greater than 450 keV as the experiment.

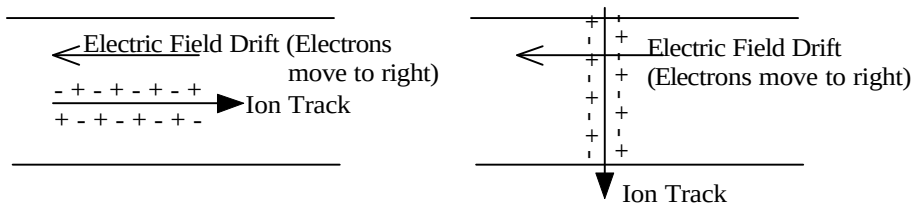


Figure 7.19. Illustration of possible variation in recombination with ion strike direction with respect to electric field.

The air gap (nitrogen) simulation:

The simulations performed in the previous discussion for the boron implanted regions cannot account for the large peak observed at 120 keV in the experimental spectra shown in Figure 7.16. A comparison of the air gap nitrogen simulation with a spectrum from KUR obtained at 1 cm depth using mixed mode irradiation is shown in Figure 7.20. The simulation was normalized to have the same number of counts as the experimental result between 120 and 450 keV. This range was selected due to the small number of counts expected from boron reactions and fast protons. The simulation provides an excellent fit to the observed data for the peak at 120 keV. The fit is not so accurate at higher energies from 300 keV to 450 keV. In this region, events are due to high angle intercepts with chord lengths in the range of 3-4 μm and an average LET of around 100 keV/μm. The poor fit is most probably due to a combination of two effects: the course modeling of the overlayer as a single thickness oxide layer and, to a lesser extent, the neglect of the TiN layer nitrogen capture reaction. The TiN layer was not simulated since we would expect approximately 7 times fewer counts (see Table 7.4).

Furthermore, the TiN spectrum should be similar to the air gap simulation due to the long range of the protons relative to the device overlayer. Despite some discrepancies, the fit particularly at 120 keV is sufficient to justify the conclusion that the spectral characteristics in the range from 100 to 450 keV are dominated by protons originating from the nitrogen within the air gap and also from the TiN layer.

The rise in counts below 80 keV is due to the contribution of fast proton recoils from neutron interactions. Protons with energies greater than 1 MeV will have an LET less than 50 keV/μm in silicon. The fast proton energy deposition spectrum displays an exponential shape as higher energy events, requiring high angle events (large chord lengths) and/or high LETs (low energy), are less probable. This spectrum shape will be seen later in fast neutron and fast proton therapy experiments described in chapters 8 and 9. The fast proton content of the microdosimetric spectrum, above the noise level of the detector, may be extracted by subtracting the air-gap simulation from the experimental spectrum. The calculation assumes that the ion-implant boron count rate in this region is negligible which is reasonable given the data displayed in Figure 7.18. The subtraction was performed over the interval from 55 keV to 250 keV with the result shown in Figure 7.20. This demonstrates that the silicon microdosimeter may be used to compare the relative dose contribution of fast protons versus boron neutron capture products since the contributions occur at different parts of the spectra. Minimization of the air gap and TiN thickness would assist in separating the fast proton component of the spectrum.

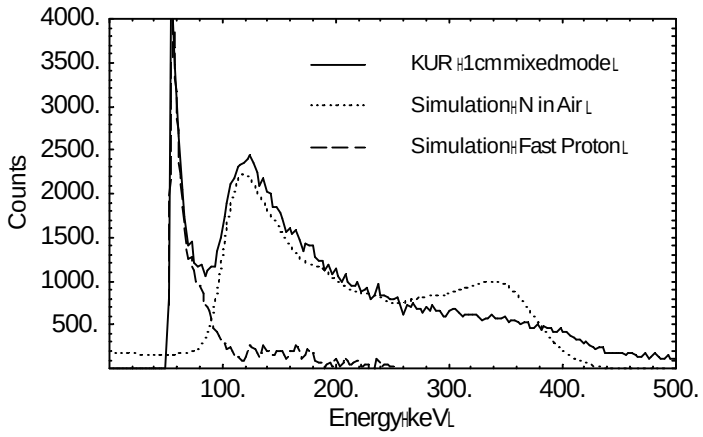


Figure 7.20. Comparison of air gap (nitrogen) simulation with energy spectrum at 1 cm depth, mixed mode irradiation at KUR. The simulation was normalized to provide the same total number of counts within the energy range of 120 to 450 keV as the experiment. The fast proton simulation curve, representing events due to fast neutron generated recoil protons, is calculated by subtracting the air simulation from the experimental data for E<250 keV.

Merged Simulation:

The air gap, ion implant and fast proton components may be added to obtain the spectrum shown in Figure 7.21. Overall, the match between experiment and simulation is reasonable except for the previously noted discrepancies.

The simulation enables calculation of the proportion of generated recoil products that reach the sensitive volume (i.e. k_r in equation (7.3)). Improvements may then be made in estimating the relative probability for thermal neutron detection via the various overlayer and implant elements. Estimates previously provided in Table 7.3 assume a k_r=1 whilst Table 7.4 is a revision using values of k_r estimated from simulations. The proportion of nitrogen (mostly from air and TiN) to ion implanted boron counts was expected to be about 0.5. The observed ratio from integration of Figure 7.21 over the appropriate regions was 5.4. This indicates that the amount of boron-10 in the device is lower than expected by a factor of 10.8 or the air gap was considerably larger than expected. The implanted isotopic abundance of boron-10 may not be 19.61% due to beam bending and design features in the ion implantation accelerator. This issue will be further addressed in the following section.

Table 7.4. Relative probability of thermal neutron detection with selected microdosimeter/overlayer elements. This is a revised and improved subset of Table 7.3.

Element/ Component	Number Atoms	Micro X-section ($s\,10^{-24}$ cm^2)	Macro X-Section (S cm^2)	k_r	Relative Prob.	Comments
^{10}B in p+ region	2.22×10^{13}	3837	8.52×10^{-8}	0.955	1	Area of p+ region is 0.022 cm^2 and boron ion implant fluence 1.5×10^{15} atoms/cm.
^{14}N in TiN	5.57×10^{15}	1.83	1.01×10^{-8}	0.5	0.06	TiN thickness = 0.1 μm, area = 0.011 cm^2, Density TiN=5.33 gm/cm^3.[267]
^{14}N in Air	1.15×10^{18}	1.83	2.11×10^{-6}	0.017	0.43	Air thickness = 300 μm, area = 10 × 10 mm

Note 1: See chapter 4 for a device description and Appendix B for additional layout information.
2: Macro X-Section = Micro X-Section × Number atoms,
Relative probability = k_r Macro X-Section/ (k_r Macro X-Section for ^{10}B in p+ region)
3: k_r is the proportion of generated recoil products that reach the sensitive volume

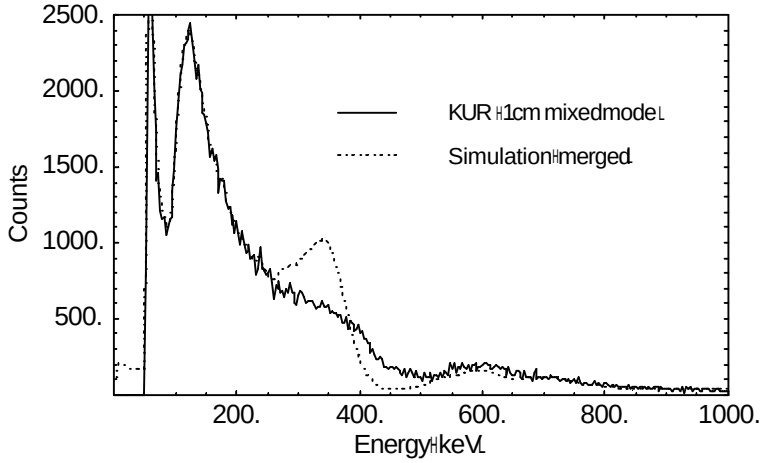


Figure 7.21. Comparison of combined boron ion implantation, nitrogen in air and fast proton simulation data with energy spectrum at 1 cm depth, mixed mode irradiation at KUR. The simulation data from Figure 7.18 and Figure 7.20 has been combined to form this plot.

7.4.2.3 Thermal neutron flux depth profile

The thermal neutron flux variation with depth may be extracted by using the counts generated from the ion-implanted boron-10. In principle, if the exact number of boron-10 atoms is known then the absolute thermal neutron flux may be measured using equation (7.3). However, the implanted isotopic abundance of boron-10 may not be 19.61% due to beam bending and ion selection design features in the ion implantation accelerator. A relative thermal neutron flux profile $F(x)$ was constructed by integrating the energy spectrum *f(E,x)* at each depth x for E greater than 450 keV and multiplying by a scale factor k. Therefore,

$$\Phi(x) = k\int_{450}^{\infty} f(E,x)dE \tag{7.8}$$

where

$$k = \frac{\Phi(1\text{ cm})}{\int_{450}^{\infty} f(E,1\text{ cm})dE} \tag{7.9}$$

and $F(1\text{ cm})$ is the flux calculated by Kobayashi [269] using gold foils (50 μm thick, 3mm diameter) at 1 cm = 3.5×10^9 n/cm^2/s (mixed mode) and 4×10^8 n/cm^2/s (epithermal mode). The energy spectra were normalized to an acquisition time of 1 second. The calculated value of k was 8.47×10^7 n/count/cm^2/s. Assuming 19.61% isotropic abundance, we may also estimate the value of k using equation (7.3). That is,

$$k = \frac{m}{k_r \Sigma} \tag{7.10}$$

where m is a factor that accounts for the boron-10 reactions that produce products with an energy deposition less than 450 keV. Both m and k_r may be calculated from the simulation spectrum for the ion implant region $g(E)$ as shown in Figure 7.18. The proportion of capture events that result in an energy deposition k_r is 0.955 and the value of m is given by

$$\begin{aligned} m &= \int_0^\infty g(E)dE \Big/ \int_{450}^\infty g(E)dE \\ &= 1.135 \end{aligned} \tag{7.11}$$

Using S from Table 7.3, which assumes natural isotopic abundance of boron-10, the value of k was estimated using equation (7.10) as 1.39×10^7 n/count/cm^2/s which is about 6 times lower than calculated using equation (7.9). Therefore, the initial assumption of natural isotopic abundance of boron-10 may be incorrect due to the nature of the ion-implantation procedure (magnetic field separation of isotopes). This result is consistent with conclusions derived in the previous section.

Using the k derived from equation (7.9), excellent agreement in the neutron flux profile, between the gold foil measurements by Kobayashi [269] and the microdosimeter, was demonstrated as shown in Figure 7.22. This result demonstrates the feasibility of using the silicon microdosimeter for simultaneous thermal neutron flux measurements and microdosimetry at a high spatial resolution. Note, the deeper penetration of the epithermal beam, although the filtering used in constructing the beam has reduced the thermal neutron flux relative to the thermal beam mode.

The microdosimeter flux measurement error depends on the total counts acquired. The 95% confidence interval on the relative error is approximately given by 3 Sqrt(counts)/counts (p75 [23]) which leads to a maximum error of 17% at x = 10 cm (epithermal mode). In general, the error is within about 10% with improved accuracy simply gained by increasing the acquisition time (currently 5 minutes). The positional accuracy achievable by the probe setup was +/- 2 mm limited by bending of the Lucite probes and alignment errors. These errors could readily be improved by redesigning the probe setup since the 3D actuator is capable of sub-millimeter accuracy.

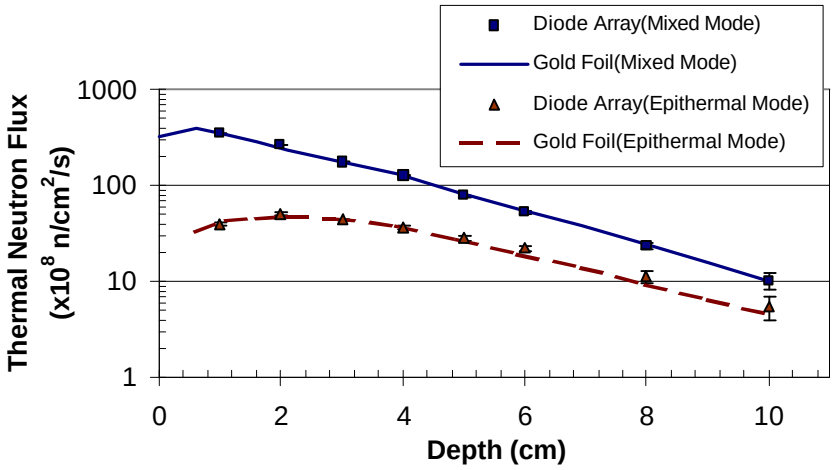


Figure 7.22. Comparison of gold foil and microdosimeter calculated thermal neutron flux profile. The depth profile for the mixed and epithermal irradiation modes are shown.

7.4.2.4 Microdosimetric comparison of irradiation modes

The energy spectrum at various depths in the water phantom is shown in Figure 7.23 for mixed mode irradiation and Figure 7.24 for epithermal mode irradiation. The spectra have been normalized so that the integral counts > 450 keV (thermal neutron events) are equal to unity. This presentation highlights differences in the fast proton contribution with energies less than 200 keV. The aim is to demonstrate the utility of the microdosimeter in analyzing the various dose components of the radiation. For the mixed mode irradiation, the proportion of energy deposition events due to fast protons versus thermal neutrons rises with depth. That is, the thermal neutrons reduce with depth at a faster rate than the higher energy neutrons that produce fast recoil protons.

A method of presenting this trend is shown in Figure 7.25. The relative ratio of fast proton events to thermal neutron events at various depths in the water phantom is presented. This was calculated by integrating the counts between 60 and 80 keV and dividing by the integral counts greater than 450 keV. The ratio is normalized to unity at a mixed mode depth = 1 cm. The features shown in Figure 7.23 and Figure 7.24 are more clearly highlighted. In particular, the epithermal mode shows a higher proportion of fast proton events then the thermal mode; an effect that is expected due to the higher energy of the neutron spectrum. The dip at 2 cm in the epithermal curve is due to the higher thermal neutron flux as shown in Figure 7.22. The relative occurrence of fast proton events at 10 cm is 5-5.5 times the occurrence at 1 cm. An improved analysis would consider dose contributions instead of event frequencies using the low noise microdosimeter prototype to obtain as much of the low energy fast proton spectrum as possible.

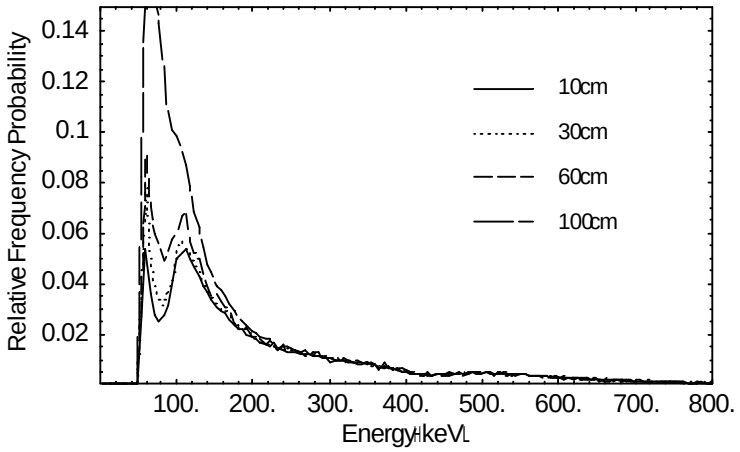


Figure 7.23. Energy spectrum for *mixed mode irradiation* at various depths in the water phantom. Spectra have been normalized so that the integral counts > 450 keV (thermal neutron events) are equal to unity. Differences in the fast proton contribution, E<200 keV, are highlighted.

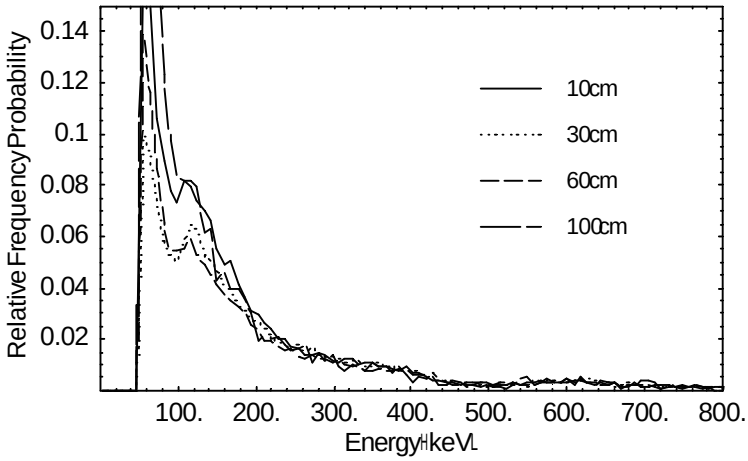


Figure 7.24. Energy spectrum for *epithermal mode irradiation* at various depths in the water phantom. Spectra have been normalized so that the integral counts > 450 keV (thermal neutron events) are equal to unity. Differences in the fast proton contribution, E<200 keV, are highlighted.

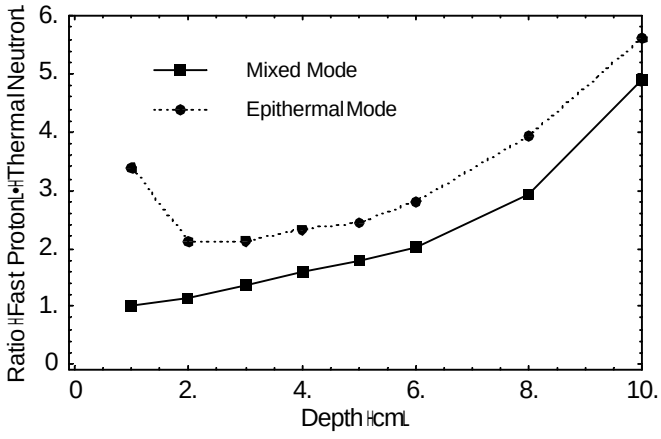


Figure 7.25. Relative ratio of fast proton events to thermal neutron events at various depths in the water phantom. Ratio is normalized to unity at a depth = 1 cm for mixed mode.

7.4.2.5 Comparison sensitive volume depth variation (2 and 5 μm SOI)

A comparison of the lineal energy spectrum for 2 μm SOI and 5 μm SOI devices under mixed mode irradiation at 1 cm depth is shown in Figure 7.26. The mean chord length (MCL) used for the 2 μm SOI device was 4.05 μm as calculated in 7.4.1.4. For the 5 μm SOI device, the MCL was adjusted so that the fast proton edge at 20 keV/μm matched with the 2 μm SOI lineal energy spectrum. The required MCL was 6.5 μm.

Three main differences are seen in this comparison. Firstly, the 5 μm SOI device is capable of measuring a lower lineal energy due to the larger signal to noise ratio. Secondly, the proton peak, originating from capture reactions with nitrogen, has a higher lineal energy in the 5 μm SOI device. The 590 keV proton with a range in silicon of 7.1 μm is almost always stopped within the 5 μm SOI. Thus, the high LET Bragg peak occurs within the sensitive volume and increases the energy deposition. Lastly, the maximum lineal energy is higher in the 2 μm SOI device. High energy events are due to high angle alpha particles emitted from the ion-implanted boron regions of the device. Thus, the energy deposited by such events will be similar for both devices. However, the lineal energy will be higher for the 2 μm SOI due to its lower MCL.

In summary, the advantage of the 5 μm SOI device is that it has a higher signal to noise ratio. The disadvantage is that it may not discriminate LET as effectively as the smaller SOI device since many particles will be stoppers and not crossers within the sensitive volume. A thin sensitive volume is desirable to maximize the sensitivity to particle LET rather than particle total energy.

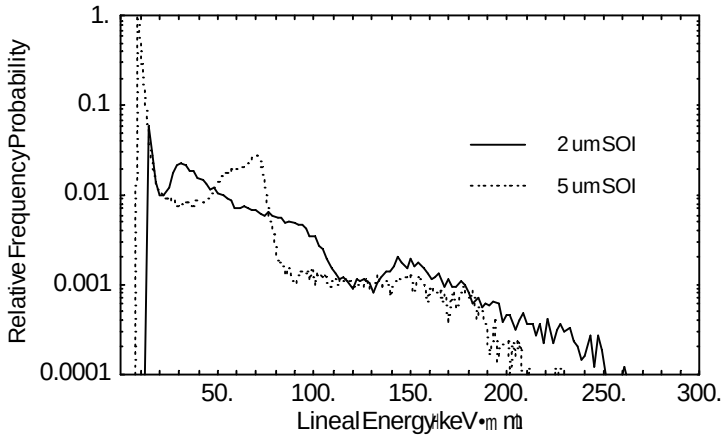


Figure 7.26. Comparison of lineal energy spectrum for 2 μm SOI and 5 μm SOI devices (small diode array 10 × 10 μm junction size) under mixed mode irradiation at 1 cm depth.

7.5 Experiments at Massachusetts Institute of Technology (*Epithermal Neutron Beam Investigation*)

Experiments were carried out at the Massachusetts Institute of Technology (MIT) Laboratory for Accelerator Beam Applications (LABA) to test the performance of the silicon microdosimeter exposed to an accelerator based thermal neutron source. The main aim was to verify the operation of a newly developed low noise silicon microdosimeter (prototype #2 see section 4.4).

7.5.1 Materials and Methods

7.5.1.1 Description of facility

A high current tandem accelerator capable of delivering multi-milliampere proton or deuteron beams at energies up to 4.1 MeV was available at LABA . The beam and target design is orientated towards the development of boron neutron capture synovectomy (BNCS). BNCS is a novel treatment for rheumatoid arthritis which uses the $^{10}B(n,\alpha)^{7}Li$ reaction to ablate the diseased synovial membrane lining the articular joints [271]. The neutron beam requirements differ from BNCT for three main reasons: (i) BNCS has much higher boron-10 concentration levels due to direct administration of boronated compounds into the synovium, (ii) the target synovium tissue is only 1.5-2 cm below the skin and (iii) the joints targeted (knee and fingers) are located far from the body's sensitive organs. The large boron-10 dose per unit incident neutron fluence allows the use of beams with more fast neutron and photon contamination than is acceptable for BNCT, since the beam will be incident on the joint for a much shorter period of time.

Neutrons were generated by bombarding a beryllium target with 1.5 MeV deuterons using the $^{9}Be(d,n)^{10}B$ reaction. The target was located within a 9 cm diameter, 23 cm length, cylindrical D_2O moderator encapsulated in an 18 cm thick graphite reflector. The heavy water reduces the neutron energy, which is initially around 1 MeV, without producing an intense photon flux. The graphite is effective at reflecting neutrons to improve the target dose rate.

7.5.1.2 Microdosimetric setup and measurements

Two microdosimetric probe assemblies were compared in these experiments. The assemblies are designated "Probe Assembly #1" and " Probe Assembly #2" and were both fully described previously in sections 4.3 and 4.4, respectively. The

microdosimeter used was the 2 μm SOI device with the small diode size (10×10 μm^2 junction) array selected and configured in its "raw" state without boronated Lucite coatings or lids. This device was selected for comparison with previous measurements and because the sensitive volume was the smallest available and offered the best LET or particle type discrimination capability given the short range of the BNCT ion products. The boron doping in the *p+* region is used as the main thermal neutron detection element. In addition, the probe has a 300 μm air gap above the chip. The charge collection characteristics of the device at the selected reverse bias voltage of 10 V were fully described in section 6.2.4.1.

A water tank with dimensions (w×l×h) 28.5×28.5×21.5 cm^3 was used as shown in Figure 7.27. For each probe assembly, the detector was placed at a depth of 1.5 cm (from the front face of the phantom) and aligned with the center of the beam axis.

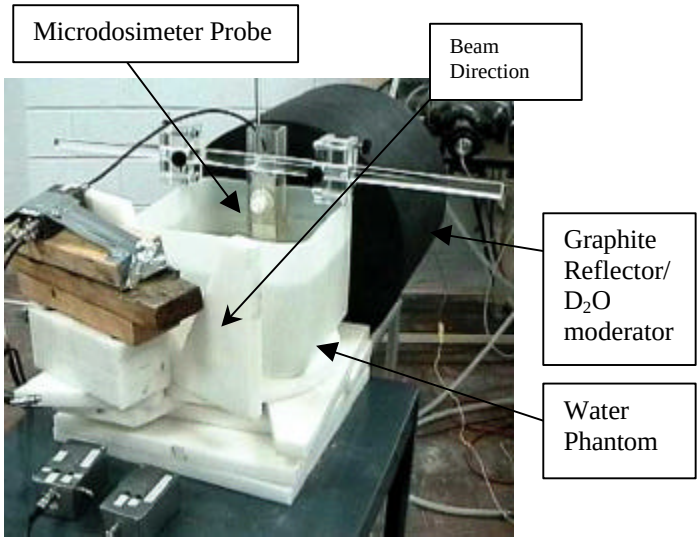


Figure 7.27. Microdosimeter probe and water phantom with the D_2O moderator/graphite reflector at MIT

7.5.2 Experimental Results and Discussion

The lineal energy spectrum in *y-f(y)* format comparing the performance of Probe Assembly #1 and the improved low noise Probe Assembly #2 is shown in Figure 7.28. The key feature of these spectra is the characteristic exponential distribution below 120 keV/μm (seen as linear on the linear-log format of Figure 7.28) and attributable to the high fast proton component in the beam. The thermal neutron component (y>120 keV/μm) is very small in comparison with the fast proton component in contrast with the BNCT lineal energy spectra shown in Figure 7.26. Longer acquisition times are required to obtain an improved spectra at higher lineal energies. In comparing the

performance of the two probes, the spectra are essentially identical down to a lineal energy of 17 keV/μm after which the early prototype begins to display increased noise characterized by a departure from the exponential distribution. A similar noise influence occurs for the low noise probe assembly although it occurs at the lower lineal energy of 10 keV/μm. This improvement in noise performance is consistent with design expectations discussed in section 4.3.

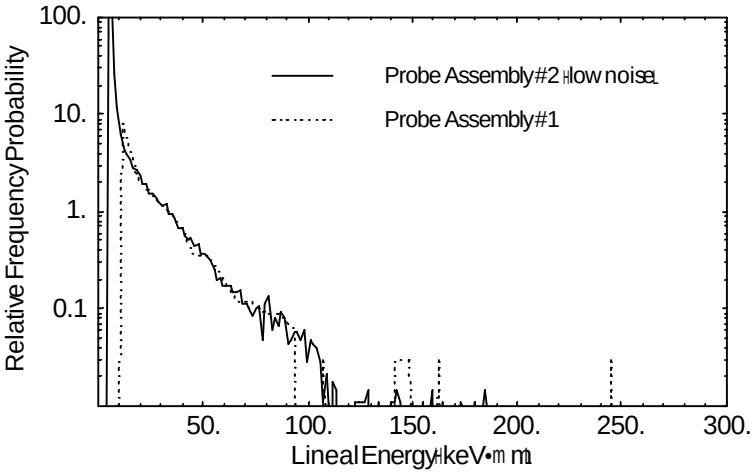


Figure 7.28. Lineal energy spectrum comparing the performance of Probe Assembly #1 and the improved low noise Probe Assembly #2.

7.6 Summary of BNCT Applications

This chapter demonstrates the first application of silicon p-n junction SOI arrays for microdosimetry in radiation oncology and particularly for BNCT. The interaction of thermal neutrons with each of the materials present in the device construction was thoroughly analyzed in section 7.2. The important materials are (in order of thermal neutron sensitivity), B-10 in a 1% Lucite coat or cover (optional, if present), B-10 in the *p*+ region, N-14 in air (if present, may not have an air gap above the device), N-14 from the TiN barrier layer.

Experiments at BNL, as presented in section 7.3, were primarily directed at investigating various converter options for the device (Lucite with B-10 and U-235) and for a comparison with a TEPC measurement. Direct coating of the device with 1% B-10 in Lucite did not change electrical characteristics and produced a microdosimetric spectrum similar to the 1% B-10 lid. Discrepancies between these spectra and Monte Carlo simulations were attributable to simplistic overlayer and charge collection modeling. More detailed investigation of charge collection modeling of high LET

particles is encouraged. In addition, preliminary results with the U235 converter suggest that the SOI p-n junction is a promising microdosimeter for heavy ion therapy provided the bias voltage is greater than 5 V to minimize recombination. Measurement of the spectra generated from B-10 deposited within the device *p*+ regions demonstrated that typical medical concentrations of B-10 may be introduced in the device design via ion implantation. Such a microdosimeter can be used under full reactor power with any device orientation.

Experiments at KUR, as presented in section 7.4, demonstrated the importance of minimizing the air gap above the device due to the large number of proton events originating from nitrogen thermal neutron reactions. Monte Carlo simulations of this effect were in good agreement with observed experimental spectrum. The ability of the 2 μm SOI microdosimeter to discriminate between fast neutron recoil protons and BNCT products facilitates simultaneous thermal neutron flux measurements and microdosimetry at a high spatial resolution. Excellent agreement in the neutron flux profile, between the gold foil measurements by Kobayashi [269] and the microdosimeter, was demonstrated as shown in Figure 7.22. The number of ion-implanted B-10 atoms within the *p*+ region used for these measurements was a factor of 6 lower than expected based on isotope natural abundance suggesting that the ion-implantation process may alter the relative isotope concentrations. If the ion-implanted B-10 proportion is known, accurate absolute thermal neutron flux may be estimated without any need for normalization to a known flux value.

The MCL was calculated using Monte-Carlo methods with values of 2.32 μm (B-10 coat) 2.26 μm (B-10 lid) and 4.05 μm (*p*+ ion implant) obtained for the various configurations. The relatively large sensitive volume compared to the range of boron capture products, and its elongated shape along with a sensitivity to the local distribution of boron are responsible for this large variation in MCL. A comparison of the 2 μm and 5 μm SOI devices further highlighted the importance of a small sensitive volume. The advantage of the 5 μm SOI device is that it has a higher signal to noise ratio. The disadvantage is that it may not discriminate LET as effectively as the smaller SOI device since many particles will be stoppers and not crossers within the sensitive volume. A thin sensitive volume is desirable to maximize the sensitivity to particle LET rather than particle total energy.

In response to the failure of traditional microdosimetry to adequately represent realistic tissue architecture and boron distribution, Solares and Zamenhof [81] have developed high-resolution quantitative autoradiography. This technique is difficult and time consuming, although it is currently the most realistic microdosimetric technique available. However, the improvements in traditional microdosimetry possible using silicon diode arrays may help to bridge the gap between proportional counter microdosimetry and the more realistic autoradiography method.

8. Application to Fast Neutron Therapy

8.1 Background to Fast Neutron Therapy

Fast neutrons, and high LET particles in general, offer therapeutic advantages in treating locally advanced or "radioresistant" tumors at certain sites. The potential advantage of neutrons rests in the high LET of the secondary particles created by neutron interactions. Densely ionizing protons, alphas and heavy ion recoil products are present that inflict a significant number of DNA double strand breaks. It is known that about 1.5 more double strand breaks (DSB) are observed after neutron irradiation than after photon irradiation of equal dose [272]. This type of radiation induced damage is generally considered lethal and unrepairable. A further advantage, evolving from the higher percentage of unrepairable DNA damage, is a reduced cell death variability across the different phases of the cell cycle. In addition, neutrons benefit from a low oxygen enhancement ratio (OER). Photon radiation causes most of its damage through the generation of free radicals and thus is dependent on the presence of oxygen in the tumor. The OER is about 3 for photons and electrons, meaning a high resistance of hypoxic cells to these low-LET particles, and only about 1.6 for neutrons [273]. Neutrons depend less on oxygen to act as a mediator and have a greater tendency to cause cell death through a direct interaction. Therefore, the hypoxic component of the tumors is spared to a lesser extent by neutron irradiation than by low-LET particle therapy.

In view of the above mentioned mechanisms the relative biological effectiveness (RBE) of neutrons used for therapy is usually in the range of 2 to 5 [111]. Note that neutrons provide no benefit over conventional therapy in terms of an improved depth-dose distribution. The depth-dose distribution for neutrons follows a similar profile to gamma photons from cobalt 60 [155]. Based on radiobiological observations, tumors with large hypoxic areas which reoxygenate slowly and well-differentiated slowly growing tumors are expected to be good candidates for neutron therapy [111].

The first use of neutron radiotherapy was performed by Stone at Berkeley in 1938 [274]. Clinical work intensified in the early 1970s starting with the fast neutron therapy programme at London's Hammersmith Hospital and the subsequent opening of several centers in Europe and the United States. There are now 14 centers in Europe alone and

approximately 15000 patients have been treated worldwide up to 1994 [272]. Unfortunately, after almost thirty years of extensive clinical trials, it appears that only a few cancer localizations benefit from the use of neutrons.

The best results have been obtained for malignant salivary gland tumors. Clinical trials have demonstrated a statistically significant improvement in loco-regional control for the neutron group (56% neutrons versus 17% photons) but with no clear improvement in overall survival [275]. This was explained by the fact that distant metastases accounted for most of the failures in the neutron group. Similar results have been seen for prostrate [276] and advanced rectal cancer [277].

Various researchers (e.g. [278]) have suggested that for a meaningful evaluation of the efficacy of neutron therapy, the neutron beam should be comparable to photon beams in terms of penetration, collimation, dose rate, isocentric capabilities etc. The fast neutron therapy facility at Harper Hospital, employed in this study, has been shown to satisfy the requirements of comparability with photon therapy [279]. An additional concern in fast neutron therapy is the dosimetric challenges imposed by the variation in RBE with neutron spectrum variations. Significant variation in beam quality occurs for neutron beams of different energies and different production mechanisms [280, 281]. Fortunately, variations in radiation quality within neutron beams irradiating homogeneous water phantoms is much less pronounced.

The traditional tool for studying the variation in radiation quality of various neutron beams is the proportional gas counter. Many microdosimetric studies have been performed on various neutron therapy beams using proportional counters. Kota [154] provides a good listing of references (e.g. [106-108]). Kota [154] also notes that in several studies [104, 105] RBE values calculated from the saturation corrected dose mean lineal energy y^* are fairly well correlated with RBE data derived from radiobiological data. The definition of y^* was developed in the theory of dual radiation action (TDRA) by Kellerer and Rossi [18] (see section 2.4.1 and 2.4.2) and will be discussed later. The correlation between y^* and RBE depends upon the specific radiobiological endpoint used. Nevertheless, the observed correlation between y^* and RBE has been used to estimate variations in RBE within beams under different irradiation conditions in a water phantom.

In this study, the performance of the silicon microdosimeter exposed to a *d(48.5 MeV)+Be* fast neutron beam is compared to results obtained by a proportional counter [154]. Both microdosimetric spectra and parameters such as $\bar{y}_d$ and y^* are compared under similar conditions. The main advantages of using a silicon microdosimeter in fast neutron therapy include ease of use (no gas system), system cost, excellent spatial resolution and the ability to operate at high clinical dose rates.

8.2 Materials and Methods

8.2.1 Description of fast neutron beam at Harper Hospital, Detroit.

The fast neutron facility at the Gershenson Radiation Oncology Center, Harper Hospital Detroit has been treating patients since 1991. Accelerated using a superconducting cyclotron, the beam is produced by the interaction 48.5 MeV deuterons with a beryllium target [279]. The neutron beam, with a maximum energy of 52.5 MeV and a mean energy of approximately 20 MeV, is shaped using a specially developed multi-rod tungsten collimator [282]. The time profile of the beam is pulsed with a pulse width of approximately 2 ms and a repetition rate of 100 Hz. Accompanying the neutron beam is a small gamma ray component originating from neutron activation within the machine and surrounding materials and from the thermal neutron capture reaction with hydrogen in the patient.

8.2.2 Description of probe assembly and phantom

The microdosimeter probe assembly used was the low noise "Probe Assembly #2" fully described previously in section 4.4. Two types of silicon microdosimeters were used in this study with SOI thickness' of 2 and 10 μm. For both devices, the small diode size (10×10 μm^2 junction) array was selected since this array has the smallest overlayer and has been used most extensively in other experiments. To correctly resolve the recoil proton component of the lineal energy spectrum a measurement down to around 1-2 keV/μm is required. The largest thickness of SOI, 10 μm, was selected to provide the highest signal to noise ratio. The smaller SOI thickness was included to gauge the effect of chord length distribution variation and sensitive volume size.

The charge collection characteristics of the devices, at the selected reverse bias voltage of 10 V, were fully described in section 6.2.4.1 and 6.2.4.2. The device bias was set to 10V so that the depletion depth is approximately 3 μm in the 10 μm device. Hence the

10 μm SOI is not fully depleted and charge collection occurs via diffusion as well as drift processes. For the 10 μm device, the charge collection efficiency was found to vary from about 0.79 in regions most distant from a diode junction to 0.86 in the center of a junction where drift collection is strongest. This relatively small variation is a result of the large minority carrier diffusion length (61 μm) in comparison to the cell dimensions (30×30×10μm). Therefore, the collection efficiency for the 10 μm SOI device may be reasonably approximated by a constant value of 0.83. For the 2 μm SOI device, the collection efficiency is also approximately constant at 0.94. Both devices have an effective thickness that is reduced not only by the collection efficiency but also due to LOCOS silicon consumption in some regions of the device. The later effect is proportionally more influential for the 2 μm SOI device.

In summary, the diode array sensitive volume may be approximated by an infinite slab with an effective charge collection thickness (averaged over the device area) of ~ 8.2 μm for the 10 μm SOI device and ~1.8 μm for the 2 μm SOI device. An infinite slab geometry is a reasonable approximation since the thickness of the devices is 2-3 orders of magnitude less than the width (1.2 mm) and length (3.6 mm) of the total array. Converting to tissue equivalent geometry using a scaling factor of 1/0.63 (as described in section 5.4), we obtain TE thickness' (h) of 12.9 μm and 2.8 μm, respectively for the 10 μm and 2 μm SOI devices. The diameter of the spherical proportional counter used in this work is 2 μm. The chord length distribution assuming μ-randomness conditions (i.e. infinite range tracks and uniform isotropic particle emission) for the infinite slabs and sphere are compared in Figure 8.1. As discussed in detail in chapter 3, the sphere is favored for its minimum CLD relative variance and isotropic response.

Microdosimetric spectra require an estimate of the detectors mean chord length (MCL or $\bar{l}$). An accurate value of $\bar{l}$ may be obtained via Monte-Carlo simulation methods which transport charged particles through the experimental setup and determine the path length traversed through the device. However, usually in proportional counter microdosimetry $\bar{l}$ is calculated analytically assuming μ-randomness. Reiterating results obtained in chapter 3, for a sphere, $\bar{l} = 2/3\ d$ where d is the sphere's diameter and for an infinite slab $\bar{l} = 2h$ where h is the slab thickness. In practice, the secondary particle ranges are not infinite and the radiation may not be isotropic. Therefore, the most

appropriate mean chord length for the infinite slab may lie somewhere between h (normally incident) and $2h$.

Due to uncertainty in selecting an appropriate mean chord length for the infinite slab, two alternative approaches are adopted in this work based on the motivation to compare the silicon microdosimeter to the proportional counter. The first method involves calculating the dose mean lineal energy $y_{d,cutoff}$ for the proportional counter and silicon microdosimeter measurements. The "cutoff" subscript signifies that the calculation is only performed over the lineal energy range measured by the silicon microdosimeter as indicated in the following expression:

$$y_{d,cutoff} = \frac{\int_c^\infty y^2 f(y)dy}{\int_c^\infty y\, f(y)dy} \tag{8.1}$$

where c is the lower lineal limit of the microdosimeter. The mean chord length for the silicon microdosimeter measurements is then iteratively adjusted to provide the same value of $y_{d,cutoff.}$ as the proportional counter. The second method for estimating $\bar{l}$ simply involves adjusting $\bar{l}$ to provide the best alpha and proton peak fit between the proportional counter and silicon microdosimeter *yd(y)* spectra. The relative merits of both methods and a comparison with the expected $\bar{l}$ range (h to $2h$) will be discussed in the results section.

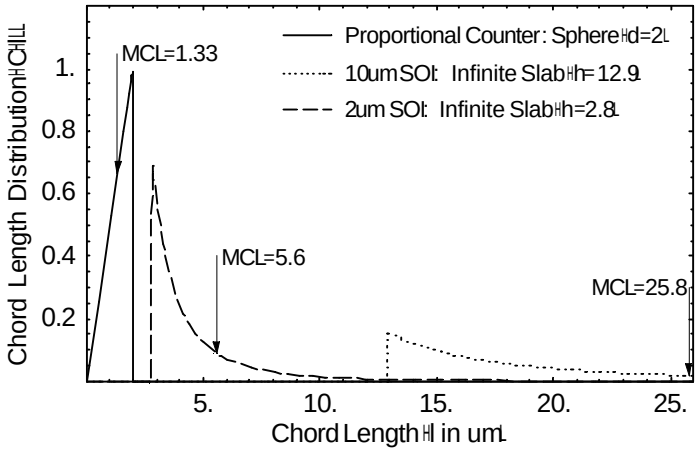


Figure 8.1. Chord length distribution for proportional counter, 10 µm SOI silicon microdosimeter and 2 µm SOI silicon microdosimeter. SOI devices are approximated by an infinite slab geometry.

8.2.3 Microdosimetric measurements

The microdosimeter probe was placed in a 30 × 30 × 30 cm water phantom constructed using 8.5 mm thick Lucite walls as shown in Figure 8.2. A specially designed Lucite holder fixed the probe assembly to the phantom walls. The water phantom was placed at a source-to-surface (SSD) distance of 183 cm. Single event spectra were recorded at a field size of 10 × 10 cm defined at the SSD. Using the 10 μm SOI device, measurements were performed along the beam central axis at a depth in the water phantom of 2.5 cm and 10 cm. In addition, a lateral measurement was performed at a depth of 10 cm and at a position 7 cm away from the central axis. For brevity, this position will be referred to as being 7 cm off-axis in the rest of the paper. Only, a single measurement, along the central axis at 10 cm, was performed using 2 μm SOI device.

The primary objective of these measurement conditions was to facilitate comparison with previous proportional counter measurements. These measurements, performed under identical experimental and beam conditions, are described in detail by Kota [154]. The proportional counter was a commercial 1/2" spherical LET counter (Far West Technology Inc., Goleta, CA) with an internal diameter of 12.7 mm and a 2.54 mm thick A-150 tissue equivalent plastic wall. The counter was filled with a propane based TE gas (CO_2 - 40.0%, N_2 - 5.0%, C_3H_8 - 55.0%) at a pressure of 8.8 kPa to simulate a unit density tissue volume of 2 μm diameter (d). Therefore, the mean chord length for the proportional counter was $\bar{l} = 2/3d = 1.33$ μm

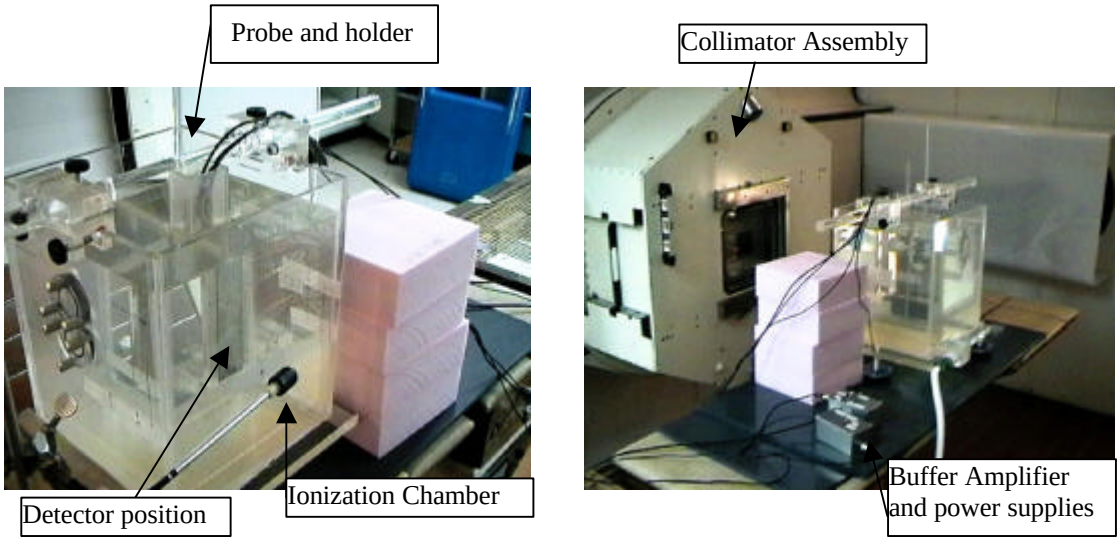
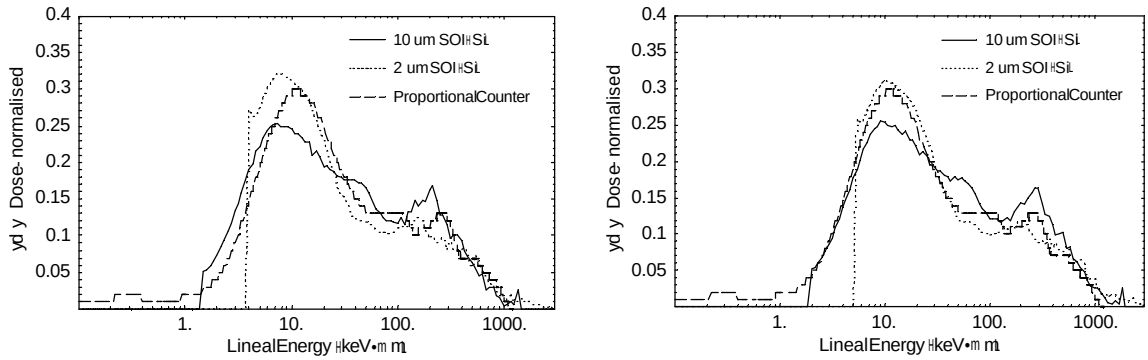


Figure 8.2. Microdosimeter probe, water phantom and collimator beam port used at Harper Hospital. The ionization chamber (Farwest Technology, 8150 TE plastic 1 cm^3) as indicated was used to monitor the total dose. Although not used in this study, the integrated charge data was collected for possible future analysis of microdosimetric spectra in terms of absolute dose.

8.3 Experimental Results and Discussion

8.3.1 Comparison of 2 μm and 10 μm SOI devices with the proportional gas counter.

The microdosimetric spectrum for the 2 μm and 10 μm SOI devices were compared with the proportional gas counter as shown in Figure 8.3. All measurements were performed at 10 cm depth on the central axis. Two presentations of the data are shown corresponding to different values of $\bar{l}$. The left side (Figure 8.3 (a)) shows the SOI diode array spectra with $\bar{l}$ set to give the same dose mean lineal energy as the proportional counter. The calculation of $\bar{y}_d$ favorably weights the data at high lineal energies, as seen by inspection of equation (8.1), resulting in the three spectra overlapping each other closely for lineal energies greater than 300 keV/μm. The right side (Figure 8.3 (b)) has $\bar{l}$ for the SOI diode array set to provide the best peak fit to the proportional counter spectrum ($\bar{l}$ ~0.75 times the left side values). The 2 μm SOI device is a remarkably close fit to the proportional counter despite its significantly different chord length distribution shown in Figure 8.1.



(a) $\bar{l}$ (2μm SOI) = 4 μm.
$\bar{l}$ (10 μm SOI) = 9.2 μm.
$\bar{l}$ (prop. counter) = 1.33 μm.

(b) $\bar{l}$ (2μm SOI) = 3 μm.
$\bar{l}$ (10 μm SOI) = 6.9 μm.
$\bar{l}$ (prop. counter) = 1.33 μm.

Figure 8.3. Comparison of microdosimetric spectra for 2 μm and 10 μm SOI devices with the proportional gas counter. Measurements were performed at 10 cm depth on the central axis. The left side (a) shows the SOI diode array spectra with a MCL set to give the same dose mean lineal energy as the proportional counter. The right side (b) has the MCL for the SOI diode array set to provide the best peak fit to the proportional counter spectrum ($\bar{l}$ ~0.75 times the left side values)

Before further discussion of the spectral features, it will prove useful to review the detailed analysis of the proportional counter spectrum provided by Kota [154]. The neutron beam has a maximum energy of 52.5 MeV, resulting in a maximum recoil proton energy of 52.5 MeV. The lineal energy corresponding to such energetic protons in the T.E. gas is ~ 2 keV/μm. Events with lineal energies lower than 2 keV/μm are due

to secondary electrons mostly arising from the gamma rays accompanying the neutron beam. The secondary electron contribution may extend as high a 15 keV/um but the relative contribution above 2 keV/μm is small in comparison to the proton component.

The prominent proton component is marked by a peak at around 10-15 keV/μm and a proton edge at ~ 130 keV/μm. The position of the proton peak is dependent on the mean neutron energy [283], with the peak shifting to higher lineal energies with decreasing mean neutron energy. The proton edge represents the maximum lineal energy that protons can have in a 2 μm diameter volume. This occurs at the end of the proton range in the Bragg peak. The energy of such protons with a range of ~2 μm in the propane based TE gas was estimated by Kota [154] from the stopping power tables in ICRU Report No. 49 [284] to be 173 keV, corresponding to a lineal energy of 130 keV/μm. For sensitive volumes that have a well defined maximum chord length, the proton edge provides an excellent and convenient calibration technique that is independent of the mean neutron energy. Above a lineal energy of 130 keV, the proportional counter spectrum is composed of contributions from alpha particles and heavy ion recoils. In particular, the spectra displays an alpha peak at ~250 keV/μm and an edge at 350 keV/μm.

In comparing the 2 μm proportional counter and the 2 and 10 μm SOI devices, five main effects contribute to differences in the observed spectrum:

1. *Noise limitation* of SOI microdosimeter.
2. Undefined upper limit to SOI microdosimeter CLD and differing CLD => Poorly defined *proton edge*.
3. Increased *relative variance of SOI microdosimeter CLD* => Spread in spectrum and possibility of very high lineal energy events.
4. Increased *gamma contribution* due to larger sensitive volume of SOI microdosimeter => Shift in the proton peak to lower lineal energy.
5. Increased *proportion of non-crossers* due to larger sensitive volume of SOI microdosimeter => (a) Shift in heavy ion recoil contribution to lower lineal energies and (b) greater influence of nuclear reactions in silicon.

The second and third effects arise from chord length distribution differences and the last two originate from sensitive volume size differences that shift the spectrum downwards. This is compensated for by the small mean chord length used in Figure 8.3(b). Effect (3) is manifest by the increased width of the proton peak and the observed events with lineal energy >1000 keV/μm. These influences will now be discussed in more detail:

1. *Noise Limitation:* The current noise limit of the silicon microdosimeter does not permit measurements below the lineal energies of $c \sim 1.2$ keV/μm for the 10 μm SOI device and $c \sim 4$ keV/μm for the 2 μm SOI device. Since the silicon microdosimeter does not measure data at the low lineal energies provided by the proportional counter, the normalization of the dose distribution spectrum *d(y)* must be modified for a correct comparison. Normally, the dose distribution *d(y)* is normalized to unity since by definition:

$$\int_0^\infty d(y)dy = 1 \tag{8.2}$$

For the silicon microdosimeter, we normalize to the proportional counter measurements as follows:

$$\int_c^\infty d_{si}(y)dy = \int_c^\infty d_{gas}(y)dy = \begin{matrix} 0.96 & \text{c} = 1.2 \text{ keV / um (10 um SOI)} \\ 0.89 & \text{c} = 4 \text{ keV / um} \quad \text{(2 um SOI)} \end{matrix} \tag{8.3}$$

2. *Proton Edge:* The proton edge technique may not simply be used for calibrating the SOI microdosimeter spectra since the maximum chord length is not well defined as discussed in section 8.2.2. The maximum chord length for the diode array with side lengths of ~1.2×3.6mm is approximately given by the diagonal equal to 3.8 mm. In practice, this chord length will almost never be traversed. (Hence the reasonable approximation to an infinite slab) The silicon microdosimeter, with its current sensitive volume, will still display a proton edge although it will not be as sharply defined as for the spherical proportional counter due to the long upper tail of the chord length distribution. Furthermore, as the sensitive volume increases in size, the proton edge will gradually move to lower lineal energies since the average LET of the longer range proton drops. The proton edge for the silicon microdosimeters

appears at ~80 keV/μm in Figure 8.3 (b) compared to ~130 keV/μm for the proportional gas counter.

3. *Relative Variance of CLD:* The possibility of large chord lengths relative to the MCL in the silicon devices increases the number of very high lineal energy events (>1000 keV/μm) for these devices as shown in Figure 8.3 (b). For Figure 8.3 (a), where the spectra have identical y_d, the main spectral features do not coincide as neatly as in Figure 8.3 (b) partly due to the increased number of high lineal energy events that leads to a shift in the silicon spectra to the left in order to satisfy $\bar{y}_d$ equivalence.

4. *Gamma Contribution:* Further distortion of the silicon microdosimetric spectra occurs due to the large sensitive volume enabling a larger gamma contribution to the spectra, particularly for the 10 μm SOI device. The effect of the larger gamma contribution is to shift the proton peak downwards and increase the prominence of the proton edge. The larger gamma contribution is a possible explanation for the relatively low $\bar{l}$ used in the spectra of Figure 8.3, particularly for the 10 μm SOI device. The $\bar{l}$ are summarised in Table 8.1. The $\bar{l}$ of the 10 μm SOI device required to match the proton peak is lower than expected since the proton peak has been shifted to lower energies due to the high gamma component.

Table 8.1. Estimated mean chord lengths for silicon microdosimeter compared with the expected range of values.

Microdosimeter	MCL (Equivalent y_d method, μm)	MCL (Peak fit method, μm)	MCL (Expected Range, h-2h) (μm)
2 μm SOI	4	3	2.8 - 5.6
10 μm SOI	9.2	6.9	12.9 - 25.8

5. *Proportion of non-crossers:* The larger sensitive volume of the silicon detector also distorts the higher lineal energies due to an increased proportion of non-crosser events such as starters, insiders and stoppers. Figure 8.4 reproduced from the work of Caswell and Coyne [285] shows the relative contribution of event types to the microdosimetric spectrum of a 1 and 32 μm spherical volume exposed to 9 MeV neutrons. The proportion of crosser events is maximized by reducing the sensitive volume dimensions relative to the range of secondary recoil products which is set by the mean neutron energy. Thus the proportion of various events in the (9 MeV

neutron,1 μm diameter) case will be comparable to the ~(20 MeV neutron-2 μm diameter) configuration used in this work. The proportion of non-crosser events in the (9 MeV neutron-32 μm diameter) case will be higher than the ~(20 MeV neutron-(10 μm SOI device)) diameter configuration due to the larger sensitive volume. Nevertheless, the general effects of large sensitive volumes on spectral characteristics shown in Figure 8.4 are illustrative.

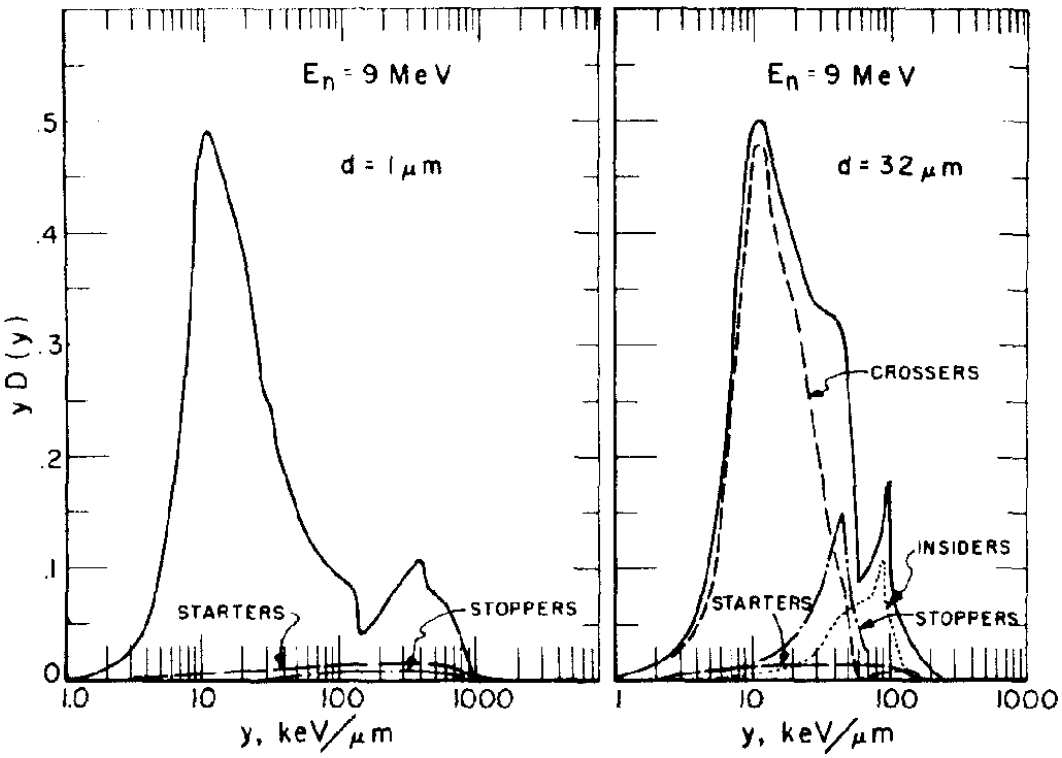


Figure 8.4. Calculated energy deposition distributions for 9 MeV neutrons in ICRU tissue for a 1 μm and a 32 μm spherical cavity, showing the contribution of insiders, starters, stoppers and crossers. For the 1 μm cavity the crossers are so close to the total, that they are not drawn on the graph, while the insiders are negligible. (Reproduced from Caswell and Coyne [285])

The effect of a high proportion of insiders and stoppers is to shift the heavy ion recoil component to lower lineal energies since the non-crosser event energy is divided by an $\bar{l}$ larger than its actual range within the sensitive volume. The 10 μm SOI device is expected to be affected by this type of spectral distortion.

The long range of proton recoils ensures that the proton peak remains at the same lineal energy despite a large variation in site size. This is an important reason for favoring the $\bar{l}$ adjustment method of maintaining a constant proton peak as shown in Figure 8.3 (b).

Another problem associated with a high proportion of non-crossers is the increasing influence of nuclear reactions with the silicon detector which will have a different

secondary recoil product spectrum than a TE material. The issue of TE is further discussed in section 8.3.3.

The difficulty in using a proton edge for calibration and the distortion of $\bar{y}_d$ by spectral changes in the prototype silicon microdosimeter are strong reasons for reducing the sensitive volume elongation and using a cubic shape. Furthermore, the cube has the minimum chord length relative variance for a RPP type volume, thus reducing chord length distribution influences on the final spectrum and providing a more clearly defined $\bar{l}$, as discussed in chapter 3. Minimization of the sensitive volume size is expected to reduce spectral deviations associated with gamma contributions and non-crosser contributions. However, to maintain an adequate signal to noise ratio with a small sensitive volume, low noise design improvements are necessary such as an on-chip pre-amplifier as discussed in section 3.5.6.

Despite the large differences in chord length distributions, the three microdosimeters display remarkably similar spectral features. A comparison of features is best performed by considering Figure 8.3 (b). The spectra have been aligned to the main proton peak. The shape of this peak is very similar for the 2 μm SOI and proportional counter since their mean chord lengths are most similar. All spectra show an alpha/ heavy ion recoil peak in the lineal energy range of 200-300 keV/μm.

In summary, the 2 μm SOI device provides a dose distribution spectra that is similar to the proportional counter but requires improvements in low noise capability. The 10 μm SOI spectrum manifests many of the key features of the proportional counter spectrum modified somewhat by the previously discussed effects. For comparison of the proportional counter with the SOI microdosimeter, the interpretation is facilitated by selecting a MCL such that the main proton recoil peaks correspond. This presentation, as given in Figure 8.3 (b), will be used for the remainder of this study.

8.3.2 Microdosimetric characterization of neutron beam using silicon microdosimeter

Given that the silicon microdosimeter spectrum reproduces the important features of the proportional gas counter spectrum, one may study the relative spatial variation in microdosimetric qualities of the neutron beam within the water phantom. The microdosimetric dose distribution measured using the 10 μm SOI silicon microdosimeter and proportional gas counter at two depths (2.5 cm and 10cm) along the

central axis of the beam are shown in Figure 8.5. The spectra at different depths are very similar to each other, suggesting that the change in the neutron energy spectrum and RBE along the central axis, if any, is minimal as concluded by Kota [154]. Thus, although the silicon microdosimeter spectrum differs in several ways from the proportional gas counter microdosimetric radiation quality variations may still be characterized.

A similar comparison may be made at 10 cm depth and 7 cm off-axis as shown in Figure 8.6. The spectrum measured off-axis shows a significantly increased gamma fraction, an enhanced proton edge, a slight increase in the lineal energy of the recoil proton peak and a significant decrease in the heavy ion component. These effects are more strongly manifested in the 10 μm SOI device due to the larger sensitive volume invoking an increased sensitivity to gamma contributions. As noted by Kota [154], the spectral changes in the off-axis measurements reflect the decrease in the primary neutron fluence and an increase in the lower-energy scattered neutron fluence in the beam penumbra. Kota [154] also states that the measured proportional counter spectrum is an integral response to a rapidly varying neutron beam in the penumbra region, since the relevant lateral dimension of the LET gas counter is approximately 1.5 cm. In this penumbra region, of rapidly varying spectral characteristics, the silicon microdosimeter offers advantages over the proportional counter due to its smaller size and higher spatial resolution. It is recommended that future comparative studies should be performed to assess the relative spatial resolution capabilities of the microdosimeters in the penumbra region.

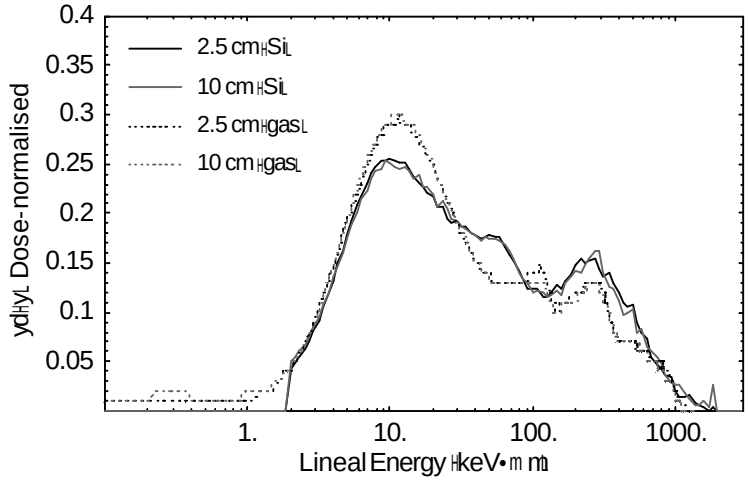


Figure 8.5. Lineal energy dose distribution measured using the 10 μm SOI silicon microdosimeter and proportional gas counter at two depths along the central axis of the beam.

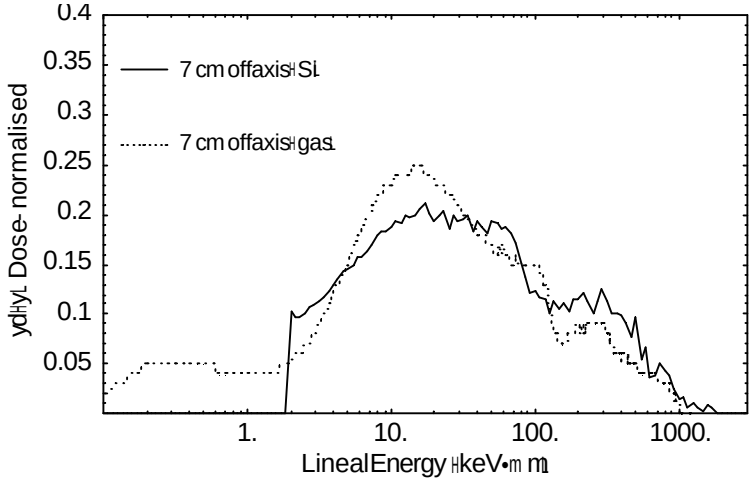


Figure 8.6. Lineal energy dose distribution measured using the 10 µm SOI silicon microdosimeter and proportional gas counter at 7 cm off-axis from the center of the beam and 10 cm depth.

The qualitative arguments presented above, in terms of the shape of the single event spectra, are quantified using $\bar{y}_d$ and y^*. Recall, that the dose mean lineal energy $\bar{y}_d$ is given by

$$\bar{y}_d = \frac{\int_0^\infty y^2 f(y)dy}{\int_0^\infty y\, f(y)dy} \tag{8.4}$$

In an effort to improve the relationship between $\bar{y}_d$ and observed biological effects, Kellerer and Rossi [18] proposed a saturation correction to account for the excessive ionization density of the high lineal energy particles over and above requirements for cell death. The saturation corrected dose mean lineal energy y^* is given by:

$$y^* = \frac{\int_0^\infty y_{sat} y f(y)dy}{\int_0^\infty y\, f(y)dy} \tag{8.5}$$

where the saturation correction function y_{sat} is given by:

$$y_{sat} = \frac{y_0^2}{y}(1 - e^{-(y/y_0)^2}) \tag{8.6}$$

with y_0 = 125 keV/µm.

The weighting function y_{sat} is shown in Figure 8.7. The weighted spectrum $y_{sat}yf(y)$ is also shown indicating the reduced emphasis on the high lineal energy events compared

to the standard spectrum $y^2f(y) = yd(y)$. Note that the "weighting" function for the standard case is simply y.

The calculated values of $\bar{y}_d$ and y^* for the various detector types and locations in the water phantom are shown in Table 8.2. The proportional counter shows a small (3%) decrease in $\bar{y}_d$ and y^* with depth along the central axis and a more pronounced decrease (5% for y^*) for the 7 cm off-axis measurement. The larger gamma component and decreased heavy ion component in the off-axis account for the decrease in $\bar{y}_d$ and y^*. These trends are not accurately reflected in the 10 µm SOI device calculations for two main reasons. Firstly, the SOI spectrum does not include data for lineal energies below ~1.2 keV/µm. More importantly, the spectrum shape is sufficiently different due to chord length distribution and sensitive volume size differences that a match with the trends of the proportional counter is not possible.

Table 8.2. Calculated values of $\bar{y}_d$ and y^* for proportional counter and 10 µm SOI device at various locations in the water phantom

Microdosimeter	$\bar{y}_d$			y^*		
	2.5 cm central	**10 cm central**	**7 cm off-axis**	**2.5 cm central**	**10 cm central**	**7 cm off-axis**
2 µm Proportional Counter	84.9	81.9	64.9	27.6	26.8	25.4
10 µm SOI device ($\bar{l}$ =9.2 µm)	81.1	84.2	74.8	29.2	29.1	28.9
10 µm SOI device ($\bar{l}$ =6.9 µm)	108.3	112.4	100	31.1	31.0	31.45

Note: The 7 cm off-axis measurement was performed at a depth of 10 cm.

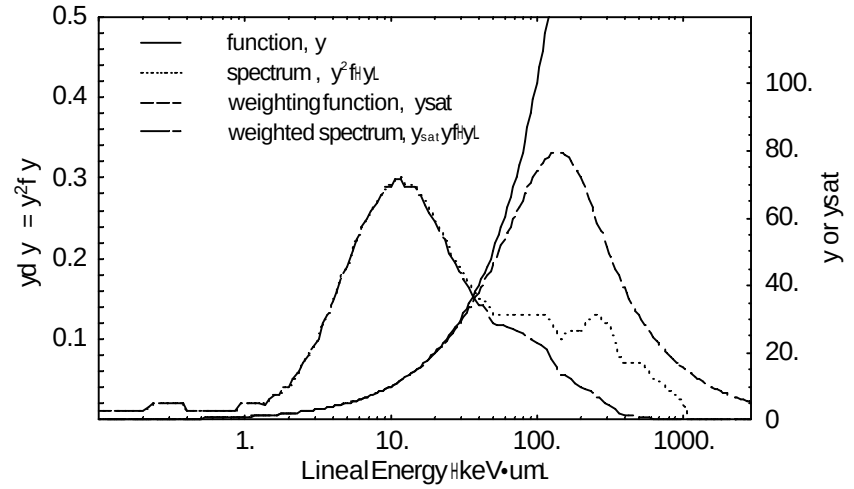


Figure 8.7. The weighting function y_{sat} used to correct the measured single event spectrum for saturation effects at lineal energies greater than 125 keV/µm. The weighted spectrum $y_{sat}yf(y)$ for the 2µm proportional counter (10 cm central axis) is shown compared to the standard spectrum $y^2f(y) = yd(y)$. The weighting function for the standard case is simply y.

8.3.3 Tissue equivalence issues using a silicon microdosimeter in fast neutron beams

The tissue equivalence of silicon microdosimeters exposed to neutron beams was discussed in some detail in section 5.5. The main conclusions are reiterated here and applied to the specific neutron beam characteristics of the Harper hospital facility.

Given identical secondary charged particle spectra, a given volume of silicon will have the same microdosimetric energy deposition as a tissue volume of equivalent shape if the dimensions of the silicon are scaled by 1/0.63. Differences in the spectra observed between the spherical proportional counter and the SOI microdosimeter arise not only from chord length distribution differences, following the above scaling procedure, but also from variations in the secondary charged particle spectra. Differences in secondary charged particle spectra arise from the use of silicon as the detector material compared to TE propane gas and dissimilar materials immediately surrounding the detector. For the SOI device, the materials surrounding the detector include SiO_2, TiN and Al overlayer structures along with the 20 mm of Lucite in the probe holder. By comparison, the proportional gas counter has a 2.54 mm thick A-150 tissue equivalent plastic wall. These large differences in materials and construction are expected to account for some of the dissimilarity in high lineal energy events seen between the proportional counter and the SOI microdosimeter.

The recoil proton spectrum originating from the Lucite converter and the A-150 TE plastic should be similar. However, the secondary charged particle spectra from nuclear interactions with the detector materials will differ. The relative importance of detector material interactions depends on the proportion of "stoppers" and "crossers" to "starters" and insiders". For sensitive volumes that are small in comparison with the secondary charged particle range, most events are due to crossers. This is the case for proportional counters with a simulated diameter of 1-2 μm as shown by Fidorra and Booz [106] (for 5.85 MeV in a site size of 1 μm diameter) and Caswell and Coyne [285] (for 9 MeV neutrons in site sizes of 1 μm and 32 μm). The 2 μm SOI device does not appear to be affected by an excessive number of starters and insiders since the spectral shape is in good comparison with the proportional counter. However, the 10 μm SOI device does have a higher heavy ion component indicative of possible nuclear interactions with the silicon.

The mean energy of the neutron beam is about 20 MeV. At this energy, the ratio of silicon to tissue kerma is ~0.2 as shown in Figure 5.16 compared to only 0.05 at neutron energies below 5 MeV. The probability of a nuclear interaction for 20 MeV neutrons is almost the same for equal thickness' of tissue and silicon as summarized in Table 5.9 extracted from Figure 5.19. Thus, it is not unreasonable to expect that some proportion of the heavy-ion recoil spectrum is due to silicon interactions particularly for the large volume 10 μm SOI device. The proportion at high lineal energies may be exacerbated by the higher probability for inelastic reactions in the silicon (~2.5 times) than tissue. The exact proportion requires more detailed calculations not performed in this work. However, one may conclude that minimizing the silicon volume is an important issue in order to reduce the proportion of silicon interactions and increase the percentage of crossers contributing to the microdosimetric spectrum. The presence of TE material surrounding the detector should also be maximized in future designs.

Table 8.3. Nuclear interaction probabilities for 20 MeV neutrons incident on silicon and muscle.

Material	Nuclear Inelastic Reactions P(interaction in 1 cm)	All Nuclear Interactions P(interaction in 1 cm)
Silicon	0.05	0.09
Muscle	0.02	0.1
Ratio(Si/Muscle)	2.5	0.9

8.4 Summary of FNT Applications

This is the first demonstration of a SOI based microdosimeter in a neutron radiation therapy beam with results sufficiently promising to confirm the feasibility of the device in this application. A detailed comparison with a proportional counter is performed. The SOI device offers several advantages in fast neutron therapy including ease of use (no gas system), system cost, the ability to operate at clinical (high) dose rates and a high spatial resolution. Shortcomings in the current design arise primarily from the large sensitive volume and the chord length distribution of the SOI device along with the need for improved low noise performance.

Despite some deficiencies in the existing design, microdosimetric radiation quality variations may still be characterized qualitatively. General trends in microdosimetric spectra as a function of position within the beam (e.g. small depth dependence, lateral variation) were in good agreement with the proportional counter. However, quantitative

analysis based on calculation of $\bar{y}_d$ and y^* is not recommended with the current design as indicated by a poor correspondence with proportional counter trends.

The study emphasizes the need for minimizing the sensitive volume of the detector to around the 1 μm region and employing a cubic shape with a smaller relative variance, well defined mean chord length and a chord length distribution more nearly approximating a sphere. Such a design will reduce the proportion of silicon interactions and increase the percentage of crossers contributing to the microdosimetric spectrum. The presence of TE material surrounding the detector should also be maximized in future designs and the design should incorporate an on-chip preamplifier to reduce noise. A more detailed analysis of neutron interactions with silicon in various sensitive volume sizes is necessary to ensure the measurement is not influenced significantly by non-TE materials.

This is the first demonstration of a SOI based microdosimeter in a neutron radiation therapy beam with results sufficiently promising to confirm the feasibility of the device in this application. A detailed comparison with a proportional counter is performed. The SOI device offers several advantages in fast neutron therapy including ease of use (no gas system), system cost, the ability to operate at clinical (high) dose rates and a high spatial resolution. Shortcomings in the current design arise primarily from the large sensitive volume and the chord length distribution of the SOI device along with the need for improved low noise performance.

Despite some deficiencies in the existing design, microdosimetric radiation quality variations may still be characterized qualitatively. General trends in microdosimetric spectra as a function of position within the beam (e.g. small depth dependence, lateral variation) were in good agreement with the proportional counter. However, quantitative analysis based on calculation of $\bar{y}_d$ and y^* is not recommended with the current design as indicated by a poor correspondence with proportional counter trends.

The study emphasizes the need for minimizing the sensitive volume of the detector to around the 1 μm region and employing a cubic shape with a smaller relative variance, well defined mean chord length and a chord length distribution more nearly approximating a sphere. Such a design will reduce the proportion of silicon interactions and increase the percentage of crossers contributing to the microdosimetric spectrum. The presence of TE material surrounding the detector should also be maximized in

future designs and the design should incorporate an on-chip preamplifier to reduce noise. A more detailed analysis of neutron interactions with silicon in various sensitive volume sizes is necessary to ensure the measurement is not influenced significantly by non-TE materials.

9. Application to Proton Therapy

9.1 Background to Proton Therapy

The use of proton beams for radiation treatment was proposed by Robert R. Wilson in 1946 [286]. Wilson referred to the ballistical aspects of the proton beam dose distribution as a rationale for the new modality. Heavy charged particles such as protons produce an energy deposition profile in tissue which is superior to profiles attainable using photon or electron irradiation. The dose distribution for a monoenergetic proton beam features a low entrance dose region followed by a slowly rising dose until the proton Bragg peak is reached, near the end of the range, where the dose rises rapidly. The beam energy is generally spread to modulate the proton range and provide a uniform high dose over the target tissue. This profile also features a moderate entrance dose and almost zero dose beyond the target [99].

In view of the excellent dose profile, proton therapy is recommended for tumors with the following characteristics [272]:

- A loco-regional evolution (thus with a low metastatic tendency)
- Cannot be totally surgically removed.
- Need high doses of radiation for cure (often more than 70 Gy)
- Lie very close to exquisitely radiosensitive organs or tissues

Particular success has been found in the treatment of uveal (or ocular) melanomas and the postoperative management of base of the skull and spinal canal malignancies. For example, Munzenrider [287] reported that enucleation (eye removal) was performed in only 57 of 1006 patients (5.7%) with uveal melanoma. Up to 1995, more than 13000 patients throughout the world had been treated with protons and almost half of them underwent treatment at the Massachusetts General Hospital in Boston [99, 272].

For patient treatment planning, knowledge of the beam RBE is vitally important. Clinical response to proton beam treatments at the Harvard Cyclotron Laboratory along with radiobiological studies led to the adoption of a universal RBE value of 1.1 for proton therapy. Studies at Loma Linda by Robertson [288] using the deactivation of V79 Chinese hamster cells *in vitro* indicated RBE values varying from 1.1 to 1.3 with

an increasing trend near the distal beam edge. Clearly, the relative biological effectiveness of the beam varies with depth. A 250 MeV proton has an initial LET of 0.4 keV/um. This rises sharply in the Bragg peak region reaching a maximum value of approximately 80 keV/μm within a few microns of the end of the range. Coutrakon [155] estimated an RBE of 1.65 at the distal edge (50% of mesa dose) based on microdosimetric measurements correlated to V79 Chinese hamster cell experiments. Microdosimetric measurements, at depths where protons enter the Bragg peak region, are particularly challenging due to the high spatial resolution required.

Further justification of the need for experimental microdosimetry in proton therapy may be seen by a brief examination of the interaction of protons with matter. Protons interact with matter by continuous slowing down as a result of Coulomb collisions with electrons and nuclei, by Bremsstrahlung radiation loss, and by nuclear reactions. The Coulomb interaction with electrons is the predominant mechanism for energy loss and is typically described by the electronic stopping power or LET of the proton [284]. Radiation loss is negligible for the energies of interest in proton therapy. However, nuclear reactions have a significant effect on the proton beam characteristics. The probability that protons in the energy range of proton therapy (<250 MeV) will undergo a nuclear interaction whilst traversing 1 gm/cm^2 is around 1% and after 20cm 1 in 4 protons will have suffered a nuclear interaction. A NIST report by Seltzer [289] and summarized by Miller [99] describes the interactions and products. Approximately 21% of the energy lost in slowing down a 250 MeV proton beam in water is due to nonelastic nuclear reactions. This fraction drops to around 4% for a 70 MeV beam. Thus nuclear interactions affect the identity and energy distribution of the secondary particles and decrease the number of primary protons in the beam.. An important characteristic of the beam is the LET spectrum of all primary and secondary particles responsible for the radiobiological properties of beam. Thus, microdosimetric measurements in a water phantom are important in high energy proton therapy installations.

Microdosimetric studies of proton beams have been performed by several investigators [155, 288, 290-293]. Typically, a spherical proportional counter containing a low-pressure tissue equivalent gas is used to obtain the spectrum of energy deposition events [1]. The millimeter resolution required in the Bragg peak region is not achievable using such a counter which normally has a diameter of 1-2 cm. Coutrakon [155] concludes a detailed study of microdosimetry and RBE measurements at Loma Linda with the

following: "More measurements using techniques to obtain spectra with finer depth resolution on the distal edge will be useful to track lineal energy and RBE changes more precisely". Parallel plate type proportional counters have been developed [291, 292] but these are still larger than the silicon microdosimeter and not as convenient to use.

The large size of the proportional counter also creates problems with pileup effects due to simultaneous multiple events during high DC current operation or when the proton beam consists of large currents produced in nanosecond to microsecond pulses. Measurements of microdosimetric spectra using a proportional counter have been reported with count rates as low as 350 counts/sec still exhibiting pileup due to the large size of the counter [292]. Therefore, proton microdosimetry requires small microdosimeters with high spatial resolution (<1mm) and small collection areas along with a short collection time in the tens of nanosecond range. Furthermore, analysis of the pulse time structure of the beam current is important for correct measurements of microdosimetric spectra.

The SOI microdosimeter developed in this work offers the potential to eliminate pile-up effects and greatly improve spatial resolution due to its small size. In this chapter, experiments at two proton therapy facilities are discussed. The experiments were conducted at the Proton Medical Research Center (PMRC) at University of Tsukuba, KEK, Japan, using a 250 MeV proton beam and at the Northeastern Proton Therapy Center (NPTC), Boston using a 230 MeV proton beam. The aim of the experiments was a preliminary study of the performance of the silicon microdosimeter to confirm its capability at measuring the expected microdosimetric features. The ability of the device to minimize pileup effects and its high spatial resolution are discussed in some detail. A comparison of experimental results with computer simulations is also presented. Two different probe assemblies are used in this work corresponding to different stages in the project development.

9.2 Experiment at PMRC-Tsukuba

The main aim of the experiment was to demonstrate the capability of the small silicon microdosimeter to perform measurements under difficult pile-up prone beam conditions for which no previous microdosimetric measurements have been performed.

9.2.1 Materials and Methods

9.2.1.1 Proton Therapy Facility at PMRC-Tsukuba

The proton therapy facility at PMRC uses the KEK 500 MeV booster synchrotron as a beam source [294]. This source was originally designed for HEP experiments and since the energy and intensity are too high for medical applications, the beam energy is degraded down to 250 MeV using carbon based degraders. Additional filters reduced this to 200 MeV for these experiments. In contrast to the NPTC facility, this synchrotron produces 50 ns pulses with an initial $2x10^9$ protons per pulse. The time interval between pulses is about 1 second in parasitic beam mode and 0.05 seconds in full beam mode. Note that the protons/pulse is the same for both parasitic mode and full beam mode. The full beam mode is used for patient treatment and provides a dose rate of approximately 200 cGy/min.

The initial beam intensity is reduced by the carbon degrader followed by a collimator such that around 10^4 protons/pulse are transported to the medical beam line. Then the beam is momentum filtered and shaped for a 10×10 cm^2 field. Thus, the beam intensity is around 4 proton/pulse/device which is much higher than at NPTC. This beam presents a difficult experimental challenge even when using the small area of the silicon based microdosimeter. Clearly, the high luminosity of this beam prevents the use of a proportional gas counter for microdosimetry due to strong pile up effects. Note that reducing the beam current does not reduce pile up effects since it usually involves a reduction in the frequency of pulses rather than the number of protons per pulse.

However, to reduce the protons per pulse one can control the momentum slit width (X) and vertical slit width (Y) which are typically set to 150 and 30 mm respectively.

9.2.1.2 Experimental Setup at PMRC-Tsukuba

This experiment was performed with "probe assembly #1" as described in section 4.3 (Note, that the improved probe assembly #2 had not been developed at this stage of the project). The 10 μm SOI device was selected to provide the highest signal to noise ratio for the measurements. The charge collection characteristics of the device, at the selected reverse bias voltage of 10 V, were fully described in section 6.2.4.2. Under these conditions, the collection efficiency was found to be reasonably approximated by a constant value of 0.82.

Microdosimetric spectra require an estimate of the detectors mean chord length $\bar{l}$. An accurate value of $\bar{l}$ may be obtained via Monte-Carlo simulation methods which transport the protons and other charged particles through the experimental setup and determine the path length traversed through the device. However, a reasonable first order approximation assumes that the beam is largely normal to the diode surface in which case we may approximate $\bar{l} \sim 8.2\mu m$. In this paper, with an emphasis on device operation, we present all results based on the silicon mean chord length without TE correction (as discussed in section 5.5). Note also, that a direct comparison with a TE proportional counter is not performed in this study.

Since the beam is largely normal to the device, it is reasonable to use the "proton edge" for calibration, a method discussed in section 8.3.1. For a normally incident proton the maximum energy deposited, at the end of the proton range, in 9.9 μm of silicon (10μm SOI - 0.1 μm LOCOS region) is 737 keV. The energy collected is then ~604 keV (0.82×737 keV) which corresponds to a maximum lineal energy of 73.7 keV/μm. Thus the proton edge will occur at around 74 keV/μm with some smoothing of the edge due to protons that are not normally incident. The spectra presented in this chapter have been calibrated to ensure the proton edge lineal energy coincides with this value. Further discussion of this spectral feature is provided in section 9.3.2.2.

The microdosimeter was placed in a 15×15×30 cm^3 Lucite phantom constructed of 2.5 cm blocks. Such a construction allowed the placement of the detector at different positions along the beam line axis. To avoid pile-up and ensure a constant energy the momentum slit was fixed at X = 3 mm whilst the vertical slit was varied from Y = 30 to 2mm. Microdosimetric spectra at a depth of 17.5 cm were recorded at various values of vertical slit width to determine the settings required to remove pile-up effects. The acquisition time for the measurements was 600 seconds. Measurements at various depths in the Lucite phantom were then performed having found the beam setup which eliminated pile-up. The integral depth-dose was measured by a MOSFET detector.

9.2.2 Results: Microdosimetric Spectra at PMRC-Tsukuba

The depth-dose curve obtained using a MOSFET detector placed at various depths in the Lucite phantom are shown in Figure 9.1. The advantageous characteristic of a MOSFET dosimeter is the extremely small dosimetric volume (~1μm) defined by the gate oxide thickness [71, 175]. High spatial resolution measurements are achievable in

the Bragg peak regions. However, the response of the MOSFET is dependent on the particle LET and angle with respect to the oxide electric field. Further investigation and comparison studies should be performed to compare the depth-dose derived from ionization chambers versus MOSFETs.

The microdosimetric spectra obtained as a function of depth in Lucite are shown in Figure 9.2. The small peaks from 30-100 keV/μm are due to statistical uncertainties. The general shift in the spectrum to higher lineal energies as depth increases from 14 cm to 17.5 cm is evident. The MOSFET depth-dose data indicates that at around 17.5 cm many of the protons will be approaching the end of their range. In this region, the protons have a higher LET, and therefore higher lineal energy, as they approach the Bragg peak. This behavior is in agreement with results obtained at NPTC and by Coutrakon [155] using a proportional counter.

The data obtained using the prototype assembly #1 exhibited significant environmental noise problems particularly when the beam RF was turned on. It is expected that the second prototype with its significantly improved shielding will avoid such difficulties. The lineal energy could not be obtained below 8 keV/μm due to the high noise levels. This was the motivation for development of the low noise prototype. Despite the limited clinical utility of the incomplete spectrum, we may still verify the capability of the device in terms of high count-rate performance.

The vertical slit was adjusted down to 2 mm from the normal value of 30 mm in order to avoid pile-up. Figure 9.3 shows a comparison of microdosimetric spectrum obtained under Parasitic-Beam and Full-Beam modes at PMRC with different vertical slit widths (depth in Lucite phantom = 17.9 cm). This example shows significant pile-up effects using the Parasitic Beam despite its much lower total intensity. To avoid pile-up in either mode the beam requires a vertical slit width of 2 mm in order to reduce the number of protons/spill. The spectra of Figure 9.2 obtained at various depths used such a slit arrangement. The results indicate that the low noise prototype applied to similar beam conditions should be capable of measuring the microdosimetric spectrum down to 1.2 keV/μm without significant pile-up complications.

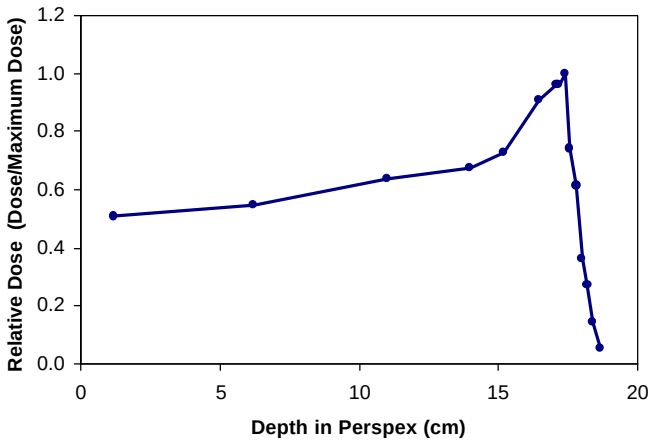


Figure 9.1: Bragg peak of 200MeV proton beam (PMRC-Tsukuba) derived by MOSFET detector in Lucite phantom. Relative dose is the dose normalized to maximum dose at depth of 17.4 cm.

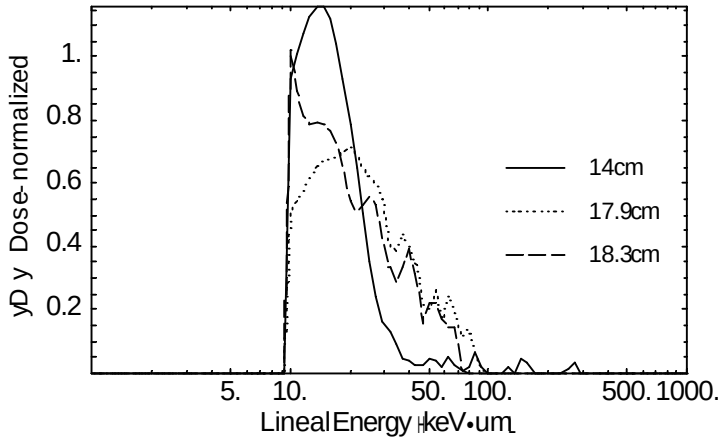


Figure 9.2: Microdosimetric spectra of 200MeV proton beam (PMRC-Tsukuba) at various depths in a Lucite phantom. Range of proton is approximately 18cm.

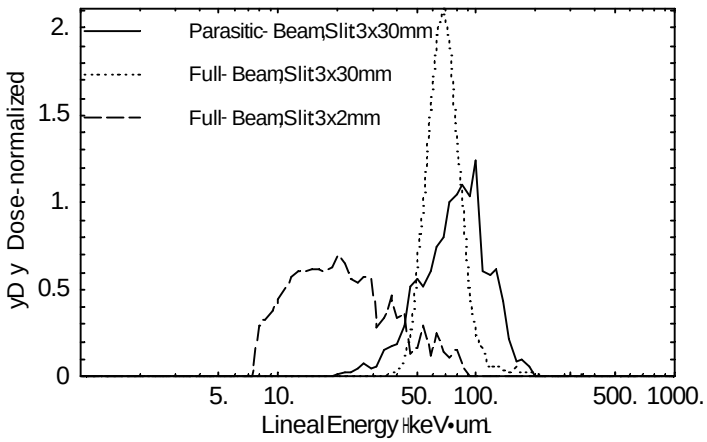


Figure 9.3: Comparison of microdosimetric spectrum obtained under Parasitic-Beam and Full-Beam modes at PMRC-Tsukuba with different vertical slit widths (depth in Lucite phantom = 17.9 cm). This example shows significant pile-up effects using the Parasitic Beam despite its much lower total intensity. To avoid pile-up in either mode the beam requires a vertical slit width of 2 mm in order to reduce the number of protons/spill.

9.3 Experiment at NPTC-Boston

9.3.1 Materials and Methods

9.3.1.1 Proton Therapy Facility at NPTC-Boston

The new proton therapy facility at NPTC utilizes a 230 MeV beam extracted from an isochronous cyclotron [295, 296]. The accelerator was built by Ion Beam Applications (IBA), Belgium and has a maximum current of 1.5 μA which is hardware limited to 300 nA in order to limit the maximum dose rate to the patient. After extraction from the cyclotron the beam passes through the Energy Selection System (ESS) designed to give a beam of any energy between 70 and 230 MeV with a user defined momentum width and emittance. The ESS uses a rapidly adjustable rotating variable thickness of graphite. Slits are provided just after the energy degrader to reduce the beam divergence to $\Delta E/E<\pm 1\%$. The facility uses a range modulator filter to create the desired spread in the proton Bragg peak. A double scattering system using a fixed scatterer and a second non-uniform thickness scatterer produce a beam with uniform intensity in the lateral profile over a 10×10 cm^2 field size.

The NPTC cyclotron operates in continuous wave mode using a 106 MHz RF frequency. Acceleration of protons occurs within 10-15 degrees of the RF wave. The time structure of the beam is therefore semi-DC with a duty-cycle of about 10% (30deg/330deg). A typical treatment beam is 2 nA equivalent to 1.25×10^{10} protons/second. So in a single RF cycle of 9.4 ns there are 118 protons spread over 0.8 ns. For the case of a 10×10 cm^2 field size (obtained using a double scattering method) we can expect 1.2 p/cm^2/cycle. Under these conditions, a microdosimeter should have a small cross-sectional area and fast collection time.

9.3.1.2 Experimental Setup at NPTC-Boston

The improved low noise "probe assembly #2" as described in section 4.4 was used for this experiment. The 10 μm SOI device was selected to provide the highest signal to noise ratio. As discussed in section 9.2.1.2 a mean chord length of 8.2 μm is used for presentation of microdosimetry spectra.

The microdosimeter selected has an active cross-sectional area of 0.044 cm^2. The minimum amplifier shaping time available was 0.25 μs and the Ortec pile-up reject system was employed to eliminate pile-up signals. Note that decreasing the amplifier

shaping time further would increase noise to unacceptable levels. In order to maintain a reasonable dead-time (less than about 20%) we require less than 1 proton per 1.25 μs striking the detector. Such a requirement may be fulfilled using a beam current of 0.25 nA in which case we expect 0.7 p/μs/(device area). In practice, higher beam currents (up to 1 nA) could be employed without excessive dead-time and distortion of the spectra due to pile-up events. The quick calculations performed above do not include losses of beam current due to scattering outside of the beam field.

The microdosimeter was placed in a Scandtronix water tank (Model RFA-300 Plus) which enabled rapid remote adjustment of the detector position. The detector position was aligned with the center of the beam and microdosimetric spectra were recorded at various distances from the beam-side wall of the tank. The depth (distance from the front wall) of the detector includes the probe overlayer materials as summarized in Table 9.1. These materials were estimated to be equivalent (in terms of stopping power) to 12mm of water. At each depth, spectra were recorded using two different gains to provide adequate dynamic range in the final merged spectrum. Initially the beam current was adjusted to ensure that the spectra were not corrupted by pile-up events. Furthermore, during measurements, the signal prior to the MCA was monitored continuously with an oscilloscope to ensure the average interval between pulses was reasonable and no pileup was present. The typical acquisition time was 600 seconds.

In addition, measurements of the depth-dose profile in the water tank were performed using a Markus ionization chamber. Measurements were made every 0.3 cm for the range 0-30 cm along the beam axis. Two measurements at each point were made using different spectroscopy amplifier gain settings (110 and 30). The results are then merged to provide a single spectrum with a higher dynamic range then the constituent spectra.

The proton beam was setup with the energy degrader in pass though position and the ESS configured to provide the full cyclotron energy of 230.5 MeV with an ΔE/E of 0.18%. The cyclotron energy is attenuated by the items identified in Table 9.2 so that the final energy (calculated using SRIM code [126]) of protons entering the water is 191.6 MeV.

Table 9.1. Probe assembly materials in front of the silicon microdosimeter and water equivalent thickness

Item	Material	Thickness (mm)	Water Equivalent Thickness (mm)
Probe Holder	Lucite	6	7.1
Shield	Al	0.4	0.8
Chip Cover	Lucite	3.5	4.1
Air on top of device	Air	0.3	0.0003
Total:			12.0

Table 9.2. Beam items in nozzle of NPTC and proton energy attenuation

Item	Material	Thickness (cm)	EnergyOut (MeV)	Energy Lost (MeV)
Cyclotron	-	-	230.5	-
Fixed scatterer	Pb	0.131	227.3	3.2
Range Modulator 1	Pb	0.4254	216.7	10.6
Range Modulator 2	C	0.0773	216.0	0.7
Beam Spread	Water Eq	3.65	199.8	16.2
Ion chambers	Water Eq	0.304	198.3	1.4
Nozzle air	Air	255	197.1	1.3
Phantom wall	Lucite	1	191.6	5.4

Water Eq: means that the effective thickness is specified in water equivalent terms. The beam spreading filter is made of lead and Lexan.

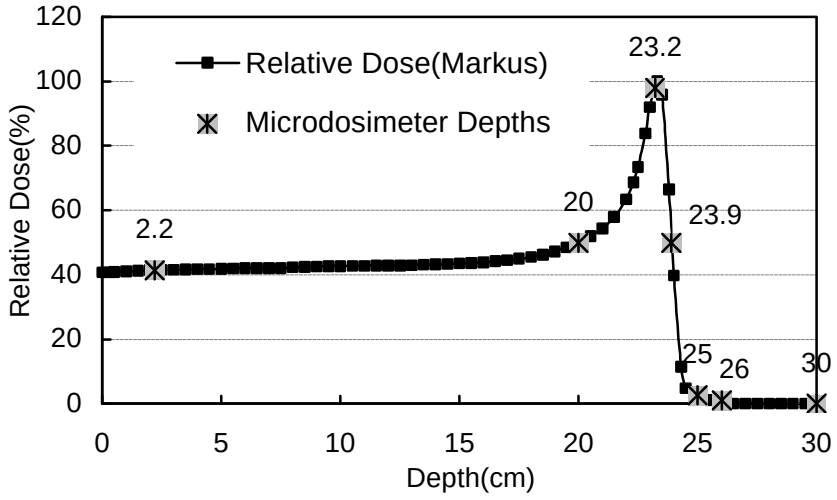


Figure 9.4: Depth-Dose curve for the NPTC 191.6 MeV proton beam in water. Relative dose is defined as Dose(Markus)/Maximum Dose(Markus). The maximum dose is at 23.2 cm and the relative dose = 1 at this point. The depths at which microdosimetric measurements are made are shown.

9.3.1.3 Simulation using SRIM and PRISM

The expected performance of the microdosimeter may be simulated using the Monte Carlo codes; SRIM (Stopping and Range of Ions in Matter) developed by Ziegler [126] and PRISM (Protons in semiconductor materials) developed by Oldfield [297]. Other

semiconductor codes such as CUPID developed by McNulty [298] may also be used for this application.

SRIM was used in the spectroscopy modeling software presented in section 6.2.1 and is capable of simulating the transport of ions through planar slabs composed of any material. SRIM results from the original work by J.P. Biersack on range algorithms [299] and the work by J.F. Ziegler on stopping theory ([184]. The program simulates elastic nuclear collision losses using the theory of Biersack [299] and inelastic atomic collisions but does not simulate inelastic nuclear collisions.

PRISM on the other hand is designed specifically for protons incident on semiconductor materials up to an energy of 450 MeV. The program models the transport of protons in a similar manner to SRIM but includes inelastic nuclear collisions between the ion and silicon target nuclei. Note that below proton energies of 8 MeV no inelastic nuclear reactions are assumed to take place and the reaction cross-section peak occurs at around 30 MeV (~650 mb). Reaction probability, residual products and energies are determined using cross-section data from a variety of sources as referenced by Oldfield [297]. For energies less than 60 MeV the work of Peterson [300] is extensively used.

The proton microdosimetry simulation was performed in three steps; the first two steps used SRIM exclusively and the last device simulation step used both SRIM and PRISM:

1. *Simulation of beam line*: The beam line as described by Table 9.2, with an initial proton energy of 230.5 MeV and an $\Delta E/E$ of 0.18%, was simulated using SRIM in order to determine the proton energy spectrum at the entrance to the water phantom. This was a crude simulation which did not consider the lateral beam spreading design since the beam spreader is a non-planer structure and thus not accurately amenable to SRIM simulation. Thus, the calculated beam energy spread (u=191.6MeV, σ=1.4MeV, $\Delta E/E$=1.7%) underestimates the true energy spread. To compensate the derived standard deviation was doubled, somewhat arbitrarily, to 2.8 MeV, a value also found to produce a reasonable correspondence between simulated microdosimetric spectrum and experimental results.

2. *Simulation of proton transport through water phantom and pre-detector probe materials*: The entrance beam proton energy at a depth of 0 cm in the water phantom was taken to be normally distributed with a mean of 191.6 MeV (Table 9.2) and standard deviation 2.8 MeV. The particle angle of incidence was taken as zero

degrees with respect to the normal. Simulations were performed for a water depth of 2.2 cm (the nearest point to the entrance) and 23.9 cm at the distal edge of the dose distribution (50% dose point as given by Figure 9.4). The output of this simulation was a distribution of proton energies at each depth along with the direction cosines of each proton simulated.

3. *Simulation of 10 mm SOI device energy deposition and charge collection*: Both SRIM and PRISM were used for this simulation. SRIM was employed using the spectroscopic modeling environment described previously in section 6.2.1 using the proton energy and angle information derived from the previous section as input. As such, the model fairly accurately accounts for the differing device regions, varying charge collection efficiency and varying incident proton energy and angle. However, the model does not consider inelastic nuclear reactions as simulated by PRISM. Thus PRISM was run, firstly for comparison with SRIM and secondly to determine the proportion of inelastic reactions originating from the silicon. PRISM accepts RPP shaped volumes and only calculates inelastic reactions with silicon. A cubic silicon volume with side length equal to the wafer thickness of 300 μm, was modeled as shown in Figure 9.5. The width and length were selected to encompass the range of most secondary particles. This simulation volume contained the detector with dimensions of 300×300×9.9 μm where 9.9 μm is the depth of the device (calculated using 10μm SOI - 0.1 μm LOCOS region) and the device overlayer was approximated as 1 μm of silicon. This is a relatively crude approximation to the device since the various oxide and aluminium overlayer regions were not included. However, a first order estimate of the proportion of events due to silicon inelastic interactions may be gauged. The charge collection efficiency of the device was modeled as a simple constant of 0.82 for the PRISM simulation whilst for the SRIM simulation the slightly more accurate collection efficiency function derived in section 6.2.4.2 was used. In addition, PRISM assumed normally incident protons unlike SRIM which used the previous water transport simulation results. Thus, only the proton energy and not the angular distribution was modeled in PRISM. For both models, the final spectra are presented with 20 keV of gaussian smoothing to simulate electronic noise and additional sources of variation consistent with the spectroscopy model of section 6.2.1.

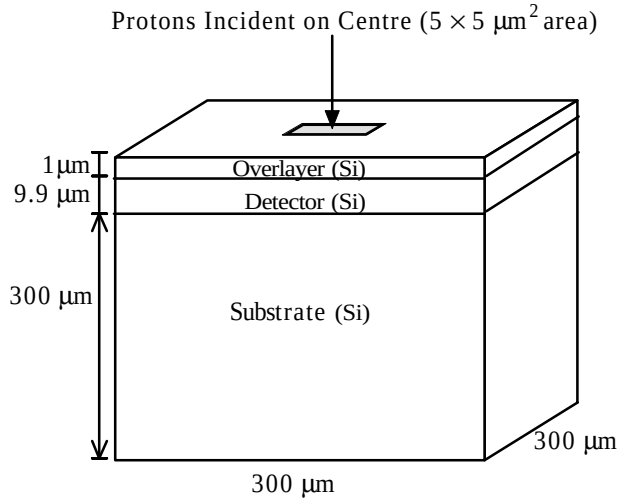


Figure 9.5. Geometry used for PRISM simulation of 10 μm SOI microdosimeter

9.3.2 Results

9.3.2.1 Microdosimetric Spectra at NPTC-Boston

The microdosimetric spectra obtained as a function of depth at NPTC are shown in Figure 9.6. One first notes the significantly improved noise performance of the low noise prototype in comparison to measurements made at PMRC. Measurements were obtained down to the noise level of about 1.2 keV/μm (Silicon). The depth-dose curve obtained using the Markus chamber and the microdosimeter measurement positions are shown in Figure 9.4. At depths less than 20cm, the large dose contribution from low lineal energy events is due to significant high energy proton and gamma contributions which both have an LET below 2 keV/μm. As we approach the Bragg peak, the LET of the protons rises as seen by the increase in the mean lineal energy and the shift of the spectra to higher lineal energies at depths between 20-26 cm. These effects were also observed using a proportional counter at the Loma Linda proton beam by Coutrakon [155] This shift is not due to pileup effects since, firstly, the signal was continuously monitored with an oscilloscope and, secondly, the count rate is lower at higher depths due to beam spreading.

Note the step decline in the microdosimetric spectra at around the maximum lineal energy of protons of 74 keV/μm. Dose contributions are evident at lineal energies above the maximum proton LET due to nuclear reaction products such as alpha particles and heavy ion recoils. However, the relative number of such events is much smaller than the proton events hence the step change above the maximum proton LET. Scattered

protons, which are not normally incident on the device, also contribute to the microdosimetric spectrum at lineal energies above 74 keV/µm.

As we exceed the maximum range of the protons, the higher lineal energy components contribute a relatively higher proportion of dose. At 30 cm, well past the primary proton range, the spectrum is comprised totally of neutron reaction products including recoil protons, alpha particles and heavy ion recoils. The neutron reaction products tend to have a large proportion of dose at higher lineal energies. The maximum lineal energy measured of around 700-800 keV/µm was limited by saturation of the multi-channel analyzer at the selected gain. An additional measurement using a lower gain and over a longer measurement time is required to obtain the small number of counts at lineal energies above the current maximum. These results will be further discussed in the next section comparing selected spectra with simulation.

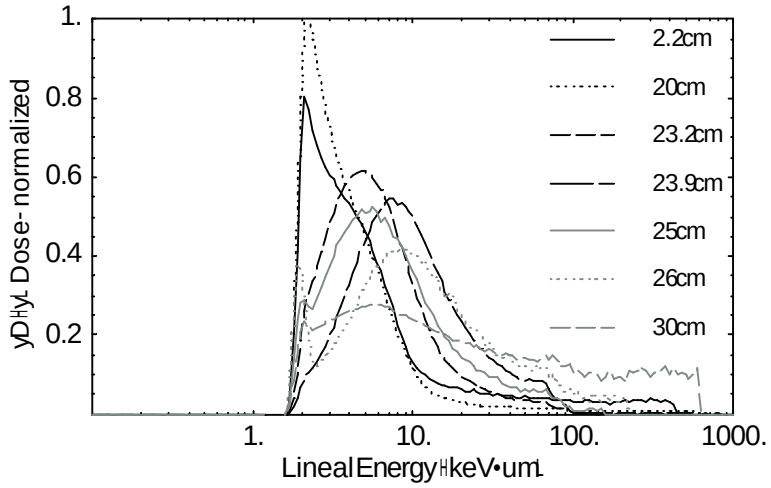


Figure 9.6: Microdosimetric spectra of 191.6 MeV proton beam at various depths in a water phantom. Range of proton is approximately 23.7 cm.

9.3.2.2 Comparison with Simulation

The energy spectrum of protons incident on the detector when placed at a depth of 23.9 cm is shown in Figure 9.7. The SRIM calculation also estimates that 48.5% of protons are stopped completely in the water; a value that coincides with the 50% maximum dose observed at a depth of 23.9 cm as shown in Figure 9.4. The energy spectrum has a large relative variance resulting in a wide variation in proton LET(Si) of between 135 (at 70 keV) and 2.5 keV/µm (at 45 MeV).

Using this energy spectrum, the expected microdosimetric spectrum was simulated and compared with the experimental spectrum as shown in Figure 9.9. Overall, the match between experimental spectrum and simulation results is quite good. The peak in lineal energy at 7.5 keV/μm was well matched and the proton edge at 73 keV/μm roughly coincides between the spectra. At lower lineal energies, the simulations do not produce as much spectral spread as the experimental spectrum due to the various simplifying approximations used in the simulations such as simple geometrical models. In addition, the shape of the spectra around the proton edge differs in all three cases.

The proton edge for the experimental data is spread from about 65 to 100 keV/μm due to a variation in the angle of incidence of the protons increasing the chord length and hence energy of these events. Such a spread is not as evident in the simulations due to inadequate modeling of the proton angular distribution. The SRIM simulation is slightly better (greater proton edge spreading) than PRISM since angle information from the previous water transport simulation was employed in SRIM whilst PRISM assumes normally incident protons. The calculated probability distribution of proton angle is shown in Figure 9.8. The SRIM water transport simulation assumes normally incident protons at a water depth of 0 cm which is a crude approximation that results in an inadequate spread in the angles incident on the device. Improved modeling would require an accurate simulation of the beam line scattering particularly the lateral spreading filters.

The experimental spectrum and simulations were also compared at 2.2 cm water depth as shown in Figure 9.10. The main point derived from this comparison is that the experimental spectrum does not have a sufficiently low noise cutoff to adequately record the spectrum. The spectrum is missing below around 2 keV/μm which severely affects the normalization process. Note, that the peak from 2-2.5 keV/μm is anomalous and was traced to a known hardware design fault in the Amptek Pocket MCA-8000. The fault only occurs at high sub-lower level discriminator count rates encountered at depths of 2.2 and 20 cm. In summary, the silicon microdosimeter probe assembly requires at least a factor of two improvement in noise performance in order to correctly measure spectra at depths less than about 20 cm. This is not a significant deficiency since the microdosimetric characteristics of the beam are not as clinically important at these depths.

The PRISM simulation enabled a calculation of the proportion of events that are due to inelastic nuclear reactions between protons and silicon in the device. It is desirable to have this proportion as low as possible since such events affect the tissue equivalence of the device operation as discussed in section 5.5.3. Of the 10000 protons transmitted through the device only 3 of the energy deposition events were due to inelastic nuclear events (all $Si^{28}(p,p)Si^{28}$ reactions). These events deposited relatively small energies from secondary proton products intercepting the sensitive volume. The energies were 56.9, 45.5 and 69.2 keV, yielding collected lineal energies of 5.7, 4.6 and 6.9 keV/μm, respectively. Prism provides a facility to increase the probability of such reactions and it was determined that only 0.043 +/- 0.004% of all events are due to inelastic reactions at 23.9 cm. At the lower simulated depth of 2.2 cm the proportion is even lower, 0.03 +/- 0.003%, due to the decreased inelastic cross-section at higher proton energies. Thus, the proportion of inelastic nuclear interaction events with silicon is negligible up to depths of around 25 cm and thus, the silicon microdosimeter with appropriate geometrical scaling may be considered tissue equivalent. At greater depths, neutron events begin to dominate the microdosimetric spectrum as discussed in the previous section. The tissue equivalence of neutron interactions was discussed in sections 5.5 and 8.3.3. Such interactions where not modeled in this simulation and future work is suggested.

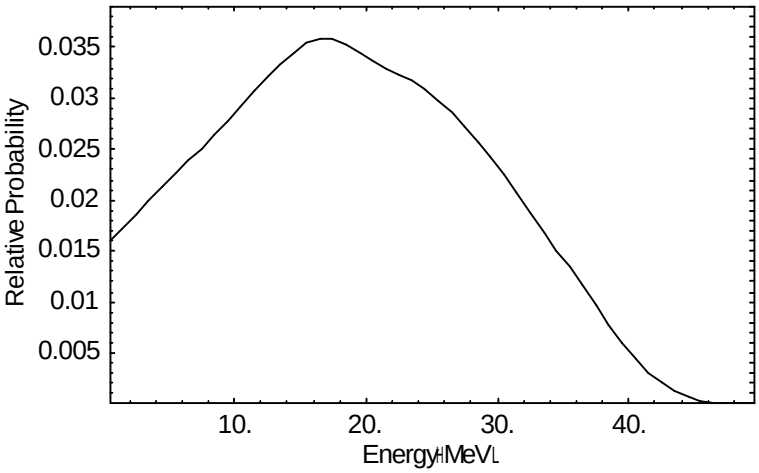


Figure 9.7. Proton energy spectrum following the transport using SRIM of 191.6 MeV protons (normal distribution with μ=191.6 MeV, σ=2.8 MeV) through 23.9 cm of water. Note also that 48.5% of protons are stopped completely in the water (i.e. E=0).

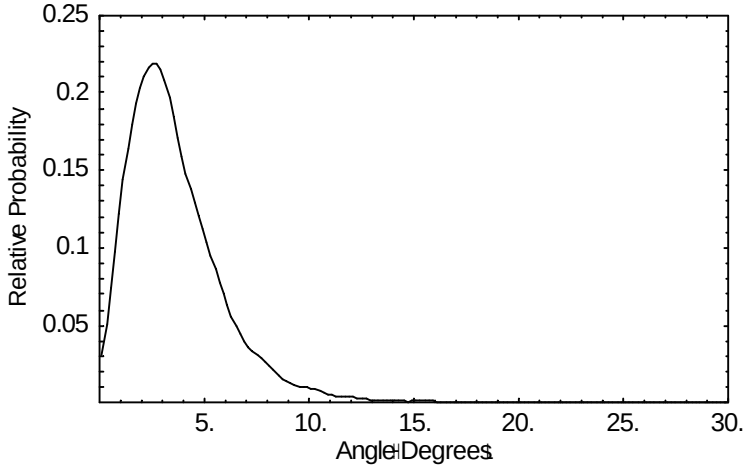


Figure 9.8. Probability distribution of proton angle of incidence with respect to the device normal. Calculated using SRIM transport of 191.6 MeV protons (normal distribution with μ=191.6 MeV, σ=2.8 MeV) through 23.9 cm of water

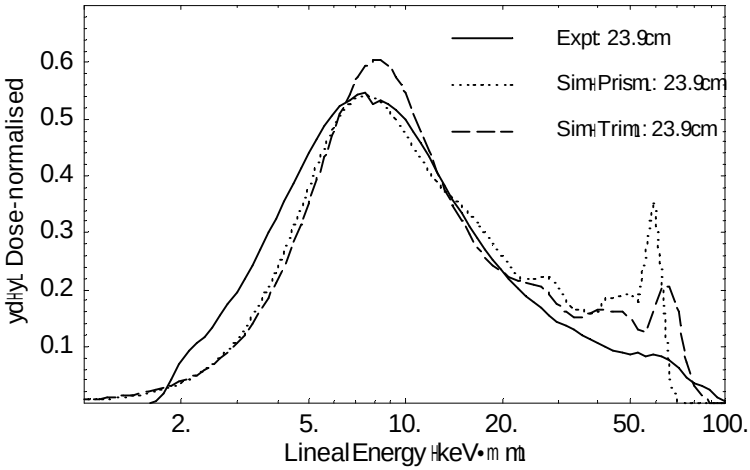


Figure 9.9. Experimental silicon microdosimeter spectrum at 23.9 cm in water phantom at NPTC compared to Monte-Carlo simulation results using PRISM and SRIM.

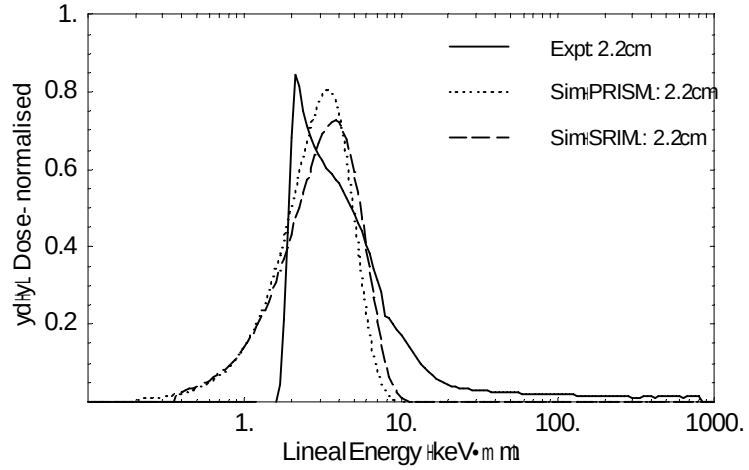


Figure 9.10. Experimental silicon microdosimeter spectrum at 2.2 cm in water phantom at NPTC compared to Monte-Carlo simulation results using PRISM and SRIM.

9.4 Summary of Proton Therapy Applications

These measurements provide valuable information for radiobiological studies of the varying effectiveness of the beam as a function of depth. Testing at the recently constructed NPTC facility in Boston demonstrated the capability of the device at recording lineal energy spectra with high spatial resolution. The spectra were consistent with simulations performed using SRIM and PRISM and qualitative expectations based on previous proportional counter measurements in protons beams and an understanding of the beam characteristics. Future work may be directed towards the analysis of beam relative biological effectiveness such as performed at Loma Linda by Coutrakon [155] at a higher spatial resolution than previously attempted.

In general, pile up and perturbation effects were avoided due to the small area (0.04 cm^2) of the total pixel array. Pileup did occur for experiments at PMRC when the vertical momentum slit width was greater than 2 mm. Under these conditions, an even smaller area detector is required. Note that the area requirements are still well within the design capability of silicon technology. The detector was coupled to a radiation-hard charge sensitive amplifier with the probe assembly capable of measuring an LET down to 1.2 keV/μm (Silicon). The device offers much improved spatial resolution compared with a proportional gas counter particularly in the critical high dose region around the proton Bragg peak.

We have demonstrated a new approach to microdosimetry in radiation oncology using a silicon SOI p-n junction array applied to proton therapy beams. Low noise, small size and good radiation hardness facilitate the application of this device in radiation oncology.

10. Conclusions and Future Recommendations

10.1 Key Findings

This work is the first comprehensive investigation of the issues confronting silicon based microdosimetry and its application to radiotherapy. The literature review and a detailed comparison of proportional counter microdosimetry to silicon microdosimetry identified four main problems requiring investigation;

1. The *requirements* of silicon microdosimetry and particularly the influence of detector *shape* have not been dealt with thoroughly in the literature.

2. The *low noise* requirements on the silicon microdosimeter are demanding and particular attention must be made in the design process to minimize electronic noise.

3. The *tissue equivalence* of silicon microdosimeters has not been addressed in detail in the literature.

4. The *sensitive volume boundary* and charge collection suffers from uncertainty in almost all previous attempts at silicon microdosimetry. *Radiation damage* may affect silicon microdosimeter performance by reducing charge collection.

An analysis of the requirements of silicon microdosimetry provided in chapters 2 and 3 enables a complete requirement summary as shown in Table 10.1. This extends the previous work of Schroder [68] presented in Table 2.1. The work of Kellerer [129] on the criteria for equivalence of spherical, cylindrical and cubic shapes was extended to include RPP shapes with an overlayer and converter structure above the detector. The effect of finite particle range on the criteria for shape equivalence was explored in greater detail. In addition, the equivalence in terms of $\bar{y}_d$ and the effect of straggling on the lineal energy spectra were determined.

The requirements for tissue equivalence were determined in chapter 5. To obtain tissue equivalence, the silicon detector/ TE converter should have a geometrical TE scaling factor of z = 0.63, a converter composition closely approximating tissue, and a minimum silicon detector size subject to shape and noise considerations (as discussed in chapters 3 and 4, respectively) in order to reduce the probability of nuclear interactions with silicon.

Table 10.1. Summary of requirements and design rules for silicon based radiation therapy microdosimetry

Detector Feature	Requirements/Findings
Shape	• A RPP with an overlayer/converter structure is appropriate. Such a structure is easily manufacturable. Furthermore, it was shown that a RPP under c-randomness is closely equivalent to a sphere and RPP under μ-randomness. The equivalence holds within 10% for particle ranges $R > 2\ (a + \bar{l})$ and within 2% for $R > 4\ (a + \bar{l})$ where a = overlayer thickness. • The elongation of the RPP should be as close to unity as practicable in order to minimize shape relative variance. A cube is the optimum RPP shape.
Size	• Given a reference tissue sphere with a MCL = $\bar{l}_{Kt}$, the required MCL of a silicon volume K is $\bar{l}_{Ksi} = \bar{l}_{Kt}\, hz$ where $hz = 0.5$ for a cube. Therefore, a silicon cube with side length 0.5 μm will have a similar TE lineal energy spectrum and $\bar{y}_d$ as a 1 μm tissue sphere. In addition, $\bar{l}_{Kt}$ (0.66 μm in this case) and not $\bar{l}_{Ksi}$ is used for calculating the TE lineal energy in the silicon volume. • The ideal silicon microdosimeter should have dimensions that approximate a tissue sphere of diameter ranging from around 13 μm (the typical cell diameter) to the minimum achievable given the device construction. Radiobiological studies such as TDRA indicate site sizes less than 2 μm are of most interest. • The detector should use an array of sensitive volumes to improve collection statistics. The total sensitive area of the volumes should be approximately 100 cm^2 for radiation protection applications and as small as 1 mm^2 for fast proton therapy measurements.
Materials	• A tissue equivalent converter should be used with a thickness greater than the maximum particle range expected to ensure charged particle equilibrium. • The overlayer thickness separating the converter and detector should be minimized (see shape comments above). • The geometrical TE scaling factor for the silicon detector (z=0.63) should apply to all ion products • The T.E converter must closely approximate tissue atomic composition with respect to atoms generating the dominant secondary charged particles. • The proportion of interactions with silicon must be negligible in comparison with converter interactions. That is, events should originate from converter recoil products or primary ions rather than from within silicon. • The range of recoil particles should be such that crossers and stoppers dominate the microdosimetric spectrum as discussed extensively in chapter 3
Operation	• An accurately defined sensitive volume. Minimization of charge collection complexity in particular diffusion and funneling effects. • Capable of measuring a lineal energy down to a minimum of ~1 keV/μm (tissue). Above this value of lineal energy the radiobiological effectiveness begins to rise above unity. Low noise design and optimization is necessary to met such requirements. • The charge collection behavior should be resistant to radiation damage at typical application fluences.

A Monte-Carlo program was developed to simulate the energy deposition of ions in a BNCT radiation field. The Monte Carlo results confirm that with appropriate geometrical scaling (z = 0.63) silicon detectors with well-known geometry will record energy deposition spectra representative of tissue cells of equivalent shape. That is, silicon is tissue equivalent for BNCT ion products under appropriate linear geometrical scaling. The scaling factor is also applicable to FNT but may need to be reduced for PT to around 0.56.

A brief study comparing tissue and silicon neutron interactions in FNT was described. For neutron energies less than 5 MeV, microdosimetric measurements in silicon volumes with dimensions of the order of 1 μm will not be significantly affected by events generated within the silicon. At higher neutron energies, the spectrum at high lineal energies may be affected by silicon elastic and inelastic reactions. A more detailed study is required to fully ascertain design requirements and the conditions under which satisfactory operation may be achieved.

The requirement for a lineal energy measurement range down to a least 1 keV/μm conflicts with the desire for a small sensitive volume that reduces the total charge collected. A noise optimization model for the microdosimeter and charge sensitive amplifier system was developed in chapter 4 that enables optimum selection of components and system parameters such as amplifier shaping time. The prototype diode array device used in this work was originally developed by Fujitsu as a test device for memory single event upset studies. Silicon-on-Insulator technology is used to assist in defining the sensitive volume and was the principle reason for selecting this test device as a prototype microdosimeter.

I-V and C-V testing of the device were performed to determine device integrity and quantify parameters required for noise optimization calculations (such as reverse bias current and capacitance). A model for device capacitance that includes metal-oxide track capacitance and the traditional pixel array depletion capacitance was presented. The method presented for calculating the model parameters (C_c, N_B, and V_{bi}) is simple and provides a reasonably accurate estimate of substrate doping concentration that corresponds well with the manufacturer's value. The model indicates the importance of minimizing metal-oxide track capacitance by having a thick oxide layer separating the metal from the substrate and ensuring a minimum metal area.

The collection efficiency and radiation hardness of silicon microdosimeters were characterized in chapter 6 using three methods; alpha and proton microbeam spectroscopy, broadbeam alpha spectroscopy and 2D and 3D device simulation. A summary comparing the methods is provided in Table 6.3. Potentially microbeam spectroscopy offers the most accurate estimation of device CE due to the unambiguous spatial information provided, the use of a proton beam to minimize funneling, a mono-energetic source, and localization of charge collection. However, in our experiments the sub-micron resolution of the microbeam system could not be achieved due to radiation damage effects limiting exposure time and thus statistical accuracy. The microbeam measurements should use the highest energy alpha available in order to minimize the influence of the overlayer. A proposed further improvement in microbeam analysis would be to use data from a minimum of two other alpha energies and simultaneously extract the CE, overlayer thickness and SOI thickness without any a-priori information regarding device structure.

The broadbeam results are used for CE definition in this work due to the greater availability of such measurements and the previously mentioned difficulties with microbeam experiments. Care must be taken in the interpretation of broad-beam data to avoid associating peaks in the spectrum directly with drift collection regions. The effect of significant lateral diffusion is to shift the spectrum to lower energies due to reduced CE. A spectroscopy software model was presented which accurately fits both broadbeam and microbeam data and assists in correctly interpreting data by including, as far as practicable, all the sources of variation that contribute to the measured spectral character.

Semiconductor device simulation was extensively used in chapter 6 to assist in understanding the charge collection process. Collection efficiency simulations described in section 6.2.2.2 and 6.2.4.1 were in poor absolute agreement with broadbeam spectroscopy modeling. The differences were attributable to inadequacies in 2D simulations. Accurate device simulation of SOI structures requires good estimation of recombination parameters, 3D device geometry and reasonable ion track models. Nevertheless, despite the possible inaccuracies of 2D simulations they do provide qualitatively useful information such as the reduction in CE away from the junction and identification of funnel dominated charge collection.

In particular, simulations on bulk devices indicated that protons would be largely immune from funneling effects in contrast to alpha particles. Radiation damage studies determined the minority carrier lifetime before and after radiation damage. Edmonds' spectroscopy method for determining lifetime was employed. Accurate results demanded, firstly, the use of proton microbeam methods to reduce funneling effects and, secondly, large area bulk diodes to conform with the Edmonds model. The reduction in lifetime with radiation damage is described by the calculated 1 MeV neutron equivalent damage constant of $K_{1MeV} = 1.5\times10^{-6}$ cm^2/n-sec. In addition, C-V measurements quantified the drop in majority carrier density from 1.6 to 1×10^{15} cm^{-3} following irradiation with 24 GeV/c protons at a fluence of 4.1×10^{13} p/cm^2.

In summary, the ability of SOI technology to create a well-defined sensitive *depth* has been confirmed by the charge collection studies. In using a p-n diode array it was initially hoped that the *lateral* charge collection would be dominated by drift in the junction region with much reduced charge collection outside that region. However, the charge collection studies demonstrated that lateral diffusion and funneling are dominant processes due to a diffusion length (61 μm) much larger than cell dimensions. Reducing diffusion by lifetime reduction methods such as radiation damage was found to also affect charge collection in drift dominated regions.

The main implication is that future SOI microdosimeter designs should introduce methods such as oxide isolation boundaries to minimize lateral diffusion. Such technology has recently (1998) been developed for radiation hard applications. The TEMIC Matra MHS D-MILL 10 MRad process available from Europractice ASIC service [253] is a good example process in which CMOS, bipolar and JFET technology are available with complete isolation between device structures. Furthermore, smaller cell volumes would reduce the dependence of charge collection on minority carrier lifetime and thus enhance radiation hardness.

Lateral diffusion has created a sensitive volume for the SOI devices that closely approximates an infinite slab (or a very elongated RPP) rather than the desired RPP, discussed in chapter 3, with small or preferably no elongation. For the 2 μm and 10μm SOI devices, the average sensitive depths (corrected for CE and SOI thickness variations) are 1.78 μm and 8.15 μm, respectively. The device width is 1214 μm and length is 3626 μm.

Despite this non-ideal shape and corresponding chord length distribution, chapters 7, 8, and 9 test the current device in BNCT, FNT and proton therapy clinical beams. The potential of the device and useful future design information may still be gauged by experimenting with the current prototype microdosimeter. Microdosimetric spectra in these studies require an estimate of the mean chord length, $\bar{l}$, for the sensitive volume which is complicated by the elongated sensitive volume. Four different methods for determining the most appropriate mean chord length for the device are discussed in section 6.4.2.

Chapter 7 demonstrates the first application of silicon p-n junction SOI arrays for microdosimetry in radiation oncology and particularly for BNCT. The interaction of thermal neutrons with each of the materials present in the device construction was thoroughly analyzed in section 7.2. The important materials are (in order of thermal neutron sensitivity), B-10 in a 1% Lucite coat or cover (optional, if present), B-10 in the $p+$ region, N-14 in air (if present, may not have an air gap above the device), N-14 from the TiN barrier layer.

Experiments at BNL, as presented in section 7.3, were primarily directed at investigating various converter options for the device (Lucite with B-10 and U-235) and for a comparison with a TEPC measurement. Direct coating of the device with 1% B-10 in Lucite did not change electrical characteristics and produced a microdosimetric spectrum similar to the 1% B-10 lid. Discrepancies between these spectra and Monte Carlo simulations were attributable to simplistic overlayer and charge collection modeling. More detailed investigation of charge collection modeling of high LET particles is encouraged. In addition, preliminary results with the U235 converter suggest that the SOI p-n junction is a promising microdosimeter for heavy ion therapy provided the bias voltage is greater than 5 V to minimize recombination. Measurement of the spectra generated from B-10 deposited within the device $p+$ regions demonstrated that typical medical concentrations of B-10 may be introduced in the device design via ion implantation. Such a microdosimeter can be used under full reactor power with any device orientation.

Experiments at KUR, as presented in section 7.4, demonstrated the importance of minimizing the air gap above the device due to the large number of proton events originating from nitrogen thermal neutron reactions. Monte Carlo simulations of this

effect were in good agreement with observed experimental spectrum. A comparison of the 2 μm and 5 μm SOI devices highlighted the importance of a small sensitive volume in order to maximize the sensitivity to particle LET rather than particle total energy. The ability of the 2 μm SOI microdosimeter to discriminate between fast neutron recoil protons and BNCT products facilitates simultaneous thermal neutron flux measurements and microdosimetry at a high spatial resolution. Excellent agreement in the neutron flux profile, between the gold foil measurements by Kobayashi [269] and the microdosimeter, was demonstrated as shown in Figure 7.22. The number of ion-implanted B-10 atoms within the *p*+ region used for these measurements was a factor of 6 lower than expected based on isotope natural abundance suggesting that the ion-implantation process may alter the relative isotope concentrations. If the ion-implanted B-10 proportion is known, accurate absolute thermal neutron flux may be estimated without any need for normalization to a known flux value.

In summary, the improvements in traditional microdosimetry possible using silicon diode arrays may help to bridge the gap between proportional counter microdosimetry in BNCT and the more realistic high-resolution quantitative autoradiography method developed by Solares and Zamenhof [81].

Chapter 8 presented the first demonstration of a SOI based microdosimeter in a neutron radiation therapy beam (Harper Hospital, Detroit) with results sufficiently promising to confirm the feasibility of the device in this application. A detailed comparison with a proportional counter is performed. Despite some deficiencies in the existing design, microdosimetric radiation quality variations may still be characterized qualitatively. General trends in microdosimetric spectra as a function of position within the beam (e.g. small depth dependence, lateral variation) were in good agreement with the proportional counter. However, quantitative analysis based on calculation of $\bar{y}_d$ and y^* is not recommended with the current design as indicated by a poor correspondence with proportional counter trends. Shortcomings in the current design arise primarily from the large sensitive volume and the chord length distribution of the SOI device along with the need for improved low noise performance.

The third and final application in which the device was tested was proton therapy as discussed in chapter 9. Testing at the recently constructed NPTC facility in Boston demonstrated the capability of the device at recording lineal energy spectra with high

spatial resolution. The spectra were consistent with simulations performed using SRIM and PRISM and qualitative expectations based on previous proportional counter measurements in protons beams and an understanding of the beam characteristics.

In general, pile up and perturbation effects were avoided due to the small area (0.04 cm^2) of the total pixel array. Pileup did occur for experiments at PMRC when the vertical momentum slit width was greater than 2 mm. Under these conditions, an even smaller area detector is required. Note that the area requirements are still well within the design capability of silicon technology. The detector was coupled to a radiation-hard charge sensitive amplifier with the probe assembly capable of measuring an LET down to 1.2 keV/μm (Silicon). The device offers much improved spatial resolution compared with a proportional gas counter particularly in the critical high dose region around the proton Bragg peak. These measurements potentially provide valuable information for radiobiological studies of the varying effectiveness of the beam as a function of depth. Future work may be directed towards the analysis of beam relative biological effectiveness such as performed at Loma Linda by Coutrakon [155] at a higher spatial resolution than previously attempted.

We have demonstrated a new approach to microdosimetry in radiation oncology using a silicon SOI p-n junction array applied to various high LET therapy beams. A consistent difficulty in experimental evaluation was the uncertainty in the mean chord length to be used evidenced by the variety of calculation methods employed for different applications. The large elongation of the devices sensitive volume (see section 6.4.2) introduces MCL uncertainty and is a compelling motivation for using unity elongation shapes such as a cube with a minimum relative variance.

Nevertheless, the potential advantages of silicon microdosimetry in radiation oncology applications are multitudinous. The diode array is a portable, low cost system without the need for gas flow technology and high voltage supplies. Of particular benefit is the devices excellent spatial resolution. Measurements, such as in proton therapy near the Bragg peak and off axis measurements in FNT, may then be performed at a spatial resolution commensurate with the application needs. The diode array also offers such advantages as a measurement in the solid phase and thus removal of wall effects, simulation of a two dimensional array of cells for improvement in collection statistics, small physical size (possible in-vivo capability), and high count rate capability that

enables operation at clinical dose rates. Furthermore, the possibility exists that future devices may be constructed with sizes and morphology more nearly representative of biological cells using real tissue cells surrounding the detector. Specific boron implantation in various cell/diode regions may be introduced along with simultaneous macrodosimetry using other detectors on the same silicon substrate. The construction of such devices may exploit the rapid development and current manufacturing capabilities (integration of components and quality control) of silicon based integrated circuit technology.

10.2 Future Recommendations and Proposed Design Outline

More work is required to completely address the four main problems confronting silicon microdosimetry. In particular, the following areas are worthy of future research:

1. The problem of determining the effect of nuclear interactions with non-TE materials in the device, such as the silicon and overlayer materials, requires further examination. In this work, the silicon device is shown to be TE provided these interactions are relatively infrequent compared to secondary products arriving from the TE converter. Hence one must maximize TE material surrounding the detector and minimize the silicon volume. The studies in clinical beams emphasized the need for minimizing the sensitive volume of the detector to around the 1 μm region and employing a cubic shape with a smaller relative variance, well defined mean chord length and a chord length distribution more nearly approximating a sphere. Such a design will reduce the proportion of silicon interactions and increase the percentage of crossers contributing to the microdosimetric spectrum. A proposed cross-section of such a device is shown in Figure 10.1. The device construction seems feasible based on recent developments in etching and 3D device construction that enable complex detector shapes as presented by Kenney [301] and Allier [302]. Monte-Carlo code, that models the interaction of neutrons (0-60 MeV) with such a device, is required to determine the relative contribution of secondary products from the TE material and the device materials as a function of sensitive volume size. For such a task, one may first attempt to modify existing code already developed for silicon and tissue materials.

2. Low noise performance may be significantly improved by integrating the charge sensitive amplifier with the detector. Achievable optimum performance for such a

system was addressed in section 4.5.6. It was estimated that an array of 2400 × 1 μm^3 diodes would have a noise level of 19 electrons and a minimum lineal energy of 0.26 keV/μm (Tissue, NB: 1 μm^3 Si cube is equivalent to 2 μm spherical TE). This noise level is sufficiently low for accurate quantitative determination of $\bar{y}_d$ and y^* in neutron therapy beams. In addition, the energy resolution of the silicon microdosimeter will now exceed the capabilities of the TEPC over the entire range of measured energies as shown in Figure 2.6. The total area of the proposed device is 200 times smaller than the prototype tested in this work. To achieve reasonable count rates for small detector arrays several detector/preamplifier channels would be required to increase the total device area. Care should be taken in the device layout design to ensure that the metal track capacitance is kept to a minimum and included in device noise modeling, as discussed in section 4.2.2.

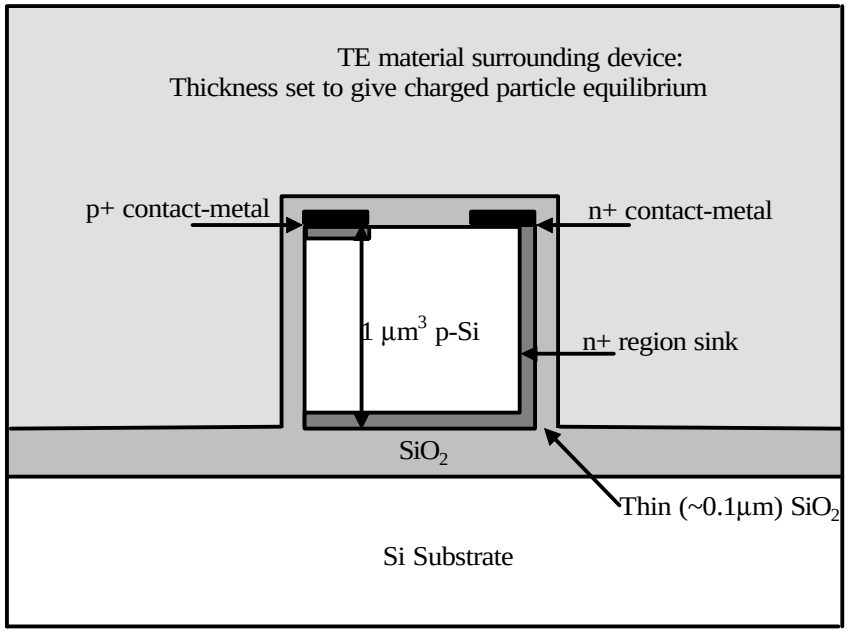


Figure 10.1. Cross-section of ideal proposed silicon microdosimeter. The TE material may be constructed with either A150, some other TE plastic or even the deposition of real tissue cells. Note that the protective qualities of the SiO_2 passivation overlayer are quite robust.

3. The next generation device should use lateral isolation technologies on a SOI substrate, as shown in Figure 10.1, to minimize lateral charge collection effects. A sensitive volume with near unity elongation (e.g. cube) may then be constructed with a well-defined sensitive volume and small chord length distribution relative variance. The detector shown in Figure 10.1 has a 1 μm^3 sensitive volume designed to approximate the response of a 2 μm diameter TE spherical proportional counter. A thin (~0.1 μm) isolation boundary of SiO_2 provides two benefits, aside from

defining the sensitive volume. Minimizing the overlayer thickness both improves TE and reduces radiation damage effects in the oxide (such as charge buildup that may increase reverse bias current noise and modify surface recombination). The oxide thickness of ~0.1 μm was selected as a reasonable minimum achievable value. Note that the oxide, metal and contact thicknesses, are all manufacturing process dependent parameters.

4. The new device should be tested using full 3D device simulation (an easier task with the smaller device dimensions). Further study of CE variations with ion type and energy is encouraged. Such future studies may use 3D device simulation with more accurate track modeling than presented in this work. Surface recombination (Si-SiO_2) will be a more significant factor than bulk recombination due to the relatively large surface area to volume ratio. Methods for determining surface recombination should be determined prior to device fabrication since a dedicated lifetime test structure on the device may be useful.

Having addressed the key issues, the next generation device should be applied to high LET applications for comparison with proportional counter performance. The device should find particular utility where spatial resolution demands are high. Such a device would provide an excellent test structure for experimental microdosimetry both in the biological domain of radiotherapy/radiation protection and for SEU studies. In the later category, an important application is the verification of neutron burst generation rate models, central to the SEU prediction software used in modern memory chip design. Applications in radiobiology include the study of dosimetry in space and avionics and radiation oncology modalities such as BNCT, heavy ion, fast neutron, and proton therapy in which dosimetry has traditionally been quite difficult.

11. References

[1] H. H. Rossi and M. Zaider, *Microdosimetry and Its Applications*. London: Springer, 1996.

[2] A. M. Kellerer, "Event simultaneity in cavities. Theory of the distortions of energy deposition in proportional counters," *Radiat. Res.*, vol. 48, p. 216, 1971.

[3] P. J. McNulty, D. R. Roth, E. G. Stassinopoulos, and W. J. Stapor, "Characterizing complex radiation environments using MORE (monitor of radiation effects)," presented at Symposium Detector Research and Development., SSC, 1990.

[4] J. N. Bradford, "Microelectronic analogues to radiobiological microdosimetry," presented at Proceedings 8th Symposium in Microdosimetry, EUR 8395, Julich, FRG, 1982.

[5] F. Dessauer, "Uber einige Wirkungen von Strahlen. I.," *Z. Phys.*, vol. 12, p. 38, 1922.

[6] I. A. Crowther, "Some considerations relative to the action of X-rays on tissue cells," *Proc. Roy. Soc.*, vol. 96, p. 207, 1924.

[7] R. E. Zirkle, D. F. Marchbank, and K. D. Kuck, "Exponential and sigmoid survival curves resulting from alpha and x-irradiation of Aspergillus spores," *J. Cell. Comp. Physiol.*, vol. 39, p. 75, 1952.

[8] L. H. Gray, "The distribution of the ions resulting from the irradiation of living cells," *Br. J. Radiol. Suppl.*, vol. 1, 1947.

[9] D. E. Lea, *Actions of Radiation on Living Cells*, 2nd ed. Cambridge: Cambridge, 1955.

[10] A. M. Kellerer and D. Chmelevsky, "Criteria for the applicability of LET," *Radiat. Res.*, vol. 63, p. 226, 1975.

[11] International Commission on Radiation Units and Measurements, *Microdosimetry (ICRU report; 36)*. Maryland: ICRU, 1983.

[12] D. T. Goodhead, "An assessment of the role of microdosimetry in radiobiology," *Radiat. Res.*, vol. 91, pp. 45-75, 1982.

[13] K. Sax, "Chromosome aberrations induced by X-rays," *Genetics*, vol. 23, pp. 494-516, 1938.

[14] D. E. Lea and D. G. Catcheside, "The mechanism of induction of radiation of chromosome aberrations in Tradescantia," *J. Genetics*, vol. 44, pp. 216-245, 1942.

[15] S. Wolff, "Interpretation of induced chromosome breakage and rejoining," *Radiat. Res. Suppl.*, vol. 1, pp. 453-462, 1959.

[16] G. J. Neary, R. J. Preston, and J. R. K. Savage, "Chromosome aberrations and the theory of RBE III. Evidence from experiments with soft X-rays, and a consideration of the effects of hard X-rays," *International Journal of Radiation Biology and Related Studies*, vol. 12, pp. 317-345, 1967.

[17] H. H. Rossi and W. Rosenzweig, "A device for the measurement of dose as a function of specific ionization," *Radiology*, vol. 64, pp. 404-411, 1955.

[18] A. M. Kellerer and H. H. Rossi, "The theory of dual radiation action," *Curr. Top. Radiat. Res. Q.*, vol. 8, pp. 85-158, 1972.

[19] D. Srdoc, "Experimental technique of measurement of microscopic energy distribution in irradiated matter using Rossi Counters," *Radiat. Res.*, vol. 43, pp. 302-319, 1970.

[20] U. Fano, "Note on the Bragg-Gray cavity principle for measuring energy dissipation," *Radiat. Res.*, vol. 1, p. 237, 1954.

[21] Y. S. Kim, "Density effect in dE/dx of fast charged particles traversing various biological materials," *Radiat. Res.*, pp. 21-27, 1973.

[22] P. Kliauga, "Microdosimetry at Middle Age: Some Old Experimental Problems and New Aspirations," *Radiat. Res.*, vol. 124, pp. 5-15, 1990.

[23] G. F. Knoll, *Radiation detection and measurement*, 2nd ed. New York: Wiley, 1989.

[24] H. H. Rossi, "Experimental limitations of microdosimetry," presented at Proceedings Second Symposium on Microdosimetry, 1970.

[25] A. M. Kellerer and D. Chmelevsky, "Concepts of microdosimetry. I. Quantities," *Radiat. Environ. Biophys.*, vol. 12, pp. 61-69, 1975.

[26] L. Lindborg and A. Brahme, "Influence of microdosimetric quantities on observed dose-response relationships in radiation therapy," *Radiat. Res.*, vol. 124, pp. 23-28, 1990.

[27] H. H. Rossi, "Energy distribution in the absorption of radiation," in *Advances in Biological and Medical Physics.*, vol. 11, 1 ed. New York: Academic Press, 1967, pp. 27-85.

[28] A. M. Kellerer, "An assessment of wall effects in microdosimetric measurements," *Radiat. Res.*, vol. 47, p. 377, 1971.

[29] U. Oldenburg and J. Booz, "Wall effects of spherical counter," presented at Proceedings of the second symposium on microdosimetry, Report No. EUR 4452, 1970.

[30] W. A. Glass and L. A. Braby, "A wall-less detector for measuring energy deposition spectra," *Radiat. Res.*, vol. 39, p. 230, 1969.

[31] W. A. Glass and W. A. Gross, "Wall-less detectors in microdosimetry," in *Topics in Radiation Dosimetry, Radiation Dosimetry Supplement 1*, vol. 1, F. J. Attix, Ed. New York: Academic Press, 1972, p. 221.

[32] International Commission on Radiation Units and Measurements, *Tissue Substitutes in Radiation Dosimetry and Measurement (ICRU report 44)*. Bethesda, Md., U.S.A.: ICRU, 1989.

[33] R. F. Shonka, J. E. Rose, and G. Failla, "Conducting plastic equivalent to tissue, air and polystyrene," in *Second United Nations International Conference on Peaceful Uses of Atomic Energy*. New York: United Nations, 1958, p. 184.

[34] H. H. Rossi and G. Failla, "Tissue equivalent ionization chambers," *Nucleonics*, vol. 14, p. 32, 1956.

[35] G. Dietze, H. G. Menzel, and G. Buhler, "Calibration of tissue equivalent proportional counters used as radiation protection dosemeters," *Radiation Protection Dosimetry*, vol. 9, pp. 245-249, 1984.

[36] P. Pihet, S. Gerdung, S. Grillmaier, R. E. Kunz, and H. G. Menzel, "Critical assessment of calibration techniques for low pressure proportional counters used in radiation dosimetry," *Radiation Protection Dosimetry*, vol. 44, pp. 115-120, 1992.

[37] U. J. Schrewe, W. D. Newhauser, H. J. Brede, and P. M. DeLuca, "Experimental estimation of kerma coefficients and dose distributions in various materials (C, N, O, Mg, Al, Si, Fe, Zr, A-150 plastic, Al2O3, AlN, SiO2 and ZrO2) for neutron energies up to 66 MeV," *Phys. Med. Biol.*, vol. 45, pp. 651-683, 2000.

[38] International Commission on Radiation Units and Measurements, *Average energy required to produce an ion pair, (ICRU report 39)*. Bethesda, Md., U.S.A.: ICRU, 1979.

[39] D. Srdoc and I. Krajer-Bronic, "Yields of ionization and excitation in irradiated matter," *IEAE CRP Atomic and Molecular Data for Radiotherapy*, 1993.

[40] L. J. Goodman and J. J. Coyne, "Wn and neutron kerma for methane-based tissue equivalent gas," *Radiat. Res.*, vol. 82, pp. 13-26, 1980.

[41] V. Radeka, "Low-Noise Techniques in Detectors," *Ann. Rev. Nucl. Part. Sci.*, vol. 38, pp. 217-277, 1988.

[42] D. Srdoc and I. Krajer-Bronic, "Statistical fluctuations in the ionization yield for low energy photons absorbed in polyatomic gases," *J. Phys. B: Atm. Molec. Phys.*, vol. 20, p. 4473, 1987.

[43] U. Fano, "Ionization yield of radiations. II. The fluctuations of the number of ions," *Phys. Rev.*, vol. 42, pp. 26-29, 1947.

[44] S. M. Sze, *Semiconductor Devices, Physics and Technology*. New York: Wiley, 1985.

[45] R. A. Langley, *Nuc. Inst. Meth. Phys. Res.*, vol. 113, p. 109, 1973.

[46] B. D. Wilkins, M. J. Fluss, S. B. Kaufman, C. E. Gross, and E. P. Steinberg, *Nuc. Inst. Meth. Phys. Res.*, vol. 92, p. 381, 1971.

[47] J. F. Dicello, H. I. Amols, M. Zaider, and G. Tripard, "A comparison of microdosimetric measurements with spherical proportional counters and solid-state detectors," *Radiat. Res.*, vol. 82, pp. 441-453, 1980.

[48] J. F. Dicello, "Microelectronics and microdosimetry," *Nuclear Instruments and Methods in Physics Research*, vol. B24/25, pp. 1044-1049, 1987.

[49] J. F. Dicello, J. N. Bradford, J. F. Dicello, P. T. Dicello, J. D. Doss, G. Johnson, W. McCabe, A. McDermott, M. Paciotti, O. M. Rivera, and M. E. Schillaci, "Microdosimetry: Measured probabilities for energy deposited by mesons in one-micron sites in silicon," *IEEE Trans. Nucl. Sci.*, vol. 33, pp. 1305-1309, 1986.

[50] M. Orlic, V. Lazarevic, and F. Boreli, "Microdosimetric counters based on semiconductors detectors," *Radiation Protection Dosimetry*, vol. 29, pp. 21-22, 1989.

[51] A. Kadachi, A. Waheed, and M. Obeid, "Performance of PIN photodiode in microdosimetry," *Health Physics*, vol. 66, pp. 577-580, 1994.

[52] A. Kadachi, A. Waheed, M.Al-Eshaikh, and M. Obeid, "Use of photodiode in microdosimetry and evaluation of effective quality factor," *Nuc. Inst. Meth. Phys. Res.*, vol. A404, pp. 400-406, 1998.

[53] International Commission on Radiation Protection, *Radiation Protection Recommendation of the International Commission on Radiation Protection (ICRP: Report 60)*. Oxford: Pergamon, 1991.

[54] J. L. Davis, "Use of computer memory chips as the basis for a digital albedo dosimeter," *Health Physics*, vol. 49, pp. 259-265, 1985.

[55] J. C. Lund, F. Sinclair, and G. Entine, "Neutron dosimeter using a dynamic random access memory as a sensor," *IEEE Trans. Nucl. Sci.*, vol. 33, pp. 620-623, 1986.

[56] A. K. M. M. Haque, J. Yates, and D. Stevens, "Soft errors in dynamic random access memories - a basis for dosimetry," *Radiation Protection Dosimetry*, vol. 17, pp. 189-192, 1986.

[57] D. G. Darambara and N. M. Spyrou, "Detection mechanisms employing single event upsets in dynamic random access memories used as radiation detectors," *Nuc. Inst. Meth. Phys. Res.*, vol. A354, pp. 67-70, 1994.

[58] W. G. Abdel-Kader, P. J. McNulty, S. El-Teleaty, J. Lynch, and A. N. Khondker, "Estimating the dimensions of the SEU-sensitive volume," *IEEE Trans. Nucl. Sci.*, vol. 34, pp. 1300-1303, 1987.

[59] P. J. McNulty, "Single event effects experienced by astronauts and microelectronic circuits flown in space," *IEEE Trans. Nucl. Sci.*, vol. 43, pp. 475-482, 1996.

[60] R. A. Reed, P. J. McNulty, W. J. Beavais, and D. R. Roth, "Charge Collection Spectroscopy," *IEEE Trans. Nucl. Sci.*, vol. 40, pp. 1876-1884, 1993.

[61] M. B. H. Breese, P. J. C. King, G. W. Grime, and F. Watt, "Microcircuit imaging using an ion beam induced charge," *J. Appl. Phys.*, vol. 72, pp. 2097-2104, 1992.

[62] F. W. Sexton, "Microbeam studies of single event upsets," *IEEE Trans. Nucl. Sci.*, vol. 43, pp. 687-695, 1996.

[63] P. J. McNulty, D. R. Roth, W. J. Beauvois, W. G. Abdel-Kader, and E. G. Stassinopoulos, "Microdosimetry in space using microelectronic circuits," presented at NATO-ASI on biological effects and physics of solar and galactic cosmic radiation, Armacaco de Pera, Portugal, 1991.

[64] D. R. Roth, P. J. McNulty, W. J. Beauvais, R. A. Read, and E. G. Stassinopoulos, "Solid-state microdosimeter for radiation monitoring in spacecraft and avionics," *IEEE Trans. Nucl. Sci.*, vol. 41, pp. 2118-2124, 1994.

[65] E. G. Stassinopoulos, C. A. Stauffer, and G. J. Brucker, "Miniature high-let radiation spectrometer for space and medical applications," *Nuclear Instruments and Methods in Physics Research*, vol. A416, pp. 531-535, 1998.

[66] O. Schroder, T. Schmitz, and M. Pierschel, "Microdosimetric dosemeters for individual monitoring based on semiconductor detectors," *Radiation Protection Dosimetry*, vol. 52, pp. 431-434, 1994.

[67] O. Schroder and T. Schmitz, "Can a personal dosemeter for neutron radiation based on a semiconductor chip match the new ICRP recommendations," *Radiation Protection Dosimetry*, vol. 54, pp. 361-364, 1994.

[68] O. Schroder and T. Schmitz, "The application of commercial semiconductor chips for personal neutron dosimetry," *Radiation Protection Dosimetry*, vol. 61, pp. 9-12, 1995.

[69] O. Schroder and T. Schmitz, "Counting protons with semiconductors - a simple approach to a personal neutron dosemeter ?," *Radiation Protection Dosimetry*, vol. 61, pp. 179-182, 1995.

[70] R. Pace, "Alpha radiation effects in integrated circuits: investigating options for sensors," in *School of Physics and Electronic Engineering*. Adelaide: University of South Australia, 1998, p. 290.

[71] A. B. Rosenfeld, G. I. Kaplan, M. G. Carolan, B. J. Allen, R. Maughan, M. Yudelev, C. Kota, and J. Coderre, "Simultaneous macro-micro dosimetry with MOSFETs," *IEEE Trans. Nucl. Sci.*, vol. 43, pp. 2693-2700, 1996.

[72] D. T. Bartlett, R. J. Tanner, and D. J. Thomas, "Active neutron personal dosemeters - a review of current status," *Radiation Protection Dosimetry*, vol. 86, pp. 107-122, 1999.

[73] J. Barthe, J. M. Bordy, and T. Lahaye, "Electronic neutron dosemeters: History and state of the art," *Radiation Protection Dosimetry*, vol. 70, pp. 59-66, 1997.

[74] A. Oed, "Microstrip gas counter," *Nuc. Inst. Meth. Phys. Res.*, vol. A263, p. 351, 1988.

[75] J. Dubeau, M. S. Dixit, E. W. Somerville, A. J. Waker, R. A. Surette, F. G. Oakham, and D. Karlen, "Experimental microdosimetry with microstrip gas counters," presented at The proceedings of the twelfth symposium on microdosimetry: An interdisciplinary meeting on radiation quality, molecular mechanisms, cellular effects and health consequences of low level ionizing radiation, Keble College, Oxford, UK, 1996.

[76] C. Hoflack, J. M. Bordy, Y. Charbonnier, T. Lahaye, M. Lemonnier, M. S. Dixit, J. Dubeau, and P. Segur, "Use of new collection systems associated with a multi cellular tissue equivalent

proportional counter for individual neutron dosimetry," presented at The proceedings of the twelfth symposium on microdosimetry: An interdisciplinary meeting on radiation quality, molecular mechanisms, cellular effects and health consequences of low level ionizing radiation, Keble College, Oxford, UK, 1996.

[77] T. Budd, C. S. Kwok, M. Marshall, and S. Lythe, "Microdosimetric properties of alpha-particle tracks measured in a low pressure cloud chamber," *Radiat. Res.*, vol. 95, pp. 217-230, 1983.

[78] T. Budd and M. Marshall, "Microdosimetric properties of electron tracks measured in a low-pressure cloud chamber," *Radiat. Res.*, vol. 93, pp. 19-32, 1983.

[79] G. P. Stonell, M. Marschall, and J. A. Simmons, "Track studies in water vapor using a low pressure cloud chamber I. Macroscopic measurements, II. Microdosimetric measurements," *Radiat. Res.*, vol. 136, pp. 341-360, 1993.

[80] J. E. Turner, S. R. Hunter, R. N. Hamm, H. A. Wright, G. S. Hurst, and W. A. Gibson, "Development of an optical digital ionisation chamber," *Radiation Protection Dosimetry*, vol. 29, pp. 9-14, 1989.

[81] G. R. Solares and R. G. Zamenhof, "A novel approach to the microdosimetry of neutron capture therapy. Part I. High-resolution quantitative autoradiography applied to microdosimetry in neutron capture therapy.," *Radiat. Res.*, vol. 144, pp. 50-58, 1995.

[82] M. Moscovitch, "The feasibility of digital neutron dosimetry using three dimensional computer optical memories," *Health Physics*, vol. 66, p. 513, 1994.

[83] M. Moscovitch and D. Emfletzoglou, "Simulation of radiation effects on three dimensional computer optical memories," *J. Appl. Phys.*, vol. 81, pp. 58-69, 1997.

[84] D. Emfietzoglou and M. Moscovitch, "A potential application to the study of microscopic energy deposition in a solid by means of heavy charged-particle induced photochromic alterations in a tissue-equivalent matrix," *Phys. Med. Biol.*, vol. 44, pp. 207-221, 1999.

[85] G. W. Phillips, A. K. Readshaw, G. O. Brown, R. G. Weiss, N. A. Guardala, J. L. Price, S. C. Mueller, and M. Moscovitch, "Investigation of 3D ORAM Materials as radiation detectors/dosimeters," *IEEE Trans. Nucl. Sci.*, vol. 47, pp. To be published Mid 2000. Presented at IEEE NSS-1999, Seattle., 2000.

[86] A. K. Readshaw, G. O. Brown, G. W. Phillips, R. G. Weiss, N. A. Guardala, J. L. Price, S. C. Mueller, and M. Moscovitch, "Investigation of 3D ORAM Materials for radiation dosimetry," *Radiation Protection Dosimetry*, vol. 85, pp. 451-454, 1999.

[87] M. Zaider, M. G. Vracko, A. Y. C. Fung, and J. L. Fry, "Electron transport in condensed water," *Radiation Protection Dosimetry*, vol. 52, pp. 139-146, 1994.

[88] M. Zaider, M. J. Bardash, and J. Ladik, "Solid State Microdosimetry," *Radiation Protection Dosimetry*, vol. 85, pp. 443-446, 1999.

[89] J. O. Stoner, "Thin sheet sensor for particle beams," *Appl. Phys. Lett.*, vol. 47, pp. 332-333, 1985.

[90] J. W. Howard, R. C. Block, H. Dussault, W. J. Stapor, P. T. McDonald, A. R. Knudson, and M. R. Pinto, "A novel approach for measuring the radial distribution of charge in a heavy-ion track," *IEEE Trans. Nucl. Sci.*, vol. 41, pp. 2077-2084, 1994.

[91] R. Cox, J. Thacker, and D. T. Goodhead, "Inactivation and mutation of cultured mammalian cells by aluminium characteristic ultrasoft x-rays II. Dose-responses of Chinese hamster and human diploid cells to aluminium x-rays and radiations of different LET," *International Journal of Radiation Biology and Related Studies*, vol. 31, pp. 561-576, 1977.

[92] D. J. Brenner and M. Zaider, "Modification of the theory of dual radiation action for attenuated fields. II. Application to the analysis of soft x-ray results," *Radiat. Res.*, vol. 99, pp. 491-501, 1984.

[93] H. H. Rossi, "Biophysical studies with spatially correlated ions. 1. Background and theoretical considerations," *Radiat. Res.*, vol. 78, pp. 185-191, 1979.

[94] A. M. Kellerer, Y. P. Lam, and H. H. Rossi, "Biophysical studies with spatially correlated ions. 4. Analysis of cell survival data for diatomic deuterium," *Radiat. Res.*, vol. 83, pp. 511-528, 1980.

[95] A. M. Kellerer and H. H. Rossi, "A generalized formulation of dual radiation action," *Radiat. Res.*, vol. 75, pp. 471-488, 1978.

[96] M. Zaider and H. H. Rossi, "On the application of microdosimetry to radiobiology," *Radiat. Res.*, vol. 113, pp. 15-24, 1988.

[97] M. Zaider, "Microdosimetry and Katz's track structure theory," *Radiat. Res.*, vol. 124, pp. 16-22, 1990.

[98] A. Wambersie, P. Pichet, and H. G. Menzel, "The Role of Microdosimetry in Radiotherapy," *Radiation Protection Dosimetry*, vol. 31, pp. 421-432, 1990.

[99] D. W. Miller, "A review of proton beam radiation therapy," *Med. Phys.*, vol. 22, pp. 1943-1954, 1995.

[100] J. R. Castro, "Results of heavy ion radiotherapy," *Radiat. Environ. Biophys.*, vol. 34, pp. 45-48, 1995.

[101] H. R. Withers and M. M. Elkind, "Microcolony survival assay for cells of mouse intestinal mucosa exposed to radiations," *Int. J. Radiat. Biol.*, vol. 17, pp. 261-267, 1970.

[102] B. J. Mijnheer, J. J. Battermann, and A. Wambersie, "What degree of accuracy is required and can be achieved in photon and neutron therapy," *Radiotherapy and Oncology*, vol. 8, pp. 237-252, 1987.

[103] E. J. Hall, H. H. Rossi, A. M. Kellerer, L. Goodman, and S. Marino, "Radiobiological studies with monoenergetic neutrons," *Radiat. Res.*, vol. 54, p. 431, 1973.

[104] T. G. Stinchcomb, F. T. Kuchnir, L. C. Myrianthopoulos, J. L. Horton, and W. K. Roberts, "Correlation of microdosimetric measurements with the relative biological effectiveness from clinical experience for two neutron therapy beams," *Med. Phys.*, vol. 13, pp. 201-206, 1986.

[105] J. L. Beach and L. R. Milavickas, "Microdosimetric measurements of radiation quality variations in homogeneous phantoms irradiated by fast neutron beams," *Med. Phys.*, vol. 9, pp. 52-60, 1982.

[106] J. Fidorra and J. Booz, "Microdosimetric investigation on collimated fast-neutron beams for radiation therapy: I. Measurements of microdosimetric spectra and particle dose fractions in a water phantom for fast neutrons from 14 MeV deuterons on beryllium," *Phys. Med. Biol.*, vol. 26, pp. 27-41, 1981.

[107] J. Fidorra and J. Booz, "Microdosimetric investigation on collimated fast-neutron beams for radiation therapy: I. The problem of radiation quality and RBE," *Phys. Med. Biol.*, vol. 26, pp. 43-56, 1981.

[108] P. M. Stafford, J. L. Horton, and P. R. Almond, "A microdosimetric characterization of a cyclotron-produced neutron beam," *Med. Phys.*, vol. 14, pp. 1015-1019, 1987.

[109] P. Pihet, "Etude microdosimetrique de fasiceaux de neutrons de haute energie. Applications dosimetriques et radiobiologiqes,". Louvain: Catholic University Louvain, 1989.

[110] P. Pihet, H. G. Menzel, R. Schmidt, M. Beauduin, and A. Wambersie, "Biological weighting function for RBE specification of neutron therapy beams. Intercomparison of 9 European centres," *Radiation Protection Dosimetry*, vol. 31, pp. 437-442, 1990.

[111] J. Gueulette, H. G. Menzel, P. Pihet, and A. Wambersie, "Specification of radiation quality in fast neutron therapy: Microdosimetric and radiobiological approach," in *Fast neutrons and high-LET particles in cancer therapy*, vol. 150, R. Engenhart-Cabillic and A. Wambersie, Eds., 1 ed. Berlin-Heidelberg: Springer-Verlag, 1998, pp. 31-53.

[112] G. Hartmann, H. G. Menzel, and H. Schulmacher, "Different approaches to determine effective quality factors and dose equivalent using the Rossi Counter," presented at Fourth symposium on neutron dosimetry, 1981.

[113] International Commission on Radiation Units and Measurements, *Quantities and Units in Radiation Protection Dosimetry (ICRU report 51)*. Bethesda, Md., U.S.A.: ICRU, 1992.

[114] L. A. Braby, G. D. Bahwar, T. J. Conroy, D. C. Elegy, and L. W. Brackenbush, "Automated systems for measuring dose and radiation quality as a function of time," *Radiation Protection Dosimetry*, vol. 52, pp. 423-426, 1994.

[115] A. Kunz, P. Pihet, E. Arnaud, and H. G. Menzel, "An easy to operate pulse height analysis system for area monitoring with TEPC in radiation protection," *Nuc. Inst. Meth. Phys. Res.*, vol. A299, pp. 696-701, 1990.

[116] D. Binder, E. C. Smith, and A. B. Holman, "Satellite anomalies from galactic cosmic rays," *IEEE Trans. Nucl. Sci.*, vol. 22, pp. 2675-2680, 1975.

[117] J. T. Wallmark and S. M. Marcus, "Minimum size and maximum packing density of nonredundant semiconductor devices," *Proc. of IRE*, pp. 286-298, 1962.

[118] J. L. Shinn, G. D. Bahdwar, M. A. Xapsos, F. A. Cucinotta, and J. W. Wilson, "An analysis of energy deposition in a tissue equivalent proportional counter onboard the space shuttle," *Radiation Measurements*, vol. 30, pp. 19-28, 1999.

[119] J. F. Bottollier-Depois, L. Lebaron-Jacobs, M. Siegrist, E. Duvivier, B. Almarcha, T. P. Dachev, J. V. Semkova, Y. N. Matviichuk, R. T. Koleva, B. T. Tomav, P. T. Baynov, V. M. Petrov, V. V. Shurshakov, V. Begin, and S. B. Koslova, "Tissue equivalent detector data obtained recently on MIR space station. Comparison with solid state detector data," *Adv. Space Res.*, vol. 18, pp. 171-174, 1996.

[120] L. Lindborg, J. E. Kyllonen, P. Beck, J. F. Bottollier-Depois, S. Gerdung, R. E. Grillmaier, and U. Schrewe, "The use of a TEPC for reference dosimetry," *Radiation Protection Dosimetry*, vol. 86, pp. 285-288, 1999.

[121] C. S. Dyer and P. R. Truscott, "Cosmic radiation effects on avionics," *Radiation Protection Dosimetry*, vol. 86, pp. 337-342, 1999.

[122] J. N. Bradford, "Single event error generation by 14 MeV neutrons reactions in silicon," *IEEE Trans. Nucl. Sci.*, vol. 27, pp. 1480-1483, 1980.

[123] J. N. Bradford, "Microvolume energy deposition from high energy proton silicon reactions," *IEEE Trans. Nucl. Sci.*, vol. 29, pp. 2085-2089, 1982.

[124] G. E. Farrell and P. J. McNulty, "Microdosimetric aspects of proton-induced nuclear reactions in thin layers of silicon," *IEEE Trans. Nucl. Sci.*, vol. 29, pp. 2012-2016, 1982.

[125] R. S. Caswell and J. J. Coyne, "Interaction of neutrons and secondary charged particles with tissue: Secondary charged particle spectra," *Radiat. Res.*, vol. 52, p. 448, 1972.

[126] J. F. Ziegler, *SRIM: The Stopping and Range of Ions in Matter*, V97.02 ed. Yorktown: IBM Research, 1997.

[127] A. M. Kellerer, "Analysis of patterns of energy distribution (Euratom Report,EUR4522,d-e-f)," presented at Second symposium on microdosimetry, Brussels, 1970.

[128] A. M. Kellerer, "Considerations on the random traversal of convex bodies and solutions for general cylinders," *Radiat. Res.*, vol. 47, pp. 359-376, 1971.

[129] A. M. Kellerer, "Criteria for the equivalence of spherical and cylindrical proportional counters in microdosimetry," *Radiat. Res.*, vol. 86, pp. 277-286, 1981.

[130] R. Coleman, "Random paths through convex bodies," *J. Appl. Prob.*, vol. 6, pp. 430-441, 1969.

[131] R. Coleman, "Intercept lengths of random probes through boxes," *J. Appl. Prob.*, vol. 18, pp. 276-282, 1981.

[132] A. M. Kellerer, "Chord length distributions and related quantities for spheroids," *Radiat. Res.*, vol. 98, pp. 425-437, 1984.

[133] M. G. Kendall and P. A. P. Moran, *Geometrical Probability*, 1 ed. London: Griffin, 1963.

[134] J. F. C. Kingman, "Mean free paths in a convex reflecting region," *J. Appl. Prob.*, vol. 2, pp. 162-168, 1965.

[135] U. Mader, "Chord length distributions for circular cylinders," *Radiat. Res.*, vol. 82, pp. 454-466, 1980.

[136] J. B. Langworthy, "A general approach to chord length distributions applied to a hemisphere," *Radiat. Res.*, vol. 118, pp. 21-36, 1989.

[137] J. N. Bradford, "A distribution function for ion track lengths in rectangular volumes," *J. Appl. Phys.*, vol. 50, pp. 3799-3801, 1979.

[138] R. Coleman, "Random paths through rectangles and cubes," *Metallography*, vol. 6, pp. 103-114, 1973.

[139] J. F. Ziegler and W. A. Lanford, "The effect of sea level cosmic rays on electronic devices," *J. Appl. Phys.*, vol. 52, pp. 4305-4312, 1981.

[140] T. B. Borak, "A method for computing random chord length distributions in geometrical objects," *Radiat. Res.*, vol. 137, pp. 346-351, 1994.

[141] Wolfram Research, *Mathematica*, V3.0 ed: Wolfram Research, 1996.

[142] A. M. Kellerer and D. Chmelevsky, "Concepts of microdosimetry. III. Mean values of the microdosimetric distributions," *Radiat. Environ. Biophys.*, vol. 12, pp. 321-335, 1975.

[143] A. M. Kellerer, "Proximity functions for general right cylinders," *Radiat. Res.*, vol. 86, pp. 264-276, 1981.

[144] P. Kliauga, "Measurement of single event energy deposition spectra at 5 nm to 250 nm simulated site sizes," *Radiation Protection Dosimetry*, vol. 31, pp. 119-123, 1990.

[145] P. Kliauga, "Nanodosimetry of heavy ions using a miniature cylindrical counter of wall-less design," *Radiation Protection Dosimetry*, vol. 52, pp. 317-321, 1994.

[146] H. I. Amols, C. S. Wuu, and M. Zaider, "On possible limitations of experimental nanodosimetry," *Radiation Protection Dosimetry*, vol. 31, pp. 125-128, 1990.

[147] T. Hartman and J. Carlsson, "Radiation dose heterogeneity in receptor and antigen mediated boron neutron capture therapy.," *Radiotherapy and Oncology*, vol. 31, pp. 61-75, 1994.

[148] J. P. A. Baak, *Manual of quantitative pathology in cancer diagnosis and prognosis*. Berlin: Springer-Verlag, 1991.

[149] M. A. Davis, J. B. Little, K. M. M. S. Ayyangar, and A. R. Reddy, "Relative biological effectiveness of the B10(n,alpha)Li7 Reaction in HeLa Cells," *Radiat. Res.*, vol. 43, pp. 534-553, 1970.

[150] D. Gabel, S. Foster, and R. G. Fairchild, "The Monte Carlo simulation of the biological effect of the B10(n,alpha)Li7 reaction in cells and tissue and its implication for boron neutron capture therapy," *Radiat. Res.*, vol. 111, pp. 14-25, 1987.

[151] T. Nguyen, G. L. Brownell, S. A. Holden, S. Kahl, M. Miura, and B. A. Teicher, "Subcellular distribution of various boron compounds and implications for their efficacy in boron neutron capture therapy by Monte Carlo simulations," *Radiat. Res.*, vol. 133, pp. 33-40, 1993.

[152] F. Poller and W. Sauerwein, "Monte Carlo Simulation of the Biological Effects of Boron Neutron Capture Irradiation with d(14)+Be Neutrons *in Vitro*," *Radiat. Res.*, vol. 142, pp. 98-106, 1995.

[153] C. Kota, R. L. Maughan, D. Tattam, and T. D. Beynon, "Use of low-pressure tissue equivalent proportional counters for the dosimetry of neutron beams used in BNCT and BNCEFNT," *Med. Phys.*, vol. 27, pp. 535-548, 2000.

[154] C. Kota and R. L. Maughan, "Microdosimetric specification of the radiation quality of a d(48.5)+Be fast neutron therapy beam produced by a superconducting cyclotron," *Med. Phys.*, vol. 23, pp. 1591-1599, 1996.

[155] G. Coutrakon, J. Cortese, A. Ghebremedhin, J. Hubbard, J. Johanning, P. Koss, G. Maudsley, C. R. Slater, C. Zuccarelli, and J. Robertson, "Microdosimetry spectra of the Loma Linda proton beam and relative biological effectiveness comparisons," *Med. Phys.*, vol. 24, pp. 1499-1506, 1997.

[156] T. P. Ma and P. V. Dressendorfer, *Ionizing radiation effects in MOS devices and circuits*. New York: John Wiley & Sons, 1989.

[157] J. F. Ziegler and G. R. Srinivasan, "Terrestrial cosmic rays and soft errors," *IBM Journal of Research and Development*, vol. 40, pp. 1-136, 1996.

[158] P. Bradley, "The effects of ionising radiation on implantable MOS electronic devices," in *Graduate School of Biomedical Engineering*. Sydney: University of New South Wales, 1996, p. 245.

[159] P. D. Bradley and E. Normand, "Single event upset in implantable cardioverter defibrillators," *IEEE Trans. Nucl. Sci.*, vol. 45, pp. 2929-2940, 1998.

[160] S. Satoh, R. Sudo, H. Tashiro, N. Higaki, and N. Nakayama, "CMOS-SRAM soft error simulation system," *IEEE/IRPS*, pp. 339-343, 1994.

[161] Y. Tosaka, H. Kanata, T. Itakura, and S. Satoh, "Simulation technologies for cosmic ray neutron induced soft errors: Models and simulation systems," *IEEE Trans. Nucl. Sci.*, vol. 46, pp. 774-779, 1999.

[162] Y. Tosaka, S. Satoh, K. Suzuki, T. Sugii, N. Nakayama, H. Ehara, G. A. Woffinden, and S. A. Wender, "Measurements and Analysis of Neutron-Reaction-Induced Charges in a Silicon Surface Region," *IEEE Trans. Nucl. Sci.*, vol. 44, pp. 173-178, 1997.

[163] Y. Tosaka, S. Satoh, K. Suzuki, T. Sugii, H. Ehara, and G. A. Woffinden, "Cosmic Ray Neutron-Induced Soft Errors in sub-half micron CMOS circuits," *IEEE Elect. Dev. Lett.*, vol. 18, pp. 99-101, 1997.

[164] Y. Tosaka, S. Satoh, T. Itakura, H. Ehara, T. Ueda, G. Woffinden, and S. A. Wender, "Measurement and analysis of neutron induced soft errors in sub-half micron CMOS circuits," *IEEE Trans. Electron Devices*, vol. 45, pp. 1453-1458, 1998.

[165] A. Cerdeira and M. Estrada, "Analytical expressions for the calculation of pixel detector capacitances," *IEEE Trans. Nucl. Sci.*, vol. 44, pp. 63-66, 1997.

[166] S. Kavadias, K. Misiakos, and D. Loukas, "Calculation of pixel detector capacitances through three dimensional numerical solution of Laplace equation," *IEEE Trans. Nucl. Sci.*, vol. 41, pp. 397-401, 1994.

[167] C. F. G. Delaney, *Electronics for the Physicist*, 1 ed. Chichester: Ellis Horwood, 1980.

[168] C. F. G. Delaney and E. C. Finch, *Radiation Detectors: Physical Principles and Applications*, 1 ed. Oxford: Clarendon Press, 1992.

[169] H. Nyquist, "Thermal agitation of electronic charge in conductors," *Physical Review*, vol. 32, pp. 110-113, 1928.

[170] W. Schottky, *Ann. Phys. (Leipzig)*, vol. 57, pp. 541-567, 1918.

[171] V. Radeka, B. Bryan, P. O'Connor, C. Britton, and A. Witenberg, "Integrated circuit front ends for nuclear pulse processing (Short Course)," presented at IEEE Nuclear Science Symposium, Seattle, 1999.

[172] E. G. G. Ortec, *Catalogue: Detectors and Instruments for Nuclear Spectroscopy*. Oak Ridge: E.G & G Ortec, 1999.

[173] D. A. Johns and K. Martin, *Analog Integrated Circuit Design*. New York: John Wiley and Sons, 1997.

[174] P. O. Connor, "Ultra low noise CMOS preamplifier-shaper for X-ray spectroscopy," *Nuclear Instrumentation and Methods in Physics Research A*, vol. A409, pp. 315-321, 1998.

[175] A. B. Rosenfeld, M. G. Carolan, G. I. Kaplan, B. J. Allen, and V. I. Khivrich, "MOSFET dosimeters: The role of encapsulation on dosimetric characteristics in mixed gamma-neutron and megavoltage X-ray fields.," *IEEE Trans. Nucl. Sci.*, vol. 42, pp. 1870-1877, 1996.

[176] T. E. Burlin, "Cavity Chambers Theory," in *Radiation Dosimetry*, vol. 1, F. H. Attix, W. C. Roesch, and E. Tochilin, Eds. New York: Academic Press, 1968, p. 332.

[177] L. H. Gray, "An ionization method for the absolute measurement of gamma ray energy," *Proc. Royal Soc.*, vol. A156, p. 578, 1936.

[178] L. H. Gray, "The absorption of penetrating radiation," *Proc. Royal Soc.*, vol. A122, p. 647, 1929.

[179] J. H. Hubbell and S. M. Seltzer, "Tables of X-Ray Mass Attenuation Coefficients and Mass Energy-Absorption Coefficients from 1 keV to 20 MeV for Elements Z = 1 to 92 and 48 Additional Substances of Dosimetric Interest,", vol. http://physics.nist.gov/PhysRefData/XrayMassCoef/cover.html, NISTIR 5632 ed. Ionizing Radiation Division, Physics Laboratory, National Institute of Standards and Technology, USA: National Institute of Standards and Technology, USA, 1996.

[180] I. C. o. R. Protection, *Report of the Task Group on Reference Man, ICRP Publication #23*. Oxford: International Commission on Radiological Protection, 1975.

[181] International Commission on Radiation Units and Measurements, *Physical Aspects of Irradiation (ICRU Report; 10b)*. Maryland: ICRU, 1964.

[182] J. B. Smathers, V. A. Otte, A. R. Smith, P. R. Almond, F. H. Attix, J. J. Spokas, W. M. Quam, and L. J. Goodman, "Composition of A-150 tissue equivalent plastic," *Med. Phys.*, vol. 4, p. 74, 1977.

[183] J. E. Turner, *Atoms, Radiation and Radiation Protection*. New York: Pergamon Press, 1986.

[184] J. F. Ziegler, J. P. Biersack, and U. Littmark, *The Stopping and Range of Ions in Solids*. New York: Pergamon Press, 1985.

[185] P. D. Bradley and A. B. Rosenfeld, "Tissue Equivalence Correction for Silicon Microdosimetry Detectors in Boron Neutron Capture Therapy," *Med. Phys.*, vol. 25, pp. 2220-2225, 1998.

[186] D. E. Charlton and B. J. Allen, "Monte Carlo calculations of ion passages through brain endothelial nuclei during boron neutron capture therapy," *Int. J. Radiat. Biol.*, vol. 64, pp. 739-747, 1993.

[187] D. E. Charlton, D. T. Goodhead, W. E. Wilson, and H. G. Paretze, *Energy deposition in Cylindrical Volumes: (a) Protons, Energy 0.3 MeV to 4.0 MeV, (b) Alpha Particles, 1.2 MeV to 20 MeV, Monograph 85/1*. Chilton: Medical Research Council, 1985.

[188] D. E. Charlton, "Energy deposition in small ellipsoidal volumes by high-LET particles application to thermal neutron dosimetry," *Int. J. Radiat. Biol.*, vol. 59, pp. 827-842, 1991.

[189] S. Green, A. C. A. Aro, G. C. Taylor, and M. C. Scott, "The development of microdosimetric detectors for investigating LET distributions in different biological tissues," *Radiation Protection Dosimetry*, vol. 31, pp. 137-156, 1990.

[190] R. S. Caswell and J. J. Coyne, "Energy deposition spectra for neutrons based on recent cross-section evaluation," presented at Sixth symposium on microdosimetry, 1978.

[191] R. S. Caswell, J. J. Coyne, and M. L. Randolph, "Kerma factors for neutron energies below 30 MeV," *Radiat. Res.*, vol. 83, p. 217, 1980.

[192] H. H. K. Tang, "Nuclear Physics of cosmic ray interaction with semiconductor materials: Particle-induced soft errors from a physicist's perspective," *IBM J. Res. Develop*, vol. 40, pp. 91-108, 1996.

[193] Brookhaven National Laboratory, "Evaluated Nuclear Data Files," *http://www.nndc.bnl.gov/nndc/endf/*, 1999.

[194] P. D. Bradley, A. B. Rosenfeld, K. K. Lee, D. Jamieson, G. Heiser, and S. Satoh, "Charge collection and radiation hardness of a SOI microdosimeter for space and medical applications," *IEEE Trans. Nucl. Sci.*, vol. 45, pp. 2700-2710, 1998.

[195] D. M. Caughey and R. E. Thomas, "Carrier mobilities in silicon empirically related to doping and field," *Proc. IEEE*, vol. 55, p. 2192, 1967.

[196] ISE Integrated Systems Engineering AG, *ISE TCAD software including (DESSIS, LIGAMENT, PROSIT, TE2DIOS)*, Release 4.0 ed. Zurich.

[197] R. N. Hall, "Electron-hole recombination in germanium," *Phys. Rev*, vol. 87, p. 387, 1952.

[198] W. Shockley and W. T. Read, "Statistics of the recombination of holes and electrons," *Phys. Rev.*, vol. 87, pp. 835-842, 1952.

[199] D. K. Schroder, "Carrier lifetimes in silicon," *IEEE Trans. Electron Devices*, vol. 44, pp. 160-170, 1997.

[200] D. K. Schroder, *Semiconductor Material and Device Characterization*. New York: Wiley, 1990.
[201] W. M. Bullis and H. R. Huff, "Interpretation of carrier recombination lifetime and diffusion length measurements in silicon," *J. Electrochem. Soc.*, vol. 143, pp. 1399-1405, 1996.
[202] L. W. Connell and F. W. Sexton, "Modeling the heavy ion cross-section for single event upset with track structure effects: the HIC-UP-TS model," *IEEE Trans. Nucl. Sci.*, vol. 43, pp. 2814-2819, 1996.
[203] E. J. Kobetich and R. Katz, "Energy deposition by electron beams and delta rays," *Physical Review*, vol. 170, pp. 391-396, 1968.
[204] R. N. Hamm, J. E. Turner, H. A. Wright, and R. H. Ritchie, "Heavy ion track structure in silicon," *IEEE Trans. Nucl. Sci.*, vol. 26, p. 4892, 1979.
[205] M. P. R. Waligorski, R. N. Hamm, and R. Katz, "The radial distribution of dose around the path of a heavy ion in liquid water," *Nucl. Tracks Radiat. Meas.*, vol. 11, pp. 309-319, 1986.
[206] I. Kanno, "Models of formation and erosion of a plasma column in a silicon surface barrier detector," *Rev. Sci. Instrum.*, vol. 58, pp. 1926-1932, 1987.
[207] R. C. Martin, N. M. Ghoniem, Y. Song, and J. S. Cable, "The size effect of ion charge tracks on single event multiple-bit upset," *IEEE Trans. Nucl. Sci.*, vol. 34, pp. 1305-1309, 1987.
[208] W. J. Stapor and P. T. McDonald, "Practical approach to ion track energy distribution," *J. Appl. Phys.*, vol. 64, pp. 4330-4434, 1988.
[209] R. Katz, K. S. Loh, L. Daling, and G. R. Huang, "An analytic representation of the radial distribution of dose form energetic heavy ions in water, Si, LiF, NaI, and SiO_2," *Radiation Effects and Defects in Solids*, vol. 114, pp. 15-20, 1990.
[210] M. J. Pruppers, H. P. Leenhouts, and K. H. Chadwick, "A track structure model for the spatial energy deposition of ionizing radiation," *Radiation Protection Dosimetry*, vol. 31, pp. 185-188, 1990.
[211] O. Fageeha, J. Howard, and R. C. Block, "Distribution of radial energy deposition around the track of energetic charged particles in silicon," *J. Appl. Phys.*, vol. 75, pp. 2317-2321, 1994.
[212] C. M. Hsieh, P. C. Murley, and R. R. O'Brien, "A field funneling effect on the collection of alpha particle generated carriers in silicon devices," *IEEE Elect. Dev. Lett.*, vol. 2, pp. 103-105, 1981.
[213] H. V. Roos, "A note on photocurrents in extrinsic semiconductors," *Solid state electronics*, vol. 22, pp. 229-232, 1979.
[214] McKelvey, *Solid state and semiconductor physics*: Harper and Row, 1966.
[215] G. C. Messenger, "Collection of charge on junction nodes from ion tracks," *IEEE Trans. Nucl. Sci.*, vol. 29, pp. 2024-2031, 1982.
[216] L. D. Edmonds, "Charge collected by diffusion from an ion track under mixed boundary conditions," *IEEE Trans. Nucl. Sci.*, vol. 38, pp. 834-837, 1991.
[217] L. D. Edmonds, "Electric currents through ion tracks in silicon devices," *IEEE Trans. Nucl. Sci.*, vol. 45, pp. 3153-3164, 1998.
[218] L. D. Edmonds, "A theoretical analysis of steady-state photocurrents in simple silicon diodes," Jet Propulsion Laboratory, Caltech, NASA, Pasadena JPL Publication 95-10, March 1995.
[219] L. D. Edmonds, "Charge collection from ion tracks in simple EPI diodes," *IEEE Trans. Nucl. Sci.*, vol. 44, pp. 1448-1463, 1997.
[220] C. Hu, "Alpha particle-induced field and enhanced collection of carriers," *IEEE Elect. Dev. Lett.*, vol. 3, pp. 31-34, 1982.
[221] F. B. McLean and T. R. Oldham, "Charge funneling in n-type and p-type Si substrates," *IEEE Trans. Nucl. Sci.*, vol. 29, pp. 2018-2023, 1982.
[222] P. E. Dodd, F. W. Sexton, and P. S. Winokur, "Three-dimensional simulation of charge collection and multiple-bit-upset in Si devices," *IEEE Trans. Nucl. Sci.*, vol. 41, pp. 2005-2017, 1994.
[223] P. E. Dodd, "Device simulation of charge collection and single event upset," *IEEE Trans. Nucl. Sci.*, vol. 43, pp. 561-575, 1996.
[224] L. D. Edmonds, "A simple estimate of funnel-assisted charge collection," *IEEE Trans. Nucl. Sci.*, vol. 38, pp. 828-833, 1991.
[225] S. Ramo, "Currents induced by electron motion," *Proceedings of the IRE*, vol. 27, pp. 584-585, 1939.
[226] H. Spieler, "Fast timing methods for semiconductor detectors," *IEEE Trans. Nucl. Sci.*, vol. 29, pp. 1142-1165, 1982.
[227] J. E. Toney, B. A. Brunett, T. E. Schlesinger, and R. B. James, "Photocurrent mapping as a probe of transport properties and electric field distributions in cadmium zinc telluride detectors," *IEEE Trans. Nucl. Sci.*, vol. 44, pp. 1684-1691, 1997.

[228] R. E. Bank, D. J. Rose, and W. Fichtner, "Numerical methods for semiconductor device simulation," *IEEE Trans. Electron Devices*, vol. 30, pp. 1031-1041, 1983.

[229] H. S. Bennett and C. L. Wilson, "Comparisons of data on band-gap narrowing in heavily doped silicon: electrical and optical measurements," *J. Appl. Phys.*, vol. 55, pp. 3582-87, 1984.

[230] H. Dussault, J. W. Howard, R. C. Block, M. R. Pinto, W. J. Stapor, and A. R. Knudson, "Numerical simulation of heavy ion charge generation and collection dynamics," *IEEE Trans. Nucl. Sci.*, vol. 40, pp. 1926-1934, 1993.

[231] P. D. Bradley, *2D animated simulation BNCT, URL: http://www.uow.edu.au/~pbradley/simulation/2Dsimulation.html*, 1.0 ed. Wollongong: University of Wollongong, 1998.

[232] D. N. Jamieson, "Structural and electrical characterisation of semiconductor materials using a nuclear microprobe," *Nuclear-Instruments-&-Methods-in-Physics-Research,-Section-B-(Beam-Interactions-with-Materials-and-Atoms).*, vol. 136-138, pp. 1-13, 1998.

[233] M. B. H. Breese, D. N. Jamieson, and P. J. C. King, *Materials analysis with a nuclear microprobe*. New York: John Wiley and Sons, 1996.

[234] G. R. Srinivasan, H. K. Tang, and P. C. Murley, "Accurate, predicative modeling of soft error rate due to cosmic rays and chip alpha radiation," *IEEE Trans. Nucl. Sci.*, vol. 41, pp. 2063-2070, 1994.

[235] MathsWorks Inc, *Matlab*, 5.2.0.3084 ed, 1998.

[236] J. S. Fu, H. T. Weaver, R. Koga, and W. A. Kolasinski, "Comparison of 2D memory SEU transport simulation with experiments," *IEEE Trans. Nucl. Sci.*, vol. 32, pp. 4145-4149, 1985.

[237] R. E. Davis, W. E. Johnson, K. Lark-Horowitz, and D. S. Siegel, "Neutron bombarded Germanium semiconductors," *Phys. Rev.*, vol. 74, p. 1255, 1948.

[238] H. W. Kramer, "Radiation damage in semiconductor detectors," *IEEE Trans. Nucl. Sci.*, vol. 29, pp. 1088-1095, 1982.

[239] G. C. Messenger and M. S. Ash, *The Effects of Radiation on Electronic Systems*, 2nd ed. New York: Van Nostrand Reinhold, 1992.

[240] G. C. Messenger, "A summary review of displacement damage from high energy radiation in silicon semiconductors and semiconductor devices," *IEEE Trans. Nucl. Sci.*, vol. 39, pp. 468-473, 1992.

[241] S. Wood, N. J. Doyle, J. A. Spitznagel, W. J. Choyke, R. M. More, J. N. McGruer, and R. B. Irwin, "Simulation of radiation damage in solids," *IEEE Trans. Nucl. Sci.*, vol. 28, p. 4107, 1981.

[242] G. P. Mueller, M. D. Wilsey, and M. Rosen, "The structure of displacement cascades in silicon," *IEEE Trans. Nucl. Sci.*, vol. 29, pp. 1493-1497, 1982.

[243] L. Edmonds, G. Swift, and A. Johnston, "Non-destructive measurements for CMOS devices using charge collection techniques," *IEEE Trans. Nucl. Sci.*, vol. 43, pp. 2833-2841, 1996.

[244] C. Leroy, P. Roy, G. L. Casse, M. Glaser, E. Grigoriev, and F. Lemeilleur, "Charge transport in non-irradiated and irradiated silicon detectors," *Nuclear Instruments And Methods In Physics Research Section A*, vol. 434, pp. 90-102, 1999.

[245] D. J. Simon and L. Durieu, "CERN report: Secondary Beams for Tests in the PS East Experimental Area," CERN, (http://www.cern.ch/CERN/Divisions/PS/Reports/PA9321/Welcome.html), Zurich PS/PA-EP Note 88-26, 8.8.88, PS/PA/Note 93-21, revised 4.8.93, 4.8.93 1993.

[246] F. Lemeilleur, "Personal Communication of CERN radiation hardness experiment conditions,"., 1997.

[247] E. A. Burke, "Energy dependence of proton-induced displacement damage in silicon," *IEEE Trans. Nucl. Sci.*, vol. 33, pp. 1276-1281, 1986.

[248] G. P. Summers, E. A. Burke, C. J. Dale, E. A. Wolicki, P. W. Marshal, and M. A. Gelhausen, "Correlation of particle induced displacement damage in silicon," *IEEE Trans. Nucl. Sci.*, vol. 33, pp. 1134-1139, 1987.

[249] G. P. Summers, E. A. Burke, P. Shapiro, S. R. Messenger, and R. J. Walters, "Damage correlations in semiconductors exposed to gamma, electron and proton radiations," *IEEE Trans. Nucl. Sci.*, vol. 40, pp. 1372-1379, 1993.

[250] R. J. Walters, S. R. Messenger, G. P. Summers, E. A. Burke, and C. J. Keavney, "Space radiation effects in InP Solar cells," *IEEE Trans. Nucl. Sci.*, vol. 38, p. 1153, 1991.

[251] E. Fretwurst, "Personal Communication of Displacement Damage Data,"., 1998.

[252] International Commission on Radiation Units and Measurements, *Photon, electron, proton, and neutron interaction data for body tissues (ICRU report 46)*. Bethesda, Md., U.S.A.: ICRU, 1992.

[253] Europractice, "Europractice ASIC service, IMEC IC manufacturing center, Kapeldreef 75, B-3001 Leuven, Belgium, http://www.imec.be.europractice,".

[254] B. Larsson, J. Crawford, and R. Weinrich, "Advances in Neutron Capture Therapy, Volume I: Medicine and Physics.," in *Proceedings of the Seventh International Symposium on Neutron Capture Therapy for Cancer*. Zürich: Elsevier, 1996.

[255] R. F. Barth, A. H. Soloway, J. H. Goodman, N. Gupta, T. E. Blue, W. Yang, and W. Tjarks, "Boron neutron capture therapy of brain tumors: An emerging therapeutic modality," *Neurosurgery*, vol. 44, pp. 433-449, 1999.

[256] J. A. Coderre and G. M. Morris, "Review: The radiation biology of boron neutron capture therapy," *Radiat. Res.*, vol. 151, pp. 1-18, 1999.

[257] R. G. Zamenhof, "Microdosimetry for boron neutron capture therapy: A review," *Journal of Neuro-Oncology*, vol. 33, pp. 81-92, 1997.

[258] G. L. Locher, "Biological effects and therapeutic possibilities of neutrons," *Ann J. Roentgenol.*, vol. 36, pp. 1-13, 1936.

[259] L. E. Farr, W. H. Sweet, J. S. Robinson, C. G. Foster, H. B. Locksley, and D. L. Sutherland, "Neutron capture therapy with boron in the treatment of glioblastoma multiforme," *Am. J. Roentgenol.*, vol. 71, pp. 279-291, 1954.

[260] D. N. Slatkin, "A history of boron neutron capture therapy of brain tumours - Postulation of a brain radiation dose tolerance limit," *Brain*, vol. 114, pp. 1609-1629, 1991.

[261] G. E. Laramore and A. M. Spence, "Boron neutron capture therapy for high-grade gliomas of the brain - a cautionary note," *Int. J. Radiat. Oncol. Biol. Phys.*, vol. 36, pp. 241-246, 1996.

[262] C. S. Wuu, H. I. Amols, P. Kliauga, L. E. Reinstein, and S. Saraf, "Microdosimetry for Boron Neutron Capture Therapy," *Radiat. Res.*, vol. 130, pp. 355-359, 1992.

[263] R. L. Maughan, M. Yudelev, and C. Kota, "A microdosimetric study of dose enhancement in a fast neutron beam due to boron neutron capture therapy," *Phys. Med. Biol.*, vol. 38, pp. 1957-1961, 1993.

[264] C. Kota, "Microdosimetric considerations in the use of the boron neutron capture reaction in radiation therapy," in *Department of Medical Physics*. Detroit: Wayne State University, 1996, p. 189.

[265] S. F. Mughabghab, M. Divadeenam, and N. E. Holden, *Neutron Cross Sections from Neutron Resonance Parameters and Thermal Cross Sections (See also http://ie.lbl.gov/ngdata/sig.htm)*. New York: Academic Press, 1981.

[266] K. S. Krane, *Introductory Nuclear Physics*. New York: John Wiley & Sons, 1988.

[267] Brycoat, "http://www.brycoat.com/physprop.html,".: Brycoat, 2000.

[268] H. B. Liu, D. D. Greenberg, J. Capala, and F. J. Wheeler, "Improved neutron collimator for brain tumor irradiations in clinical boron neutron capture therapy," *Med. Phys.*, vol. 23, pp. 2051-2060, 1996.

[269] T. Kobayashi, Y. Sakurai, and K. Kanda, "Characteristics of neutron irradiation facility and dose estimation method for neutron capture therapy at Kyoto University Research Reactor Institute," presented at Proceeding of the IAEA Technical Committee Meeting, 1999.

[270] T. Kobayashi, Y. Sakurai, K. Kanda, Y.Fuijita, and K. Ono, "The remodeling outline of the neutron irradiation facility of the Kyoto University Research Reactor mainly for neutron capture therapy," presented at Proceeding of the IAEA Technical Committee Meeting, 1999.

[271] J. C. Yanch, S. Shortkroff, R. E. Shefer, S. Johnson, E. Binello, D. Gierga, A. G. Jones, G. Young, C. Vivieros, A. Davison, and C. Sledge, "Boron neutron capture synovectomy: Treatment of rheumatoid arthritis based on the 10B(n,alpha)7Li nuclear reaction," *Med. Phys.*, vol. 26, pp. 364-375, 1999.

[272] J. M. Cosset, M. Maher, and J. L. Habrand, "New particles in radiotherapy: an introduction," *Radiat. Environ. Biophys.*, vol. 34, pp. 37-39, 1995.

[273] S. Field, "A historical survey of radiobiology and radiotherapy with fast neutrons," *Curr. Top. Rad. Research*, vol. Q 11, pp. 1-86, 1976.

[274] R. S. Stone and J. C. Larkin, "Treatment of cancer with fast neutrons," *Radiology*, vol. 39, pp. 608-620, 1942.

[275] G. E. Laramore, J. M. Krall, T. W. Griffin, W. Duncan, M. P. Richter, K. R. Saroja, M. H. Maor, and L. W. Davis, "Neutron versus proton irradiation for unresectable salivary gland tumors: Final report of an RTOG-MRC Randomized clinical trial," *International Journal of Radiation Oncology, Biology, and Physics*, vol. 2, pp. 235-240, 1993.

[276] T. Griffin, J. Krall, G. Aramore, R. Parker, M. Burneson, and L. Peters, "Neutron versus photon irradiation for locally advanced prostrate cancer: report of a randomized clinical trial," presented at Proc. Int. Congr on Radiation Oncology, Kyoto, Japan, 1993.

[277] R. Engenhart-Cabillac, J. Debus, F. J. Prott, R. Potter, K. H. Hover, N. Breteau, and A. Krull, "Use of neutron therapy in the management of locally advanced nonresectable primary or

recurrent rectal cancer," in *Fast neutrons and high-LET particles in cancer therapy*, vol. 150, R. Engenhart-Cabillic and A. Wambersie, Eds., 1 ed. Berlin-Heidelberg: Springer-Verlag, 1998, pp. 113-124.

[278] D. K. Bewley, *The Physics and Radiobiology of Fast Neutron Beams*, 1 ed. Bristol: Hilger, 1989.

[279] R. L. Maughan, W. E. Powers, and H. G. Blosser, "A superconducting cyclotron for neutron radiation therapy," *Med. Phys.*, vol. 21, pp. 779-785, 1994.

[280] P. Pihet, J. Gueulette, H. G. Menzel, R. E. Grillmaier, and A. Wambersie, "Use of microdosimetric data of clinical relevance in neutron therapy planning," *Radiation Protection Dosimetry*, vol. 23, pp. 471-474, 1988.

[281] H. G. Menzel, P. Pihet, and A. Wambersie, "Microdosimetric specification of radiation quality in neutron radiation therapy," *Int. J. Radiat. Biol.*, vol. 57, pp. 865-883, 1990.

[282] R. L. Maughan, D. G. Kruger, G. F. Blosser, E. B. Blosser, M. Yudelev, J. D. Forman, H. G. Blosser, and W. E. Powers, "A multi-rod collimator for neutron therapy," *International Journal of Radiation Oncology, Biology, and Physics*, vol. 34, pp. 411-420, 1996.

[283] H. G. Menzel and H. Schuhmacher, "The application of tissue equivalent proportional counters to problems in neutron dosimetry," presented at Proceedings 4th symposium on neutron dosimetry, Munich-Nehherberg, 1981.

[284] International Commission on Radiation Units and Measurements, *Stopping powers for protons and alpha particles (ICRU report 49)*. Bethesda, Md., U.S.A.: ICRU, 1993.

[285] R. S. Caswell and J. J. Coyne, "Microdosimetric spectra and parameters of fast neutrons," presented at Fifth symposium on microdosimetry, Verbania Palanza(Italy), 1975.

[286] R. R. Wilson, "Radiological use of fast protons," *Radiology*, vol. 47, p. 487, 1946.

[287] J. Munzenrider, E. Gragoudas, E. Seddon, J. Sisterton, P. McNulty, S. Birnbaum, K. Johnson, M. Austin-Saymour, J. Slater, M. Goitein, L. Verhey, M. Urie, D. Ruotolo, K. Egan, and F. Osuna, "Conservative treatment of uveal melanoma: probability of eye retention after proton treatment," *International Journal of Radiation Oncology, Biology, and Physics*, vol. 15, pp. 533-558, 1988.

[288] J. B. Robertson, J. M. Eaddy, J. O. Archambeau, G. B. Coutrakon, D. W. Miller, M. F. Moyers, J. V. Siebers, J. M. Slater, and J. F. Dicello, "Relative biological effectiveness and microdosimetry of a mixed energy field of protons up to 200 MeV," *Adv. Space Res.*, vol. 14, pp. 271-275, 1994.

[289] S. M. Seltzer, *An assessment of the role of charged secondaries from nonelastic nuclear interactions by proton therapy beams in water*. Gaithersberg,MD: U.S Dept of Commerce, 1993.

[290] P. J. Kliauga, R. D. Colvett, Y. L. Lam, and H. H. Rossi, "The relative effectiveness of 160 MeV protons. I. Microdosimetry," *International Journal of Radiation Oncology, Biology, and Physics*, vol. 4, pp. 1001-1008, 1978.

[291] V. P. Cosgrove, A. C. Aro, S. Green, M. C. Scott, G. C. Taylor, D. E. Bonnett, and A. Kacperek, "Studies relating to 62 MeV proton cancer therapy of the eye," *Radiation Protection Dosimetry*, vol. 44, pp. 405-409, 1990.

[292] V. P. Cosgrove, S. Delacroix, S. Green, A. Mazal, and M. C. Scott, "Microdosimetric studies on the Orsay proton synchrocyclotron at 73 and 200 MeV," *Radiation Protection Dosimetry*, vol. 70, pp. 493-496, 1997.

[293] R. Becker, J. Bienen, U. Carl, and P. Cloth, "Biophysical investigations of therapeutic proton beams," *Radiation Protection Dosimetry*, vol. 70, pp. 485-492, 1997.

[294] T. Matsuda and K. Inamura, "Computer controlled multi-leaf conformation radiotherapy," *Nippon Act. Radiol.*, vol. 41, pp. 965-974, 1981.

[295] A. Smith, M. Goitein, H. Suit, S. Durlacher, J. Flanz, K. Gall, A. Levine, S. Rosenthal, and S. Woods, "The Massachusetts General Hospital Northeast Proton Therapy Center, Boston Massachusetts," presented at Proceedings of NIRS International Seminar on the application of heavy ion accelerator to radiation therapy of cancer in connection with XXI PTCOG meeting, Chiba, Japan, 1994.

[296] J. Sisterton, J. B. Flanz, and J. E. Burns, "A new proton irradiation facility at the Northeastern Proton Therapy Center,", vol. In press, 1999.

[297] M. K. Oldfield and C. I. Underwood, "PRISM- a tool for modeling proton energy deposition in semi-conductor materials," *IEEE Trans. Nucl. Sci.*, vol. 43, pp. 2715 -2723, 1996.

[298] P. J. McNulty and G. E. Farrell, "Proton induced nuclear reactions in silicon," *IEEE Trans. Nucl. Sci.*, vol. 28, p. 4007, 1981.

[299] J. P. Biersack and L. G. Haggmark, "A Monte Carlo computer program for the transport of energetic ions in amorphous targets," *Nuc. Inst. Meth. Phys. Res.*, vol. 174, pp. 257-269, 1980.

[300] E. Petersen, "Nuclear reactions in semiconductors," *IEEE Trans. Nucl. Sci.*, vol. 27, p. 1494, 1980.

[301] C. Kenney, S. Parker, J. Segal, and C. Storment, "Silicon Detectors with 3-D Electrode Arrays: Fabrication and Initial Test Results," *IEEE Trans. Nucl. Sci.*, vol. 46, p. 1224, 1999.

[302] C. P. Allier, R. W. Hollander, P. M. Sarro, and C. W. E. v. Ejik, "Thin photodiodes for a scintillator-silicon well detector," *IEEE Trans. Nucl. Sci.*, vol. 46, pp. 1948-1956, 1999.

Appendices

Appendix A: Prototype Fujitsu Silicon Microdosimeter, Packaging and Processing

A.1. Device Packaging

- The IC is packaged in a 28 pin DIL package.
- 4 diode arrays are on each IC. The arrays and pin-outs are summarised below
- The devices are fabricated on 4 different wafers SOI (2μm,5μm 10μm)+ bulk
- Substrate is p-type($1.5x10^{15}cm^{-3}$)

Array	Diode Size	Array size	Pin(p side)	Pin(n+ side)	Comments
1	100x100um	30x50=150 diodes	1	4	Note 1
2	100x100um	10x5=50	2	3	
3	10x10um	120x120=14400	25	28	Faulty all devices
4	10x10um	40x120=4800	26	27	Note 1

NOTE 1: To *reverse bias* diode connect +Vdd to Pin(n+ side) and earth to Pin(p side)

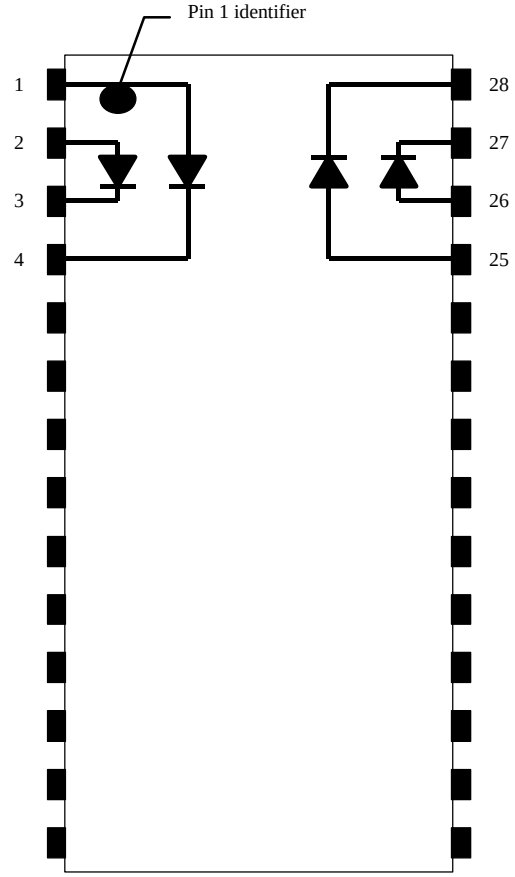


Figure A.1. Package pin-out diagram

A.2. Device Processing

The following pages contain mask details at various scales. The processing steps are summarized in the table below and the mask details are provided in the following figures.

Table A.1. Processing steps for microdosimeter device construction

	Step	Pre-process	Parameters	Post-process	Comments
1.	Crystallization	Czochralski Crystal growth	SOI wafer bonding		SOI formed by bonding wafers in oven with 0_2
2.	Pad Oxidize		50A, 800°C, dry 0_2		To reduce thermal expansion stress during oxidation
3.	SiN CVD		1150 A		
4.	<FL>	HMDS	Oxide Mask Photoresist		
5.	FL etch		SiN (1150A), TEL580	RS	
6.	Field Oxidation		3500A, 900°C, Wet 0_2		
7.	SiN Washout			RS	
8.	Thin Oxide		50A, 800°C, Wet 0_2		
9.	<FN>	HMDS	n+ Mask Photoresist		
10.	Ion Implant n+		As+, 30keV, 5E15 /cm^2	RS	
11.	<FP>	HMDS	P+ Mask Photoresist		
12.	Ion Implant p+		B+, 30keV, 5E15 /cm^2	RS	
13.	LTO CVD		4000A		
14.	Anneal		1000°C, 10s, RTA		Removes ion-induced lattice damage
15.	<NA>	HMDS	Mask Photoresist		
16.	SiO_2 Wet Etch			RS	
17.	Ti/TiN Sputtering		Ti(200A)/TiN(1000A)		Radio Frequency sputtering
18.	Barrier Anneal		450°C, 30min, N_2		
19.	Al Sputtering		6000A		
20.	<LA>	HMDS	Mask Photoresist		
21.	AL RIE				
22.	Sinter		450°C, 30min, N_2/H_2		
23.	LTO CVD		2000A		
24.	<C>	HMDS	Mask Photoresist		
25.	SiO_2 RIE			RS	
26.	Back Process		Process back side		Includes 2000A Au deposit

Acronyms:
SOI = Silicon On Insulator
CVD = Chemical Vapor Deposition
LPCVD = Low Pressure CVD
HMDS = Hexamethyldisilizene (primer for photoresist)
RS = Resist Strip
LTOCVD = Low Temperature Oxide CVD
RTA = Rapid Thermal Anneal
RIE = Reactive Ion Etching

Mask codes:
<FL> = Field oxide mask
<FN> = n+ ion-implant mask
<FP> = p+ ion-implant mask
<NA> = Ohmic contact mask
<LA> = Aluminium metal mask
<C> = Pad Contact mask

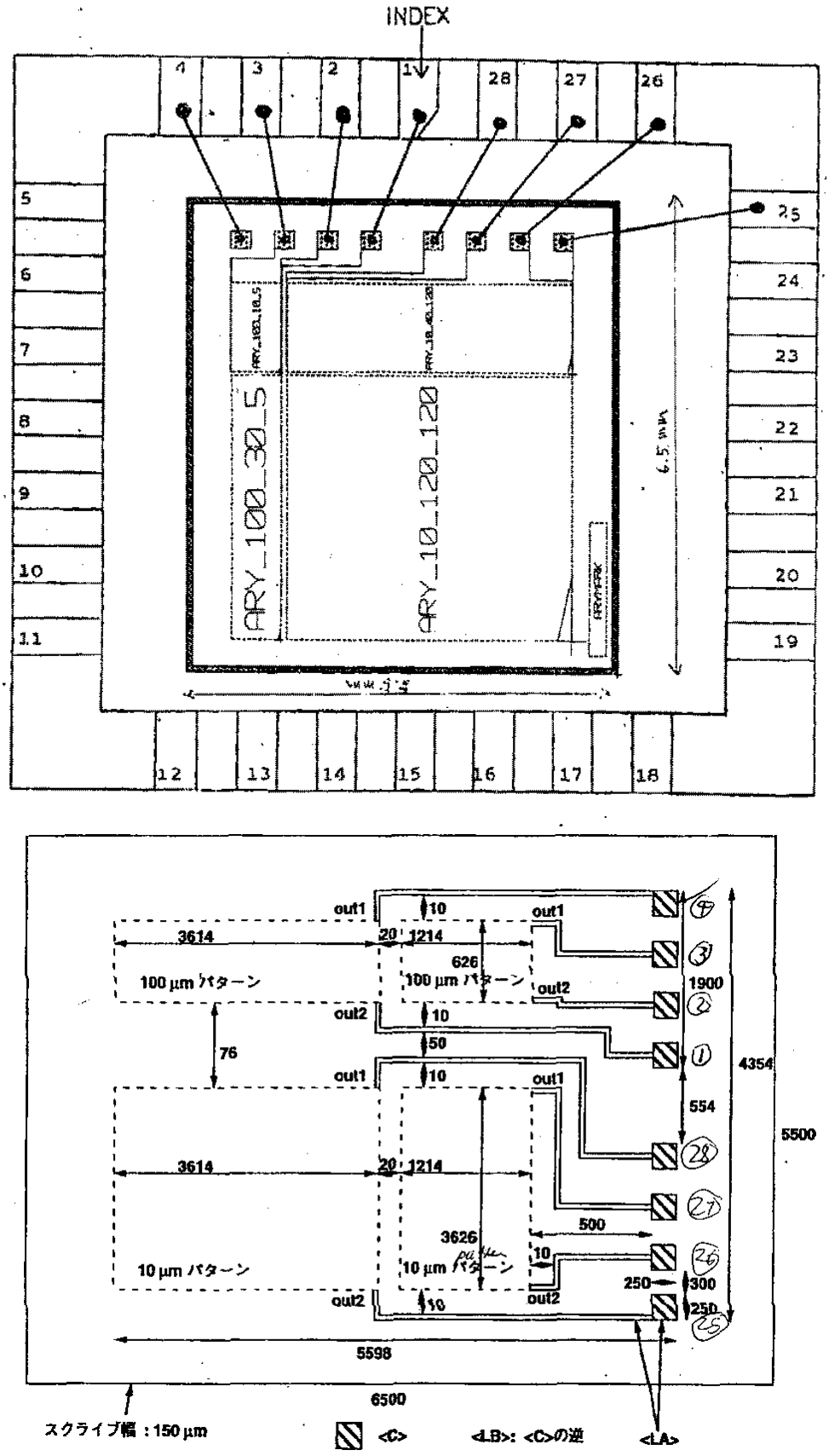


Figure A.2. Layout of arrays and silicon die.

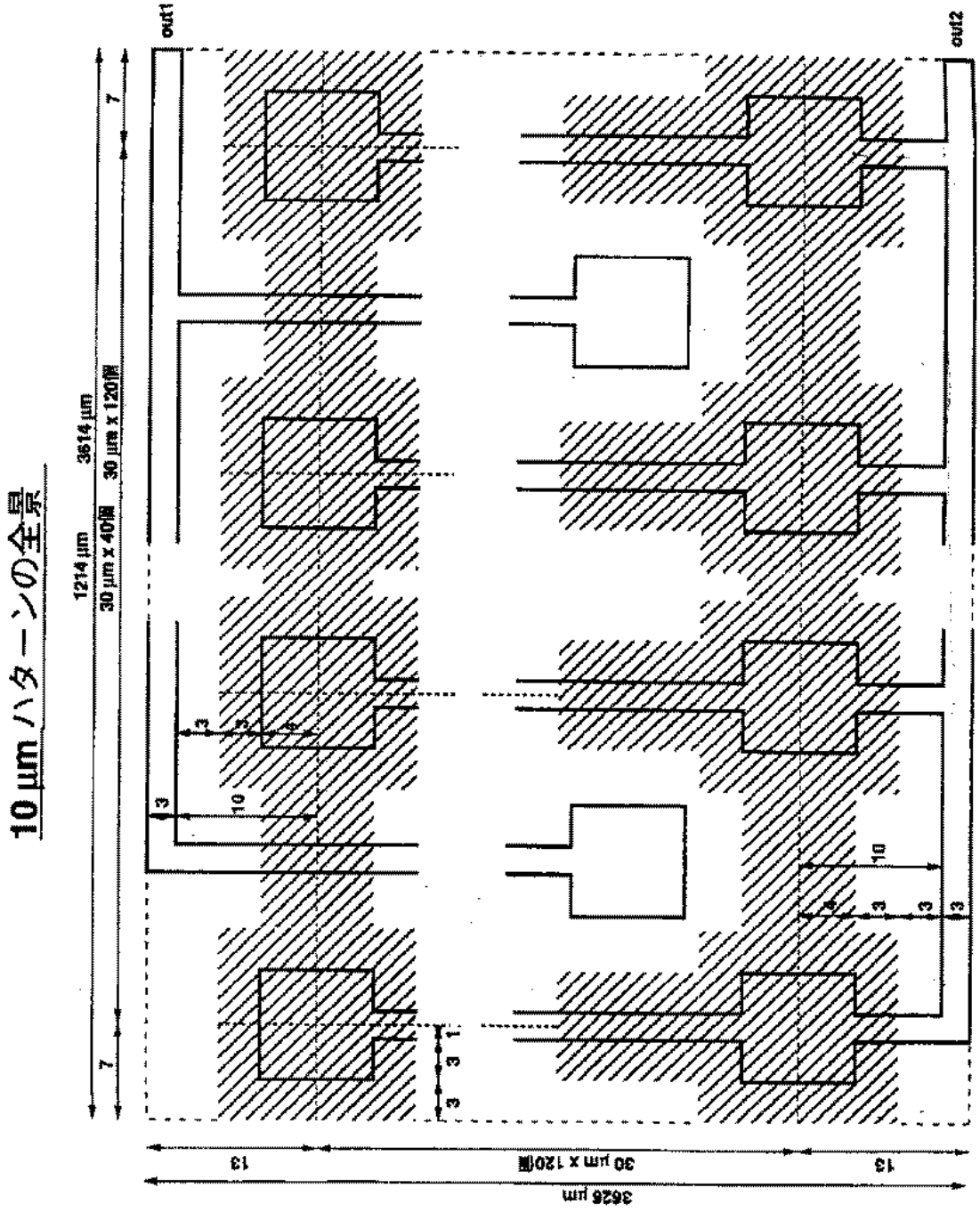


Figure A.3. Large scale layout of 10×10 μm^2 junction arrays

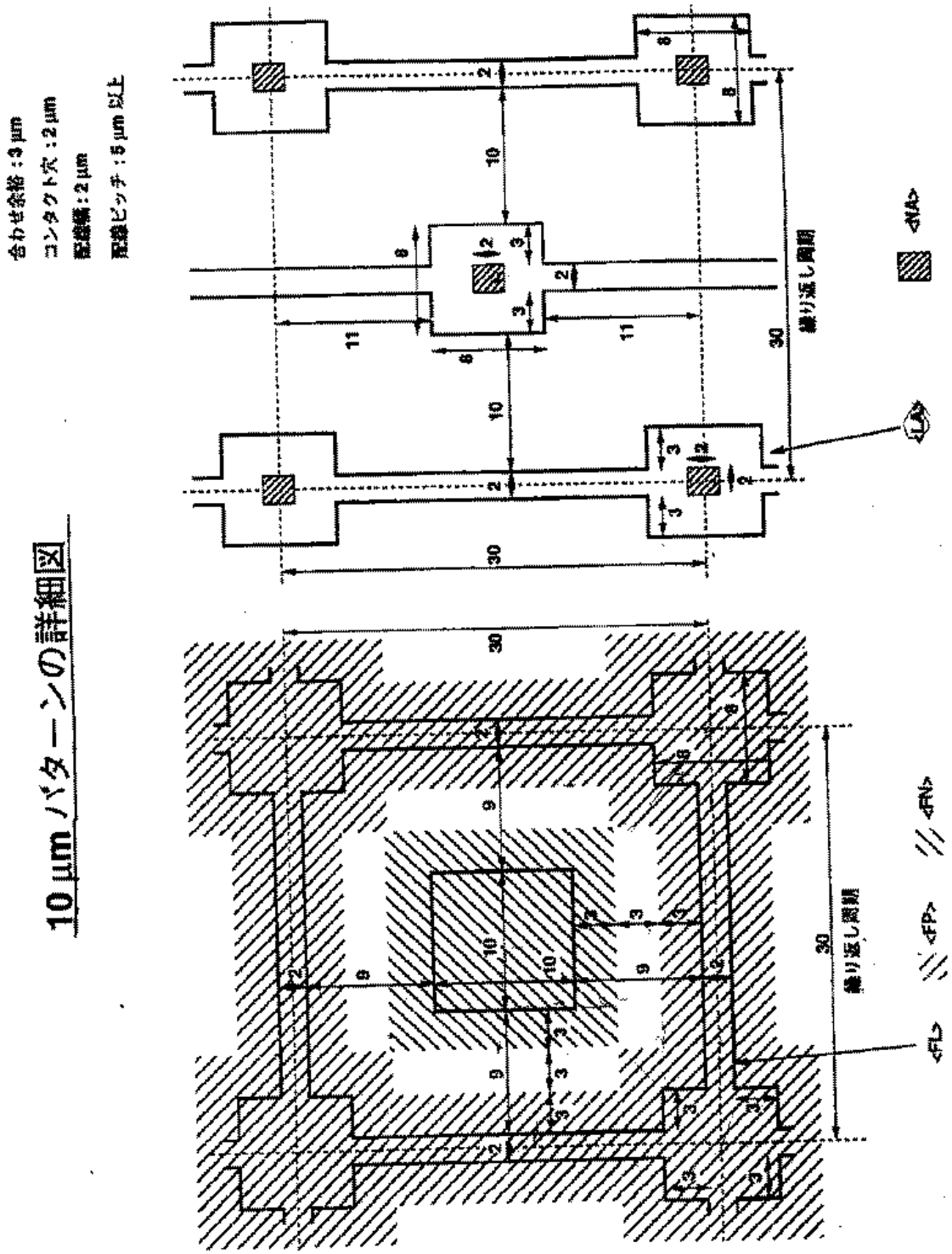


Figure A.4. Small scale layout of 10×10 μm^2 individual cell

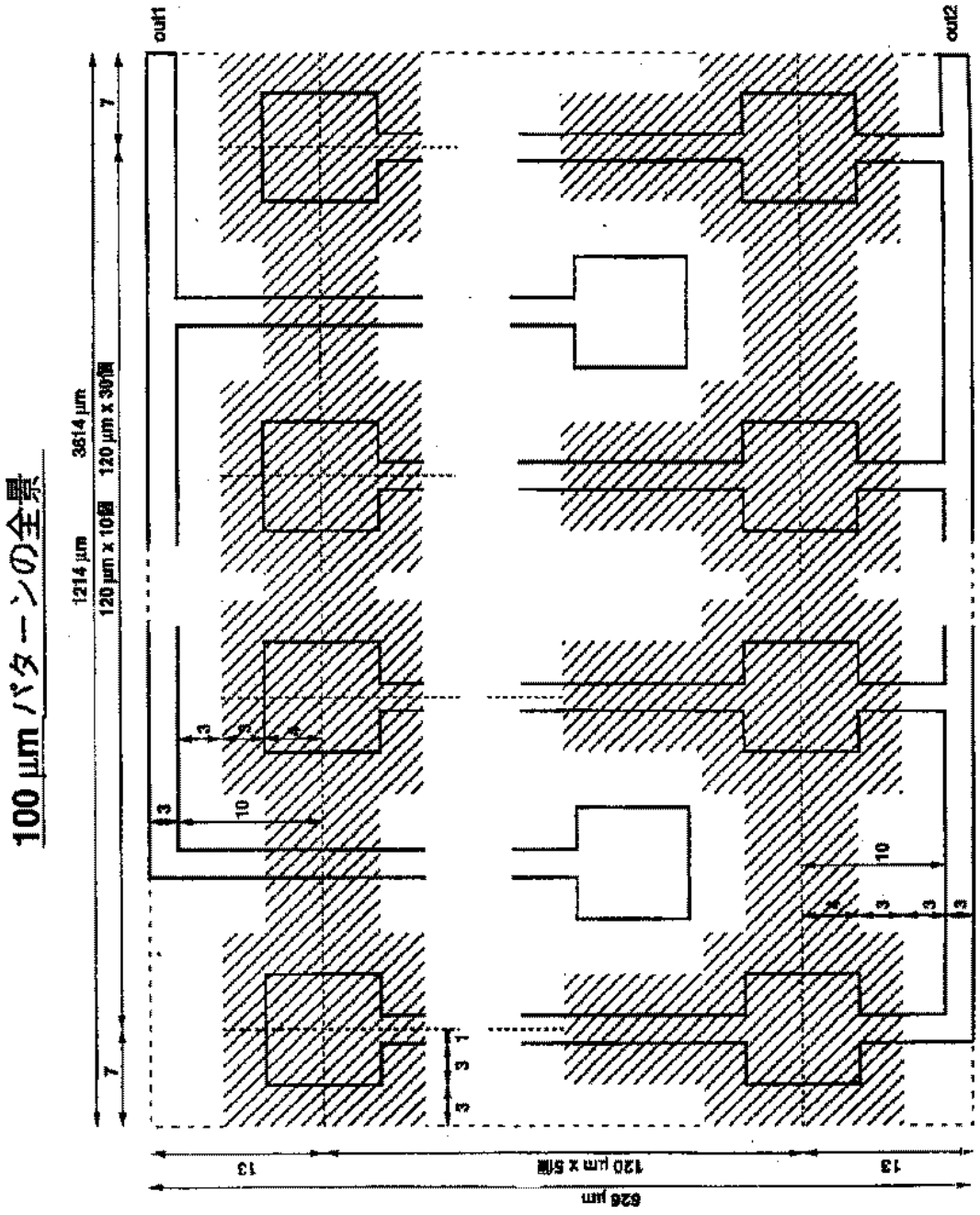


Figure A.5. Large scale layout of 100×100 μm^2 junction arrays

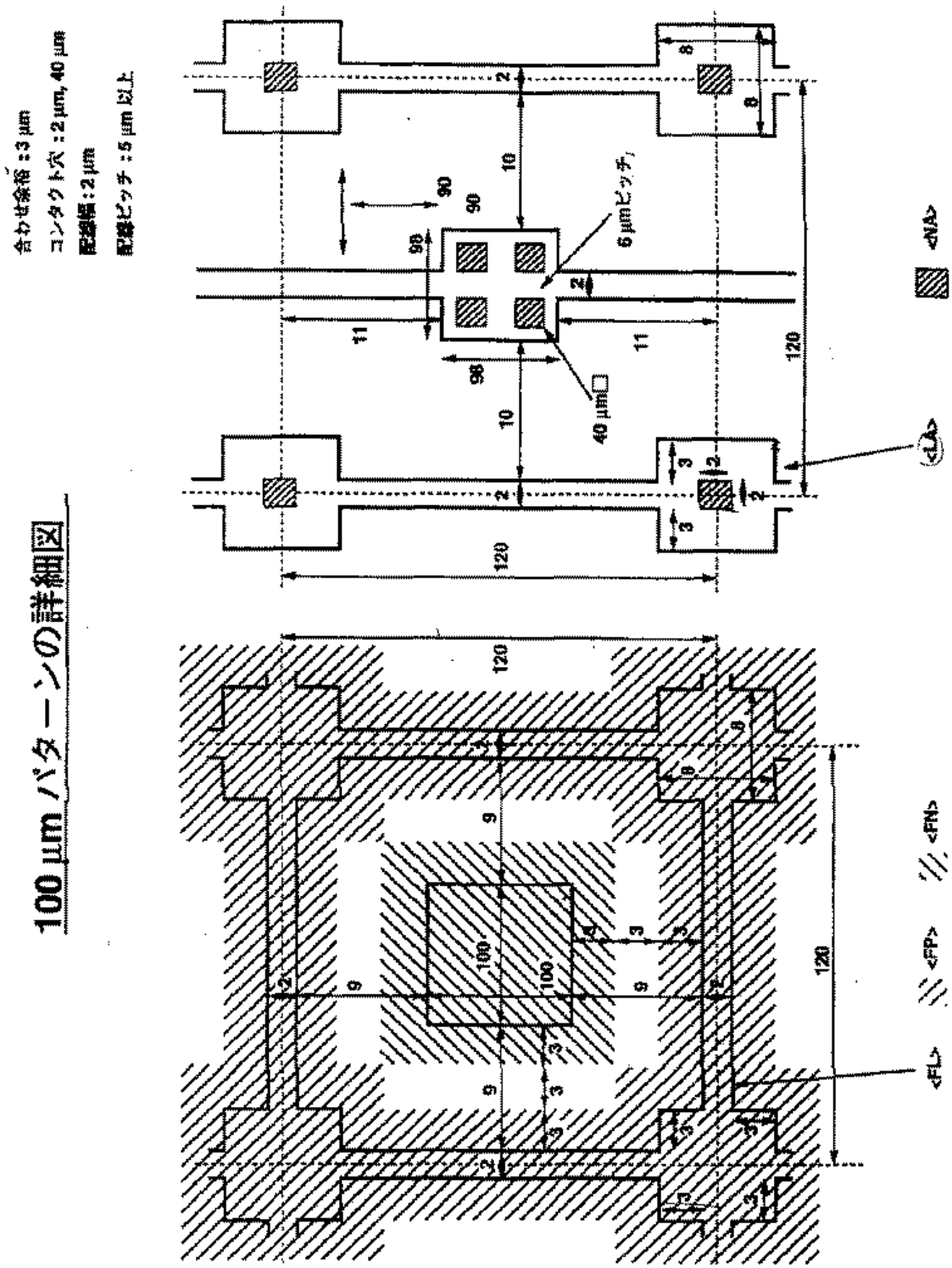


Figure A.6. Small scale layout of 100×100 μm^2 individual cell

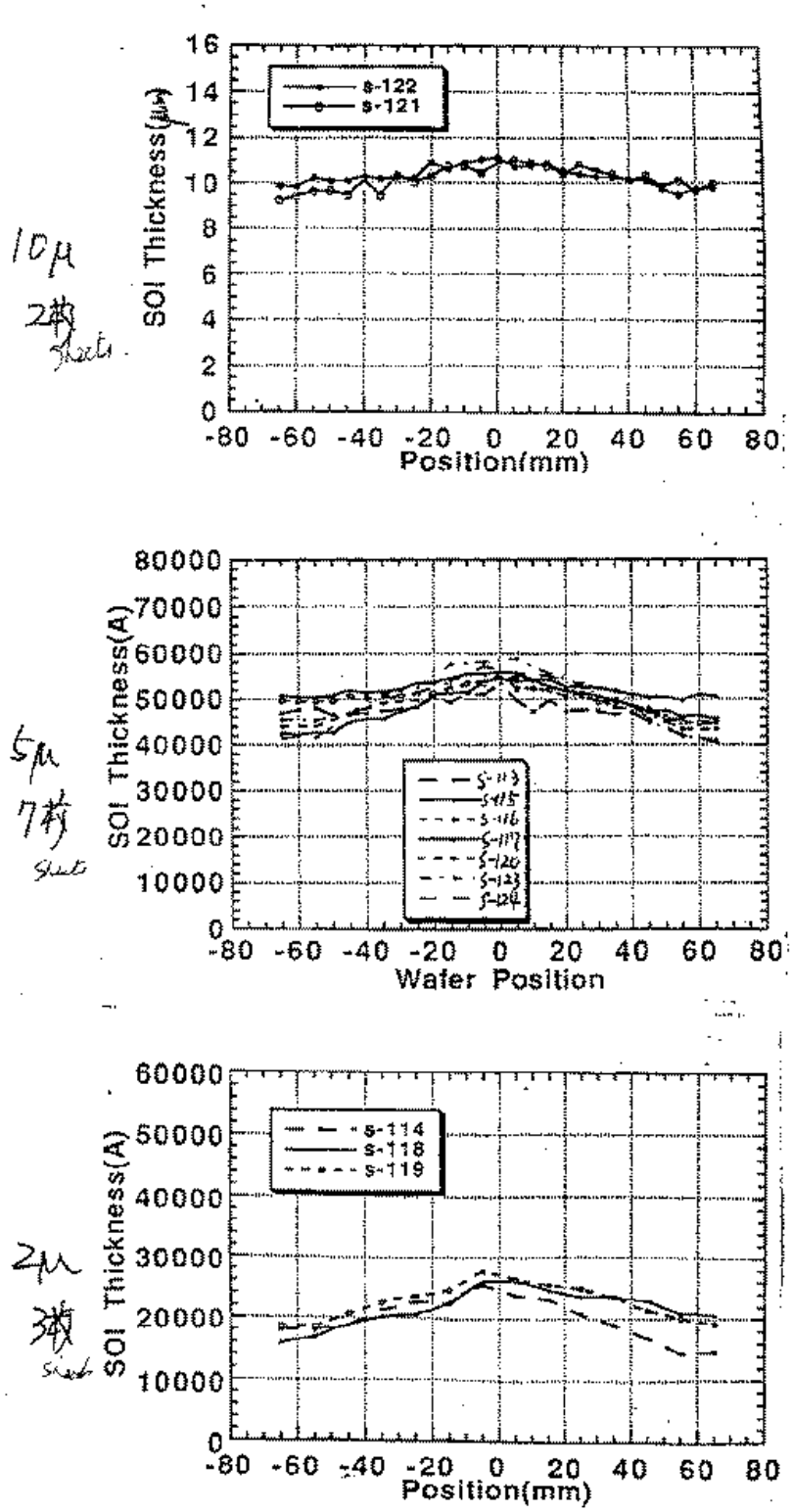


Figure A.7. Thickness of SOI substrates measured by Fujitsu as a function of wafer position and processed wafer

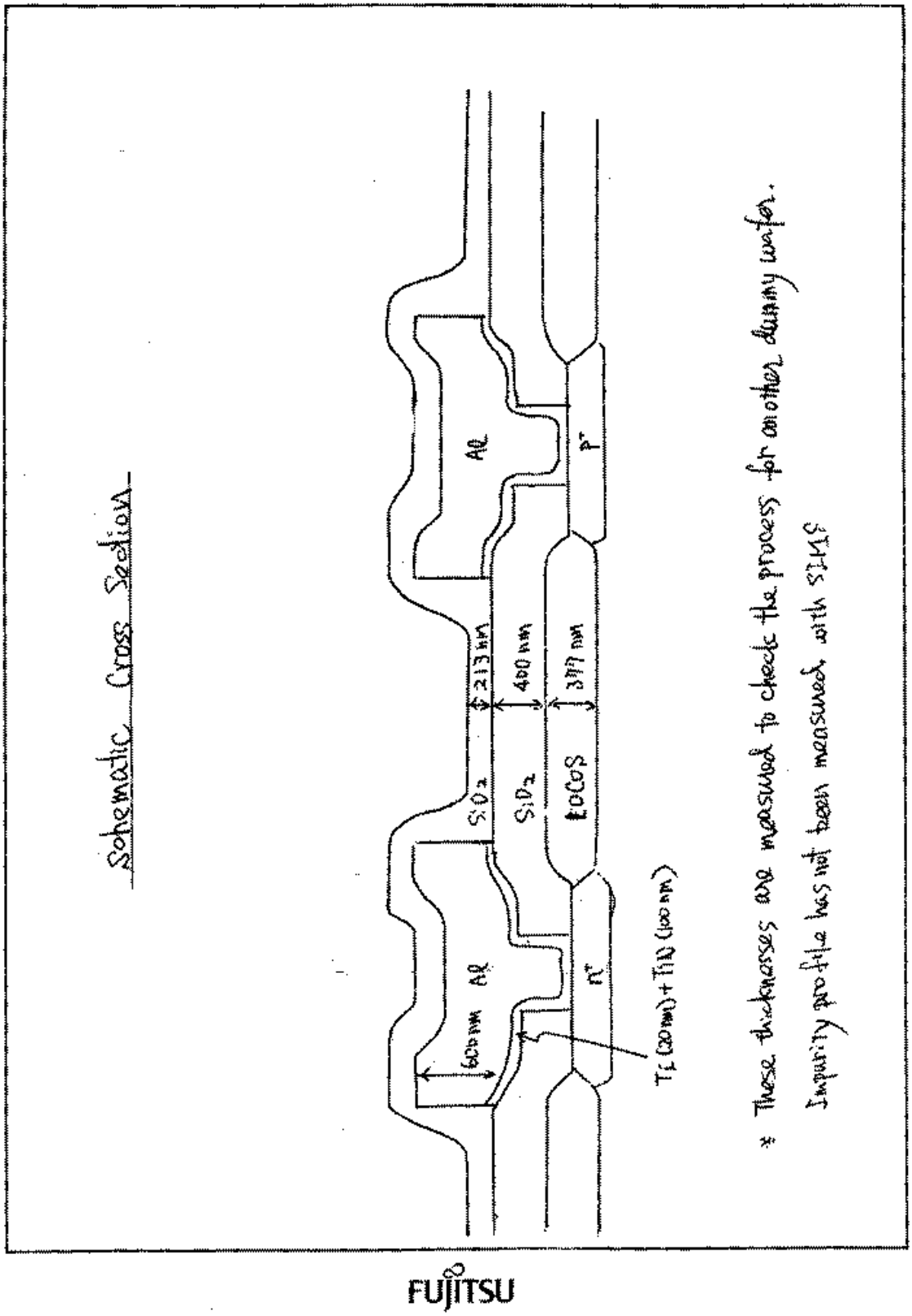


Figure A.8. Basic device cross-section as supplied by Fujitsu.

Appendix B:
Mathematica Notebook - Analytical and Monte-Carlo Calculations of Chord and Segment Length Distributions in Various Shapes

This is an outline of the Mathematica [141] based notebook constructed to analyse and compare the SLD and CLD of various shapes. The entire notebook contents are too lengthy to present. The file (and other useful microdosimetric material) along with this thesis document will be available at the Radiation Physics Group (University of Wollongong) web site:

URL: http://www.uow.edu.au/eng/phys/rpg/rpghome.htm

1 Introduction
2 Chord Length Distributions under u-randomness
- 2.1 CLD for Sphere
- 2.2 CLD for Hemisphere
- 2.3 CLD for Spheroid
- 2.4 CLD for Cylinder
- 2.5 CLD for Infinite slab
- 2.6 CLD for Cube
- 2.7 CLD for Rectangular parallelepiped (RPP)
- 2.8 Plot Chord Length Distributions
- 2.9 Plot CLD for 2 um SOI device and 10 um SOI device compared with a 2 um diameter proportional counter
- 2.10 Plot distributions for literature review
- 2.11 Calculate Relative Variance

3 Segment length distributions (u-randomness with finite range)
- 3.1 SLD for Sphere
- 3.2 SLD for Cube
- 3.3 SLD for Rectangular parallelepiped (RPP)
- 3.4 SLD for Infinite Slab with overlayer and converter

4 Comparison of Dose Average Lineal Energy (yd)
- 4.1 Section Introduction
- 4.2 yd and geometric reduction factor for a sphere
- 4.3 yd and geometric reduction factor for a cylinder
- 4.4 yd and geometric reduction factor for a RPP and cube
- 4.5 yd calculation for infinite slab with overlayer and converter
- 4.6 yd calculation for RPP (cube in particular) with overlayer and converter

5 Comparison of spectrum including straggling
- 5.1 Chord length distributions under u-randomness with straggling
- 5.2 Segment length distributions under u-randomness(finite range) with straggling
- 5.3 Segment length distributions under c-randomness with straggling

6 Monte-Carlo Simulation of segment length distribution for RPPs (Analysis of Converter/Overlayer/RPP sensitive volume geometry)
- 6.1 3D display of simulation geometry set-up
- 6.2 CLD Monte Carlo simulation using Link to C routine
- 6.3 Basic Software Verification Tests
- 6.4 Calculate $\overline{y}_d$ and spectra for converter/overlayer/sensitive volume(50x50x2)

Appendix C:
Low Noise Microdosimeter Probe Design (Prototype #2)

